Searching for new physics with tau leptons and silicon tracker upgrades in the ATLAS detector

by

Theodore Georgio Zorbas

A thesis submitted for the degree of

Doctor of Philosophy

in Physics

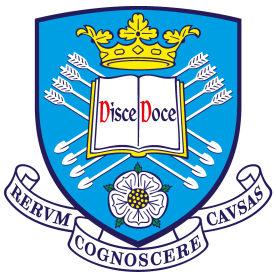

The University Of Sheffield.

Department of Physics and Astronomy

The University of Sheffield

Supervisor: **Dr. Trevor Vickey**

December 2020

Abstract

This thesis discusses an analysis searching for new physics beyond the Standard Model, particularly for heavy neutral resonances such as additional H/A Higgs bosons proposed by the Minimal Supersymmetric Standard Model, as well as heavy Z' bosons. The search is conducted through the di-tau lepton final state, with focus in this thesis on the leptonic-hadronic decay channel. The analysed data was collected by the ATLAS detector, recording $139\,\text{fb}^{-1}$ integrated luminosity of proton-proton collisions within the Large Hadron Collider at 13 TeV during its Run-2. The analysis also incorporates the latest Athena Release 21 software for event reconstruction, delivering significant improvements to tau lepton identification and electron rejection algorithms which are also studied in this thesis. The result of the analysis finds no significant excess beyond the Standard Model, but sets record exclusion limits on the proposed models, in the mass range of 0.2 to 2.5 TeV, extending the result by 4 to 5 times that of previous analyses. The outlook to the ATLAS Phase-2 upgrade is also discussed, through the installation of a new all-silicon Inner Tracker. Prototype barrel strip detector modules are assembled and tested throughout this research programme, with focus on developing improvements to the construction tooling and procedures, whilst transitioning to the testing of fully electrical components.

Declarations

The author of this thesis, myself, *Theodore Georgio Zorbas*, will be commonly referred to in the third person throughout the text as "the author". This thesis is submitted to *The University of Sheffield* for awarding the degree of *Doctor of Philosophy in Physics* (PhD) to the author, with supervision by *Dr. Trevor Vickey*.

The writing of and the work presented in this thesis is that of the author's own development, between August 2016 and July 2020. Any similarities in the writing to other texts are purely coincidental. While many of the projects which will be discussed throughout this thesis are collaborative efforts, often continuing on from existing work by others, the text will attempt to highlight the areas where the author had specifically contributed to the advancement of these projects. This includes denoting which of the presented results were created by the author, or are otherwise referenced from another source.

The author will have also earned authorship credit on publications submitted by the *ATLAS collaboration* since 2017. This was granted through the completion of a *qualification task* (QT) in the first year of the PhD, forming part of the work presented in this thesis from Sections 4.3 and 4.3.2. This authorship was sustained through continued contributions to the collaboration, awarded via *Operation Task Planner* (OTP) points, particularly for the work discussed in Sections 2.3.5, 3.4 and 6.

Regarding units of energy (eV), momentum (eV/c) and mass (eV/c^2), this thesis will often assume *natural units*, where the speed of light, c, is set equal to 1, such that all of these quantities are given in units of eV.

Acknowledgements

The author would like to thank *The University of Sheffield* (TUoS) for the opportunity and resources in achieving this degree. This includes the members of the *Department of Physics and Astronomy*, the *High Energy Physics* (HEP)/*Particle Physics and Particle Astrophysics* (PPPA) groups, and all of colleagues whom the author had worked alongside from the *Sheffield ATLAS* (ShATLAS) group.

A special thanks to *Dr. Trevor Vickey* who greatly supervised the author's work that went into forming this thesis.

The author would also like to thank CERN and the ATLAS collaboration for providing the usage of their experiment and resources. In particular, the author would like to thank the colleagues from ATLAS whom they had worked closely with over the years, especially from the Tau CP group, the xTauFramework developers, the BSM di-tau analysis team and the ITk community.

Thanks from the author to the *UK Research and Innovation* (UKRI)/*Science and Technology Facilities Council* (STFC) for their funding which enabled for this work to progress.

Lastly, but not least, the author would like to thank their family and friends for their continued support over these challenging years.

Contents

Chapter 1: Theory

This section will briefly introduce a general overview of the underlying models used in modern particle physics, and highlight some of their remaining problems, while offering a few popular solutions towards them. These solutions are to be probed by the analysis as the main feature of this thesis, on which the author primarily contributes towards, later in Chapter 5.

1.1 The Standard Model of particle physics

The Standard Model (SM) of particle physics is a theory that describes all currently observed fundamental particles and the types of forces that act between them. The SM unifies quantum field theories, which describe the fundamental particles and interactions, with gauge invariance that preserves local symmetries in the model [1]. These symmetries can be described as the product of (special) unitary groups given by Equation 1.1.1, where each group relates to the strong, the weak and the electromagnetic forces, respectively [2].

$$SU(3)_C \otimes SU(2)_L \otimes U(1)_Y \tag{1.1.1}$$

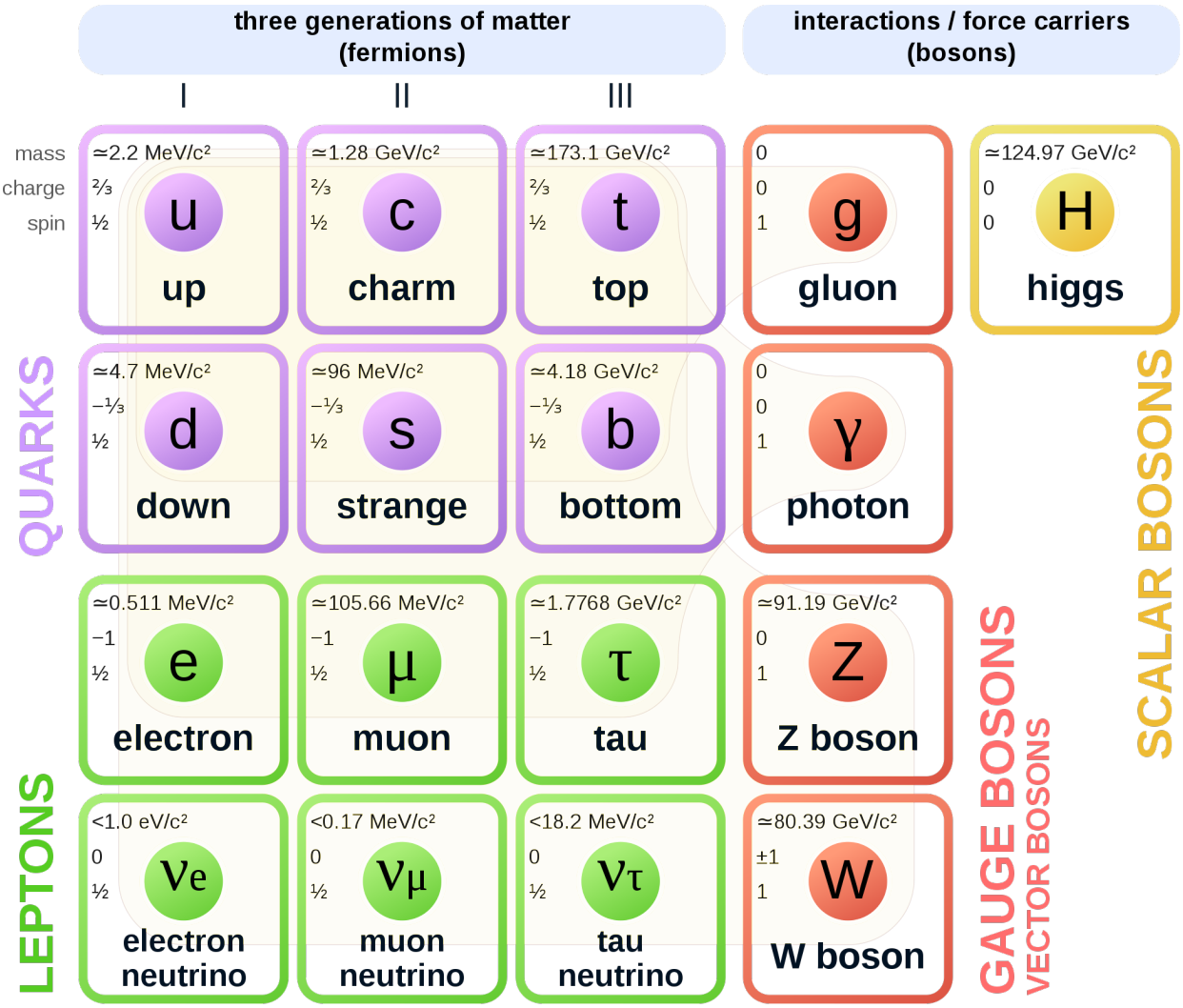

Figure 1.1.1: Elementary particles and some of their observed properties in the Standard Model [3].

The SM also includes the Higgs mechanism, which introduces spontaneous symmetry breaking at energies of the electroweak scale, approximately on the order of 100 GeV. This refers to the combination of the electromagnetic and weak forces, where the photon, Z and $W^{\pm}$ bosons join states to become the B and $W_3^{0,\pm}$ bosons, propagators of the electroweak force. This mechanism also generates a Higgs field which gives the property of mass to particles that interact with it, especially for the notably heavier weak bosons, and can be described by an $SU(2)$ doublet state, consisting of a neutral and a charged scalar field, each in order to model the electromagnetic charges of the Z and $W^{\pm}$ bosons, respectively [1]. This field is governed by the scalar Higgs boson which was first discovered in 2012 [4][5], thus completing the expected inventory of elementary SM particles. The SM is able to explain many experimental observations in particle physics up to the energies of the electroweak scale. All known elementary particles with some of their experimentally observed properties are shown in Figure 1.1.1.

1.2 Problems and limitations of the Standard Model

While the SM has successfully explained much of physics up to the electroweak scale, a significant number of questions still remain, especially those at even higher energies. It seems that these questions can't be explained with the current SM and observed fundamental particles. This section will introduce some of the most major and pressing failures of the SM, followed by how they could be resolved, especially in relation to the work derived from this thesis.

One of such mysteries is named the *Hierarchy problem*, which questions why the Higgs boson mass is as small as it is was discovered to be ($\sim$125 GeV). It is expected that virtual quantum loop corrections, an example of such shown in Figure 1.2.1 below, should inflate the Higgs mass up to the Planck scale ($\mathcal{O}(10^{19}$ GeV)). Instead it appears that there is an unnatural fine-tuning of parameters in the SM that is constraining the mass around the electroweak scale, which is not a satisfying solution to the theory, but possible nonetheless [1].

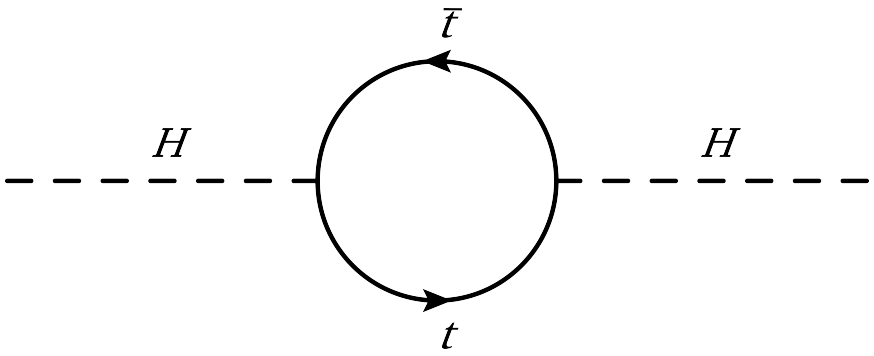

Figure 1.2.1: Feynman diagram of a virtual quantum loop via a top-antitop quark pair, coupled to the Higgs boson, based on Reference [6].

Another question is raised by astronomical observations, suggesting that ∼85 % of the matter in the Universe consists of an invisible fundamental substance not known to the SM — it has been given the name *dark matter*, to allude its mysterious composition [7]. Observations commonly suggest that these particles are weakly-interacting, if at all, with all of the forces known to the SM, with the exception of gravity (also not explained by the SM), and greatly heavy in mass, thus earning the name *Weakly-Interacting Massive Particles* (WIMPs) [1].

While it is assumed in the SM that neutrinos should be completely massless, experimental observations have in fact shown that they possess a non-zero sub-eV-scale mass [1]. This failure of the SM also does not predict their behaviour in oscillating between their flavour eigenstates as they travel over some distance. These observations also begin to raise questions as to whether the neutrino is in fact its own antiparticle, referred to as a *Majorana particle* [1].

It is expected that the Standard Model is merely a low energy approximation of a *Grand Unified Theory* (GUT). Having seen that the electromagnetic and weak interactions can combine into the electroweak on the $\mathcal{O}(100\,\text{GeV})$, a similar combination is also expected with the strong interaction by introducing an additional gauge symmetry group of size at least $SU(5)$. Such phenomenon would be expected to occur on the $\mathcal{O}(10^{15}\,\text{GeV})$ or higher [1].

1.3 Solutions beyond the Standard Model

From these failures of the SM, it is already clear that there are needs for corrections in order to explain these observed phenomena. In the arguments to be discussed throughout the following sections, it is proposed that some of these limitations can be resolved through the inclusion of new physics beyond the Standard Model (BSM). In the context of this thesis, only a few of many theories will be discussed as possible extensions to the SM, and how they are tested for in the analysis discussed in Chapter 5.

1.3.1 Supersymmetry and the Two-Higgs-Doublet Model

One of the more popular extensions to the SM, *Supersymmetry* (SUSY) introduces a whole new set of particles known as *superpartners* which shadow their counterparts in the SM, analogous to antimatter. In general, *sparticles*, as they are also known, differ in spin to their SM-equivalent by a half-integer, such that fermions become bosons and vice versa. Through interactions, R-parity conservation is derived as an alternative to baryon and lepton number conservation, such that SM particles have an R-parity value of $+1$ and sparticles with -1. In SUSY models, a level of symmetry breaking occurs such that the couplings and masses of sparticles also differ and are generally significantly heavier than the electroweak scale [6].

SUSY provides an alternative and satisfyingly natural answer to the Hierarchy problem. For every virtual quantum loop in the SM coupling to the Higgs, as previously demonstrated in Figure 1.2.1, there will be a sparticle-equivalent with an inverse contribution, as shown in Figure 1.3.1, such that upon summation will cancel each other out, thus renormalising the Higgs mass to the electroweak scale [6].

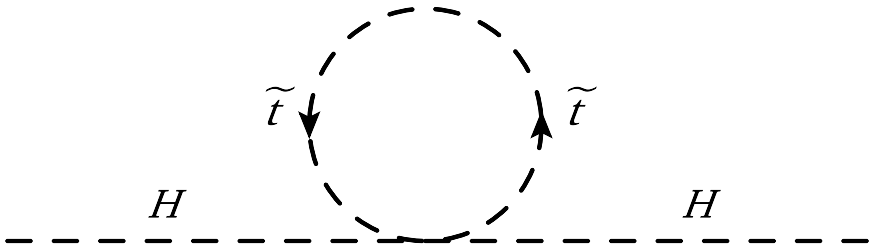

Figure 1.3.1: Feynman diagram of a virtual quantum loop via a supersymmetric stop-antistop squark pair, coupled to the Higgs boson, based on Reference [6].

A popular theoretical scenario of SUSY is the *Minimal Supersymmetric Standard Model* (MSSM), since it has one of the fewest number of additional tuneable parameters (∼100) [6][8]. The particles that are introduced by the MSSM are given in Table 1.3.1, reflecting very similarly the SM beyond the electroweak scale. The gauginos and scalinos (the SUSY counterparts to the gauge and scalar bosons) can form mixed eigenstates, which are then seen as new elementary particles, namely four neutralinos ($\widetilde{\chi}^0_{1,2,3,4}$) and two charginos ($\widetilde{\chi}^\pm_{1,2}$). It is a common hypothesis that the lightest of these neutralinos ($\widetilde{\chi}^0_1$) cannot decay without violating R-parity conservation, so must be stable, and therefore a candidate WIMP-like particle for the dark matter mystery [7].

<table>
<tr><th colspan="5">Bosons</th><th colspan="4">Fermions</th></tr>
<tr><td rowspan="2">Squarks</td><td>$\widetilde{u}$
sup</td><td>$\widetilde{c}$
scharm</td><td>$\widetilde{t}$
stop</td><td rowspan="2"></td><td rowspan="3">Gauginos</td><td>$\widetilde{g}$
gluino</td><td rowspan="3">Scalinos</td><td rowspan="2">$\widetilde{H}^{0,+}_u$
$\widetilde{H}^{0,-}_d$
Higgsino</td></tr>
<tr><td>$\widetilde{d}$
sdown</td><td>$\widetilde{s}$
sstrange</td><td>$\widetilde{b}$
sbottom</td><td>$\widetilde{B}$
Bino</td></tr>
<tr><td rowspan="2">Sleptons</td><td>$\widetilde{e}$
selectron</td><td>$\widetilde{\mu}$
smuon</td><td>$\widetilde{\tau}$
stau</td><td rowspan="2"></td><td>$\widetilde{W}^{0,\pm}_3$
Wino</td><td rowspan="2"></td></tr>
<tr><td>$\widetilde{\nu}_e$
selectron
sneutrino</td><td>$\widetilde{\nu}_\mu$
smuon
sneutrino</td><td>$\widetilde{\nu}_\tau$
stau
sneutrino</td><td colspan="2">$\widetilde{\chi}^0_{1,2,3,4}$
neutralino</td><td colspan="2">$\widetilde{\chi}^\pm_{1,2}$
chargino</td></tr>
</table>

Table 1.3.1: The additional elementary particles in the Minimal Supersymmetric Standard Model [6].

The MSSM can be described by a Type-II *Two-Higgs-Doublet Model* (2HDM) [9], where two Higgsino doublet fields are required in the theory to break electroweak symmetry, as opposed to one in the SM [10]. In a Type-II 2HDM, each gauge eigenstate doublet, H_u and H_d, couple to isospin up- and down-type fermions, respectively. Given the symmetric nature of SUSY, this implies that there must also be additional non-SUSY Higgs bosons with R-parity of +1. Upon electroweak symmetry breaking, these doublet states materialise into *five* physical Higgs bosons, as represented in Figure 1.3.2.

Figure 1.3.2: Comical representations of the five fundamental Higgs bosons posited by the 2HDM [11].

Two important parameters in the 2HDM are $\tan\beta$, defined as the ratio of the vacuum expectation values between the two Higgs doublets (H_u/H_d), and m_A, the mass of the CP-odd A boson [9]. The experimental results in this thesis will place limits on the values of these parameters in order to constrain the theory, as will be demonstrated in Chapter 5.

The 2HDM can be interpreted in different benchmark scenarios of the MSSM, such as hMSSM, $m_h^{\text{mod+}}$ [12] and various models of M_h^{125} [13]. These models are chosen for study on recommendation by the LHC Higgs Cross-Section Working Group [14]. In the case of the hMSSM, the mass of the lightest CP-even h boson is set to the experimentally-measured value of the SM Higgs boson, while in the $m_h^{\text{mod+}}$ scenario, the stop squark mixing paramater X_t is tuned such that the h boson mass is similar to the SM Higgs boson measurement [12]. For the analysis in Chapter 5, it is expected for the $m_h^{\text{mod+}}$ scenario to possess a reduced branching ratio to tau leptons and therefore weaker ability to constrain, compared to the hMSSM, due to the inclusion of low-mass neutralinos into the model [15].

The base M_h^{125} benchmark model is similar to the hMSSM [13], but instead it is assumed that there are very weak non-zero couplings between the heavy neutral H/A bosons and the MSSM sparticles. Further modifications to this scenario include the $M_h^{125}(\widetilde{\chi})$, where of those sparticles, the H/A bosons strongly couple exclusively with neutralinos, or similarly the $M_h^{125}(\widetilde{\tau})$, where instead the coupling is only strong with staus. Lastly, the M_h^{125}(align) model assumes that the H/A boson couplings are aligned with those of the SM Higgs boson.

Additional M_h^{125} benchmarks have also been proposed by theorists [13], but are not probed by the analysis on recommendation in Chapter 5. It should also be noted that while the MSSM can incorporate the 2HDM, it is still generally possible for a 2HDM to exist independently of SUSY [9]. For example, it has been suggested by certain neutrino theories that incorporating a 2HDM could also attempt to explain neutrino oscillations and whether they are Majorana particles [16].

The decay channels of the heavy neutral H/A bosons behave differently for certain ranges of $\tan\beta$. At high $\tan\beta$ ($\gtrsim$10), the heavy neutral Higgs' couple more strongly to down-type fermions, relative to that of the SM Higgs, nearly exclusively decaying to either a bottom-antibottom quark pair ($b\bar{b}$) with $\sim$90 % probability or tau-antitau lepton pair ($\tau^-\tau^+$) with $\sim$10 % probability [10]. At low $\tan\beta$, the H/A bosons couple strongly to up-type fermions, nearly exclusively decaying into a top-antitop quark pair ($t\bar{t}$), assuming that the H/A mass is more than double the top quark mass. There is also a small chance that the H may decay into di-boson pairs, such as $W^+W^-/ZZ/hh$, while A would decay into hZ. These probabilities are enhanced to a few percent (comparable to the SM Higgs decay into ZZ) at low $\tan\beta$ and for lower masses of H/A ($<$500 GeV). In the context of this thesis, these additional Higgs bosons are searched for in Chapter 5, with focus primarily on the heavy neutral H/A bosons decaying into a pair of tau leptons.

1.3.2 Additional heavy weak bosons

The extension onto the Standard Model to include weak Z' and $W'^{\pm}$ bosons arises in a vast array of BSM theories which include an additional $SU(2)$ gauge group [17]. These additional heavy weak bosons are often required by theories attempting to form a GUT based on groups larger than $SU(5)$. However the masses of the Z' and $W'^{\pm}$ bosons are not well constrained by theories, allowing it to be anywhere between the electroweak and the GUT scales [18].

In the context of this thesis, only the neutral Z' boson decaying into a pair of tau leptons is searched for in Chapter 5. The results from this search are analysed in two benchmark scenarios, chosen from internal recommendation by the ATLAS Exotics Working Group: the *Sequential Standard Model* (SSM) and the *Strong Flavour Model* (SFM), while several other benchmarks have also been proposed by theorists [17].

The SSM assumes that the couplings of the Z' boson are identical to that of its SM counterpart, the Z boson [17]. However, from the results to be presented in Chapter 5, it may also be trivial for the SSM to be later reinterpreted into a wider array of alternative models, when studying the effect on the signal by further tuning these couplings [15].

The SFM, also known as the Non-Universal (NU) G(221) model [19][20], postulates that the Z' boson, represented by a second $SU(2)$ electroweak gauge group, potentially couples more strongly to third-generation fermions, which may provide an explanation for their significantly higher masses compared to the lower generations [21]. This coupling is governed by a mixing parameter $\sin^2\phi$ between these two electroweak gauge groups, where $\sin^2\phi < 0.5$ corresponds to such stronger coupling with third-generation fermions, or otherwise preferential to first- and second-generation fermions as in the first $SU(2)$ group, for a TeV-scale mass Z' boson.

Chapter 2: Experimental facilities

This chapter will introduce the experimental facilities used in recording the physics data, on which the feature BSM search analysis will be performed. The components for how this data is produced via high-energy collisions of particles and recorded by detectors will be broken down into their corresponding technologies and discussed in detail throughout the following sections. Where the author had also played a role in supervising the operation of these facilities will also be discussed.

2.1 The Large Hadron Collider

The *Large Hadron Collider* (LHC) is at time of writing the world's largest and most powerful circular particle accelerator and collider. It was built by the *European Organization for Nuclear Research* (CERN), approximately 100 m below the area around Geneva in Switzerland and the French border, with a 26.7 km circumference [22].

The LHC has been running since 2008, where the accelerator has recently finished operating through its second run of data-taking (Run-2), lasting four years from 2015 to 2018. During this phase, the LHC has been able to collide protons with protons at a *centre of mass* (CoM) energy of $\sqrt{s} = 13\,\text{TeV}$. The protons are grouped together into bunches comprised of approximately 10^{11} protons each, since this would give more feasible probabilities for collision events. The collisions deliver an *instantaneous luminosity*, L, on the order of $10^{34}\,\text{cm}^{-2}\,\text{s}^{-1}$, in relation to the number of collision events per second N_{event} and the cross-section of that event σ_{event}, as given by Equation 2.1.1 [22]. Over time, the total delivery of collisions can then be quantified as *integrated luminosity* $\int L\,\text{d}t$. The accelerator is also capable of colliding heavy ions such as lead and xenon with both themselves and protons.

$$L = \frac{N_{\text{event}}}{\sigma_{\text{event}}} \tag{2.1.1}$$

The protons collided in the LHC are sourced from a cylinder of hydrogen gas, ionised to just their proton nuclei. They begin their journey through a linear accelerator LINAC2, bringing their energy up to 50 MeV, as shown in Figure 2.1.1. The protons are then further accelerated through a series of progressively larger circular accelerators; many of which themselves were once experiments like the LHC throughout CERN's history. First they encounter the *Proton Synchrotron Booster* (PSB) raising the energy to 1.4 GeV, followed by the *Proton Synchrotron* (PS) taking this to 25 GeV, and lastly through the *Super Proton Synchrotron* (SPS) increasing the energy to 450 GeV. Eventually, the protons are injected into the LHC forming a collimated beam, where they are then accelerated to their final energy of 6.5 TeV.

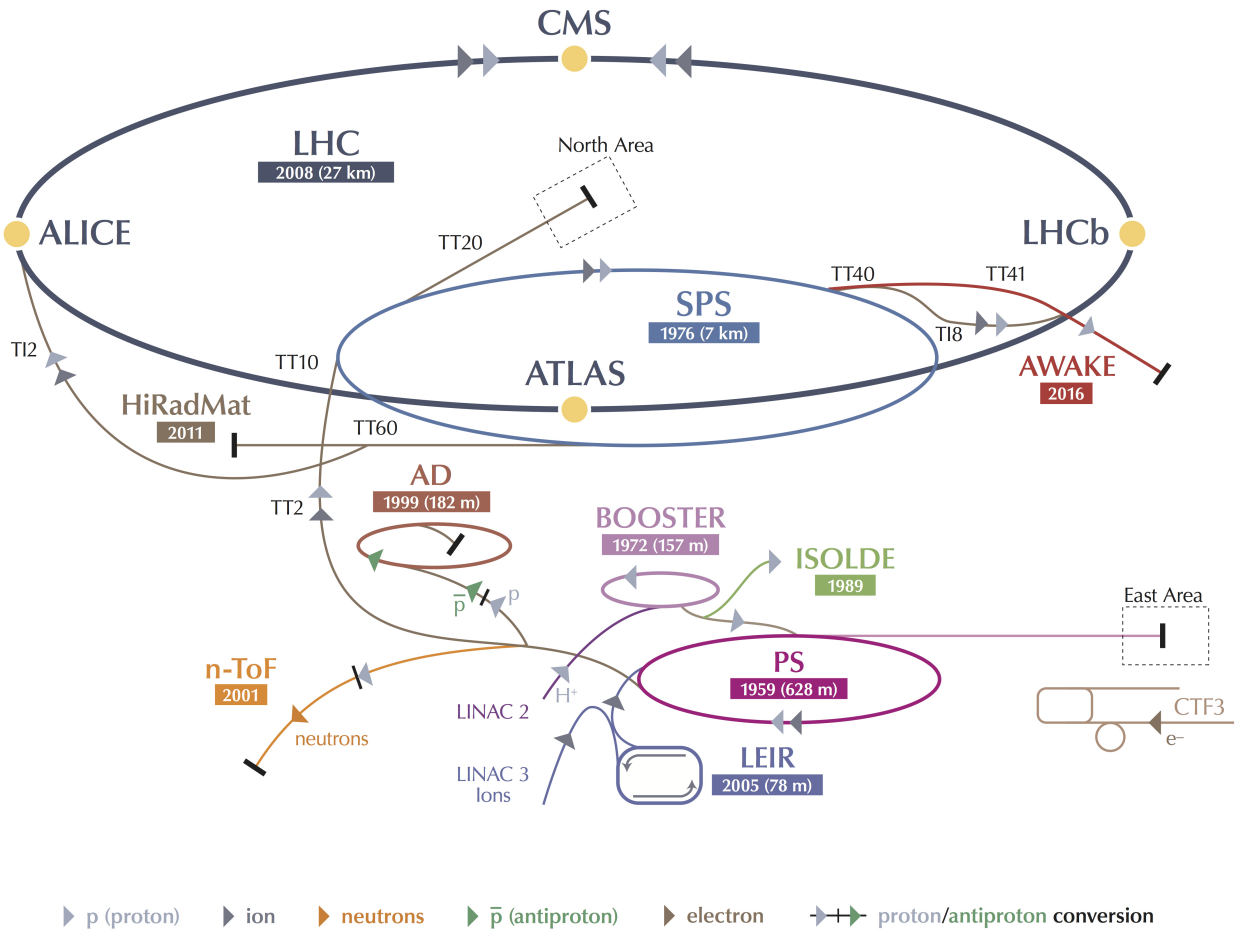

Figure 2.1.1: Schematic of the CERN accelerator complex increasing proton energy from the LINAC2 up to the LHC [23].

The protons are constrained into bunches by radio frequency (RF) cavities, situated at multiple points along the LHC. These cavities accelerate and decelerate protons which are outside of the target energy or timing, such that they fall into these bunches within a controlled RF bucket occupying the volume of the beam pipe, each being spaced apart with a time difference of 25 ns from each other.

The protons are circulated around the LHC in opposite directions while they are accelerated and then collided together. Despite protons having the same electromagnetic charge, they can be accelerated while close together using superconducting dipole magnets spaced along the LHC, making for a compact pipe design as shown in Figure 2.1.2. These magnets produce fields with two apertures where each of the opposing beams reside within a pair of parallel pipes while benefiting from the same acceleration mechanism.

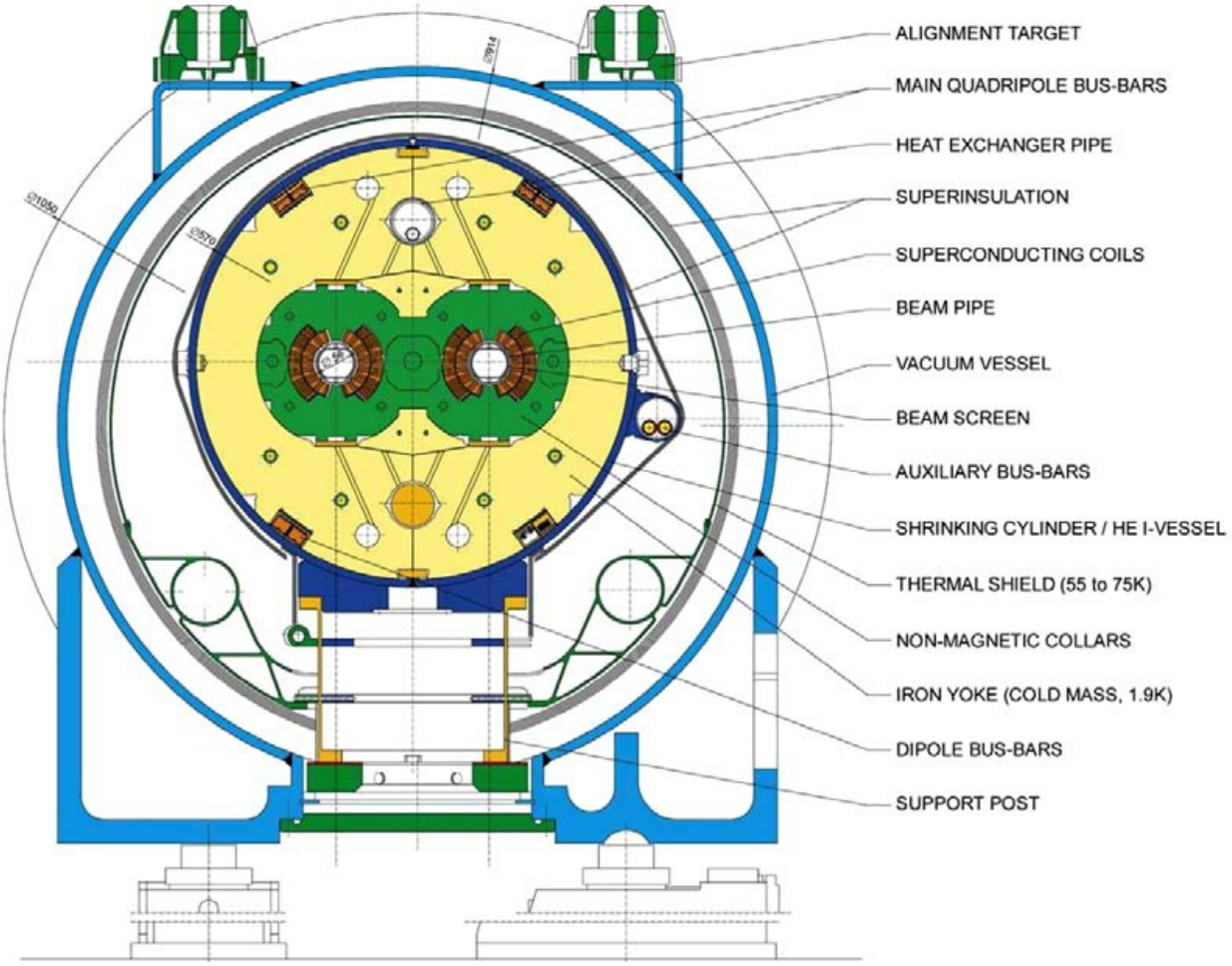

Figure 2.1.2: Schematic of the cross-section of a dipole magnet used to constrain and accelerate proton beams in the LHC [22].

The protons are brought together for collision at various interaction points around the LHC, by using higher-order quadrupole magnets to squeeze the beams into focus. Positioned around these points are numerous detectors, of which there are four major experiments: ATLAS [24], CMS [25], LHCb [26] and ALICE [27]; each are shown on Figure 2.1.3.

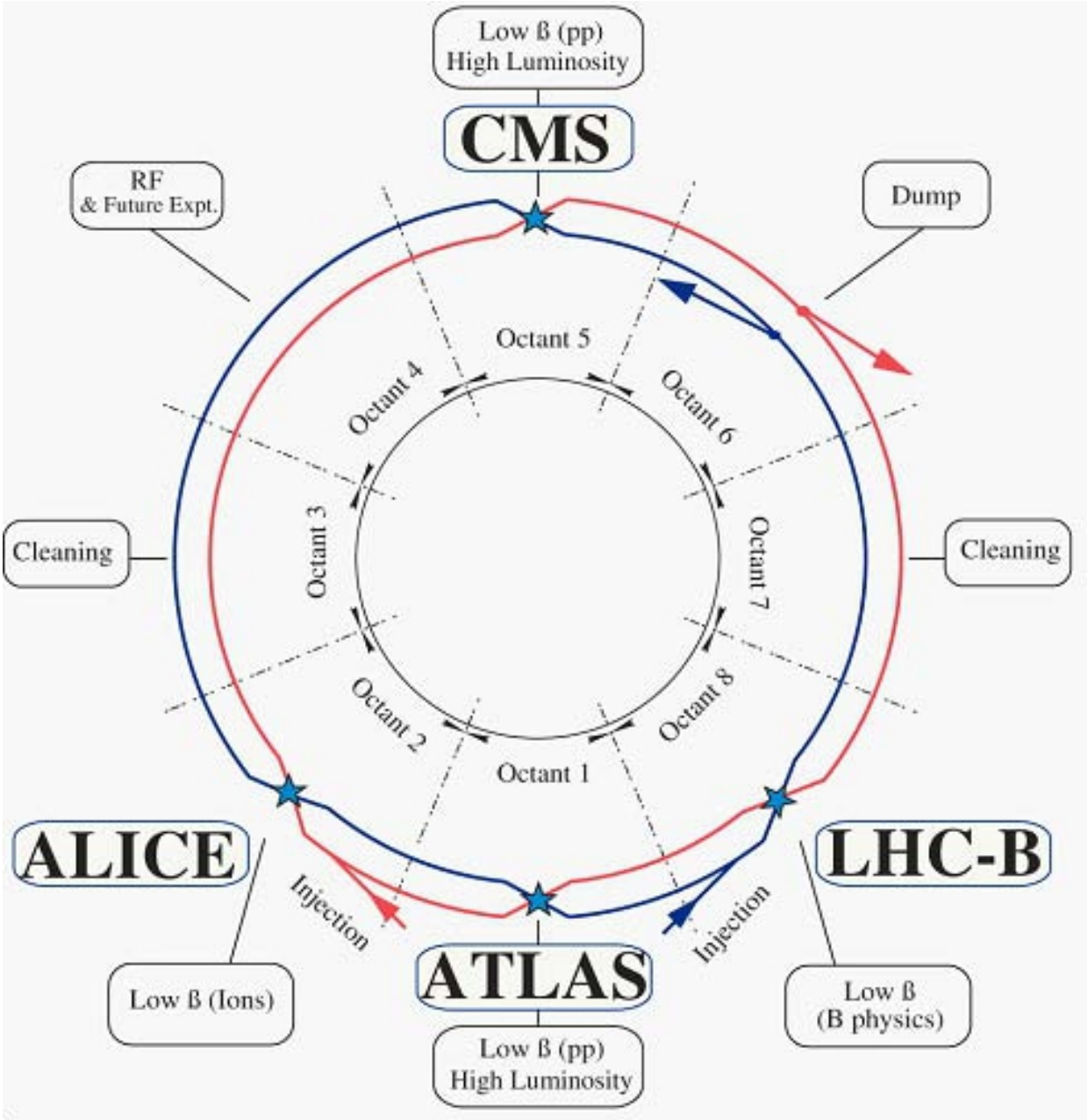

Figure 2.1.3: Schematic of the LHC, labelled with the positions of each of the four major experiments [22].

ATLAS and CMS are general purpose detectors which primarily focus on studying *proton-proton* (p-p) collisions in search for new physics at high energy, the nature of which is discussed in this thesis using the ATLAS detector. LHCb differs in that it uses lower statistics of p-p collisions to specifically analyse bottom quark physics, while ALICE specialises in studying heavy ion collisions.

2.2 Collision event rates

Since the p-p collisions during Run-2 are timed 25 ns apart, this corresponds to a frequency of 40 MHz. Depending on the instantaneous luminosity delivered in each year of data-taking, as shown in Figure 2.2.1, there are between ∼10 to 70 p-p interactions per bunch-crossing, with an average of ∼34, as presented in Figure 2.2.2.

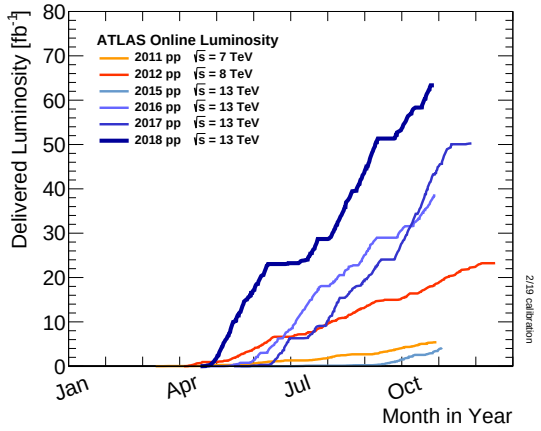

Figure 2.2.1: Delivered luminosity accumulated daily for each year of both Run-1 and Run-2 data-taking [28].

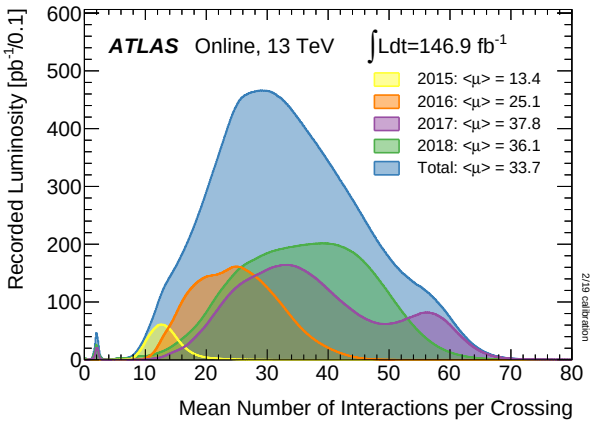

Figure 2.2.2: Distributions of the number of interactions per bunch-crossing for each year of Run-2 data-taking [28].

These coincidental interactions are commonly known as *pileup* [29], with an example visualised in Figure 2.2.3. Not only is pileup a challenge for detector tracking systems due to the excessive density of tracks, but would also deliver a total of ∼1 GHz of collision events which is far beyond what is capable or reasonable of being recorded by a detector or its software at the time of operation (referred to as *online* operation). This problem will be addressed later in Section 2.3.4 through the use of triggers in the ATLAS detector.

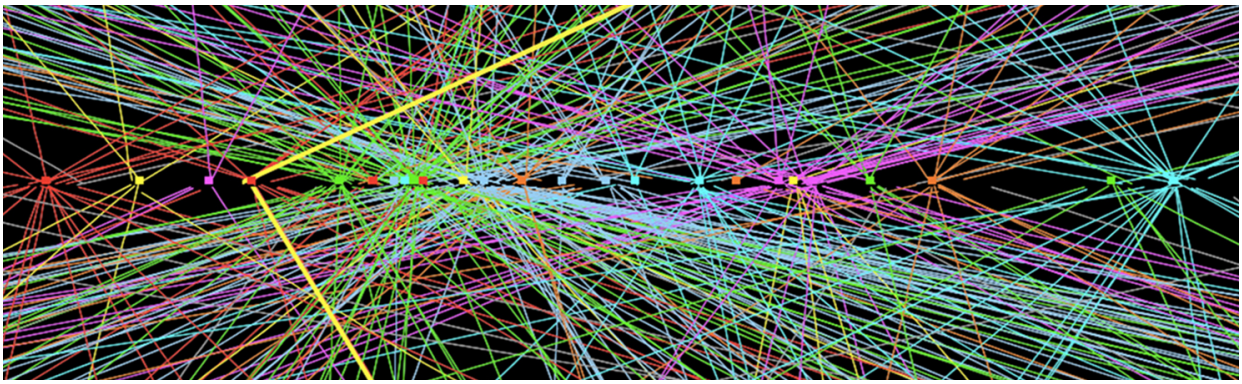

Figure 2.2.3: An example visualisation of a proton-proton bunch-crossing, with multiple interactions (∼25) along the beam pipe generating a dense particle track environment, known as pileup [30].

2.3 The ATLAS detector

The ATLAS detector (*A Toroidal LHC ApparatuS*) is one of two major general purpose detectors situated along the LHC, primarily analysing high-luminosity p-p collision data [24]. The cylindrical detector surrounds the LHC beam pipe, as shown in Figure 2.3.1, with the origin centred on the nominal interaction point of the collision. The detector measures 44 m in length and 25 m in diameter.

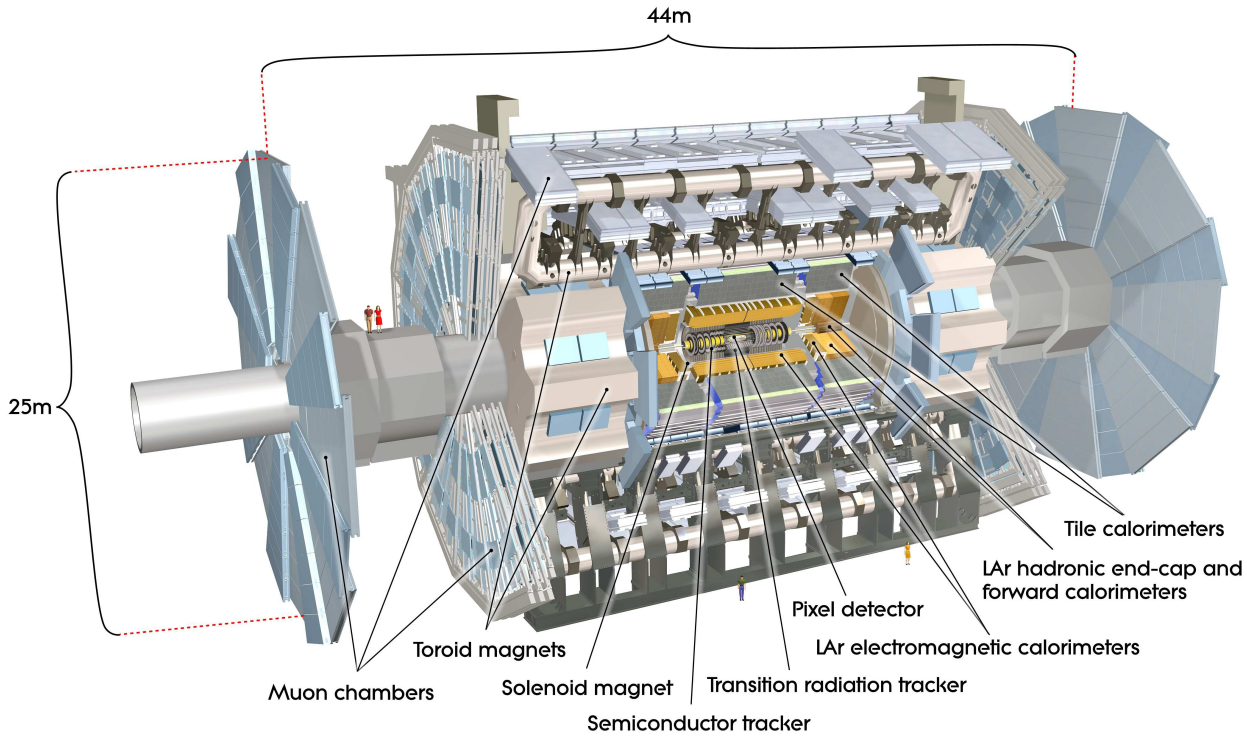

Figure 2.3.1: The ATLAS detector with key components and sub-detectors labelled [24].

ATLAS is formed of a series of modular sub-detectors, each assisting with a unique role in identifying and measuring the particles produced from the collision. Working outwards from the interaction point, the major sub-systems encountered by the particles in flight are: the *Inner Detector* (InDet), the *Calorimeters* (Calo) and the *Muon Spectrometer* (MS).

ATLAS can also be divided into two regions: the *barrel* and the *end-caps*. The barrel resides in the central region of ATLAS, while the end-caps reside on both ends along the beam pipe.

In a right-handed Cartesian coordinate system, the positive x-axis is defined towards the centre of the LHC ring, the positive y-axis as vertically upwards, and therefore the positive z-axis is defined along the direction of the anticlockwise beam. In a polar coordinate system, the azimuthal angle ϕ rotates around the beam pipe, while the polar angle θ deviates perpendicularly from the beam pipe, and therefore moving away with radius R. On either side of the interaction point along the beam pipe, and azimuthally, the detector is symmetrical.

Visualised by Figure 2.3.2, the *pseudorapidity* η is often used as a simple alternative to describe the polar angle θ within the detector, as defined by Equation 2.3.1. This is preferred since differences in pseudorapidity ($\Delta\eta$) are Lorentz-invariant, a necessary requirement to circumvent the significant Lorentz boosts applied by high-energy collisions when observed in the reference frame of the LHC. Therefore the angular separation ΔR between two objects in the $\eta - \phi$ plane can be described by Equation 2.3.2:

$$\eta = -\ln\tan\left(\frac{\theta}{2}\right) \tag{2.3.1}$$

$$\Delta R = \sqrt{(\Delta\eta)^2 + (\Delta\phi)^2} \tag{2.3.2}$$

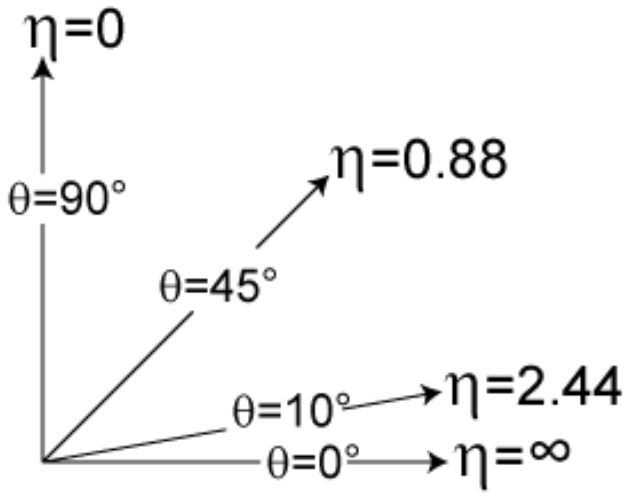

Figure 2.3.2: Visualisation of the polar angle θ with pseudorapidity η in the Cartesian $z - y$ plane of the ATLAS detector [31].

The detector measures the energy E and momentum p of particles produced from the collision as they pass through. Idealistically, the invariant mass m could then be derived as a result of Equation 2.3.3. However, in reality, the detector resolution would be limited, and so the invariant mass is usually estimated from its visible component instead. Furthermore, it is unknown what the exact initial kinematics of each of the protons or their constituents are at the time of the collision along the beam pipe, and that there is commonly less interest in studying soft scattering collisions close to the beam direction. Therefore, it is often preferable to take the *transverse* component of these kinematic variables, running perpendicularly to the beam, since it is guaranteed that there should be no initial component in this direction at the time of collision. This gives the *transverse energy* E_{T} and the *transverse momentum* p_{T} in this component, and will be commonly used in the analyses throughout this thesis.

$$E^2 = (pc)^2 + (mc^2)^2 \tag{2.3.3}$$

Due to their weakly-interacting nature, the ATLAS detector is not sensitive to neutrinos that may be produced in the collisions, and in some addition of any possible inefficiencies or gaps within the detector itself, will result in some missing component to the energy reconstruction. Taking this from the transverse direction, this gives the *transverse missing energy* $E_{\mathrm{T}}^{\mathrm{miss}}$, calculated from the vectorial sum of all reconstructed momenta measured by the detector (and converted to energy), then as inferred by the conservation of momentum law, must be defined in the opposite direction.

2.3.1 Inner Detector

The InDet provides tracking and momentum measurements of charged particles, as shown in Figure 2.3.3. The complete InDet measures 6.2 m in length and 2.1 m in diameter. Given the heavy rate of collisions produced from the LHC, especially those from pileup, the InDet is required to distinguish individual charged particles from a highly dense region of tracks.

In order to achieve this high resolution and deliver precision measurements, the InDet is comprised of three major components, starting from the centre: the *Pixel* detector, the *Semiconductor Tracker* (SCT) and the *Transition Radiation Tracker* (TRT).

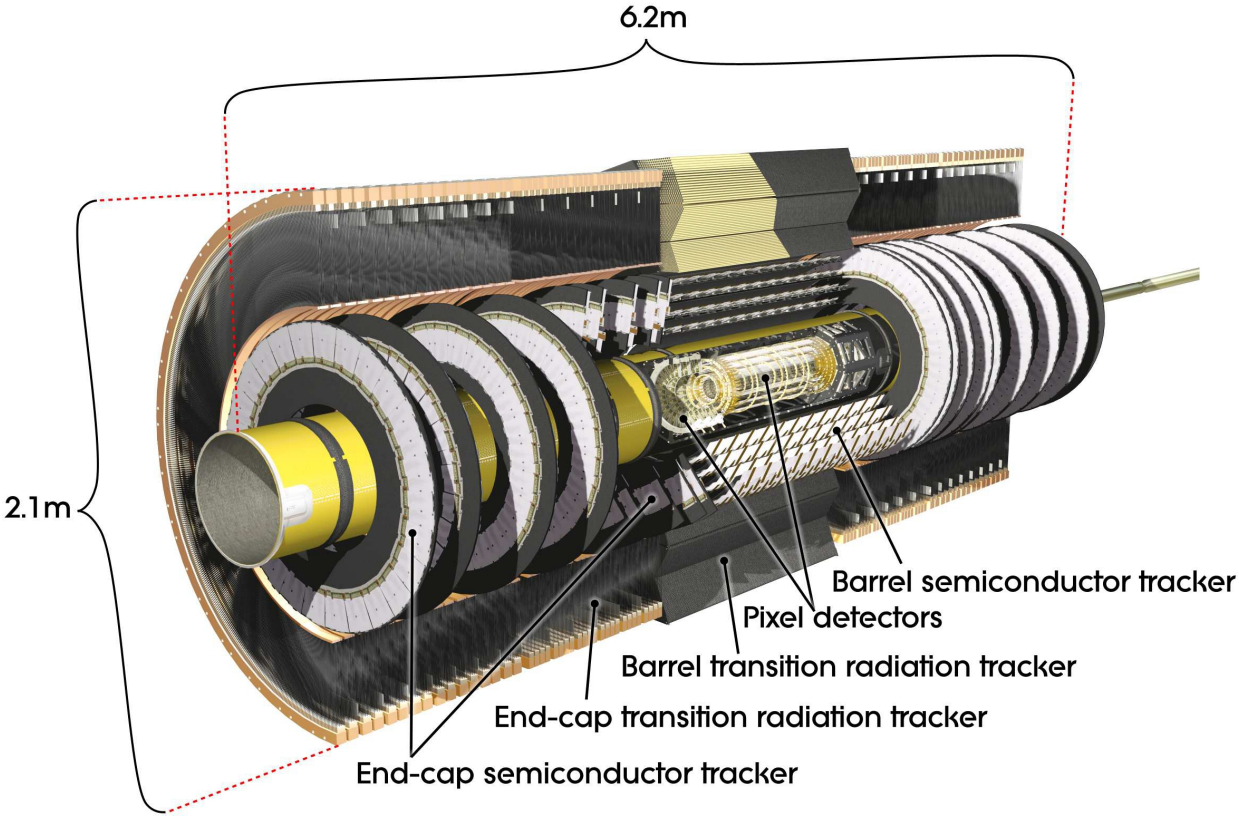

Figure 2.3.3: The ATLAS Inner Detector surrounding the LHC beam pipe, with key components and sub-detectors labelled [24].

In the barrel region, the three InDet trackers are arranged concentrically as cylinders parallel to the beam pipe, as shown in Figure 2.3.4. The Pixel and SCT detectors extend over the region $|\eta| < 2.5$, covering the inner radii of the InDet between 5.05 to 12.25 cm for the Pixel and 29.9 to 51.4 cm for the SCT. The TRT spans the region $|\eta| < 2.0$, covering the outer radii of the InDet between 55.4 to 108.2 cm. In the end-cap regions, the InDet trackers are arranged perpendicularly to the beam pipe in a radial pattern.

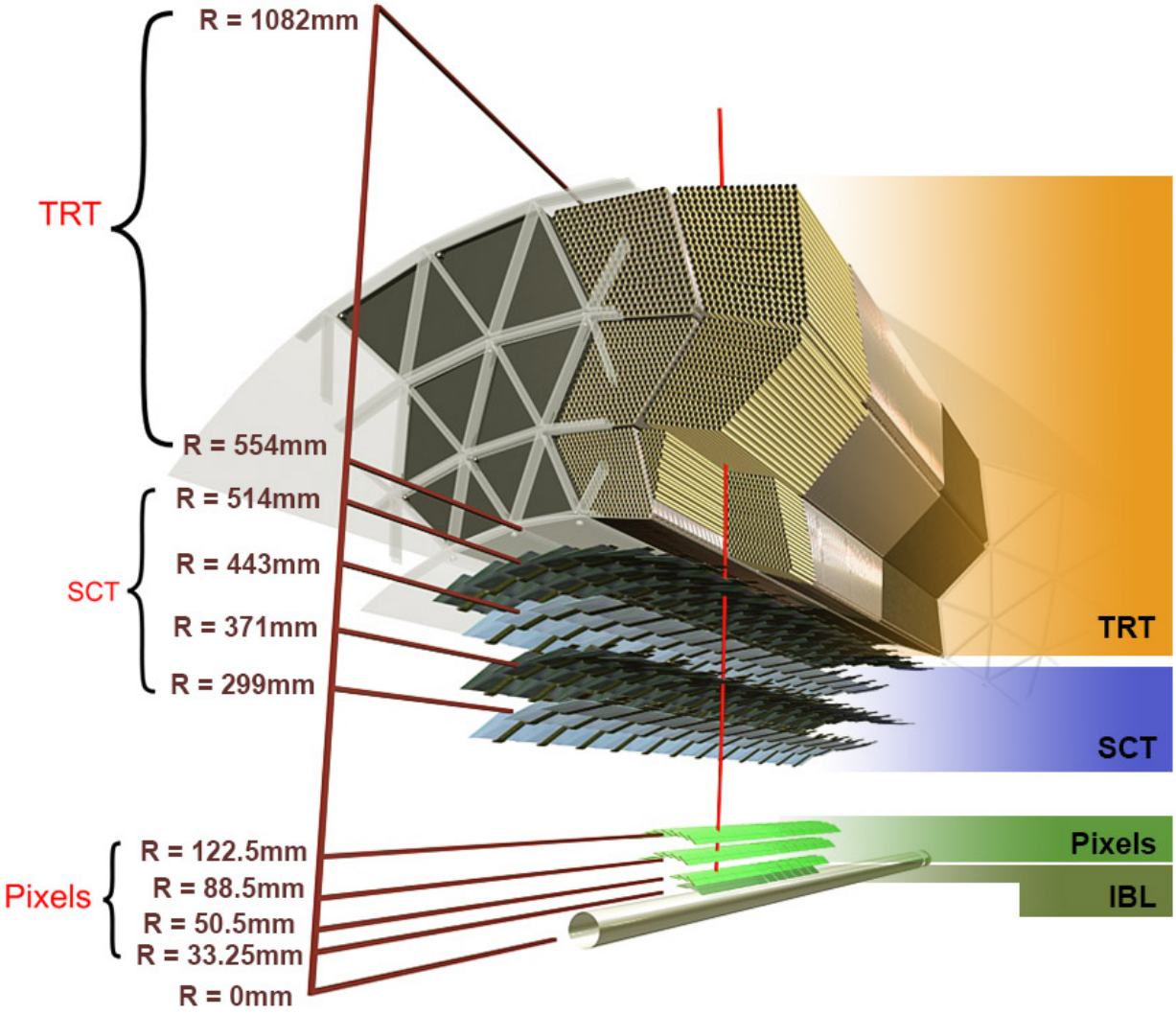

Figure 2.3.4: The barrel region of the ATLAS Inner Detector labelled with each of its three tracking components [32].

The Pixel detector is formed of 1744 rectangular modules of size $19 \times 63\,\text{mm}^2$ each, facing the incoming particle direction. Each module contains 47,232 n-type silicon sensors of size $50 \times 400\,\mu\text{m}^2$ with thickness 250 µm each. They are arranged into 3 layers in the barrel and 3 in each end-cap region, providing ∼80.4 million readout channels. This fine granularity provides the high resolution required in the dense track region for the innermost radii of the InDet, measuring at 10 µm in the $R - \phi$ plane and 115 µm in z/R for the barrel/end-caps. It also enables measuring secondary vertices from short-lived particles decaying in this innermost region, such as tau leptons.

Before Run-2 operations, a fourth *Insertable B-Layer* (IBL), also shown in Figure 2.3.4, was introduced between the innermost Pixel barrel layer and the beam pipe at a radius of 3.325 cm. This improved tracking performance at smaller radii in order to meet the increases in luminosity and compensate for radiation damage [33].

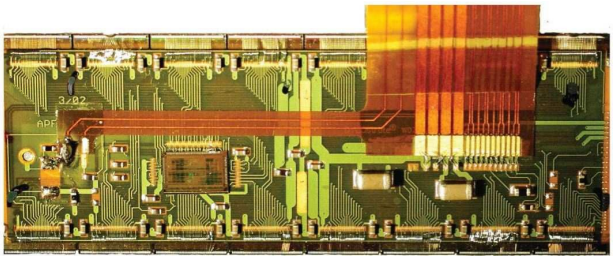

Figure 2.3.5: Photograph of a Pixel module used in the barrel region of the ATLAS Inner Detector [24].

The SCT is formed of 4088 p-in-n-type silicon microstrip modules of sensor thickness 285 µm each. The 2112 rectangular modules in the barrel are of size $64 \times 128\,\text{mm}^2$ each, while the remaining 1976 modules in the end-caps are trapezoidal with similar but decreasing lengths. They are arranged into 4 layers in the barrel and 9 in each end-cap region, providing ∼6.3 million readout channels. Compared to the Pixel detector, the SCT provides a larger area of coverage for particle detection where the track density is reduced at higher radii, but at the cost of a lower resolution in order to maintain design practicality, with 17 µm in the $R - \phi$ plane and 580 µm in z/R. An example photograph of a single SCT microstrip module is shown in Figure 2.3.6.

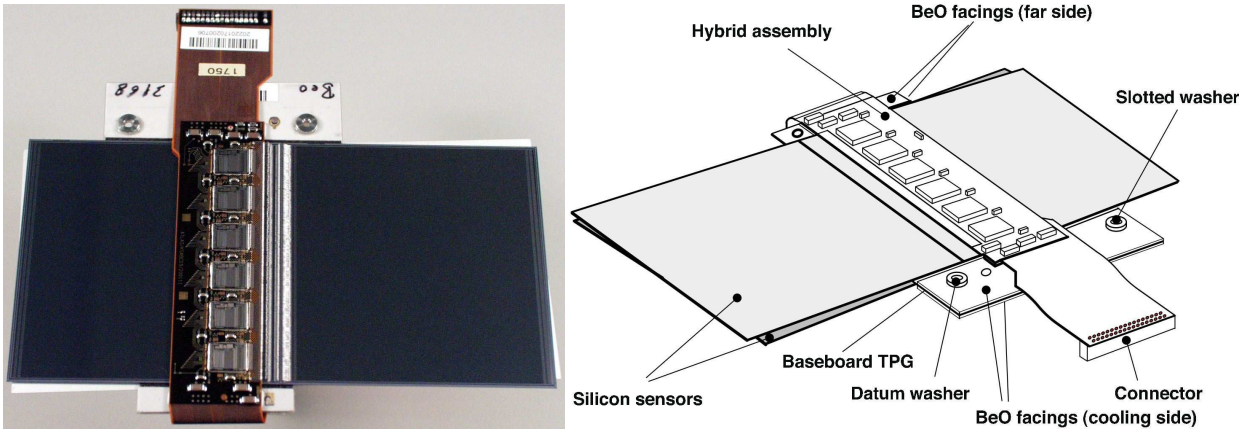

Figure 2.3.6: Photograph (left) and schematic (right) of a SCT microstrip module used in the barrel region of the ATLAS Inner Detector [24]. Each of the 6 chips on the module readout circuit contains 256 channels.

The TRT consists of 298,304 layered straw tubes filled with a mixture of primarily Xe gas with CO_2 and O_2, running perpendicularly to the incoming particle direction. Each 4 mm diameter straw tube contains a thin conducting wire running down its centre to the readout, and in between the tubes are filled with transition radiation-inducing materials such as polypropylene fibres, creating a dielectric boundary with the gas. The straw tubes are grouped together into modules, forming 96 modules over 3 layers in the barrel with ∼500 straws each and 20 modules in each of the end-caps with 6144 straws each, providing a total of ∼351,000 readout channels. Although the TRT provides a much lower resolution compared to the silicon trackers, at 130 µm in $R - \phi$, this is compensated by extending out far at the larger radii, allowing it to reconstruct much longer track information. Utilising this transition radiation phenomenon, the TRT is also immediately capable of specifically identifying electrons, due to their unique X-ray signature.

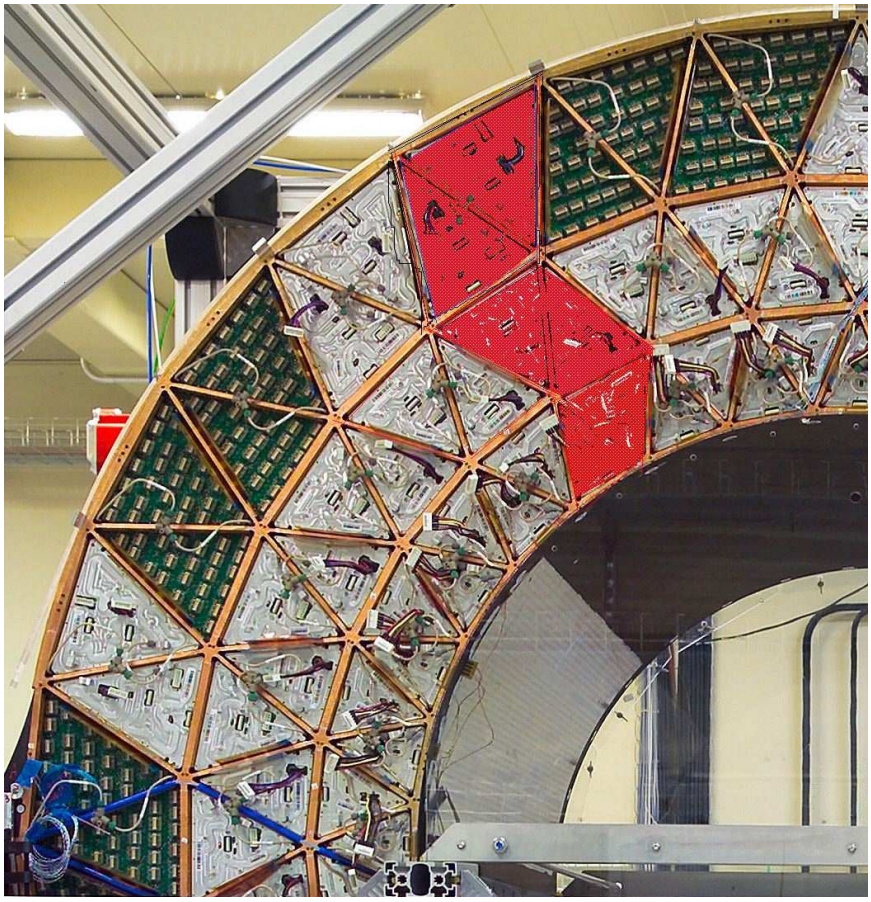

Figure 2.3.7: Photograph of a segment of the TRT used in the barrel region of the ATLAS Inner Detector. Highlighted in red are individual modules in each of its three layers [24].

The Pixel and SCT are cooled between -5 to $-10\,°\text{C}$ using a *chlorofluorocarbon* (CFC)-based evaporative cooling system, in order to reduce thermal noise and ensure protection from overheating during their operation. The TRT is kept balanced at room temperature ($\sim$20 °C) through surrounding heating elements as to ensure its gaseous state.

The InDet is surrounded by a superconducting solenoid magnet providing a 2 T axial magnetic field, strongly bending charged particle tracks and therefore enabling measurements of their momentum. All of the components in the InDet compliment each other to provide precise measurements on particle momentum, identification, impact parameters and vertex tracking.

While this chapter explains the current status of the LHC and the ATLAS detector as they were operated during Run-2, various upgrades to both are planned for future data-taking runs. Of particular interest to this thesis are the plans to replace the InDet of the ATLAS detector with a new tracker in preparation for Run-4, with the author's work specifically focusing on the construction of the SCT-like component which will form part of the upgrade, all to be discussed later in Chapter 6.

2.3.2 Calorimeters

Surrounding the InDet are the Calo sub-systems, providing energy measurements of showering particles, as shown in Figure 2.3.8. Since calorimetry depends on the showering of these particles and the nature of the shower depends on the particle type, the Calo is therefore split into two major sub-detectors, working outwards from the centre: the *Electromagnetic Calorimeter* (EMCal) and the *Hadronic Calorimeter* (HCal).

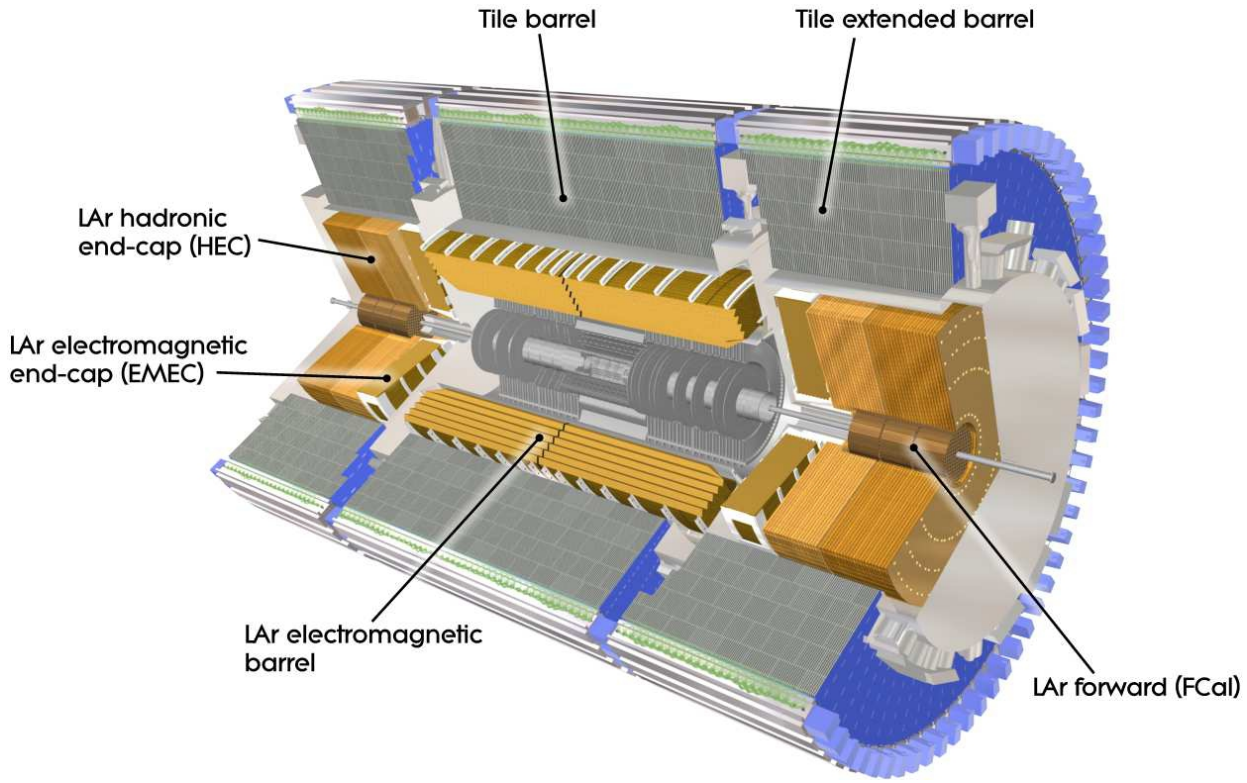

Figure 2.3.8: The ATLAS Calorimeters surrounding the Inner Detector, with key components and sub-detectors labelled [24].

The EMCal is optimised to measure the showers of electrons and photons, covering a range up to $|\eta| < 3.2$ between the barrel and end-cap regions. The EMCal consists of a sampling *liquid argon* (LAr) active detector segmented by lead absorber plates, alternating along strip or square-like cells facing perpendicularly to the incoming particle direction, as shown in Figure 2.3.9. They are arranged into an accordion-like geometry so as to ensure maximum coverage with no gaps between, with a fine granularity for resolving $\sim 0.025 \times 0.025$ in $\Delta\eta \times \Delta\phi$, adequate for measuring EM showers, and cell length of 470 mm in order to ensure maximum containment of the shower, covering $\sim$22 radiation lengths, while minimising interference with muons so that they may reach the MS at higher radii unstirred. The EMCal provides 163,968 readout channels.

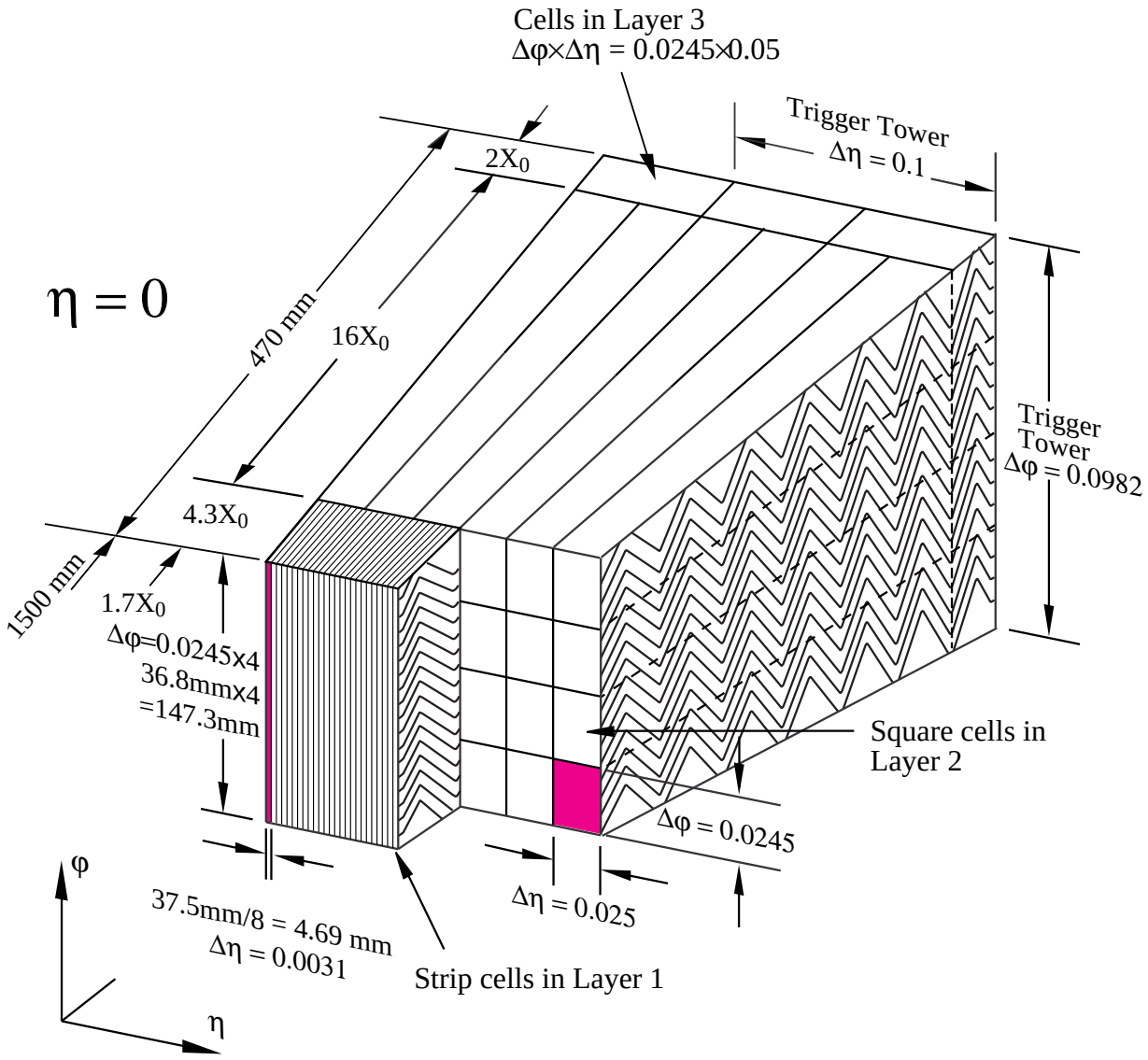

Figure 2.3.9: Schematic of an Electromagnetic Calorimeter cell used in the barrel region of the ATLAS detector. [24].

This is then followed by the HCal designed to be appropriate for measuring showers from hadronic jets. The HCal utilises differing technologies in the barrel and end-cap regions. In the barrel, this consists of an active scintillating *Tile Calorimeter* (TileCal) interspaced with steel absorber plates, covering $|\eta| < 1.0$. In the end-caps, the TileCal extends from the barrel without any rotation between $0.8 < |\eta| < 1.7$, along with two additional active LAr calorimeter sub-systems layered with copper absorbers: the *Hadronic End-cap Calorimeter* (HEC) ranging $1.5 < |\eta| < 3.2$, and the *Forward Calorimeter* (FCal) covering $3.1 < |\eta| < 4.9$. The FCal is intended to identify both EM and hadronic showers, but at these extreme values of η close to the beam pipe. Compared to the EMCal, the HCal have a much coarser granularity of $\sim 0.1 \times 0.1$ for resolution, but still sufficient for probing hadronic jet showers. The TileCal and HEC provide a total of 15,484 readout channels, while the FCal provides 3524 channels.

2.3.3 Muon Spectrometer

Finally, the Calo are encased within the MS, specifically designed to track and measure the momenta of muons, as shown in Figure 2.3.10. This sub-system is required since muons possess a much higher penetration depth through the detector than other types of particles, typically appearing invisible to most of the other sub-systems, with the exception of the InDet tracker, so the energy information would be lost otherwise. Utilising this distance between the InDet and the outermost radii of the ATLAS detector allows for the MS to determine muon momenta through the spectrometry of magnetic deflection as opposed to calorimetry.

The MS is supported by a superconducting air-core toroid magnet surrounding the entire detector. Like the InDet, the magnetic field bends the muon tracks with a power between 1 to 7.5 T m depending on the region in the detector. This enables the MS to make precise measurements for even the highest muon momenta of $\sim$3 TeV.

The MS consists of three layers of sub-detectors encountered in order: the *Monitored Drift Tubes* (MDT) ranging $|\eta| < 2.7$, and the *Cathode Strip Chambers* (CSC) covering $2.0 < |\eta| < 2.7$, in both the barrel and end-cap regions; then followed by either the *Resistive-Plate Chambers* (RPC) in the barrel ($|\eta| < 1.05$), or the *Thin-Gap Chambers* (TGC) in the end-caps ($1.05 < |\eta| < 2.7$).

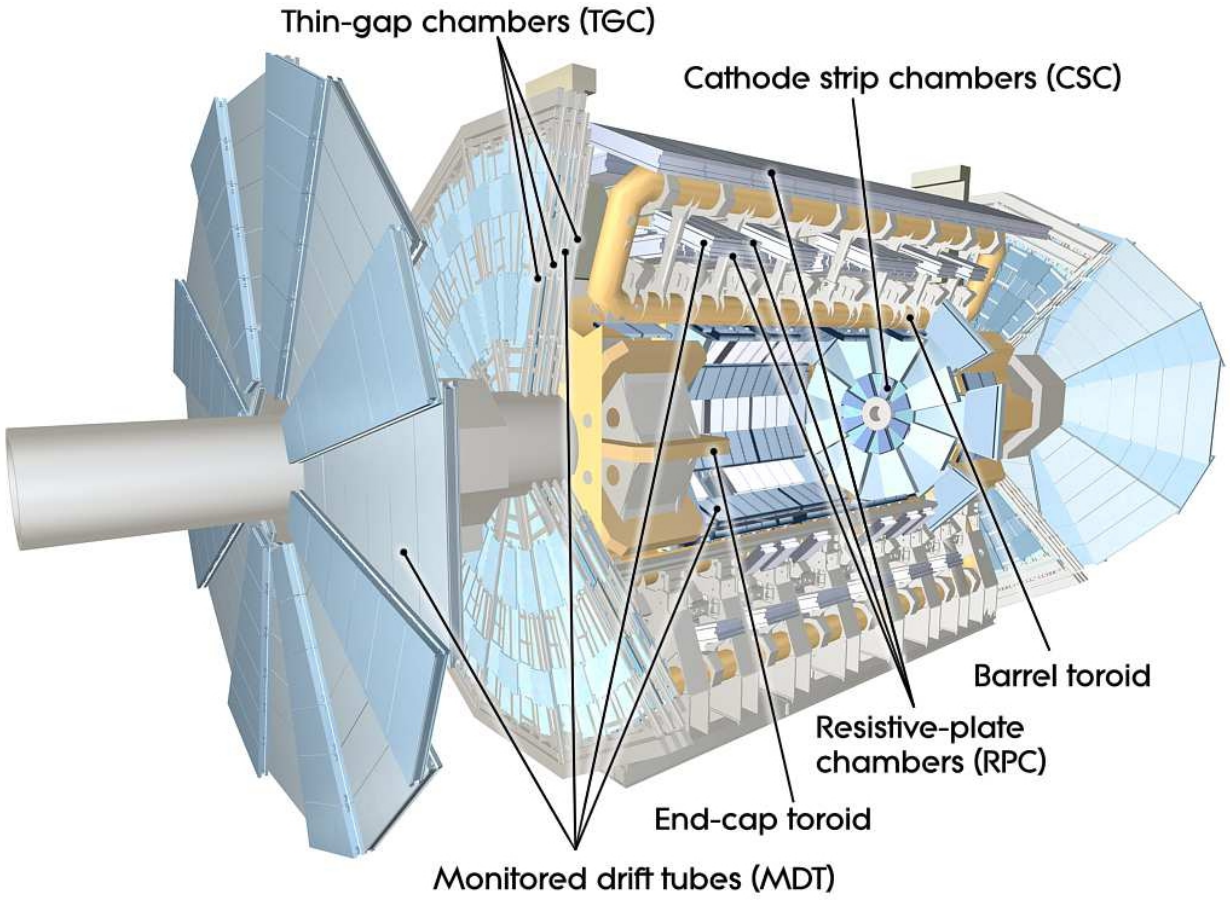

Figure 2.3.10: The ATLAS Muon Spectrometer surrounding the Calorimeters, with key components and sub-detectors labelled [24].

The inner MDT and CSC sub-systems provide precision measurements on tracking muons, while the outer RPC or TGC detectors act as additional coordinate references, as well as delivering rapid trigger response. The MS provides a total of ∼1.1 million readout channels across all of its sub-systems.

2.3.4 Trigger and Data Acquisition system

As mentioned in Section 2.2, in order to cope with this overwhelming stream of information, especially from pileup, the ATLAS detector is fitted with a *Trigger and Data Acquisition* (TDAQ) system [24], as represented by Figure 2.3.11.

The trigger system aims to rapidly measure and identify the resultant particles produced from the collision based on information provided by the sub-detectors. Only if these particles meet a certain threshold criterion, such as by energy, then the collision data for that event would be stored for further analysis. Given that many of these events may not generally contain particles of physics interest, such as those which soft scatter or common backgrounds, these triggers help to drastically reduce the recorded event frequency to ∼1 kHz, which is far more comfortable for detector readout and data storage operations.

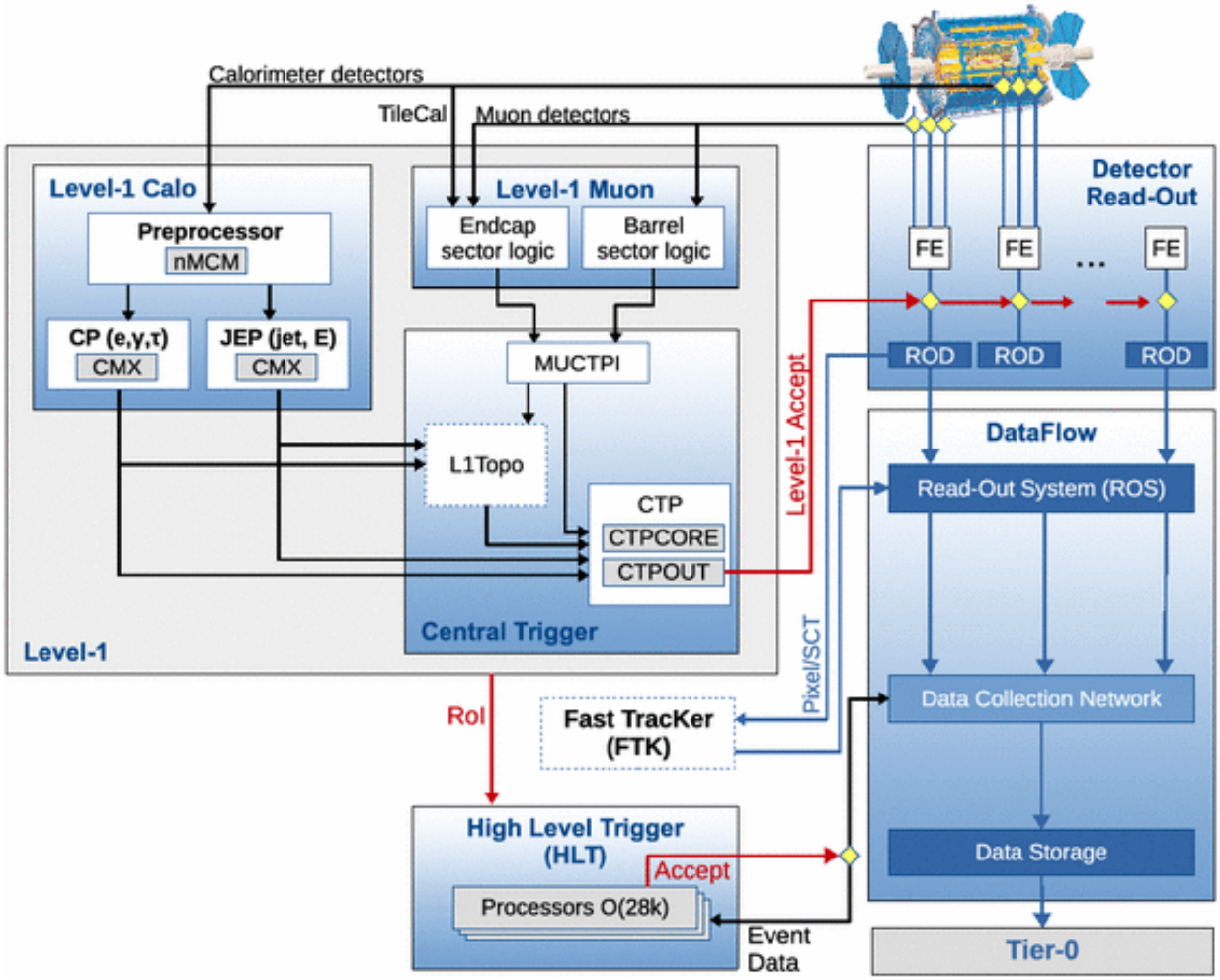

Figure 2.3.11: A diagram of the TDAQ system representing the flow of data from detector to storage, passing through each of the labelled trigger sub-systems [34].

The TDAQ can be divided into two major components: a hardware-based *Level-1* (L1) trigger and a software-based *High-Level Trigger* (HLT) system. The L1 trigger considers information provided by the Calo (*L1Calo*) and MS (*L1Muon*) systems, enabling it to make decisions rapidly based on the energy of objects. This means the L1 must be able to respond within 2.5 µs, before its electronics accrue dead-time from the subsequent collisions and thus resulting in loss of data (a caution the author would have monitored during the shifting discussed in Section 2.3.5).

For those objects which pass the L1 trigger, a *Region-of-Interest* (RoI) is demarcated which informs the HLT of a starting location for further processing. These events are buffered by the *Read-Out System* (ROS) before processed by the HLT's algorithms, which returns a decision within a further ∼4 s. Similarly, this buffer must be flushed by the HLT quick enough so as to avoid the system running busy and therefore incurring loss of data. The HLT considers additionally detailed information from the Calo and MS as well as the InDet when making its decision, including more precise track and hit measurements, particle identification and isolation criteria.

As a result, a collection of threshold criteria produced by the L1 and HLT based on their energy and type are also provided as a "trigger menu" for use by physics analyses, examples of which will be utilised for both of the analyses in Chapters 4 and 5.

2.3.5 ATLAS Control Room shifting

The truly final component of the detector are the people who operate it, remotely from the *ATLAS Control Room* (ACR) on the surface. With this in mind, the author contributed towards this effort during Run-2 operations, amounting to 184 hours of shift work over the course of several months in 2018, both during day and night of all days of the week. Shifting involves monitoring the detector status, ensuring continuous and safe operation, good data-taking quality, and taking action where needed or otherwise communicating between shifters and on-call experts to resolve problems as quickly as possible.

Supervising and controlling the detector is enabled through the *Detector Control System* (DCS) which allows shifters to observe and instruct each and every sub-component of ATLAS [35]. The ACR is usually divided into sections each with at least one shifter posted on eight hour cycles to monitor a single major sub-system. For the author, this meant supervising the InDet, while others would monitor the Calo, the MS and the trigger system. There would also be stationed a shift leader, run coordinator, data quality inspector and safety officer. The DCS treats the sub-components of the detector with a *finite-state machine* (FSM) hierarchy, such that, for example, if a single module in the SCT reports an error, this state propagates upwards through the detector in layers, in turn indicating a problem with the SCT and therefore with the InDet. This allows the shifter to be able to find and respond to problems quickly as they navigate downwards through the FSM operator interface, an example of which is shown in Figure 2.3.12.

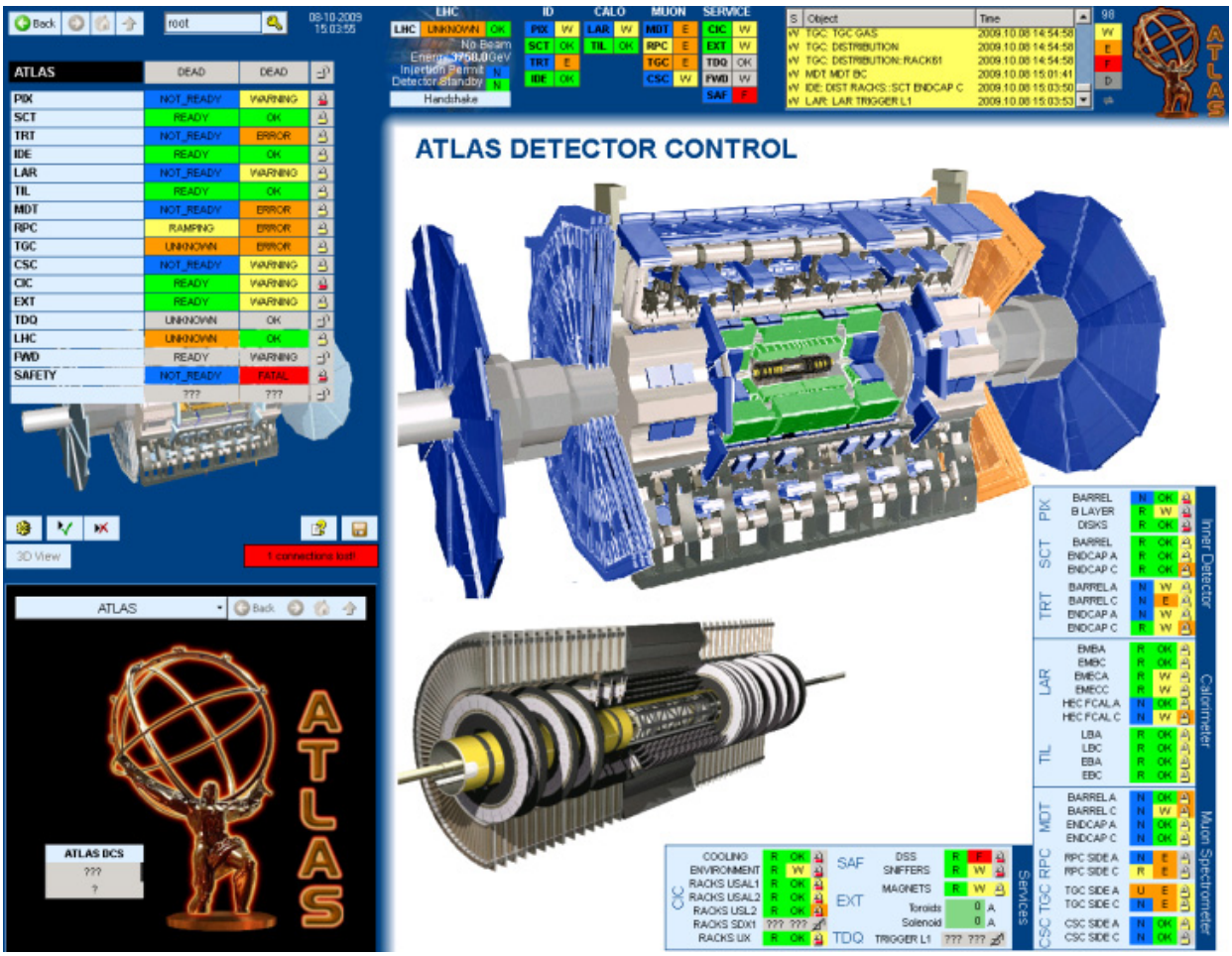

Figure 2.3.12: An example of the finite-state machine operator interface reporting a variety of detector states, used in the ATLAS Control Room [36].

Chapter 3: ATLAS computing

In this chapter, the downstream processing of the recorded collision data will be discussed, declaring the final amount of good quality data that was collected during Run-2 operations at 139 fb^{-1} of integrated luminosity, and how the core structure of that data is formatted into ROOT-based file types known as AODs. The generation of Monte Carlo-simulated physics used for comparing expected SM backgrounds against the recorded data will also be briefly discussed. This will then be followed by further size reduction and the general strategy for analysis processing of the data, into reduced formats known as DAODs and eventually Ntuples. The software frameworks and tooling deployed to achieve these goals will be introduced, namely ATLAS' own Athena framework covering the majority of the main upstream processing and generation, but with more focus on the author's primary involvement with the xTauFramework for the processing of Ntuples, relevant to the tau lepton-based analyses discussed in this thesis. An overview of the computing resources required and available will be covered, including the use of CERN's Worldwide LHC Computing Grid for large-scale cluster computing. Finally, the long-term preservation of the recorded and analysed data, as well as efforts by the author in improving the robustness of software, will be briefly discussed.

3.1 Data collection and formatting

Throughout Run-2 operations, the LHC delivered a total of 156 fb^{-1} integrated luminosity of p-p collision data, as shown in Figure 3.1.1, with an increasing amount in each passing year. However the ATLAS detector and its operation still have some inefficiencies in capturing all of this, e.g. due to malfunctions or beam instabilities, recording only 147 fb^{-1}, corresponding to ~94 % efficiency. While data is being recorded by the detector, the measured luminosity are divided into blocks of time, namely *lumiblocks*, each corresponding to roughly a few minutes of data-taking, and can be identified by an increasing numeric value [29]. For each consecutive period of data-taking, these lumiblocks are combined into *runs* (not to be confused with the LHC operation periods), with each of these usually lasting on the order of several hours since they often correlate with the LHC operation cycle.

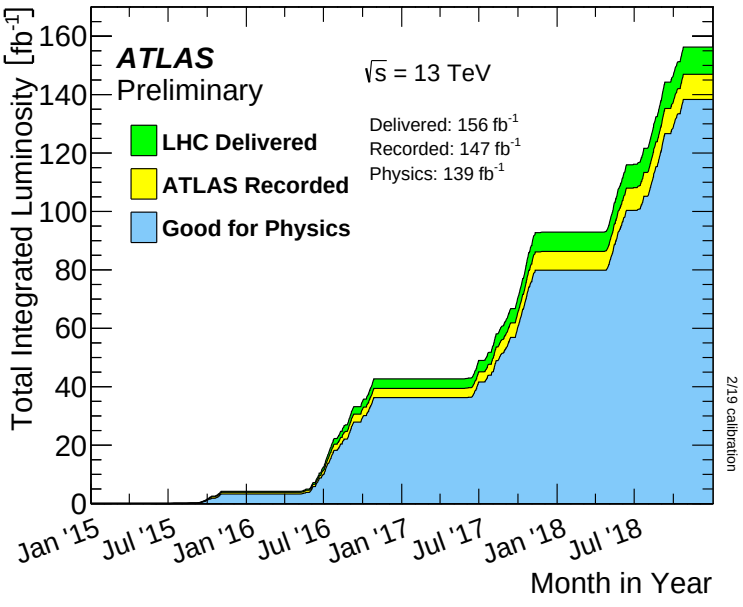

Figure 3.1.1: Progression of the total integrated luminosity during Run-2 data-taking delivered by the LHC, recorded by the ATLAS detector and marked good quality for physics analyses [28].

This segmentation of the data allows it to be further monitored before use in physics analyses, where they must pass the inspection of a dedicated *Data Quality* (DQ) group. For example, the data would be excluded if it was found that it was recorded at a time of detector malfunction. The author assisted in this effort while on the InDet shifts from Section 2.3.5, by comparing the live recorded data against references, confirming that the sub-detectors were in a functional state, and thus assessing if that data was reliable. Those runs and lumiblocks which are approved by DQ are recorded to a *Good Runs List* (GRL), identifying to analysers which parts of the data are safe and useful. This means that for the Run-2 total, a final $139\,\text{fb}^{-1}$ of good standard physics data recorded by ATLAS is ready for analysis, such as that which will be discussed for the BSM search in Chapter 5, an efficiency of $\sim$95 % of the recorded data.

Each collision event recorded by the detector has an information size of $\sim$1.5 MB [37]. With a collision readout rate of $\sim$1 kHz, this would total $\sim$1.5 GB of data being stored per second. The events saved by the TDAQ system are originally stored in a file format based on CERN's *ROOT* analysis software, labelled as `RAW` since it represents the raw live data. However, after the data has been recorded and reconstructed (in *offline* operation), the raw format is further processed into a container known as a *(ROOT-readable) Analysis Object Data* ((x)AOD), which reconstructs the information into the different physics objects useful for analyses to work with. For the full Run-2 data, including on the order of billions of events, these AODs would amount to an order of PB size of information, which can be difficult and slow to process through offline analysis software.

3.2 Monte Carlo simulation

It is generally common in high energy physics experiments for the recorded data to be compared and modelled against a *Monte Carlo* (MC) simulation. MC is commonly used in analyses to either predict the known SM background, which are usually irreducible within the processes being studied, or to provide an estimate of the expected signal as part of some BSM search or SM precision measurement. These MC samples are studied and generated on request in ATLAS by a dedicated *Physics Modelling Group* (PMG) [38], where each various sample individually accounts for a single physics process, with particular properties. For example, a single MC sample could be used to estimate the background contribution from a $Z/\gamma^* \to \tau\tau$ process, specifically within some mass slice between 120 to 180 GeV, as such examples would be seen in the analyses from Chapters 4 and 5. It is then typical that the total number of MC samples processed, each individually predicting all possible background processes at various ranges, summed together and compared with the data by analyses, are on the order of 100.

The majority of the MC samples used in ATLAS are created using common physics generators, such as `Powheg`, `Pythia`, `Sherpa`, `aMC@NLO`, `Herwig` and `MadGraph` [38], to name just a popular handful. MC generation in p-p collision physics is usually devolved into two major roles: the base event generation by the calculation of the processes' quantum *matrix elements* (ME), followed by corrections sourced from its subsequent *parton showers* (PS). For example, it is common in ATLAS for many MC samples to use `Powheg` for ME, in tandem with `Pythia` for PS. The physics processes are often generated at their *leading order* (LO), but can sometimes include multiples of their *next-to-leading order* (NLO, NNLO, etc.) processes, each considering higher quantum perturbation order corrections.

Once the MC processes have been generated, the simulated events are then digitised using the `GEANT` software [38], as if they were actual data that would be recorded by the ATLAS detector. This includes modelling the behaviour of the MC events in passage through the detector material, and how they would appear as signals through the readout electronics. At this stage, then just as with the recorded data, the MC would follow through the reconstruction software and procedures, forming AOD files.

However, since MC is generated through computer simulation, it can widely vary, depending on the complexity of the physics process, the amount of time it takes to produce the simulation for that particular sample. It can be typical that samples take several months of processing in order to *fully simulate* (FullSim) an adequate number of events, which usually matches approximately the amount of recorded data statistics in a typical analysis' event selection, on the order of millions of events. As a solution to this problem, if the accuracy of the MC simulation is not so important to the analysis, and high numbers of event statistics are prioritised, ATLAS provides a *fast simulation* (FastSim) alternative which removes some of the detailed digitisation and reconstruction calculations, thus greatly reducing the generation time by many months. These FastSim samples are more commonly used for signal-based MC, which only serve as a baseline estimation for their abundance within typical analyses, as would be seen in the BSM search in Chapter 5.

On this topic of event statistics, as Run-2 operations have progressed, the amount of recorded data has been increasing, thus also demanding increased statistics in the available MC, which in itself has been a great challenge for computing and software in general. While the number of MC events do not have to be exactly the same as the data, since the MC can be scaled appropriately, it should still be generally approximate such as to avoid incurring too much statistical uncertainty in this estimation. As mentioned throughout the previous sections, during Run-2, between the years of 2015 and 2018, a total of $139\,\text{fb}^{-1}$ integrated luminosity of data was recorded. This can be broken down into three major *campaigns*: 2015–2016 with $36\,\text{fb}^{-1}$, 2017 with $44\,\text{fb}^{-1}$ and 2018 with $59\,\text{fb}^{-1}$. Beginning with the 2016-level of major MC development, labelled as `MC16`, campaigns were launched to generate the adequate MC statistics for each subsequent year of data-taking: these are labelled as `MC16a`, `MC16d` and `MC16e`, respectively. Extrapolating from their differences in luminosity, this implies a multiple of $\sim$1.2$\times$ of additional events generated between MC16a and MC16d, and $\sim$1.6$\times$ with MC16e.

In addition to the increasing statistics recorded in each subsequent campaign, then as seen previously in Figure 2.2.2, the pileup distribution for each year of data-taking has also evolved and increased. For MC16a, this has averaged around 25 interactions, MC16d with 38 interactions and MC16e with 36 interactions per bunch-crossing, all with very different shapes of profile. Thus for these reasons also, the MC generation campaigns must be divided in this way per-year during reconstruction, in order to account for the different pileup distributions. However, it is overall difficult to accurately predict the effect of pileup interactions in MC simulation, especially on a per-sample basis. As such, it is common in downstream analyses to correct for these interactions per MC sample through the use of a *Pileup Reweighting* (PRW) tool. This tool makes use of configuration files generated per MC sample (initially by the analysis and therefore very often by the author, but later made centrally available), to consider the pileup and luminosity information in each campaign and correct the baseline pileup model for that physics process. The luminosity information per-lumiblock is also able to account for the good quality data by which the MC should be reweighted, when taking into account the GRL for that year of data-taking.

3.3 Data processing

For the sake of brevity throughout the remainder of this chapter, *data* will refer to both the collision data recorded by the detector and the generated MC simulation, since they share similar software formats and will be processed in the same way, unless where otherwise stated.

3.3.1 Derived format reduction

As mentioned in Section 3.1, AODs are generally too large a file format to process for physics analyses. In practice, the widely varying analyses studying the data from ATLAS will usually focus on a smaller subset of events and their information stored relevant to their physics involved. As such, a storage model is currently adopted for Run-2, and strongly recommended for analyses to use, which divides the AODs into smaller formats known as DAODs (*Derived AOD*), typically reducing the size to an order of TB and take around a month to process. A visualisation of this reduction workflow is represented by Figure 3.3.1.

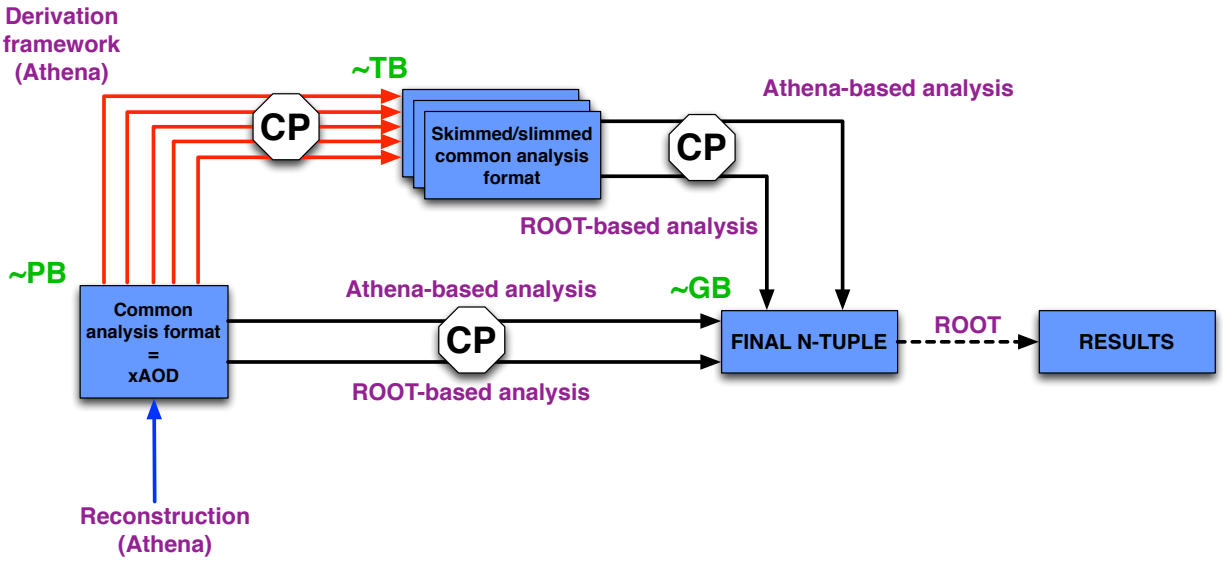

Figure 3.3.1: A typical ATLAS analysis workflow for data size reduction adopted for Run-2 [37].

There are ∼100 subsets of DAOD separated out for different physics contents. For example, these are labelled such as `DAOD_TAUX` for tau lepton-based analyses or `DAOD_HIGGX` for Higgs boson-based analyses, along with further divisions of physics where represented by the `X` (specific examples of these will be discussed for the analyses in Chapters 4 and 5).

These DAODs remove information in three different ways, depending on how they are relevant to that analysis (with mock examples described in the context of `DAOD_TAUX`): entire events are *skimmed* (e.g. those which contain no tau leptons), physics objects from events are *thinned* (e.g. not interested in photons), and properties from objects are *slimmed* (e.g. not interested in raw detector track and hit variables).

However, reducing the file size is not the only objective for DAODs, as they also serve as an opportunity to *augment* the data. This can take form in a number of ways: a chance to calculate and include additional physics information that analyses may find useful (e.g. calculating and storing the invariant mass for pairs of tau leptons), apply any technical corrections for issues found with the original AOD format as an *AODFix* without having to reproduce them from scratch, or other forms of recommended physical corrections and calibrations for individual objects.

In the case of the latter, these calibrations are studied by dedicated groups for each physics object known as *Combined Performance* (CP). These groups strive to improve upon the quality and efficiency of reconstructing their object of focus. For instance, more will be discussed specifically on tau lepton CP later in Chapter 4.

Until now, several instances of different software-based objectives and workflows have been discussed. In summary, these have included the HLT decision system, AOD object reconstruction, MC simulation, DAOD size reduction and augmentation with the application of CP-recommended calibrations. But achieving all of these goals are in fact enabled by the core of ATLAS software: the *Athena* framework, divided into multiple tools each responsible for these different objectives. It is also from this framework that analyses would often base their software on, as will be discussed throughout the following sections.

3.3.2 Analysis format reduction

Once centrally available, the typical ATLAS analysis begins with processing the DAODs, but how exactly they intend to do this does widely vary and is completely optional. For instance, many analyses may still find that the DAOD format is still too large and slow to process, so they wish to further reduce the size. Others also find that the *Event Data Model* (EDM) within these AOD-based formats, which structures the objects into vector-based containers, is too complex and difficult to access [39]. One method which will be used frequently in this thesis was mentioned in Figure 3.3.1, where the DAODs are processed into a final analysis input format known as an *Ntuple*. These Ntuples are still ROOT-based formats but exhibit a flat vector-less structure, where the stored event and object information are non-abstract and so trivially accessible. Since this serves as an opportunity for an analysis to constrain their format to just the information needed for their personal physics criteria, Ntuples are capable of reducing the size to the order of GB and usually take a week to process depending on the complexity, making them very easy to store and process quickly in a downstream analysis' software.

This additional step after DAODs, be they Ntuples or other, also allows freedom for analyses to augment their format with any specific properties and calculations they may require. It is also commonplace that further CP recommendations and corrections are to be applied, especially since they are regularly updated and so analyses need a rapid response time to include them, usually on the order of once a month. The application of these CP recommendations are usually provided through Athena as individual tools which can be imported through a standalone *AnalysisBase* library. But the post-DAOD software themselves are usually independently-written and varying at this stage.

In this thesis, much of the author's analysis work involves the use of the Ntuple-producing *xTauFramework* (xTFW) software [40]. Here the xTFW imports AnalysisBase and runs in a pure ROOT environment known as *EventLoop*, providing a common engine to process DAOD events with ease. As the name suggests, the xTFW is used extensively by several tau lepton-related analyses, including various SM physics studies. For the author, this is deployed for the analyses in this thesis which will be discussed with more detail in Chapters 4 for Tau CP and 5 for the BSM search. In general, the author's contributions would involve regularly producing, developing and testing the Ntuples for these analyses, which usually include: applying and tuning selection criteria to skim events, augmenting the output with custom variables of interest or slimming those which are not, investigating and applying the CP recommendations, including pileup corrections for MC estimation, and calculating their systematic uncertainties. To achieve many of these objectives, the xTFW allows individual analyses to use freely-configurable options to steer hundreds of individual parameters as they wish. Otherwise users are free to write their own EventLoop code within the xTFW for processing their analysis.

Beyond the specific analysis applications, the author was also a joint project responsible and maintainer for the xTFW: overseeing and reviewing all developments both generic and analysis-specific, as well as working on technical software and performance improvements, some of which will also be discussed later in Sections 3.4.2 and 4.

3.4 Software management

3.4.1 Computing resources

For the author and many others affiliated with CERN, typical computing work involves the use of dedicated desktops, often via remotely, with Linux-based *operating systems* (OS) installed and usually through a *Command Line Interface* (CLI). Initially, *Scientific Linux 6* was CERN's primary choice of OS, until 2019 when this was migrated to the more modern *CentOS 7* distribution, which also required some validation work by the author on numeral software frameworks, such as the xTFW, to ensure a continued operation. These desktops were provided by both TUoS' HEP group and CERN's LXPLUS, and usually have enough resources for most post-Ntuple analysis processing, plotting and other general work. However, there are often occasions where additional computational power is needed, so computer clusters formed by these services (scheduled by HTCondor) are available to tackle the problem through the division and parallelisation of the workload.

But in the cases of Ntuple processing with the xTFW, upstream AOD-based formatting and MC generation, increased processing power and storage space are necessary to handle the large number of events contained on the order of millions. For these large-scale purposes, jobs can be submitted to the *Worldwide LHC Computing Grid* (WLCG), a network of computer clusters and dedicated nodes stationed all around the world [41]. The WLCG is a collaboration of over 170 institutes in 40 countries [42], contributing over 800,000 CPU cores and storage for over 300 PB of data [43].

Each site of the WLCG is allocated a tier representing their available resources and priority for usage, as shown in Figure 3.4.1, split into three major levels: a single Tier-0 computing centre located within CERN for the processing and storage of the initial raw data and the highest-level reconstruction such as with AODs, 13 Tier-1 typically *High-Performance Computing* (HPC) clusters for the subsequent reprocessing at large scales such as with DAODs, and the remaining ∼160 Tier-2 institute computing clusters for common analysis work such as with Ntuple productions.

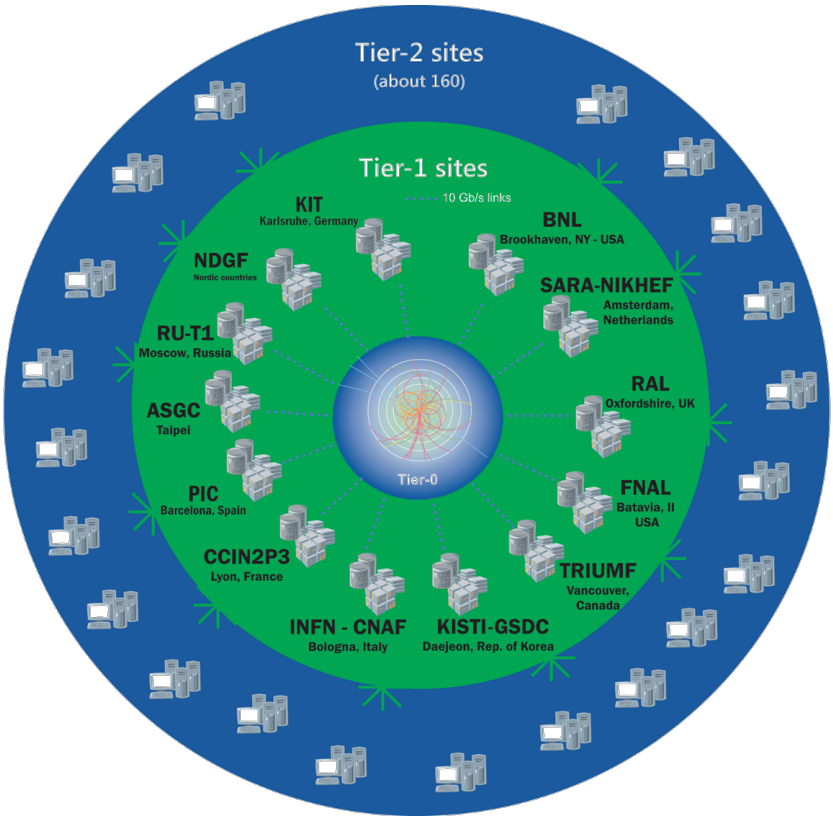

Figure 3.4.1: A diagram representing the three-tier site system of the WLCG with Tier-1 site names and locations [43].

The author made regular use of the WLCG when it came to submission of the xTFW for processing Ntuples, adopting official production roles for both the Higgs physics and Tau CP groups. For example, as illustrated by Figure 3.4.2, when a task is submitted, a compressed copy of the xTFW source code as pre-compiled libraries is uploaded to multiple allocated sites on the WLCG where the input DAOD is available for each divided sample. A build job will unpack the uploaded software which is then temporarily stored onto the site. From there, the software will run on the sample, looping over all events available as the xTFW would locally. Once complete, the resulting output Ntuple will be stored on the WLCG for approximately two weeks, where it can be downloaded locally to a workspace, usually shared, via a *Distributed Data Management* (DDM) system [38], ready for further post-Ntuple analysis.

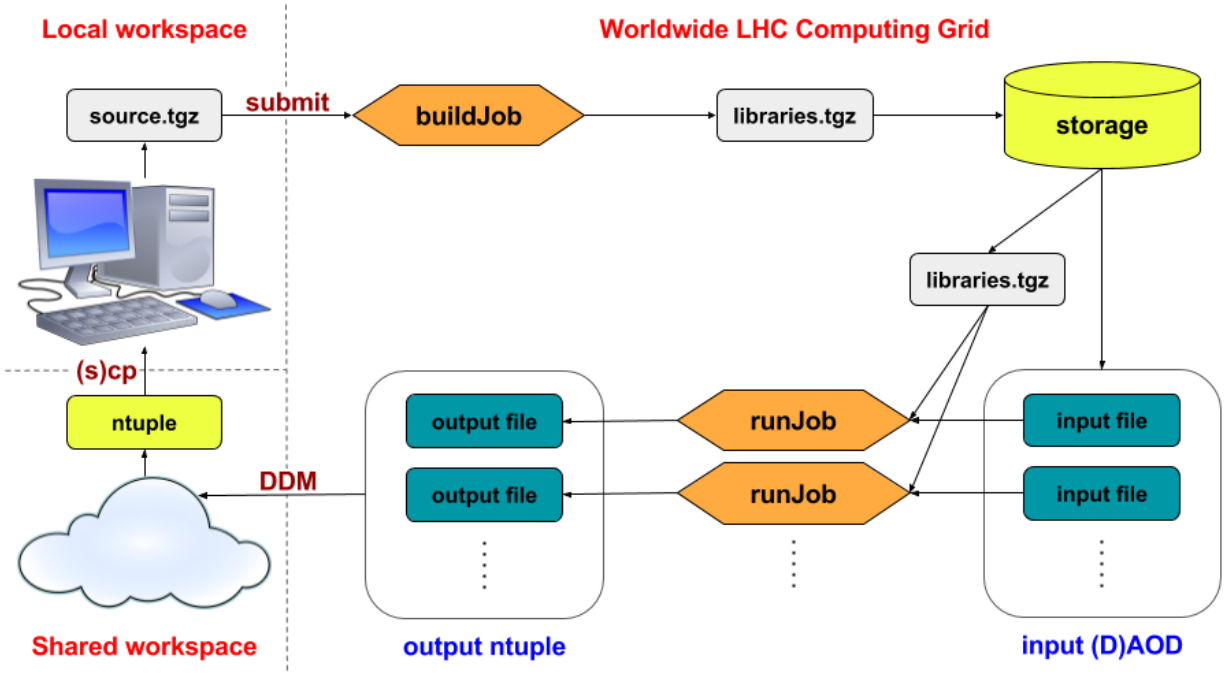

Figure 3.4.2: A schematic visualising the workflow of a job submission to the WLCG.

During this process, it was also the author's responsibility to test the framework, both locally and on the WLCG, as well as monitor and resubmit tasks as necessary, whilst resolving any transient problems that are occasionally encountered specifically with the WLCG. These challenges include manually allocating memory and processing power for each task, replicating the input data across sites to ensure availability, and quickly responding to site outages and malfunctions. The author managed and verified the download of the Ntuples to a shared storage space, carefully observing quota limitations when keeping a history of Ntuples.

3.4.2 Analysis preservation

As with any software in general, with focus on those in ATLAS such as Athena and the xTFW, it's important for the codebase to be saved and protected from loss. As this is a collaborative effort, it helps to be able to communicate and share software developments with colleagues whilst reviewing and documenting changes. For these reasons, implementing a *version control system* (VCS) is essential to everyday software operation, and has evolved at CERN during Run-2. Prior to 2017, CERN utilised the *Apache Subversion* (SVN) VCS supported by the *Trac* [44] web service. This choice was later restructured around using *Git* as the primary VCS, alongside the *GitLab* [45] web service as its hosting environment, due to common criticisms about the lack of user flexibility and review control in SVN/Trac which GitLab resolved. This also involved work by the author to ensure a smooth transition of existing software repositories, such as the xTFW, between the two VCSs.

Using a web-based VCS enables individual physics analyses to control and label how their software is used, especially when producing and publishing their results. This leads towards an elegant solution for a critical problem that has generally been facing modern science — can those results be reproduced, and can they be re-analysed differently? This is the philosophy behind *analysis preservation* (AP), an effort CERN has greatly accelerated during Run-2. For instance, Git offers the ability to tag a specific point in history of a software repository, allowing for the exact codebase as used to calculate the results published by an analysis to be retrieved indefinitely, as well as enabling the opportunity for it to be reprocessed and further modified in additional studies.

However, while a useful feature for productivity, using a VCS with a tagged history alone does not provide a full solution for attempting to indefinitely preserve an analysis. The code itself usually requires dependencies on the computing environment it is run on, as those mentioned in Section 3.4.1. Naturally, computers and their software will update with time for standard security and performance reasons, meaning that such a task of recalculating the results a few years from the design of that codebase will likely become incompatible with a future system, either by introducing a variety of inconsistencies with the original results or perhaps even completely unable to execute the software. In order to resolve this problem, the compiled analysis codebase should be packaged with all of its dependencies, as would be used at the time of its original execution. This practice is commonly referred to as *containerisation*. This ensures that the analysis software would be independent of the system it is run on, and the interfacing is handled globally by the container platform instead. This guarantees a long-term solution for preserving the analysis, or simply allowing the freedom to be able to deploy the software immediately on any system without a rigorous overhead pre-configuration. For these goals, CERN uses the *Docker* [46] containerisation platform.

In the case of the author's work, adoption of the modern VCS and containerisation strategies have appeared in all aspects of this thesis, where it was particularly beneficial for preserving the BSM search analysis as to be discussed in Chapter 5. Predominantly, the author invested the most AP-related time introducing this system fully into the xTFW, since it is used to produce the Ntuples for the aforementioned analysis, as well as for the benefit of many others. As already established in Section 3.3.2, the xTFW requires a ROOT-based environment with the AnalysisBase libraries and CP calibration files. Since most of these requirements are common to many analyses in ATLAS, a container for AnalysisBase and all of these tooling have already been generated and centrally provided for each Athena release. Using the containerisation software, the compiled xTFW is simply packaged on top of the AnalysisBase container, ready to be deployed on any system. Combined with similar containerisation efforts for software in the rest of the analysis chain, this leads to the long-term preservation and full reproducibility of the BSM search analysis.

In the ideal scenario, the software taken from any point in time should be preserved so that it may allow for freedom when re-investigating the analysis. However this would require constant compilation and generation of the containers which can be arduous and time consuming. The GitLab web service offers a solution to automate this procedure through the use of a *Continuous Integration and Continuous Deployment* (CI/CD) pipeline. The CI/CD can be instructed to run a series of jobs through a progressively-staged pipeline as each previous job successfully completes. These jobs are automatically launched on the web server onto a runner node for every change committed to the software base. For instance, this was deployed by the author for use in the xTFW, with an example pipeline shown in Figure 3.4.3. The framework is automatically compiled through its own local scripts — this in itself provides a form of confirmation testing that the software should be operational. When the software has successfully compiled, the pipeline is instructed to package the result into a container, and publish it to an online registry where they can be accessed indefinitely.

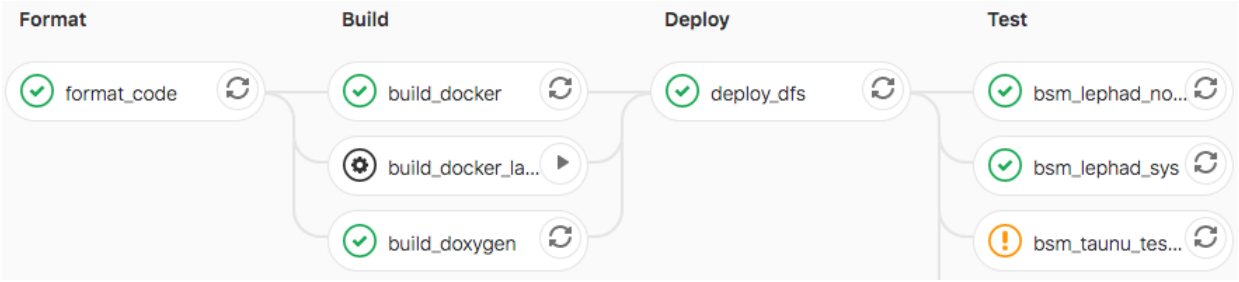

Figure 3.4.3: An example of a CI pipeline web interface automatically running on the xTFW, with individual jobs organised into progressive stages, those mostly passing marked with a green tick where others return warnings marked with an orange exclamation.

In addition to automating this AP construction, the CI/CD was also deployed onto the xTFW pipeline to format the code before it is compiled, in order to adhere to coding style standards through the use of industry tooling such as *clang-format* [47] for C++ and *YAPF* [48] for Python code formatting. It is also used to automatically compile and publish documentation of the code onto a website written through the *Doxygen* [49] software.

However, with particular focus on the final stage of the pipeline, where the author had spent a significant time developing, the container is loaded for system *Run-Time Testing* (RTT) for each available analysis configured on the xTFW. This is enabled through a sub-package within the framework which can also be executed locally, as a means to run through an analysis over a small subset of events, within a fixed set of input samples obtained from a remote server, in order test and confirm whether a full execution would succeed. Not only does this allow users to easily check the functionality of their analysis while in development, and without the need to handle large input files themselves, but also provides an opportunity on the CI/CD to confirm that their analyses would continue to successfully operate when any changes have been committed to the framework. This helps to ensure a robust operation of the software for all analyses and quickly address problems so that time can be spent more efficiently elsewhere.

3.5 Athena Release 21 development

The Athena software framework is versioned into major releases. In 2016, near the start of Run-2, the Athena version used by the author was *Release 20.7* (R20), until 2017, around halfway through Run-2, when it was upgraded to *Release 21.2* (R21), and used until the end of Run-2 and beyond. This upgrade meant several significant changes to both the software and the physics behind the results for all analyses in ATLAS.

From the software perspective, this coincided with the migration from the SVN to Git VCS discussed in Section 3.4.2. This also meant a change in the build and compilation system that would have been used to construct all software in ATLAS, such as the xTFW — this involved a migration from using ATLAS' own *RootCore* [50] build system to a more commercially-available one known as *CMake* [51], enabling longer-term support for the software.

As these migrations take place, then in order to continue with the author's studies, such as those in Section 4.3.2 for Tau CP and the BSM search analysis to be discussed in Chapter 5, the author had spent significant development time in completing these essential migrations, particularly for the xTFW and the downstream analysis software. This involved ensuring that the software continues to be able to compile with the new build systems and tooling, accounting for any changes to the EDM and DAOD structure that the new Athena release had introduced, while scrutinising the differences in the results, all as part of an ATLAS-wide effort.

But the most significant importance of the new Athena release were the improvements from the physics perspective. The new Athena release meant substantial improvements to reconstruction for MC simulation, especially in accounting for the variations in the pileup distribution, and increasing dataset sizes, for each passing year of data-taking in Run-2, as well as methods and techniques used across all CP groups and tools. For example, this would have included significant improvements to tau lepton identification algorithms by the Tau CP group, to be discussed in more detail in Section 4.2.

As a consequence of these upgrades to the new Athena R21, the results shown for BSM search analysis in Chapter 5 would have greatly benefited from them. For instance, Athena R21 introduced improvements which rivals that of what would have been expected from the just increase in integrated luminosity alone, to $139\,\text{fb}^{-1}$, from the time of the partial Run-2 dataset available, at $\sim 36\,\text{fb}^{-1}$, used with Athena R20. The significance of this improvement will be highlighted in more detail in Section 5.5.

Chapter 4: Tau Combined Performance

As introduced in Section 3.3.1, the ATLAS collaboration devolves calibration studies on each particle type into *Combined Performance* (CP) groups. This chapter will specifically focus on the techniques used by the Tau CP group for the study of tau leptons, as well as highlighting where the author contributed to this process, particularly around developing electron rejection algorithms and deriving their corrections. These studies aim to ensure a good modelling of tau leptons so that they may be used effectively by downstream physics analyses interested in them, such as the BSM search analysis relevant to this thesis which will be later discussed in Chapter 5.

The tau lepton (τ^-) is a third-generation fermion with a mass of 1776.86 MeV/c^2 and mean lifetime of 290.3 fs [52] (corresponding to a relativistic decay length of 2.449 mm for a typical 50 GeV tau). While the tau may decay into its lighter lepton (ℓ^-) generations, the electron (e^-) and the muon (μ^-), it is also unique in that it is massive enough to also decay into hadrons ($h^{0,\pm}$), all through a W^- boson. Table 4.0.1 demonstrates some of the primary decay modes for the tau expressed as *Branching Ratios* (BR), revealing that a majority of ∼65 % decay hadronically (τ_{had}), while the remaining ∼35 % decay leptonically (τ_{lep}).

Decay mode ($\tau^- \to$)	NpXn	BR (%)
$\ell^-\bar{\nu}_e + \nu_\tau$	0p0n	∼35
$e^-\bar{\nu}_e + \nu_\tau$	0p0n	17.39
$\mu^-\bar{\nu}_\mu + \nu_\tau$	0p0n	17.82
$h^- + \nu_\tau$	1p0n	11.51
$\pi^- + \nu_\tau$	1p0n	10.82
$K^- + \nu_\tau$	1p0n	0.696
$\pi^- + \pi^0 + \nu_\tau$	1p1n	25.49
$\pi^- + \pi^0\pi^0 + \nu_\tau$	1p2n	9.26
$\pi^- + \pi^0\pi^0\pi^0 + \nu_\tau$	1p3n	1.04
$\pi^-\pi^+\pi^- + \nu_\tau$	3p0n	8.99
$\pi^-\pi^+\pi^- + \pi^0 + \nu_\tau$	3p1n	2.74
$\pi^-\pi^+\pi^- + \pi^0\pi^0 + \nu_\tau$	3p2n	0.1

Table 4.0.1: Summary of the most prominent tau lepton decay modes, expressed in the NpXn hadronic labelling scheme (see text for details) with their branching ratios in percent [52].

Leptonic tau decays assume lepton universality, such that they should be evenly split between electrons and muons around ∼17.5 % each. In order to preserve lepton flavour conservation, all tau decays will produce tau neutrinos (ν_τ), while leptonic decays will include additional electron ($\bar{\nu}_e$) or muon ($\bar{\nu}_\mu$) anti-neutrinos. However, since neutrinos are invisible to the ATLAS detector, these will certainly result in an overall $E_{\text{T}}^{\text{miss}}$ component, especially for leptonic decays.

The majority of the hadronic daughters are pions ($\pi^{0,\pm}$) (∼94 % of $h^{0,\pm}$) with a smaller amount of kaons ($K^{0,\pm}$) (∼6 %). In order to conserve charge, the tau may only decay into an odd number N of charged hadrons, where mainly either $N = 1$ (∼77 % of N) or 3 (∼23 %). Since these charged particles will be seen as tracks within the InDet, these are commonly referred to as "N-prong" decays (Np). However, tau decays may also include any additional number X of neutral hadrons (Xn) if any at all, since they have no constraint by charge nor will be visible to the InDet. The most dominant modes are $X = 1$ for 1-prong decays (∼55 % of X) and $X = 0$ for 3-prong decays (∼76 %). In total, this forms a common simplified hadronic decay labelling scheme for stating the number of charged and neutral daughters, NpXn.

The most common tau decay mode is therefore the hadronic 1p1n with pions (25.49 %). It is assumed that all anti-tau (τ^+) decays and BRs are identical when conjugating the daughters' charges and lepton numbers appropriately for anti-particles. As such, any further notation of $\tau^\pm$ will be simplified to τ in this thesis.

The Tau CP group partly specialises in improving *hadronic* tau reconstruction, in developing identification and rejection algorithms, and calibrating the tau energy against the Calo [53]. The primary focus on studying hadronic taus comes as a result of the more complex nature of hadronic decays, presenting a larger challenge for accurately delivering calibrations, as well as distinguishing them from other sources of hadronic processes [53]. In comparison, the leptonic tau decays are generally considered simpler to identify from the reconstruction of their constituent lighter leptons, and therefore these calibrations are deferred to the their own responsible CP groups (Electron/Photon (e/γ) CP and Muon CP, respectively).

Some of the software tools developed by the Tau CP group will be introduced, since they play an essential role in delivering these calibrations and recommendations. As already introduced in Section 3.3.2, this will also endorse the use of the xTFW, and while the author's contribution in generally maintaining the xTFW have been discussed, further production of Ntuples and analysing them on behalf of the Tau CP group will also form a key part of the author's electron rejection algorithm studies which will be discussed later in this section.

4.1 Tau reconstruction and energy scale calibration

Since taus are relatively short-lived compared to lighter leptons, only their reconstructed decay products are visible to the detector, and therefore commonly denoted in ATLAS as $\tau_{\text{had-vis}}$ for hadronic taus. A hadronic tau candidate can be detected from charged tracks found within the InDet and energy deposits in the Calo. The hadronic tau decay acts as the seed for producing an expanding jet of hadrons. In ATLAS, all forms of jets, whether they are sourced from hadronic taus or other processes, are reconstructed within cones. Figure 4.1.1 illustrates the cone for an example hadronic tau-jet decaying into several pions.

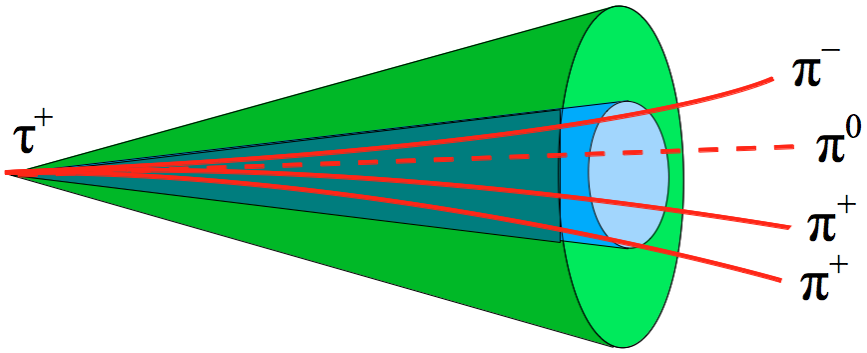

Figure 4.1.1: Visualisation of an example hadronic tau decaying into a conical jet formed from pions (3p1n), separated into the core (inner) and isolation (outer) regions [54].

All standard jets are reconstructed using the anti-k_t algorithm [55], with a conical radius of $\Delta R = 0.4$ in the $\eta - \phi$ transverse plane. The hadronic tau candidate is required to have a $p_{\mathrm{T}} > 10\,\mathrm{GeV}$ and found wholly within the InDet ($|\eta| < 2.5$), excluding the gap between the TileCal and the FCal ($1.37 < |\eta| < 1.52$). The vertex of this tau-jet is chosen from the vertex of the track with the largest momentum within that jet, for tracks with a significant length and $p_{\mathrm{T}} > 1\,\mathrm{GeV}$. Tracks found within the cone of a hadronic tau candidate are divided into a core ($0 < \Delta R < 0.2$) and an isolation ($0.2 < \Delta R < 0.4$) region. The direction of the tau-jet is calculated from the vector sum of visible tracks within the core region. Additional hadronic tau candidates or other objects found to be geometrically overlapping within the isolation region are rejected.

Calibrating the energy scale of all reconstructed jets must be derived with respect to the deposition measured in the Calo. A *tau energy scale* (TES) is specifically associated for hadronic taus, but in order to do so, the mass of the tau candidate is first defined to be zero, such that the transverse momentum and energy are equivalent. The true TES is then extracted and calibrated by comparing the measured energy deposition by the tau-jet with the average energy from the sum of its hadronic decay products as predicted in MC simulation.

4.2 Tau identification and machine learning techniques

The most dominant background to hadronic taus are jets initiated from other quark and gluon processes. In order to *identify* (ID, not to be confused with the InDet) which reconstructed objects are hadronic taus, *machine learning* (ML) techniques are used to train algorithms which will quantify the tau ID significance on each reconstructed object.

The resulting tau ID algorithm is usually classified into two parameters: efficiency and rejection. Efficiency represents the fraction of hadronic tau candidates which are reconstructed as $\tau_{\text{had-vis}}$ and pass the requirements of the ID algorithm (true positive) [56]. Likewise, rejection then corresponds to the inverse of the efficiency of the algorithm for incorrectly identifying the background as a hadronic tau (false positive). As a result, efficiency would be proportional to the quantity of the hadronic tau signal leftover by a selection criterion, while rejection would be proportional to the amount of background that is removed. Therefore, in an ideal situation, one would prefer to keep as much signal statistics and thus as high efficiency as possible, along with the smallest background and so maximum rejection. However, in practice, the relationship between efficiency and rejection can be described by the inverse of a *receiver operating characteristic* (ROC) curve (rejection against efficiency) [57], examples of which will be seen from the results to be discussed in Figure 4.3.1. This means that an increase in efficiency would lead to a decrease in rejection, and vice versa.

As such, when requiring a selection criterion based on the tau ID algorithm's parameters, compromises must be made per-analysis as to whether they prefer a higher efficiency, a higher rejection or anywhere in between. To meet this demand, a *working point* (WP) classification scheme is provided by the Tau CP group to pre-define specifically recommended values of efficiency and rejection across the ROC curve, where individual analyses would then decide which WP they prefer to use in their selection (or vetoing) criteria. Commonly in ATLAS, these WPs are labelled in range from *loose* to *medium* to *tight*, each corresponding to a decreasing level of efficiency and with increasing rejection, with efficiency values to be given as a result of these studies in Table 4.2.1, differently for 1- and 3-prong tau decays. For example, low-statistics analyses may prefer choosing a looser WP over a tighter one, if they could not afford to reject that many events. This WP approach is not unique to the Tau CP group, and is used in classifying all object types in ATLAS by each of their respective CP groups — the ID algorithm techniques however may vary.

Throughout Run-2, ML techniques have been used to train algorithms for tau ID. Until 2020, a *Boosted Decision Tree* (BDT) [58][59] was the chosen method of ML for achieving this goal [53]. They were later replaced with an alternative technique known as a *Recurrent Neural Network* (RNN) [60]. These BDT algorithms were trained using MC simulated samples of Drell-Yan $Z/\gamma^* \to \tau\tau$ processes acting as the signal, against di-jet processes observed in the recorded data serving as the background. The training was performed separately for 1 and 3-prong tau candidates.

BDTs are trained on the principle of a *multivariate analysis* (MVA) [61], where some multitude of input kinematic variables are used to discriminate the tau signal from the background, and often different choices of variables for 1- and 3-prong decays. The learning trials decisions based on each variable consecutively to form a tree structure and derives weightings based on their effectiveness. The process is repeated through numeral trees in succession to boost the decision accuracy. The resulting algorithm efficiency is independent of the transverse momentum of the tau, as well as the pileup distribution. The signal efficiency values for each recommended WP derived from the BDT training for 1 and 3-prong taus are provided in Table 4.2.1. The factor of background rejection increases with the tighter WPs, but the value will depend on how much background is available in the analysis it is applied to (an example will be discussed in the BSM analysis in Chapter 5).

N-prong tau	1-prong			3-prong		
Working point	Loose	Medium	Tight	Loose	Medium	Tight
Efficiency (%)	60	55	45	50	40	30

Table 4.2.1: Signal efficiencies for tau ID derived from a BDT-trained algorithm, for each recommended working point, for 1 and 3-prong taus [53].

4.3 Electron rejection

A second background to hadronic taus are electrons which may be misidentified as a tau candidate by the ID algorithms. This section will discuss the progression of techniques used to combat against these misidentifications and how the Tau CP group delivers the resulting corrections, especially in detail where the author had contributed towards this effort. As such, this concept of electron rejection and the study behind it is commonly referred to as *eVeto*. However, the significance of this background does widely vary as it depends on each individual analyses' selection criteria. But in the case of this thesis, the eVeto contribution will be important to the BSM analysis to be discussed in Chapter 5.

The eVeto study is divided into two components in this thesis: firstly, additional algorithms are developed, similarly to those from the previous Section 4.2, dedicated to rejecting the misidentified electrons from the selection. The following section will discuss some of the modern developments to these algorithms during Run-2 where the author was briefly involved.

Secondly, where these rejection algorithms are then applied in practice, a global normalisation mismatch between the recorded data and MC simulation is observed. In order to correct for this, a *scale factor* (SF) is calculated and applied to the MC to ensure that it agrees well with the data. For the major part of this section, the author contributed to the analysis behind this SF study.

4.3.1 Algorithm training

Until 2017, approximately halfway through Run-2, the eVeto was initially modelled by a non-ML-based *log-likelihood* (LLH) technique [56], separating the true tau signal from the misidentified electron background. However, with an aim to improve upon its performance, a BDT method was preferred and offered an increased rejection which will be discussed in this section. Likewise, the BDT was used for eVeto until 2020, at the end of Run-2, when it was then superseded by an RNN [60]. In order to differentiate these eVeto techniques from their ID equivalents, they will be referred to as eLLH, eBDT and eRNN, respectively.

To begin the eBDT training, MC samples of $\gamma^* \to \tau\tau$ are used as the tau signal, while $Z \to ee$ at low mass and increasing mass-slices of $Z/\gamma^* \to ee$ processes are used for the electron background. The samples are sourced from a reduced AOD-based format known as a *Mini AOD* (M(x)AOD), generated as an alternative to DAODs, customised specifically for the Tau CP group's purposes, although otherwise very similar. The MxAODs are generated by the group's own developed *Tau Harmonisation and Optimisation Resources* (THOR) software framework, and reduce the file size to an order of GB (much smaller than the usual DAOD, and more comparable to an Ntuple size). THOR produces output MxAODs divided into various streams, each used by many of the different studies investigated by the Tau CP group, including the TES and ID training.

The sample inputs were taken from THOR's *Main* stream and used in tandem with another software framework, *Lots Of Kewl Images* (LOKI), designed for training the eBDTs and creating the performance plots to validate them, which is where the author was briefly involved. LOKI tunes the eBDT across different regions of η (in the barrel (*Bar*) for $|\eta| < 1.37$, within the inner end-caps (*End1*) between $1.37 < |\eta| < 2.00$ and the outer end-caps (*End23*) for $|\eta| > 2.0$) and provides a range of eVeto WPs with 75% (tight), 85% (medium) and 95% (loose) tau signal efficiency (and therefore decreasing electron rejection). Figure 4.3.1 demonstrates the performance results of the eBDT training as plotted by LOKI. It is clear from the ROC curves that the newest eBDT algorithm globally outperforms the eLLH rejection, while increasing the minimum accepted efficiency.

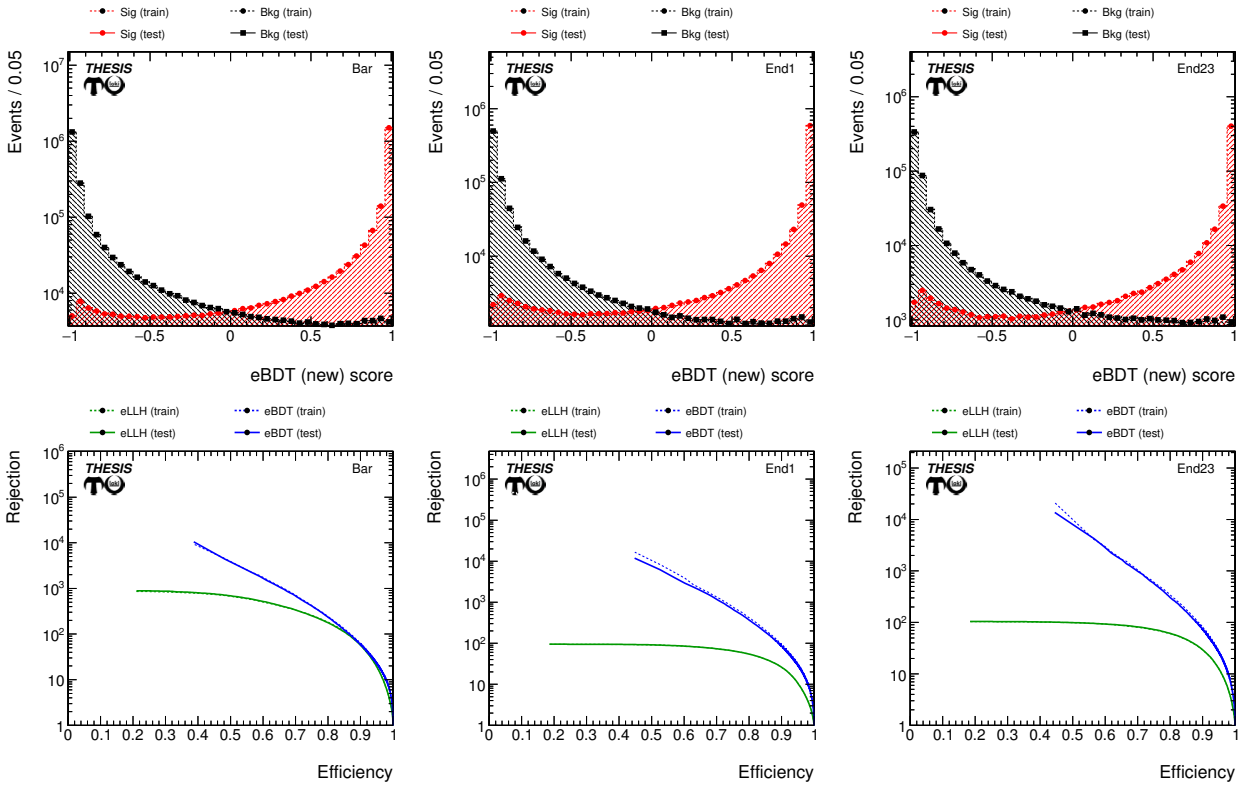

Figure 4.3.1: Performance plots of the new eBDT trained by LOKI, across each region of η from left to right (*Bar*: $|\eta| < 1.37$, *End1*: $1.37 < |\eta| < 2.00$, *End23*: $|\eta| > 2.0$). The upper plots show the scores on the new eBDT algorithm separating clearly between the tau signal (sig) and electron background (bkg), while comparing the behaviours of the training and testing datasets. The lower plots show the inverse ROC curves for each algorithm under scrutiny: these include the original eLLH and the new eBDT as trialled by the author.

The eBDT results are extracted from LOKI as XML-based calibration weight files and applied in augmentation during the creation of DAODs, which will be used by analyses and further investigated in the following Section 4.3.2.

4.3.2 Scale factor measurements

As introduced in Section 4.3, when the eVeto rejection algorithms are applied to an analysis in practice, it is often found that there is a normalisation disagreement between the recorded data and MC simulation, despite being treated equally and identically in both datasets. Examples of this difference will be presented in the following sections. In order to correct for this, the Tau CP group derives a SF to be applied to the MC which would account for the difference. In reality, the application of SFs are not unique to the Tau CP group and are in fact commonplace in ATLAS, as it is often encountered where MC would disagree with the data in a fashion similar to this — such is the nature of simulation.

For the eVeto, the SF is calculated as the ratio of electron rejection efficiencies, ε, between data and MC, as given by Equation 4.3.1:

$$\mathrm{SF} = \frac{\varepsilon_{\mathrm{data}}}{\varepsilon_{\mathrm{MC}}} \tag{4.3.1}$$

Event selection

The eVeto analysis samples are based on the DAOD_TAUP1 derivation, designed to contain only events and preliminary calibrations relevant to Tau CP-related studies (this way, the eVeto algorithm can be trialled before distributed to the rest of the general physics analysis derivations). In the case of this sub-derivation, the processes are modelled by a di-tau production, where one tau decays hadronically and the other leptonically, specifically to electrons ($\tau_{\mathrm{e}}\tau_{\mathrm{had}}$).

The eVeto derivations are processed regularly through the xTFW into Ntuples by the author, where they will then be provided as inputs to an informal analysis software previously created solely for this study named *Zeescalation* (which has since been deprecated for other more commonly used frameworks). At the time of this study, the results will include only the 2015 and 2016 years of Run-2 operation, amounting to $\sim$36 fb^{-1} of integrated luminosity.

The efficiencies are measured in a *tag-and-probe* analysis, where the effect of electrons produced in a $Z \to ee$ process being misidentified as hadronic taus can be studied in detail. This means that such a real electron expected from a τ_{e} signal is *tagged* with stringent requirements, so that the τ_{had} can be *probed* for electron misidentification from this dominant $Z \to ee$ background. Events are selected to contain at least one electron and one hadronic tau. The tagged leading-p_{T} electron is critically selected to have $p_{\mathrm{T}} > 25$ GeV, be isolated and pass a tight ID requirement. The probed leading-p_{T} hadronic tau is only required to meet a $p_{\mathrm{T}} > 20$ GeV criterion, although the SF will be estimated individually with all available tau ID WPs applied. Both are required to reside within $|\eta| < 2.47$, excluding the crack between $1.37 < |\eta| < 1.52$. Any events containing muons or bottom quark-initiated jets are excluded. While there has been some desire for 3-prong tau corrections, the eVeto study has only focused on delivering recommendations for 1-prong taus as these suffer the most.

A *signal region* (SR) for electron-misidentified taus is defined to further enrich the $Z \to ee$ process (Z-SR). The tag electron is additionally required to have a more stringent $p_{\mathrm{T}} > 30\,\mathrm{GeV}$, while the invariant mass of the tag electron and probe tau must be within a window of the Z mass peak, between 80 to 100 GeV. The *transverse mass*, m_{T}, between the electron and $E_{\mathrm{T}}^{\mathrm{miss}}$ must also be $< 40\,\mathrm{GeV}$ in order to suppress the contribution from W+jets processes, where m_{T} is given generally for some lepton ℓ by Equation 4.3.2.

$$m_{\mathrm{T}}(\mathbf{p}_{\mathrm{T}}{}^{\ell}, \mathbf{E}_{\mathrm{T}}^{\mathrm{miss}}) = \sqrt{2p_{\mathrm{T}}^{\ell} E_{\mathrm{T}}^{\mathrm{miss}}[1 - \cos\Delta\phi(\mathbf{p}_{\mathrm{T}}{}^{\ell}, \mathbf{E}_{\mathrm{T}}^{\mathrm{miss}})]} \tag{4.3.2}$$

Within this Z-SR, the efficiency for electron rejection can be calculated as the ratio of included events after passing the eVeto algorithm over the total number of events, as given by Equation 4.3.3. The Z-SR is then divided into its *numerator* component for the rejection algorithm under study (Z-SR-numer) and its *denominator* serving as a validation region where its modelling can be investigated before applying the eVeto (Z-SR-denom). SFs will be derived for all available eVeto algorithms, including the eLLH, each WP of the eBDT and combinations of both.

$$\varepsilon = \frac{\text{Z-SR events, pass eVeto}}{\text{all Z-SR events}} \tag{4.3.3}$$

Background estimation

In practice, the Z-SR is not composed purely of $Z \to ee$ events and contains other significant background processes which cannot be reduced and so continue to affect its modelling ability. These backgrounds mainly include events from multi-jet and W+jets processes. In order to constrain the modelling of these two backgrounds, *control regions* (CR) are invented to enrich each of these processes and derive any necessary corrections from them which will need to be applied back to the Z-SR, typically as a normalisation weighting factor. In both CRs, no more than a single electron is required in the event, and the invariant mass is instead required to avoid the Z mass peak with a selection $< 80\,\mathrm{GeV}$. Other smaller backgrounds and irreducible signals include events from $Z \to \tau\tau$ and top quark processes as estimated by MC, as well as a contribution from events where the tag electron and probe tau have the *same sign* of charge (SS), in contrast to having *opposite sign* (OS) as would usually be expected from di-object production.

For multi-jet (or QCD) processes, a Q-CR is defined with an inverted tag electron anti-isolation requirement. A normalisation factor, r_{QCD}, is calculated from the ratio of OS to SS events, where the MC estimation is subtracted from the data, as given by Equation 4.3.4. r_{QCD} would then be applied back onto the SS contribution to correct for any mismodelling. However, it can also be noticed that the Q-CR has a small contribution from W+jets processes and so will also depend on its derived normalisation factor. Figure 4.3.2 shows the final modelling in the Q-CR after all normalisation factors have been applied back. Table 4.3.1 lists the values of those derived factors for r_{QCD} in each selection.

$$r_{\mathrm{QCD}} = \frac{(\mathrm{data} - \mathrm{MC}_{W\mathrm{jets},Z\ell\ell,Z\tau\tau,\mathrm{top}})^{\mathrm{OS}}}{(\mathrm{data} - \mathrm{MC}_{W\mathrm{jets},Z\ell\ell,Z\tau\tau,\mathrm{top}})^{\mathrm{SS}}} \tag{4.3.4}$$

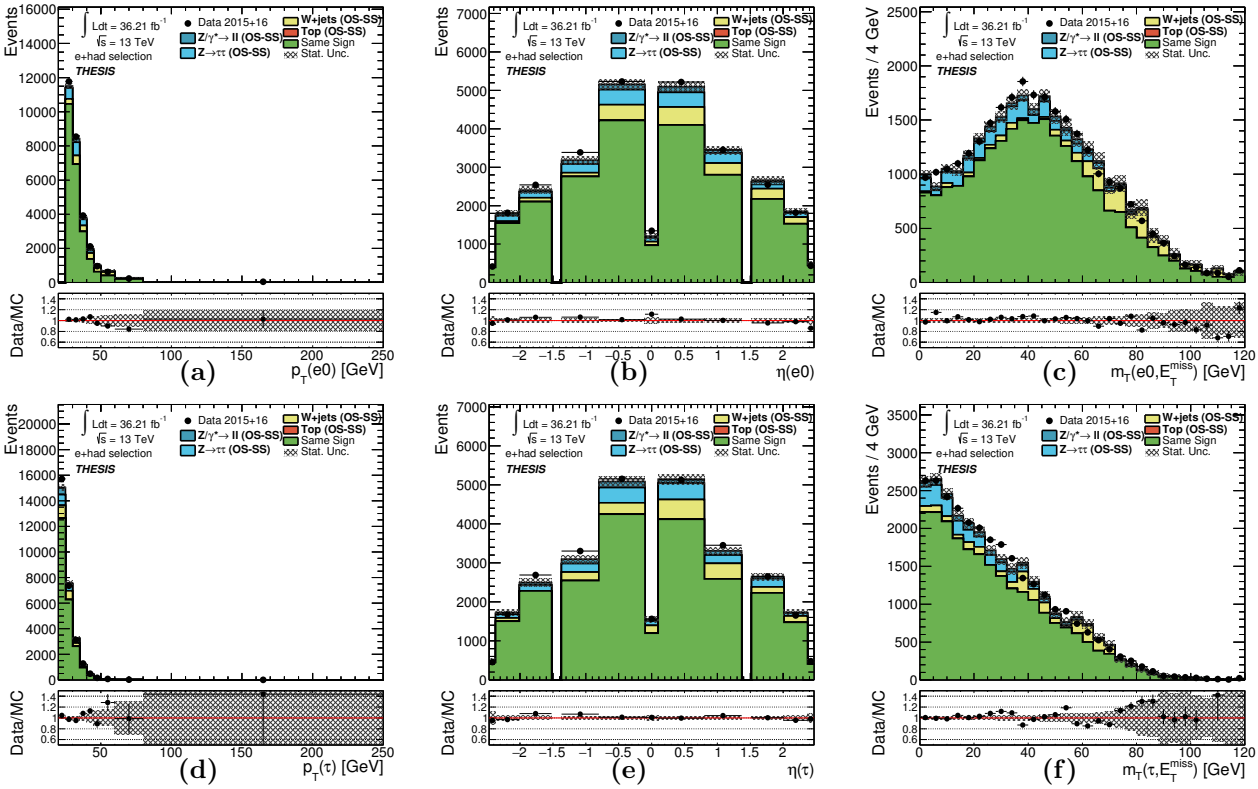

Figure 4.3.2: Plots of the tag electron (top) and probe hadronic tau (bottom), representing their p_{T}, η and m_{T} (from left to right), as observed in the QCD control region, with a medium tau ID applied.

For W+jets processes, a W-CR is defined with a high $m_{\mathrm{T}} > 70\,\mathrm{GeV}$ selection so that it may enrich its events, as well as a high $E_{\mathrm{T}}^{\mathrm{miss}} > 30\,\mathrm{GeV}$ requirement. As the W-CR features a significant contribution from SS events, it heavily depends on a calculation of r_{QCD} to first be applied. Another normalisation weight representing the W+jets k-factor, k_W, is calculated from the ratio of data with MC subtraction against the simulated $Z \to ee$ contribution, as given by Equation 4.3.5. The k_W factor is calculated separately for both OS and SS-enriched events. Figure 4.3.3 shows the final modelling in the W-CR after all normalisation factors have been applied back. Table 4.3.1 also lists the values of those derived factors for k_W in each selection.

$$k_W = \frac{\mathrm{data} - \mathrm{MC}_{W\mathrm{jets,top},Z\tau\tau}}{\mathrm{MC}_{Z\ell\ell}} \tag{4.3.5}$$

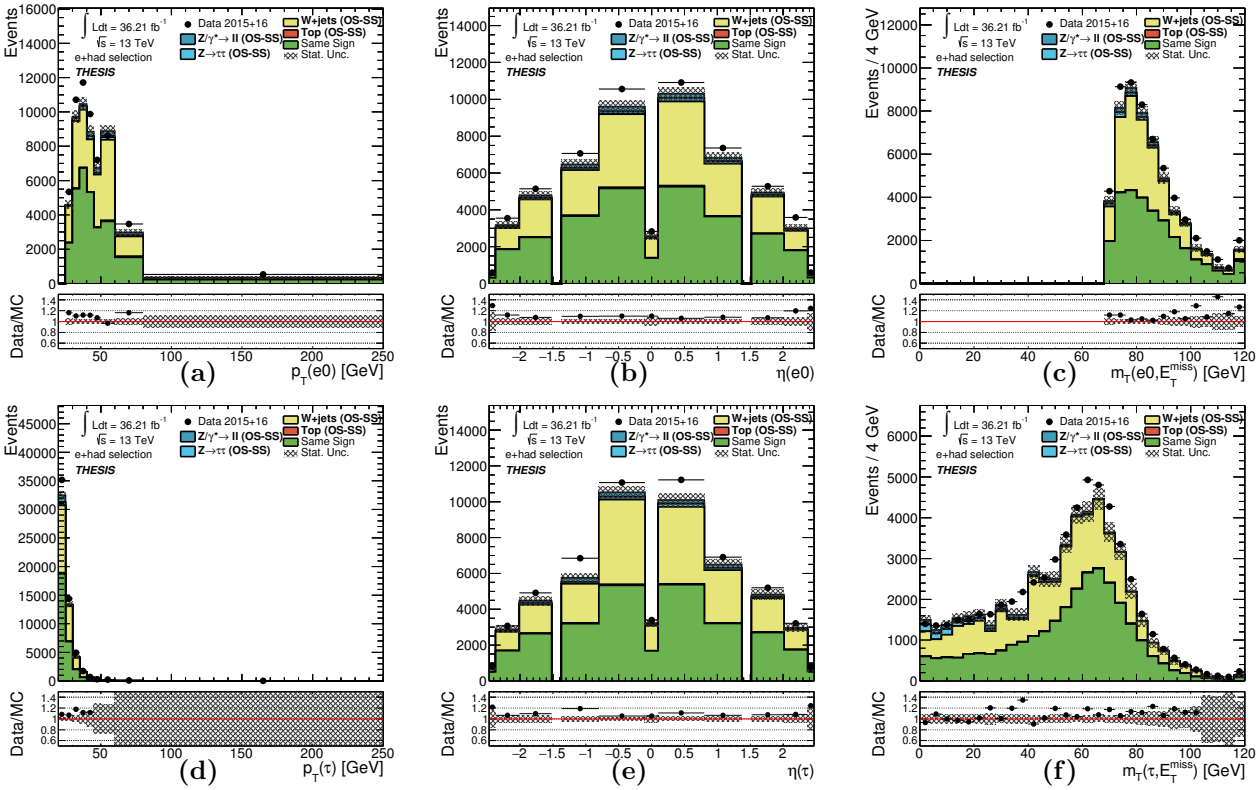

Figure 4.3.3: Plots of the tag electron (top) and probe hadronic tau (bottom), representing their p_{T}, η and m_{T} (from left to right), as observed in the W+jets control region, with a medium tau ID applied.

Tau ID selection	$e\tau$ **charge**	k_W	r_{QCD}
None	OS	0.9950 ± 0.0039	1.0620 ± 0.0044
	SS	1.0037 ± 0.0046	
Medium	OS	1.210 ± 0.017	1.222 ± 0.023
	SS	1.194 ± 0.026	

Table 4.3.1: Values of k_W and r_{QCD} iteratively calculated from the W+jets and QCD control regions. The values consider regions with and without a medium hadronic tau ID selection. For k_W, there is a value for both the OS and SS charge regions.

Since the r_{QCD} and k_W calculations have shown to be mutually dependent on each other, they are recalculated iteratively until differences are $<1\,\%$. The resulting background estimation in the Z-SR as weighted by these normalisation factors is therefore calculated as Equation 4.3.6. This modelling is finally verified by the Z-SR-denom region, where the results are shown in Figure 4.3.4 for each selection.

$$\mathrm{BG}^{\mathrm{OS}}_{Zee} = r_{\mathrm{QCD}} \times (\mathrm{data}^{\mathrm{SS}} - (k_W^{\mathrm{SS}} W^{\mathrm{SS}} + Z\tau\tau^{\mathrm{SS}} + \mathrm{top}^{\mathrm{SS}})) + (k_W^{\mathrm{OS}} W^{\mathrm{OS}} + Z\tau\tau^{\mathrm{OS}} + \mathrm{top}^{\mathrm{OS}}) \qquad (4.3.6)$$

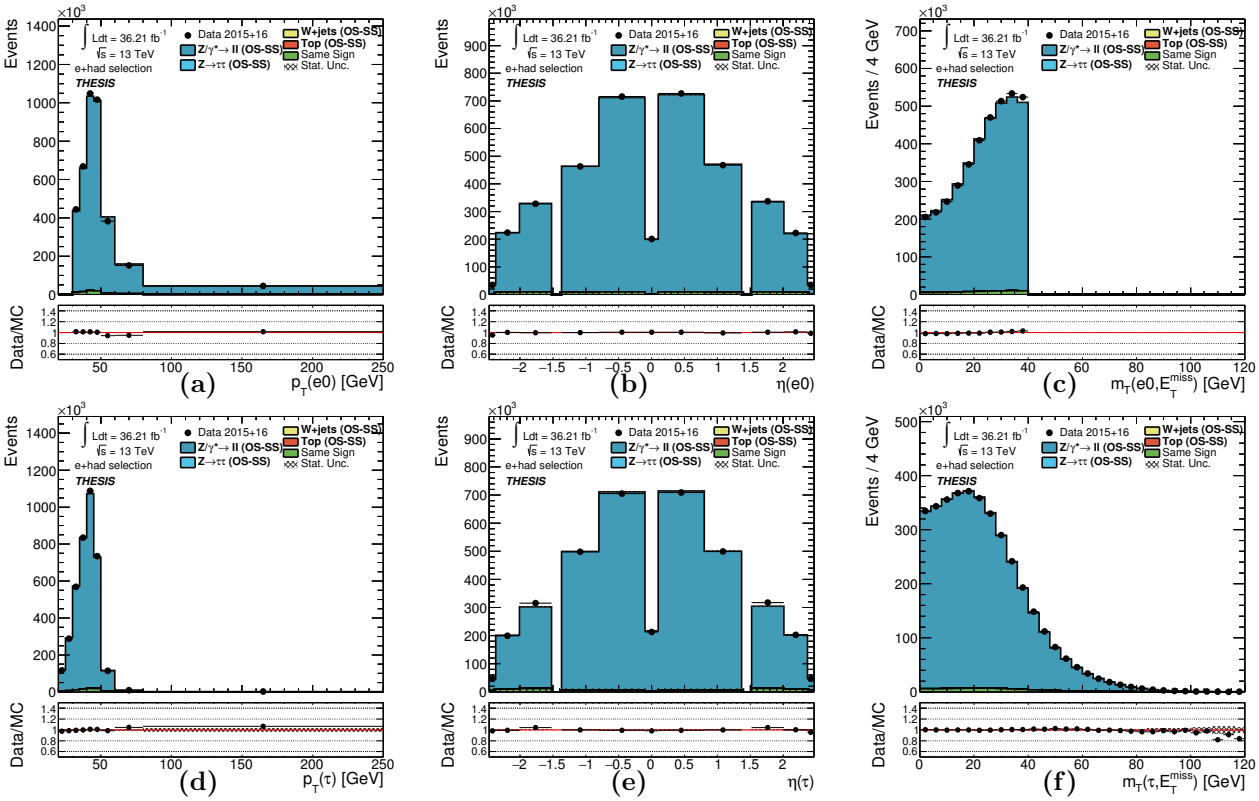

Figure 4.3.4: Plots of the tag electron (top) and probe hadronic tau (bottom), representing their p_{T}, η and m_{T} (from left to right), as observed in the $Z \to ee$ signal denominator validation region, with a medium tau ID applied. The selection criterion in electron $m_{\mathrm{T}} < 40\,\mathrm{GeV}$ is clearly visible.

Signal and scale factor results

Having confirmed decent modelling in the Z-SR-denom, the same normalisation factors are also applied to the Z-SR-numer region. The eVeto algorithms are applied for eLLH and eBDT at 75%, 85% and 95% efficiency, where their SFs are calculated individually. They are also applied for combinations of eLLH+eBDT at each efficiency. The results for each of these are shown in Figure 4.3.5.

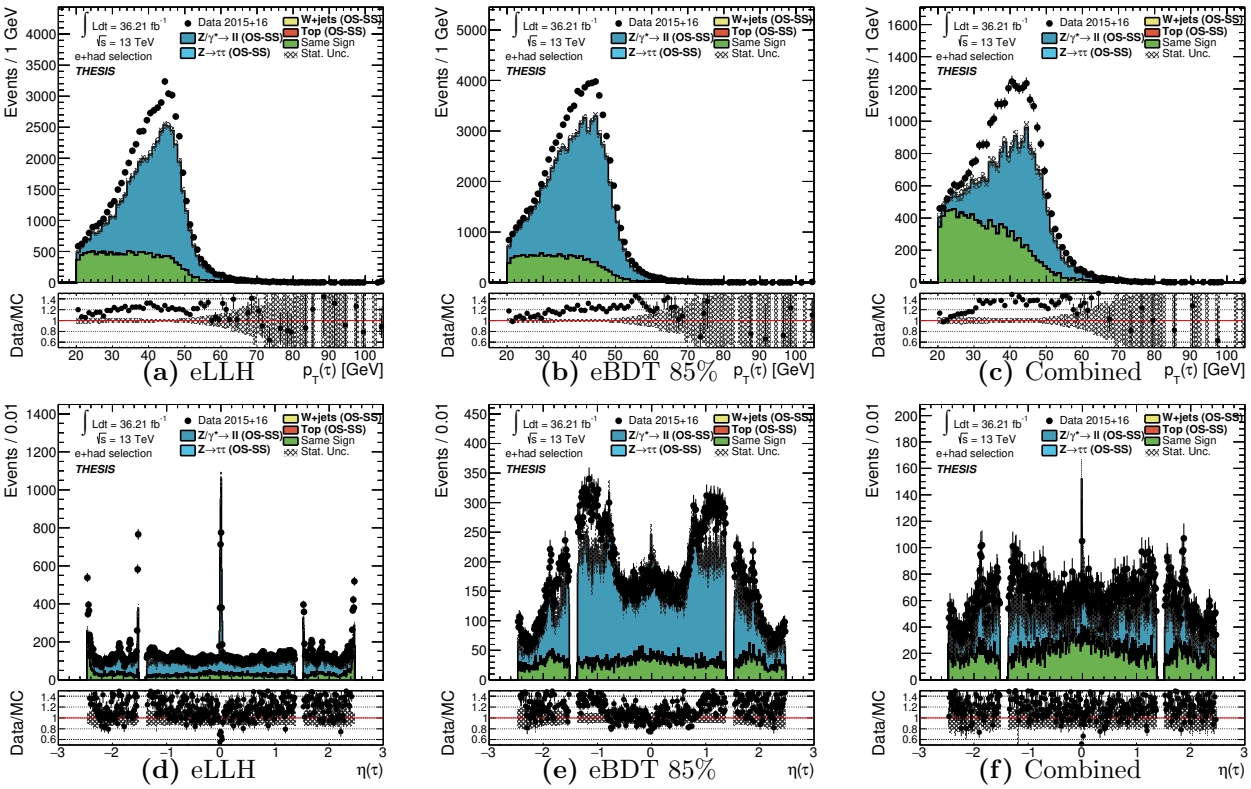

Figure 4.3.5: Plots of the probe hadronic tau p_{T} (top) and η (bottom), for eVeto algorithms applied with eLLH, eBDT @ 85% and both applied simultaneously (from left to right), as observed in the $Z \to ee$ signal numerator region, with a medium tau ID applied. These plots exemplify the typical disagreement between data and simulation.

The rejection efficiencies are then calculated from the division of the Z-SR-numer and Z-SR-denom for data and MC, and the resulting SF as the ratio between them. These are both shown in Figure 4.3.6.

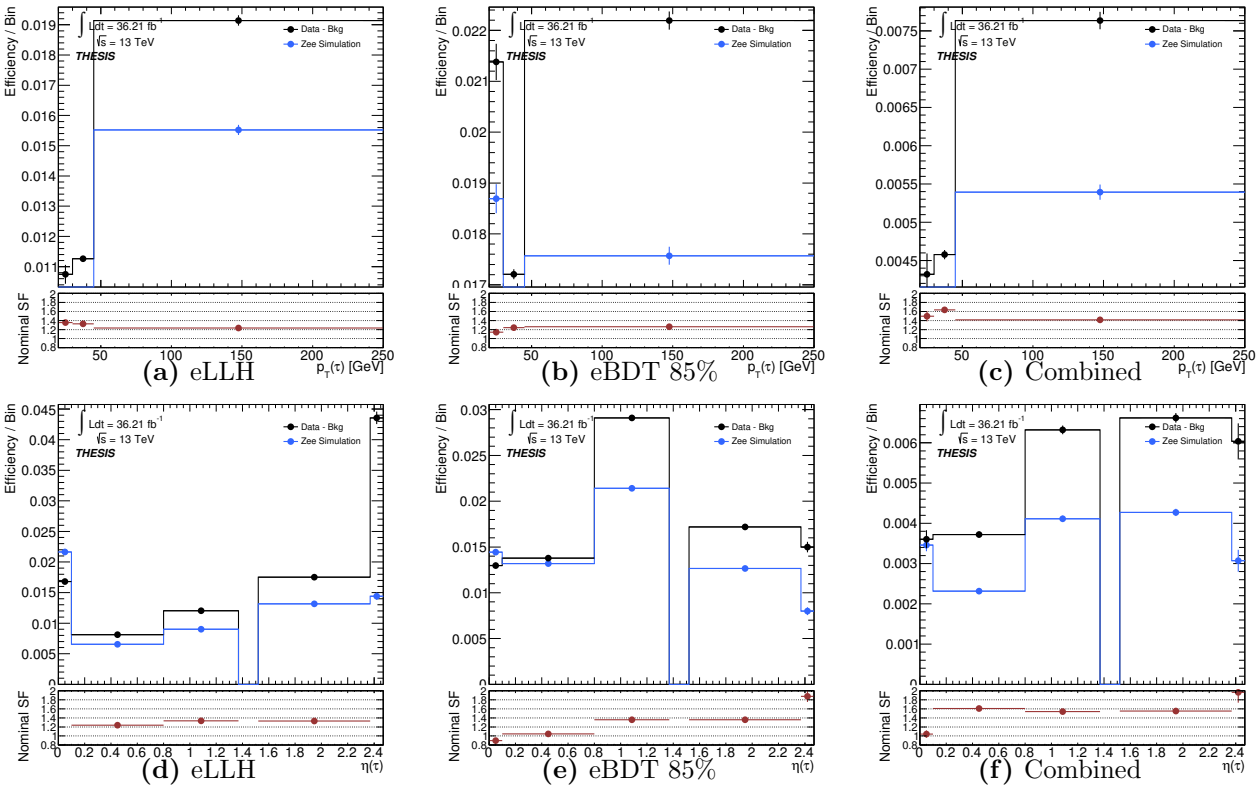

Figure 4.3.6: Efficiency plots of the probe hadronic tau p_{T} (top) and η (bottom), for eVeto algorithms applied with eLLH, eBDT @ 85% and both applied simultaneously (from left to right), as observed in the divided $Z \to ee$ signal region, with a medium tau ID applied. These plots exemplify the typical disagreement between data and simulation. Therefore, the ratio of data to MC is taken in the lower section of these plots, indicating the resulting scale factor. The binning is chosen to optimise the statistical uncertainty.

It is immediately clear, from the significant normalisation difference between data and MC in these plots, the fundamental reason for why these SFs are needed from this study, in order to correct for this. It can be seen that the SF mainly varies with tau η while remaining mostly flat for tau p_{T}. The bin widths are chosen such that there is a fair amount of statistics and therefore minimised uncertainty in each. While at first the SF was parameterised in the binning of η and a single value applied for p_{T}, the approach was later generalised into a 2-dimensional classification considering both η against p_{T}. These 2D SFs are shown in Figure 4.3.7.

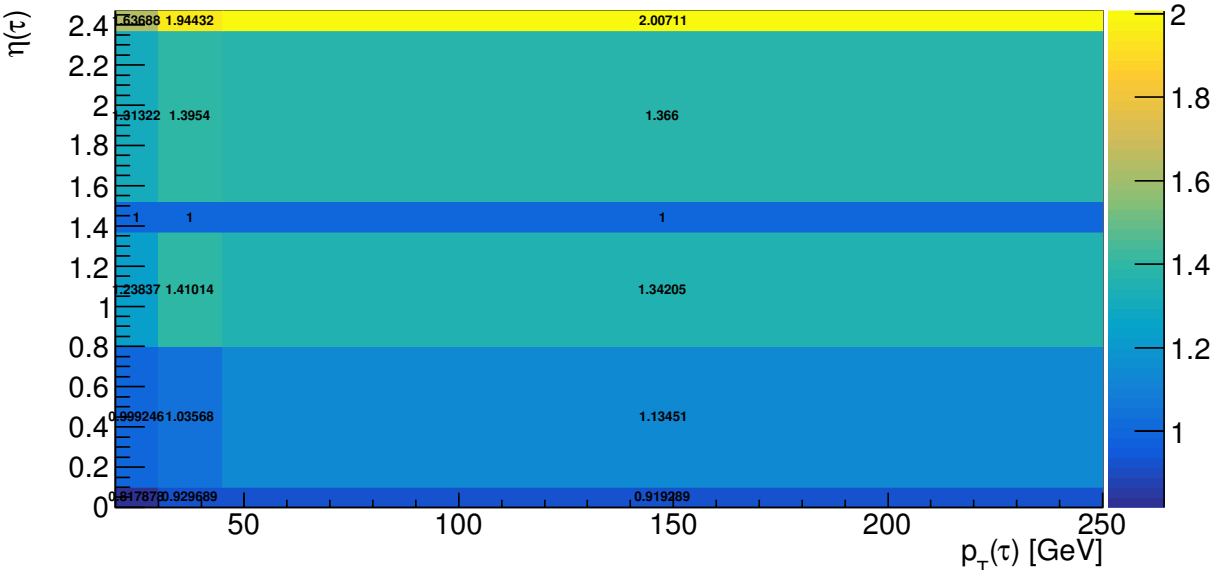

Figure 4.3.7: A 2-dimensional scale factor binned in tau η against tau p_{T}, derived for the eBDT @ 85% WP.

In order to deliver these corrections to analyses, the SFs are provided as a ROOT file through the Athena framework, introduced in Section 3.3.1. A sub-tool for tau-related physics is used to distribute several Tau CP corrections, including the eVeto SFs, known as *TauAnalysisTools* (TAT). The corrected electron rejection algorithms can be applied, with configuration to the TAT interface, onto events during the Ntuple production step, or at least saving the result as a boolean flag within the Ntuple which can be later selected in downstream analysis software.

Systematic uncertainties

The values for the SFs are also calculated and delivered with uncertainty, so that downstream analyses may consider this as a systematic variation to their own results. While part of this is sourced from the statistical uncertainty within this eVeto study, it also comes with systematic variations from the sources which this analysis depends on. The systematic uncertainties are calculated for each individual SF based on each of the eVeto rejection WPs, and applied to each bin for how the SF is separated.

Some of the most significant sources of systematic uncertainty come from pileup reweighting, e/γ CP corrections and the r_{QCD} and k_W calculations. Overall, the systematic variation ranges between 1 to 2 %, while the statistical uncertainties are more dominating as they vary between 1 to 3 %. This should not be too surprising as these results only feature a smaller fraction of the Run-2 dataset. The combined uncertainties for each SF bin across η in each eVeto algorithm can be seen in Table 4.3.2.

Combined:

bin-center	SF	stat	sym sys	stat [%]	sym sys [%]
0.05	0.777	0.020	0.004	2.6	0.5
0.45	1.238	0.022	0.011	1.8	0.87
1.08	1.334	0.023	0.013	1.7	0.99
1.45	1.000	0.000	0.000	0.0	0.0
1.95	1.330	0.020	0.009	1.5	0.7
2.42	3.026	0.145	0.038	4.79	1.3

Combined:

bin-center	SF	stat	sym sys	stat [%]	sym sys [%]
0.05	0.898	0.029	0.015	3.3	1.7
0.45	1.045	0.013	0.009	1.3	0.8
1.08	1.360	0.014	0.015	1.1	1.1
1.45	1.000	0.000	0.000	0.0	0.0
1.95	1.359	0.022	0.013	1.6	0.94
2.42	1.876	0.124	0.029	6.60	1.5

Combined:

bin-center	SF	stat	sym sys	stat [%]	sym sys [%]
0.05	1.041	0.080	0.023	7.7	2.2
0.45	1.608	0.050	0.023	3.1	1.5
1.08	1.538	0.040	0.021	2.6	1.4
1.45	1.000	0.000	0.000	0.0	0.0
1.95	1.550	0.043	0.019	2.8	1.2
2.42	1.966	0.228	0.033	11.6	1.7

Table 4.3.2: Tables of statistical (stat) and systematic (sys) uncertainties on the scale factor (SF), in the centre of each bin of η. The systematic uncertainties are combined and averaged such that it is symmetrical around the point (sym), and uncertainties are also expressed as a percentage of the SF. The tables are given for each eVeto algorithm applied, for the eLLH, eBDT @ 85% and both combined (from top to bottom), with a medium tau ID applied.

Chapter 5: Search for new physics decaying into di-tau leptons

As part of the title of this thesis and the summation of the discussion thus far, the author's work primarily focuses on the analysis of the ATLAS data recorded during Run-2, in the search for new BSM heavy neutral resonances decaying into a di-tau ($\tau^+\tau^-$) final state. The search is mainly conducted independent of any theoretical model, but towards the end of the process, a handful of scenarios from those introduced in Section 1.3 are benchmarked against the results. In particular, these include searches for additional MSSM-based Higgs bosons, as were denoted H/A, as well as some studies aiming for the heavy weak Z' boson.

Over the course of Run-2 operations, multiple papers dedicated to this search have been submitted [62][15][63], where in the more recent publications [15][63] the author had significantly contributed to their development and evolution. The majority of the results presented in this thesis are based on those published in the most recent paper [63] featuring a dataset size of 139 fb^{-1} integrated luminosity from the full Run-2 operation.

The production mechanisms studied in this analysis for such $H/A/Z'$ bosons are shown in Figure 5.0.1 at their lowest order. The H/A production features the *gluon fusion* (ggH) mechanism which is already a familiar process to the SM Higgs. However, in this regime searching for higher mass resonances, the *b-associated production* (bbH) mechanism becomes more prominent, especially with higher values of the MSSM parameter $\tan\beta$. As a means to distinguish the analysed data between the two production mechanisms, the events are categorised based on the presence of bottom quark-flavoured jets (b-jets): ggH processes are typically associated with events containing no b-jets (b-veto), while the bbH mechanisms are attributed to events with at least one b-jet present (b-tag). The Z' production is based on a typical Drell-Yan (DY) process.

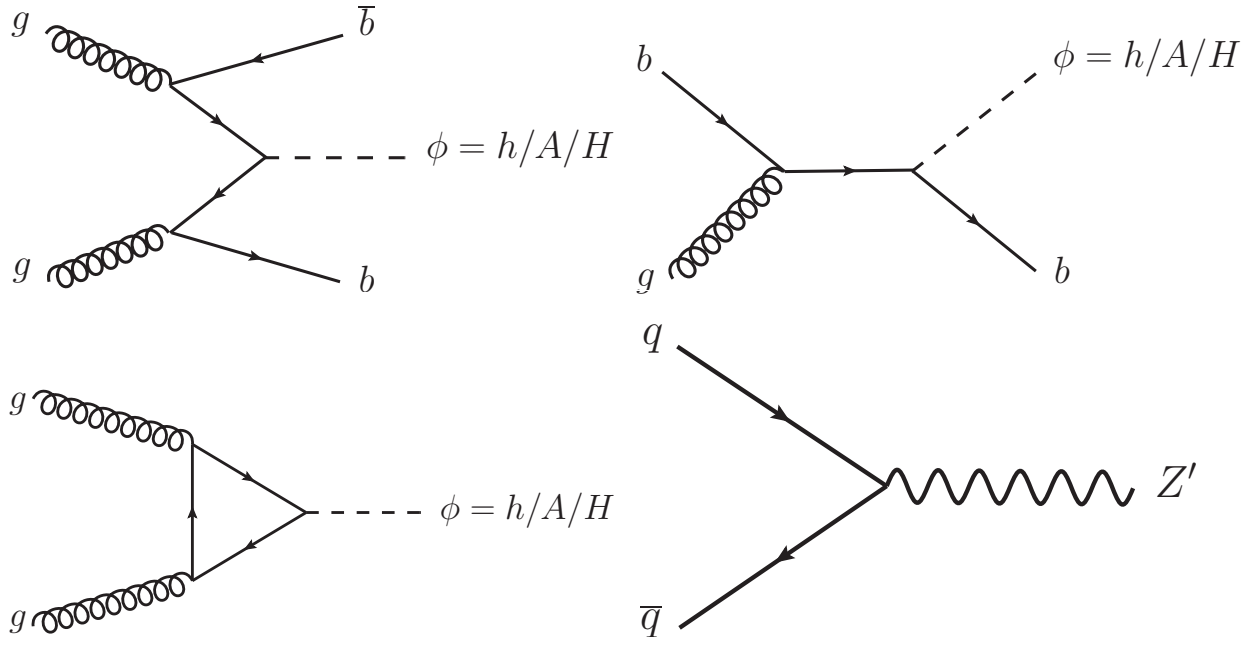

Figure 5.0.1: Lowest-order Feynman diagrams for the b-associated production mechanism in the four-flavour (top-left) and five-flavour (top-right) schemes, and gluon fusion (bottom-left) of the H/A bosons, and Drell-Yan production (bottom-right) of the Z' boson [15].

As learned from Chapter 4, since each tau may decay either leptonically (τ_{lep}) or hadronically (τ_{had}), this BSM $\rightarrow \tau\tau$ analysis is divided into two sub-channels of focus depending on the decay combination: a semi-leptonic di-tau decay $\tau_{\text{lep}}\tau_{\text{had}}$ channel occurring with ∼46 % probability, and a fully-hadronic $\tau_{\text{had}}\tau_{\text{had}}$ channel occurring with ∼42 % probability. While this suggests a $\tau_{\text{lep}}\tau_{\text{lep}}$ decay would occur with ∼12 % probability, the channel is currently not significant enough to warrant interest for a dedicated study in ATLAS. The author is involved in the analysis of the $\tau_{\text{lep}}\tau_{\text{had}}$ channel, so this is where the discussion and results presented in this thesis will be focussed on.

5.1 Event selection

A series of event selection criteria are applied to the recorded data and MC simulation in order to designate a *signal region* (SR), enriched in potential events from high-mass BSM physics. The analysis strategy that will be described here, as with many analyses in ATLAS, will share this common formula with what was already discussed for the eVeto scale factor analysis in Section 4.3.2. Furthermore, while this BSM analysis also shares the concept of studying taus, in particular the $\tau_{\text{lep}}\tau_{\text{had}}$ channel may use very similar selection techniques to the eVeto study.

In general, the BSM $\rightarrow \tau^+\tau^-$ analysis selection requires two oppositely-charged tau leptons, decaying approximately back-to-back to each other in the transverse plane ($|\Delta\phi(\tau_1, \tau_2)| \approx \pi$ rad), assuming a non-Lorentz boosted two-body decay. For the $\tau_{\text{lep}}\tau_{\text{had}}$ channel, this is selected at $|\Delta\phi(\tau_{\text{lep}}, \tau_{\text{had}})| > 2.4$ rad, while in the $\tau_{\text{had}}\tau_{\text{had}}$ channel, selected at $|\Delta\phi(\tau_{\text{had}}, \tau_{\text{had}})| > 2.7$ rad. The hadronically-decaying tau candidate ($\tau_{\text{had-vis}}$) in either channel is selected from its visible decay products, with the methods as discussed from Tau CP in Chapter 4, from either 1- or 3-prong decays and no more than two neutral daughters. This means the $\tau_{\text{had-vis}}$ must continue to reside within the InDet, $|\eta| < 2.5$, while excluding the transition region, $1.37 < |\eta| < 1.52$.

For the $\tau_{\text{lep}}\tau_{\text{had}}$ channel selection, the highest p_{T}-leading hadronic tau (τ_{had}) is required to possess a minimum $p_{\text{T}} > 25$ GeV and pass the medium tau ID selection using a BDT algorithm, as recommended for best performance by the Tau CP, where the ID working points were defined in Section 4.2. The leptonically-decaying tau candidate (τ_{lep}) is treated as a lighter lepton, ℓ, as either an electron (e) or a muon (μ). As such, the $\tau_{\text{lep}}\tau_{\text{had}}$ channel is commonly divided into its constituent $e\tau_{\text{had}}$ and $\mu\tau_{\text{had}}$ sub-channels for detailed study. The leptons are matched with CP-recommended single-lepton triggers with p_{T} thresholds ranging between 20 to 140 GeV, with the full list of triggers given in Table B.1.1. The selected p_{T}-leading lepton is required to have $p_{\text{T}} > 30$ GeV, pass a medium ID selection and remain isolated from other objects within $\Delta R < 0.2$. Leptons must be contained within the InDet, $|\eta| < 2.47$, while muons should also be located within the MS, $|\eta| < 2.5$.

For the $\tau_{\text{had}}\tau_{\text{had}}$ channel selection, the highest p_{T}-leading hadronic tau ($\tau_{\text{had-1}}$) is matched with a single-tau trigger with a p_{T} threshold at either 80, 125 or 160 GeV (depending on the year of Run-2 data-taking), where the required p_{T} must be 5 GeV above the respective threshold, and must meet a medium ID requirement. The second-highest sub-leading-p_{T} hadronic tau ($\tau_{\text{had-2}}$) is only required to possess a minimum $p_{\text{T}} > 65$ GeV and pass the loose ID selection.

The τ_{had} ID algorithm is capable of a rejection factor of 20 at the loose WP for 1-prong taus and 200 for the 3-prong, while for the medium WP a rejection of 30 and 500 for the 1- and 3-prong taus is achieved, respectively, when applied against multi-jet events [63].

The $\tau_{\text{lep}}\tau_{\text{had}}$ channel also imposes additional requirements on lepton $m_{\text{T}} < 40\,\text{GeV}$, as was defined in Equation 4.3.2, in order to suppress contributions from W+jets processes, where $E_{\text{T}}^{\text{miss}}$ will certainly be present due to the neutrino daughters from tau decays. A selection rejecting events based on the invariant mass is applied in the $e\tau_{\text{had}}$ sub-channel between 80 to 110 GeV (around the Z mass peak) so as to avoid $Z \to ee$ processes. The electron rejection eLLH algorithm from Section 4.3 is also applied, providing a rejection factor on electrons misidentified as hadronic taus of up to 200 [15].

Any other jets involved are required to meet $p_{\text{T}} > 20\,\text{GeV}$ and found within $|\eta| < 2.5$, so as to remove the contribution from soft-scattering and emission events. A jet vertex-tagging algorithm is also applied with $p_{\text{T}} < 60\,\text{GeV}$ and $|\eta| < 2.4$, in order to determine the origin of the jet and thus mitigate pileup effects. b-jets are identified with an ATLAS-common $MV2c10$ algorithm [64], working at 70 % efficiency.

Both the $\tau_{\text{lep}}\tau_{\text{had}}$ and $\tau_{\text{had}}\tau_{\text{had}}$ channels base their analyses on the DAOD input files introduced in Section 3.3, to then produce Ntuples and their furthering studies via different means. Both channels use the DAOD_HIGG4X series of derivations, designed to select events containing di-tau decays with all of the latest CP calibrations applied, and especially useful to Higgs-related studies. For $\tau_{\text{lep}}\tau_{\text{had}}$, the X denotes the `DAOD_HIGG4D2` sub-derivation relevant for such semi-leptonic decays and shared with SM Higgs studies, while for $\tau_{\text{had}}\tau_{\text{had}}$, `DAOD_HIGG4D4` is used for fully-hadronic decays but especially in a higher mass regime as would be expected for BSM.

Since the author's involvement lies with the $\tau_{\text{lep}}\tau_{\text{had}}$ channel, the remaining discussion will focus purely on these studies. As mentioned repeatedly since Section 3.3.2, the author has made use of the xTFW for the production of Ntuples, and this was mainly the case for the $\tau_{\text{lep}}\tau_{\text{had}}$ channel, where the usual responsibilities previously discussed continue to apply. In addition to processing the full Run-2 recorded dataset, ∼165 individual MC background and signal samples were processed, for each of the three data-taking campaigns, as introduced in Section 3.2. The full list of MC DAOD samples processed into Ntuples are given in Listing B.1.1.

While many of the most basic signal selection criteria are applied at the Ntuple-level, some still remain open as they will be utilised differently in background estimation, which will be discussed in the following section. Once these Ntuples have been produced, they are passed onto a software framework used by the $\tau_{\text{lep}}\tau_{\text{had}}$ analysis for further study known as the *Common Analysis Framework* (CAF), used by several analyses across ATLAS. In practice, CAF serves as the core for an expanding framework tailored specifically to the $\tau_{\text{lep}}\tau_{\text{had}}$ analysis, which has then taken on the name of *BSMtautauCAF*, where the remaining selection criteria are applied and their following results will have been created from by the author.

5.2 Background estimation

For the $\tau_{\text{lep}}\tau_{\text{had}}$ channel, backgrounds (or *bkg* for short) include processes which can also produce a genuine τ_{had}, such as those from $Z/\gamma^* \to \tau\tau$ and $t\bar{t} \to b\bar{b} + \tau^+\tau^- + \nu_\tau\bar{\nu}_\tau$ (each dominant in the b-veto and b-tag categories, respectively). Since these backgrounds are irreducible, they are estimated with MC simulation. Other similar backgrounds with smaller contributions, or those which produce ℓ as a τ_{lep} decay would, come from $Z/\gamma^* \to \ell\ell$, di-boson and single top processes.

However, some of the most dominant background contributions come from jets being misidentified as one of the candidate τ_{had} or ℓ, despite various selection criteria and algorithms applied — these are commonly referred to as *fakes*. For instance, QCD-based *multi-jet* processes (MJ) could be misidentified as a ℓ, and W+jets (in b-veto) or $t\bar{t}$ (in b-tag) could fake a τ_{had}. While MC simulation has some effectiveness in estimating these fake backgrounds, a data-driven correction is still required. As such, the fakes are estimated using a *fake factor* (FF) technique, calculated as the ratio of the number of events N in the recorded data which pass a certain selection criterion over those which fail it, as given by Equation 5.2.1. Subsequently, in its re-arranged form, the pre-determined value of the FF can be used to estimate the scale of these fake background processes when extrapolated from the events which fail the selection criterion in the SR.

$$\text{X-FF} = \frac{(N_{\text{data}} - N_{\text{bkg}})^{\text{pass}}}{(N_{\text{data}} - N_{\text{bkg}})^{\text{fail}}}\bigg|_{\text{X-FR}} \tag{5.2.1}$$

In order to estimate the fake contributions from the different processes, *fake regions* (FR) are defined to enrich the contributions from these fake processes so that they may be accurately measured with a FF calculation attributed to each. The $\tau_{\text{lep}}\tau_{\text{had}}$ analysis categorises the fake components into two major FRs: where MJ processes fake leptons in a *Lepton Fake Region* (L-FR), and where W+jets or $t\bar{t}$ processes fake τ_{had} in a *W+jets/Top Fake Region* (W/T-FR). This results in a set of fake factors and regions, X-FF and X-FR, where X $\in$ [L, W, T]. However, while the FRs are aimed to enrich the fake background and therefore purely modelled by data, in reality, there will still be some contribution from genuine processes that can be estimated by MC, so a background subtraction is applied in the FF calculation.

For the L-FR, the FF pass/fail requirement is distinguished on the lepton isolation condition of the selected ℓ — those which fail the isolation (ISO) condition are referred to as *anti-ISO*. In contrast, for the W/T-FR, the differentiating FF requirement is on the τ_{had} ID, so similarly those failing the condition are referred to as *anti-ID*. Likewise, the W+jets/$t\bar{t}$ contributors are generally sourced from quark-initiated jets, while MJ processes also include sources from gluon-initiated jets.

5.2.1 Multi-jet fake estimation

The L-FR is defined quite differently to the SR event selection, with the main difference being the lepton ISO requirement being toggled for FF calculation. The opposite-charge and back-to-back $|\Delta\phi|$ conditions are no longer required, the τ_{had} minimum p_{T} lowered to 20 GeV, while its ID quality must be worse than loose (an efficiency less than 1 %), the lepton m_{T} selection criterion is reduced to less than 30 GeV and the $e\tau_{\text{had}}$ invariant mass rejection is removed. Additionally, the L-FR also forces that there must be exactly one lepton available in the event.

Using the BSMtautauCAF analysis software, the L-FR is drawn with the xTFW Ntuples as input and the further selection criteria applied. The L-FR also contains a minor contribution from W+jets fakes, but estimating this with the data-driven method would first require the calculation of the W-FF from the W-FR, which in turn also needs the L-FF derived here, so indicating a cyclical analysis strategy. Instead, since its significance in the L-FR is small, it is adequate to estimate the W+jets fakes process with MC simulation, thus truncating the procedure for simplicity. The L-FF is calculated from the resulting data as per Equation 5.2.1, parameterised in histogram bins as a function of the p_{T}^{ℓ} and $|\Delta\phi(\ell, E_{\text{T}}^{\text{miss}})|$, separately for the $e\tau_{\text{had}}$ and $\mu\tau_{\text{had}}$ sub-channels. The binning is organised across the full range of p_{T}^{ℓ}, but segmented across $|\Delta\phi(\ell, E_{\text{T}}^{\text{miss}})|$ into four bins for the b-veto category and three for the b-tag: these are defined in steps starting from 0 to 0.5, to 1, to 2 and to π rad for the b-veto, and from 0 to 0.5, to 1 and to π rad for the b-tag. This results in a total of fourteen L-FF calculations. A visualisation of this binning for the calculated L-FF are shown in Figures 5.2.1–5.2.4.

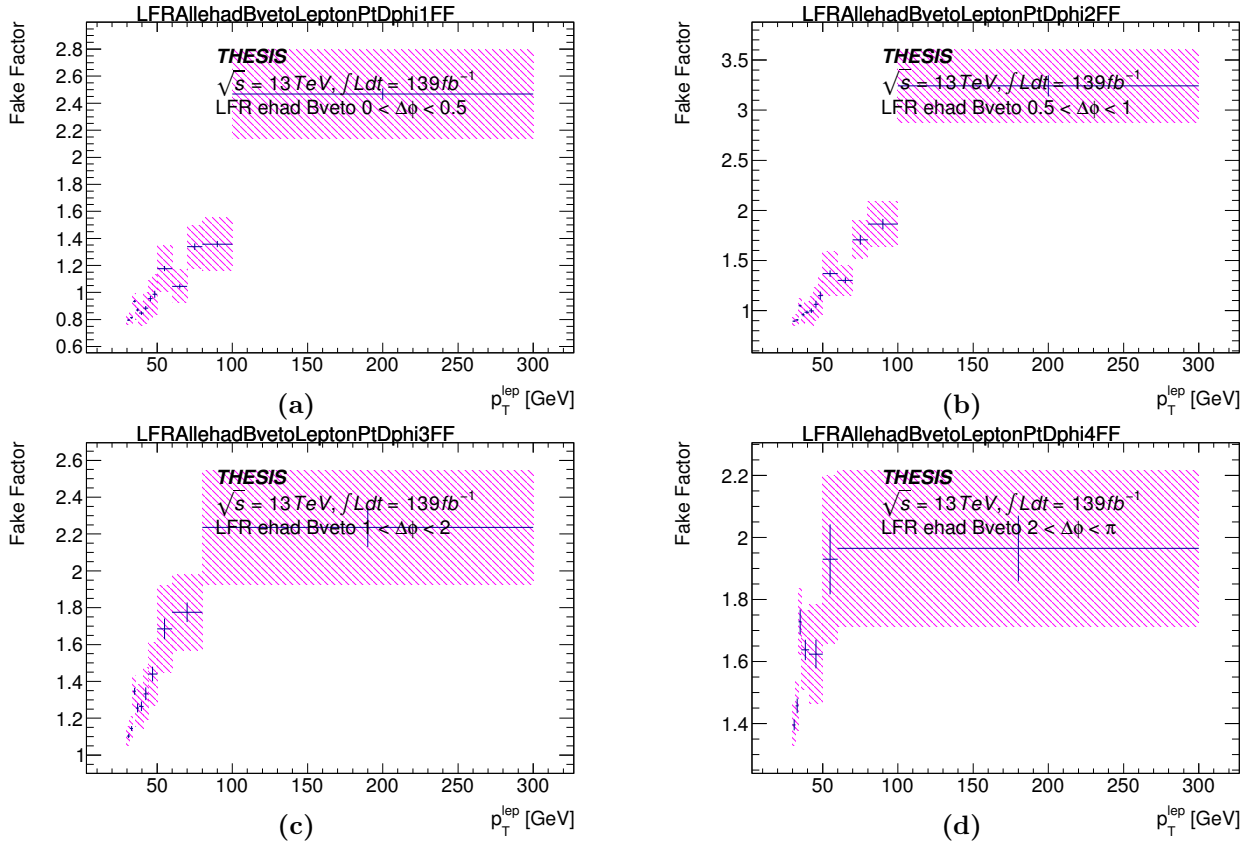

Figure 5.2.1: Plots of the Lepton Fake Factor distribution across the selected lepton p_{T}, as calculated from the Lepton Fake Region, for each binning range of $|\Delta\phi(\ell, E_{\text{T}}^{\text{miss}})|$ (from top left to bottom right). The fake factors are parameterised in the b-veto category, representing the $e\tau_{\text{had}}$ sub-channel.

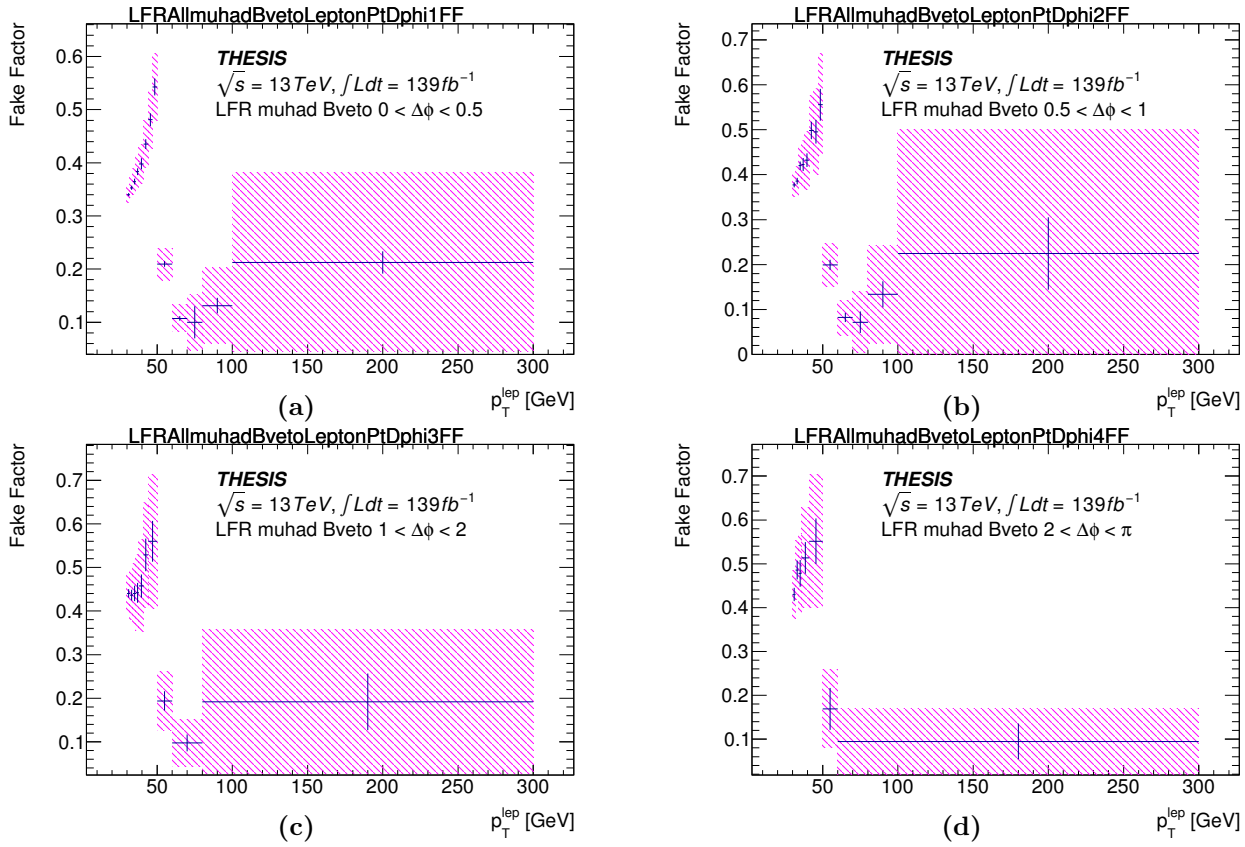

Figure 5.2.2: Plots of the Lepton Fake Factor distribution across the selected lepton p_{T}, as calculated from the Lepton Fake Region, for each binning range of $|\Delta\phi(\ell, E_{\mathrm{T}}^{\mathrm{miss}})|$ (from top left to bottom right). The fake factors are parameterised in the b-veto category, representing the $\mu\tau_{\mathrm{had}}$ sub-channel.

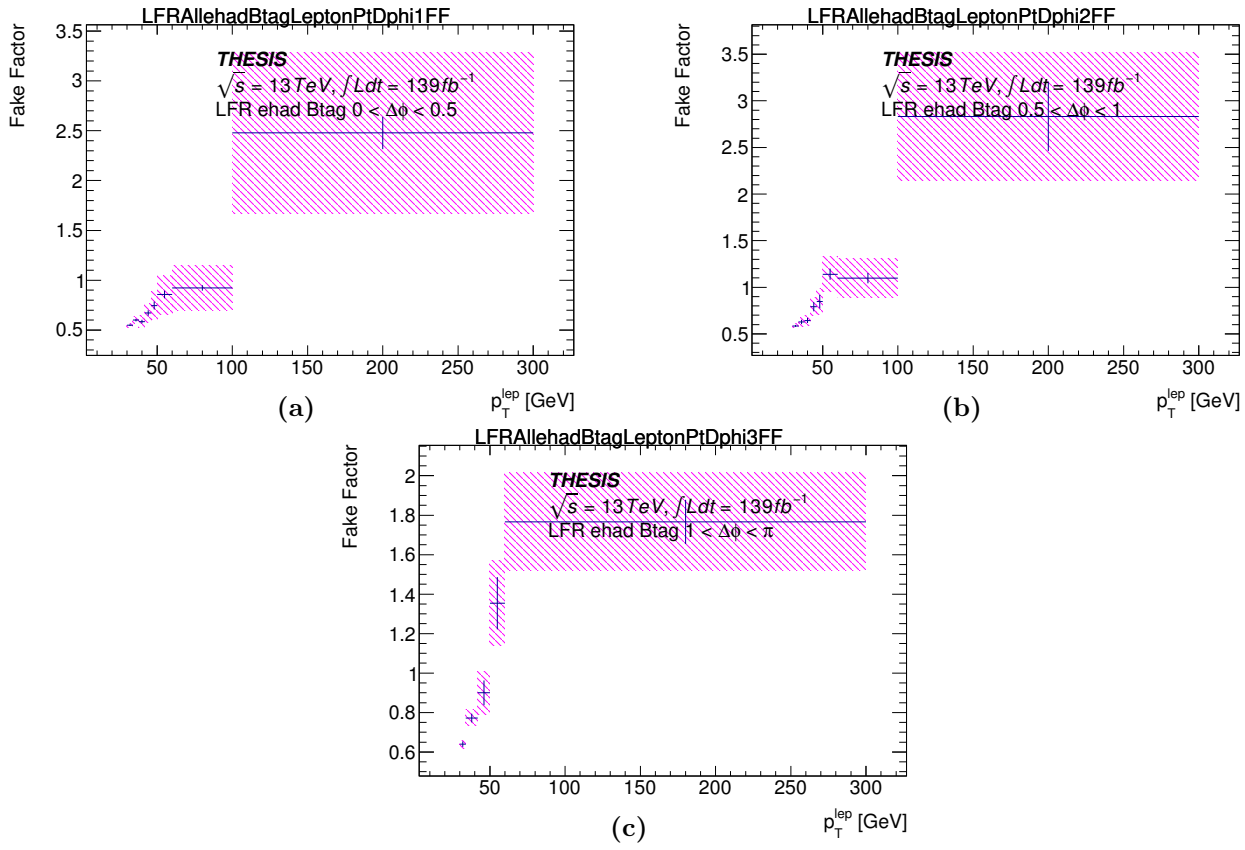

Figure 5.2.3: Plots of the Lepton Fake Factor distribution across the selected lepton p_{T}, as calculated from the Lepton Fake Region, for each binning range of $|\Delta\phi(\ell, E_{\mathrm{T}}^{\mathrm{miss}})|$ (from top left to bottom right). The fake factors are parameterised in the b-tag category, representing the $e\tau_{\mathrm{had}}$ sub-channel.

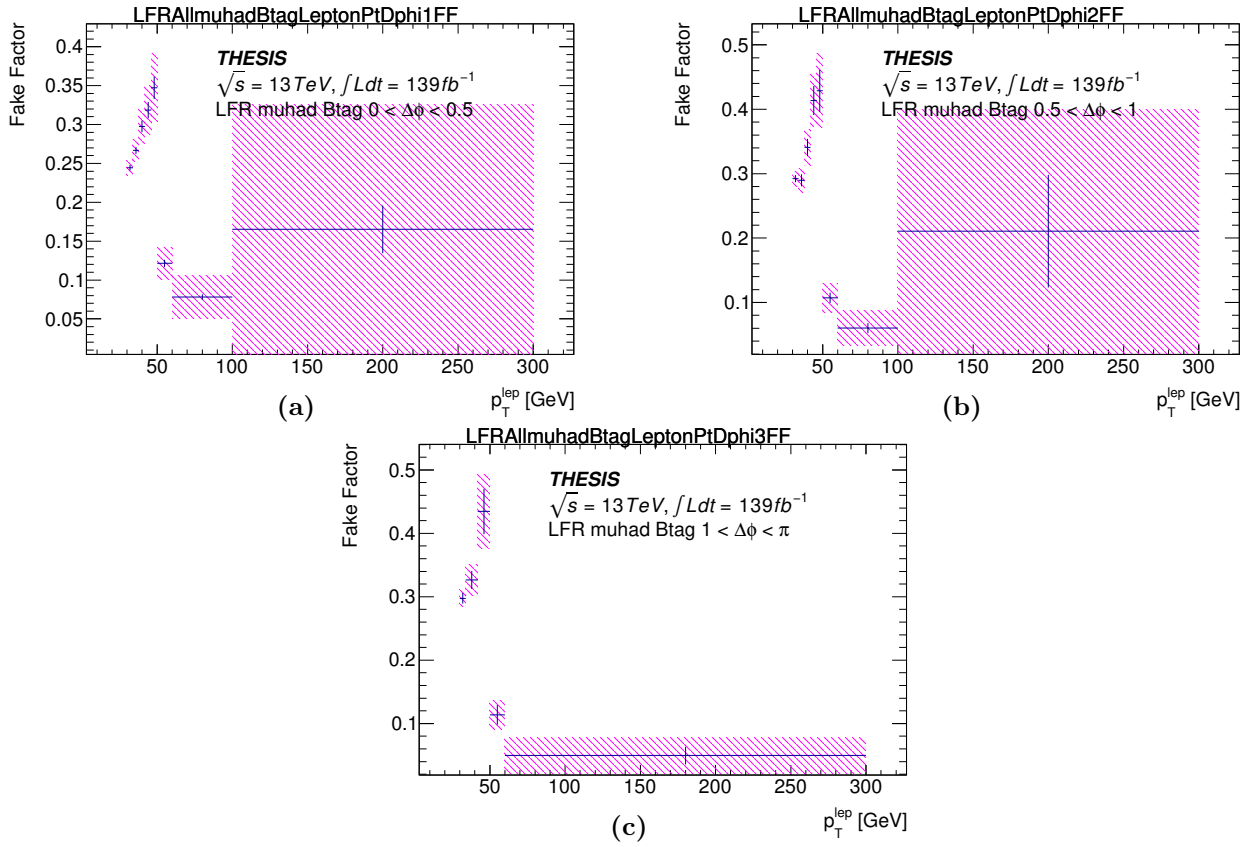

Figure 5.2.4: Plots of the Lepton Fake Factor distribution across the selected lepton p_{T}, as calculated from the Lepton Fake Region, for each binning range of $|\Delta\phi(\ell, E_{\mathrm{T}}^{\mathrm{miss}})|$ (from top left to bottom right). The fake factors are parameterised in the b-tag category, representing the $\mu\tau_{\mathrm{had}}$ sub-channel.

From these results, it can be seen that the overall value of the L-FF ranges between ∼0 to 3 in the $e\tau_{\mathrm{had}}$ sub-channel from Figures 5.2.1 and 5.2.3, and ∼0 to 0.5 in $\mu\tau_{\mathrm{had}}$ from Figures 5.2.2 and 5.2.4. The L-FF distribution in $e\tau_{\mathrm{had}}$ typically increases with the lepton p_{T} across this range, while although the $\mu\tau_{\mathrm{had}}$ shares a similar behaviour, there is a significant discontinuation around 50 GeV. This is expected to be caused by boundary conditions within the CP-recommended isolation algorithms applied to muons, such that different techniques are applied for low and high p_{T} muon regimes around the 50 GeV mark. Overall, these values and distributions for the L-FF are typically expected. Generally, the bin widths are chosen such as to provide sufficient statistics in each.

In order to confirm a successful calculation, the L-FF is applied back into the L-FR as a contribution from QCD fakes, so as to ensure a continued fair modelling, especially in the other non-parameterised variables of interest, such as p_{T}^{τ}. This MJ fake contribution in the region where events pass the ISO requirement is derived from the re-arrangement of Equation 5.2.1, such that the L-FF is multiplied by the number of anti-ISO events to estimate the number of those which would pass. The result of this complimented L-FR can be seen in Figures 5.2.5 and 5.2.6, and a breakdown of the anti-ISO events themselves as they would be used in the calculation of L-FF are also shown in Figures 5.2.7 and 5.2.8.

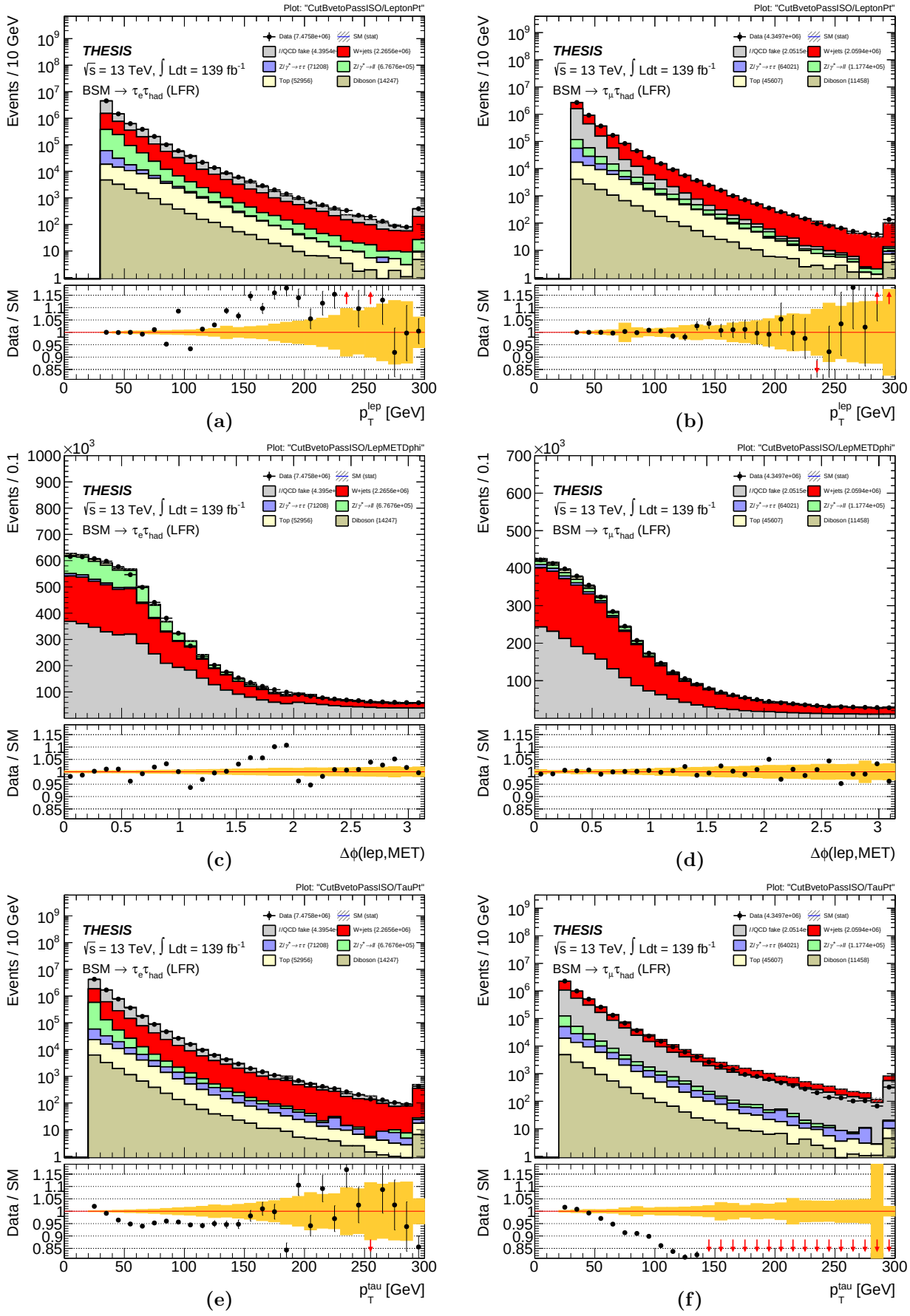

Figure 5.2.5: Plots of the Lepton Fake Region which pass the lepton isolation requirement with the Lepton Fake Factor applied back, representing lepton p_{T}, $|\Delta\phi(\ell, E_{\mathrm{T}}^{\mathrm{miss}})|$ and tau p_{T} (from top to bottom). The region is divided into the $e\tau_{\mathrm{had}}$ (left) and $\mu\tau_{\mathrm{had}}$ (right) sub-channels, representing the b-veto category.

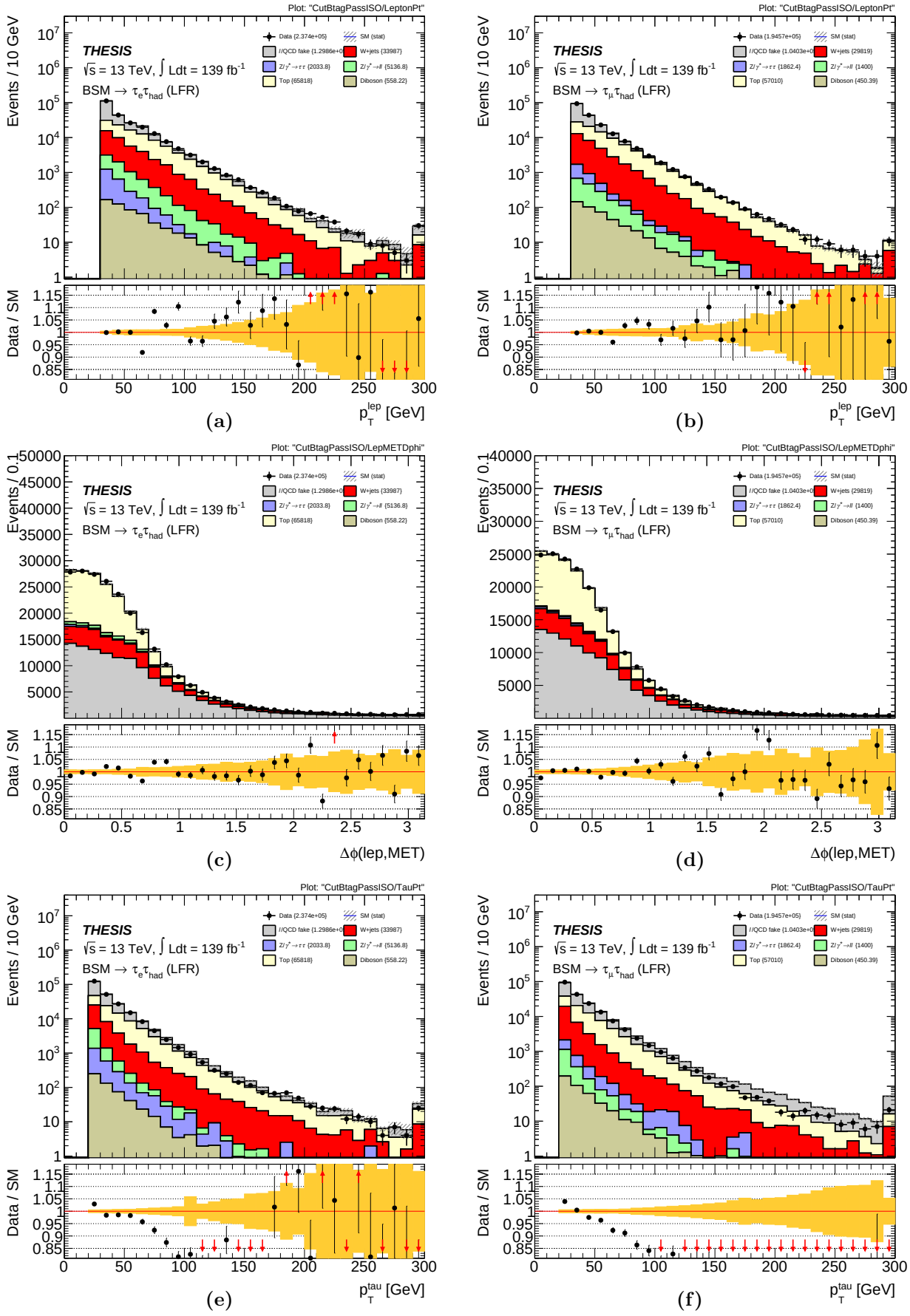

Figure 5.2.6: Plots of the Lepton Fake Region which pass the lepton isolation requirement with the Lepton Fake Factor applied back, representing lepton p_{T}, $|\Delta\phi(\ell, E_{\mathrm{T}}^{\mathrm{miss}})|$ and tau p_{T} (from top to bottom). The region is divided into the $e\tau_{\mathrm{had}}$ (left) and $\mu\tau_{\mathrm{had}}$ (right) sub-channels, representing the b-tag category.

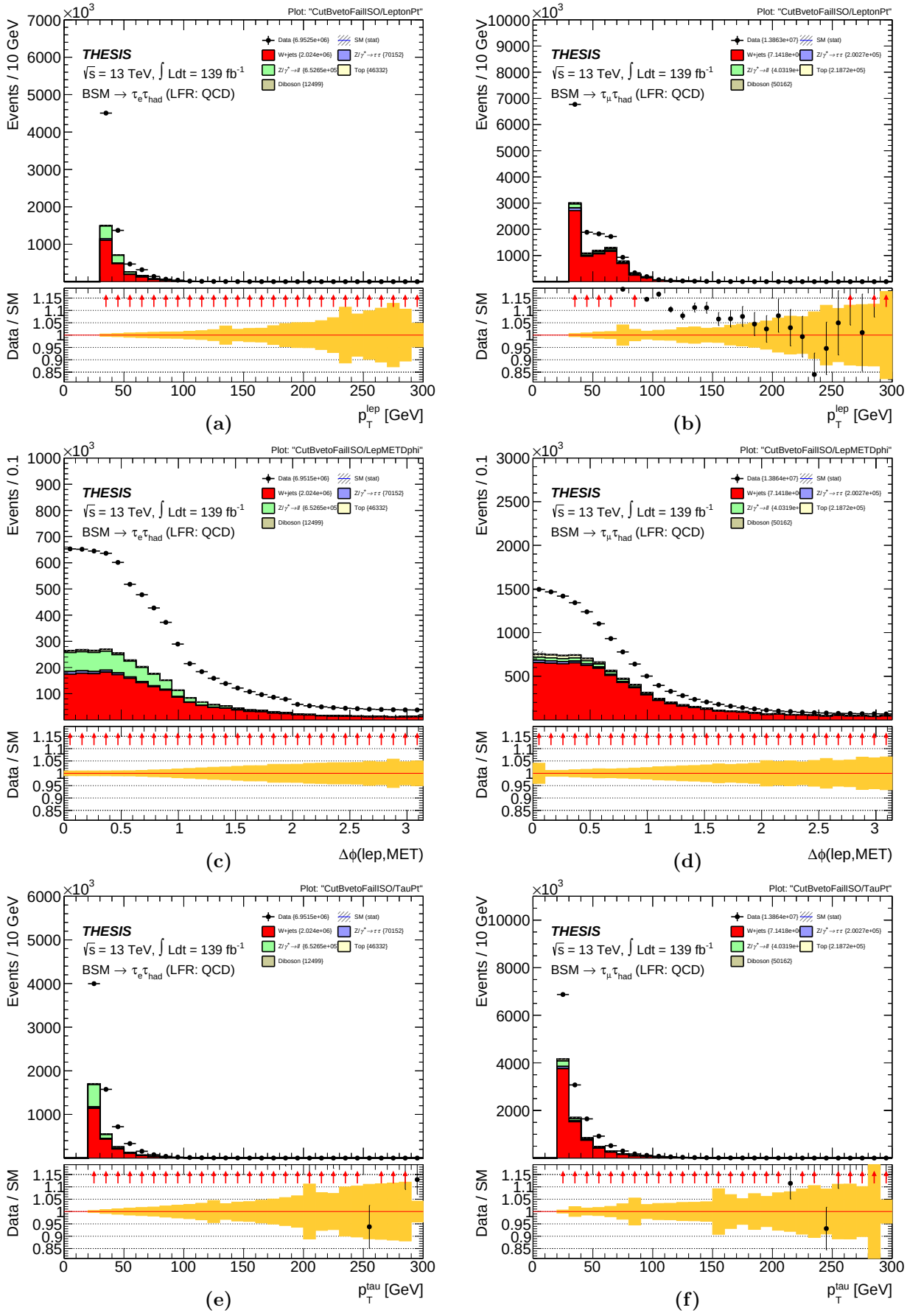

Figure 5.2.7: Plots of the QCD fake component which fail the lepton isolation requirement within the Lepton Fake Region as used in the calculation of the Lepton Fake Factor, representing lepton p_{T}, $|\Delta\phi(\ell, E_{\mathrm{T}}^{\mathrm{miss}})|$ and tau p_{T} (from top to bottom). The region is divided into the $e\tau_{\mathrm{had}}$ (left) and $\mu\tau_{\mathrm{had}}$ (right) sub-channels, representing the b-veto category.

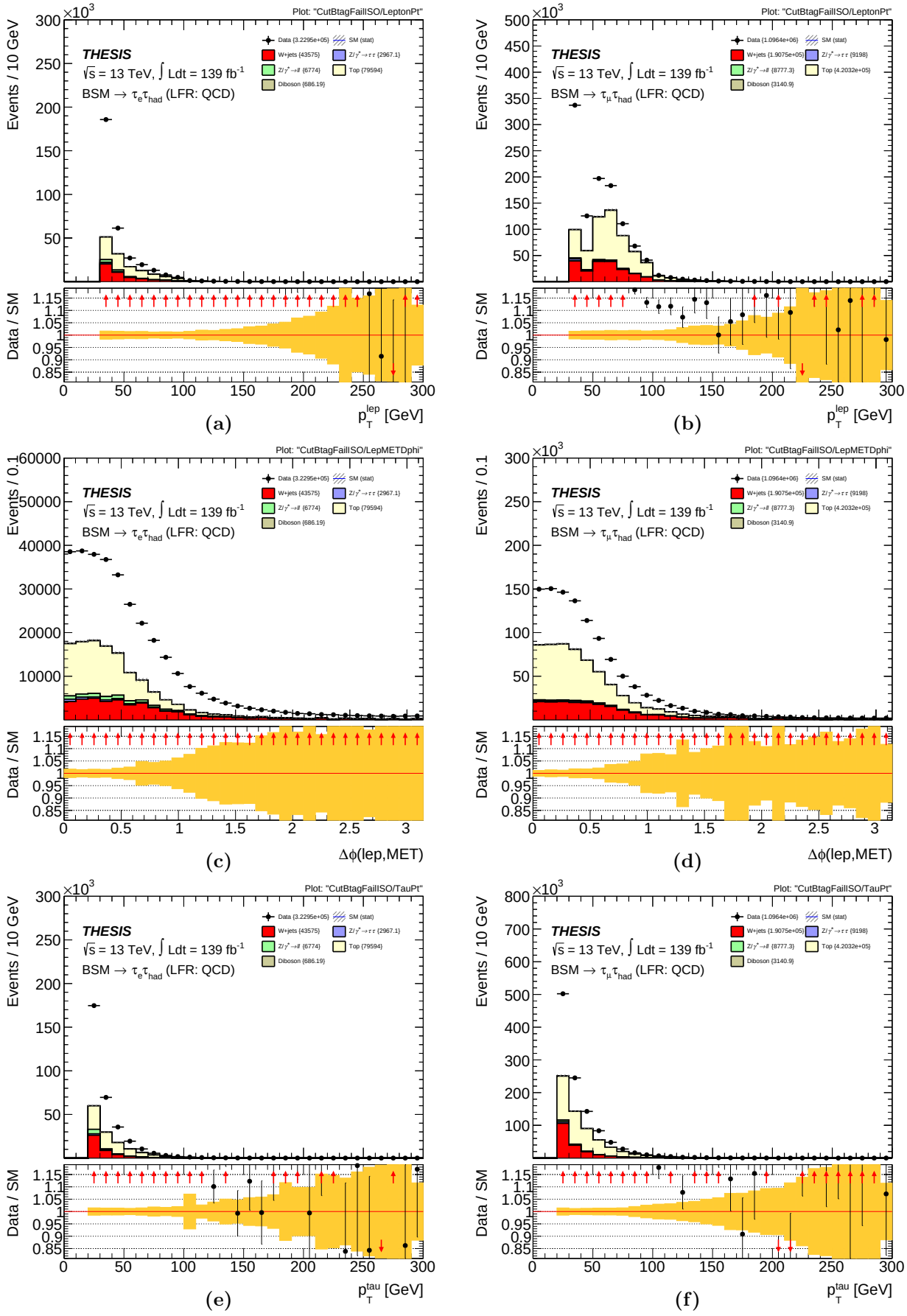

Figure 5.2.8: Plots of the QCD fake component which fail the lepton isolation requirement within the Lepton Fake Region as used in the calculation of the Lepton Fake Factor, representing lepton p_{T}, $|\Delta\phi(\ell, E_{\mathrm{T}}^{\mathrm{miss}})|$ and tau p_{T} (from top to bottom). The region is divided into the $e\tau_{\mathrm{had}}$ (left) and $\mu\tau_{\mathrm{had}}$ (right) sub-channels, representing the b-tag category.

Since the L-FR should now have all processes completely represented, and expect that the recorded data and MC simulation would agree, it can also be considered to serve as a *control region* (CR), as a means to further constrain the background independently of the SR. However, upon inspection of both Figures 5.2.5f and 5.2.6f, it is of most concern that there is still a significant level of mismodelling between the data and MC prediction which is visible in p_{T}^{τ} for the $\mu\tau_{\mathrm{had}}$ channel. After $\sim$50 GeV, the prediction consistently overestimates the data by an increasing factor of up to $\sim$3, the result of which would have an adverse effect on the fake estimation.

In order to correct for this, a *scale factor* (SF) is derived such as to force the QCD fake contribution closer to that of the data. So for the L-FR, the L-SF is parameterised in the mismodelled variable of concern, p_{T}^{τ}, but also like the L-FF calculation, in bins of $|\Delta\phi(\ell, E_{\mathrm{T}}^{\mathrm{miss}})|$ with the same binning ranges as for the b-veto and b-tag categories. The L-SF is calculated only for the $\mu\tau_{\mathrm{had}}$ channel, thus resulting in seven distributions which can be seen in Figures 5.2.9 and 5.2.10.

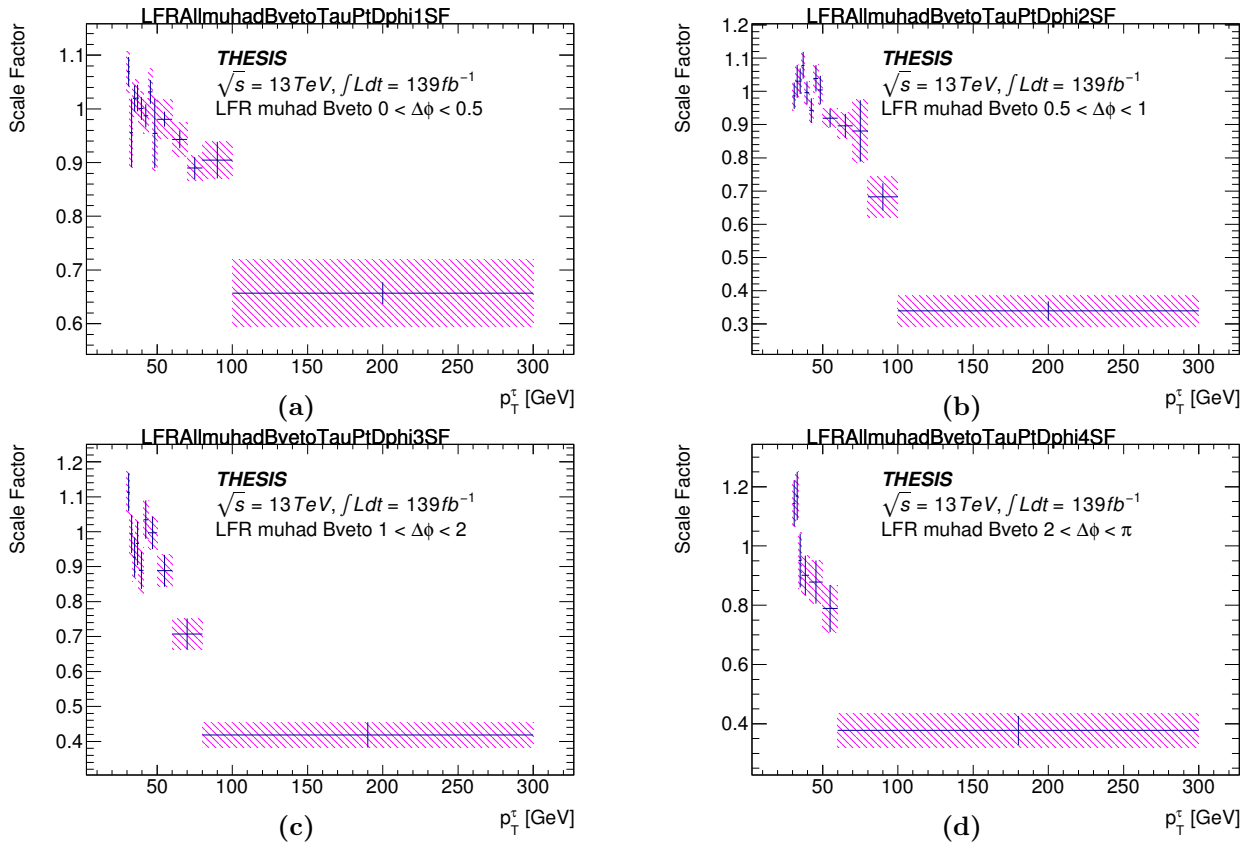

Figure 5.2.9: Plots of the Lepton Scale Factor distribution across the selected tau p_{T}, as calculated from the Lepton Fake Region, for each binning range of $|\Delta\phi(\ell, E_{\mathrm{T}}^{\mathrm{miss}})|$ (from top left to bottom right). The scale factors are parameterised in the b-veto category, representing the $\mu\tau_{\mathrm{had}}$ sub-channel.

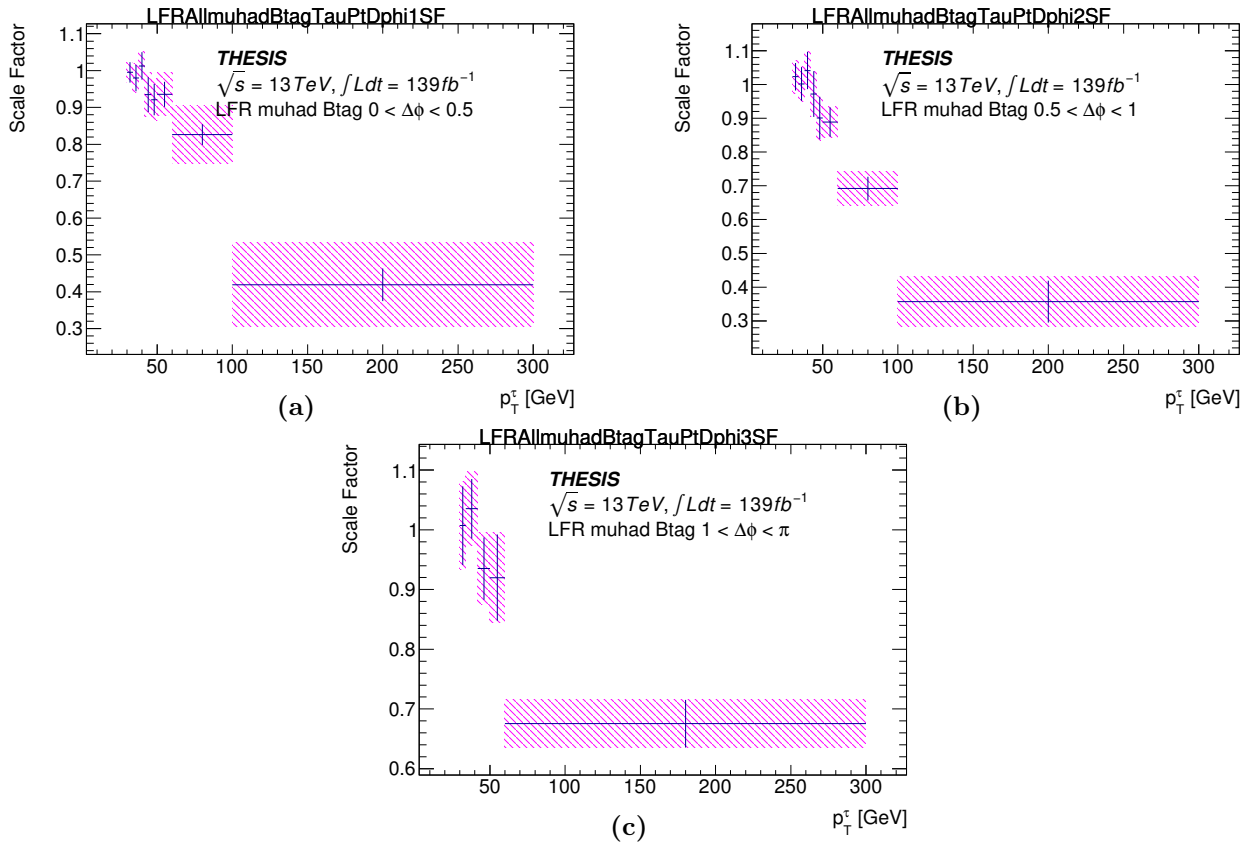

Figure 5.2.10: Plots of the Lepton Scale Factor distribution across the selected tau p_{T}, as calculated from the Lepton Fake Region, for each binning range of $|\Delta\phi(\ell, E_{\mathrm{T}}^{\mathrm{miss}})|$ (from top left to bottom right). The scale factors are parameterised in the b-tag category, representing the $\mu\tau_{\mathrm{had}}$ sub-channel.

Once again, the newly derived L-SF is applied back into the L-FR in order to cross-check the modelling a final time. Since the L-SF is parameterised only for the $\mu\tau_{\mathrm{had}}$ channel, only the results shown in Figure 5.2.11 would be affected. When comparing the results with those seen in Figures 5.2.5 and 5.2.6 before the L-SF calculation, the agreement in p_{T}^{τ} is now much more satisfactory, with the majority of the prediction evenly within a reasonable 15 % of the data, especially when considering the increasing statistical uncertainties of this order at high p_{T}^{τ}. Upon further inspection, cases of any remaining mismodelling, such as in Figure 5.2.11e, are still expected to be accounted for by systematic uncertainties should they be represented, the likes of which will be calculated for the SR in Section 5.4. Furthermore, any other unsolved disagreement beyond this which has a significant effect on the downstream analysis will be accommodated by being derived as an additional systematic uncertainty in the final result.

This success concludes the L-FR studies, and the result provides the remainder of the BSMtautauCAF analysis with two new parameters for the MJ fake background estimation: the L-FF and the L-SF, along with their statistical uncertainties which will be propagated as a systematic uncertainty in the final SR analysis, as to be discussed in Section 5.4.

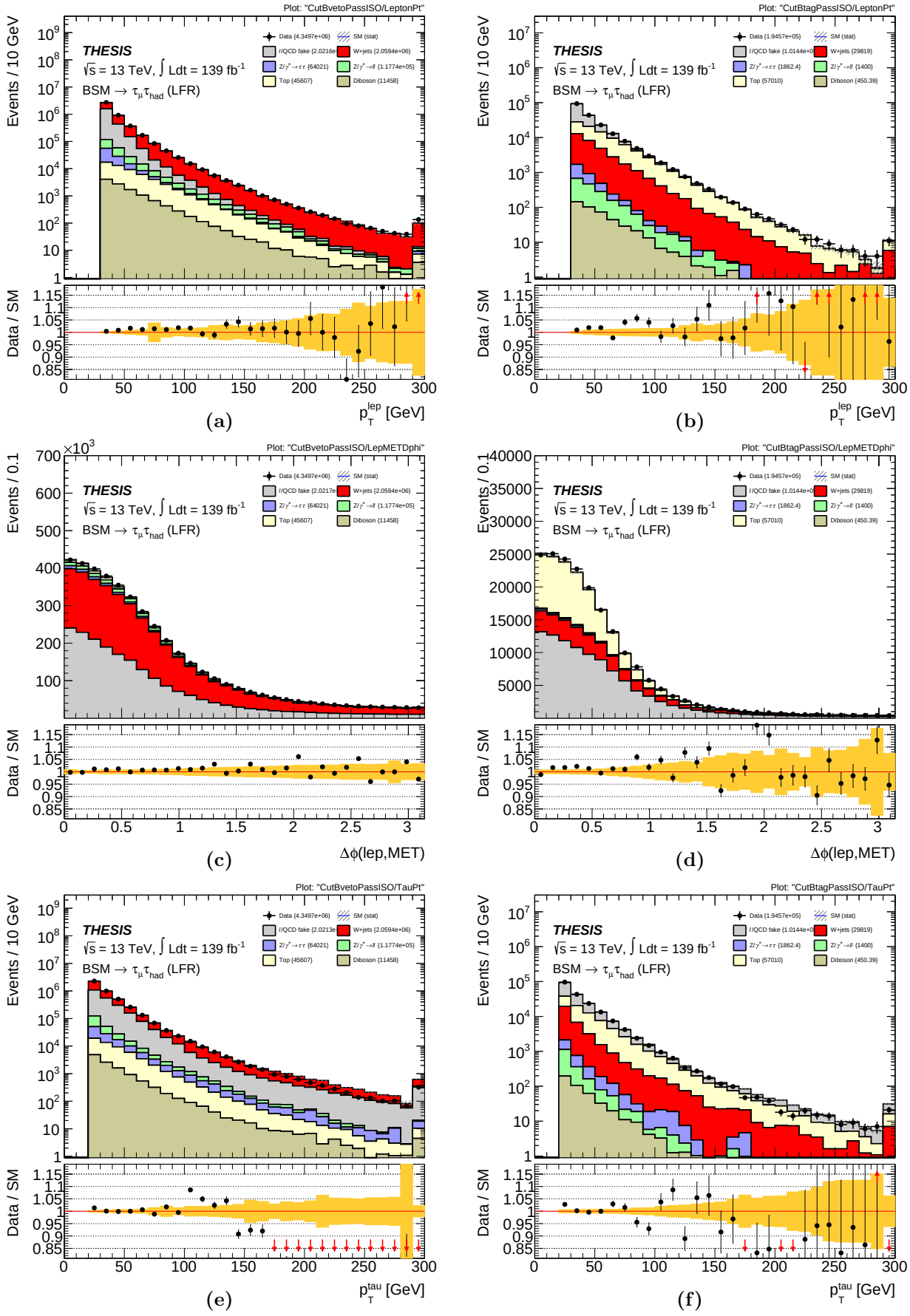

Figure 5.2.11: Plots of the Lepton Fake Region which pass the lepton isolation requirement with the Lepton Scale Factor applied back, representing lepton p_{T}, $|\Delta\phi(\ell, E_{\mathrm{T}}^{\mathrm{miss}})|$ and tau p_{T} (from top to bottom). The region is divided into the b-veto (left) and b-tag (right) categories, representing the $\mu\tau_{\mathrm{had}}$ sub-channel.

5.2.2 W boson and top quark fake estimation

In contrast to the L-FR, the W/T-FR is defined much more similarly to the SR event selection, where this time the FF calculation focuses on toggling the tau ID requirement. The exceptions apply to the lepton m_{T} criterion now altered to be at least 60 GeV (so as to not suppress the W+jets contribution anymore), with a maximum at 150 GeV in the b-veto category and 110 GeV in the b-tag. The W-FR and T-FR independently are differentiated by the b-veto and b-tag category selections, respectively.

As briefly mentioned in Section 5.2.1, the W/T-FR also contains a contribution from QCD fakes, so the calculation of the L-FF and its corrective L-SF are first required. In the same way as in the L-FR, the W/T-FFs are calculated from Equation 5.2.1, with their parameterisation set across only p_{T}^{τ}, for each of the $e\tau_{\mathrm{had}}$ and $\mu\tau_{\mathrm{had}}$ channels, but now also separated for 1- and 3-prong tau selections. The W-FF is calculated solely in the b-veto category and the T-FF in the b-tag. This results in a total of eight W/T-FF calculations, which are presented in Figures 5.2.12 and 5.2.13.

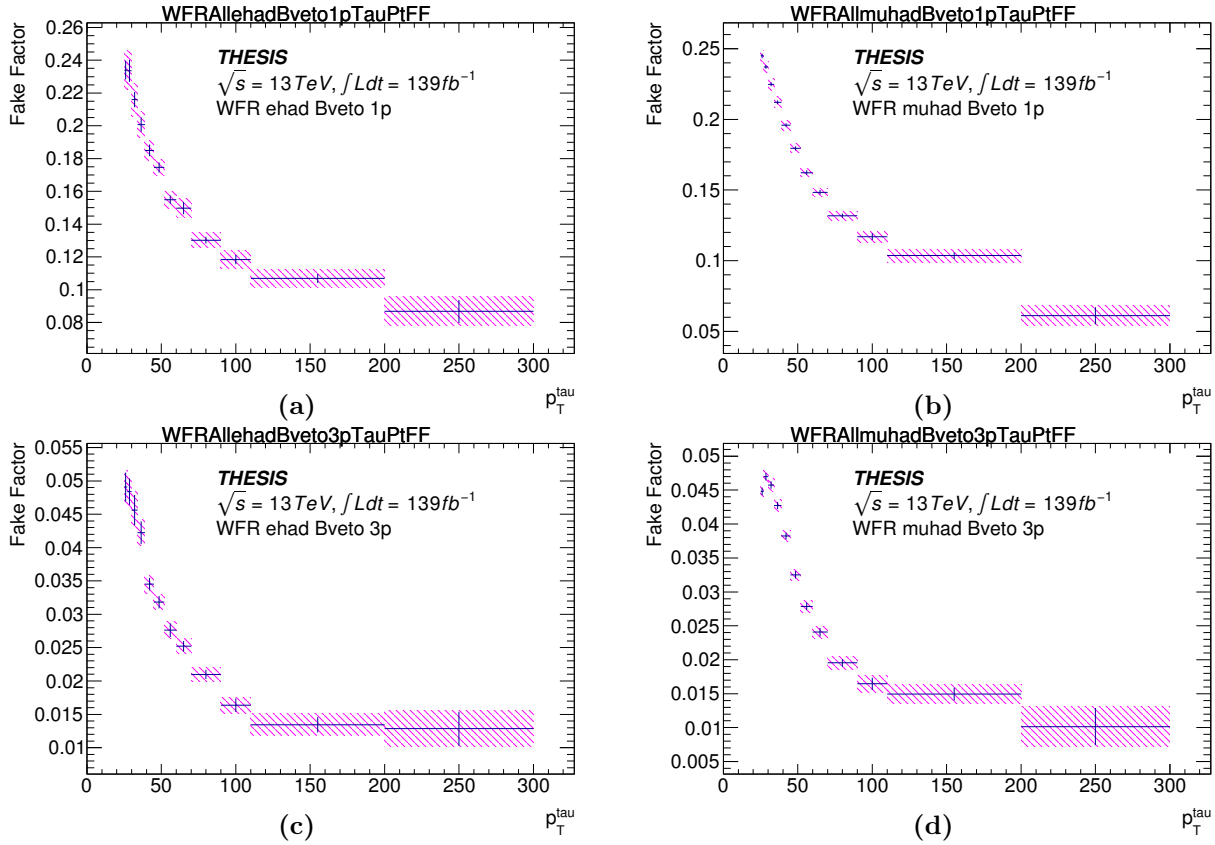

Figure 5.2.12: Plots of the W+jets/Top Fake Factor distribution across the selected tau p_{T}, as calculated from the W+jets/Top Fake Region, representing the $e\tau_{\mathrm{had}}$ (left) and $\mu\tau_{\mathrm{had}}$ (right) sub-channels, for 1- (top) and 3-prong (bottom) tau decay modes. The fake factors are parameterised in the b-veto category (for W+jets fakes).

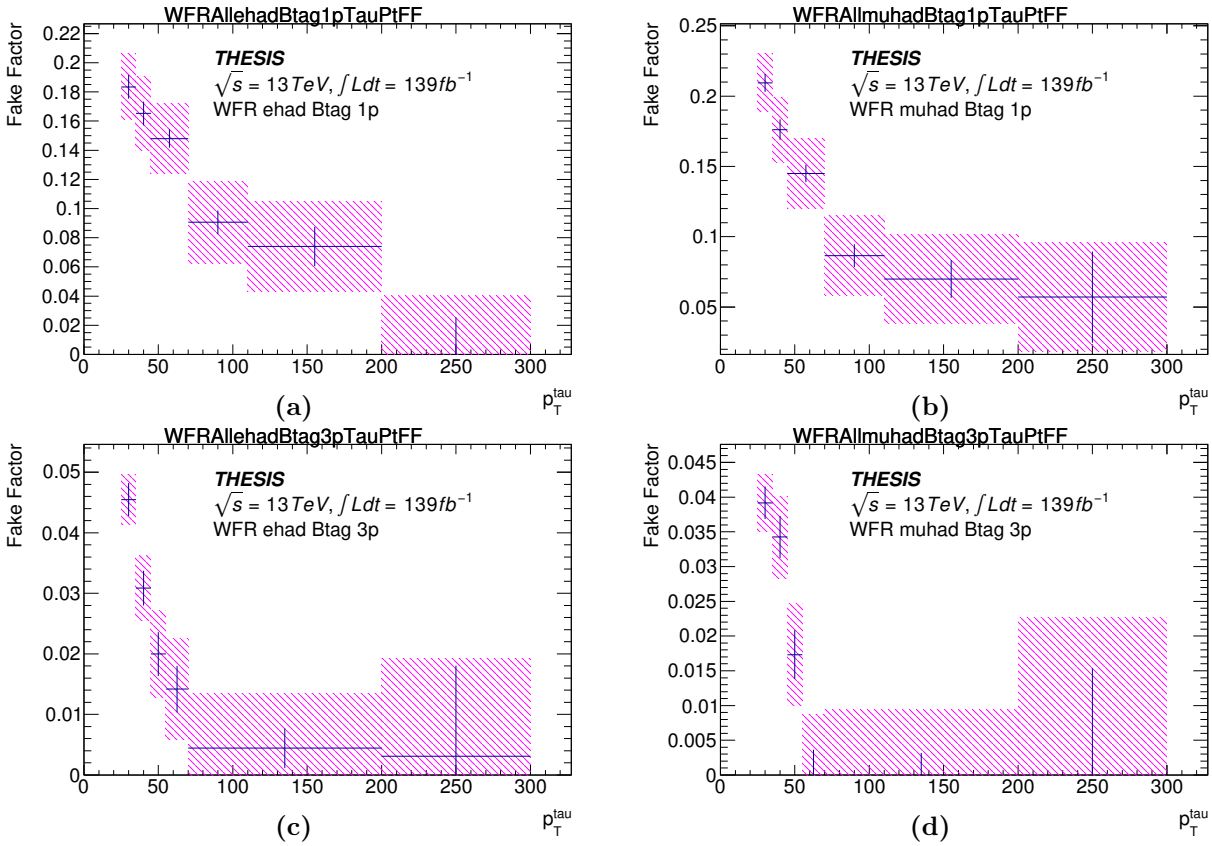

Figure 5.2.13: Plots of the W+jets/Top Fake Factor distribution across the selected tau p_{T}, as calculated from the W+jets/Top Fake Region, representing the $e\tau_{\mathrm{had}}$ (left) and $\mu\tau_{\mathrm{had}}$ (right) sub-channels, for 1- (top) and 3-prong (bottom) tau decay modes. The fake factors are parameterised in the b-tag category (for top quark fakes).

The results show that the overall values of the W/T-FF range between ∼0 to 0.25 for 1-prong tau decays and ∼0 to 0.05 for 3-prong, for the W-FF in b-veto category, as seen in Figure 5.2.12, while the T-FF in b-tag ranges between ∼0 to 0.2 for 1-prong and ∼0 to 0.05 for 3-prong, seen in Figure 5.2.13. The W/T-FF distributions all smoothly decrease with the tau p_{T} across these ranges, and are typically expected of the results.

Again, the W/T-FFs are applied back into the W/T-FR as contributions from W+jets/$t\bar{t}$ fake processes, as a means to cross-check the completed results — this can be seen in Figures 5.2.14 and 5.2.15 for W+jets, 5.2.16 and 5.2.17 for $t\bar{t}$ fakes.

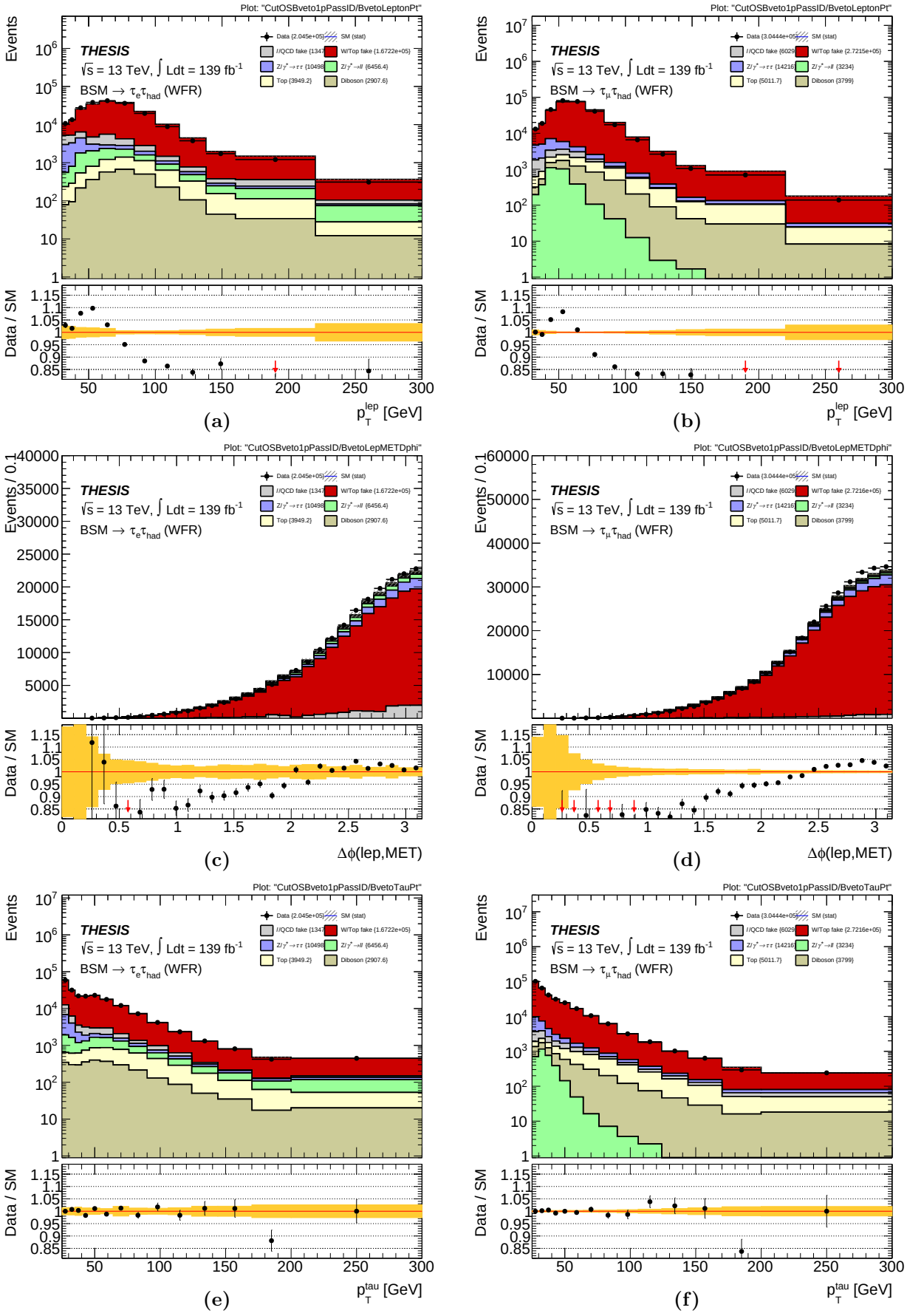

Figure 5.2.14: Plots of the W+jets Fake Region which pass the tau identification requirement with the W+jets Fake Factor applied back, in the b-veto category, for the 1-prong tau decay mode, representing lepton p_{T}, $|\Delta\phi(\ell, E_{\mathrm{T}}^{\mathrm{miss}})|$ and tau p_{T} (from top to bottom). The region is divided into the $e\tau_{\mathrm{had}}$ (left) and $\mu\tau_{\mathrm{had}}$ (right) sub-channels.

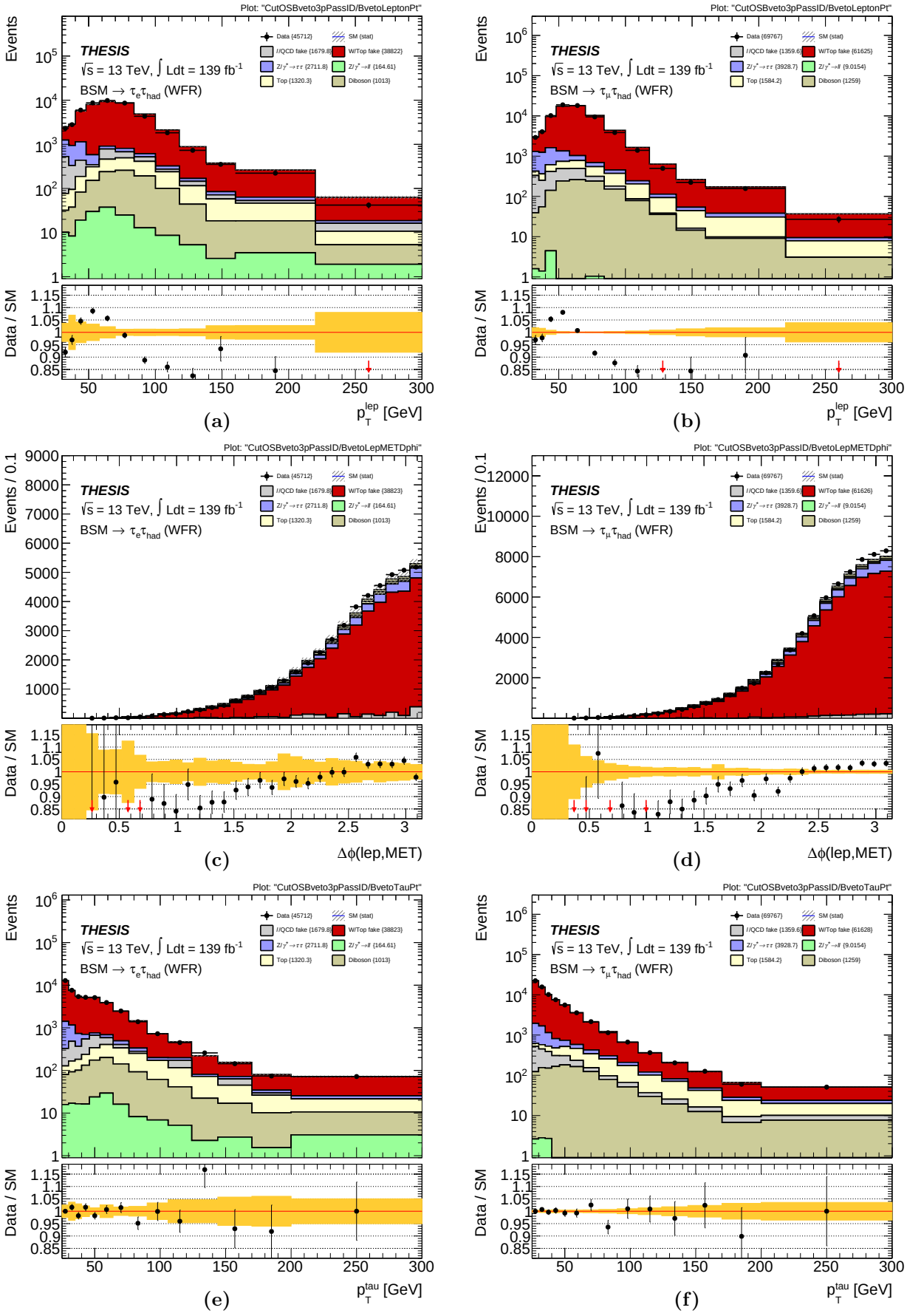

Figure 5.2.15: Plots of the W+jets Fake Region which pass the tau identification requirement with the W+jets Fake Factor applied back, in the b-veto category, for the 3-prong tau decay mode, representing lepton p_{T}, $|\Delta\phi(\ell, E_{\mathrm{T}}^{\mathrm{miss}})|$ and tau p_{T} (from top to bottom). The region is divided into the $e\tau_{\mathrm{had}}$ (left) and $\mu\tau_{\mathrm{had}}$ (right) sub-channels.

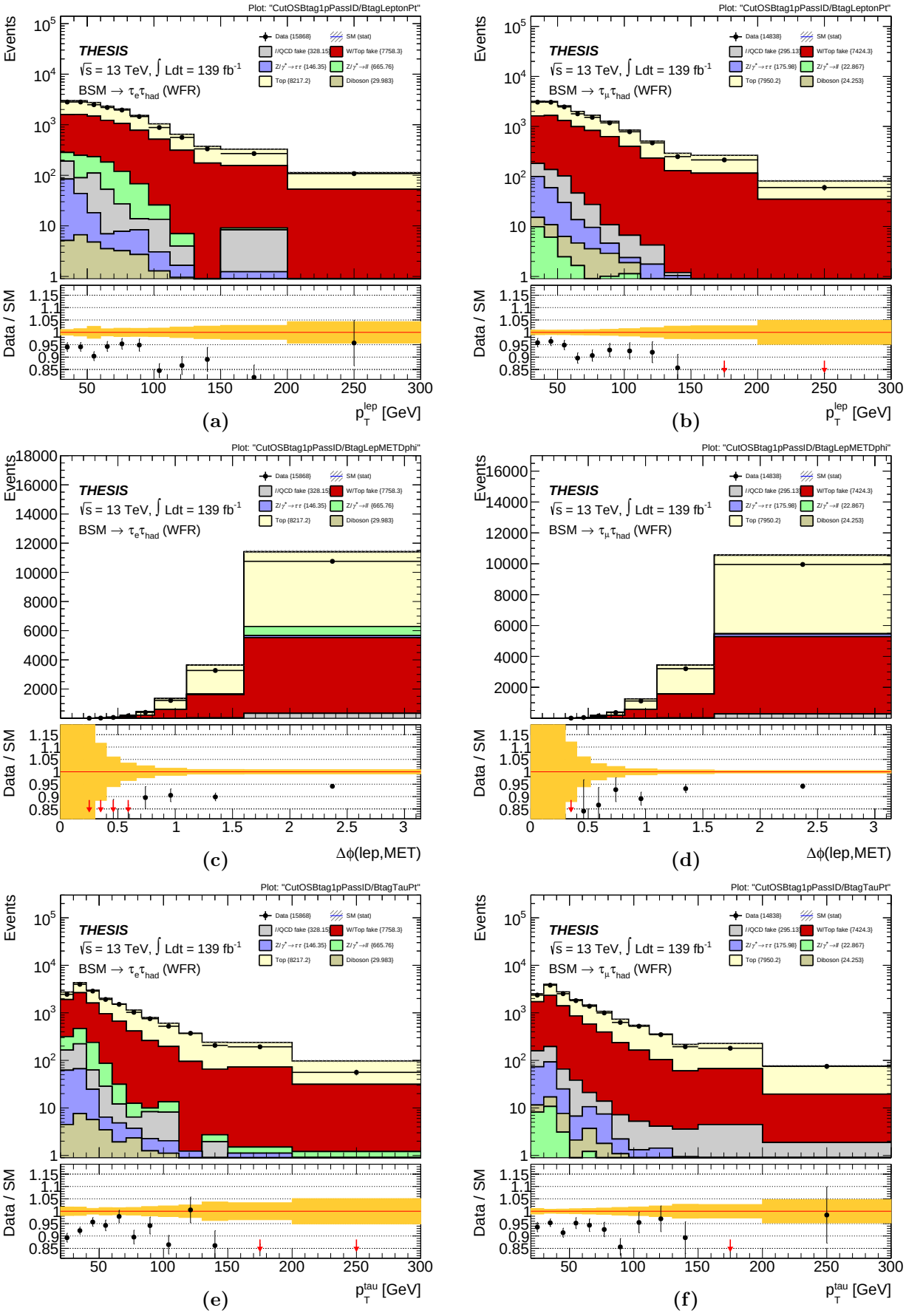

Figure 5.2.16: Plots of the Top Fake Region which pass the tau identification requirement with the Top Fake Factor applied back, in the b-tag category, for the 1-prong tau decay mode, representing lepton p_{T}, $|\Delta\phi(\ell, E_{\mathrm{T}}^{\mathrm{miss}})|$ and tau p_{T} (from top to bottom). The region is divided into the $e\tau_{\mathrm{had}}$ (left) and $\mu\tau_{\mathrm{had}}$ (right) sub-channels.

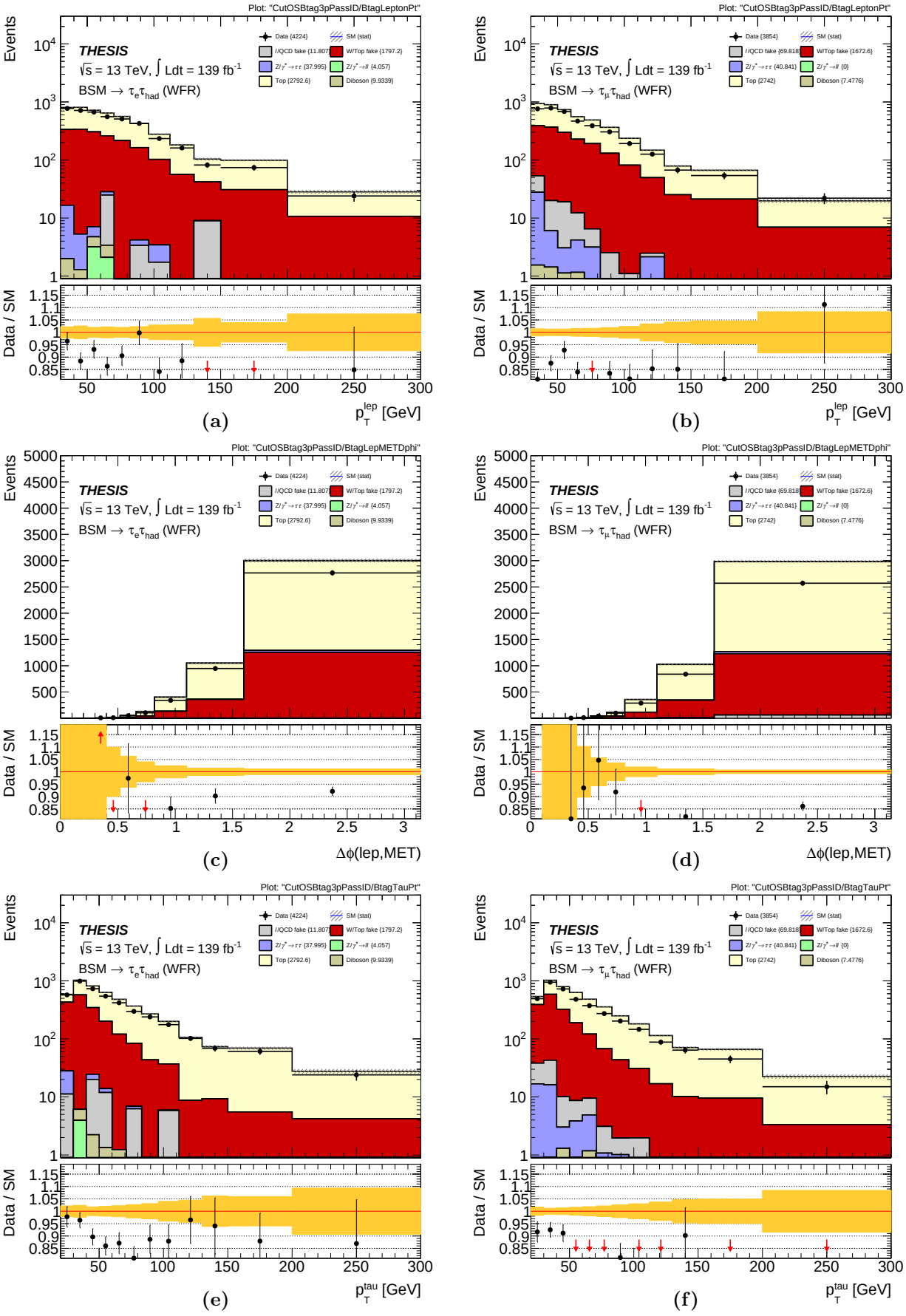

Figure 5.2.17: Plots of the Top Fake Region which pass the tau identification requirement with the Top Fake Factor applied back, in the b-tag category, for the 3-prong tau decay mode, representing lepton p_{T}, $|\Delta\phi(\ell, E_{\mathrm{T}}^{\mathrm{miss}})|$ and tau p_{T} (from top to bottom). The region is divided into the $e\tau_{\mathrm{had}}$ (left) and $\mu\tau_{\mathrm{had}}$ (right) sub-channels.

As before, reviewing the applied results of the W/T-FR reveals a significant mismodelling of concern in p_{T}^{ℓ} for the b-veto category (the W-FR). This can be seen in Figures 5.2.14a, 5.2.14b, 5.2.15a and 5.2.15b, where the disagreement between the prediction and data approaches larger than 20 % at $p_{\mathrm{T}}^{\ell} > 50\,\mathrm{GeV}$, well outside of the statistical uncertainty.

As such, a W-SF is derived in order to correct for this, where the parameterisation is separated between the $e\tau_{\mathrm{had}}$ and $\mu\tau_{\mathrm{had}}$ channels, as well for 1- and 3-prong taus. This generates four W-SFs which are represented in Figure 5.2.18.

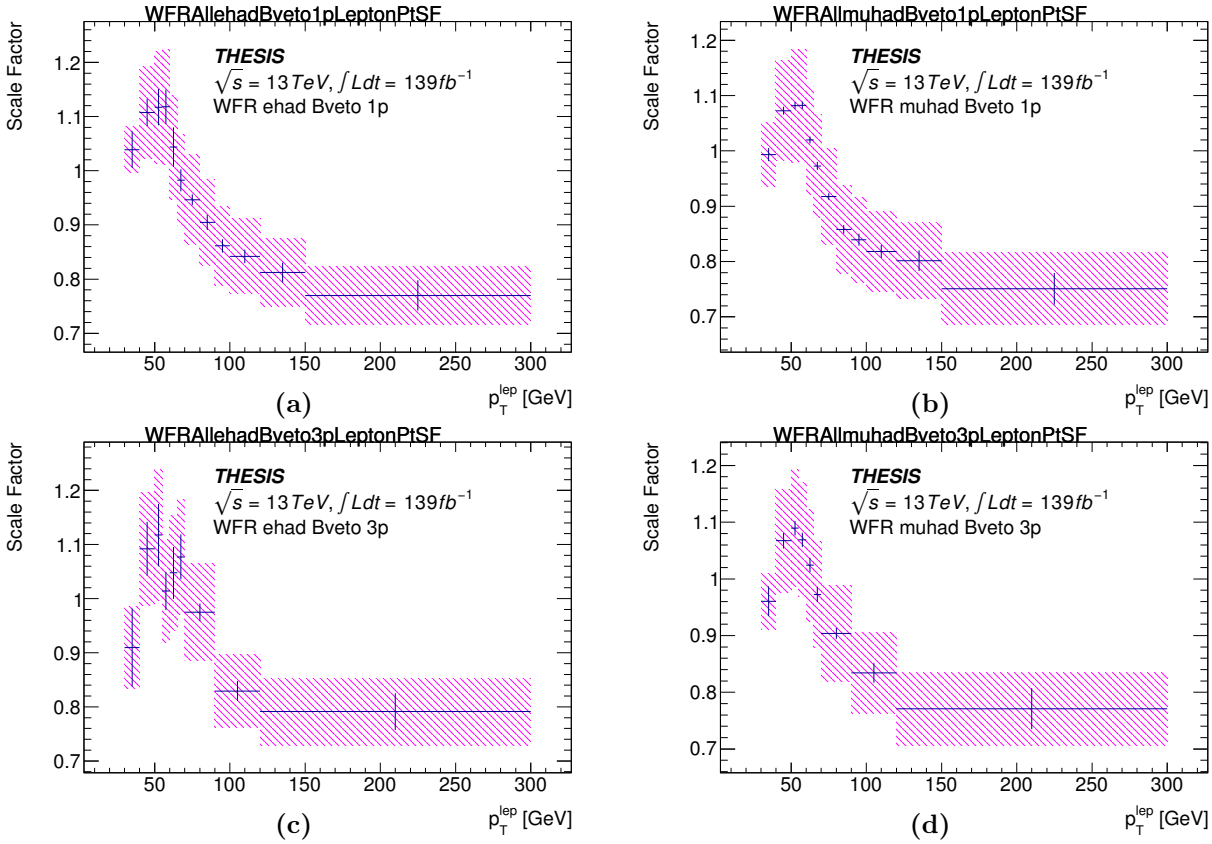

Figure 5.2.18: Plots of the W+jets Scale Factor distribution across the selected lepton p_{T}, as calculated from the W+jets Fake Region, representing the $e\tau_{\mathrm{had}}$ (left) and $\mu\tau_{\mathrm{had}}$ (right) sub-channels, for 1- (top) and 3-prong (bottom) tau decay modes.

Additionally, it can also be seen that there is a strong disagreement in p_{T}^{τ} for the b-tag category (the T-FR). However, this appears to be attributed to the significant genuine top quark contribution in the region, forming approximately 50 % of the residual background within the top quark fake component. As will be further discussed in Section 5.2.3, a CR dedicated to constraining the genuine top quark process (the T-CR) through the calculation of a T-SF will be required for the final background estimation, but its significant presence already demands the correction to be applied in the T-FR estimation. This leads to another cyclical analysis strategy, since the T-CR will first require an estimation of its top fake contribution, as calculated in the T-FR. To circumvent such an iterative process, the T-FF is no longer applied to the b-tag category for the T-FR, thus serving no further use, and instead the W-FF calculated from the b-veto takes its place with an additional normalisation factor — this is acceptable as it turns out the modelling of p_{T}^{τ} between the b-veto and b-tag categories are not too dissimilar. The normalisation factor is calculated from the ratio of the overall (single bin) FF between the original T-FF and the W-FF, separately for 1- and 3-prong taus, at approximately $\sim$0.8. This W-FF-based alternative for the T-FF is then applied into the T-CR as the top fake contribution, the result of which can be seen in Figures 5.2.19 and 5.2.20. This allows the T-CR to calculate its T-SF much sooner for genuine tops, which will then also subsume the correction to the T-FR and thus nullifying the dependency problem. The T-SF calculation is parameterised in p_{T}^{τ}, also for 1- and 3-prong taus, but rather as the full $\tau_{\mathrm{lep}}\tau_{\mathrm{had}}$ combination of the $e\tau_{\mathrm{had}}$ and $\mu\tau_{\mathrm{had}}$ sub-channels. This provides two T-SF distributions which are shown in Figure 5.2.21.

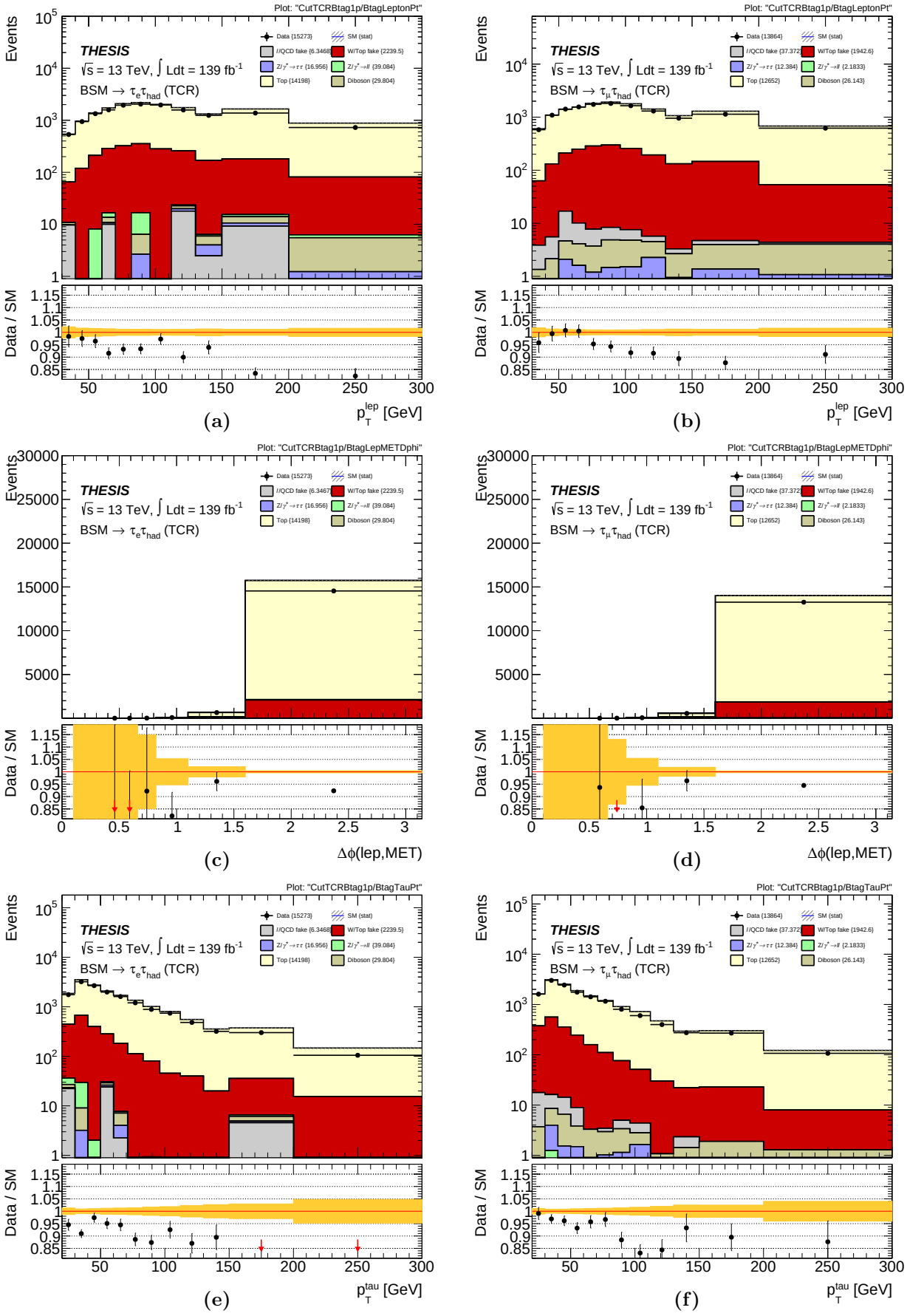

Figure 5.2.19: Plots of the Top Control Region with the W+jets-derived Top Fake Factor applied back, in the b-tag category, for the 1-prong tau decay mode, representing lepton p_{T}, $|\Delta\phi(\ell, E_{\mathrm{T}}^{\mathrm{miss}})|$ and tau p_{T} (from top to bottom). The region is divided into the $e\tau_{\mathrm{had}}$ (left) and $\mu\tau_{\mathrm{had}}$ (right) sub-channels.

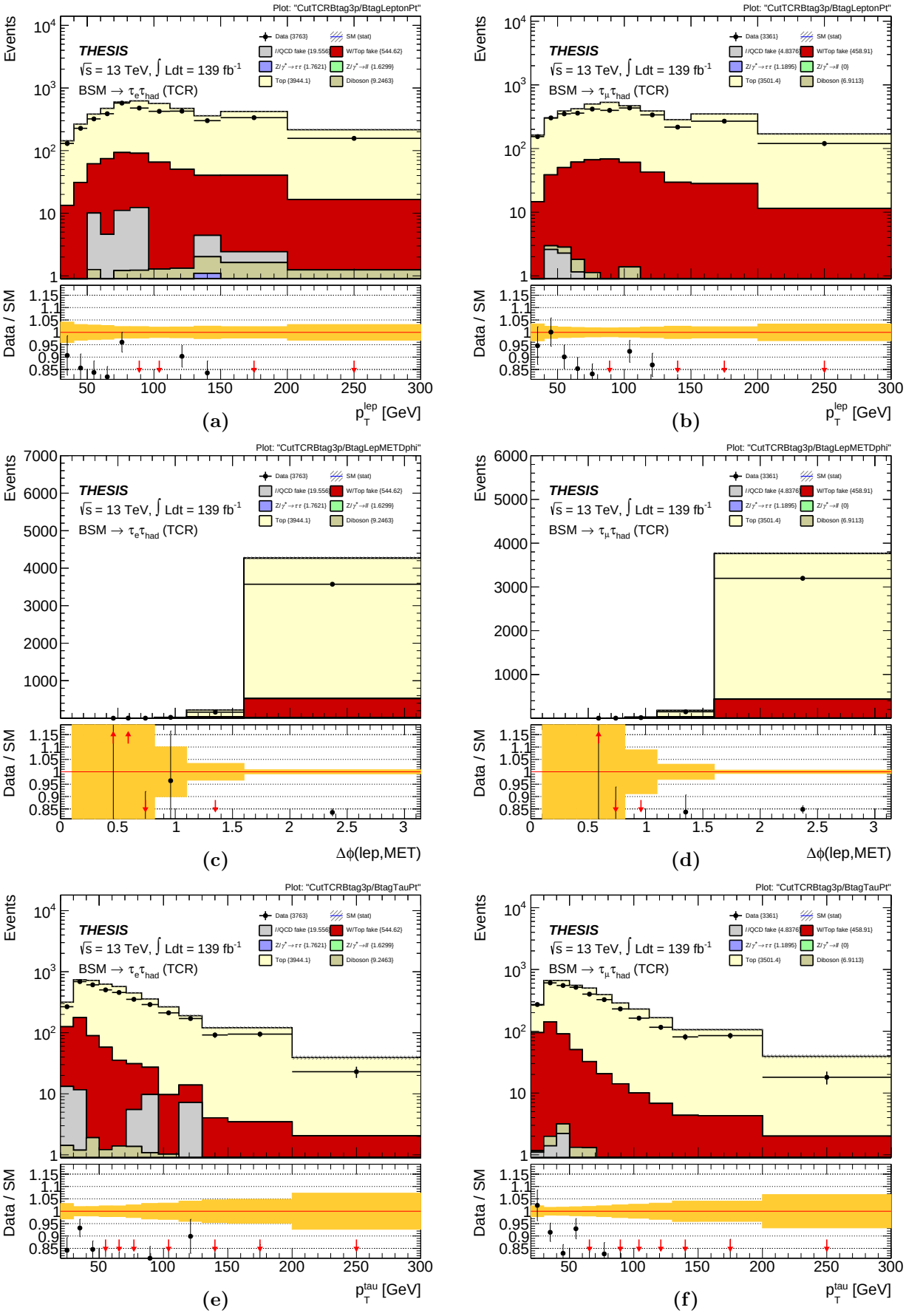

Figure 5.2.20: Plots of the Top Control Region with the W+jets-derived Top Fake Factor applied back, in the b-tag category, for the 3-prong tau decay mode, representing lepton p_{T}, $|\Delta\phi(\ell, E_{\mathrm{T}}^{\mathrm{miss}})|$ and tau p_{T} (from top to bottom). The region is divided into the $e\tau_{\mathrm{had}}$ (left) and $\mu\tau_{\mathrm{had}}$ (right) sub-channels.

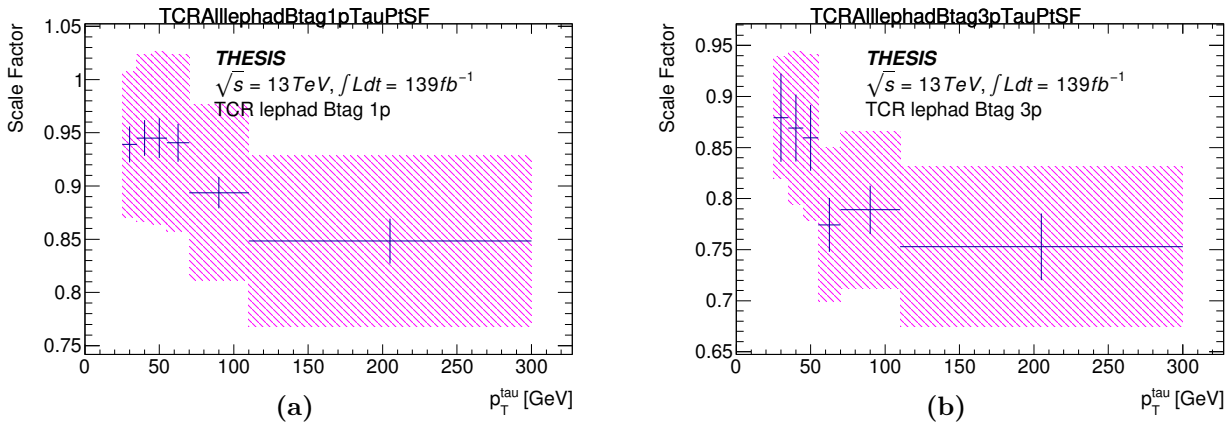

Figure 5.2.21: Plots of the Top Scale Factor distribution across the selected tau p_{T}, as calculated from the Top Control Region, representing the inclusive $\tau_{\mathrm{lep}}\tau_{\mathrm{had}}$ channel, for 1- (left) and 3-prong (right) tau decay modes, parameterised in the b-tag category.

Concluding the W/T-FR study, four new parameters were derived: the W-FF and the W-FF-cum-T-FF for the estimation of W+jets and $t\bar{t}$ fakes, respectively, along with corrections from the W-SF and the T-SF, where the T-SF was sourced in advance from the genuine T-CR. All newly calculated SFs are applied back into the W/T-FR to confirm decent modelling in Figures 5.2.22 and 5.2.23 for W+jets, 5.2.24 and 5.2.25 for $t\bar{t}$ fakes. Just as with the L-FR, any remaining discrepancies, such as in Figure 5.2.22f, are either negligible, accountable by systematic uncertainty, or otherwise propagated as its own systematic uncertainty in the final result.

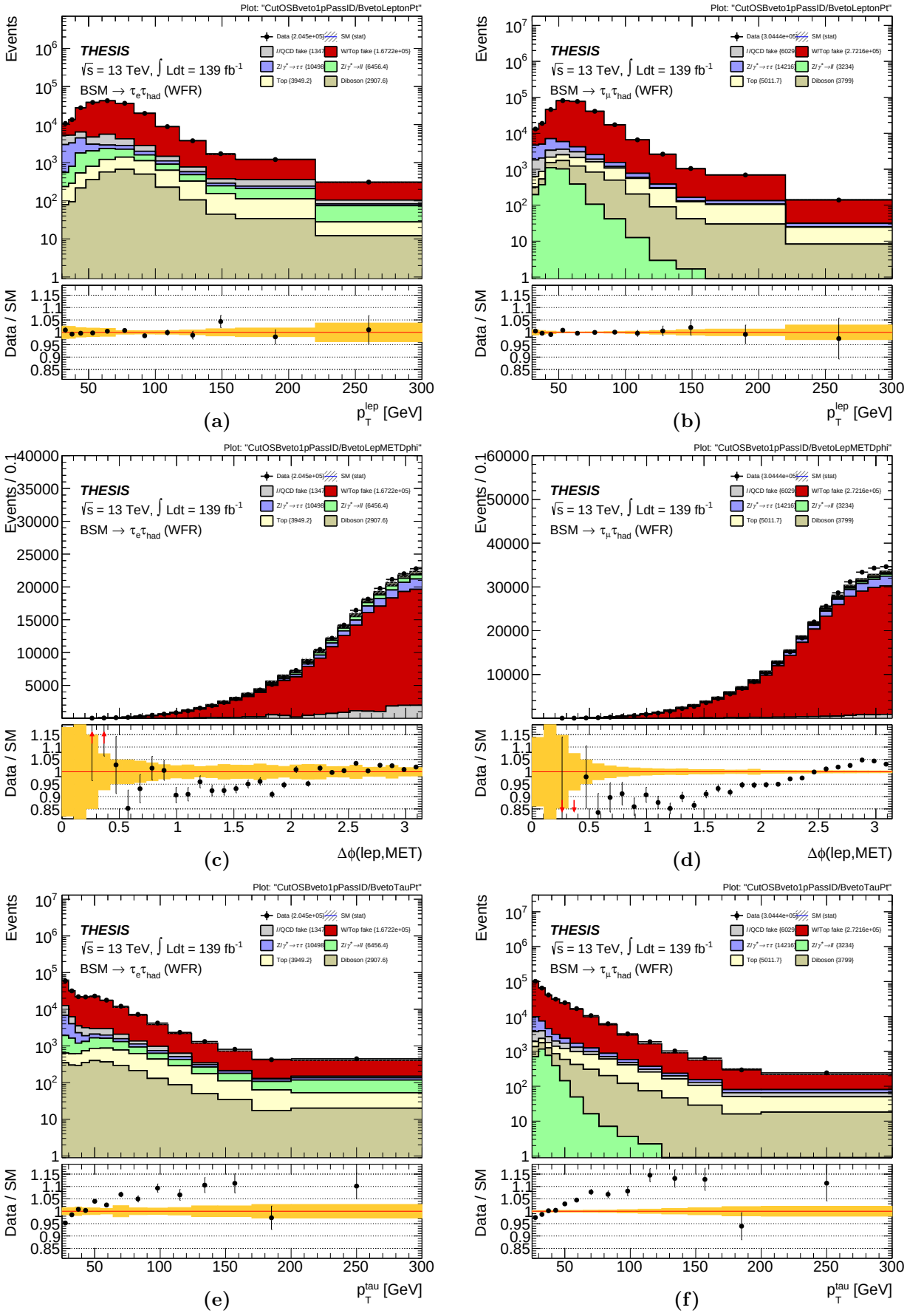

Figure 5.2.22: Plots of the W+jets Fake Region which pass the tau identification requirement with the W+jets Scale Factor applied back, in the b-veto category, for the 1-prong tau decay mode, representing lepton p_{T}, $|\Delta\phi(\ell, E_{\mathrm{T}}^{\mathrm{miss}})|$ and tau p_{T} (from top to bottom). The region is divided into the $e\tau_{\mathrm{had}}$ (left) and $\mu\tau_{\mathrm{had}}$ (right) sub-channels.

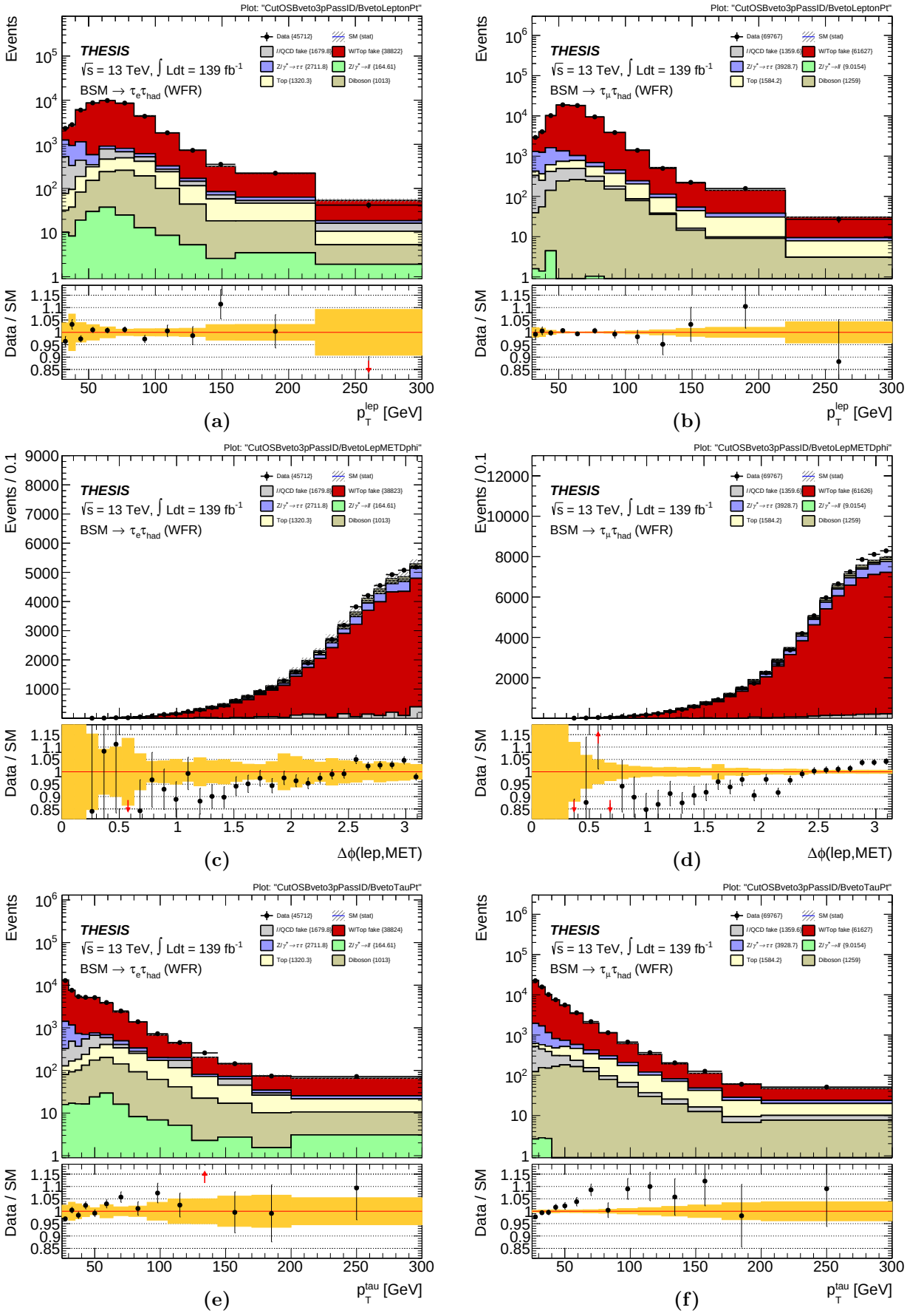

Figure 5.2.23: Plots of the W+jets Fake Region which pass the tau identification requirement with the W+jets Scale Factor applied back, in the b-veto category, for the 3-prong tau decay mode, representing lepton p_{T}, $|\Delta\phi(\ell, E_{\mathrm{T}}^{\mathrm{miss}})|$ and tau p_{T} (from top to bottom). The region is divided into the $e\tau_{\mathrm{had}}$ (left) and $\mu\tau_{\mathrm{had}}$ (right) sub-channels.

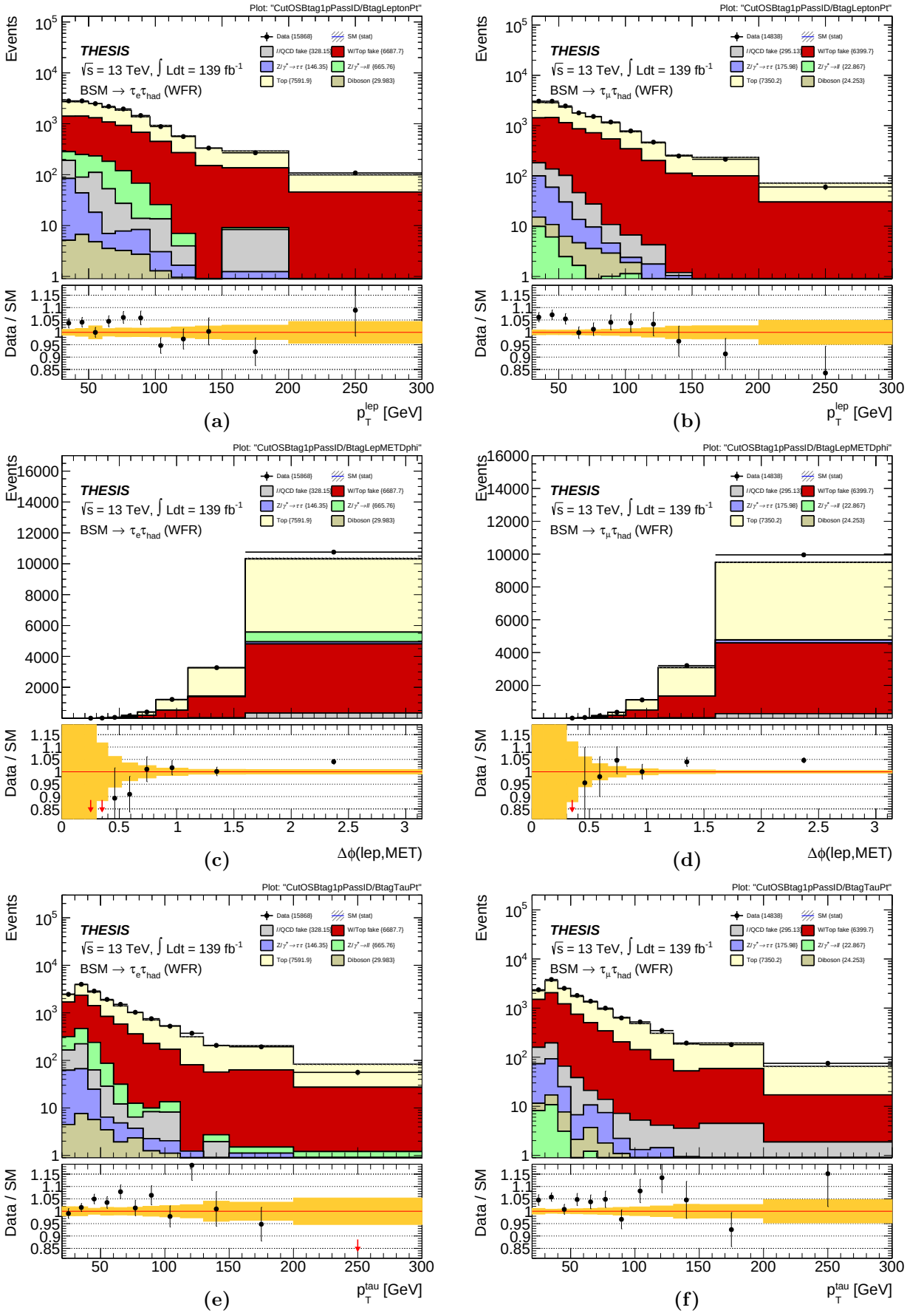

Figure 5.2.24: Plots of the Top Fake Region which pass the tau identification requirement with the Top Scale Factor applied back, in the *b*-tag category, for the 1-prong tau decay mode, representing lepton p_{T}, $|\Delta\phi(\ell, E_{\mathrm{T}}^{\mathrm{miss}})|$ and tau p_{T} (from top to bottom). The region is divided into the $e\tau_{\mathrm{had}}$ (left) and $\mu\tau_{\mathrm{had}}$ (right) sub-channels.

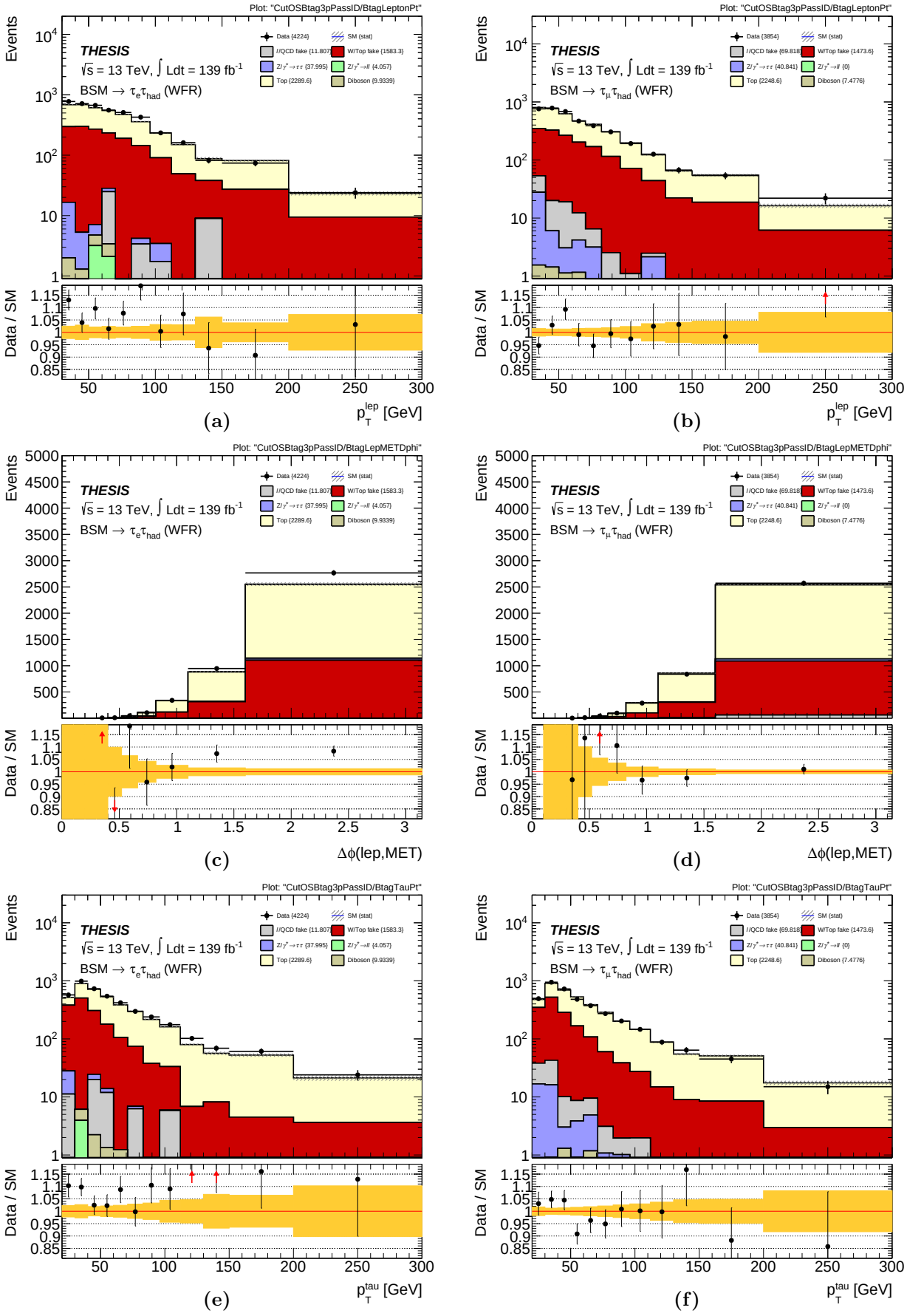

Figure 5.2.25: Plots of the Top Fake Region which pass the tau identification requirement with the Top Scale Factor applied back, in the b-tag category, for the 3-prong tau decay mode, representing lepton p_{T}, $|\Delta\phi(\ell, E_{\mathrm{T}}^{\mathrm{miss}})|$ and tau p_{T} (from top to bottom). The region is divided into the $e\tau_{\mathrm{had}}$ (left) and $\mu\tau_{\mathrm{had}}$ (right) sub-channels.

5.2.3 Top quark estimation and validation

As already briefly introduced in Section 5.2.2, the T-CR is designed to observe and model the contribution from genuine top quark processes, a background more prevalent in the b-tag category. The T-CR is defined quite closely to the SR event selection, where instead the lepton m_{T} is required to be at least 60 GeV, such as to enrich events from $t\bar{t}$ processes, and the $e\tau_{\mathrm{had}}$ invariant mass rejection is no longer required.

The intention of the T-CR is to cross-check the modelling between data and MC, as with the other (fake) CRs, and derive a T-SF to correct for any disagreement, particularly in p_{T}^{τ}. However, given the complex circumstances raised by the T-FR studies in Section 5.2.2, the T-CR and its calculation for a T-SF has already been deployed. As such, the application of the T-SF back into the T-CR to confirm a complete modelling agreement are shown in Figures 5.2.26 and 5.2.27. The T-CR will then play an instrumental role towards deriving the systematic uncertainty and fitting procedures, to be discussed later in Section 5.4.

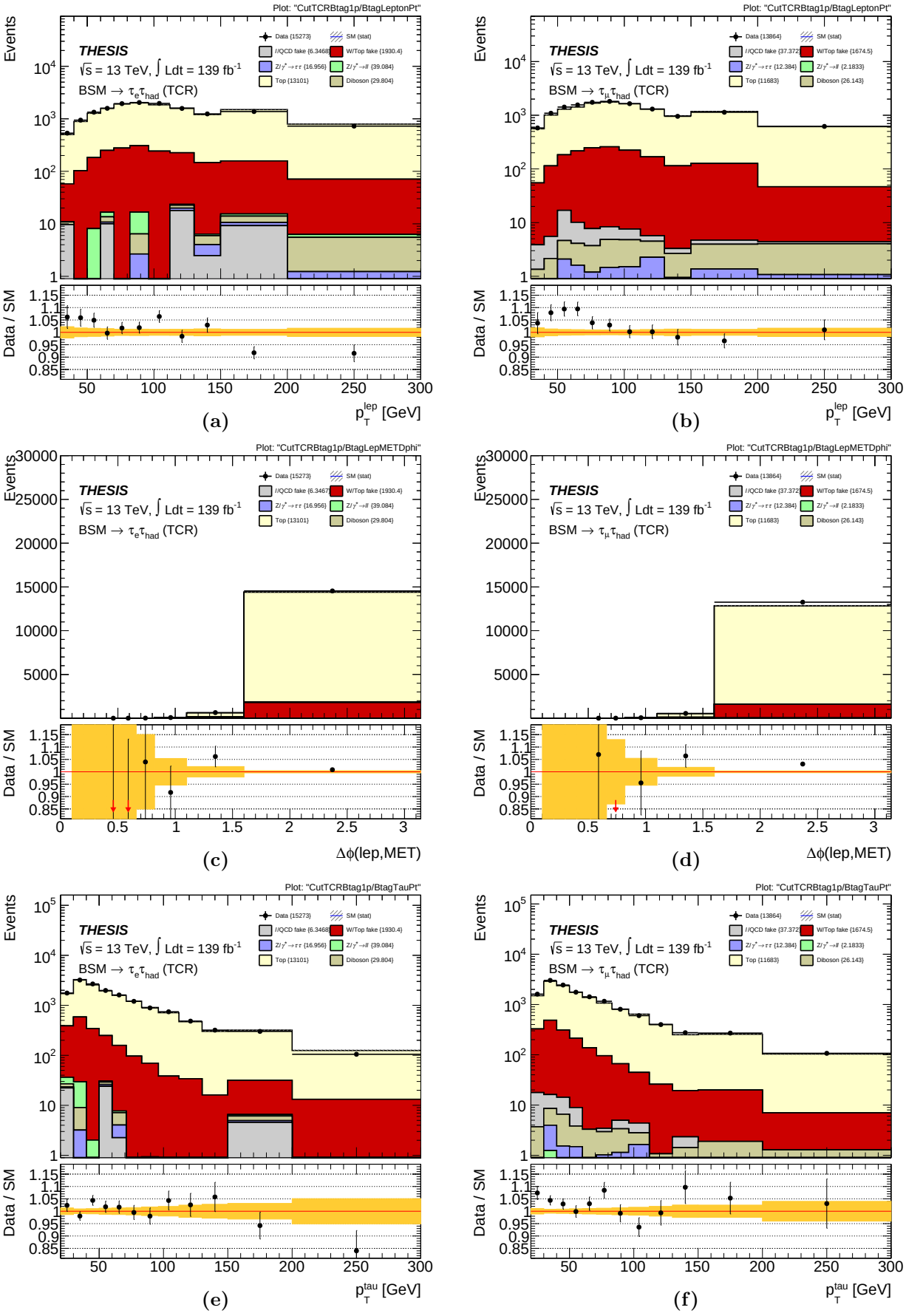

Figure 5.2.26: Plots of the Top Control Region with the Top Scale Factor applied back, in the b-tag category, for the 1-prong tau decay mode, representing lepton p_{T}, $|\Delta\phi(\ell, E_{\mathrm{T}}^{\mathrm{miss}})|$ and tau p_{T} (from top to bottom). The region is divided into the $e\tau_{\mathrm{had}}$ (left) and $\mu\tau_{\mathrm{had}}$ (right) sub-channels.

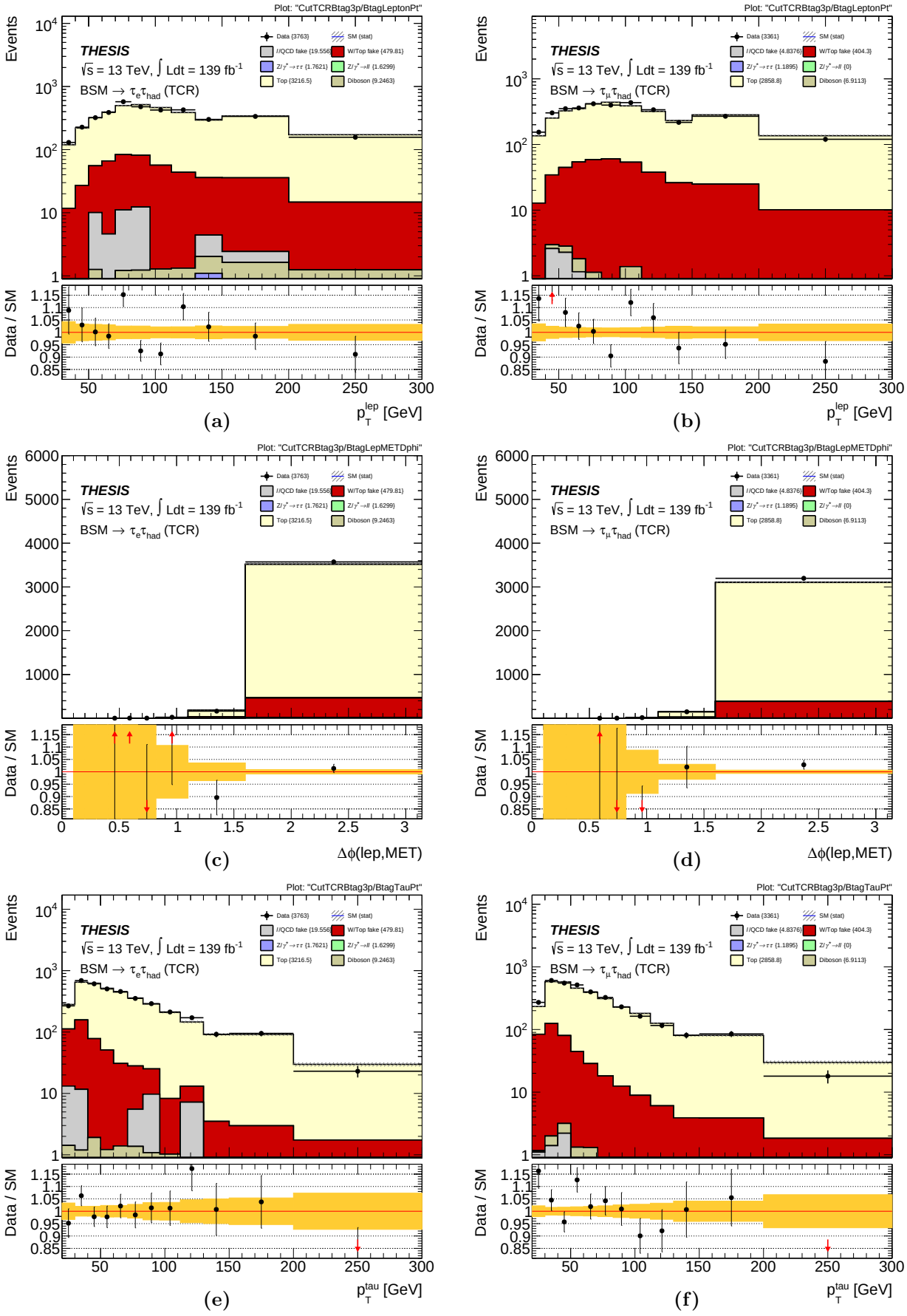

Figure 5.2.27: Plots of the Top Control Region with the Top Scale Factor applied back, in the b-tag category, for the 3-prong tau decay mode, representing lepton p_{T}, $|\Delta\phi(\ell, E_{\mathrm{T}}^{\mathrm{miss}})|$ and tau p_{T} (from top to bottom). The region is divided into the $e\tau_{\mathrm{had}}$ (left) and $\mu\tau_{\mathrm{had}}$ (right) sub-channels.

So far, a number of (fake) CRs have been defined to constrain the background modelling for different individual processes before it is revealed in the SR. In summary, these have included the L-FR, the W/T-FR and the T-CR, which have all derived a number of correction factors, all to be passed on to the final signal calculation. However, it is important to note that these assumptions are only valid on two primary conditions. Firstly, the event kinematic selections as defined in the CRs are sufficiently independent to those of the SR, such as to avoid any bias in modelling background events which may contain a potential BSM signal. Secondly, the kinematics in the CRs must still be at least similar enough to the SR, so that their derived factors are reasonably applicable to the SR selection.

In order to satisfy these conditions, an approach is commonly used in ATLAS when defining CRs and SRs, known as the *ABCD method*. The name refers to an allocation of four regions, each arbitrarily labelled [A, B, C, D], when parameterised across two independent variables of interest, with an example illustrated in Figure 5.2.28. Based on this example, the SR would be labelled by region D, while the CR is labelled by region A. The key point is that the parameter space utilised by regions A and D are completely orthogonal to each other, thereby ensuring the independency of the event selection between the CR and SR, as required by the first condition. In the context of the BSM $\tau_{\text{lep}}\tau_{\text{had}}$ analysis, this is largely ensured by the variation on the lepton m_{T} selection criterion between all of these regions.

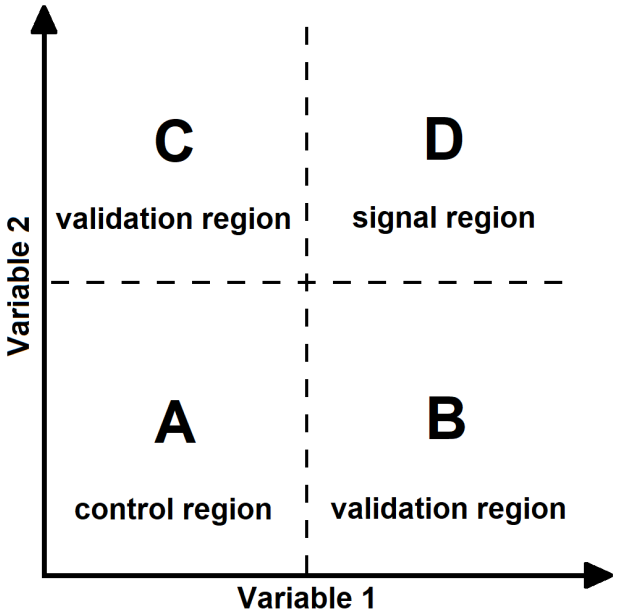

Figure 5.2.28: A generic representation of the ABCD method for dividing Control, Validation and Signal Regions across a two-parameter space.

As for regions B and C, while these are still largely independent to the SR through one of the variables, as represented by region D, there is still some partial overlap in the parameter space which runs a risk, albeit likely negligible, of signal contamination. Therefore, while these regions would not be adequate to serve as a formal CR, they are however useful for establishing a smooth transition in the kinematic selections between the CR and SR. This allows for the analysis to inspect the validity of the assumptions made in the CRs, as questioned by the second condition, and so commonly referred to as a *validation region* (VR). The VR event selection is defined in the $\tau_{\text{lep}}\tau_{\text{had}}$ analysis to be very close to the SR, where the only difference lies with the lepton m_{T} selection, now between 40 to 60 GeV.

The VR will culminate and test all of the correction factors derived in the (fake) background CRs thus far, to a region that is similar to the SR and so probing their accuracy. The results of this VR are shown in Figures 5.2.29–5.2.32. In order to efficiently distinguish a potential BSM signal, observed in the data, from the SM background, predicted by MC, a discriminant variable is defined as the *total transverse mass* of the di-tau system, $m_{\mathrm{T}}^{\mathrm{tot}}$, as given by Equation 5.2.2. While this mass reconstruction had previously been estimated through various complex algorithm techniques [65], experience had shown difficulty with handling the abundance of undetected neutrinos from these tau decays, offering little-to-no improvement in the sensitivity over this kinematic estimation, especially given its increase in computational demand.

$$m_{\mathrm{T}}^{\mathrm{tot}} \equiv \sqrt{(p_{\mathrm{T}}^{\tau_1} + p_{\mathrm{T}}^{\tau_2} + E_{\mathrm{T}}^{\mathrm{miss}})^2 - (\mathbf{p}_{\mathrm{T}}{}^{\tau_1} + \mathbf{p}_{\mathrm{T}}{}^{\tau_2} + \mathbf{E}_{\mathrm{T}}^{\mathrm{miss}})^2} \tag{5.2.2}$$

It can be seen from the results in the VR that there is still some significant mismodelling remaining in p_{T}^{τ} and $|\Delta\phi(\tau, E_{\mathrm{T}}^{\mathrm{miss}})|$, for example in Figure 5.2.29d. As such, a V-SF is extrapolated from the difference between data and MC, with parameterisation across p_{T}^{τ}, for both the $e\tau_{\mathrm{had}}$ and $\mu\tau_{\mathrm{had}}$ channels, and for 1- and 3-prong taus. Additionally, the parameterisation is divided in the b-veto and b-tag categories, such that extra binning through $|\Delta\phi(\tau, E_{\mathrm{T}}^{\mathrm{miss}})|$ is also applied in the b-veto, with three steps defined from 0 to 1, to 2 and to π rad. This provides a total of sixteen V-SF calculations, all of which are shown in Figures 5.2.33–5.2.36. However, unlike the other SFs derived in this analysis, the V-SF will not be applied back as a weight into the SR, since the VR doesn't serve as a CR. Instead, the V-SF is intended to represent a new systematic uncertainty based on the remnant mismodelling from the background estimation thus far, which will be seen in Section 5.4.

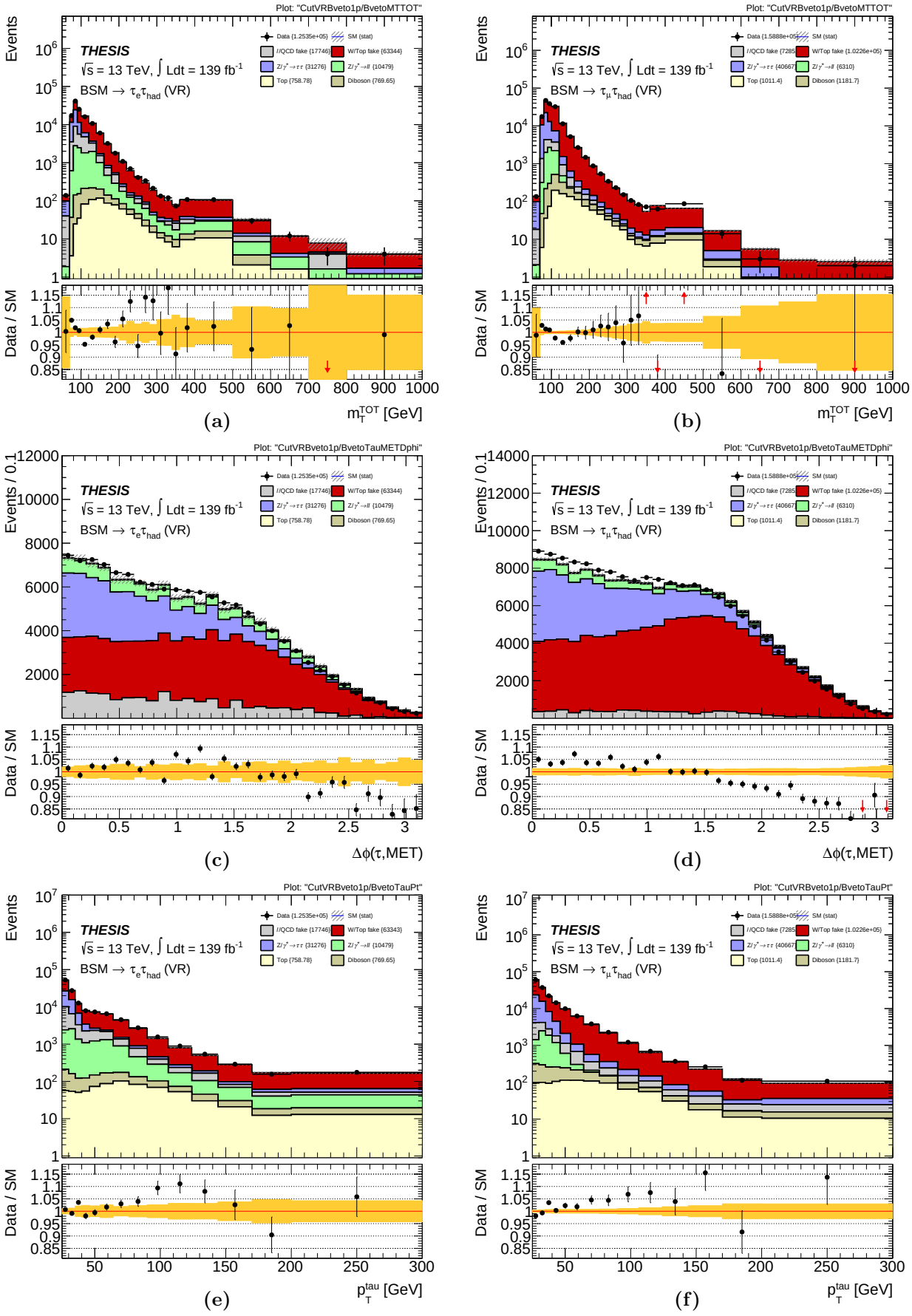

Figure 5.2.29: Plots of the Validation Region with all derived factors applied back, in the b-veto category, for the 1-prong tau decay mode, representing the signal discriminant $m_{\mathrm{T}}^{\mathrm{tot}}$, $|\Delta\phi(\tau, E_{\mathrm{T}}^{\mathrm{miss}})|$ and tau p_{T} (from top to bottom). The region is divided into the $e\tau_{\mathrm{had}}$ (left) and $\mu\tau_{\mathrm{had}}$ (right) sub-channels.

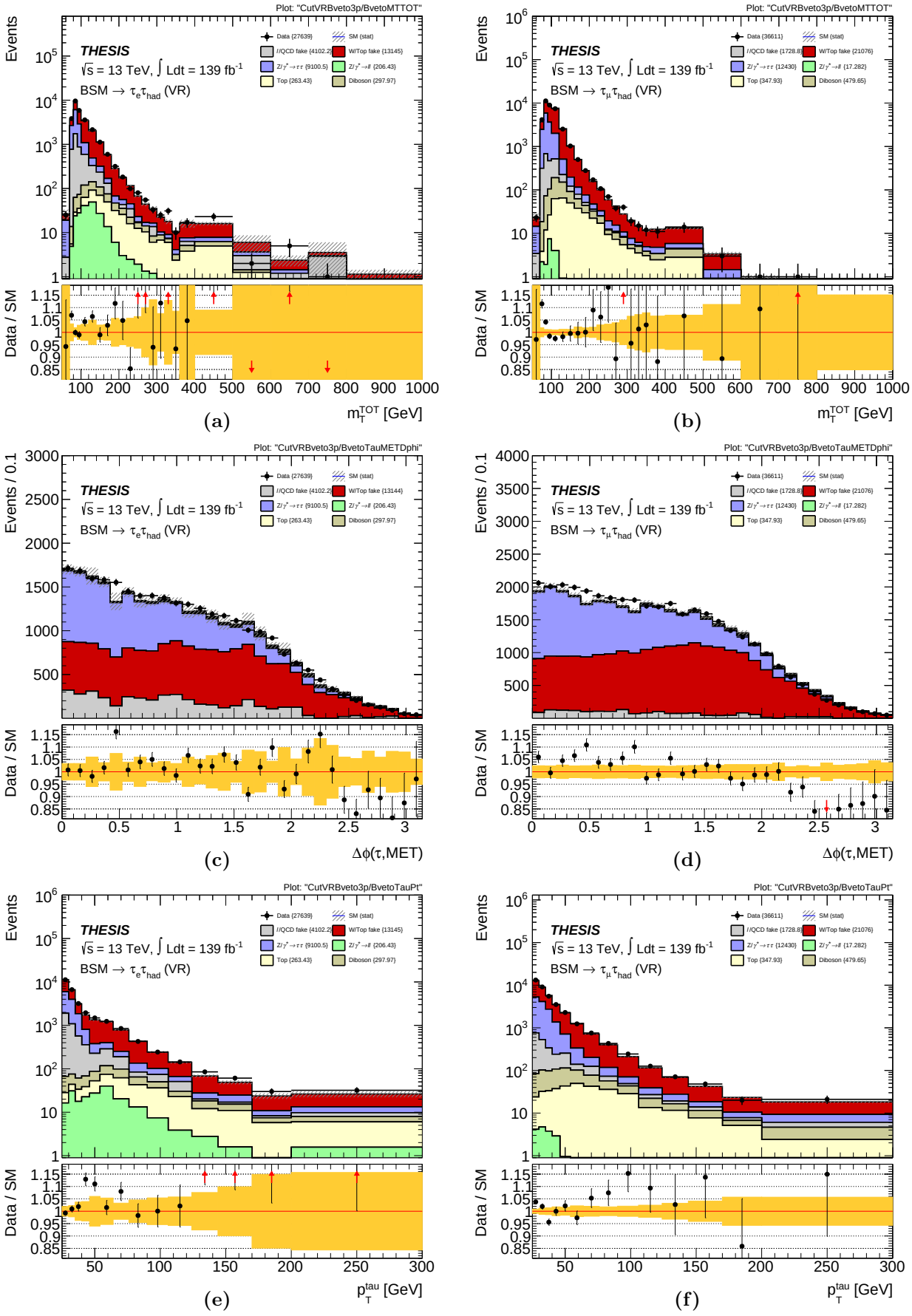

Figure 5.2.30: Plots of the Validation Region with all derived factors applied back, in the b-veto category, for the 3-prong tau decay mode, representing the signal discriminant $m_{\mathrm{T}}^{\mathrm{tot}}$, $|\Delta\phi(\tau, E_{\mathrm{T}}^{\mathrm{miss}})|$ and tau p_{T} (from top to bottom). The region is divided into the $e\tau_{\mathrm{had}}$ (left) and $\mu\tau_{\mathrm{had}}$ (right) sub-channels.

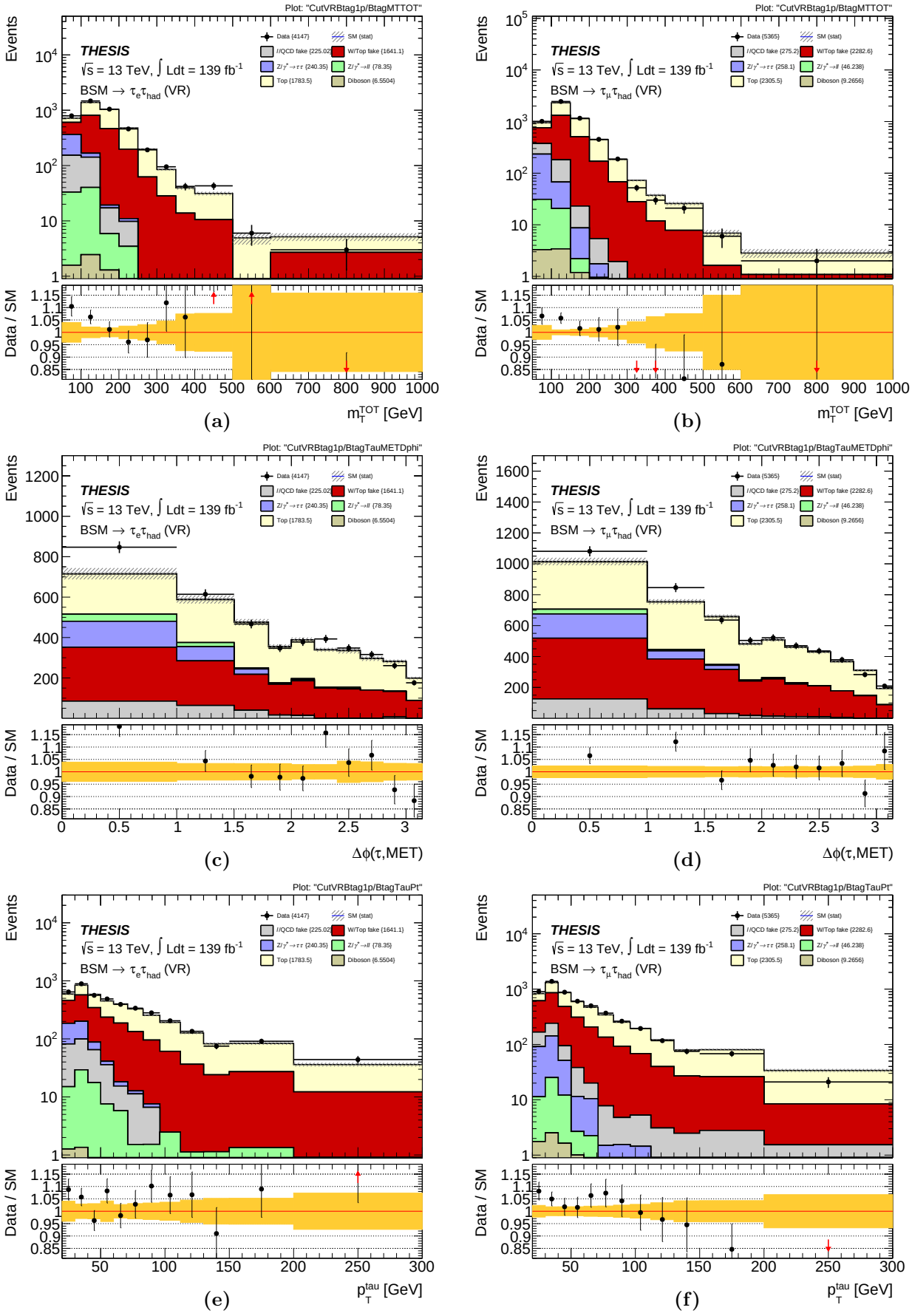

Figure 5.2.31: Plots of the Validation Region with all derived factors applied back, in the b-tag category, for the 1-prong tau decay mode, representing the signal discriminant $m_{\mathrm{T}}^{\mathrm{tot}}$, $|\Delta\phi(\tau, E_{\mathrm{T}}^{\mathrm{miss}})|$ and tau p_{T} (from top to bottom). The region is divided into the $e\tau_{\mathrm{had}}$ (left) and $\mu\tau_{\mathrm{had}}$ (right) sub-channels.

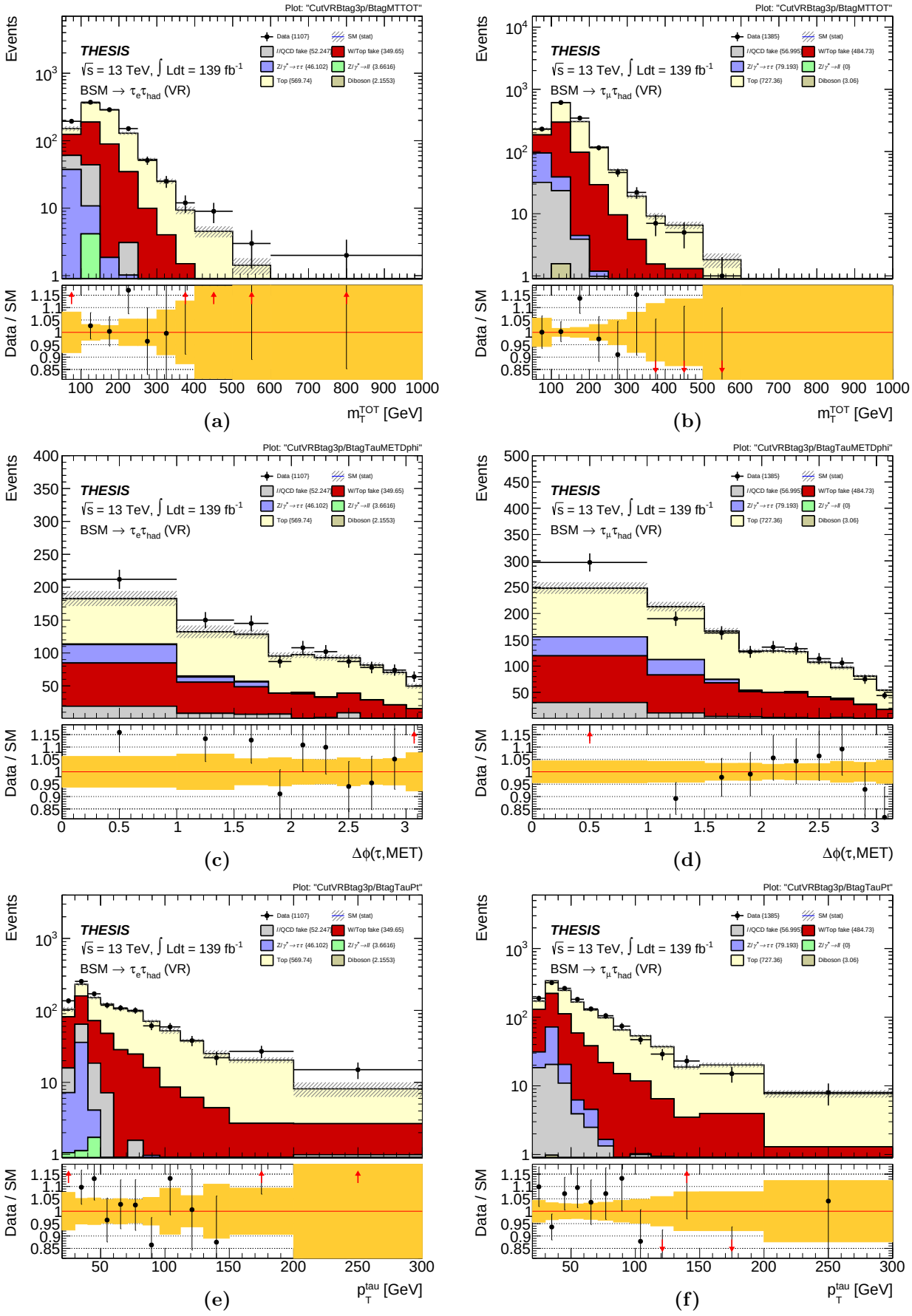

Figure 5.2.32: Plots of the Validation Region with all derived factors applied back, in the b-tag category, for the 3-prong tau decay mode, representing the signal discriminant $m_{\mathrm{T}}^{\mathrm{tot}}$, $|\Delta\phi(\tau, E_{\mathrm{T}}^{\mathrm{miss}})|$ and tau p_{T} (from top to bottom). The region is divided into the $e\tau_{\mathrm{had}}$ (left) and $\mu\tau_{\mathrm{had}}$ (right) sub-channels.

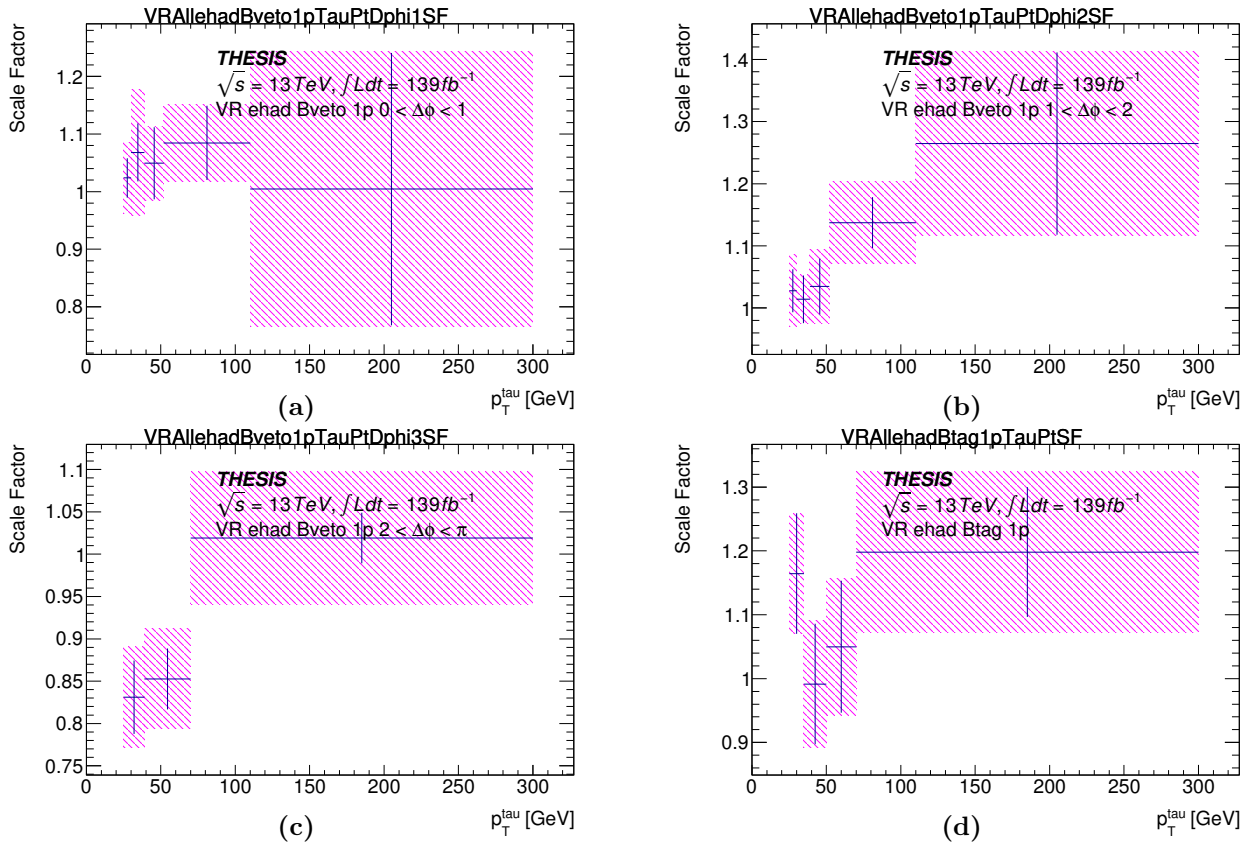

Figure 5.2.33: Plots of the Validation Scale Factor distribution across the selected tau p_{T}, as calculated from the Validation Region, for each binning range of $|\Delta\phi(\tau, E_{\mathrm{T}}^{\mathrm{miss}})|$ in the b-veto category followed by the b-tag (from top left to bottom right). The scale factors are parameterised in the $e\tau_{\mathrm{had}}$ sub-channel, representing the 1-prong tau decay mode.

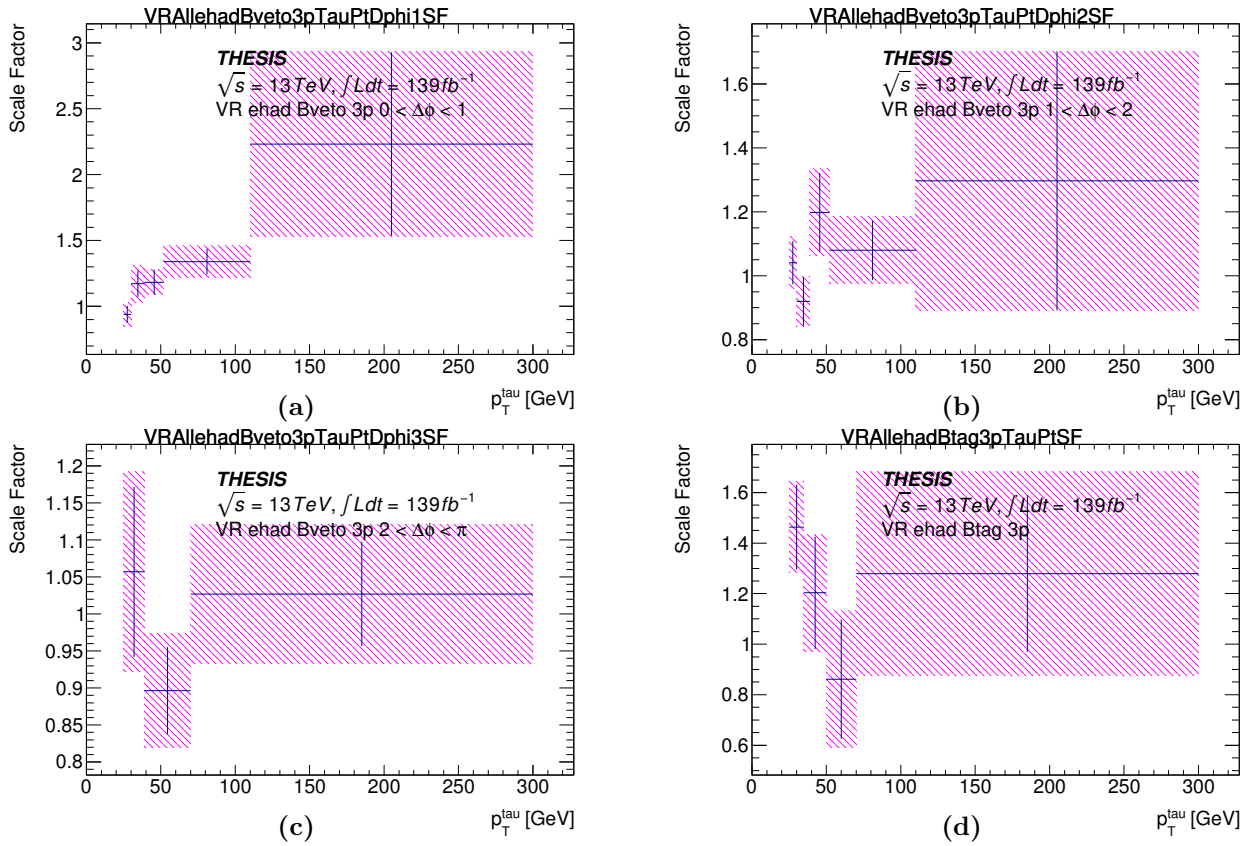

Figure 5.2.34: Plots of the Validation Scale Factor distribution across the selected tau p_{T}, as calculated from the Validation Region, for each binning range of $|\Delta\phi(\tau, E_{\mathrm{T}}^{\mathrm{miss}})|$ in the b-veto category followed by the b-tag (from top left to bottom right). The scale factors are parameterised in the $e\tau_{\mathrm{had}}$ sub-channel, representing the 3-prong tau decay mode.

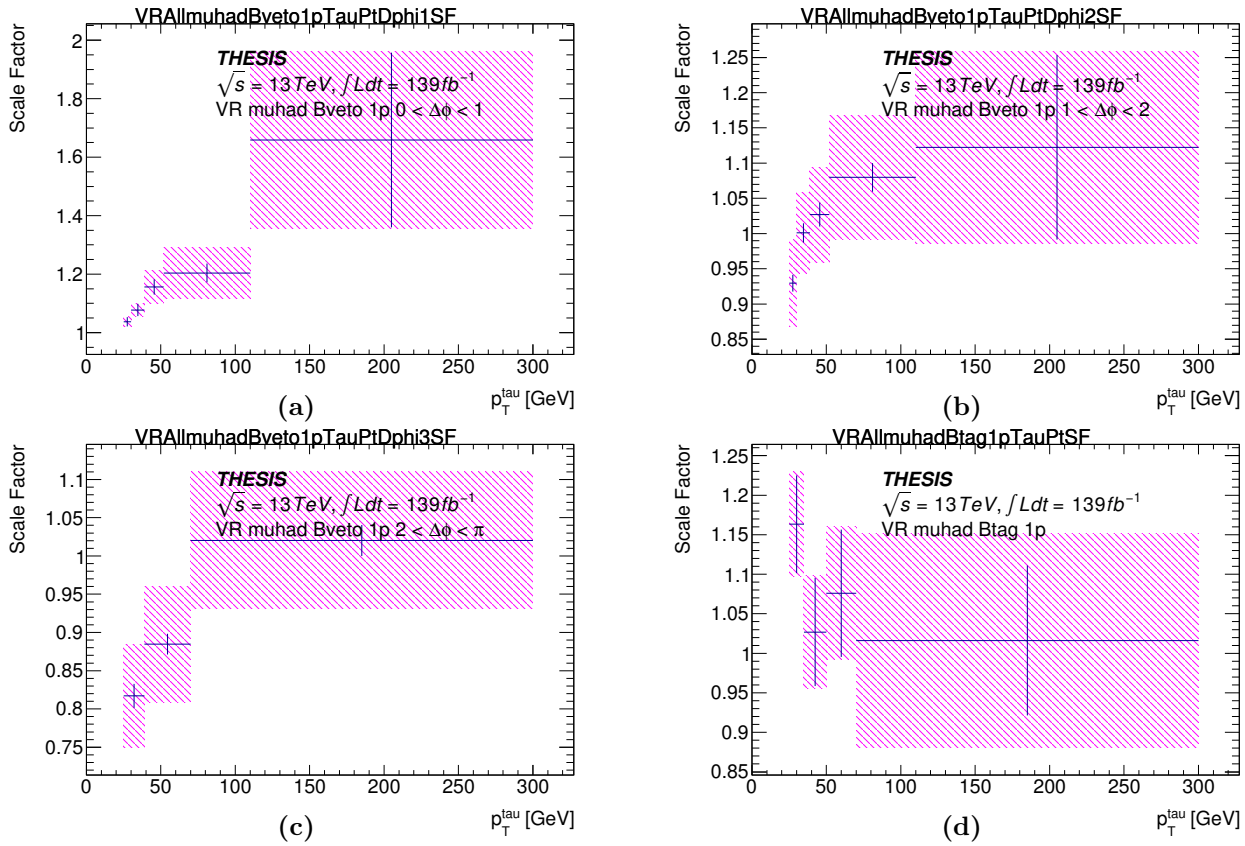

Figure 5.2.35: Plots of the Validation Scale Factor distribution across the selected tau p_{T}, as calculated from the Validation Region, for each binning range of $|\Delta\phi(\tau, E_{\mathrm{T}}^{\mathrm{miss}})|$ in the b-veto category followed by the b-tag (from top left to bottom right). The scale factors are parameterised in the $\mu\tau_{\mathrm{had}}$ sub-channel, representing the 1-prong tau decay mode.

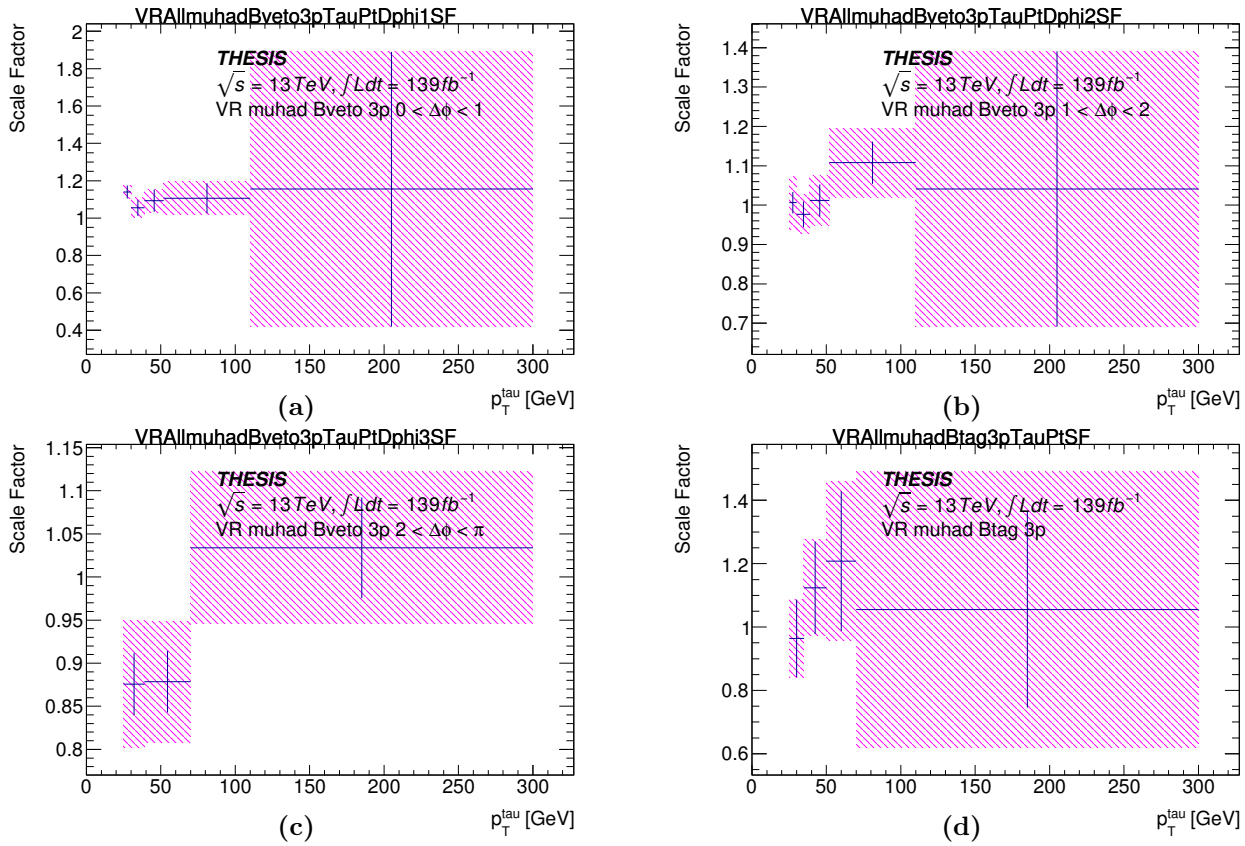

Figure 5.2.36: Plots of the Validation Scale Factor distribution across the selected tau p_{T}, as calculated from the Validation Region, for each binning range of $|\Delta\phi(\tau, E_{\mathrm{T}}^{\mathrm{miss}})|$ in the b-veto category followed by the b-tag (from top left to bottom right). The scale factors are parameterised in the $\mu\tau_{\mathrm{had}}$ sub-channel, representing the 3-prong tau decay mode.

5.3 Signal results

With all major background processes now estimated and modelled through numerous correction factors, all are then applied back into the SR. In order to avoid any bias, subconscious or other, whilst interpreting the results, it is a common ATLAS strategy for the recorded data in the SR to first be *blinded*, such that the result is hidden and only the MC prediction is shown. This also helps to serve as a final means to investigate any problems with the BSM $\tau_{\mathrm{lep}}\tau_{\mathrm{had}}$ analysis or in the CAF software itself. Once the background studies are complete and an approval within the ATLAS hierarchy is made, Figures 5.3.1–5.3.4 reveal the unblinded results for the SR, and therefore concluding the estimation part of the analysis.

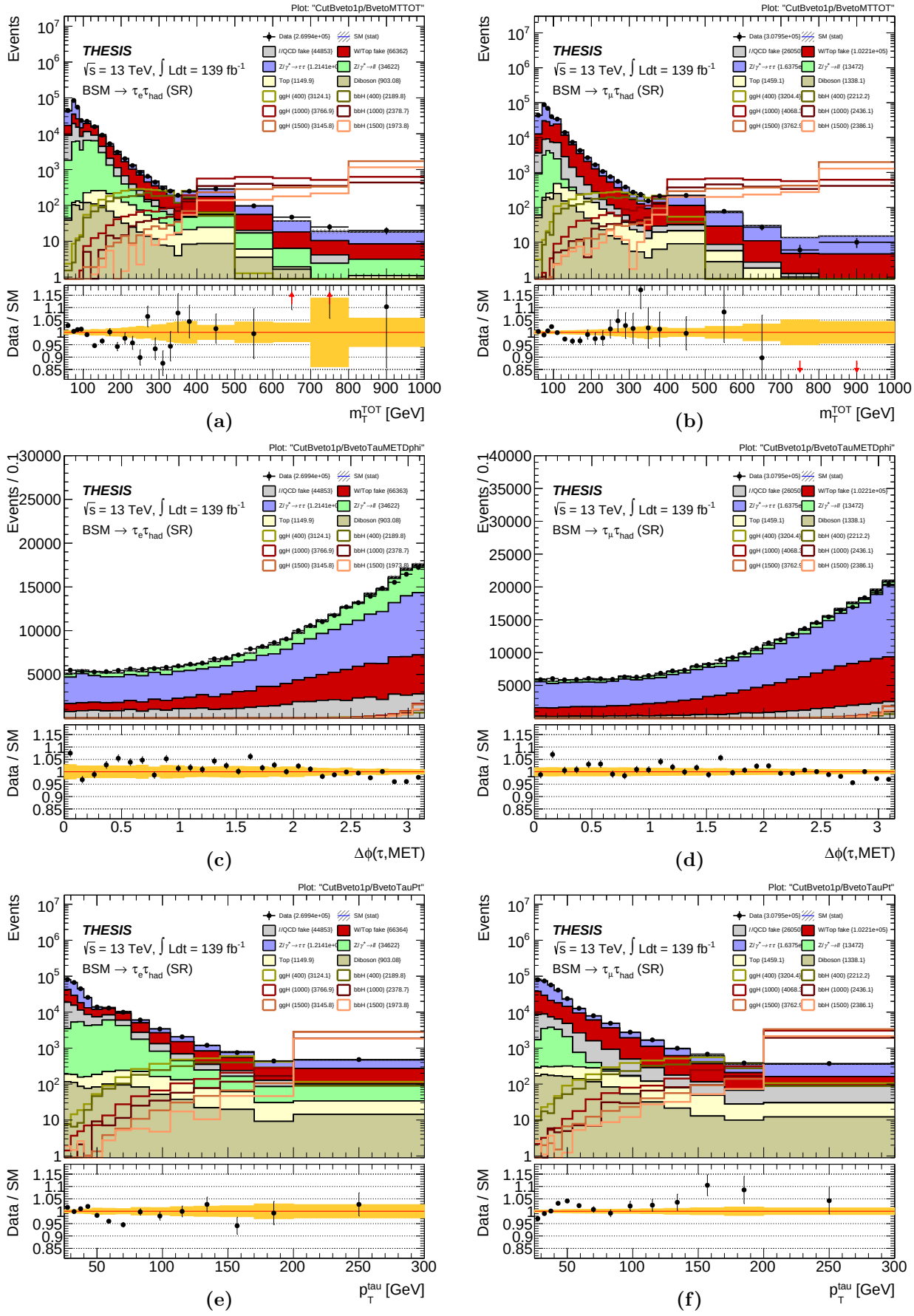

Figure 5.3.1: Plots of the unblinded Signal Region with all derived factors applied back, in the b-veto category, for the 1-prong tau decay mode, representing the signal discriminant $m_{\mathrm{T}}^{\mathrm{tot}}$, $|\Delta\phi(\tau, E_{\mathrm{T}}^{\mathrm{miss}})|$ and tau p_{T} (from top to bottom). The region is divided into the $e\tau_{\mathrm{had}}$ (left) and $\mu\tau_{\mathrm{had}}$ (right) sub-channels. In addition, example signal predictions are overlaid with varying masses in GeV for H/A bosons from the hMSSM model, generated through the ggH and bbH mechanisms.

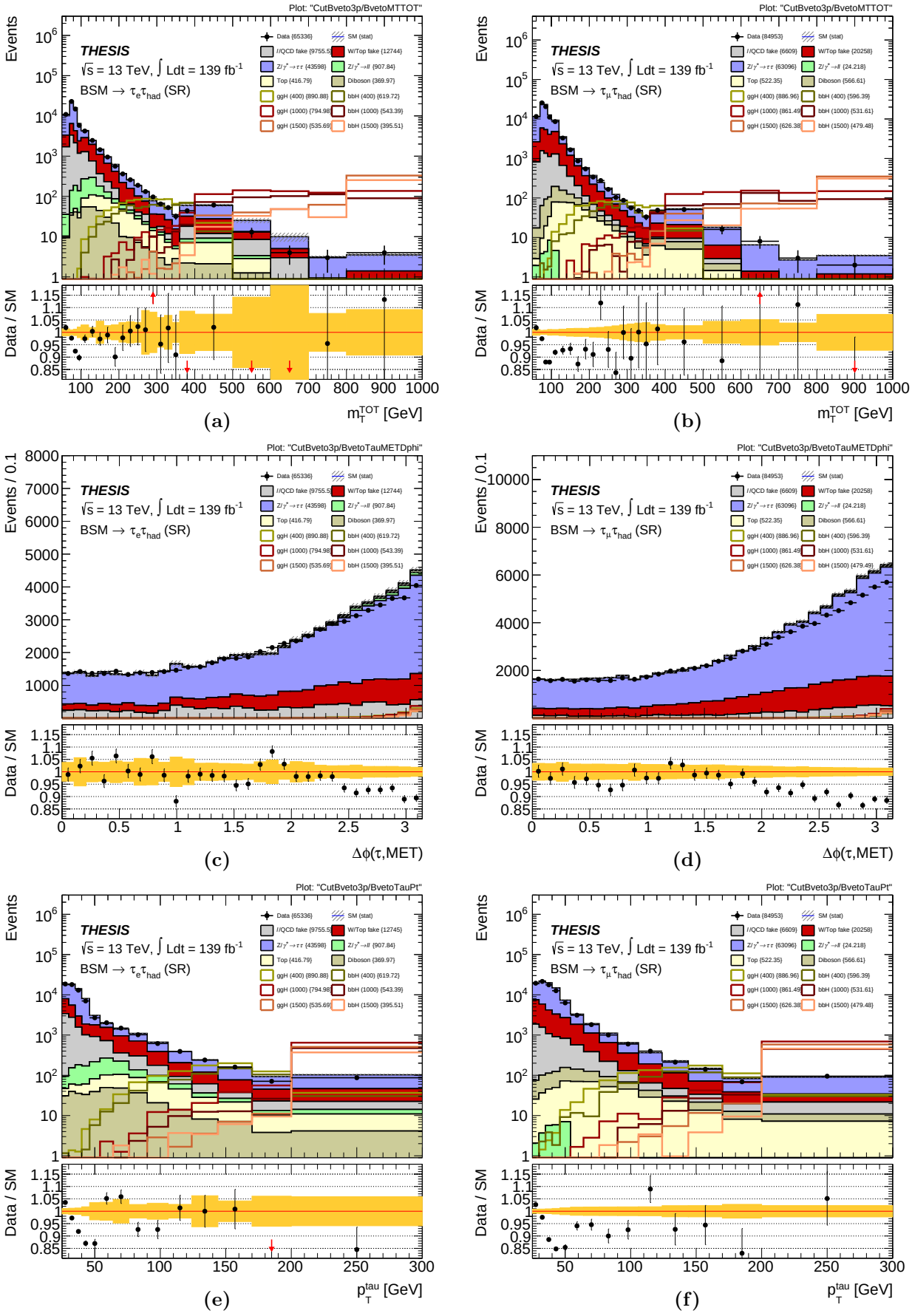

Figure 5.3.2: Plots of the unblinded Signal Region with all derived factors applied back, in the b-veto category, for the 3-prong tau decay mode, representing the signal discriminant $m_{\mathrm{T}}^{\mathrm{tot}}$, $|\Delta\phi(\tau, E_{\mathrm{T}}^{\mathrm{miss}})|$ and tau p_{T} (from top to bottom). The region is divided into the $e\tau_{\mathrm{had}}$ (left) and $\mu\tau_{\mathrm{had}}$ (right) sub-channels. In addition, example signal predictions are overlaid with varying masses in GeV for H/A bosons from the hMSSM model, generated through the ggH and bbH mechanisms.

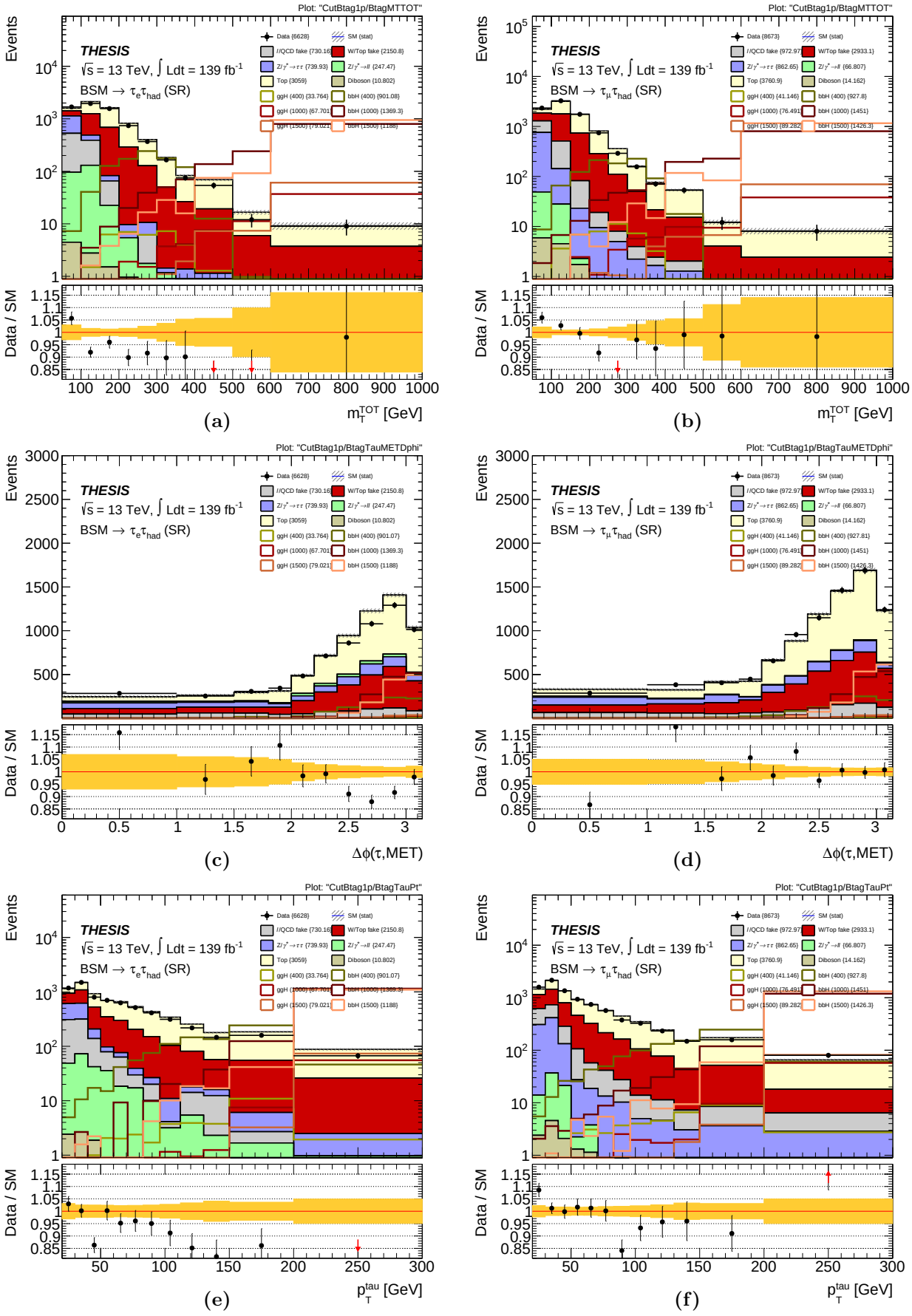

Figure 5.3.3: Plots of the unblinded Signal Region with all derived factors applied back, in the b-tag category, for the 1-prong tau decay mode, representing the signal discriminant $m_{\mathrm{T}}^{\mathrm{tot}}$, $|\Delta\phi(\tau, E_{\mathrm{T}}^{\mathrm{miss}})|$ and tau p_{T} (from top to bottom). The region is divided into the $e\tau_{\mathrm{had}}$ (left) and $\mu\tau_{\mathrm{had}}$ (right) sub-channels. In addition, example signal predictions are overlaid with varying masses in GeV for H/A bosons from the hMSSM model, generated through the ggH and bbH mechanisms.

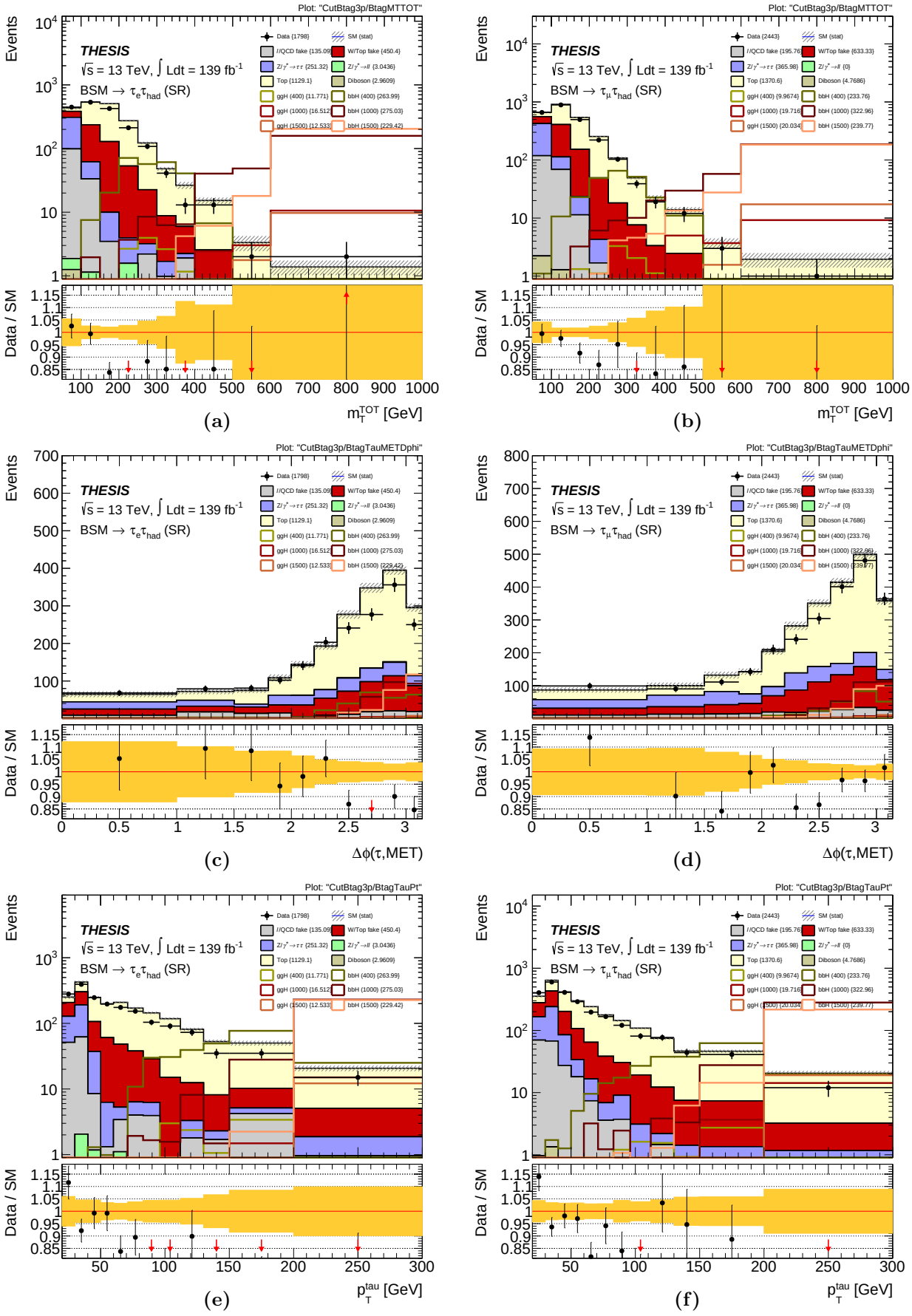

Figure 5.3.4: Plots of the unblinded Signal Region with all derived factors applied back, in the b-tag category, for the 3-prong tau decay mode, representing the signal discriminant $m_{\mathrm{T}}^{\mathrm{tot}}$, $|\Delta\phi(\tau, E_{\mathrm{T}}^{\mathrm{miss}})|$ and tau p_{T} (from top to bottom). The region is divided into the $e\tau_{\mathrm{had}}$ (left) and $\mu\tau_{\mathrm{had}}$ (right) sub-channels. In addition, example signal predictions are overlaid with varying masses in GeV for H/A bosons from the hMSSM model, generated through the ggH and bbH mechanisms.

Before making any interpretations, it should be noted that at this stage the uncertainty attributed to the MC/background estimation represents only the statistical uncertainty. While the dataset luminosity has increased throughout Run-2 data-taking, the statistical uncertainty becomes less prominent, and so the systematic uncertainty starts to play the more dominant role, which will be calculated in the following Section 5.4.

5.4 Systematic uncertainties

Systematic uncertainties are present in many forms in ATLAS and the analysis itself. Many are from the detector calibrations, which in turn propagate into the derived CP corrections for each object subgroup. Others are theory uncertainties when attempting to accurately model a particular MC process. Some are created during the analysis chain, such as those from the fake background estimations in Section 5.2, mainly as an artefact of the remaining mismodelling in the CRs.

When estimating systematics in ATLAS, they commonly apply in two forms: *weight* and *kinematic* systematics. Weight systematics represent those as a variation to a weighting factor distribution (such as FFs and SFs), which affect the normalisation of events. These weight systematics may be included in parallel to the regular *nominal* weight within the Ntuple, as an alternative variable to the same event. However, kinematic systematics require a complete re-evaluation of the event itself, as they would often vary some property closely related to the detector, to the point that the result of some applied selection criteria will be entirely different.

For the BSM $\tau_{\text{lep}}\tau_{\text{had}}$ analysis, these systematics are packaged into the Ntuple level using the xTFW, where the weight systematics are simply added as additional variables alongside the nominal result, while the kinematic systematics essentially require the entire Ntuple to be processed repeatedly for each variation, which can be very computationally intensive. As with any uncertainty, the systematic variations are independently provided in their 1σ standard deviation up and down directions, although more than often they are symmetrical, and will be combined later in the final result. Using BSMtautauCAF, the TCR, VR and SR event selections are processed repeatedly for each systematic variation, delivering a full result which represents how the analysis would look like assuming the full 1σ deviation. The systematic uncertainty is then calculated as the event difference between this result and the nominal result, as a percentage event yield value which is then applied back into the original result as a means to visualise the systematic uncertainty band in addition to the statistical uncertainty.

While there are many sources of systematic uncertainty available in ATLAS, the $\tau_{\text{lep}}\tau_{\text{had}}$ analysis only needs to estimate those which would at least be significant, typically considering those with a yield of at least $\sim$0.01 %, especially when summed together. For those derived during the analysis, these include: 8 from the L-FF calculation (for $e\tau_{\text{had}}/\mu\tau_{\text{had}}$ and b-veto/b-tag), 4 from the L-SF (for b-veto/b-tag), 8 from the W/T-FF (for b-veto/b-tag and 1/3-prong), 16 from the W/T-SF (for b-veto/b-tag, 1/3-prong and $e\tau_{\text{had}}/\mu\tau_{\text{had}}$) and 8 from the V-SF (for b-veto/b-tag and 1/3-prong), a total of 44 weight variations from the analysis (including both 1σ up/down directions). Other general systematics are sourced during the Ntuple production, providing 72 CP-based weight variations (e.g. tau ID efficiency), with 6 more from top quark MC theory and 24 from BSM theory, a total of 102 weight variations, and 60 CP-based kinematic variations (e.g. tau energy scale). This provides a total of 206 systematic variations to evaluate during the analysis runtime. The full list of systematics and ranked by their resulting yields for each region, channel, category and prong are given in Appendix B.3. Where the resulting systematic bands are calculated, Figures 5.4.1 and 5.4.2, 5.4.3–5.4.6, and 5.4.7–5.4.10 represent the TCR, VR and SR, respectively, identical to those as seen previously in Figures 5.2.26 and 5.2.27, 5.2.29–5.2.32, and 5.3.1–5.3.4, but now with the inclusion of the systematic uncertainty.

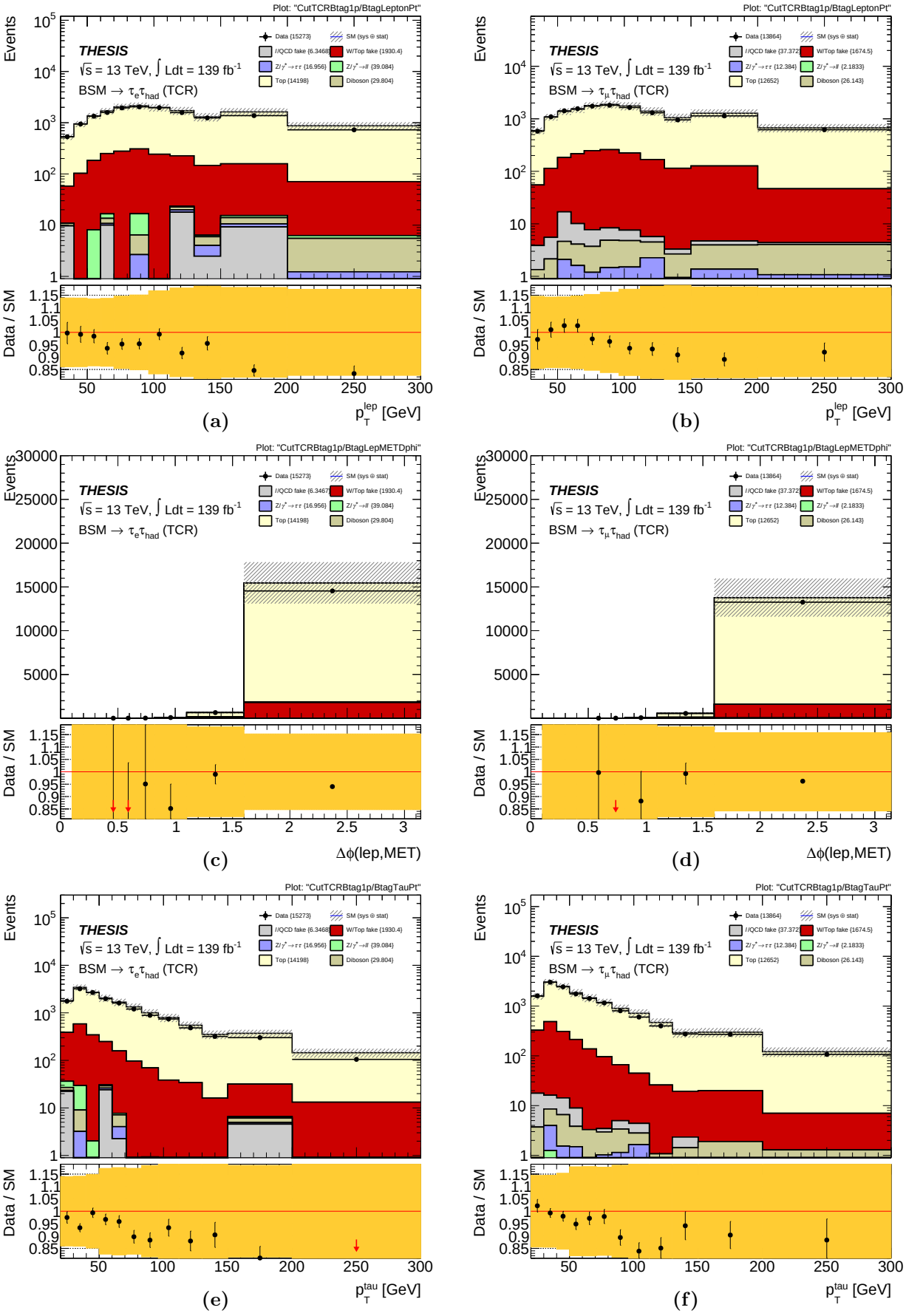

Figure 5.4.1: Plots of the Top Control Region with the systematic uncertainty included, in the b-tag category, for the 1-prong tau decay mode, representing lepton p_{T}, $|\Delta\phi(\ell, E_{\mathrm{T}}^{\mathrm{miss}})|$ and tau p_{T} (from top to bottom). The region is divided into the $e\tau_{\mathrm{had}}$ (left) and $\mu\tau_{\mathrm{had}}$ (right) sub-channels.

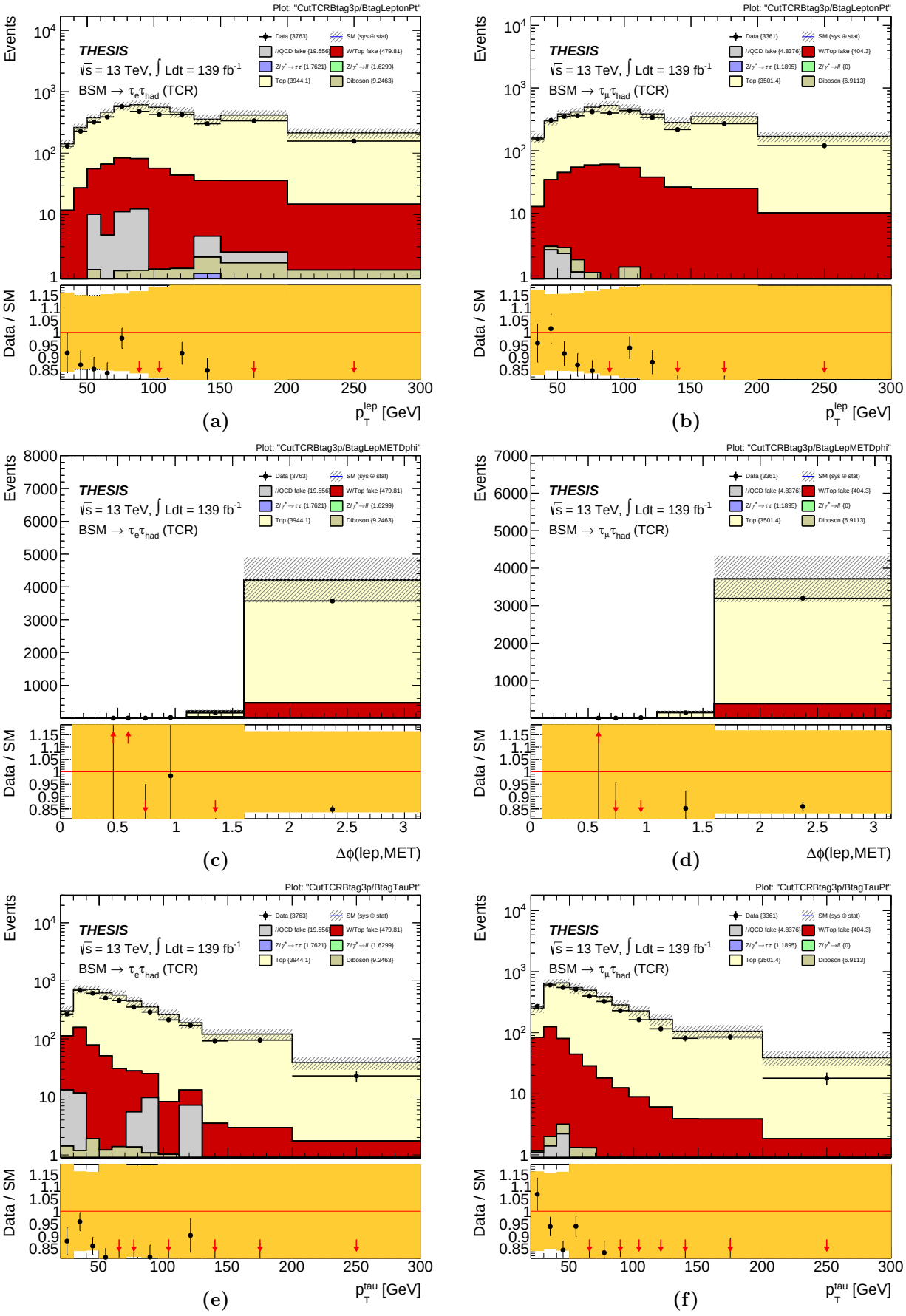

Figure 5.4.2: Plots of the Top Control Region with the systematic uncertainty included, in the b-tag category, for the 3-prong tau decay mode, representing lepton p_{T}, $|\Delta\phi(\ell, E_{\mathrm{T}}^{\mathrm{miss}})|$ and tau p_{T} (from top to bottom). The region is divided into the $e\tau_{\mathrm{had}}$ (left) and $\mu\tau_{\mathrm{had}}$ (right) sub-channels.

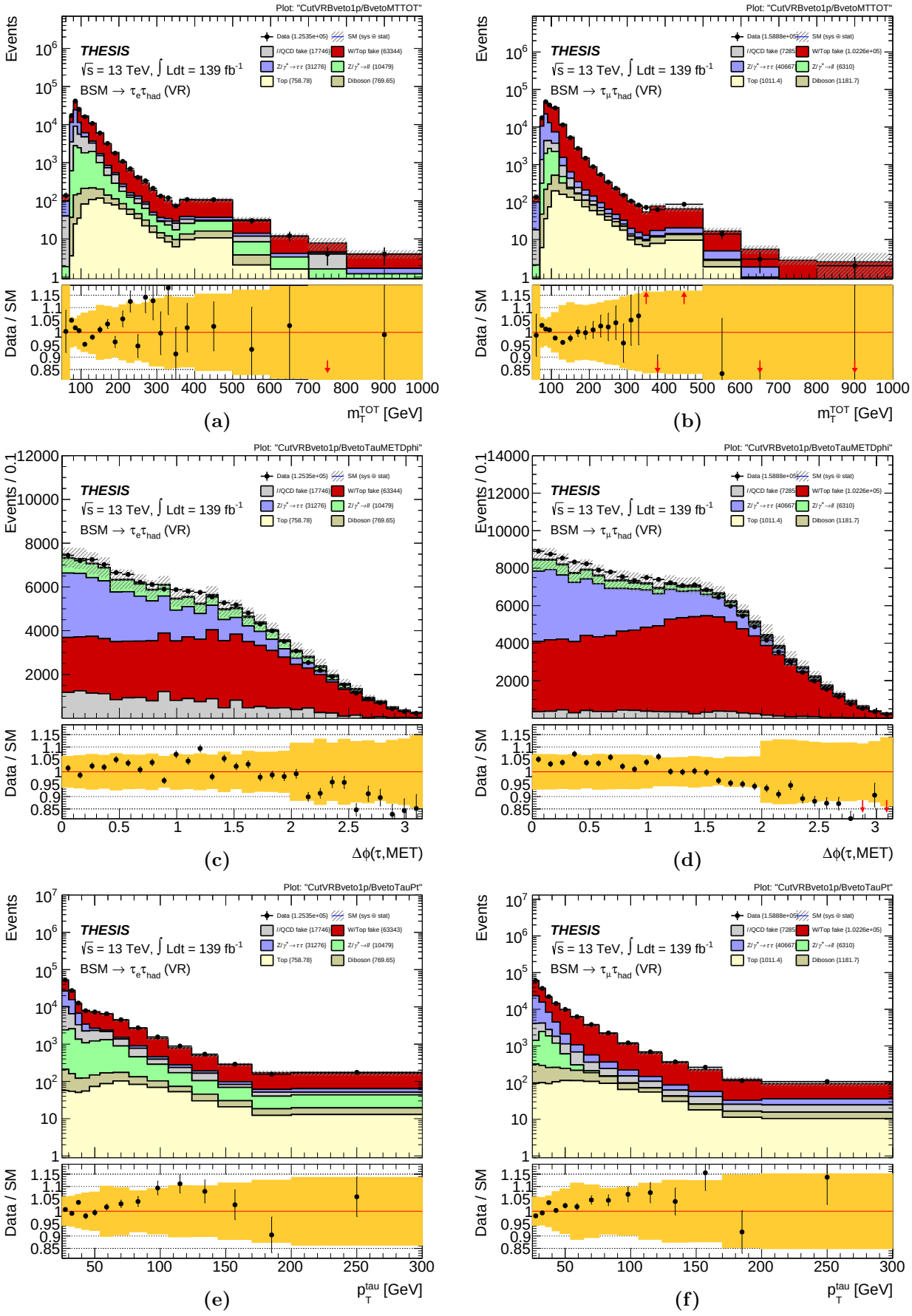

Figure 5.4.3: Plots of the Validation Region with the systematic uncertainty included, in the b-veto category, for the 1-prong tau decay mode, representing the signal discriminant $m_{\mathrm{T}}^{\mathrm{tot}}$, $|\Delta\phi(\tau, E_{\mathrm{T}}^{\mathrm{miss}})|$ and tau p_{T} (from top to bottom). The region is divided into the $e\tau_{\mathrm{had}}$ (left) and $\mu\tau_{\mathrm{had}}$ (right) sub-channels.

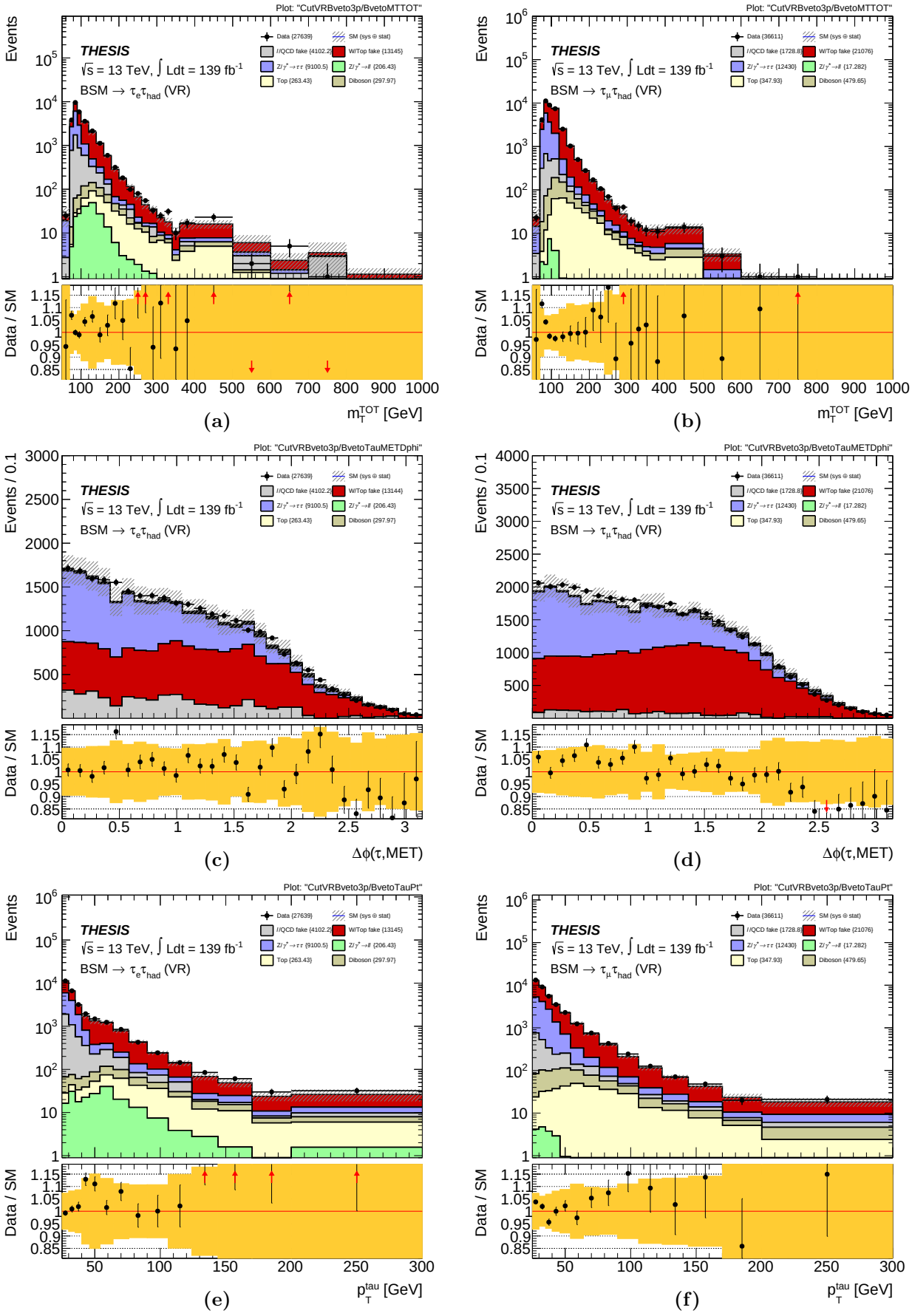

Figure 5.4.4: Plots of the Validation Region with the systematic uncertainty included, in the b-veto category, for the 3-prong tau decay mode, representing the signal discriminant $m_{\mathrm{T}}^{\mathrm{tot}}$, $|\Delta\phi(\tau, E_{\mathrm{T}}^{\mathrm{miss}})|$ and tau p_{T} (from top to bottom). The region is divided into the $e\tau_{\mathrm{had}}$ (left) and $\mu\tau_{\mathrm{had}}$ (right) sub-channels.

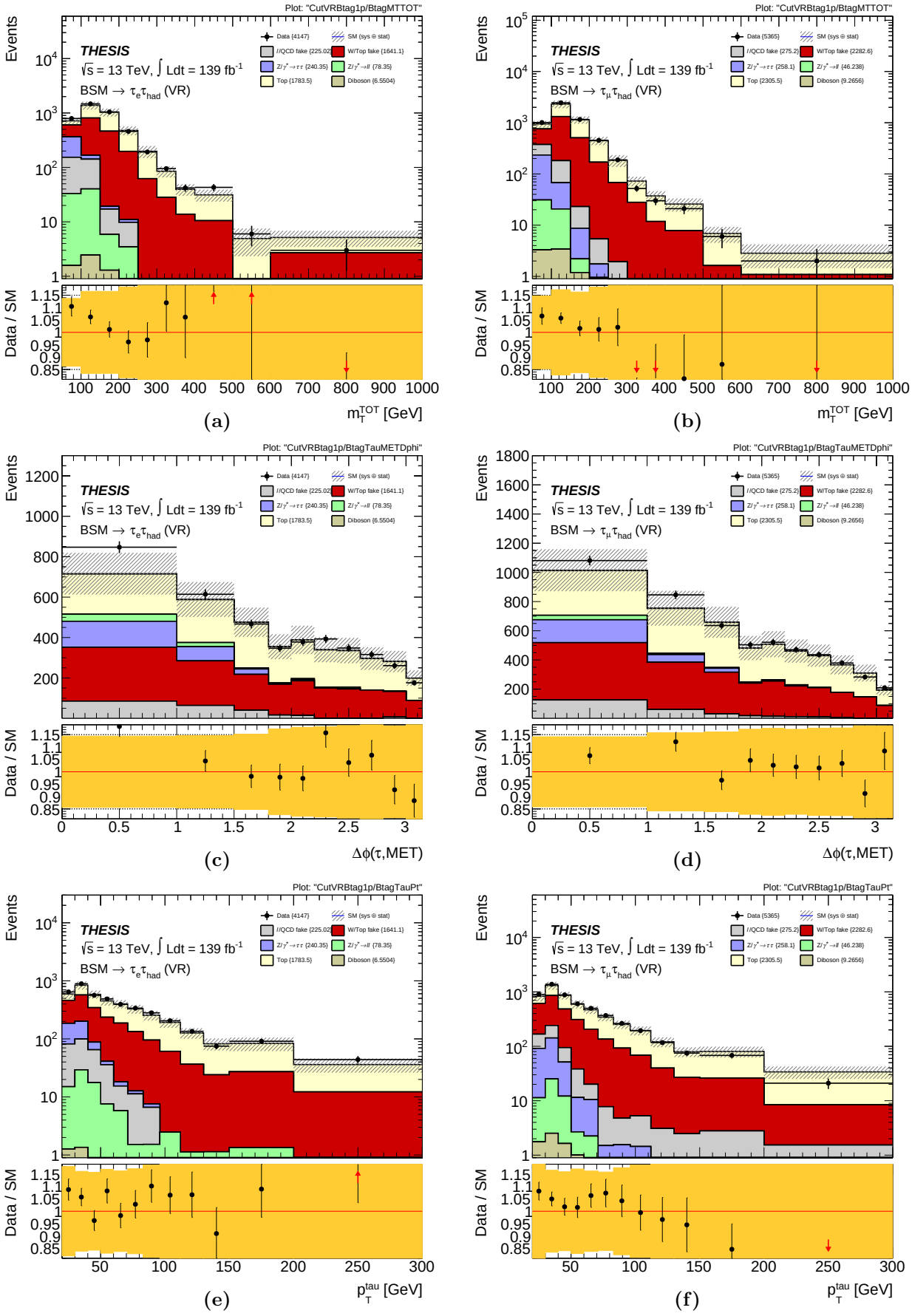

Figure 5.4.5: Plots of the Validation Region with the systematic uncertainty included, in the b-tag category, for the 1-prong tau decay mode, representing the signal discriminant $m_{\mathrm{T}}^{\mathrm{tot}}$, $|\Delta\phi(\tau, E_{\mathrm{T}}^{\mathrm{miss}})|$ and tau p_{T} (from top to bottom). The region is divided into the $e\tau_{\mathrm{had}}$ (left) and $\mu\tau_{\mathrm{had}}$ (right) sub-channels.

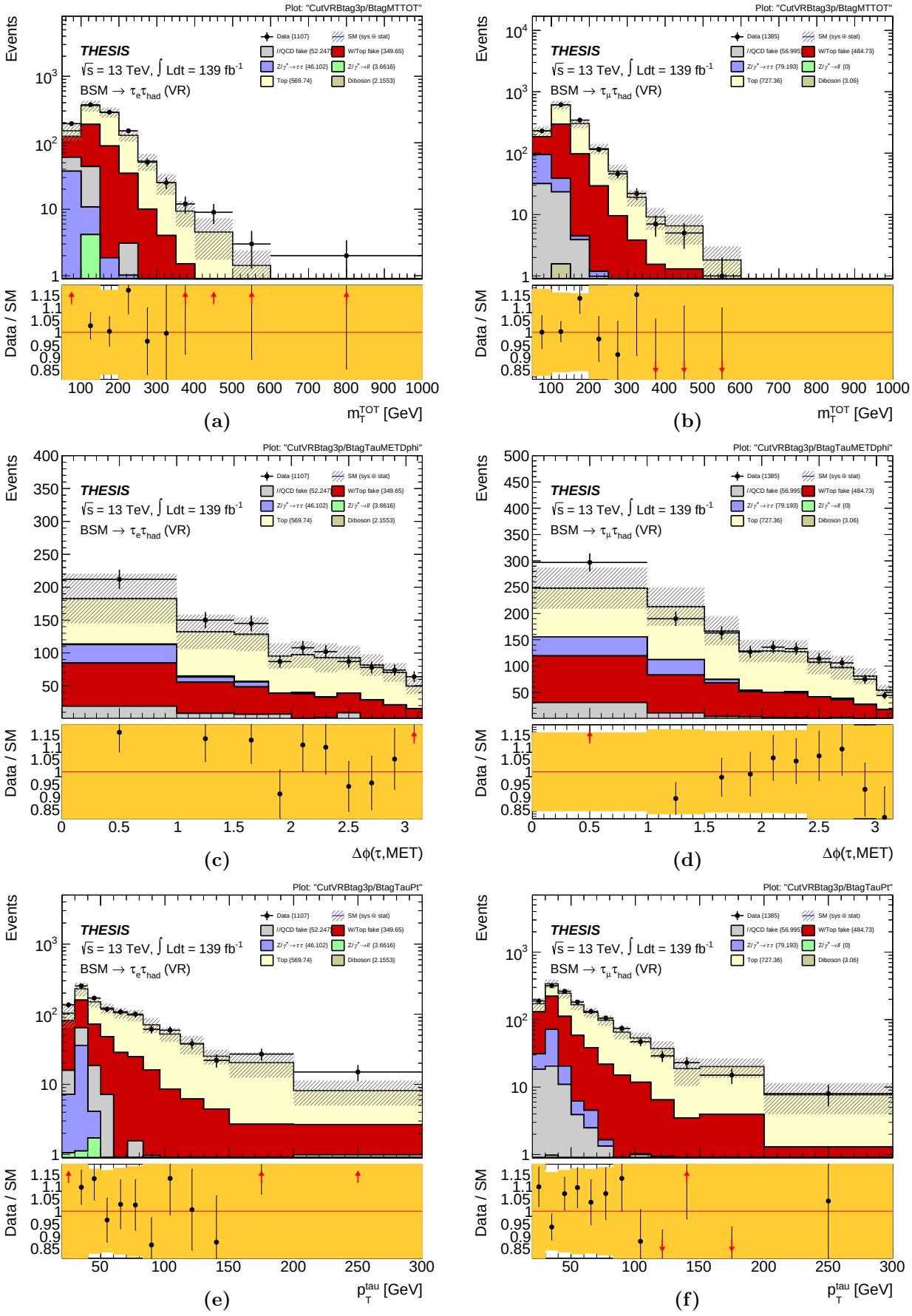

Figure 5.4.6: Plots of the Validation Region with the systematic uncertainty included, in the b-tag category, for the 3-prong tau decay mode, representing the signal discriminant $m_{\mathrm{T}}^{\mathrm{tot}}$, $|\Delta\phi(\tau, E_{\mathrm{T}}^{\mathrm{miss}})|$ and tau p_{T} (from top to bottom). The region is divided into the $e\tau_{\mathrm{had}}$ (left) and $\mu\tau_{\mathrm{had}}$ (right) sub-channels.

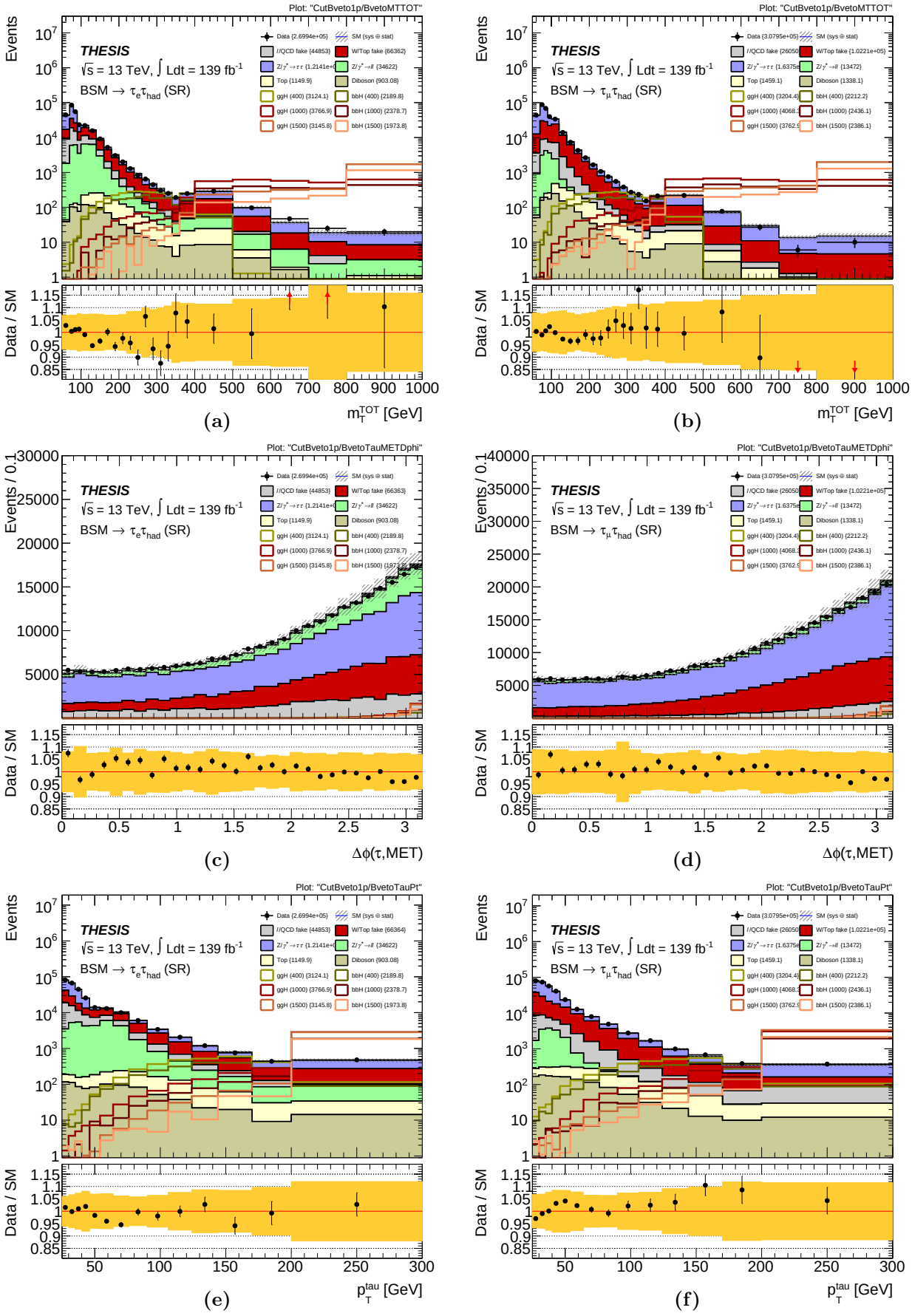

Figure 5.4.7: Plots of the unblinded Signal Region with the systematic uncertainty included, in the b-veto category, for the 1-prong tau decay mode, representing the signal discriminant $m_{\mathrm{T}}^{\mathrm{tot}}$, $|\Delta\phi(\tau, E_{\mathrm{T}}^{\mathrm{miss}})|$ and tau p_{T} (from top to bottom). The region is divided into the $e\tau_{\mathrm{had}}$ (left) and $\mu\tau_{\mathrm{had}}$ (right) sub-channels. In addition, example signal predictions are overlaid with varying masses in GeV for H/A bosons from the hMSSM model, generated through the ggH and bbH mechanisms.

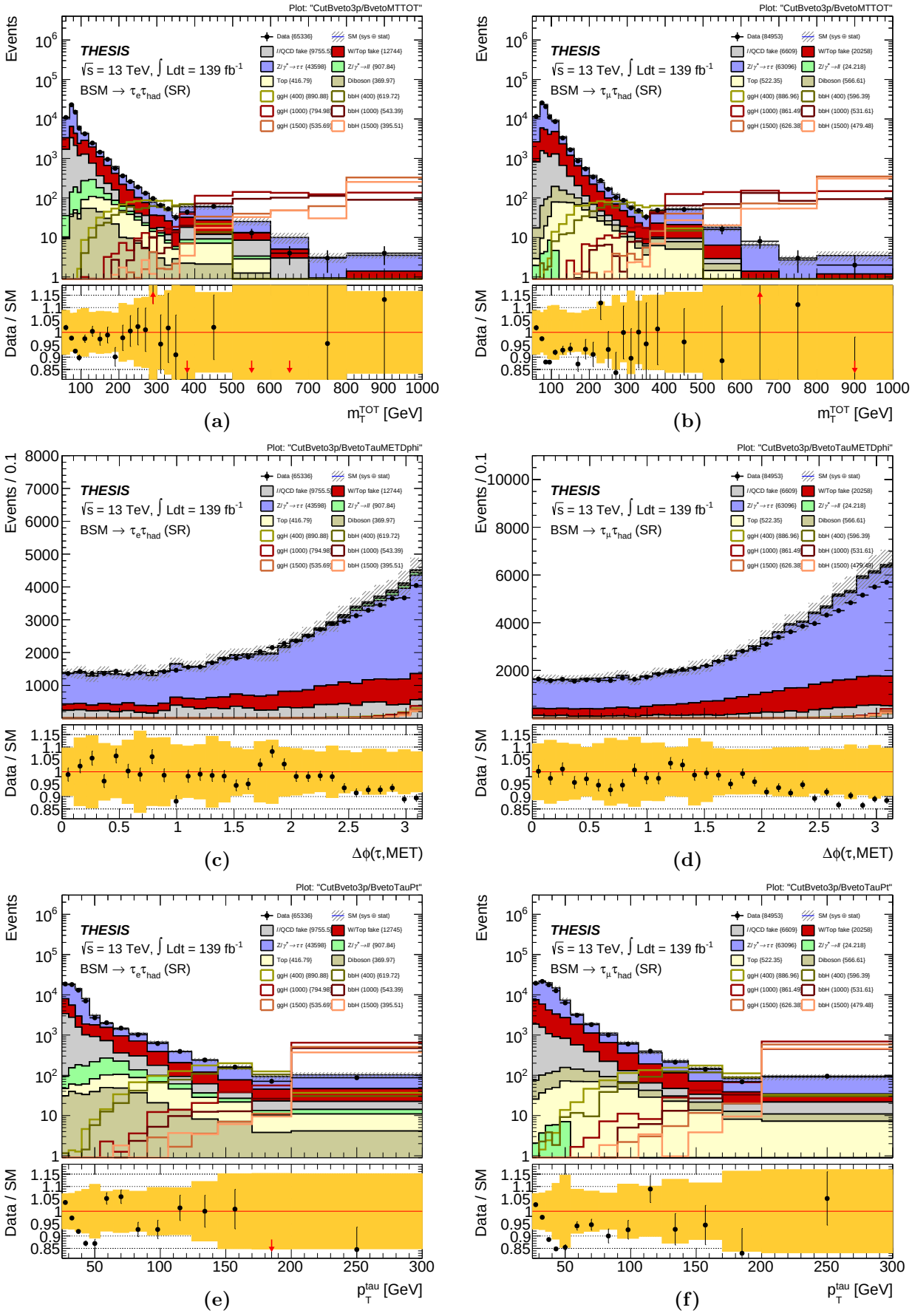

Figure 5.4.8: Plots of the unblinded Signal Region with the systematic uncertainty included, in the b-veto category, for the 3-prong tau decay mode, representing the signal discriminant $m_{\mathrm{T}}^{\mathrm{tot}}$, $|\Delta\phi(\tau, E_{\mathrm{T}}^{\mathrm{miss}})|$ and tau p_{T} (from top to bottom). The region is divided into the $e\tau_{\mathrm{had}}$ (left) and $\mu\tau_{\mathrm{had}}$ (right) sub-channels. In addition, example signal predictions are overlaid with varying masses in GeV for H/A bosons from the hMSSM model, generated through the ggH and bbH mechanisms.

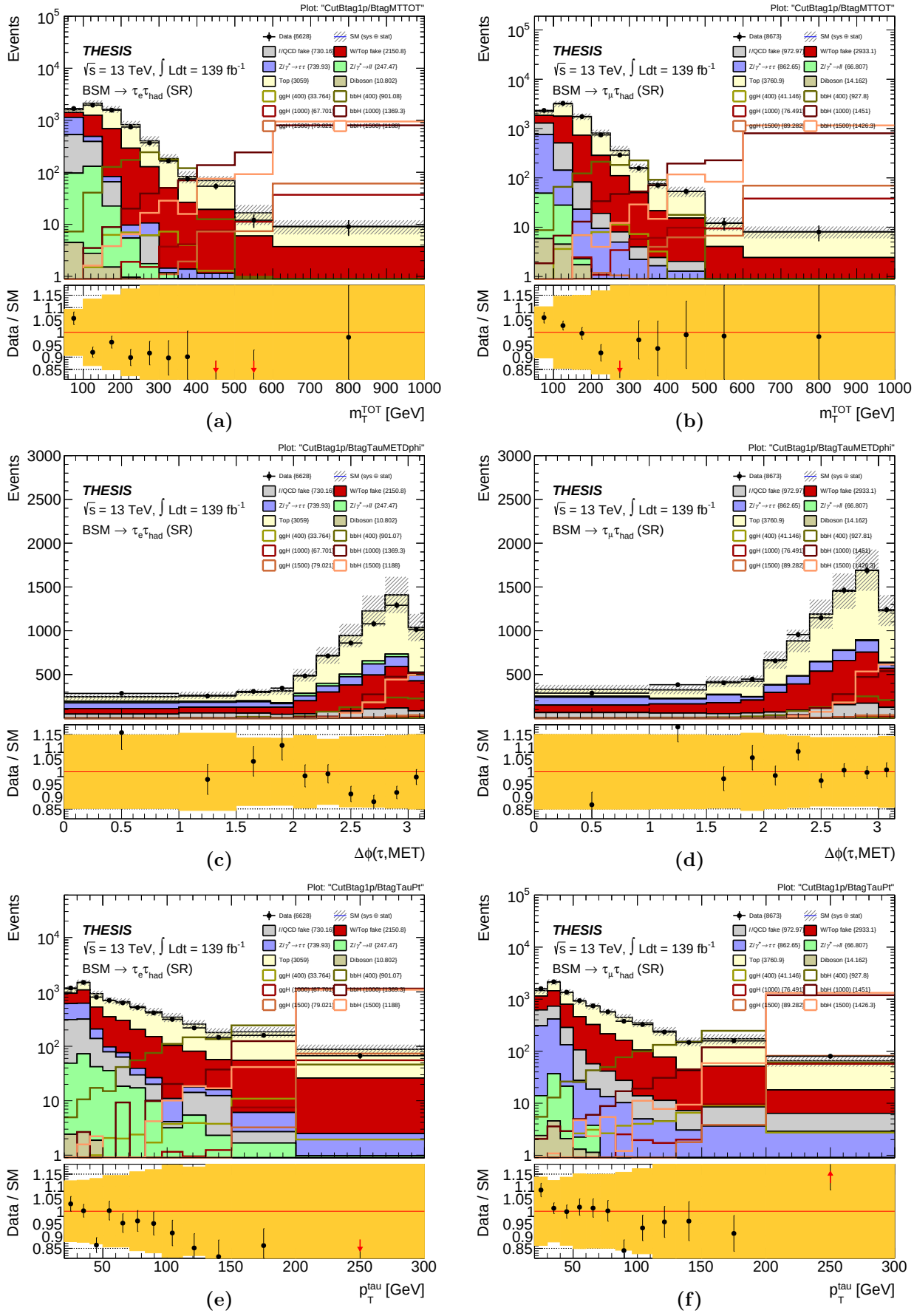

Figure 5.4.9: Plots of the unblinded Signal Region with the systematic uncertainty included, in the b-tag category, for the 1-prong tau decay mode, representing the signal discriminant $m_{\mathrm{T}}^{\mathrm{tot}}$, $|\Delta\phi(\tau, E_{\mathrm{T}}^{\mathrm{miss}})|$ and tau p_{T} (from top to bottom). The region is divided into the $e\tau_{\mathrm{had}}$ (left) and $\mu\tau_{\mathrm{had}}$ (right) sub-channels. In addition, example signal predictions are overlaid with varying masses in GeV for H/A bosons from the hMSSM model, generated through the ggH and bbH mechanisms.

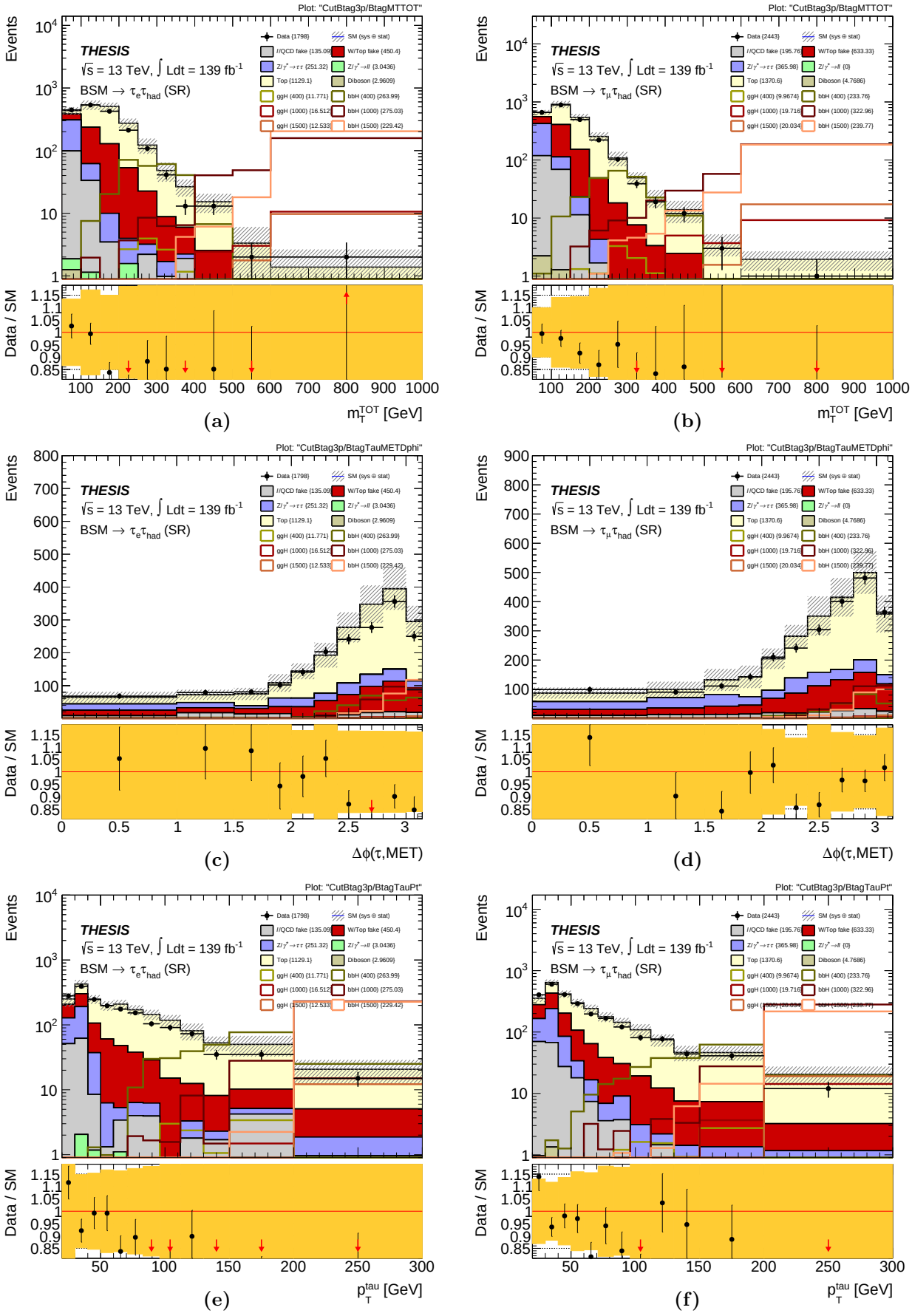

Figure 5.4.10: Plots of the unblinded Signal Region with the systematic uncertainty included, in the b-tag category, for the 3-prong tau decay mode, representing the signal discriminant $m_{\mathrm{T}}^{\mathrm{tot}}$, $|\Delta\phi(\tau, E_{\mathrm{T}}^{\mathrm{miss}})|$ and tau p_{T} (from top to bottom). The region is divided into the $e\tau_{\mathrm{had}}$ (left) and $\mu\tau_{\mathrm{had}}$ (right) sub-channels. In addition, example signal predictions are overlaid with varying masses in GeV for H/A bosons from the hMSSM model, generated through the ggH and bbH mechanisms.

Firstly, it can be seen in the T-CR and VR that any of the remaining disagreement between data and MC, which originally appeared significantly beyond the statistical uncertainty, is now well expected within the systematic uncertainty. This assures that the background modelling is well understood and accounted for. Secondly, any deviation that was present in the SR, which could have potentially led to indications of some BSM discovery, are in fact also well expected within the systematic uncertainty. It is then apparent that, with the increasing luminosity dataset available, the systematic uncertainty is generally becoming more dominant over its statistical counterpart, with exceptions still remaining in the more rarer event selections typically attributed to either the b-tag category or with 3-prong taus, or with masses above $\sim$0.6 TeV [63]. As such, while these results from the BSMtautauCAF concludes a major part of the $\tau_{\text{lep}}\tau_{\text{had}}$ analysis chain, as well as for much of author's contribution, and providing a first indication of a whether there is a BSM result, the systematic uncertainty can still be further constrained and inspected in more detail through post-fitting procedures, which will be briefly discussed in the following Section 5.5.

5.5 Fitted results and exclusion limits

As was seen in Section 5.4, the systematic uncertainties on the $\tau_{\text{lep}}\tau_{\text{had}}$ results dominate most of the uncertainty in the SR. As a means of constraining this uncertainty to provide a clearer result, the SR undergoes a likelihood fitting procedure on the signal discriminant $m_{\text{T}}^{\text{tot}}$ variable. The results are first converted from their CAF format into a generic ROOT file, and then passed onto various statistical software frameworks made within ATLAS. The binning widths are optimised in order to provide sufficient statistics and enhance the signal strength. The fit also considers the T-CR, as much of the systematic uncertainty is strongly correlated with the top quark theory estimation. At this stage, the $\tau_{\text{had}}\tau_{\text{had}}$ analysis also undergoes similar fitting procedures, having completed their background and signal estimation studies, and the two channels start to be combined for the final result. Figure 5.5.1 represents the final post-fitted SR results, as presented in the latest publication [63], in both the $\tau_{\text{lep}}\tau_{\text{had}}$ and $\tau_{\text{had}}\tau_{\text{had}}$ channels, for the $m_{\text{T}}^{\text{tot}}$ discriminant.

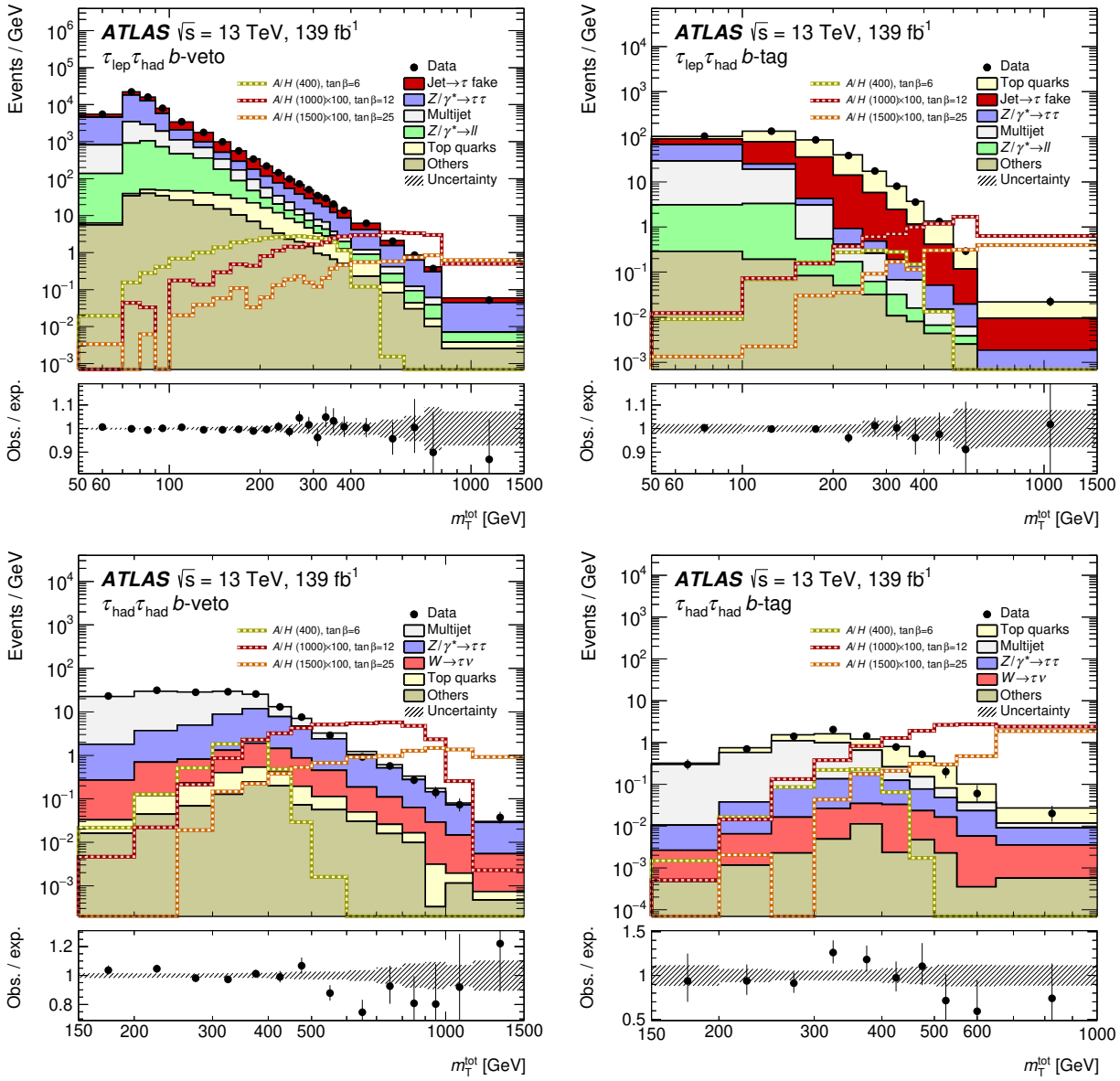

Figure 5.5.1: Distribution of the signal discriminant $m_{\mathrm{T}}^{\mathrm{tot}}$ in the $\tau_{\mathrm{lep}}\tau_{\mathrm{had}}$ (top) and the $\tau_{\mathrm{had}}\tau_{\mathrm{had}}$ (bottom) channels, in the b-veto (left) and b-tag (right) categories [63]. In addition, example signal predictions are overlaid with varying masses in GeV for H/A bosons from the hMSSM model, combined from both of the ggH and bbH mechanisms.

The results show that the data are in agreement with the background predicted by the SM, with no significant excess of a BSM signal observed. As a consequence, it can be reliably stated that the existence of such a BSM model in the parameter space explored in this analysis can be excluded. This is still useful for such theories to constrain the parameters in their models, which in turn allows them to be better understood and thus limit the search area. The author was briefly involved with deriving these exclusion limits in the context of the BSM models interested in this analysis, particularly for the MSSM Higgs. The results are generated by an independent plotting framework made by the BSM $\tau\tau$ analysis team, while the applied models themselves are inherited from a dedicated theory working group.

The exclusion limits are presented in two primary cases: those which are independent of any specific benchmark model, and therefore representing the limit only on the production mechanisms, which are seen for the ggH and bbH mechanisms in Figure 5.5.2, and those which are dependent on the variety of benchmark models which were introduced in Section 1.3.1, shown for the hMSSM and the range of M_h^{125} benchmark scenarios in Figure 5.5.3, between the masses of 0.2 to 2.5 TeV. The behaviour around 350 GeV and $\tan\beta < 10$ reflects the kinematic transition to the dominant $H/A \to t\bar{t}$ decay mode in this region, thereby limiting the exclusion ability for this analysis.

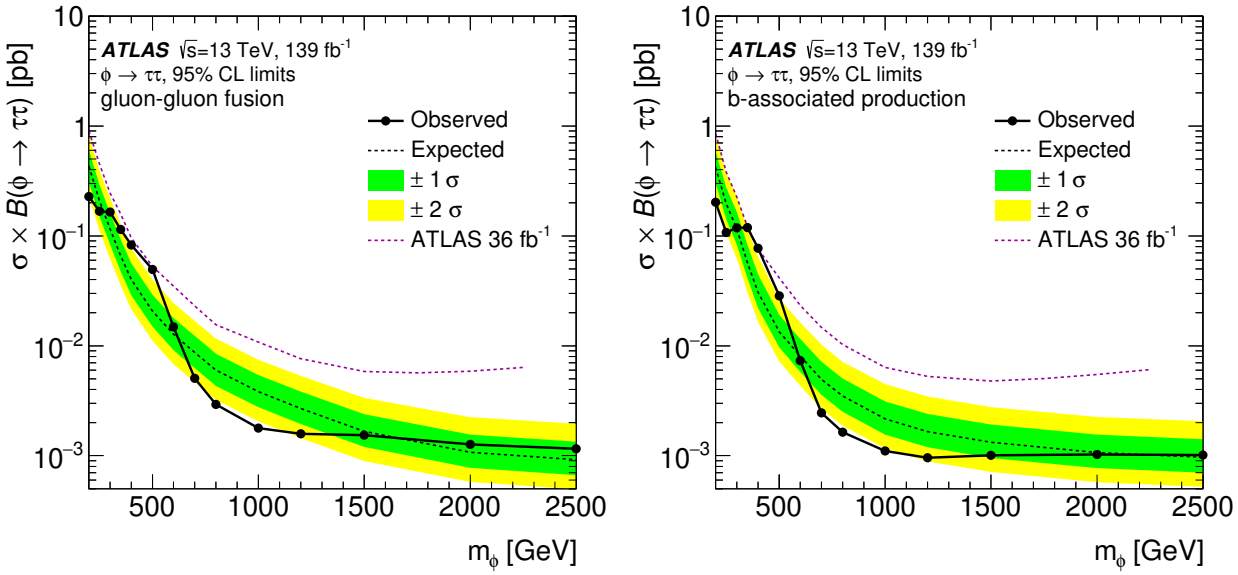

Figure 5.5.2: Observed and expected upper limits with 95% confidence level (CL) on the production cross-section σ multiplied by the branching ratio B of $\phi \to \tau\tau$, against the mass of the scalar boson $\phi = H/A$, combined from the $\tau_{\text{lep}}\tau_{\text{had}}$ and $\tau_{\text{had}}\tau_{\text{had}}$ channels for the gluon fusion (left) and b-associated production (right) mechanisms of the H/A bosons [63]. The expected limit is hypothesised by the given model, attributing a deviation by 1σ uncertainty in green and 2σ in yellow. The observed limit is the result of the analysed data, the majority of which are within the 2σ expectation, while the largest variations are seen with 2.2σ in ggH and 2.7σ in bbH, both at 400 GeV. The plot also shows the observed limit from the previous 36 fb^{-1} result [15].

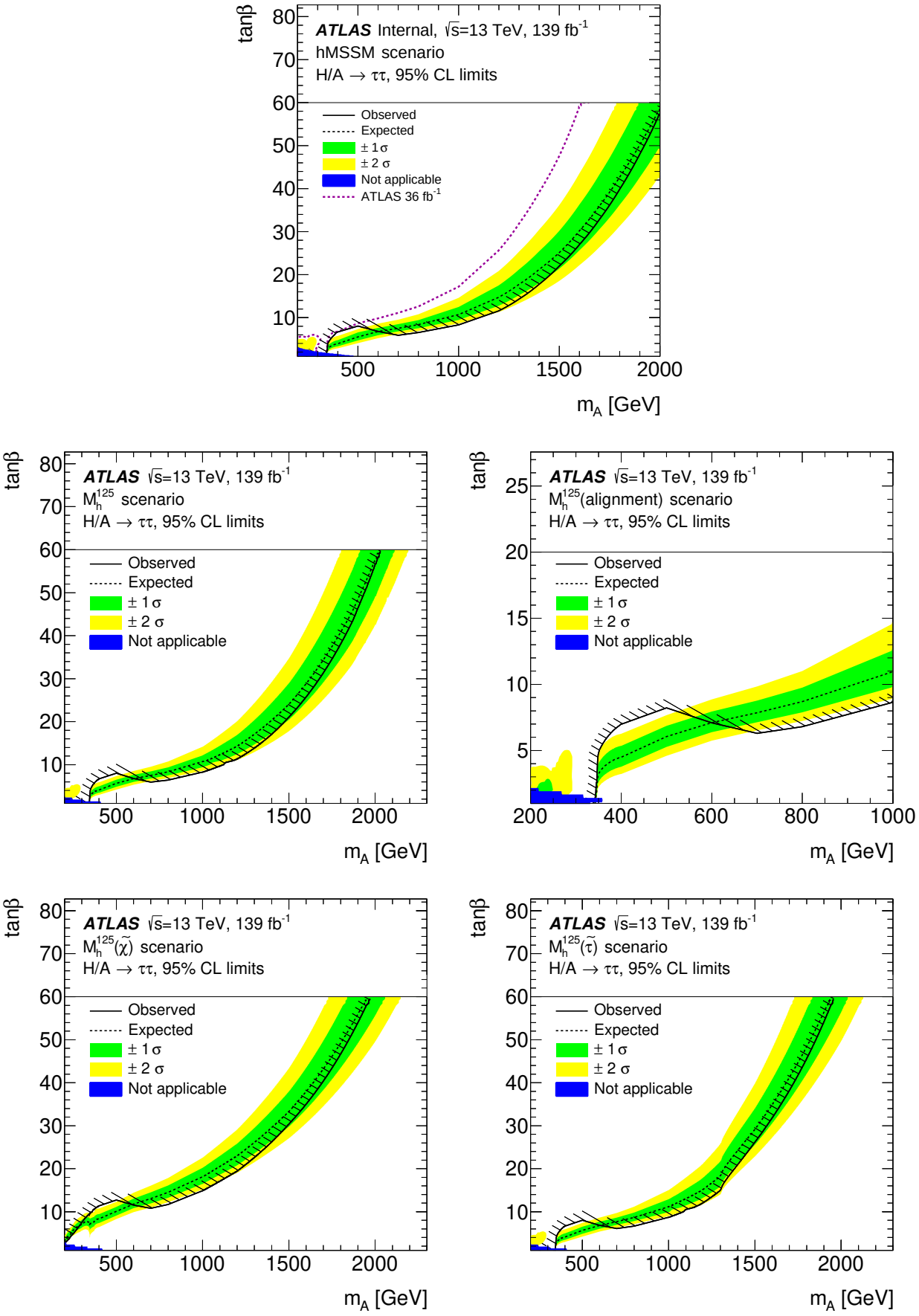

Figure 5.5.3: Observed and expected upper limits with 95% confidence level (CL) on the benchmark model parameters $\tan\beta$ against m_A, combined from the $\tau_{\text{lep}}\tau_{\text{had}}$ and $\tau_{\text{had}}\tau_{\text{had}}$ channels, for the hMSSM (top) and each of the four M_h^{125} (bottom) benchmark scenarios of the H/A bosons [63]. The hMSSM plot also shows the observed limit from the previous 36 fb^{-1} result [15].

These results have substantially extended the exclusion limits and mass range from the previous search with 36 fb^{-1} luminosity of 2015 and 2016 data [15]. For instance, the limits have improved by 4 to 5 times for masses between 0.7 to 2.5 TeV [63]. However, while much of this additional exclusion power may be sourced from the increase in luminosity, there is certainly also a significant benefit from the upgrade in using Athena Release 21 over Release 20 for the tau reconstruction, as discussed previously in Section 3.5.

In addition to these results presented in the most recent publication [63] with 139 fb^{-1} integrated luminosity, the exclusion limits interpreted in the context of the Z' scenario are featured in the previous iteration of publication [15], with 36.1 fb^{-1} from the 2015 and 2016 partial Run-2 datasets. Figure 5.5.4 shows the model independent limit for the Drell-Yan production mechanism, between the masses of 0.2 to 4 TeV, while both Figures 5.5.4 and 5.5.5 represent the exclusion limit in context of the SSM and SFM benchmark models.

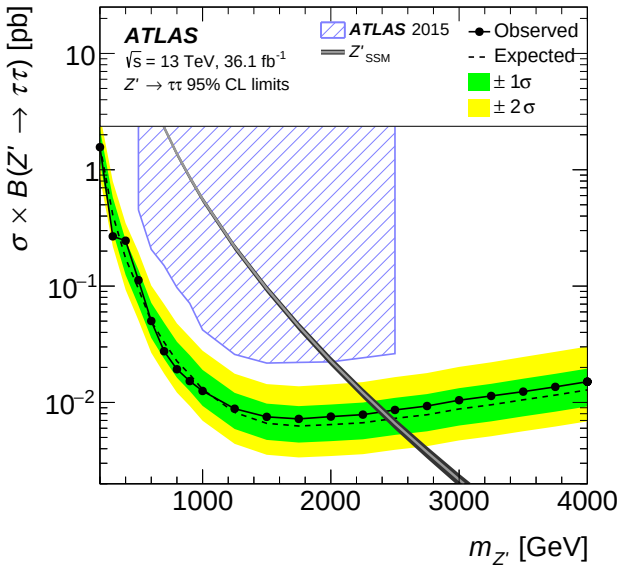

Figure 5.5.4: Observed and expected upper limits with 95% confidence level (CL) on the production cross-section σ multiplied by the branching ratio B of $Z' \to \tau\tau$, against the mass of the Z' boson, combined from the $\tau_{\text{lep}}\tau_{\text{had}}$ and $\tau_{\text{had}}\tau_{\text{had}}$ channels, for the Drell-Yan production mechanism of the Z' boson. Included is the predicted cross-section of the Z' boson in the SSM benchmark scenario, with uncertainty [15].

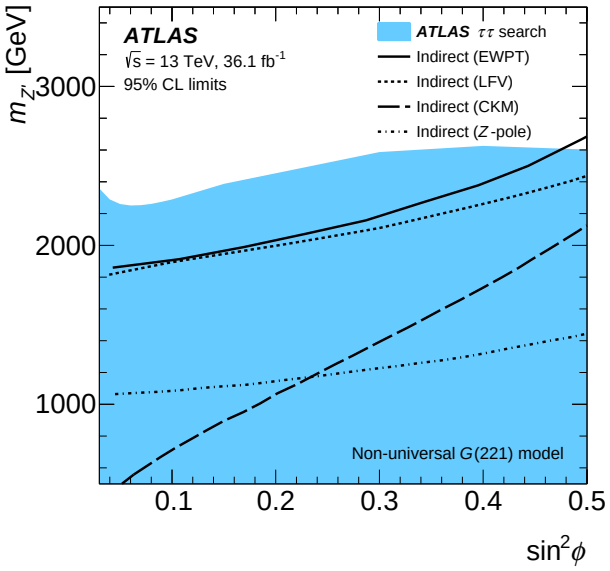

Figure 5.5.5: Observed exclusion limit with 95% confidence level (CL) on the benchmark model parameters $m_{Z'}$ against $\sin^2\phi$ combined from the $\tau_{\text{lep}}\tau_{\text{had}}$ and $\tau_{\text{had}}\tau_{\text{had}}$ channels, for the SFM benchmark scenario of the Z' boson [15]. Included are indirect upper limits from electroweak precision measurements (EWPT), lepton flavour violation (LFV), CKM unitarity and Z-pole measurements.

While there may not have been an opportunity to repeat this Z' interpretation in the latest publication [63], there are still prospects for the analysis to potentially reintroduce the study in the future, as well as possibly from alternative BSM models.

5.6 CMS comparison

As introduced in Section 2.1, the ATLAS detector is only one of four major experiments around the LHC. Another similar general purpose detector, CMS (*Compact Muon Solenoid*) [25], has also published similar results on this BSM di-tau search analysis [66], most recently using the partial Run-2 2015 and 2016 datasets, which records at 35.9 fb^{-1} of good quality integrated luminosity for the CMS detector.

To keep the comparison with ATLAS fair in recorded luminosity, Figure 5.6.1 shows again the model independent limits on the ggH and bbH production mechanisms for both the CMS and the 36.1 fb^{-1} ATLAS [15] results. This is followed by a similar comparison on the model dependent limits in the context of the hMSSM and $m_h^{\text{mod+}}$ benchmark scenarios in Figure 5.6.2.

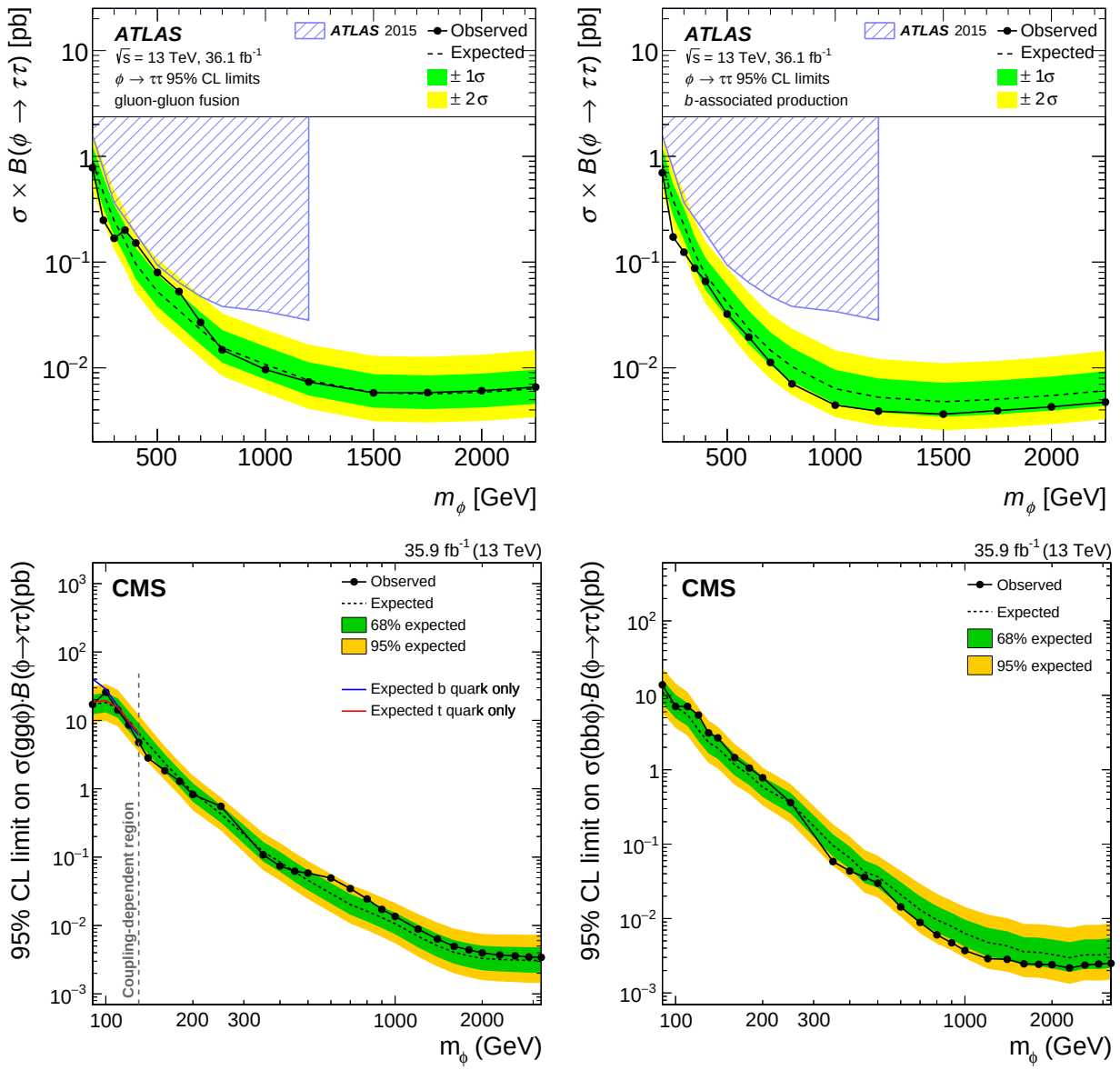

Figure 5.6.1: Observed and expected upper limits with 95% confidence level (CL) on the production cross-section σ multiplied by the branching ratio B of $\phi \to \tau\tau$, against the mass of the scalar boson $\phi = H/A$, for the gluon fusion (left) and b-associated production (right) mechanisms of the H/A bosons, as presented by the 36.1 fb^{-1} ATLAS (top) and 35.9 fb^{-1} CMS (bottom) searches.

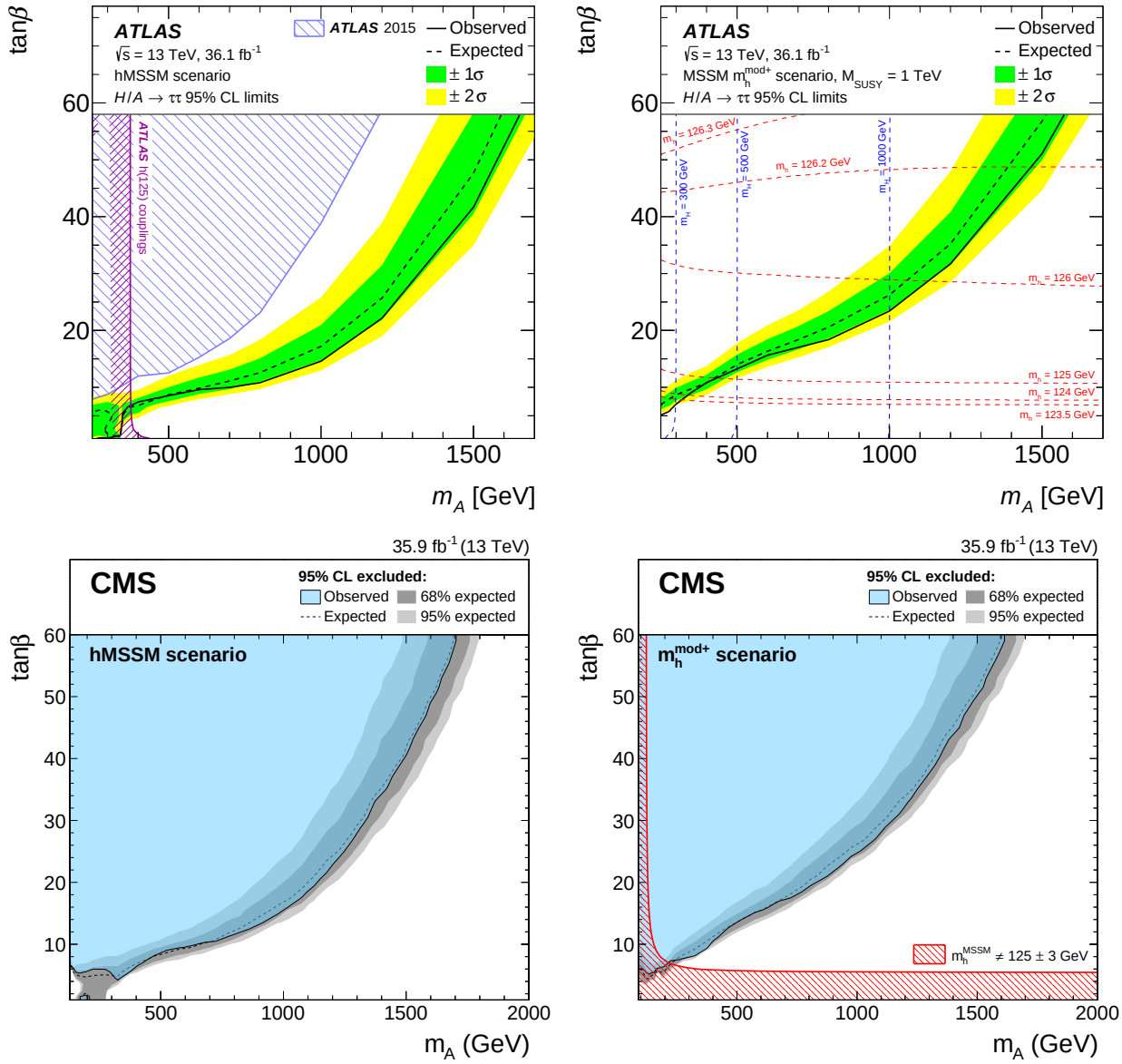

Figure 5.6.2: Observed and expected upper limits with 95% confidence level (CL) on the benchmark model parameters $\tan\beta$ against m_A, for the hMSSM (left) and $m_h^{\text{mod+}}$ (right) benchmark scenarios of the H/A bosons, as presented by the 36.1 fb^{-1} ATLAS (top) and 35.9 fb^{-1} CMS (bottom) searches.

Generally, it seems that both ATLAS and CMS agree very closely on these exclusion limits. In addition to these older benchmark scenarios used in this previous ATLAS search, the CMS result had also interpreted the exclusion limits in the context of the various M_h^{125} models, with the exception of the M_h^{125}(align) scenario, as shown in Figure 5.6.3.

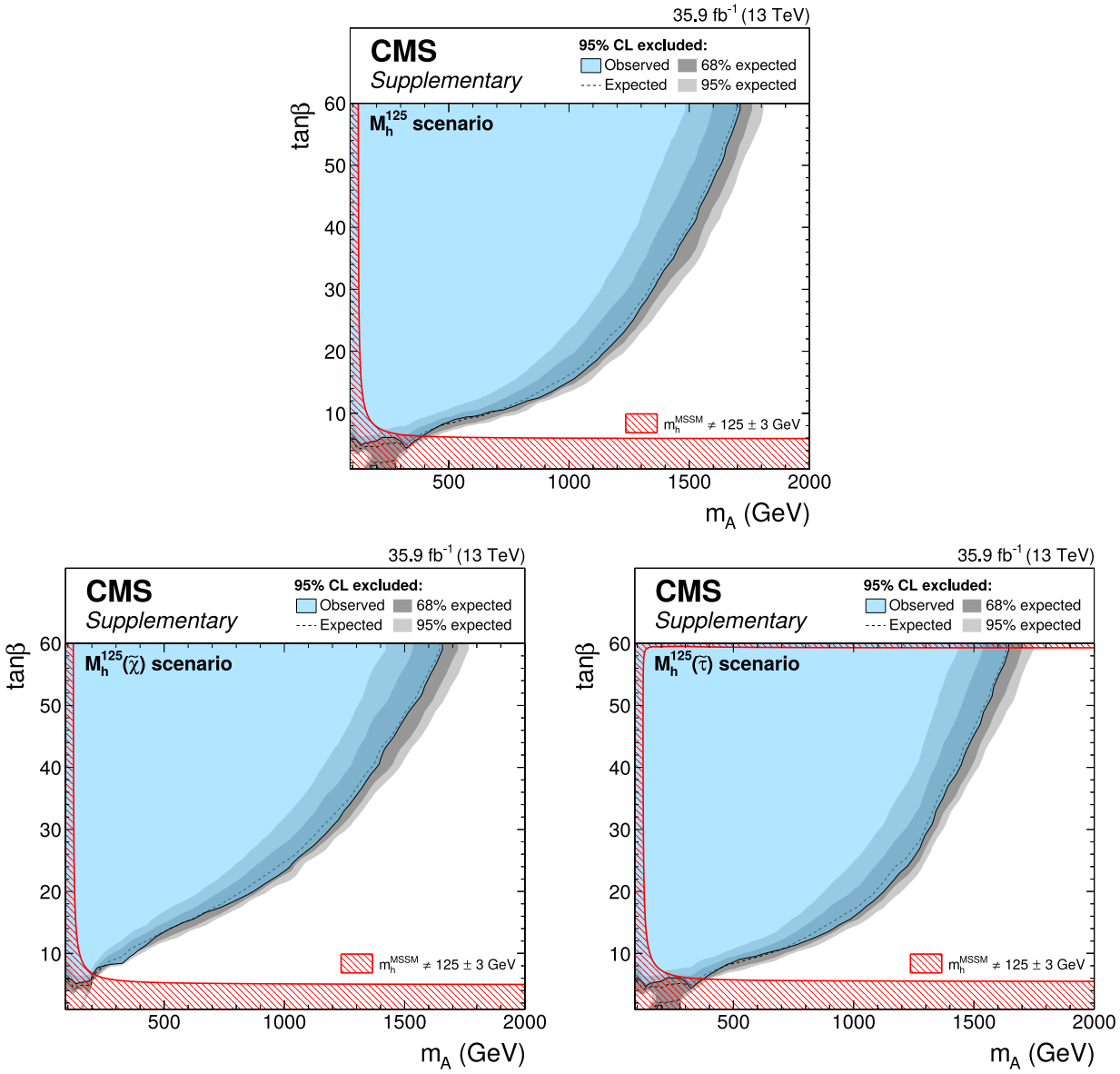

Figure 5.6.3: Observed and expected upper limits with 95% confidence level (CL) on the benchmark model parameters $\tan\beta$ against m_A, for each M_h^{125} benchmark scenario of the H/A bosons, as presented by the 35.9 fb^{-1} CMS search.

Chapter 6: ATLAS Phase-2 silicon Inner Tracker upgrade

As discussed in Chapter 2, the ATLAS detector has recorded 139 fb^{-1} luminosity of data at 13 TeV during the LHC's Run-2, between 2015 to 2018. Following the programme described in Figure 6.0.1, the LHC is currently undergoing a second *Long Shutdown* (LS2) since 2019 for ∼2 years, where it will implement Phase-1 upgrades [67]. It will then resume with Run-3 operations from around 2022 to 2024, whilst possibly operating at an increased energy of 14 TeV, and expected to double both the current instantaneous and recorded integrated luminosity to ∼300 fb^{-1}.

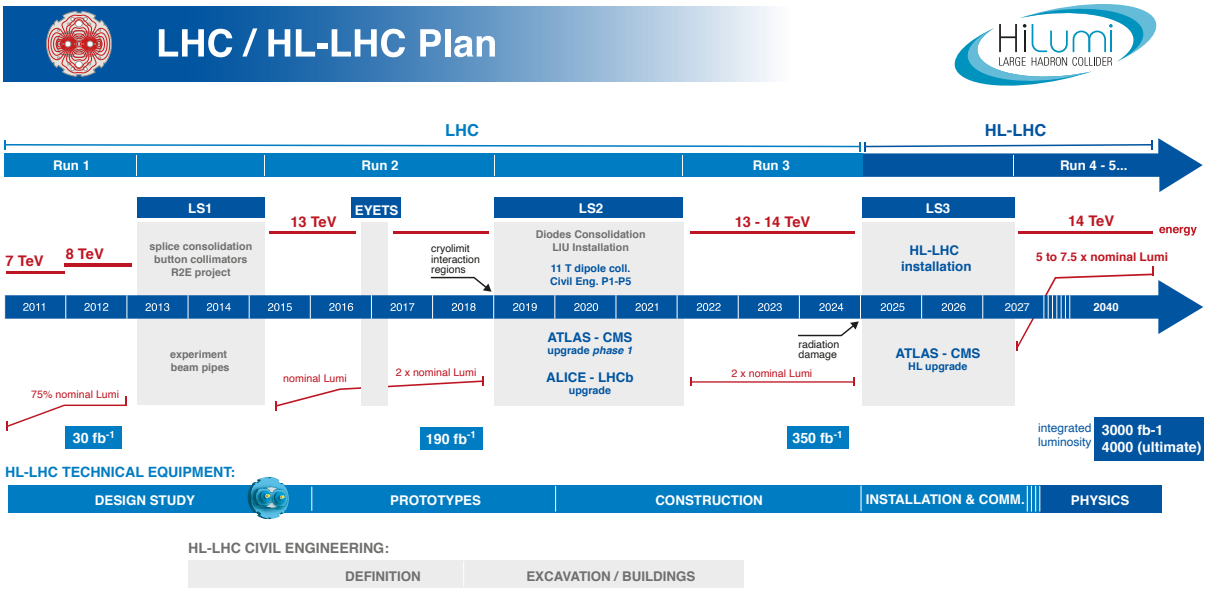

Figure 6.0.1: The projected LHC programme from its operation since 2011 to the HL-LHC starting in 2026 [68].

However, the main focus of this chapter will be following LS3, and the implementation of Phase-2 LHC upgrades in advance of Run-4 operations starting in ∼2027. The Phase-2 upgrade plans a major increase to the instantaneous luminosity delivered, approximately between 5 to 7 times of that currently in Run-2, and so expected to reach ∼3000 to 4000 fb^{-1} of recorded data over a >10 year run [69], whilst possibly continuing to operate at 14 TeV. For this reason, the project has been dubbed the *High Luminosity LHC* (HL-LHC) [70].

In order to cope with this major increase in instantaneous luminosity, the ATLAS' InDet will also require a proportionate upgrade, otherwise it would not be able to sustain sufficient recording in a far denser particle track environment, as a result of the increased pileup of ∼200 interactions per crossing [67]. This is especially the case given that by Run-4 operations, the InDet will also have suffered several years of built-up radiation damage and so its recording efficiency significantly declined, worsened by heavier radiation doses by ten-fold that would be delivered by the HL-LHC. As such, the InDet, formed from the Pixel, SCT and TRT sub-detectors, as mentioned in Section 2.3.1, will be replaced by a new and improved *Inner Tracker* (ITk).

The ITk will feature an all-silicon detector, comprised only of an upgraded Pixel and a new SCT-like sub-detectors, where the SCT-like component is renamed as the *Strip* detector while extending over the range formally occupied by the TRT. Figure 6.0.2 represents a view of the new ITk design, with contrast to the InDet from Figure 2.3.3, while Figure 6.0.3 describes the radii and pseudorapidity coverage by each of the ITk components. In comparison to the current InDet, the Pixel and Strip detectors will have approximately doubled in radius (within the barrel region) to completely fill the space of the original InDet, whilst vastly extending the coverage to $|\eta| < 4.0$.

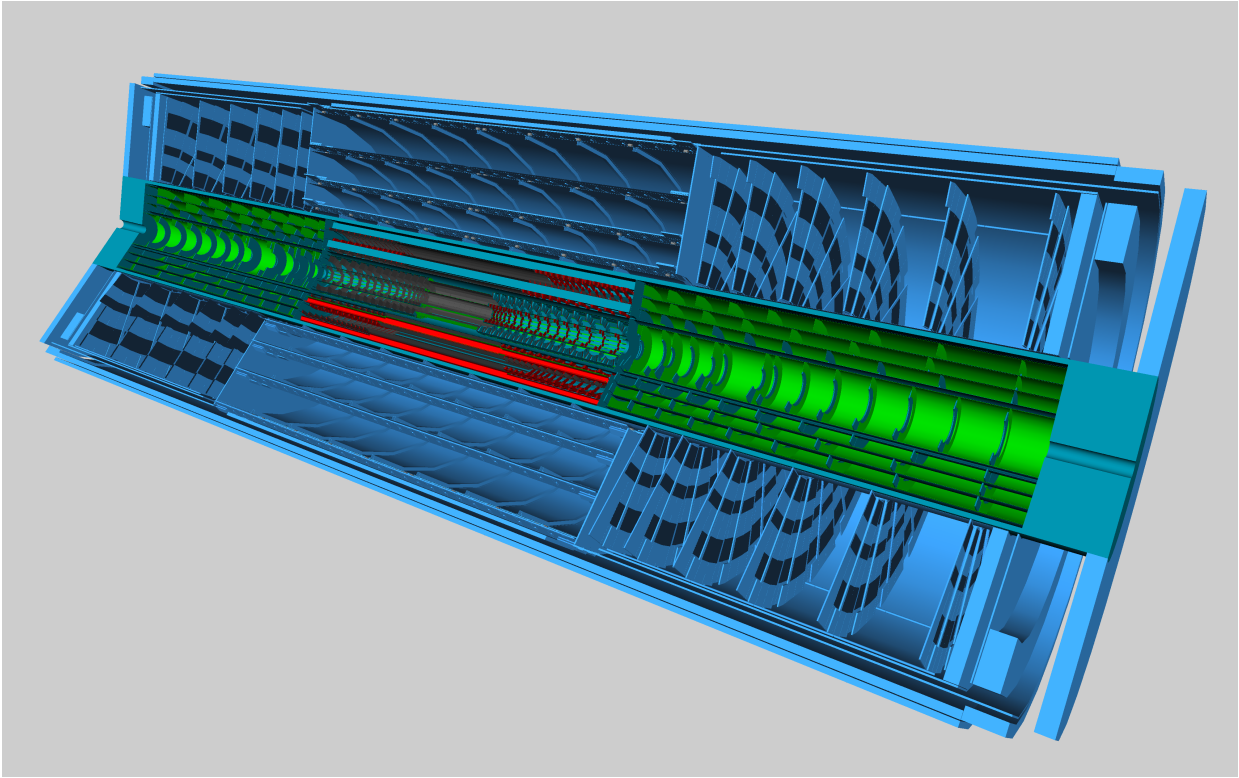

Figure 6.0.2: A simulated view of the ITk, featuring the Pixel detector running through the centre, and surrounded by the Strip detector, extended to fill the region formally occupied by the Inner Detector [69].

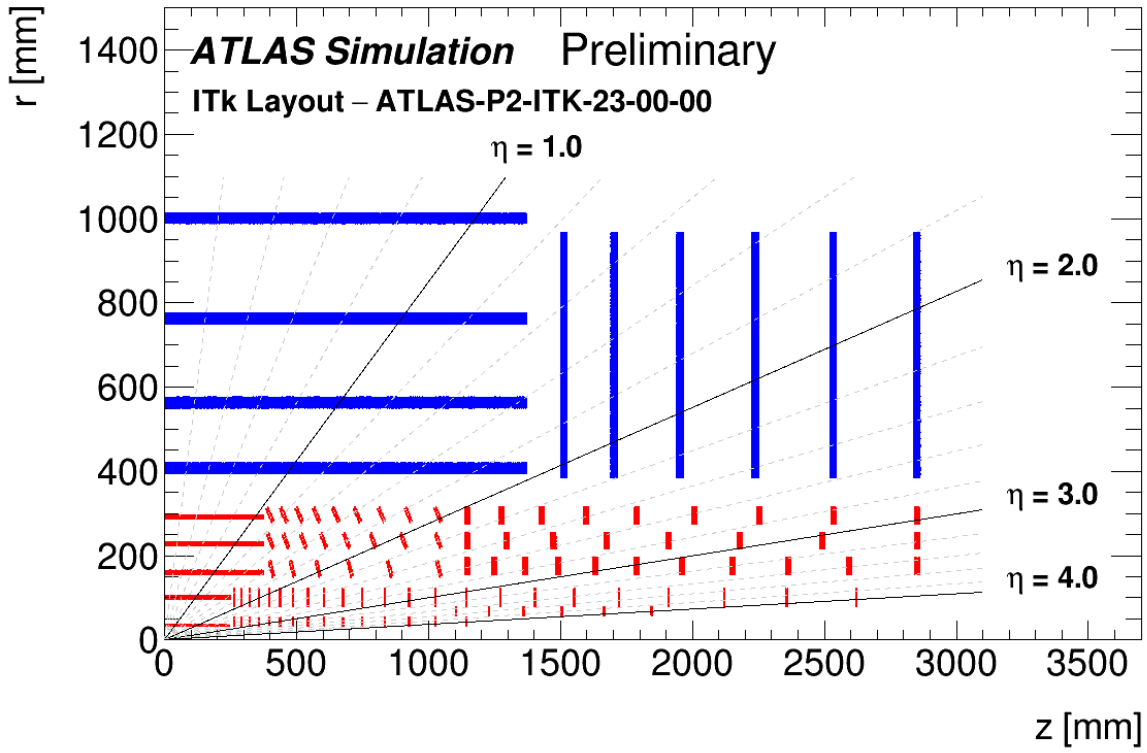

Figure 6.0.3: Latest proposed layout of the ITk in the ATLAS detector with radius R and length z from the interaction point, where pseudorapidity η has also been labelled, revealing the inner Pixel detector (red) and the outer Strip detector (blue) [71].

In contrast to the current InDet Pixel detector, the new ITk Pixel detector will be formed of >10,000 modules, similar in design and arrangement to the previous, but with a smaller (target) module size of $19.2 \times 20\,\text{mm}^2$, each containing 153,600 silicon sensors of size $50 \times 50\,\mu\text{m}^2$ and thickness 150 µm each, in order to improve the resolution as demanded by the HL-LHC [69]. The ITk Pixel is organised into five layers extended across both the barrel and end-cap regions, as seen in Figure 6.0.3, where the end-cap modules are inclined roughly perpendicularly to those in the barrel, which also allows for the increased coverage in pseudorapidity. This provides a significantly increased total of readout channels of at least 100 times that of the InDet Pixel. An example ITk Pixel module is shown in Figure 6.0.4.

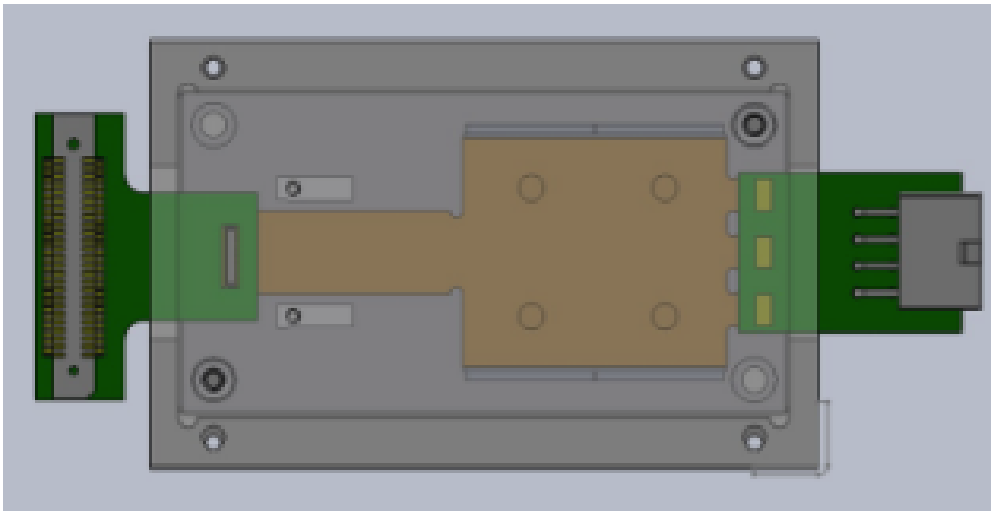

Figure 6.0.4: Schematic drawing of an ITk Pixel module [69]. The centre brown area represents the sensor itself, mounted onto the grey module frame, with green data and power connectors.

The ITk Strip detector closely relates to the current InDet SCT, continuing the silicon micro-strip design totalling 17,888 modules of thickness ∼300 µm each [67]. Unlike the p-in-n SCT sensors, the Strip sensor is composed of an n^+-in-p silicon wafer, primarily chosen due to its improved performance after long-term radiation exposure. Within the barrel region are 10,976 square modules with sensor size $\sim 97 \times 97\,\mathrm{mm}^2$ each, and 6912 similarly-sized trapezoidal modules in the end-caps. The Strip modules are organised into four layers in the barrel and six in each end-cap region, as seen in Figure 6.0.3, also providing a significantly increased 59.87 million readout channels compared to the SCT. An example ITk Strip module for the barrel region is shown in Figure 6.0.5. Further description of the barrel Strip detector will follow in Section 6.1.

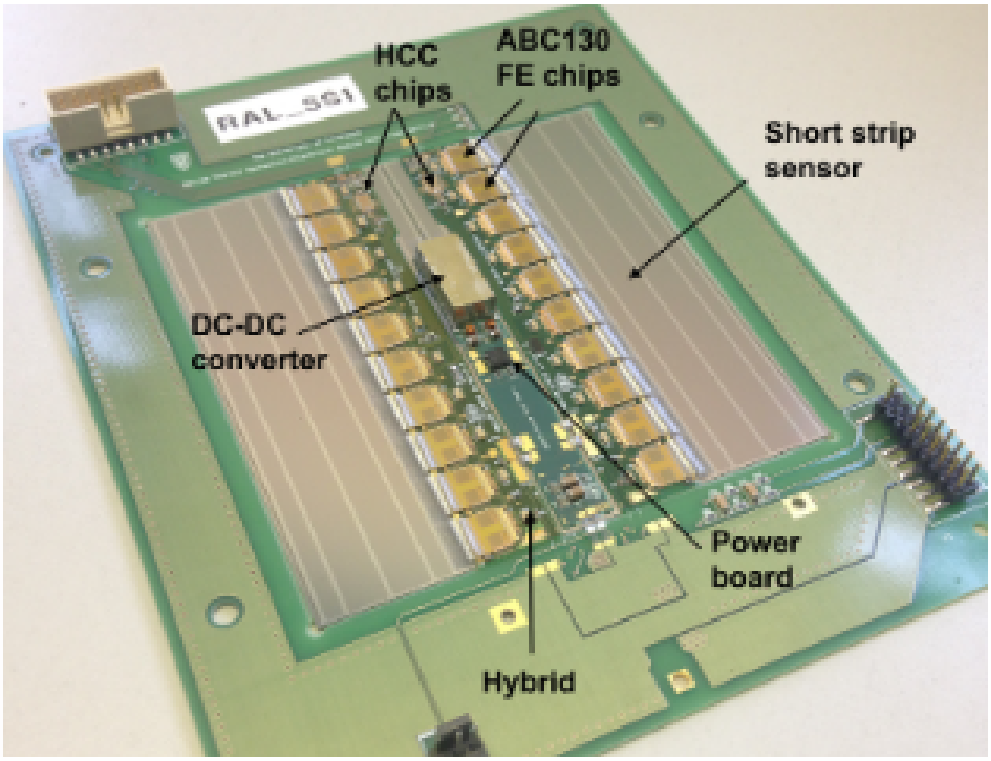

Figure 6.0.5: Photograph of a prototype ITk Strip module used in the barrel region [67]. The centre dark reflective component is the sensor itself, with dark green readout electronic boards attached and mounted to a light green module frame, with data and power connectors.

This thesis will follow the author's contributions towards the research, development, construction and testing of prototype ITk Strip detector modules, particularly for the barrel region in ATLAS. The components forming the Strip modules and how they are assembled together will be discussed in detail, where the author had regularly built such variety of prototypes throughout the project. The description and figures of these techniques will be primarily based on those of the most recent module designs, although the evolution of the general process over the years has not drastically changed. Particular emphasis lies on setting up a construction and testing site at TUoS in preparation for Phase-2, while improving such methods and tooling for quality assurance and ease of construction, as based on the feedback from these prototype experiences.

6.1 Barrel Strip detector

Following on from the Strip detector discussion in Section 6, the barrel Strip modules are mounted onto 392 long, flat, double-sided supporting staves of 1.4 m length, an example of one shown in Figure 6.1.1, running across the length of the detector on each side of the interaction point, while each stave holds 14 modules on each face. The module power supply and readout data transfer are handled externally via an *End-of-Substructure* (EoS) card attached to the end of the stave.

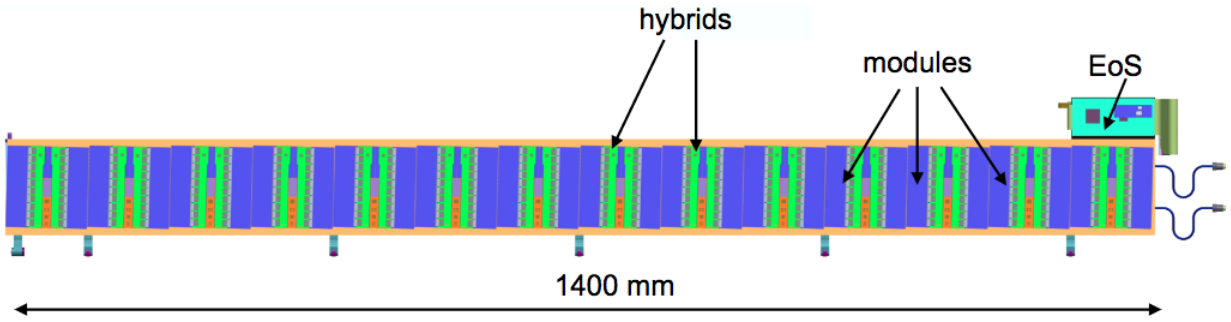

Figure 6.1.1: Schematic of a single barrel stave (orange) holding 14 Strip modules (dark blue) seen on one of its faces, each module containing two hybrids (green) channeling power and data towards an EoS card (light blue) on the end of the stave [67].

Visualised by Figure 6.1.2, a barrel Strip module consists of the commercially-produced square silicon sensor mentioned in Section 6, where the pitch between strips is 75.5 µm. The data is read out by either one or two *Printed Circuit Boards* (PCB) named *hybrids*, which are glued onto the sensor itself. Out of these barrel Strip modules, 3808 of them reside within the inner two layers of the barrel Strip detector, each containing two hybrids glued back-to-back around the centre of the sensor, and each individually accessing the channels facing on their side — these are referred to as *short-strip* (SS) modules, with a strip length of 24.1 mm. The remaining 7168 modules residing within the outer two layers contain only a single hybrid attached to one side of the sensor, and the channels are effectively bridged across the centre of the sensor to form a *long-strip* (LS) module, with strip length 48.2 mm.

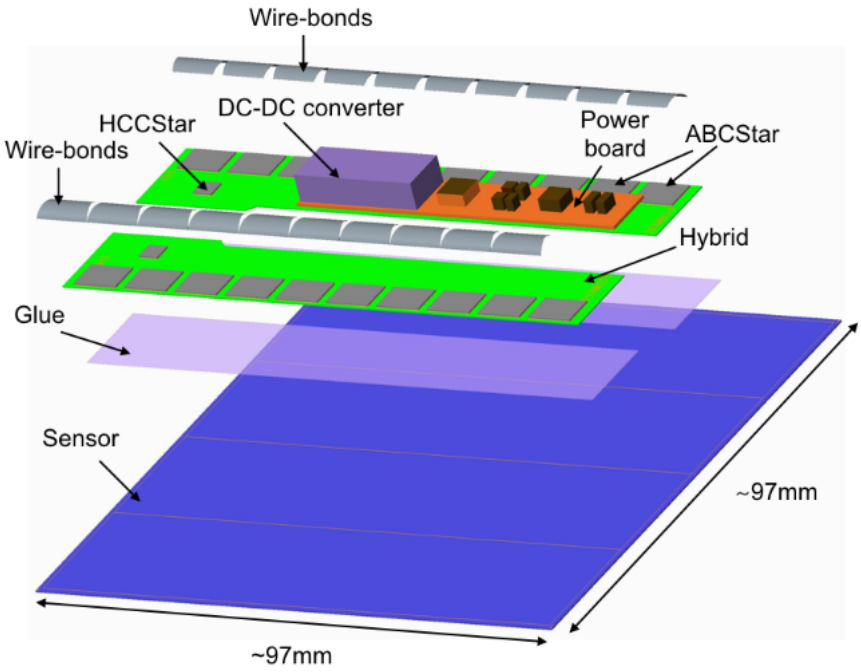

Figure 6.1.2: Exploded schematic of a barrel short-strip module, containing a silicon sensor (blue), two hybrids (green) and a power board (orange) with a DC-to-DC converter (purple), all glued and wire bonded together. The AMAC would be the large chip represented next to the DC-to-DC converter. Each hybrid holds ten ABC(Star)s and a HCC(Star) (grey) [67].

Each hybrid holds eleven commercial silicon *Application-Specific Integrated Circuit* (ASIC) chips with glue, ten of which are named *ATLAS Binary Chip* (ABC), positioned on the front-end of the hybrid and wire bonded to 256 channels each across the sensor, processing the readout into a binary signal. The final ASIC named the *Hybrid Controller Chip* (HCC) governs the communication and timings between the ABCs and the rest of the readout system. The data and power are both channeled through a *power board* towards the stave's EoS card, which is glued onto the sensor and wire bonded to each hybrid, where the power is delivered through a (*direct current*) DC-to-DC converter and supervised by an *Autonomous Monitor And Control* (AMAC) chip mounted onto the board.

While these supporting electronics are powered by a *low-voltage* (LV) supply, with more details to be covered through the electrical testing in Section 6.3, the sensor itself is additionally powered with negative bias from a *high-voltage* (HV) supply. This bias generates an electric field within the silicon that forces any charged particles to drift towards the surface of the sensor (and therefore along the channeled readout strips), thus enabling the material to be highly sensitive to the passage of charged particles, as would be produced from the LHC collisions.

The design of the silicon hybrid chips, namely the ABCs and the HCC, have gone through a number of versions throughout the years in this project (for example: ABCN, ABC250, ABC130, to name a few). The values typically indicate the semiconductor processing technology used in the chips as measured in nm. Denoting the final design as to be constructed and inserted into the ITk, these are labelled as the *Star/** version. While the Star chipset will continue to use the 130 nm technology, this design also changes the communication path architecture between the ABCs and the HCC, shifting from a chained ABC pattern to a direct single ABC-to-HCC star-like one, and thus significantly improving readout bandwidth. This also coincides with the compatible tooling design as used to assemble them, which will be discussed throughout the following sections. This thesis and the author's experience will primarily focus on the studies involving the penultimate ABC130 chipset and the progression onto ABCStar.

6.2 Barrel Strip module construction

In the following sections, the construction procedure for a single barrel Strip module will be described in detail. TUoS will be involved with the production process of the barrel Strip modules, expected to construct ∼10 % of the total number of modules over a 3-4 year period once begun in ∼2021, whilst working closely with several institutes across the UK, the USA, China and CERN. In the meantime, a production facility with the appropriate tooling has been set up at TUoS, while research and development into the techniques of the construction procedures and testing are being investigated and practised, with involvement of the author, as will be discussed throughout the sections that follow.

Modules are built inside of an *ISO class 5* (100 particles per cubic feet) cleanroom environment, where example images of such are shown in Figure 6.2.1. Cautious clothing procedures are in place for workers, such as wearing specialised overcoats, shoes, gloves and hairnets, in order to minimise the unwelcome introduction of dust and dirt, as well as delivering protection from *electrostatic discharge* (ESD) which could damage sensitive electrical components.

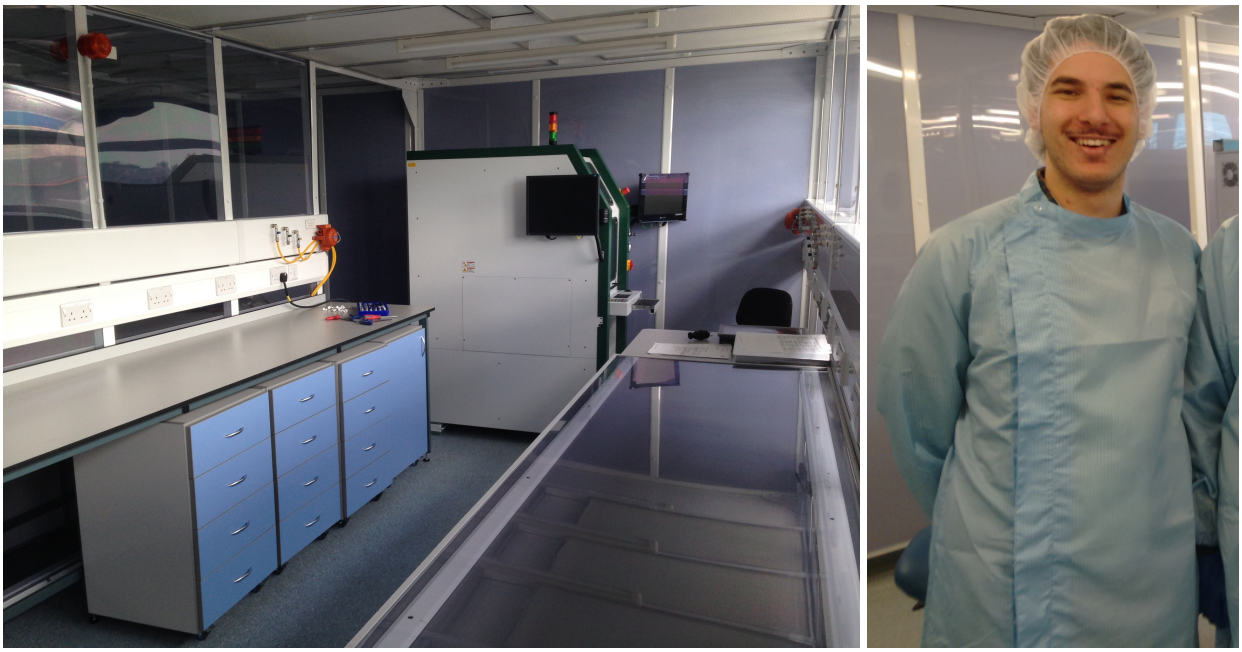

Figure 6.2.1: Photograph of the cleanroom at The University of Sheffield (left) and an example of the required protective clothing as donned by the author (right).

In order to safely and inexpensively practise the production of prototype hybrids and modules, before using the final components in production, as well as trial and test the tooling used, low-grade silicon or (patterned) glass is used as substitute for sensors and ABCs in the construction of earlier prototypes. While these materials do not possess any electrically-conductive properties which could be readout tested, on which more is to be discussed in Section 6.3, they do still exhibit *thermo-mechanical* (TM) properties similar to the high-grade *fully-electrical* (EL) silicon which would be used in the final construction. This allows for testing of the physical behaviour of the constructed module when passed through thermal cycling and mechanical strain, as a means of understanding how it would withstand over time once installed within the ITk environment. As such, these prototypes have appropriately been referred to as TM or EL modules throughout the project, each serving different uses for study. Alternatively, in the mixed case of EL hybrids attached to a TM sensor, these are referred to as MS (*mechanical sensor*) modules, which allow for partial readout testing without imposing high EL sensor costs. Once these prototype modules had been constructed, they are also used for testing their installation and readout on prototype staves.

The construction process involves the assembly of the chips onto the hybrids, followed by the hybrids and power board onto the sensor, then wire bonding the components together and taking measurements for quality control. While the discussion will focus on the latest design, tooling and techniques used by the final ABCStar chipset, there will be some highlights on how changes and improvements were reached through experience with the ABC130 programme, simplifying the construction process and guaranteeing quality assurance.

6.2.1 Hybrid assembly

The assembly of a barrel Strip module from its individual fabricated components begins with the hybrid construction, with the primary objective of gluing the ABCs and HCC to the hybrid. Chip-unpopulated hybrids are received from other collaborating institutes (within the UK) mounted onto a roughly A4 paper-sized PCB panel, shown in Figure 6.2.2, where the design has varied from containing approximately two to four pairs of hybrids per panel. The hybrids are paired with opposite left/right handedness, labelled as Y/X-type, respectively.

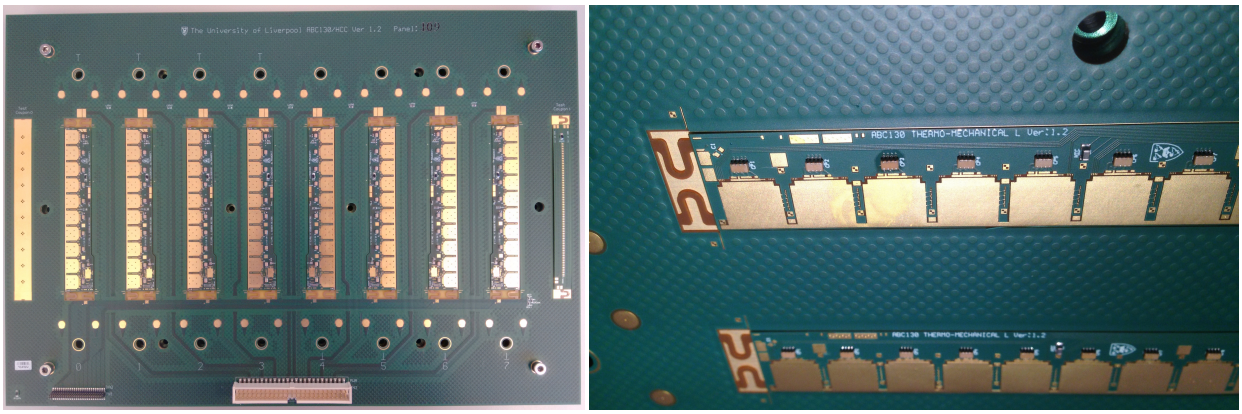

Figure 6.2.2: Photographs of an example hybrid PCB panel (left) of newer ABC130 design, with four pairs of blank hybrids ready for assembly, and a close-up of one of these hybrids (right) from a different panel of older ABC130 design, where it can be seen in comparison that the chip pads do not have grooves which would guide the glue as newer models do.

When assembling a single hybrid, ten ABCs and one HCC are carefully placed upright into a custom-designed slotted tray using a common vacuum suction pen, shown in Figure 6.2.3, aligned to their relative positions matched to the hybrid, and opposing HCC slots for those intended for a Y/X-type hybrid. The addition of the HCC slot into this chip tray was one of the key but simple developments throughout this process, as originally this was being done by hand with great difficulty.

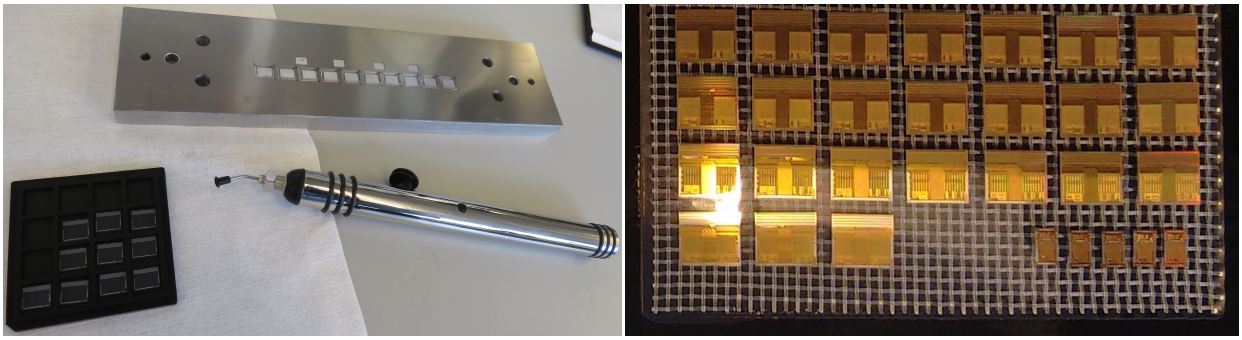

Figure 6.2.3: Photographs of the chip tray, vacuum pen and example glass ABCs (left), where the chip tray is of older design without the HCC slots, and example electrical ABC130 chips (right) with HCCs in the bottom-right corner.

A custom vacuum pick-up tool matching the eleven chip positions is then lowered onto the tray, shown in Figure 6.2.4, made with two opposing holes to align the tool's pins into position, in order to simultaneously pick-up all of the chips while maintaining their relative positions.

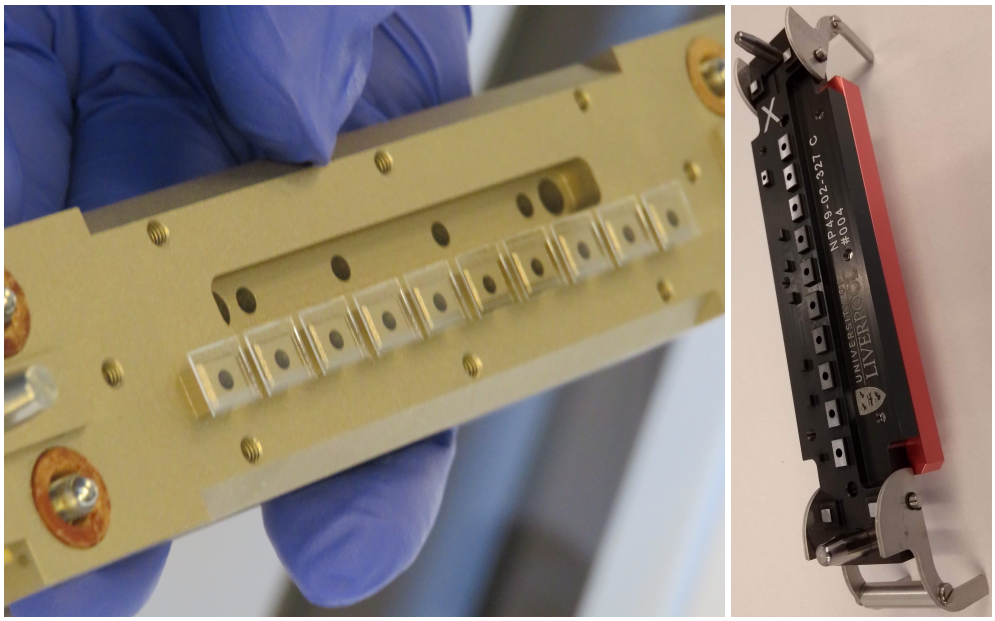

Figure 6.2.4: Photographs of the undersides of a vacuum hybrid pick-up tool, of older ABC130 design (left) holding ten glass ABCs as example but without a HCC slot, and of the newest ABCStar design (right) with a HCC slot available in the top-left corner for an X-type hybrid.

The pick-up tool can then be safely rested atop of a stand with the chips facing upwards, shown in Figure 6.2.5, and the stand will hold the tool securely, either by vacuum or by clamps in more recent designs.

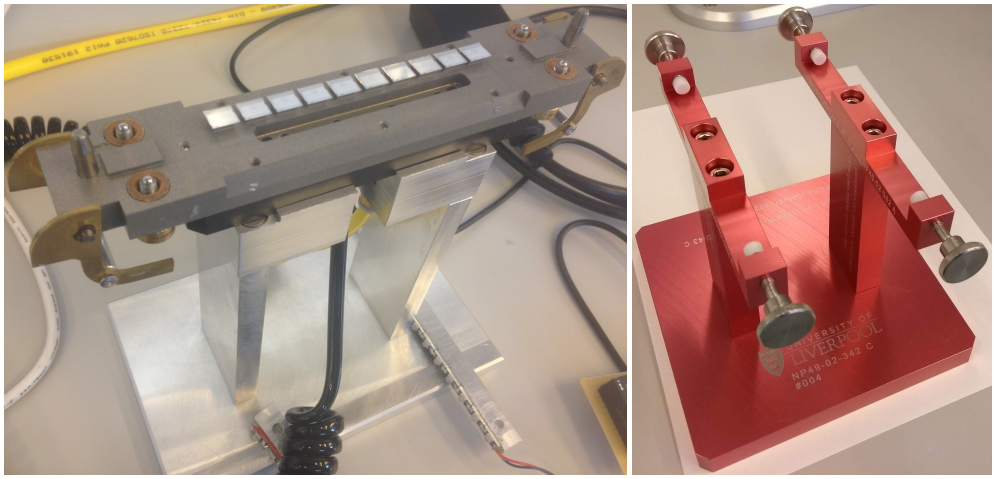

Figure 6.2.5: Photographs of a stand where the hybrid pick-up tool can be securely rested, as shown (left) with the held chips facing upwards, and the pick-up tool held down by vacuum, or instead by clamps (right) in the newest ABCStar design.

A custom gluing stencil is lowered onto the chips, shown in Figure 6.2.6, again with holes on either side aligned for the pick-up tool's pins, and four additional feet on the tool to adjust the exact height the stencil rests at above the chips. The stencil features a five-crossed hole pattern, much like that on the side of a dice, for each of the ABCs, and something similar but smaller for the HCC. This pattern had also widely evolved throughout the project before settling on this final design, in order to ensure that the chips remain strong and stable on the hybrid, especially when thermally cycled.

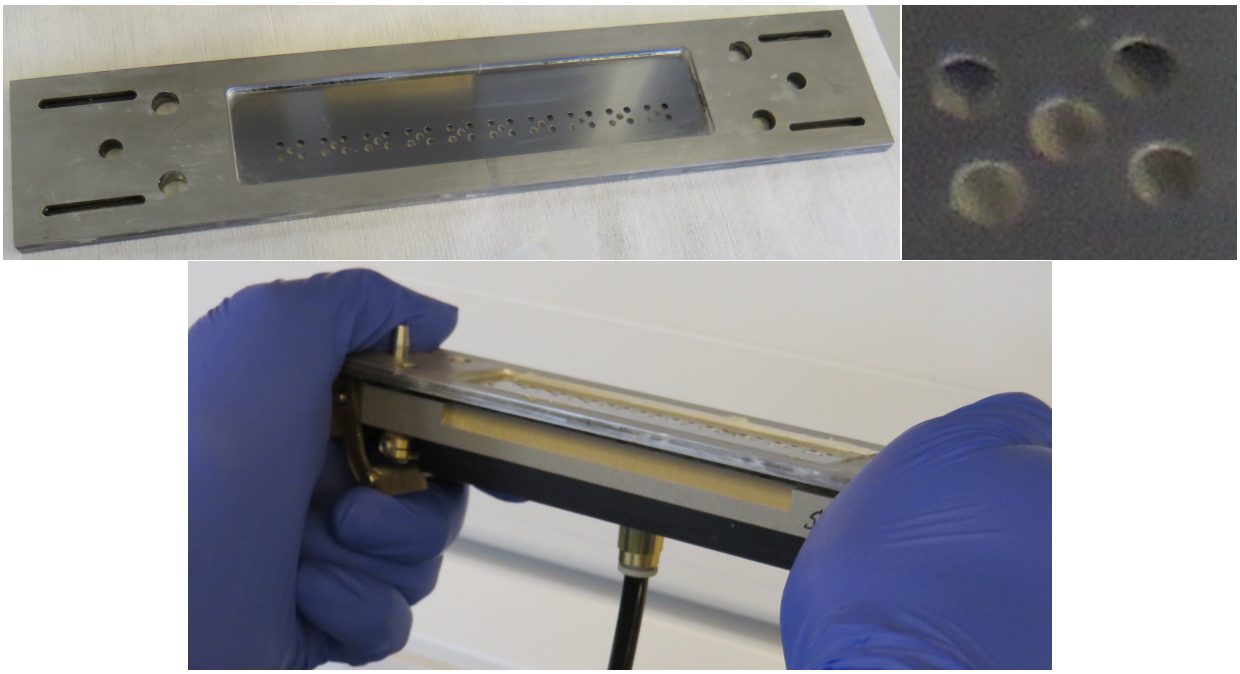

Figure 6.2.6: Photographs of the hybrid-chip gluing stencil (top-left) of older ABC130 design with no pattern for the HCC, featuring the five-crossed hole pattern zoomed in (top-right), and the stencil being attached to the hybrid pick-up tool with the chips held in between (bottom).

With the stencil's holes aligned over the underside of each chip, the glue can be placed in strategic position with a precise quantity and thickness, such as to ensure robustness whilst minimising seepage that could obstruct wire bonding. The final choice of procedure is using an *ultraviolet light* (UV)-curable glue (*Loctite 3525*, or alternatively *Dymax 6-621* [67]) which is carefully injected into each hole of the stencil through a pneumatically-powered needle, shown in Figure 6.2.7, dispensing a small and specific amount of glue.

Figure 6.2.7: Photographs of the UV glue-dispensing container (left) without its needle, and the process of the glue being pneumatically-injected through the hybrid stencil (right), with the exception that this photograph features an earlier trial where the glue was placed on the hybrids rather than the chips.

This choice of glue was also a hot topic of study throughout the research programme, where in earlier designs a silver epoxy glue (*TRA-DUCT 2902, BIPAX* [67]) was originally used, applied by smearing the glue across the holes of the stencil rather than by injection. However, while it is important to have a suitable choice of glue that is able to meet the stability conditions imposed by radiation in the ITk environment, there are also the matters of practicality and supply during the production process which the silver epoxy was failing to meet, in that its curing time was too slow (on the order of hours) and that there could not be a guarantee of having a sufficient, long-life stock during the production phase.

The hybrid remains fixed to the panel, and the panel is attached to a custom matching-sized vacuum jig, where vacuum lines run underneath the panel to keep the hybrid down flat, since it has a tendency to move or bow slightly and thus cause misalignments as a result. The stencil is removed and the pick-up tool holding the glued chips is carefully lowered onto the hybrid, again where the panel has holes for its alignment pins. A solid weight block is placed on top of the pick-up tool and the vacuum remains open, shown in Figure 6.2.8, in order to keep the chips above the hybrid at the exact target height, intended between ∼60 to 100 µm. In more recent designs, the blank pads on the hybrid where each chip would be placed also have slight grooves which match the stencil pattern, so as to assist the alignment of the glue. Two UV *light-emitting diode* (LED) bars are placed on both sides of the hybrid, also shown in Figure 6.2.8, where modern panel designs have troughs in place to align them comfortably, and emit for ∼5 min in order to rapidly cure the glue.

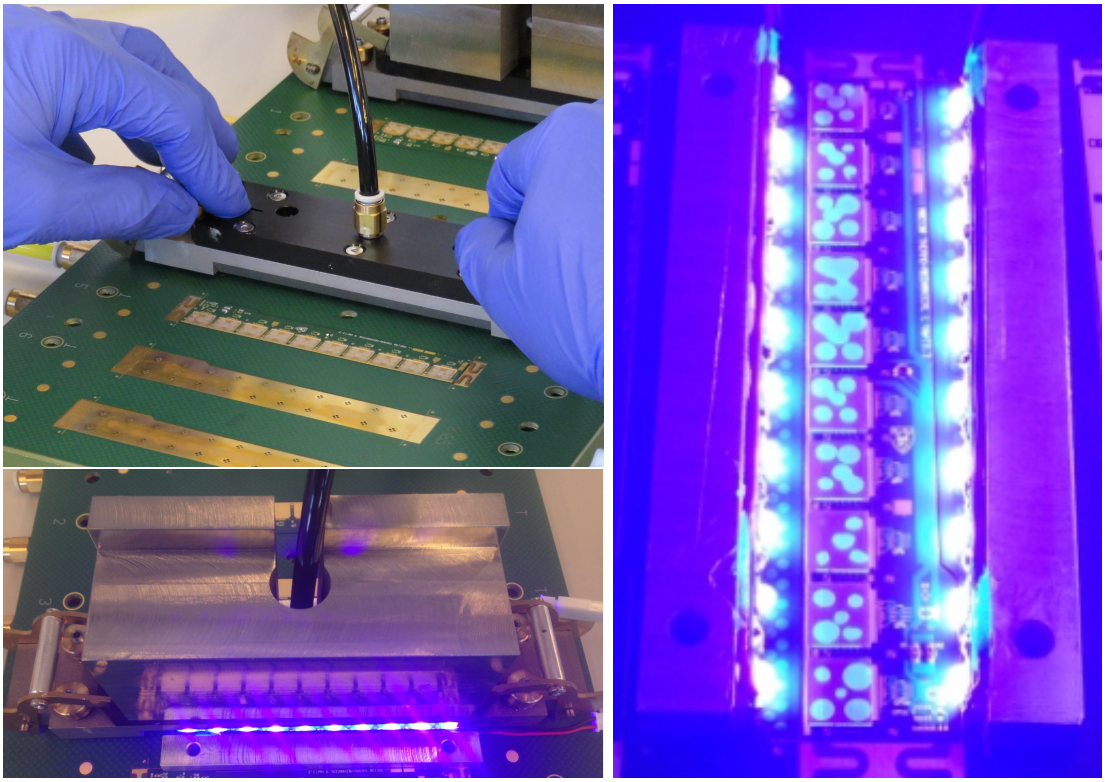

Figure 6.2.8: Photographs of the hybrid pick-up tool, holding glued chips, being lowered onto an older ABC130 panel (top-left), followed by a weight block being placed on top of the pick-up tool (bottom-left) with two UV LED bars surrounding the hybrid and left to cure the glue, where the effect of the UV light on the glue without any tooling blocking the view (right) highlights the glue pattern through the glass chips, such that in this example trial the positioning and quantity of each dot is not perfect.

When the curing is complete, the pick-up tool's vacuum is disconnected and lifted away from the hybrid, leaving behind the chips securely glued to the hybrid at the intended height, with the completed product shown in Figure 6.2.9. In practice, a caveat should be noted that by the time of the final official production phase, TUoS will not continue assembling hybrids and instead would be receiving the completed product, as described here, from the associate institutes, only to proceed with the module assembly which will be discussed in the following section.

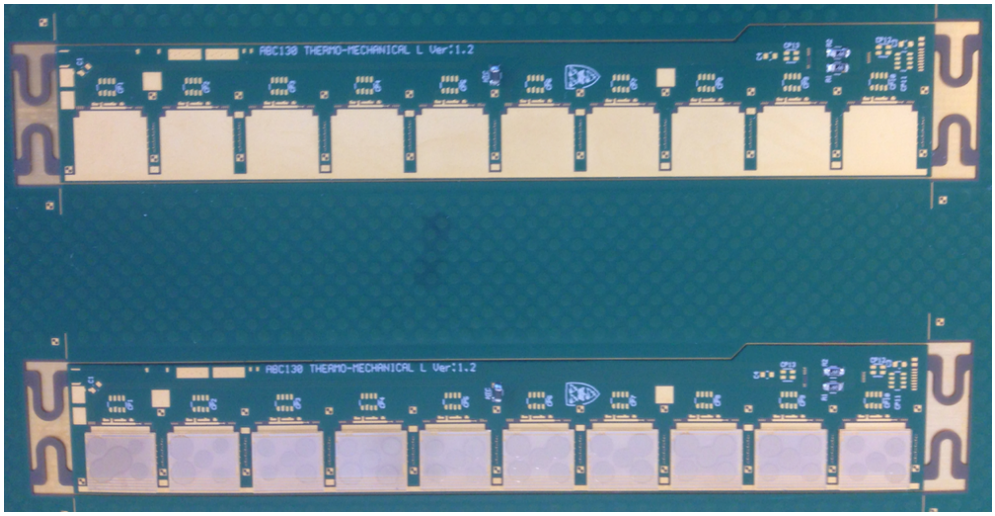

Figure 6.2.9: Photograph of a completed hybrid assembly (bottom) featuring an older ABC130 design with UV-glued glass ABCs, compared to an unpopulated hybrid (top).

6.2.2 Module assembly

While it may be expected for TUoS to construct a mixture of both SS and LS modules, the majority of the research project so far and thus this thesis will focus on the production of SS modules, where the main objective of the module assembly is to glue the two opposite-handedness hybrids onto the sensor, followed by the power board, which overall is quite similar to the hybrid assembly procedure. In practice, the only difference with LS module assembly is avoiding the addition of the second hybrid.

The module assembly procedure begins by carefully releasing a completed hybrid from the panel, while being held down by the panel vacuum jig. This is achieved by either cutting two thin tabs with a scalpel on either side of the hybrid in earlier designs, as seen in Figure 6.2.9, or by removing the hybrid as it is held down by double-sided Kapton tape — this design has widely varied throughout the project to make this step as easy and clean as possible. The same vacuum pick-up tool used for the chip assembly is used to pick up the hybrid by its chips after disconnecting the panel jig vacuum, and rested securely atop the same stand with the underside of the hybrid revealed upwards.

Very similarly to the hybrid assembly procedure, another custom stencil of different design is lowered across the hybrid, shown in Figure 6.2.10. The final stencil pattern, which has also varied greatly over the years, features a long thin rectangular gap running across the backbone of the hybrid, with approximately five shorter interspaced gaps along where the ABCs reside, and a wider one underneath the HCC area of the hybrid. This design ensures a continued strong connection of glue when met with thermal stress, while minimising the appearance of air bubbles during the gluing process which could compromise that integrity.

Figure 6.2.10: Photographs of the module-sensor gluing stencil, used in older ABC130 designs (top) and the latest ABCStar (bottom).

While the rapidly-curing UV glue would still be the preferable choice as it was for the hybrid assembly, it was found there was difficulty in sufficiently transmitting UV light from the LED bars into the gap between the sensor and the hybrid, particularly because these components are wider in comparison to the hybrid assembly, and in placing the LED bars into a position without damaging the sensor. Since this proved itself to be impractical, the original technique of using an epoxy glue smeared across the stencil, shown in Figure 6.2.11, filling in the gaps to the complete thickness, remains with the final module construction procedure. However, the choice is an electrical grade *Fuller Epolite FH-5313* epoxy [67] which should still be adequate for hybrid-to-sensor gluing and supplied in enough quantity, also shown in Figure 6.2.11.

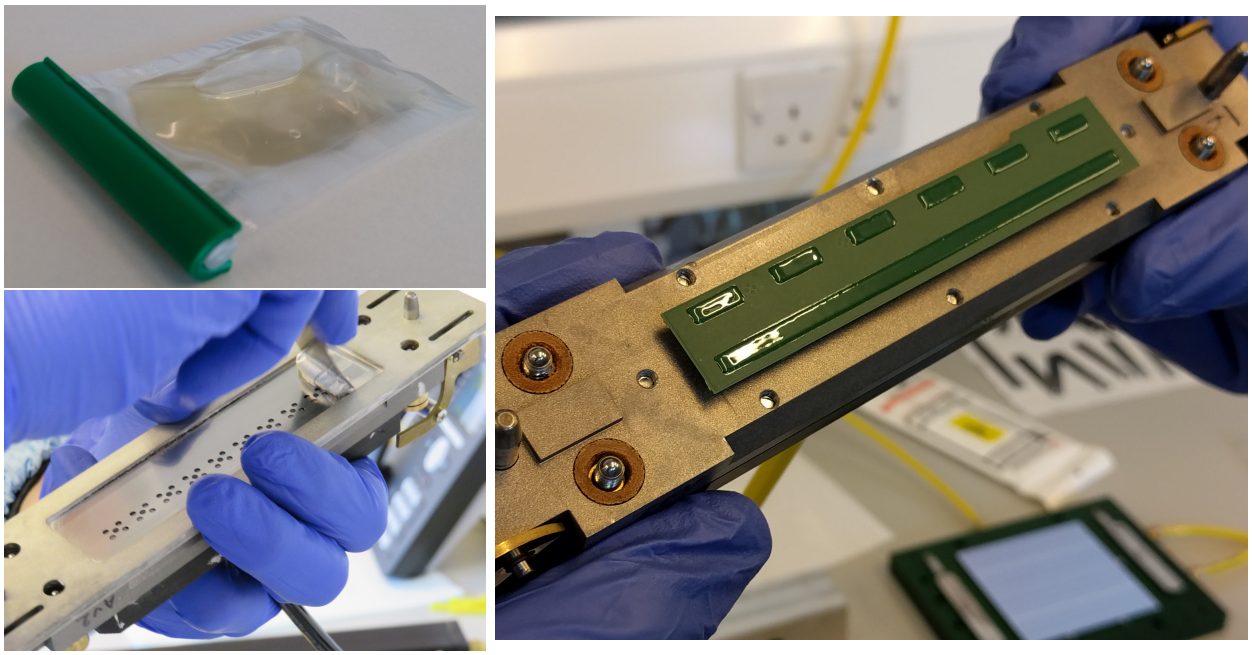

Figure 6.2.11: Photographs of the module epoxy glue in its packaging (top-left) and the technique by which it would be smeared across the stencil (bottom-left), with that caveat that this example photograph represents a hybrid-chip stencil smearing an older silver epoxy glue instead, followed by the glued hybrid once the stencil has been removed (right) held by the pick-up tool.

The sensor is prepared by placing it on top of a custom vacuum jig, shown in Figure 6.2.12, where the edges can be aligned by three pins running across a corner. The design of the sensor vacuum jig itself has also evolved to include additional holes for the underlying vacuum lines, so as to ensure an even distribution of suction and therefore strain on the sensor, which would have resulted in a slight bowing otherwise. Just as with the hybrid assembly, the glued hybrid is lowered from the pick-up tool onto the sensor vacuum jig, aligned with holes for its pins on either side. In order to ensure that the hybrid of a certain handedness is placed into the correct position and orientation on top of the sensor, later developments to the pick-up tool have adjusted the thickness of its two pins to differing sizes, and the holes on the jigs to match, so that they cannot be placed the wrong way round by accident. This is further assisted by markings on all of the tooling as a visual reminder to the worker. Again, the pick-up tool vacuum remains on and a weight placed on top, also shown in Figure 6.2.12, to keep the hybrid-sensor glue height between ∼80 to 160 µm, and left to cure for ∼12 h, making this one of the slowest parts of the module construction procedure.

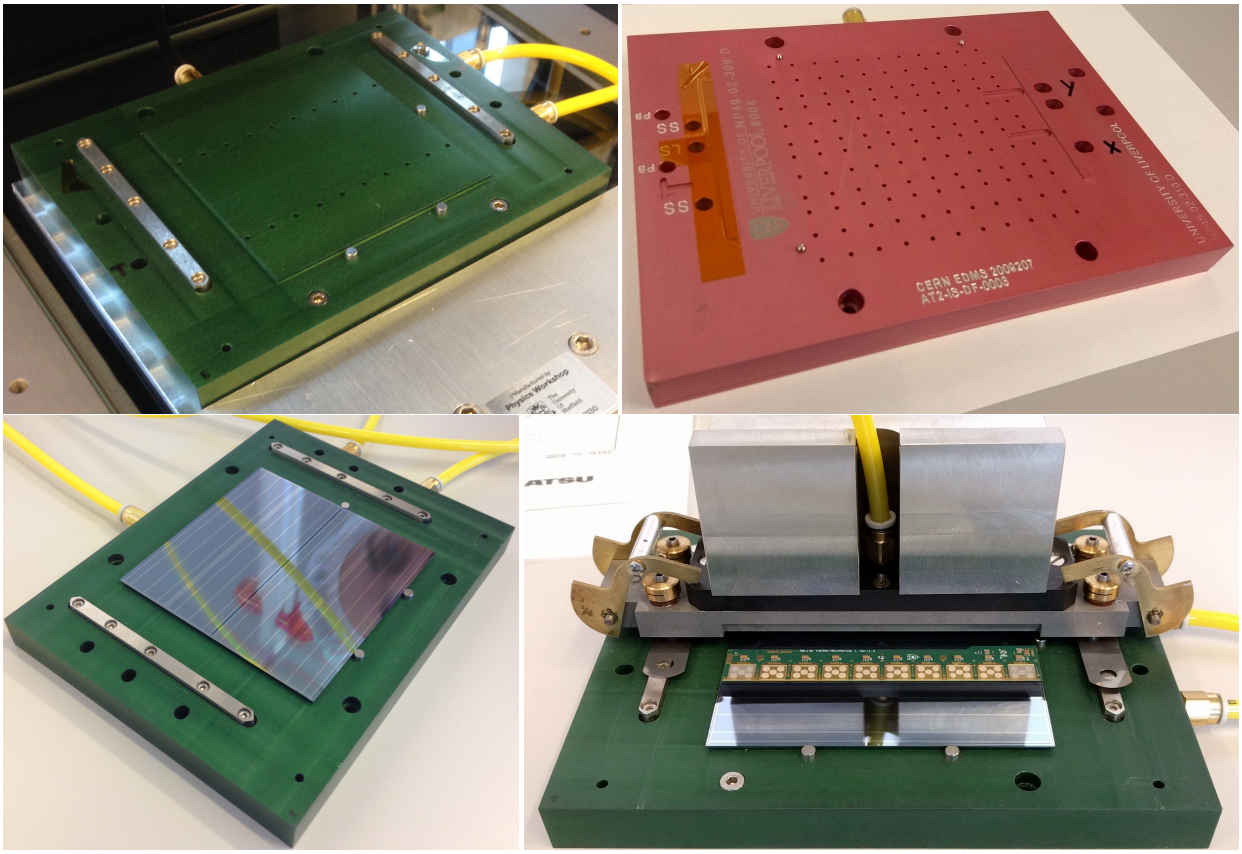

Figure 6.2.12: Photographs of the module sensor vacuum jig, with the older ABC130 design (top-left), and the latest ABCStar (top-right) where the vacuum hole configuration is spread across the whole surface of the sensor. This is followed by an example thermo-mechanical silicon sensor placed atop of the older ABC130 jig (bottom-left), where the epoxy-glued hybrid is lowered onto with the pick-up tool, with a weight block placed on top and left to cure (bottom-right), with a second hybrid already glued in front previously.

For SS modules only, the exact same procedures are performed in mirror for the second, opposite-handedness hybrid, with the advantage in the most modern tooling that there is enough space for both hybrids to be glued down to the sensor and cured simultaneously, drastically reducing the production time. Once both hybrids have finished curing and their pick-up tools removed, the module assembly is completed by gluing the power board onto the sensor. As discussed previously in Section 6.2, the power board is only necessary for EL/MS modules which would possess an electrical behaviour, and since the power board stock was limited, this step was not common during the TM programme — where it was, the gluing was done by hand with great difficulty. Otherwise, the ultimately final procedure for attaching the power board to the sensor is identical to that of the hybrids using their own appropriate tooling, with the exceptions that a differently-optimised stencil pattern is used, along with a special vacuum pick-up tool that safely holds the power board by its DC-to-DC converter housing, shown in Figure 6.2.13. An example of a completed SS barrel module, with two hybrids and one power board, was shown previously in Figure 6.0.5.

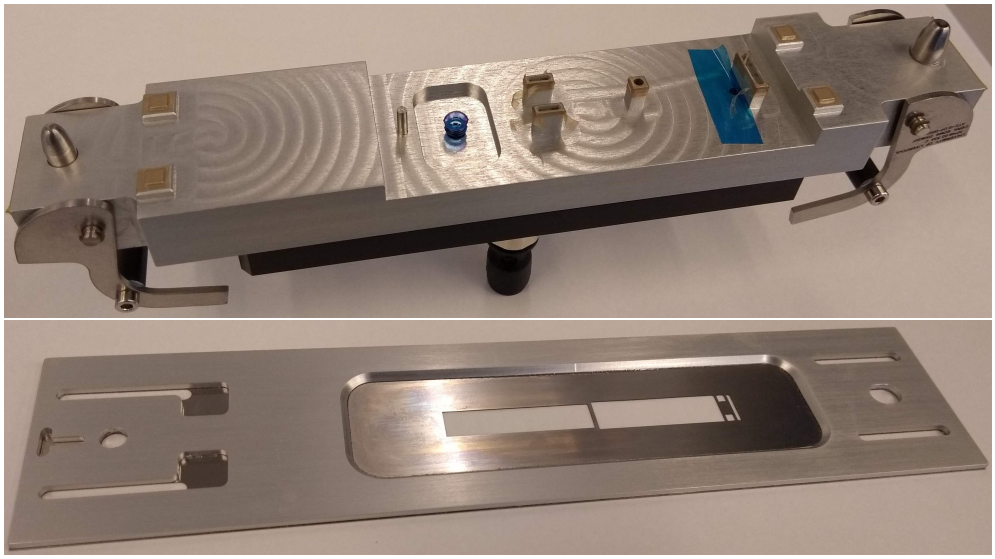

Figure 6.2.13: Photographs of the alternative vacuum pick-up tool (top) and sensor-gluing stencil (bottom) for the power board from the latest ABCStar design.

6.2.3 Glue height metrology

As mentioned in the previous Sections 6.2.1 and 6.2.2, the nominal glue heights of chip-to-hybrid and hybrid-to-sensor should be between ∼60 to 100 µm and ∼80 to 160 µm, respectively [67]. Not only is this required to maintain the structural and thermal strength requirements that would be challenged in the ITk environment, but also restricts the performance of the wire bonding procedures which will be discussed in the following section.

To verify that these target glue heights have been satisfied during the assembly procedures, metrology is performed on the hybrids and module using a probing microscope (*OGP SmartScope Flash CNC 200* [67]), connected to a computer as shown in Figure 6.2.14. With the sample placed underneath, the microscope primarily uses a laser to reflect off an opaque surface, in order to measure a vertical distance through time-of-flight. Alternatively, where the surface is not opaque (as was in the case of TM transparent glass substitutes) and so the laser is not able to reflect off the target surface, a mechanical touch probe can be used instead with less precision and higher risk of damage to the sample, so generally this method is not preferable.

In the ideal situation, with many developments over time adding these features to the samples, solid dull pads/stripes on the silicon components and fiducial markings on the hybrids can be used as suitable laser reference points for each height measurement, an example of which is also displayed in Figure 6.2.14.

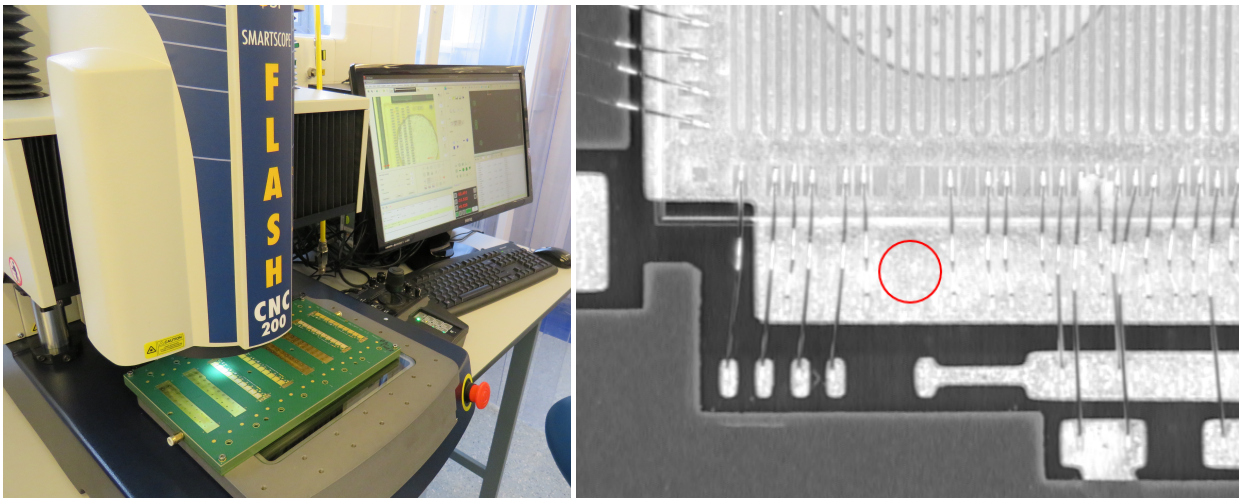

Figure 6.2.14: Photograph of the laser probing microscope and computer used for glue height metrology, with a hybrid panel underneath for testing (left), and a close-up of an ABC-hybrid pad with a patterned glass chip glued and wire bonded as seen by the microscope software (right).

By taking numerous measurements across the sample, planes can be constructed using the microscope's computer software, representing the top surface level of that component, and so the distance between two planes can be taken as the glue thickness, while subtracting for the known thickness of the component itself (where the chip thickness is 300 µm and the hybrid thickness is 275 µm). The glue height measurements can then be compared with expectation for quality control, otherwise the sample would simply be rejected from the production line. An example result of such a glue height measurement is shown in Figure 6.2.15.

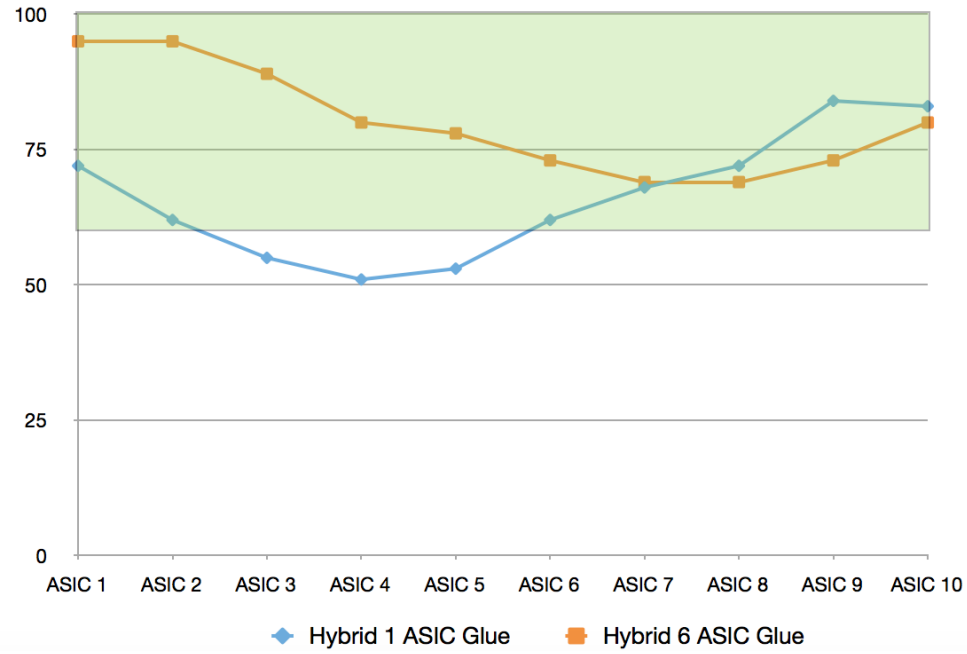

Figure 6.2.15: An example result of a laser measurement for a pair of hybrid-ASIC/ABC glue heights. The y-axis represents the actual glue height in µm, where the accepted tolerance band between ∼60 to 100 µm is highlighted green. The uncertainty in each measurement (∼0.1 µm) is too small to represent on this scale. It is clear from these results that while the hybrid labelled number 6 (orange) lies entirely within acceptance, hybrid 1 (blue) falls beneath this requirement on chips 3, 4 and 5.

For the majority of the research programme so far, these measurements on the glue heights have been taken manually with the probing microscope, in that the laser position was driven using joystick controls by the worker, with the computer screen as visual reference, as well as instructing the software to construct planes and calculate differences. Since during the production phase many more modules will be constructed and need to be tested quickly, these manual methods are too slow, taking on the order of half an hour to complete, as well as running some risks for human error.

As such, the author investigated into creating an automated measurement routine, built-in as an available feature within the microscope's graphical software interface, which was successfully tested on a few of the prototypes built at TUoS. By fixating the sample to a consistent and approximately aligned position underneath the microscope, the software is able to determine the exact location of fiducial markings and components using image edge detection, giving the routine a reference starting point. Then, given that the relative positions of markings and components are known from design, and the edge detection is used to account for any horizontal uncertainties, the routine can be instructed to move the laser from point-to-point taking numerous measurements far more rapidly and consistently than by manual. The routine will then automatically calculate the planes and differences, and producing the glue height metrology results, with appropriate data formatting, in just a few minutes. However, since this depends on pre-emptively knowing the design of the components, and these designs have been rapidly evolving throughout the project, development and scrutinisation of these routines are still an ongoing effort.

6.2.4 Wire bonding

Once the module assembly from Section 6.2.2 is complete, and the metrology from Section 6.2.3 confirms the glue heights are suitable, the electrical connections can be made between the sensor to the chips, the chips to the hybrid, and the hybrids to the power board, thus completing the assembly of an EL module. This is performed using a wire bonding machine, shown in Figure 6.2.16. The machine threads a 25 µm wire through a needle which ultrasonically welds the wire to allocated bonding pads patterned across the module components. Photographs of this process, and a wire bonded module, are also shown in Figure 6.2.16.

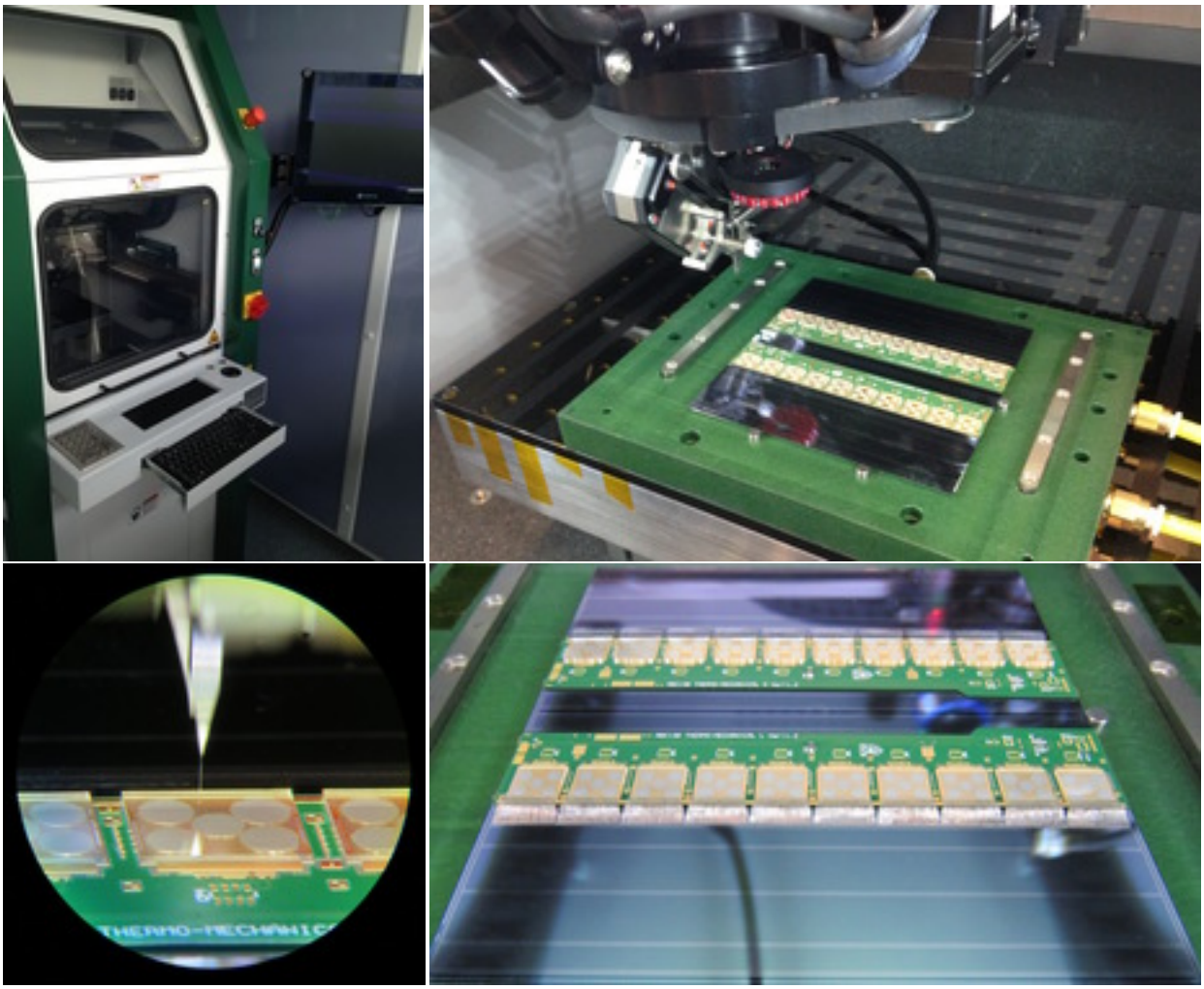

Figure 6.2.16: Photographs of the wire bonding machine. These feature the wire bonder machine itself (top-left), the needle inside the wire bonder with module underneath (top-right), a close-up of the needle wire bonding a patterned glass ABC to the sensor (bottom-left), and a fully wire bonded module (bottom-right).

6.3 Data acquisition testing

In addition to the detector hardware being upgraded for the ITk, so must the detector readout electronics and data acquisition (DAQ) software, in order to cope with the higher rates of information and number of channels. In order to conduct these tests, a fully wire bonded electrical hybrid/module is required so that it may be read out by a local DAQ testing system.

The author was responsible for setting up a DAQ testing facility at TUoS within an *ISO class 7* (10,000 particles per cubic feet) cleanroom, which involved managing and installing the required DAQ hardware, devices, tooling, components and software. In the early days of this setup programme, a number of travelling DAQ loads with fully electrical mini-sensor modules were transported to numerous institutes across the world, including TUoS, as a means in assisting them to set up, practice, identify issues and missing components, and obtain referenceable results with their DAQ system, as well as test the robustness of the delivery transportation methods itself. These developments and upgrades led onto the opportunity to independently test and quality control several EL hybrids on panels, and EL or MS modules, while uploading those results and cataloguing the components to a shared online database, which will be discussed throughout the following sections.

6.3.1 Hardware setup

To begin the DAQ testing, the necessary electronic components to interface with a hybrid or module to a computer are first required. This is performed using a commercially-available *Field-Programmable Gate Array* (FPGA) board as the acting DAQ system, shown in Figure 6.3.1 — the choice of which has evolved throughout the project, originally using the *Atlys* [72] FPGA model, but later switching to the *Nexys* [73], with perhaps further options to consider in the future.

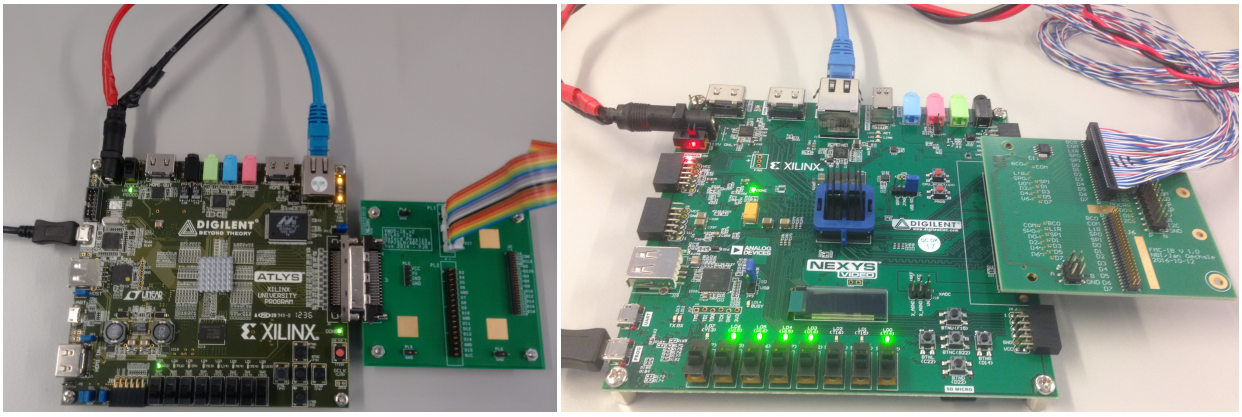

Figure 6.3.1: Photographs of the older Atlys (left) and newer Nexys (right) FPGA boards, acting as the core of the DAQ testing readout system. Attached to the right of each FPGA are the VMOD-IB (Atlys) and FMC-IB (Nexys) adapter interface boards.

The FPGA board is connected to a computer through a gigabit ethernet cable and powered with a LV power supply (*Aim-TTi MX180TP*), shown in Figure 6.3.2 (5 V/3 A voltage/current for the Atlys FPGA, 12 V/3 A for the Nexys). Firmware on the FPGA can be flashed with software via a USB cable from the computer.

Figure 6.3.2: Photograph of a low-voltage power supply delivering power to the various components within the DAQ testing system. From left to right, the channels shown are powering the Nexys FPGA, the SLVS buffer board and a single hybrid-on-panel.

The FPGA data is then connected to either a hybrid or a module through a variety of interfaces, additional boards and adapters, all depending on the situation and FPGA board model, which has greatly evolved throughout the programme. For example, focusing on the latest Nexys model and DAQ setup design, the Nexys FPGA is interfaced with an additional *FPGA Mezzanine Card Interface Board* (FMC-IB) adapter (*VMOD-IB* for the Atlys), also shown attached in Figure 6.3.1, which then connects to a *Scalable Low-Voltage Signaling* (SLVS) buffer board through a ribbon cable, as shown in Figure 6.3.3. The SLVS buffer takes additional LV power supply at 4.5 V/0.3 A, and the data connects to the hybrid/module or other load as the *device-under-test* (DUT) via the panel/frame they are held within using a ribbon cable or other, also shown in Figure 6.3.3.

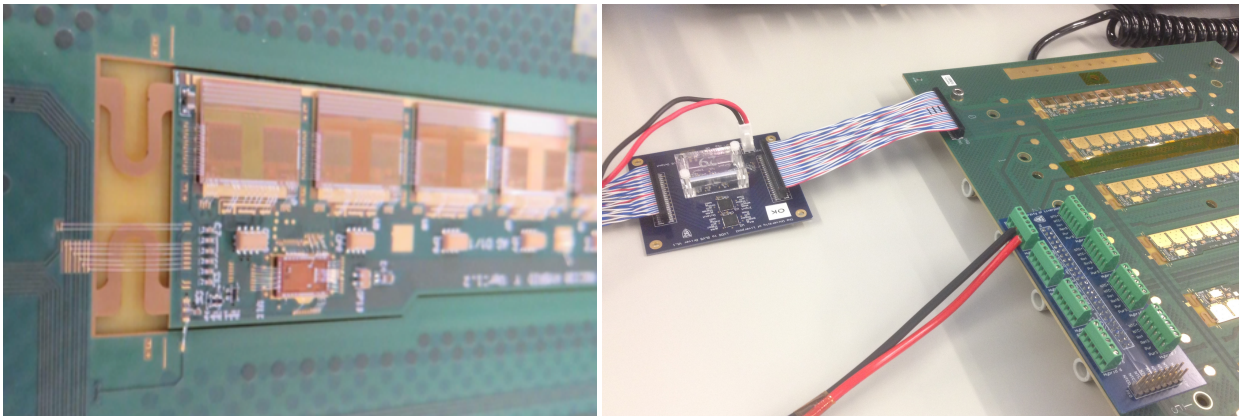

Figure 6.3.3: Photographs of an example electrical hybrid on panel with wire bonds (left) and the panel connected with the SLVS buffer board through a ribbon cable (right).

The hybrids are also powered with a LV supply nominally at 1.5 V/1.1 A per hybrid, where in the case of a complete module the connection is made through the power board itself to the hybrids. Figure 6.3.4 summarises the general schematic of these electronic boards, connections and power, while Figure 6.3.5 display a complete photograph of an example setup.

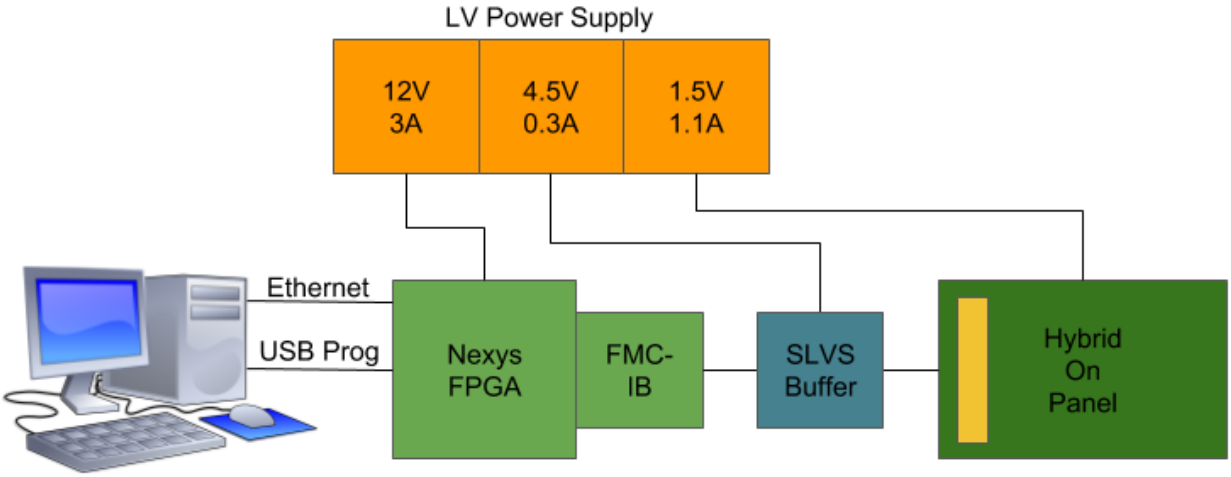

Figure 6.3.4: Schematic of the computer, electronic boards, connections and power used in DAQ testing, for an example single electrical hybrid on panel, using the most recent Nexys-based FPGA setup.

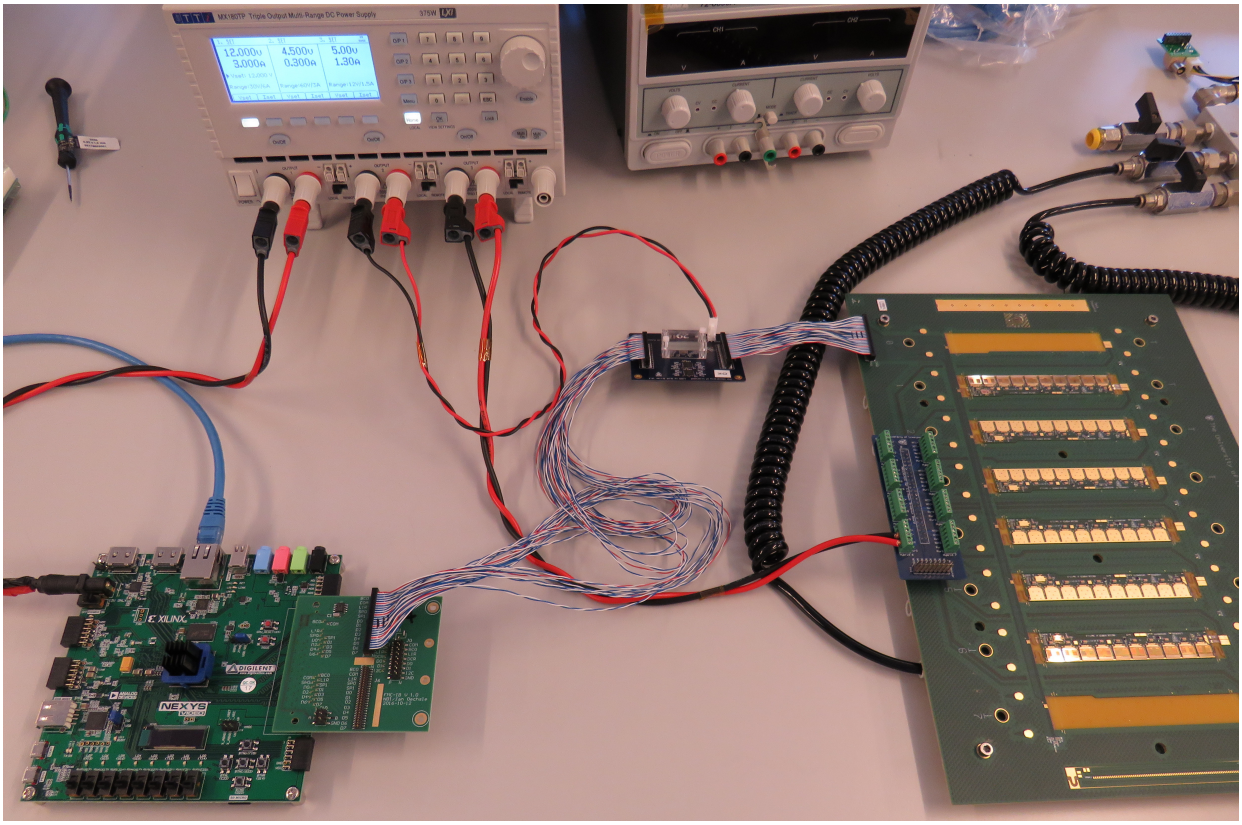

Figure 6.3.5: Photograph of the an example complete DAQ testing setup, using the Nexys FPGA system for testing a single hybrid-on-panel, with LV power supply, FMC-IB, SLVS buffer board and the various cabling.

In the case of fully EL modules, while its hybrids' electronic operations are powered by the LV, the sensor is also negatively biased with a HV power supply (*Keithley 2410 SourceMeter*), as shown in Figure 6.3.6, at approximately 500 V with current compliance on the order of a µA. While this bias is usually needed to activate the sensor's sensitivity in detector operation, it also benefits the DAQ testing by suppressing the sensor's internal thermal noise, while there are no collisions to monitor, as any stray background charges will be swept away by the silicon's electric field.

Figure 6.3.6: Photograph of a high-voltage power supply delivering a negative bias to the module sensor, as a means to suppress noise during the DAQ testing.

To mitigate any further sources of background noise, the module can be stored inside of a dark sealed box during the DAQ testing, an example shown in Figure 6.3.7, which should at least remove any noise caused by the natural visible light. A dry nitrogen gas supply is fed into the box for a few minutes to flush, in order to reduce the relative humidity to less than 5 %, since excessive humidity introduces additional noise or causes the sensor to break down and fail to hold its voltage. The humidity can be monitored using a portable electronic thermohygrometer placed inside of the box, producing an example graph as shown in Figure 6.3.8. For similar reasons, to ensure that the humidity causes no problems to any of the components at any time during the construction or testing, be they noise or damage related, all sensitive parts are stored away within a temperature-controlled, dry nitrogen-flushed cabinet when not in use.

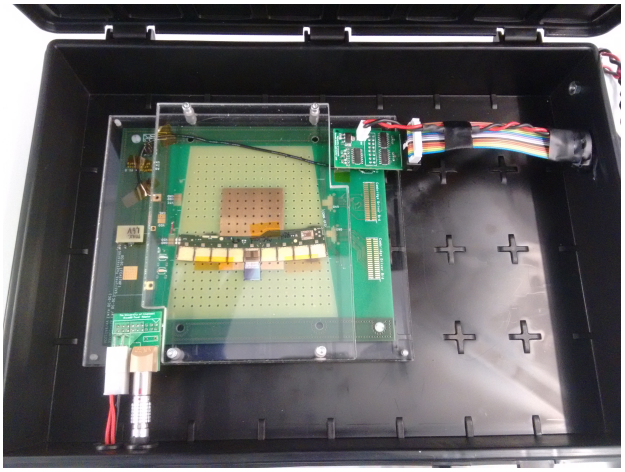

Figure 6.3.7: Photograph of a sealable box with an example DAQ load DUT inside, used to create a dry nitrogen-flushed, dark environment as a means to reduce noise.

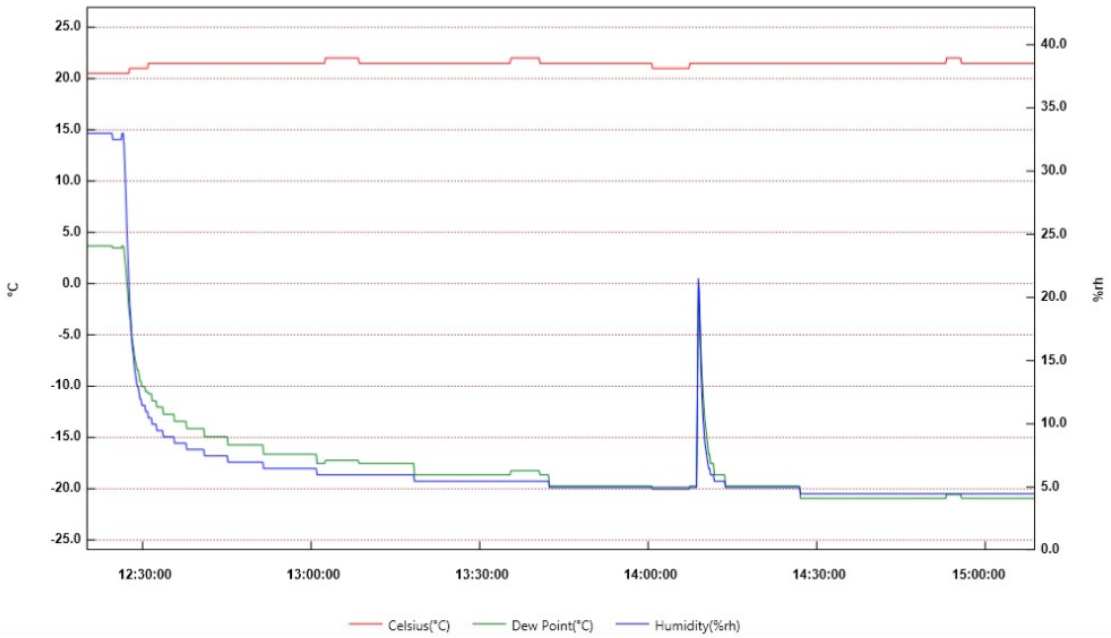

Figure 6.3.8: Example graphs of temperature (red), dew point (green) and relative humidity (blue) with the time of day, inside of a sealed box where a module under DAQ testing would be stored, while it was being flushed with dry nitrogen. There is a clear exponential decrease in humidity (and dew point) as the dry nitrogen started to flow into the box. The spike in humidity was caused by briefly opening the lid of the box, reintroducing water vapour from the surrounding air. Temperature remains mostly constant.

While under testing, particularly for modules, the electronics can begin to overheat and may cause damage to them if left running for too long. But as certain DAQ tests may require these lengthy operations, and just as modules would be exposed to in practice within the ITk environment, additional cooling mechanisms are required. Usually, modules under test are placed and held down atop of a vacuum jig, as shown in Figure 6.3.9, similar to those used for the sensor during their construction. While often it is enough for the jig itself, made from a thick block of metal, to dissipate the heat with the vacuum maintaining surface contact with the module, additional coolant lines can be pumped through the jig via a chiller so as to enhance its cooling ability. Using an anti-freezed water-glycol mixture as coolant, the chiller will regulate the temperature of the module around 10 °C throughout the DAQ testing. For the larger-scale nearing final production, a dedicated cold testing box with a capacity for up to approximately four modules in parallel is also under design and testing, also useful for performing the thermal cycling tests [67].

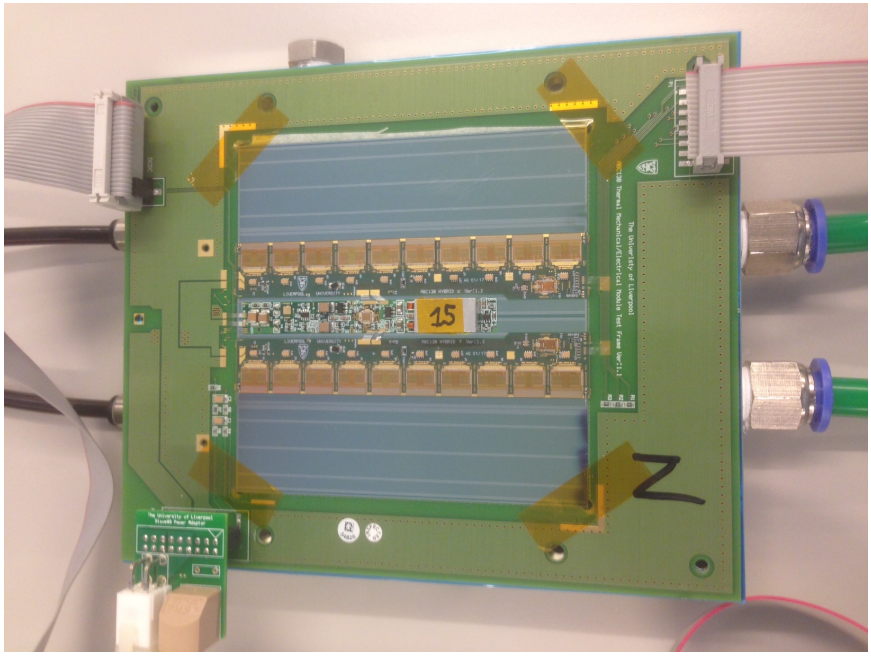

Figure 6.3.9: Photograph of an example module, wire bonded to a frame and mounted on top of a vacuum jig (with additional Kapton tape), where the vacuum connection lines can be seen on the left, and the chiller coolant lines can be seen on the right. The DAQ data ribbon cable can also be seen on the top-right, the LV power connector on the top-left, and the HV at the bottom-left.

6.3.2 Software setup

To obtain the readout from the DAQ system, custom software must be installed on the connected computer. Descendant of the current *SCTDAQ* software used for the SCT monitoring, as encountered during the ACR shifting discussed previously in Section 2.3.5, *ITSDAQ* is under development and testing for acquiring the data from ITk Strips [74]. ITSDAQ communicates with the DAQ system to run a series of tests, ultimately with the goal of measuring the input noise and gain of the DUT, and verifying those results for quality control in the natural expectation of possessing consistent low noise and high gain.

With reference to example results from an MS module, the full testing procedure carried out by ITSDAQ is as follows: the ABC and HCC IDs are first scanned to confirm that the DAQ system is able to communicate with them from the hybrids, and that they are assigned to the correct address. An example of this output confirming that this is the case is shown in Figure 6.3.10, where there should be ten ABCs and one HCC present per hybrid. The 256 channels on each ABC are also divided into two streams, denoted *Stream 0* and *Stream 1*, of 128 channels each, where the Stream 1 wire bonding pads are positioned in a row behind those of Stream 0 on the edge of the chip. This dual configuration of streams is more important for dividing the long and short strips of LS modules, and has little effect on SS modules [67].

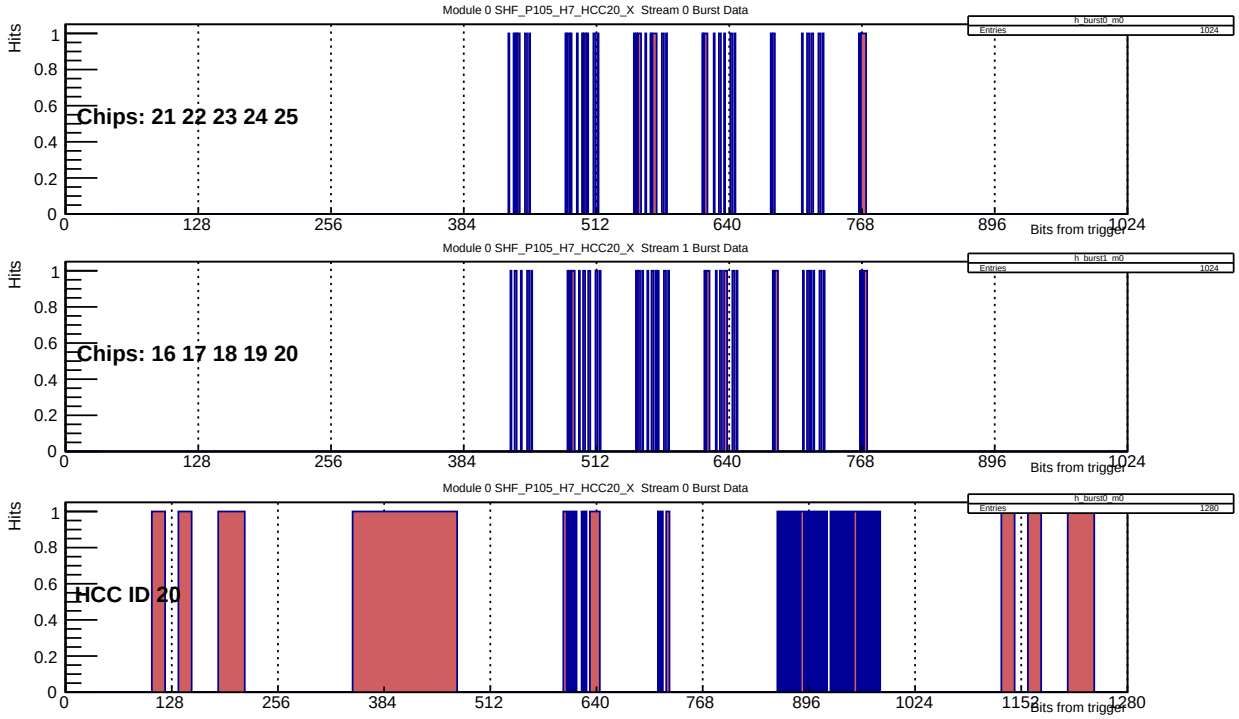

Figure 6.3.10: ITSDAQ results representing the ABC and HCC IDs from the X-type hybrid on an MS SS module labelled *SHF_MS04*, where the ABC IDs are shown for both streams. All expected addresses are correctly being received.

A *Strobe Delay* (SD) test is then performed to calibrate the readout timing delays registered for each ABC on the hybrid, which will have an effect on the subsequent tests. Figure 6.3.11 shows an example result of these SDs set to each ABC, with the goal of synchronising their individual readout timings. An expected delay should be set to approximately 20 µs, but does also depend on the temperature of the DUT.

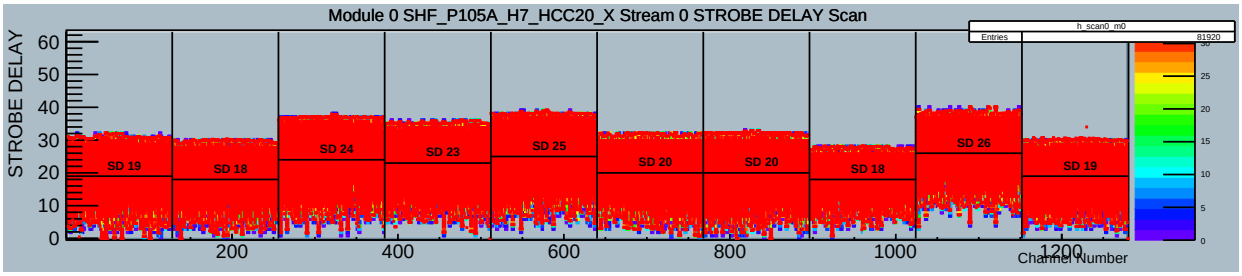

Figure 6.3.11: ITSDAQ results representing the Strobe Delay test from the X-type hybrid on an MS SS module labelled *SHF_MS04*, for ABC Stream 0. The registered timing delays for each ABC all appear to be reasonably near the expected 20 µs.

This is followed by a *Three-Point Gain* (3PG) test injecting three different charges, at 0.5, 1.0 and 1.5 fC, to perform a threshold scan with the voltage, using a linear fit on the results, and thus extracting the input noise and gain of the DUT. The results of this test are shown in Figure 6.3.12.

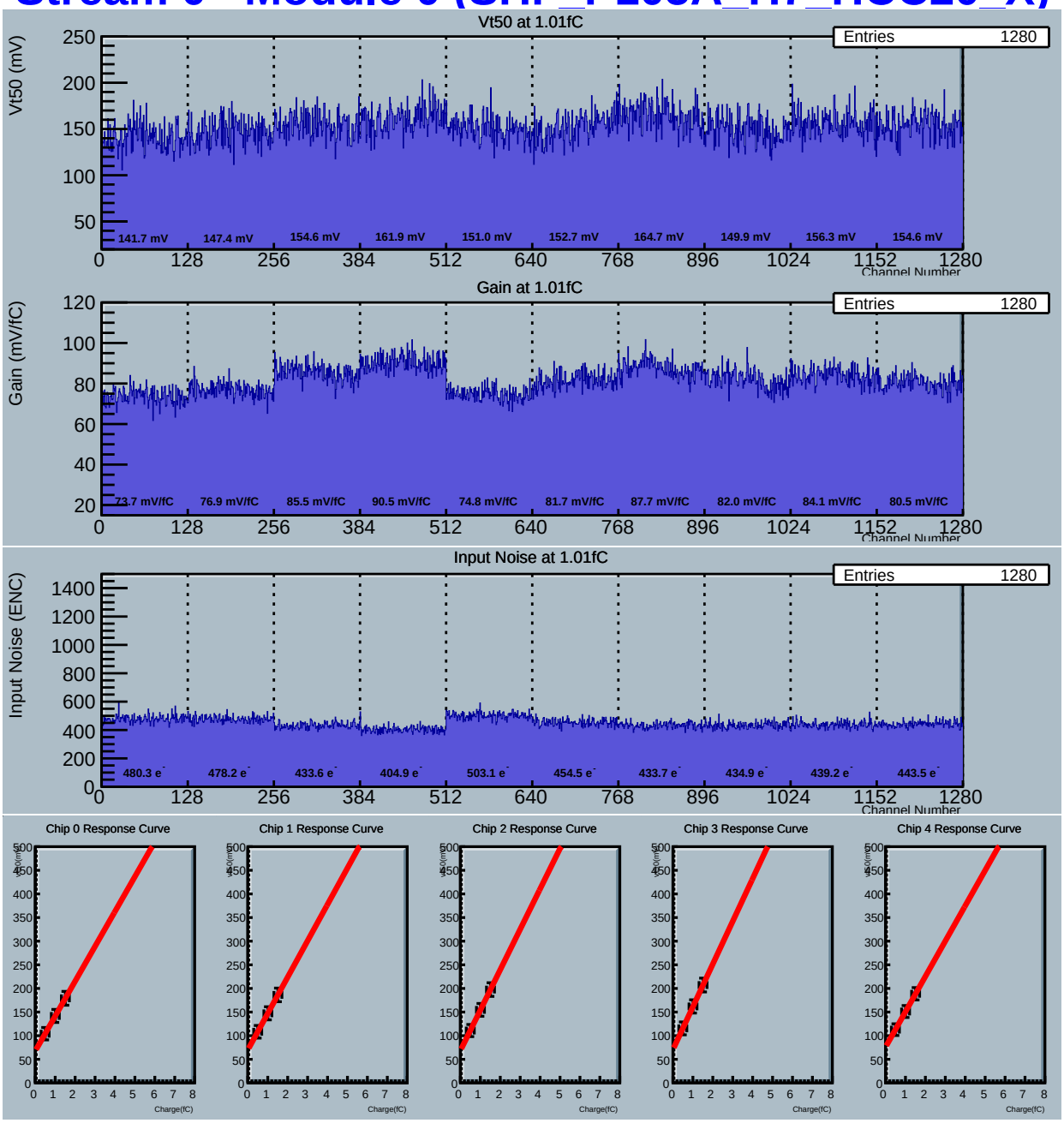

Figure 6.3.12: ITSDAQ results representing the Three-Point Gain test from the X-type hybrid on an MS SS module labelled *SHF_MS04*, for ABC Stream 0. The plots show the threshold voltage, the gain, the input noise and the 3-point response curve as linear fit, for each ABC.

Considering the results of this 3PG test, a *Trim Range* (TR) test is used to minimise variations which would be encountered in the response, by trimming each individual channel in the ABCs at different voltage thresholds. Any other anomalous channels are completely masked also, where it is usually reasonable if only one or two channels along the hybrid have been masked as a result. Figure 6.3.13 shows the results of the 3PG test again but with the trims and masks applied.

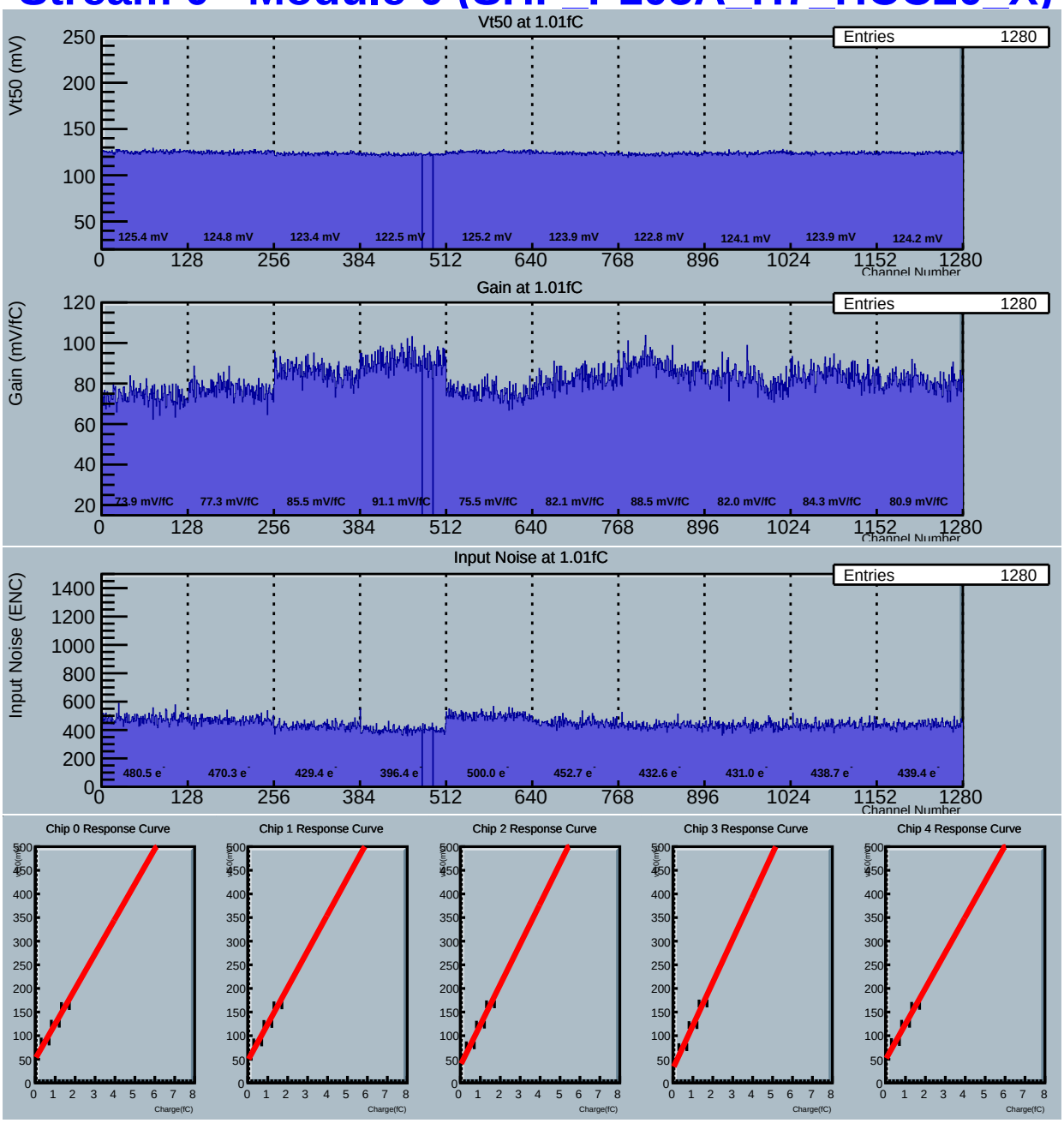

Figure 6.3.13: ITSDAQ results representing the Three-Point Gain test, with trims and masks applied, from the X-type hybrid on an MS SS module labelled *SHF_MS04*, for ABC Stream 0. The plots show the threshold voltage, the gain, the input noise and the 3-point response curve as linear fit, for each ABC. The threshold voltage and their uncertainties in the response fit are constrained by the trim, while 2 channels in the 4th ABC have been masked, which is fairly reasonable.

With all of these confirmations and calibrations in place, a *Response Curve* (RC) test is identical to the 3PG test, but instead injecting ten different charges, between 0.2 to 6.0 fC, and performing an exponential fit to the result. This test takes more time but produces a more accurate result for the input noise and gain. Figure 6.3.14 shows the results of the RC test, where the final input noise and gain information are taken from into review.

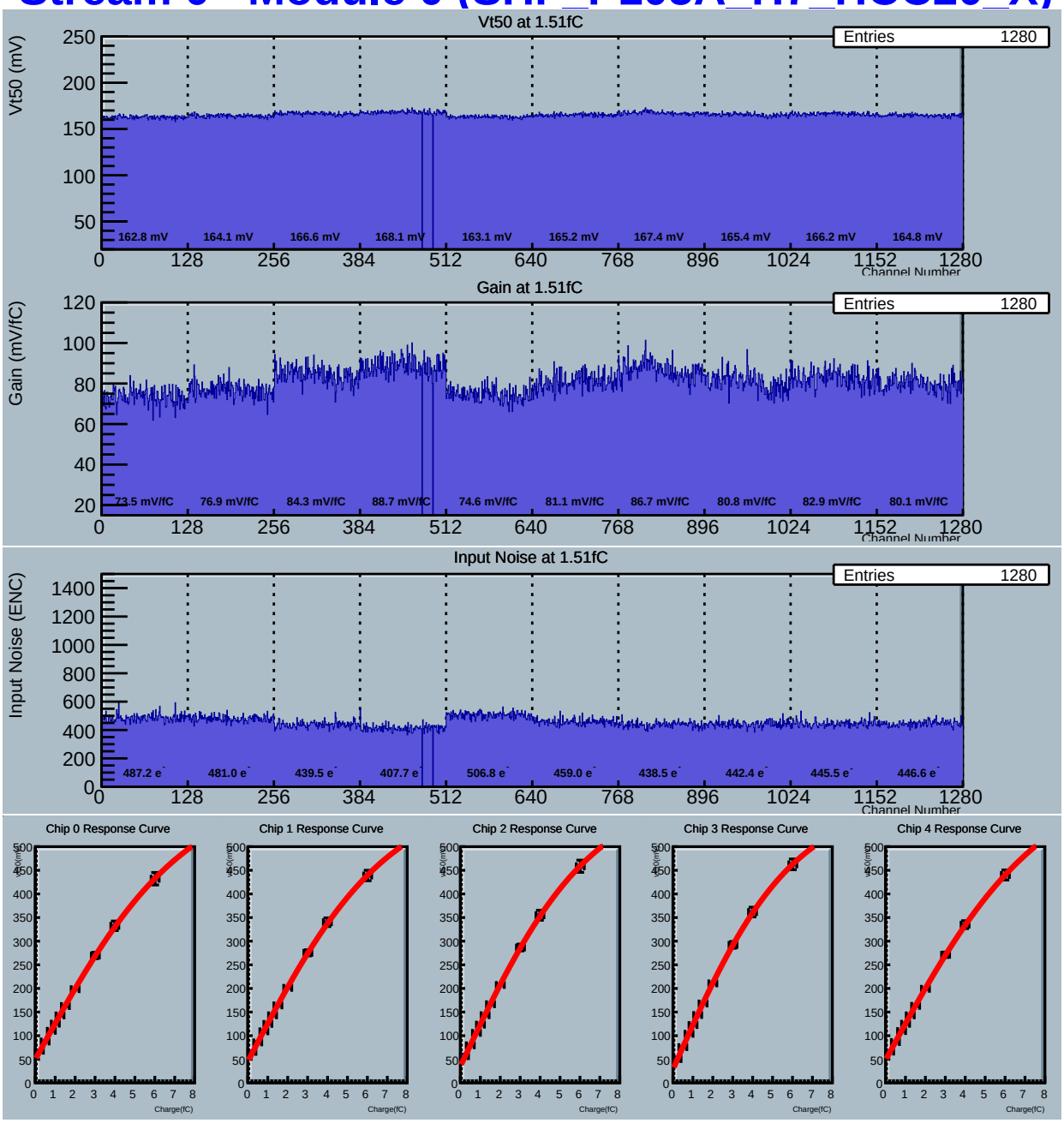

Figure 6.3.14: ITSDAQ results representing the Response Curve test from the X-type hybrid on an MS SS module labelled *SHF_MS04*, for ABC Stream 0. The plots show the threshold voltage, the gain, the input noise and the 10-point response curve as exponential fit, for each ABC. As desired, the final input noise is reasonably minimal and the gain is maximal, while both are mostly consistent between ABCs.

The final *Noise Occupancy* (NO) test injects no charges, and measures the noise as a function of the threshold scan. These results are shown in Figure 6.3.15.

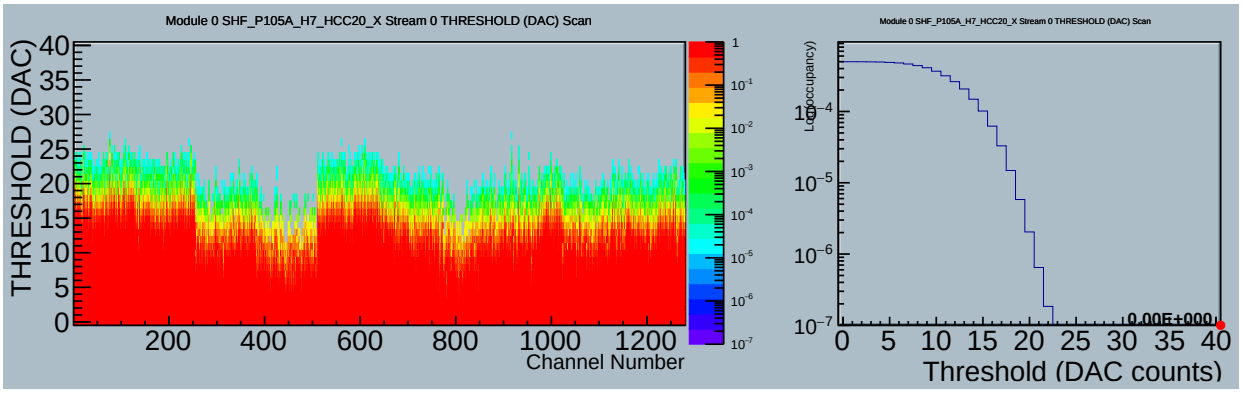

Figure 6.3.15: ITSDAQ results representing the Noise Occupancy test from the X-type hybrid on an MS SS module labelled *SHF_MS04*, for ABC Stream 0. The plots show the threshold scan across each channel of the ABCs, and the resulting occupancy as a function of the threshold.

6.3.3 Cataloguing and results database

As the project approaches the official production schedule, the formalised tracking of parts and constructed modules will become necessary. As a means to assist with this, an online shared database has been set up to catalogue all of these components, with information such as their type, where they are stored, what their status is and in which modules they have been assembled to, as well as the metrology and DAQ test results allocated to them. The author was briefly involved in registering a number of the prototype modules to this database as part of a trial scheme, as well as uploading their DAQ test results.

In order for the constructed modules to be uniquely identifiable in the database, they must adhere to some specific naming scheme. As would have been briefly seen in the DAQ results from the previous section, the example module that was under test was given the name `SHF_MS04`, where SHF denotes that the module was constructed at TUoS, and that it was the fourth MS module to be assembled. This module was of SS design, containing two hybrids, one of which mentioned was labelled `SHF_P105A_H7_HCC20_X`, where `P105A` denotes the panel the hybrid was sourced from, `H7` as the number of the hybrid on that panel, `HCC20` as the HCC ID address and it was of X-type handedness. However, this naming scheme is still very much under deliberation, but generally makes it clearer going forward how these components can start to be separated.

Navigating through the database, `SHF_MS04` can be found registered as a completed module with DAQ test results passing requirements, as automatically determined by the system against some reference. It can then be seen that the module is parent to two hybrids, one of which is `SHF_P105A_H7_HCC20_X`, as well as a power board and a sensor, and that this hybrid is parent to ten ABCs, one HCC and a PCB. All of these individual base components also have unique reference IDs, where there are plans for them to be scannable through a barcode-like system when transported between institutes.

6.4 Physics outlook

Returning to the BSM di-tau search analysis from Chapter 5, prospective studies have also been investigated for the ∼3000 fb^{-1} of data expected to be collected during Run-4 operations and beyond, utilising the ITk upgrades whilst operating at 14 TeV collision energy [10]. Figure 6.4.1 demonstrates a substantial extension in the exclusion limits on the hMSSM parameter space, as achieved by such an increase in luminosity of this order.

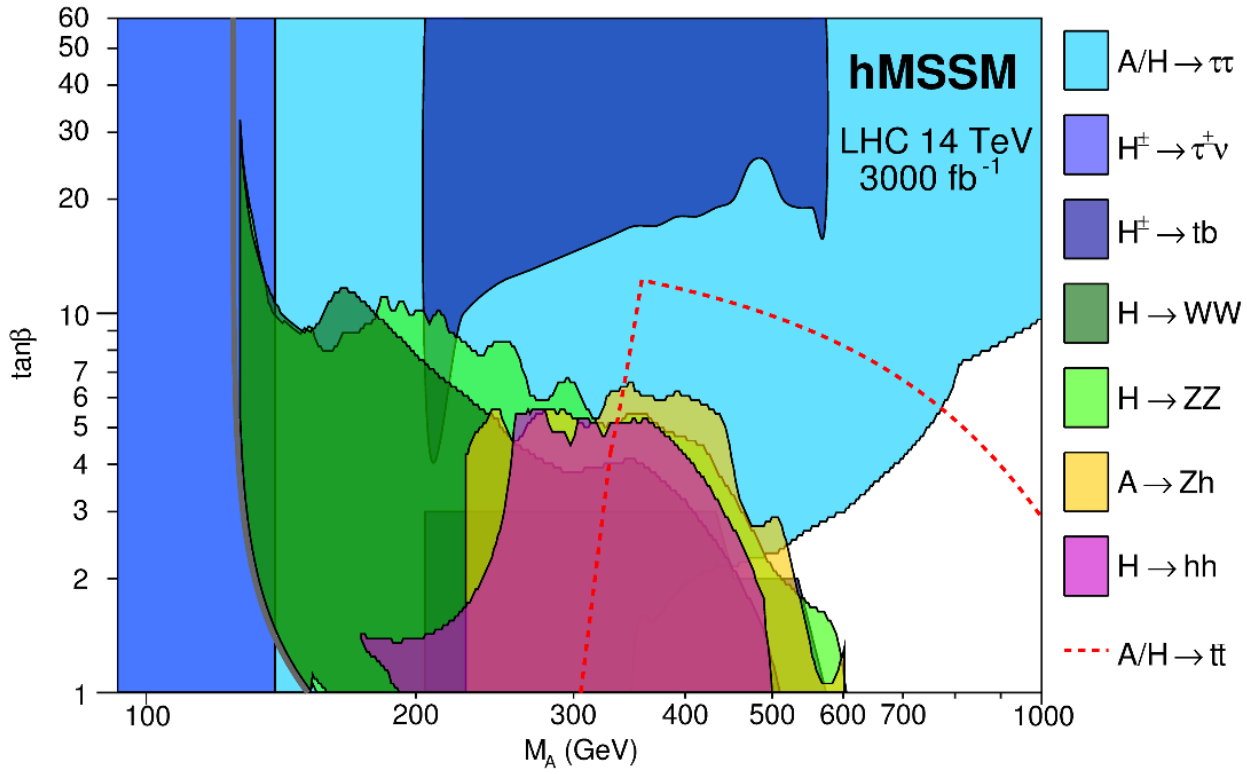

Figure 6.4.1: Projected exclusion upper limits with 95 % confidence level in the $m_A - \tan\beta$ parameter space of the hMSSM benchmark scenario, from a combination of various analyses including the BSM $H/A \to \tau\tau$ search, after collecting 3000 fb^{-1} of data throughout Run-4 operations and beyond [10].

However, if compared with the current exclusion limits at 139 fb^{-1} as presented in Figure 5.5.3, it should also be kept in mind that this prediction is based on results produced in the same generation as Athena Release 20, whilst the author's analysis is based on Release 21 and delivers a very comparable result, highlighting also the importance of software improvements in short timescales.

Chapter 7: Summary

From Chapter 2, the LHC and the ATLAS detector were introduced, operating through Run-2 during 2015 to 2018 and recording a total of $139\,\text{fb}^{-1}$ integrated luminosity of data at $\sqrt{s} = 13\,\text{TeV}$ p-p collisions. Chapter 1 introduced a number of new BSM physics scenarios, particularly those which build upon additional heavy neutral MSSM H/A Higgs bosons, namely the hMSSM, $m_h^{\text{mod+}}$ and variations of M_h^{125}, as well as heavy Z' boson interpretations benchmarked through the SSM and the SFM.

In Chapter 5, these BSM models were searched for in an analysis utilising this full Run-2 dataset, in the decay mode of the BSM resonances to a di-tau lepton final state, particularly for the $\tau_{\text{lep}}\tau_{\text{had}}$ channel. The backgrounds to this analysis were estimated through MC simulation as introduced in Chapter 3, with further calculations and corrections through the use of fake factors for estimating the quantity of misidentified events. Additional physics improvements were also incorporated through the use of the latest Athena Release 21 software for event reconstruction, also introduced in Chapter 3, including the improvements to tau lepton identification and electron rejection algorithms discussed in Chapter 4. Through the combination of these analysis methods, improved statistical uncertainties from the expanded Run-2 dataset and systematic uncertainties well-constrained through the developing background estimation techniques, the culminating result finds the data to be in agreement with the expected SM background, and therefore setting record exclusion limits over previous analyses. These limits are set to constrain each of the proposed BSM model benchmarks, as well the model independent scenarios for their ggH and bbH production mechanisms, between the masses of 0.2 to 2.5 TeV, and see an improvement by 4 to 5 times that of a previous analysis based on $36\,\text{fb}^{-1}$ of data.

In addition, Chapter 6 finalises with the outlook to the ATLAS Phase-2 Inner Tracker upgrade, introducing the prospective timeline for a replacement of the current Inner Detector in time for Run-4 operation starting around 2027. Until then, emphasis lies with the assembly and testing of prototype silicon components for barrel strip modules forming the outer part of this new Inner Tracker. The development programme has seen a number of versions of these components produced, as well as changes and improvements to the tooling used to construct them, but particularly with significant progress made in transitioning studies from thermo-mechanical to fully electrical silicon testing. The programme will continue with these electrical developments, establishing methods for quality control and preparing for the final production phase.

Bibliography

[1] M. Thomson, *Modern particle physics*, Cambridge University Press, 2013.

[2] A. Bettini, *Introduction to Elementary Particle Physics*, Cambridge University Press, 2008.

[3] MissMJ, Cush, *Standard Model of Elementary Particles*, 17 September 2019, https://commons.wikimedia.org/wiki/File:Standard_Model_of_Elementary_Particles.svg.

[4] ATLAS Collaboration, *Observation of a new particle in the search for the Standard Model Higgs boson with the ATLAS detector at the LHC*, Phys. Lett. B **716** (2012) 1, arXiv:1207.7214 [hep-ex].

[5] CMS Collaboration, *Observation of a new boson at a mass of 125 GeV with the CMS experiment at the LHC*, Phys. Lett. B **716** (2012) 30, arXiv:1207.7235 [hep-ex].

[6] S. P. Martin, *A Supersymmetry primer*, Adv. Ser. Direct. High Energy Phys. **18** (1998) 1, arXiv:hep-ph/9709356 [hep-ph].

[7] G. Bertone, *Particle Dark Matter: Observations, Models and Searches*, Cambridge University Press, 2010.

[8] S. Dimopoulos and D. W. Sutter, *The Supersymmetric flavor problem*, Nucl. Phys. **B452** (1995) 496, arXiv:hep-ph/9504415 [hep-ph].

[9] G. C. Branco et al., *Theory and phenomenology of two-Higgs-doublet models*, Phys. Rept. **516** (2012) 1, arXiv:1106.0034 [hep-ph].

[10] A. Djouadi et al., *Fully covering the MSSM Higgs sector at the LHC*, JHEP **06** (2015) 168, arXiv:1502.05653 [hep-ph].

[11] Julie Peasley, *The Particle Zoo*, 2 May 2017, https://www.particlezoo.net.

[12] M. Carena, S. Heinemeyer, O. Stål, C. Wagner, and G. Weiglein, *MSSM Higgs boson searches at the LHC: benchmark scenarios after the discovery of a Higgs-like particle*, Eur. Phys. J. C **73** (2013) 2552, arXiv:1302.7033 [hep-ph].

[13] E. Bagnaschi, H. Bahl, E. Fuchs, T. Hahn, S. Heinemeyer, S. Liebler, S. Patel, P. Slavich, T. Stefaniak, C. E. M. Wagner, and et al., *MSSM Higgs boson searches at the LHC: benchmark scenarios for Run 2 and beyond*, The European Physical Journal C **79** (2019) 617, http://dx.doi.org/10.1140/epjc/s10052-019-7114-8.

[14] LHC Higgs Cross Section Working Group, *Handbook of LHC Higgs Cross Sections: 4. Deciphering the Nature of the Higgs Sector*, arXiv:1610.07922 [hep-ph].

[15] ATLAS Collaboration, *Search for additional heavy neutral Higgs and gauge bosons in the ditau final state produced in* 36 fb^{-1} *of pp collisions at* $\sqrt{s} = 13$ *TeV with the ATLAS detector*, Journal of High Energy Physics **2018** (2018) 055, http://dx.doi.org/10.1007/JHEP01(2018)055.

[16] D. Atwood, S. Bar-Shalom, and A. Soni, *Neutrino masses, mixing and leptogenesis in a two Higgs doublet model "for the third generation"*, Physics Letters B **635** (2006) 112–117, http://dx.doi.org/10.1016/j.physletb.2006.02.033.

[17] M. Cvetic and S. Godfrey, *Discovery and identification of extra gauge bosons*, Adv. Ser. Direct. High Energy Phys. **16** (1995) 383, arXiv:hep-ph/9504216.

[18] A. Leike, *The Phenomenology of extra neutral gauge bosons*, Phys. Rept. **317** (1999) 143, arXiv:hep-ph/9805494.

[19] K. Hsieh, K. Schmitz, J.-H. Yu, and C.-P. Yuan, *Global Analysis of General SU(2) x SU(2) x U(1) Models with Precision Data*, Phys. Rev. D **82** (2010) 035011, arXiv:1003.3482 [hep-ph].

[20] D. J. Muller and S. Nandi, *Top flavor: A Separate SU(2) for the third family*, Phys. Lett. B **383** (1996) 345–350, arXiv:hep-ph/9602390.

[21] E. Malkawi, T. Tait, and C.-P. Yuan, *A model of strong flavor dynamics for the top quark*, Phys. Lett. B **385** (1996) 304, arXiv:hep-ph/9603349.

[22] L. Evans and P. Bryant, *LHC Machine*, JINST **3** (2008) S08001.

[23] J. Haffner, *The CERN accelerator complex*, OPEN-PHO-ACCEL-2013-056, http://cds.cern.ch/record/1621894.

[24] ATLAS Collaboration, *The ATLAS Experiment at the CERN Large Hadron Collider*, JINST **3** (2008) S08003.

[25] CMS Collaboration, *The CMS experiment at the CERN LHC*, JINST **3** (2008) S08004.

[26] LHCb Collaboration, *The LHCb Detector at the LHC*, JINST **3** (2008) S08005.

[27] ALICE Collaboration, *The ALICE experiment at the CERN LHC*, JINST **3** (2008) S08002.

[28] ATLAS Collaboration, *LuminosityPublicResultsRun2*, https://twiki.cern.ch/twiki/bin/view/AtlasPublic/LuminosityPublicResultsRun2.

[29] G. Duckeck, D. Barberis, R. Hawkings, R. Jones, N. McCubbin, et al., *ATLAS Computing: technical design report*, ATLAS-TDR-17, http://cds.cern.ch/record/837738.

[30] L. R. F. Castillo, *The Search and Discovery of the Higgs Boson*, Morgan & Claypool Publishers, 2015.

[31] JabberWok, *A graphic showing the relationship between angle and pseudorapidity*, 16 May 2007, https://commons.wikimedia.org/wiki/File:Pseudorapidity2.png.

[32] K. Potamianos, *The upgraded Pixel detector and the commissioning of the Inner Detector tracking of the ATLAS experiment for Run-2 at the Large Hadron Collider*, in *Proceedings, 2015 European Physical Society Conference on High Energy Physics (EPS-HEP 2015): Vienna, Austria, July 22-29, 2015*. 2015. arXiv:1608.07850 [physics.ins-det].

[33] ATLAS Collaboration, *ATLAS Insertable B-Layer Technical Design Report*, ATLAS-TDR-19, 2010, https://cds.cern.ch/record/1291633.

[34] ATLAS Collaboration, *Performance of the ATLAS Trigger System in 2015*, Eur. Phys. J. C **77** (2017) 317, arXiv:1611.09661 [hep-ex].

[35] A. B. Poy, H. Boterenbrood, H. J. Burckhart, J. Cook, V. Filimonov, S. Franz, O. Gutzwiller, B. Hallgren, V. Khomutnikov, S. Schlenker, and F. Varela, *The detector control system of the ATLAS experiment*, Journal of Instrumentation **3** (2008) P05006–P05006, http://dx.doi.org/10.1088/1748-0221/3/05/p05006.

[36] O. Gutzwiller, H. Burckhart, S. Franz, S. Schlenker, S. Filiminov, V. Khomutnikov, L. Sargsyan, and Y. Armenia, *Status of the ATLAS Detector and Common Infrastructure Control System*, in *Proceedings of the Japan Academy*, vol. TUP103. August, 2010.

[37] J. Catmore, J. Cranshaw, T. Gillam, E. Gramstad, P. Laycock, et al., *A new petabyte-scale data derivation framework for ATLAS*, J. Phys.: Conf. Ser. **664** (2015) 072007.

[38] ATLAS Collaboration, *The ATLAS Simulation Infrastructure*, Eur. Phys. J. C **70** (2010) 823, arXiv:1005.4568 [hep-ex].

[39] A. Buckley, T. Eifert, M. Elsing, D. Gillberg, K. Koeneke, A. Krasznahorkay, E. Moyse, M. Nowak, S. Snyder, and P. van Gemmeren, *Implementation of the ATLAS Run 2 event data model*, Journal of Physics: Conference Series **664** (2015) 072045, https://doi.org/10.1088%2F1742-6596%2F664%2F7%2F072045.

[40] ATLAS Collaboration, *xTauFramework (CERN Internal)*, https://gitlab.cern.ch/ATauLeptonAnalysiS/xTauFramework.

[41] C. Eck, J. Knobloch, L. Robertson, I. Bird, K. Bos, et al., *LHC computing Grid: Technical Design Report*, CERN-LHCC-2005-024, https://cds.cern.ch/record/840543.

[42] ATLAS Collaboration, *ATLAS Computing Acknowledgements 2016–2017*, ATL-GEN-PUB-2016-002, https://cds.cern.ch/record/2202407.

[43] CERN, *Worldwide LHC Computing Grid*, https://wlcg.web.cern.ch.

[44] Edgewall Software, *Trac Subversion*, https://trac.edgewall.org/wiki/TracSubversion.

[45] GitLab Inc., *GitLab*, https://about.gitlab.com.

[46] Docker, Inc., *Docker*, https://www.docker.com.

[47] LLVM Developer Group, *ClangFormat*, https://clang.llvm.org/docs/ClangFormat.html.

[48] Google Inc., *YAPF*, https://github.com/google/yapf.

[49] Dimitri van Heesch, *Doxygen*, https://www.doxygen.nl.

[50] ATLAS Collaboration, *RootCore*, https://twiki.cern.ch/twiki/bin/view/AtlasComputing/RootCore.

[51] Kitware, Inc. and Contributors, *CMake*, https://cmake.org.

[52] M. Tanabashi et al. (Particle Data Group), *Review of Particle Physics*, Phys. Rev. D **98** (2018) 030001.

[53] ATLAS Collaboration, *Measurement of the tau lepton reconstruction and identification performance in the ATLAS experiment using pp collisions at* $\sqrt{s} = 13$ *TeV*, ATLAS-CONF-2017-029, 2017, https://cds.cern.ch/record/2261772.

[54] Y. Sakurai, *The ATLAS Tau Trigger Performance during LHC Run 1 and Prospects for Run 2*, in *Proceedings, 2nd Conference on Large Hadron Collider Physics Conference (LHCP 2014): New York, USA, June 2-7, 2014*. 2014. arXiv:1409.2699 [hep-ex].

[55] M. Cacciari, G. P. Salam, and G. Soyez, *The anti-k_t jet clustering algorithm*, JHEP **04** (2008) 063, arXiv:0802.1189 [hep-ph].

[56] ATLAS Collaboration, *Reconstruction, Energy Calibration, and Identification of Hadronically Decaying Tau Leptons in the ATLAS Experiment for Run-2 of the LHC*, ATL-PHYS-PUB-2015-045, 2015, https://cds.cern.ch/record/2064383.

[57] T. Fawcett, *An introduction to ROC analysis*, Pattern Recognition Letters **27** (2006) 861 – 874.

[58] L. Breiman, J. Friedman, R. Olshen, and C. Stone, *Classification and Regression Trees*, Chapman & Hall, 1984.

[59] Y. Freund and R. E. Schapire, *A Decision-Theoretic Generalization of On-Line Learning and an Application to Boosting*, J. Comput. Syst. Sci. **55** (1997) 119.

[60] ATLAS Collaboration, *Run 2 Tau Performance (The Taucronomicon)*, to be submitted for publication, expected late 2020.

[61] A. Hocker et al., *TMVA - Toolkit for Multivariate Data Analysis*, arXiv:physics/0703039.

[62] ATLAS Collaboration, *Search for Minimal Supersymmetric Standard Model Higgs bosons H/A and for a Z' boson in the $\tau\tau$ final state produced in pp collisions at $\sqrt{s} = 13$ TeV with the ATLAS Detector*, Eur. Phys. J. C **76** (2016) 585, arXiv:1608.00890 [hep-ex].

[63] ATLAS Collaboration, *Search for Heavy Higgs Bosons Decaying into Two Tau Leptons with the ATLAS Detector Using pp Collisions at $\sqrt{s} = 13$ TeV*, Phys. Rev. Lett. **125** (2020) 051801, https://link.aps.org/doi/10.1103/PhysRevLett.125.051801.

[64] ATLAS Collaboration, *ATLAS b-jet identification performance and efficiency measurement with $t\bar{t}$ events in pp collisions at $\sqrt{s} = 13$ TeV*, Eur. Phys. J. C **79** (2019) 970, arXiv:1907.05120 [hep-ex].

[65] M. Norlin, *Mass reconstruction techniques in di-Higgs events with τ-leptons and b-quarks in the ATLAS experiment at the LHC*, Dissertation, 2016, http://urn.kb.se/resolve?urn=urn:nbn:se:uu:diva-310314.

[66] CMS Collaboration, *Search for additional neutral MSSM Higgs bosons in the $\tau\tau$ final state in proton-proton collisions at $\sqrt{s} = 13$ TeV*, JHEP **09** (2018) 007, arXiv:1803.06553 [hep-ex].

[67] ATLAS Collaboration, *Technical Design Report for the ATLAS Inner Tracker Strip Detector*, ATLAS-TDR-025, 2017, https://cds.cern.ch/record/2257755.

[68] CERN, *HL-LHC Project Schedule*, https://project-hl-lhc-industry.web.cern.ch/content/project-schedule.

[69] ATLAS Collaboration, *Technical Design Report for the ATLAS Inner Tracker Pixel Detector*, ATLAS-TDR-030, 2018, https://cds.cern.ch/record/2285585.

[70] CERN, *The High-Luminosity LHC Project. 298th Meeting of Scientific Policy Committee*, CERN/SPC/1068. CERN/FC/6014. CERN/3255, Jun, 2016, https://cds.cern.ch/record/2199189.

[71] ATLAS Collaboration, *ITK-2020-002, Updates in the ITk Pixel Layout following the smaller radius decision*, https://atlas.web.cern.ch/Atlas/GROUPS/PHYSICS/PLOTS/ITK-2020-002.

[72] Digilent Inc., *Atlys overview*, December 2017, https://reference.digilentinc.com/atlys/atlys/refmanual.

[73] Digilent Inc., *Nexys Video overview*, December 2017, https://reference.digilentinc.com/reference/programmable-logic/nexys-video/start.

[74] Carlos Garcia Argos, *ATLAS ITk Strips DAQ System With 130 Chipset: User and Troubleshooting Guide*, CERN Internal, July, 2018.

Appendix A: Tau Combined Performance

A.1 Electron rejection

A.1.1 Algorithm training

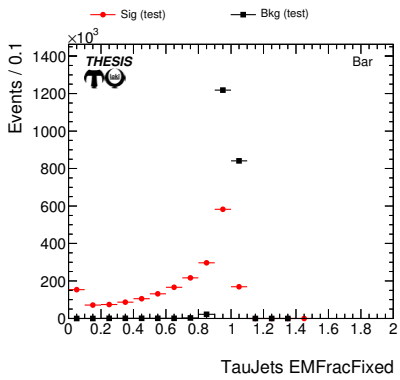

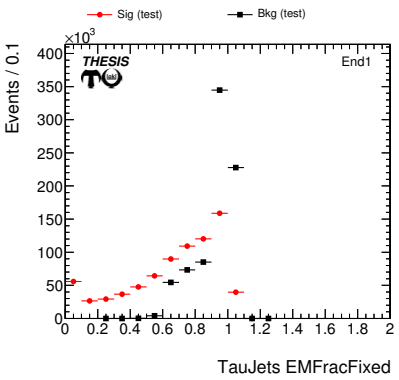

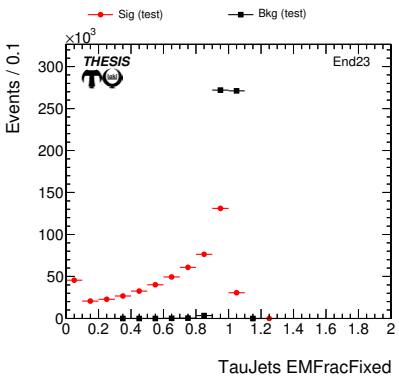

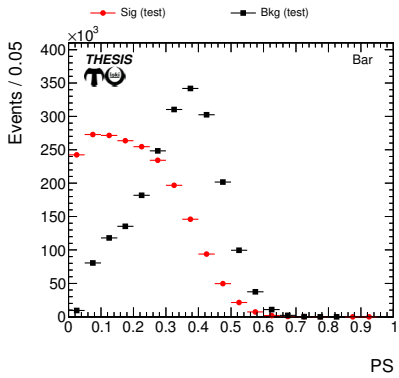

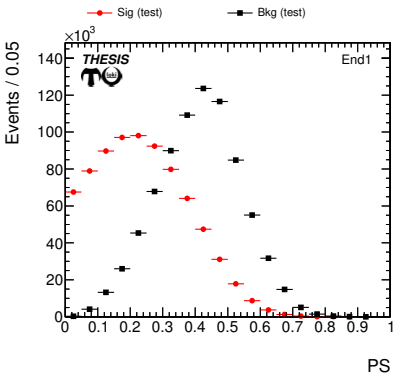

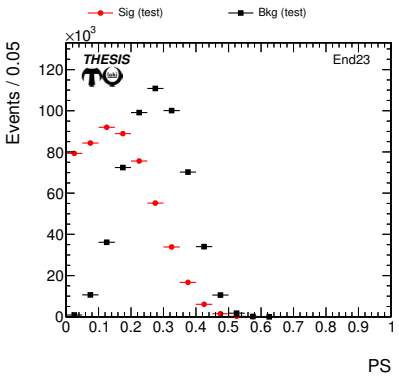

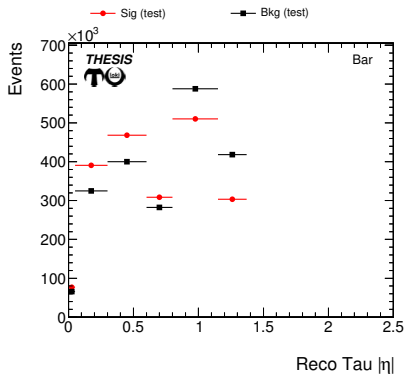

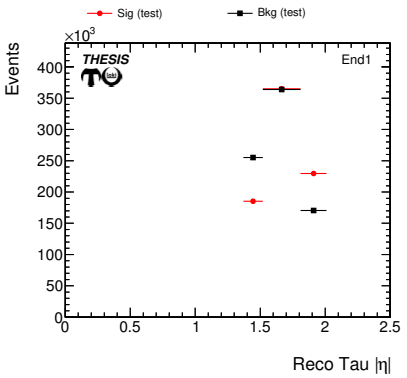

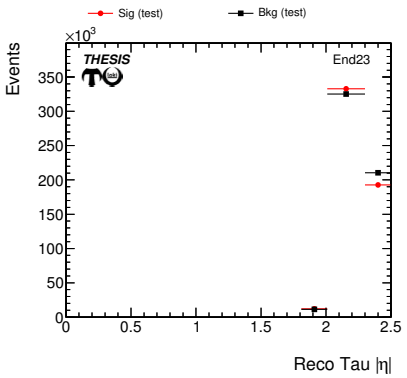

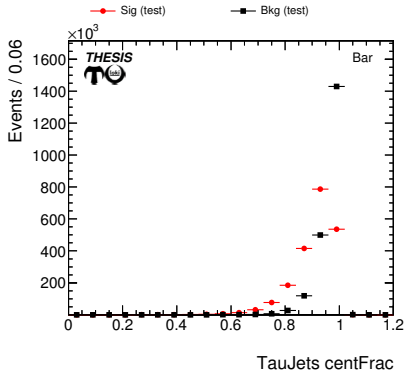
Sig (test)
Bkg (test)
THESIS
Bar
Events / 0.06
TauJets centFrac

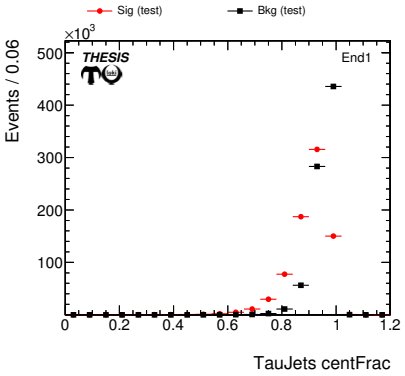
Sig (test)
Bkg (test)
THESIS
End1
Events / 0.06
TauJets centFrac

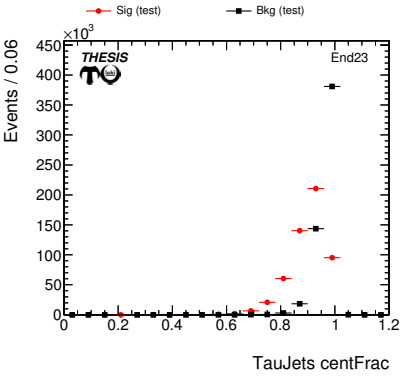
Sig (test)
Bkg (test)
THESIS
End23
Events / 0.06
TauJets centFrac

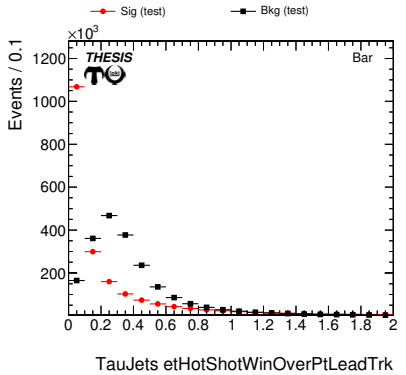
Sig (test)
Bkg (test)
THESIS
Bar
Events / 0.1
TauJets etHotShotWinOverPtLeadTrk

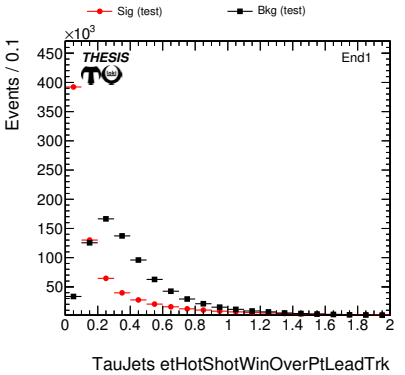
Sig (test)
Bkg (test)
THESIS
End1
Events / 0.1
TauJets etHotShotWinOverPtLeadTrk

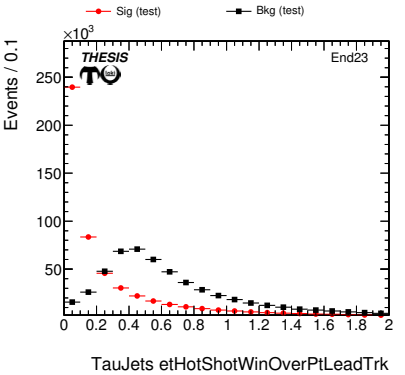
Sig (test)
Bkg (test)
THESIS
End23
Events / 0.1
TauJets etHotShotWinOverPtLeadTrk

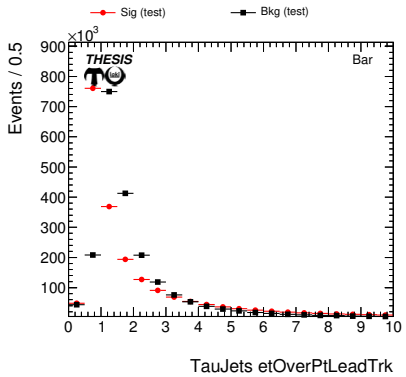
Sig (test)
Bkg (test)
THESIS
Bar
Events / 0.5
TauJets etOverPtLeadTrk

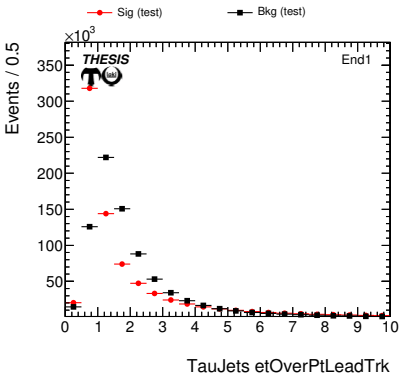
Sig (test)
Bkg (test)
THESIS
End1
Events / 0.5
TauJets etOverPtLeadTrk

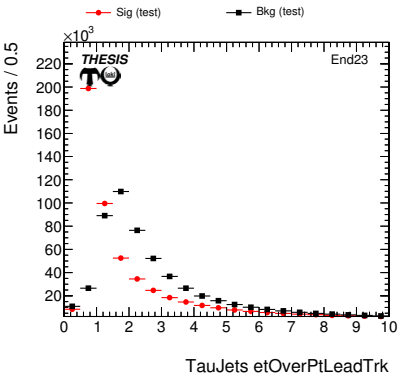
Sig (test)
Bkg (test)
THESIS
End23
Events / 0.5
TauJets etOverPtLeadTrk

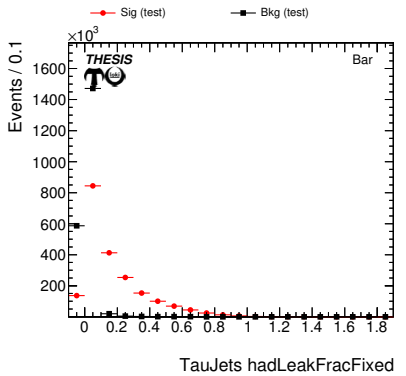
Sig (test)
Bkg (test)
THESIS
Bar
Events / 0.1
TauJets hadLeakFracFixed

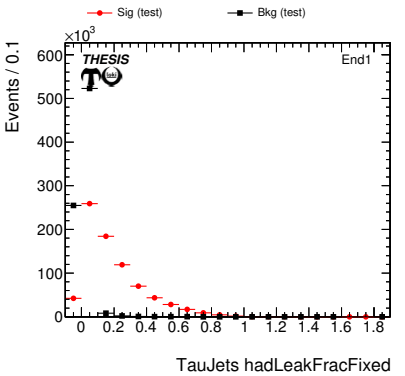
Sig (test)
Bkg (test)
THESIS
End1
Events / 0.1
TauJets hadLeakFracFixed

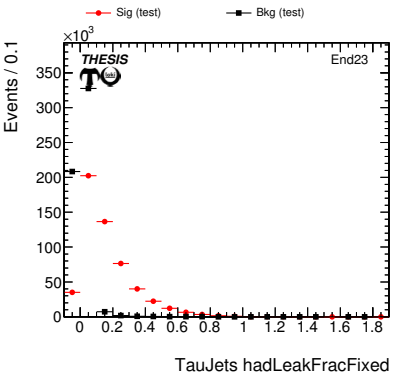
Sig (test)
Bkg (test)
THESIS
End23
Events / 0.1
TauJets hadLeakFracFixed

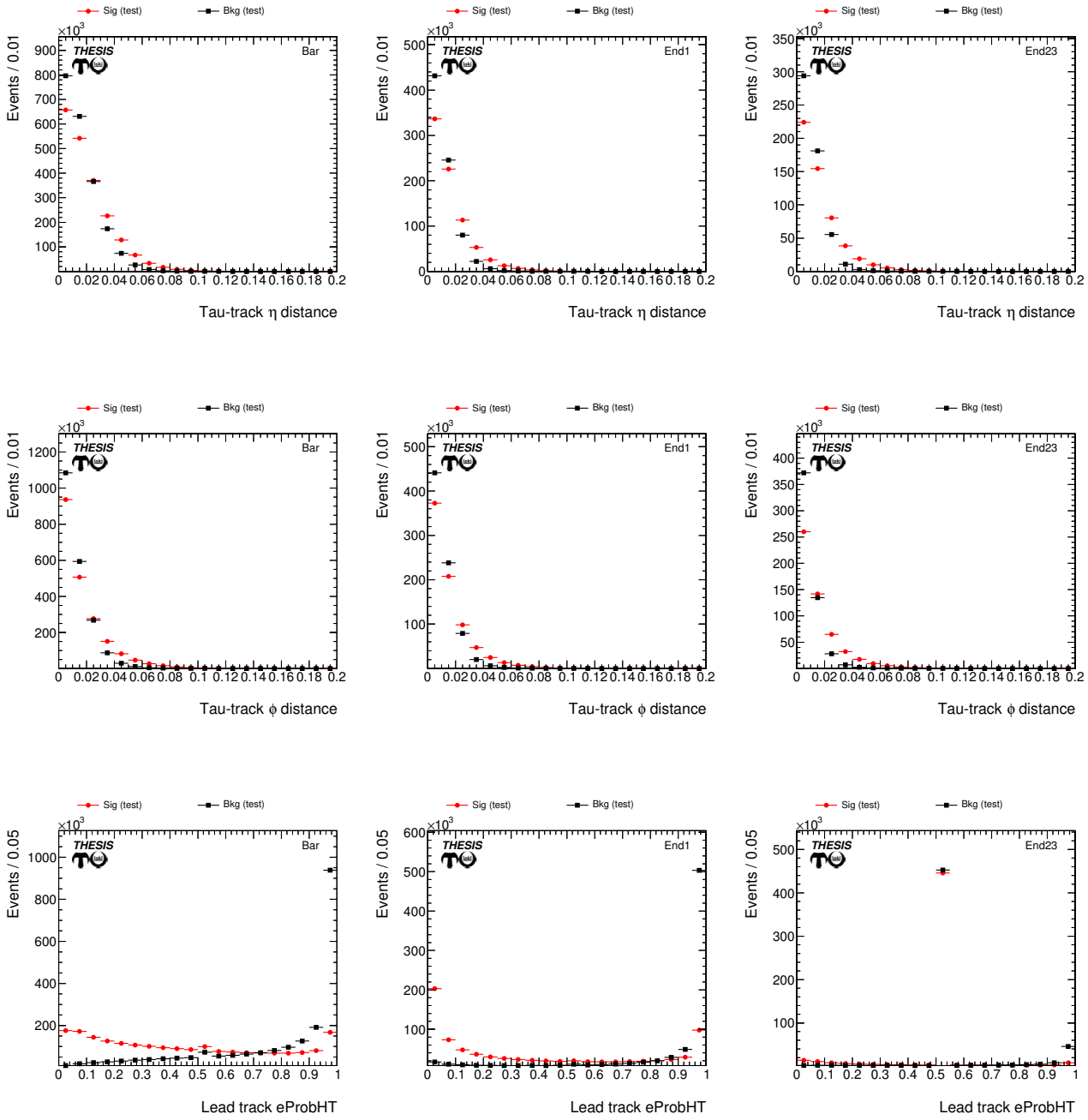

Figure A.1.1: Performance plots of the new eBDT trained by LOKI, across each region of η from left to right. The plots show the distributions of ten variables (from top to bottom) used in training the new eBDT algorithm in separating the tau signal (sig) and electron background (bkg) for the testing dataset.

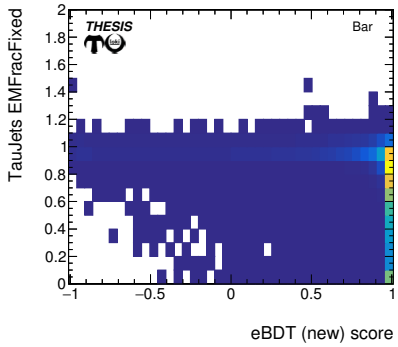
THESIS
Bar
TauJets EMFracFixed
eBDT (new) score

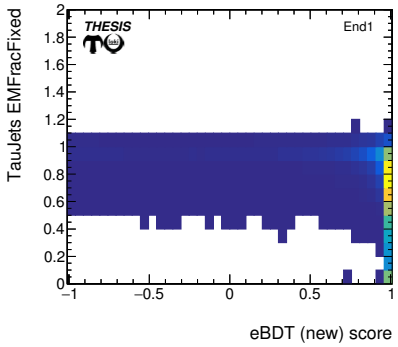
THESIS
End1
TauJets EMFracFixed
eBDT (new) score

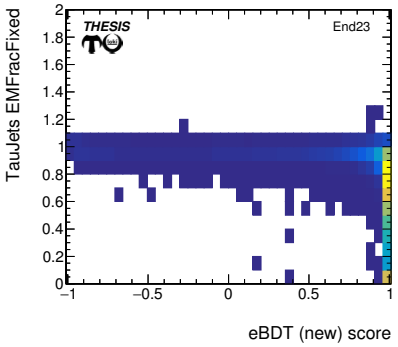
THESIS
End23
TauJets EMFracFixed
eBDT (new) score

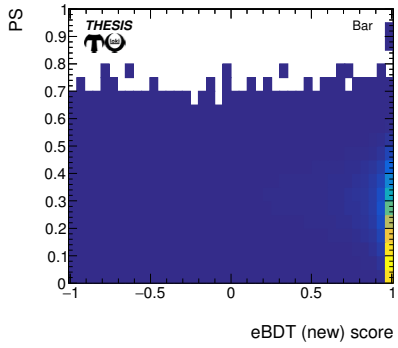
THESIS
Bar
PS
eBDT (new) score

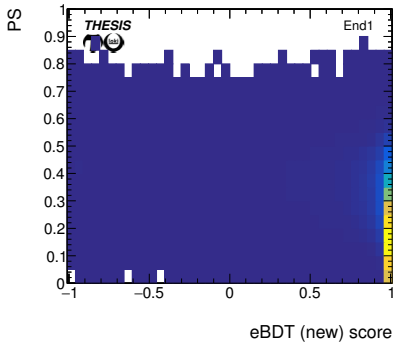
THESIS
End1
PS
eBDT (new) score

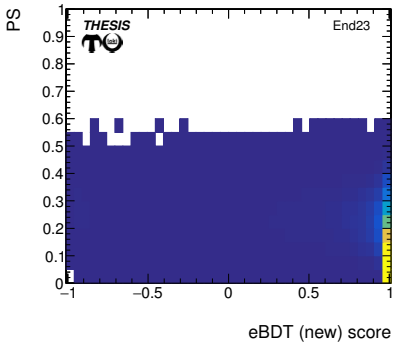
THESIS
End23
PS
eBDT (new) score

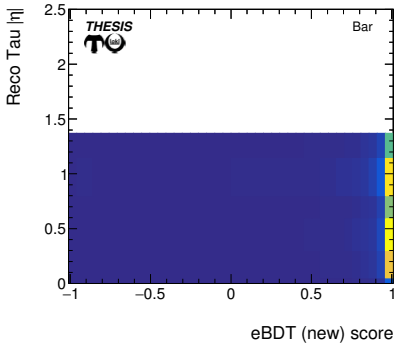
THESIS
Bar
Reco Tau |η|
eBDT (new) score

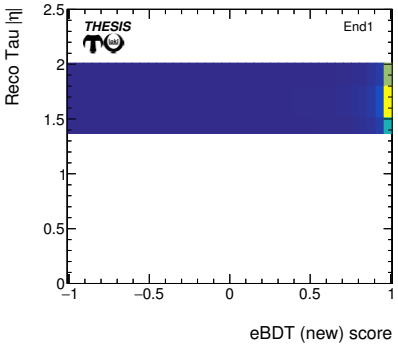
THESIS
End1
Reco Tau |η|
eBDT (new) score

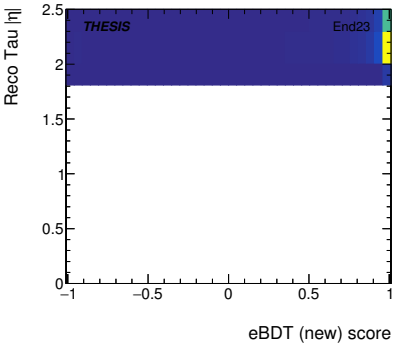
THESIS
End23
Reco Tau |η|
eBDT (new) score

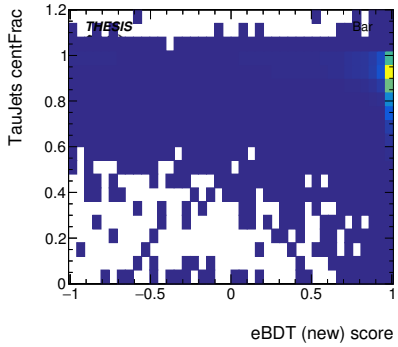
THESIS
Bar
TauJets centFrac
eBDT (new) score

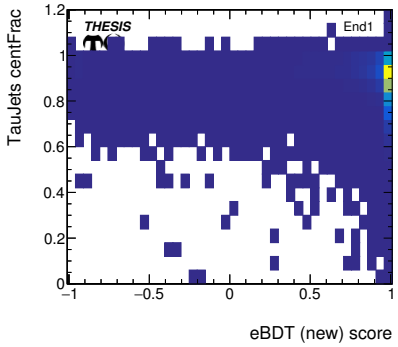
THESIS
End1
TauJets centFrac
eBDT (new) score

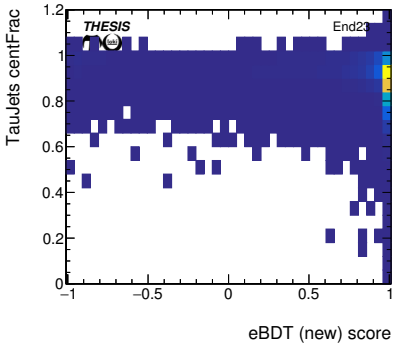
THESIS
End23
TauJets centFrac
eBDT (new) score

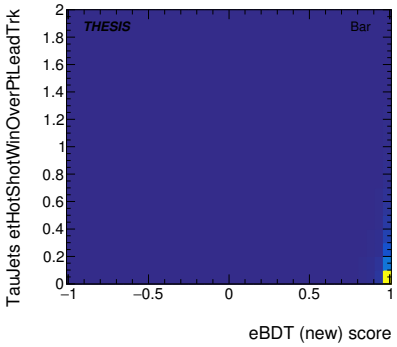
THESIS
Bar
TauJets etHotShotWinOverPtLeadTrk
eBDT (new) score

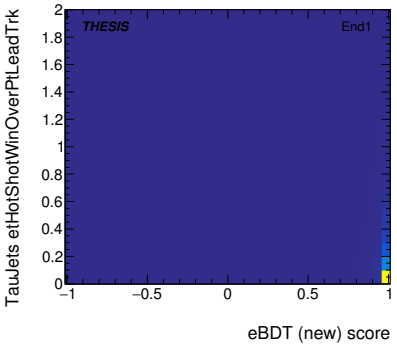
THESIS
End1
TauJets etHotShotWinOverPtLeadTrk
eBDT (new) score

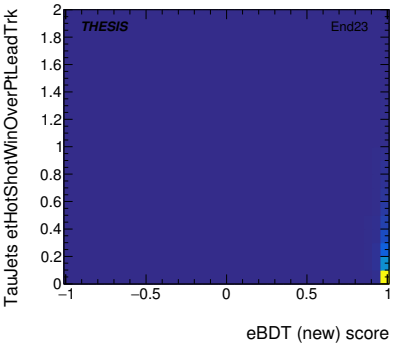
THESIS
End23
TauJets etHotShotWinOverPtLeadTrk
eBDT (new) score

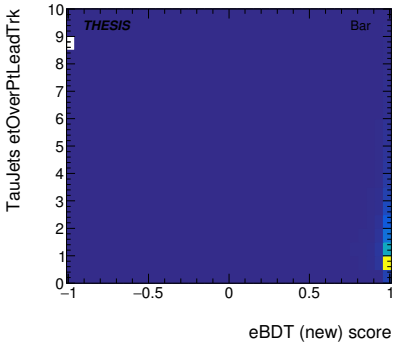
THESIS
Bar
TauJets etOverPtLeadTrk
eBDT (new) score

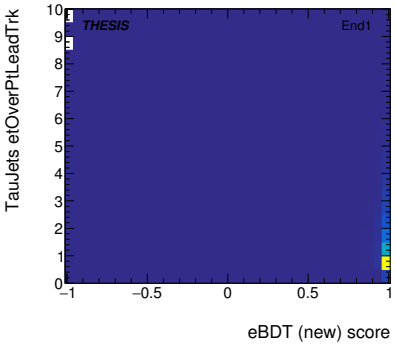
THESIS
End1
TauJets etOverPtLeadTrk
eBDT (new) score

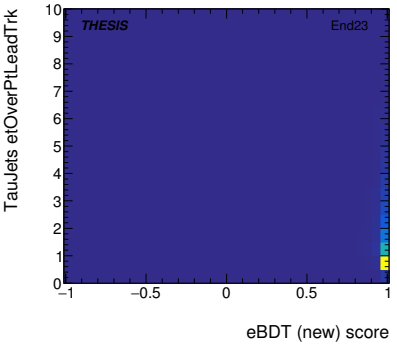
THESIS
End23
TauJets etOverPtLeadTrk
eBDT (new) score

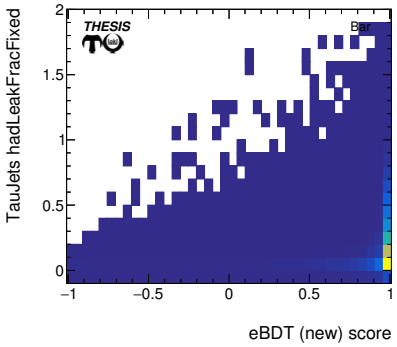
THESIS
Bar
TauJets hadLeakFracFixed
eBDT (new) score

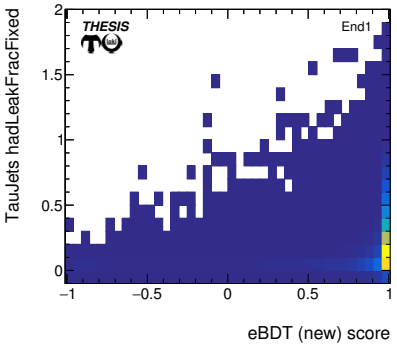
THESIS
End1
TauJets hadLeakFracFixed
eBDT (new) score

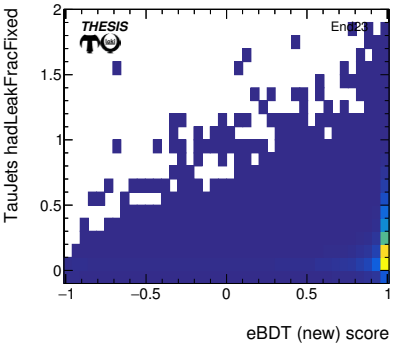
THESIS
End23
TauJets hadLeakFracFixed
eBDT (new) score

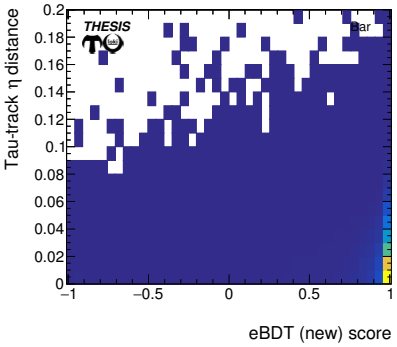
THESIS
Bar
Tau-track η distance
eBDT (new) score

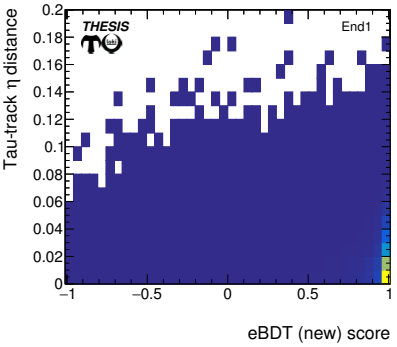
THESIS
End1
Tau-track η distance
eBDT (new) score

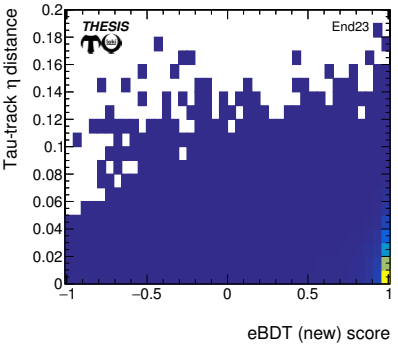
THESIS
End23
Tau-track η distance
eBDT (new) score

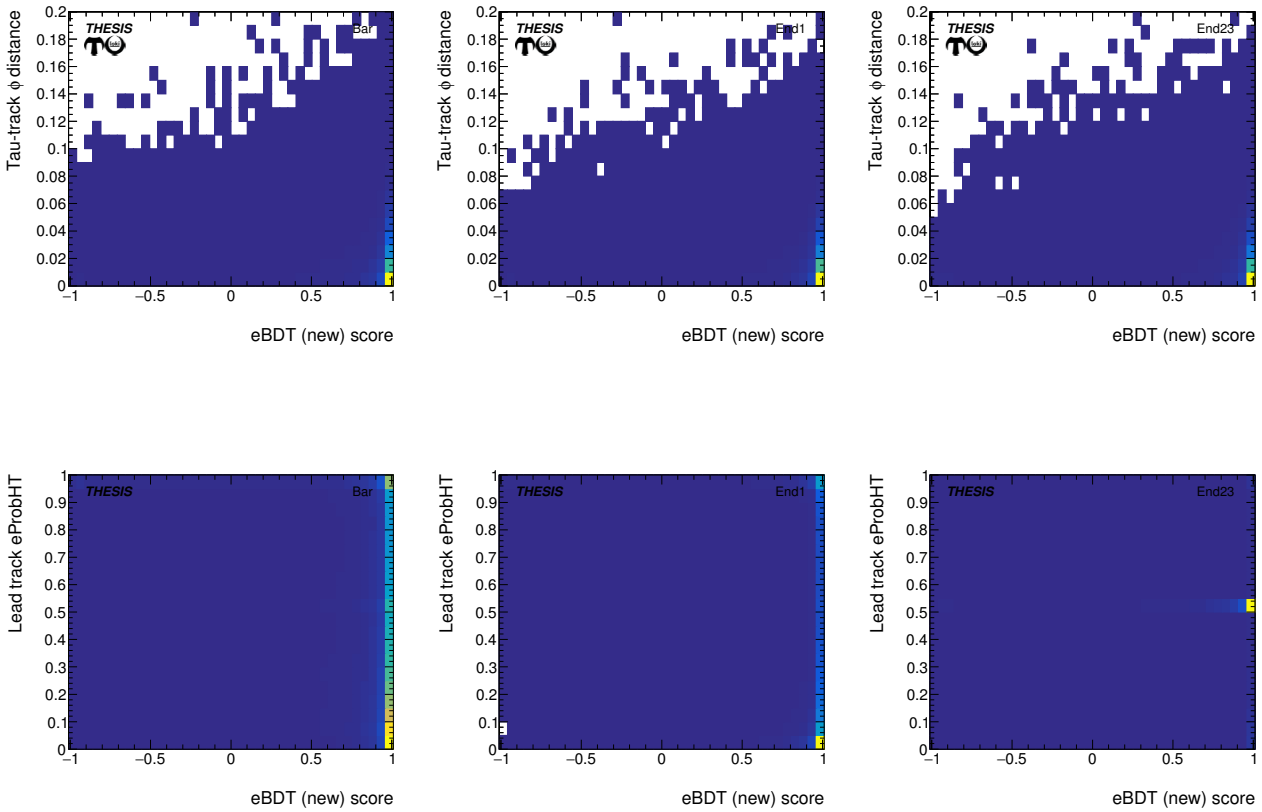

Figure A.1.2: Performance plots of the new eBDT trained by LOKI, across each region of η from left to right. The plots show the correlations between ten variables (from top to bottom) used in training the new eBDT algorithm and its score in separating the tau signal and electron background. The correlation strength is colour-coded, from its weakest (blue) to its strongest (yellow).

A.1.2 Scale factor measurements

Background estimation

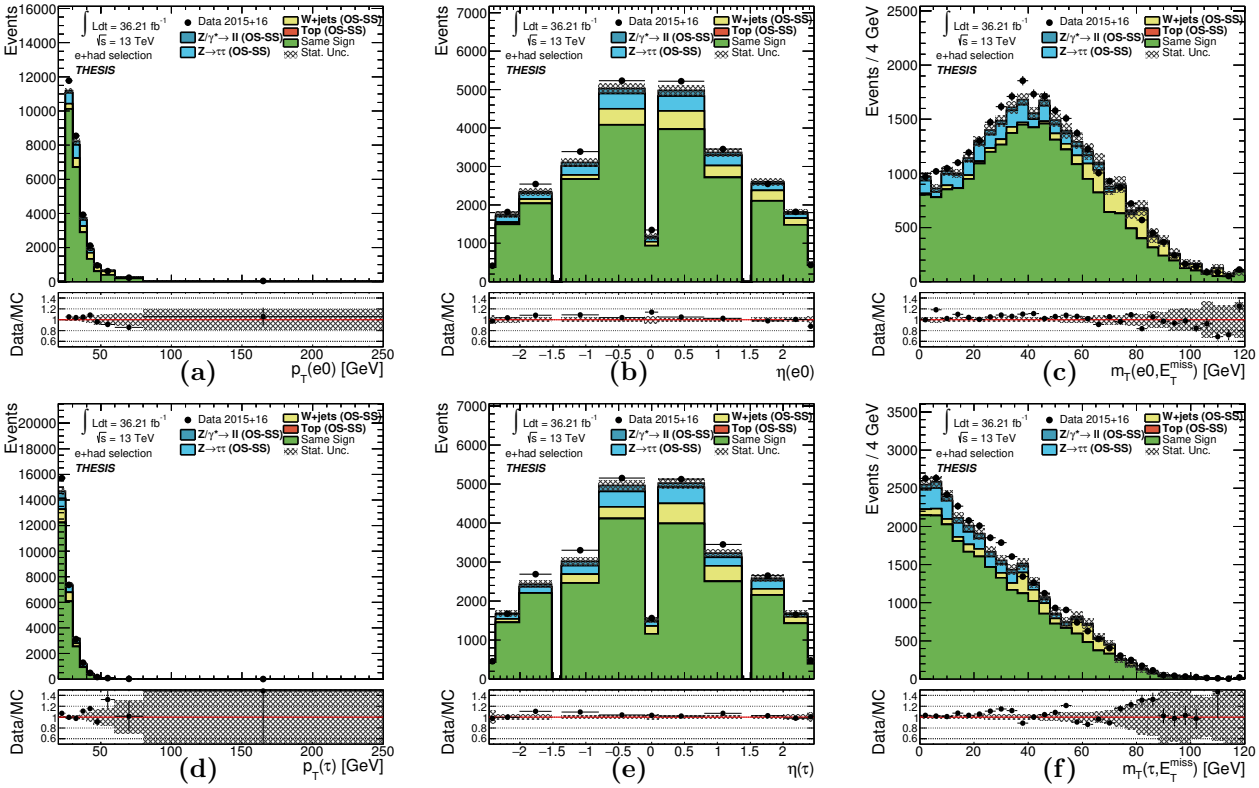

Figure A.1.3: Plots of the tag electron (top) and probe hadronic tau (bottom), representing their p_{T}, η and m_{T} (from left to right), as observed in the QCD control region, with a medium tau ID applied. These represent their state before any normalisation factors are derived.

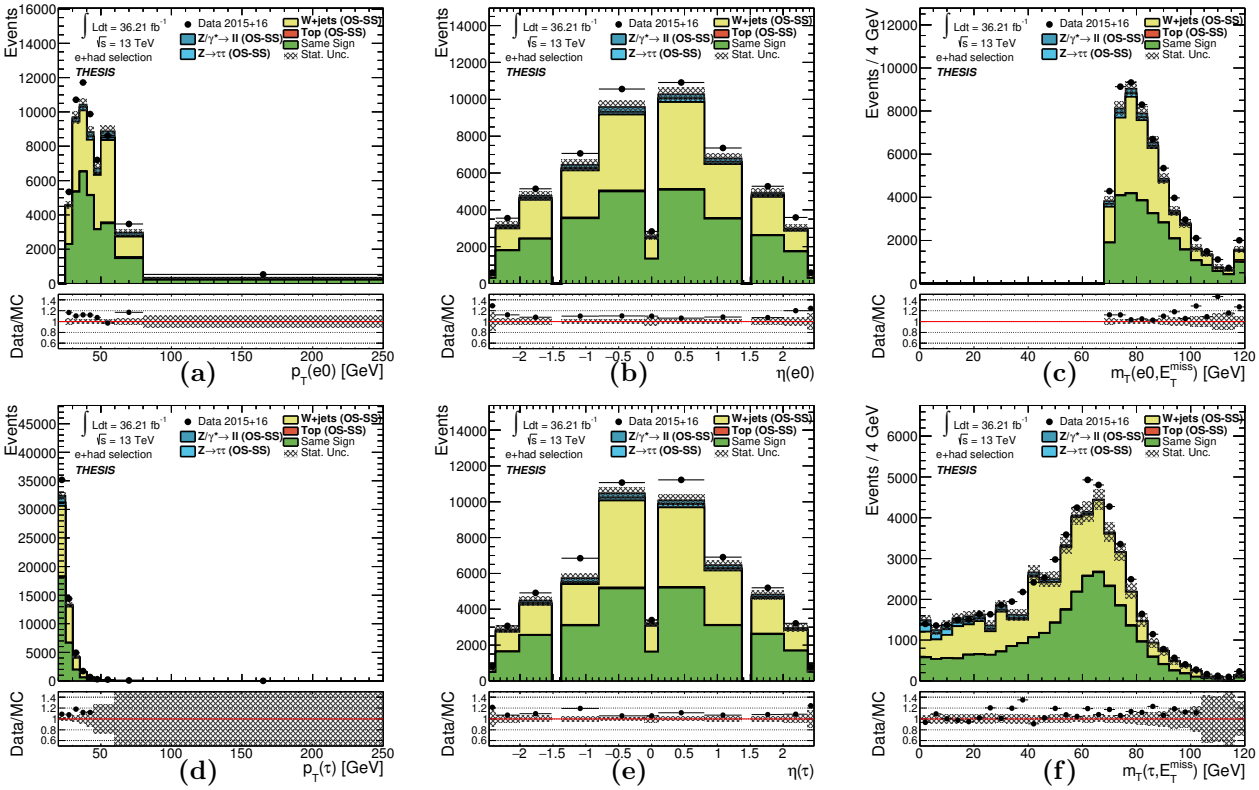

Figure A.1.4: Plots of the tag electron (top) and probe hadronic tau (bottom), representing their p_{T}, η and m_{T} (from left to right), as observed in the W+jets control region, with a medium tau ID applied. These represent their state before any normalisation factors are derived.

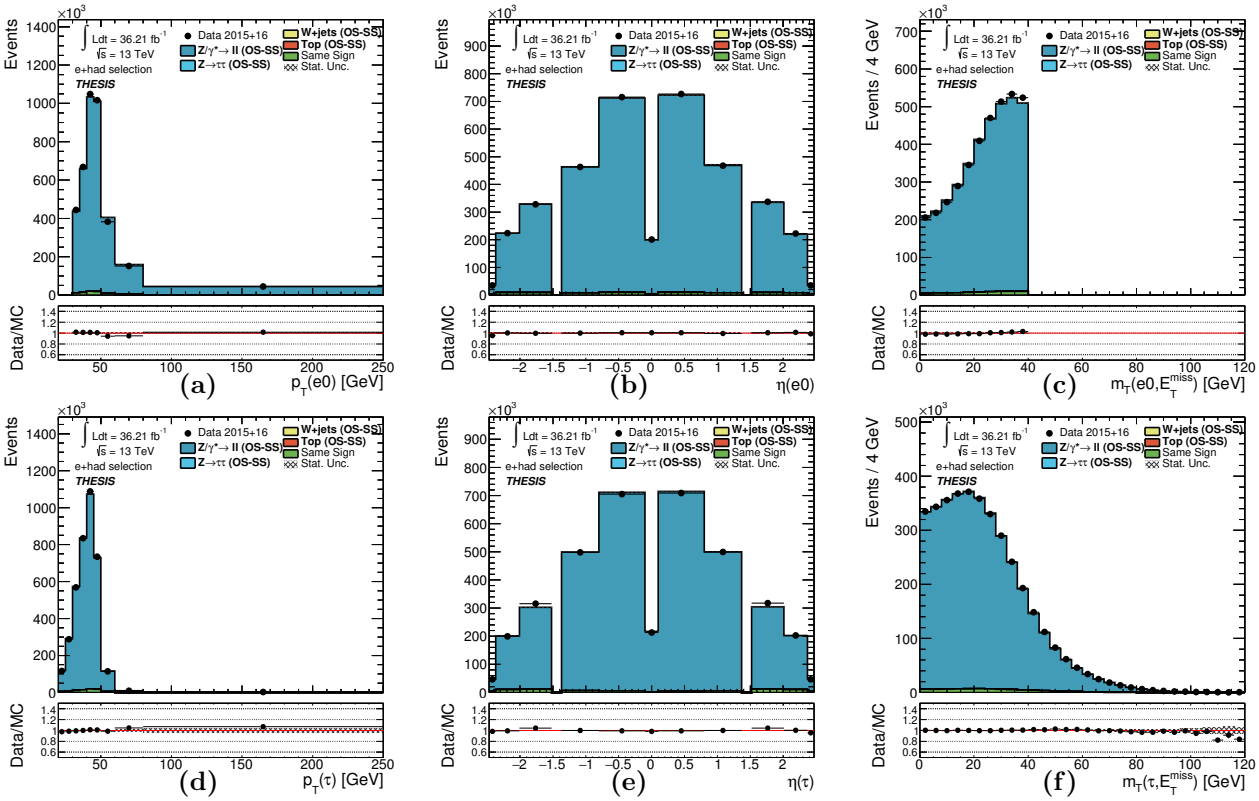

Figure A.1.5: Plots of the tag electron (top) and probe hadronic tau (bottom), representing their p_{T}, η and m_{T} (from left to right), as observed in the $Z \to ee$ signal denominator validation region, with a medium tau ID applied. These represent their state before any normalisation factors are derived.

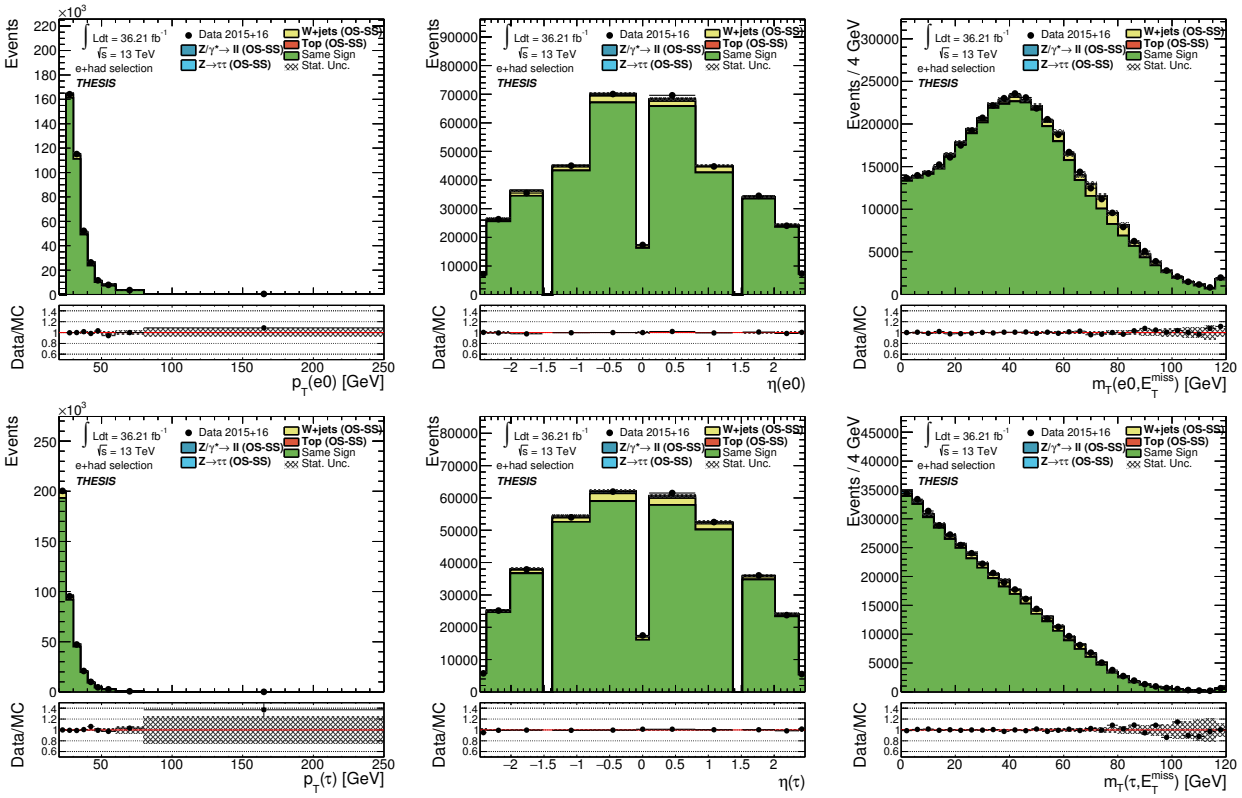

Figure A.1.6: Plots of the tag electron (top) and probe hadronic tau (bottom), representing their p_{T}, η and m_{T} (from left to right), as observed in the QCD control region, with no tau ID applied.

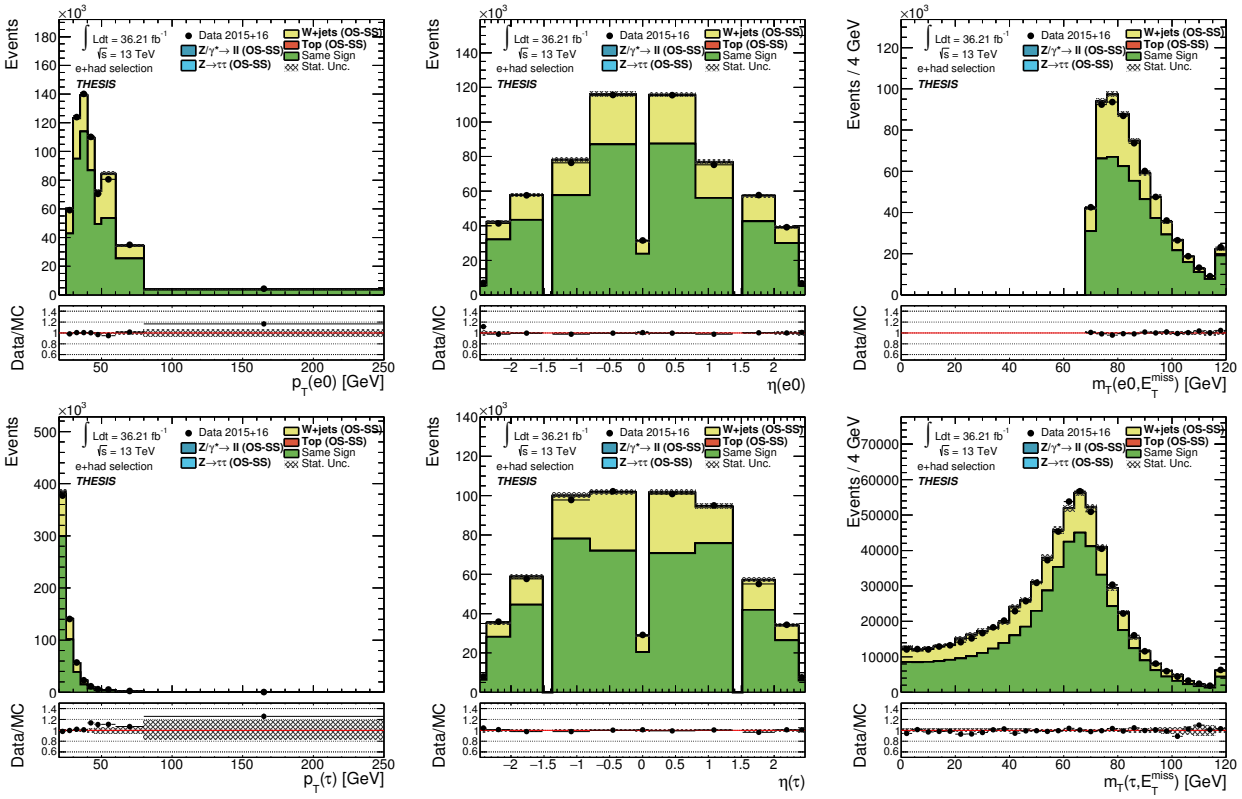

Figure A.1.7: Plots of the tag electron (top) and probe hadronic tau (bottom), representing their p_{T}, η and m_{T} (from left to right), as observed in the W+jets control region, with no tau ID applied.

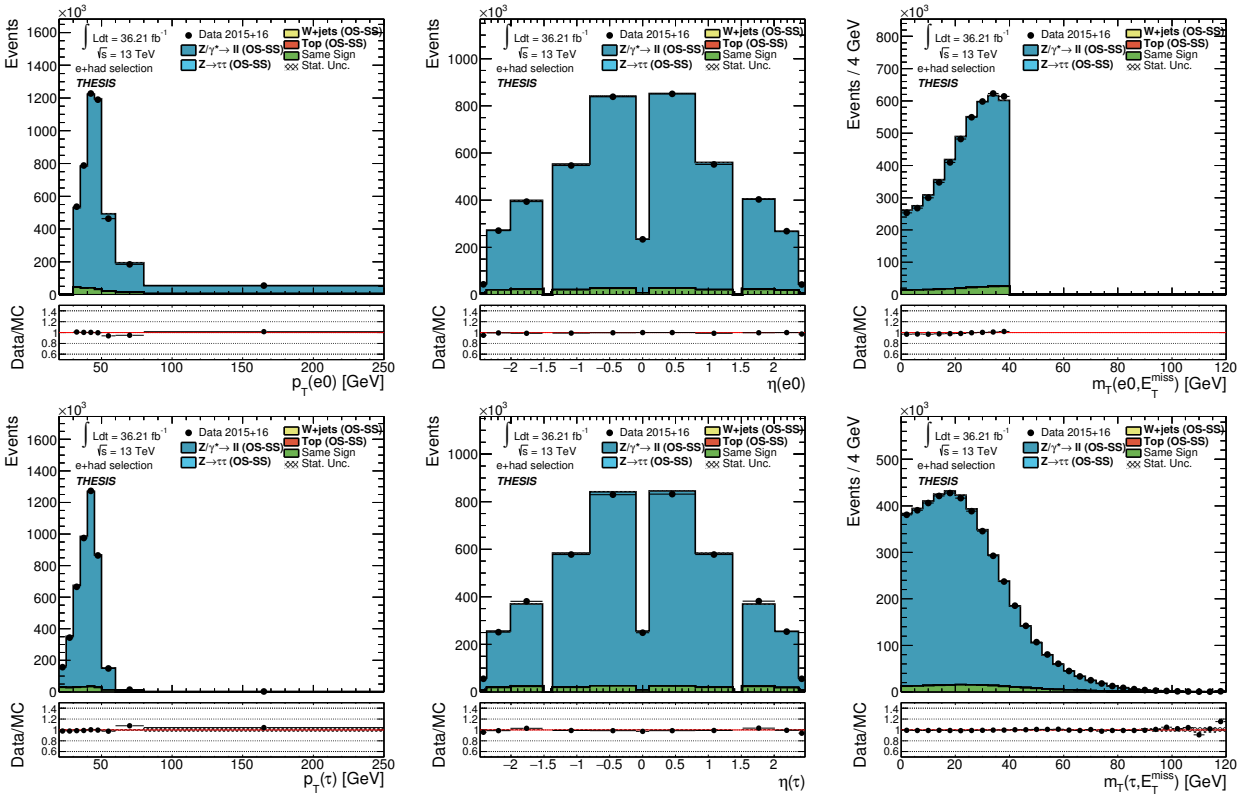

Figure A.1.8: Plots of the tag electron (top) and probe hadronic tau (bottom), representing their p_{T}, η and m_{T} (from left to right), as observed in the $Z \to ee$ signal denominator validation region, with no tau ID applied. The selection criterion in electron $m_{\mathrm{T}} < 40\,\mathrm{GeV}$ is clearly visible.

Signal and scale factor results

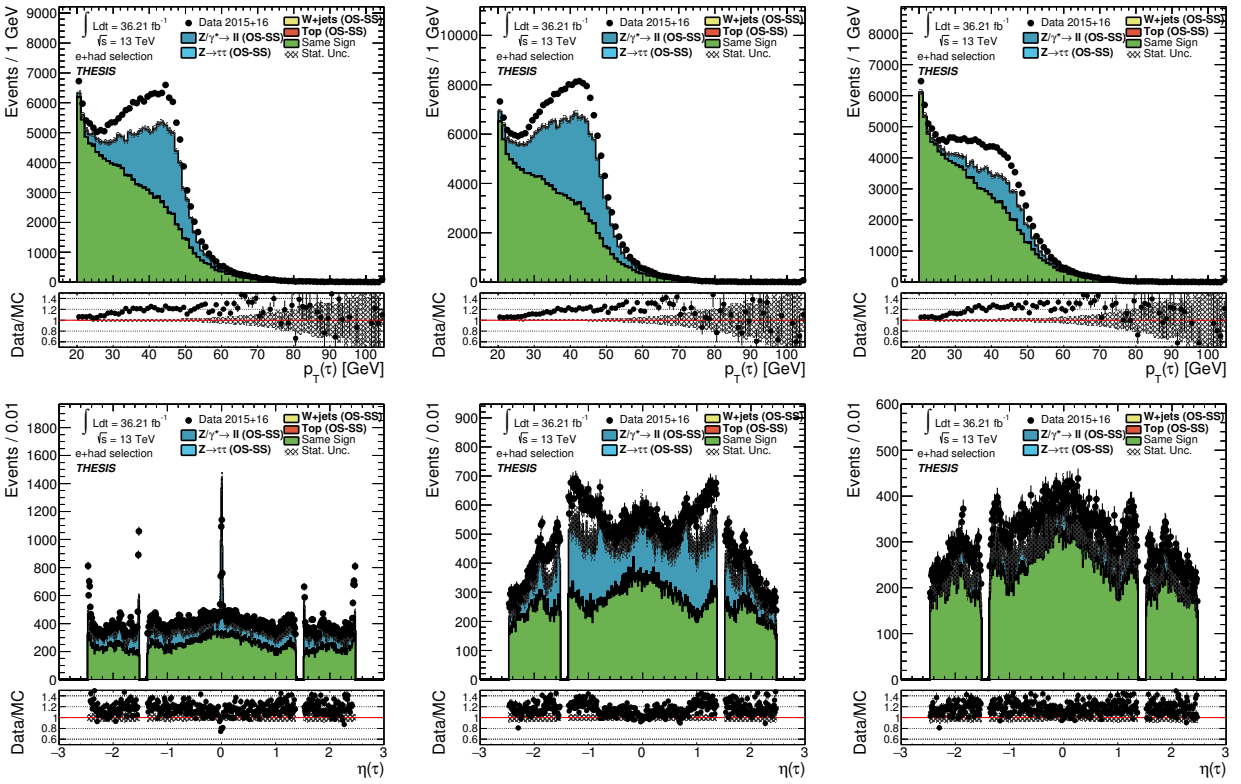

Figure A.1.9: Plots of the probe hadronic tau p_{T} (top) and η (bottom), for eVeto algorithms applied with eLLH, eBDT @ 85% and both combined (from left to right), as observed in the $Z \to ee$ signal numerator region, with no tau ID applied.

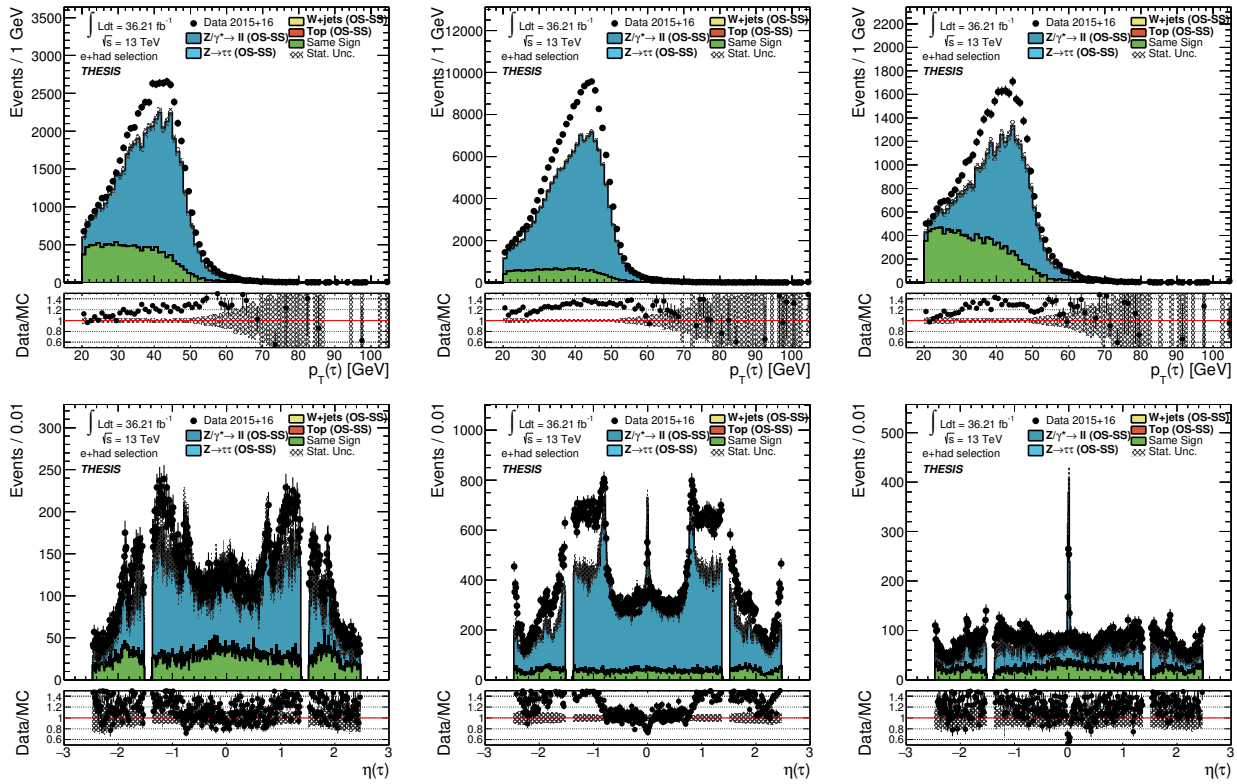

Figure A.1.10: Plots of the probe hadronic tau p_{T} (top) and η (bottom), for eVeto algorithms applied with eBDT @ 75%, 95% and 95% with eLLH (from left to right), as observed in the $Z \to ee$ signal numerator region, with a medium tau ID applied.

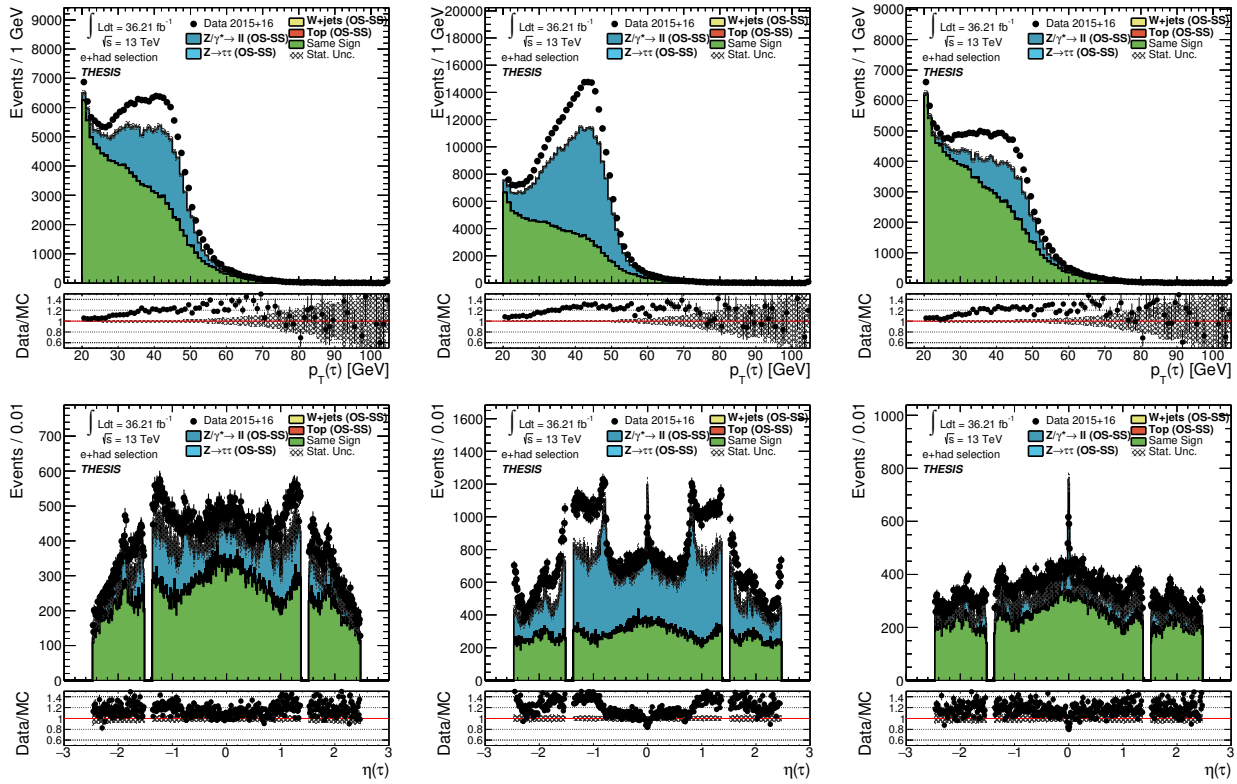

Figure A.1.11: Plots of the probe hadronic tau p_{T} (top) and η (bottom), for eVeto algorithms applied with eBDT @ 75%, 95% and 95% with eLLH (from left to right), as observed in the $Z \to ee$ signal numerator region, with no tau ID applied.

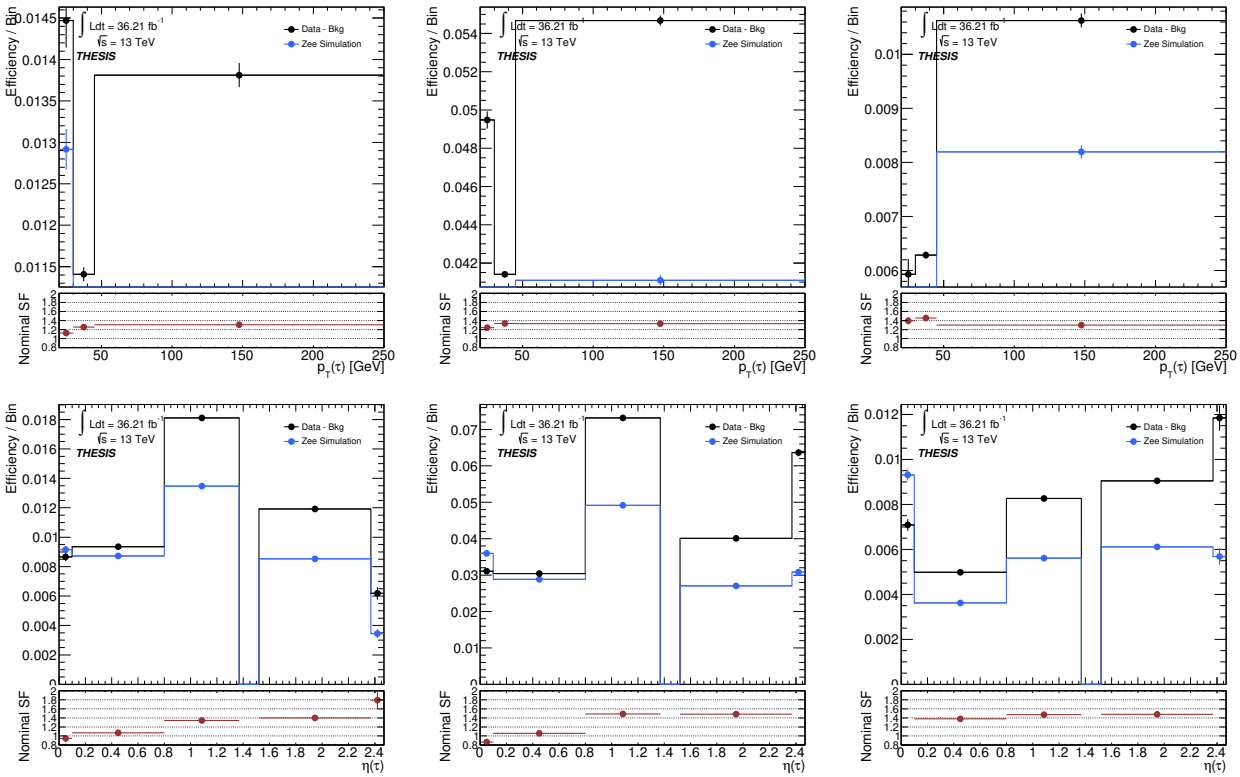

Figure A.1.12: Efficiency plots of the probe hadronic tau p_{T} (top) and η (bottom), for eVeto algorithms applied with eBDT @ 75%, 95% and 95% with eLLH (from left to right), as observed in the divided $Z \to ee$ signal region, with a medium tau ID applied. The ratio of data to MC is taken in the lower section of these plots, indicating the resulting scale factor.

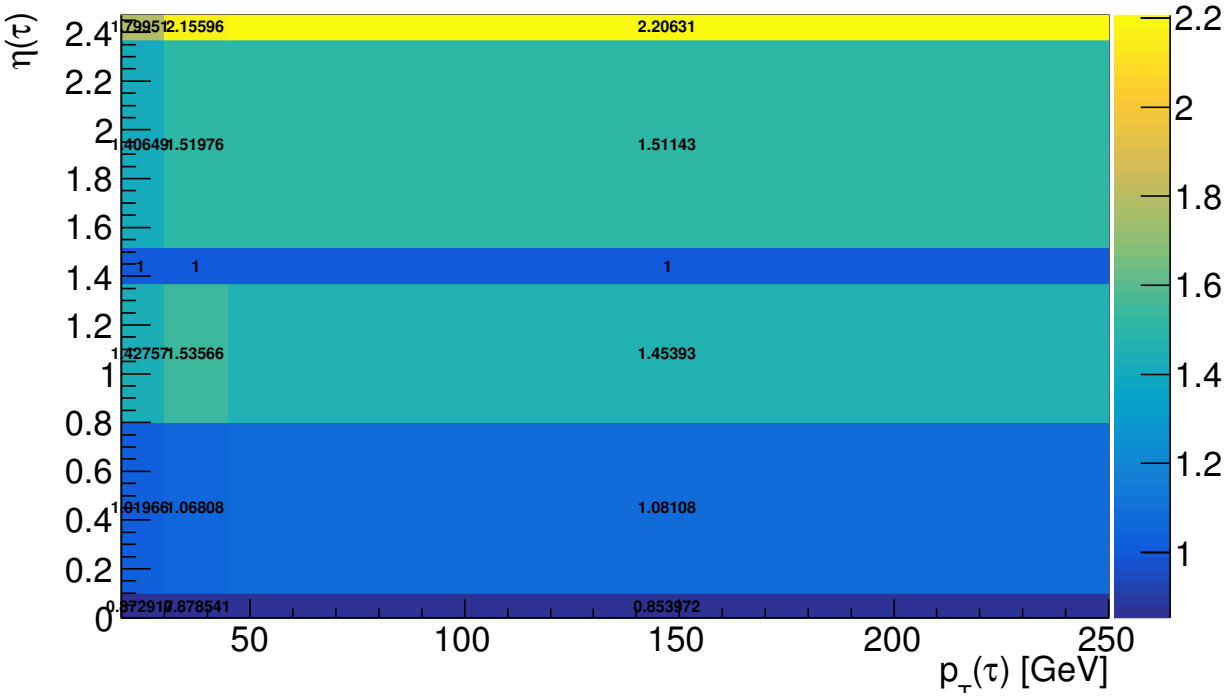

Figure A.1.13: A 2-dimensional scale factor binned in tau η against tau p_{T}, derived for the eBDT @ 95% WP.

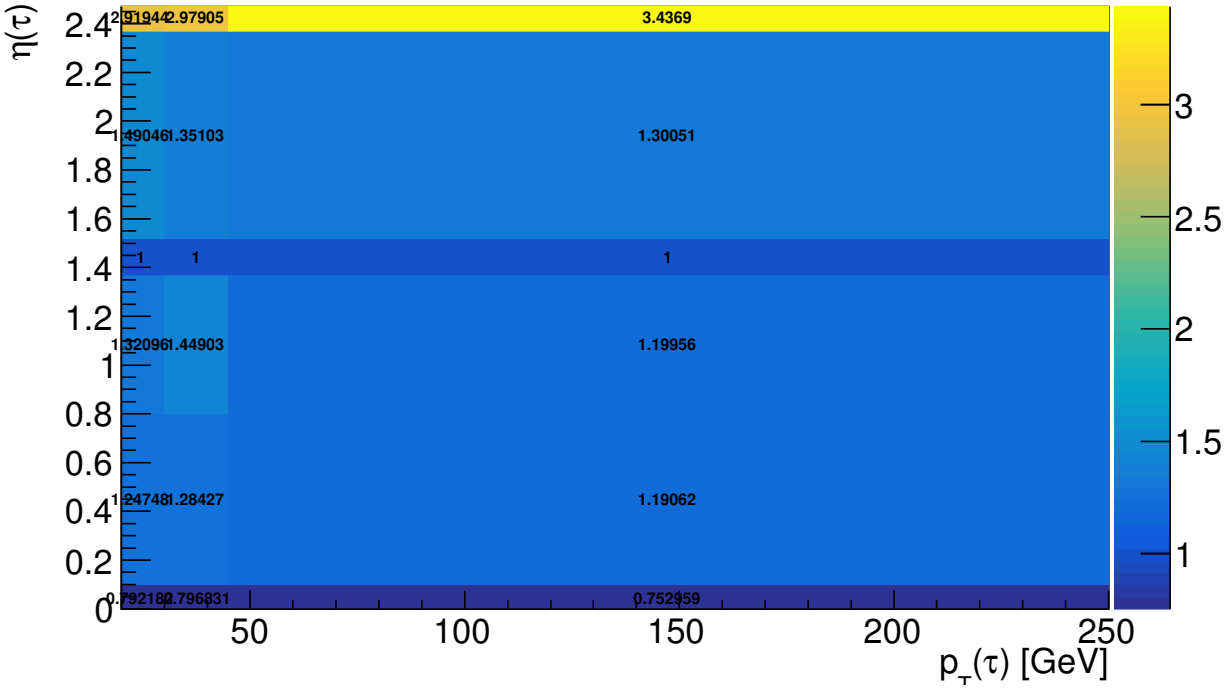

Figure A.1.14: A 2-dimensional scale factor binned in tau η against tau p_{T}, derived for the eLLH WP.

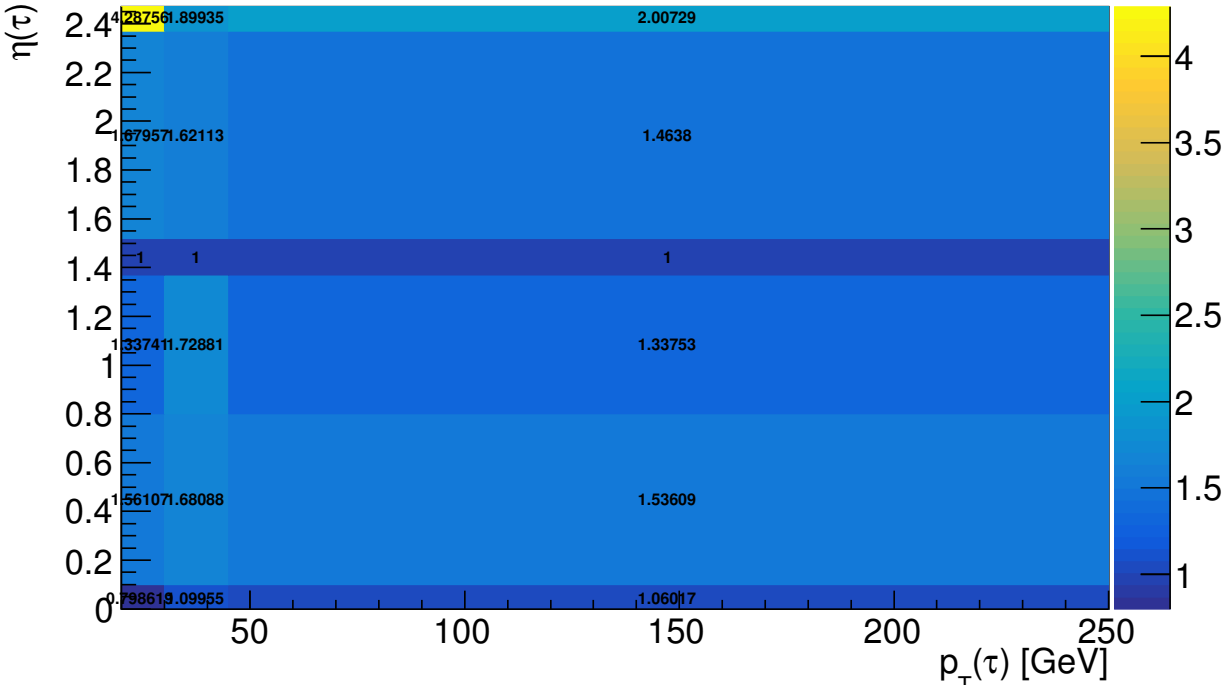

Figure A.1.15: A 2-dimensional scale factor binned in tau η against tau p_{T}, derived for the eBDT @ 85% with eLLH WP.

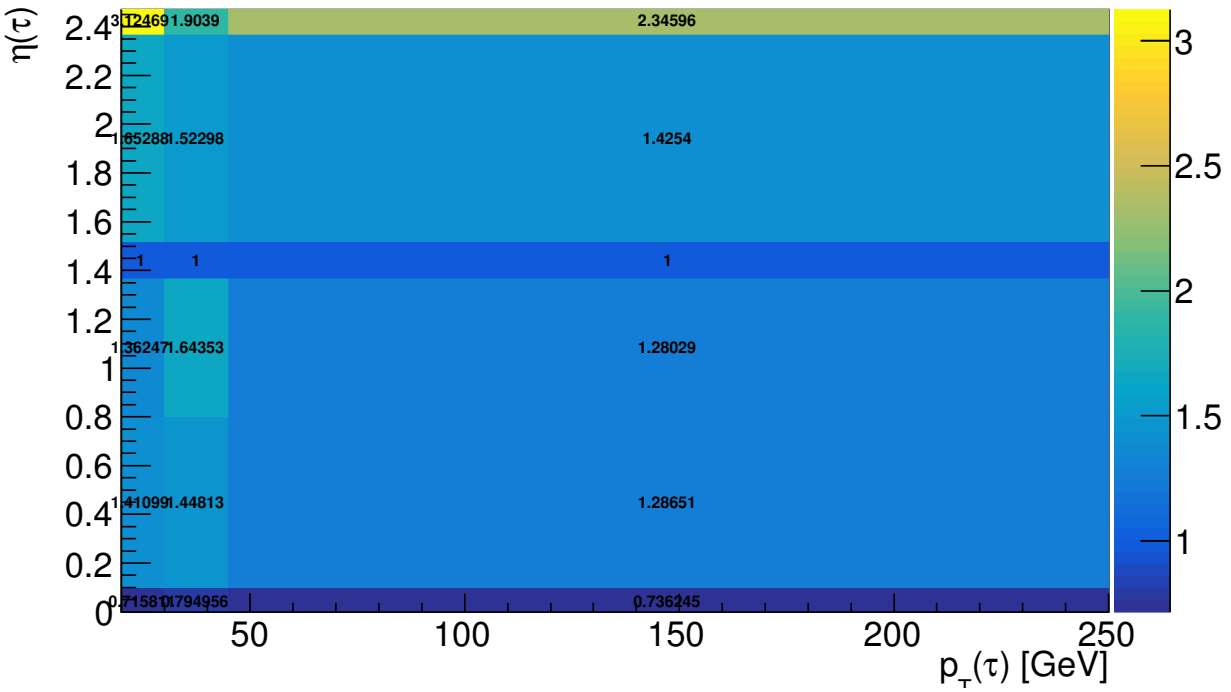

Figure A.1.16: A 2-dimensional scale factor binned in tau η against tau p_{T}, derived for the eBDT @ 95% with eLLH WP.

Systematic uncertainties

Combined:

bin-center	SF	stat	sym sys	stat [%]	sym sys [%]
0.05	0.945	0.040	0.017	4.232	1.750
0.45	1.072	0.017	0.008	1.597	0.726
1.08	1.344	0.019	0.015	1.389	1.093
1.45	1.000	0.000	0.000	0.000	0.000
1.95	1.398	0.028	0.014	2.015	0.990
2.42	1.791	0.196	0.033	10.940	1.843

Combined:

bin-center	SF	stat	sym sys	stat [%]	sym sys [%]
0.05	0.864	0.017	0.012	1.913	1.337
0.45	1.056	0.008	0.012	0.792	1.137
1.08	1.489	0.010	0.021	0.658	1.418
1.45	1.000	0.000	0.000	0.000	0.000
1.95	1.483	0.015	0.020	0.984	1.331
2.42	2.066	0.061	0.037	2.958	1.815

Combined:

bin-center	SF	stat	sym sys	stat [%]	sym sys [%]
0.05	0.761	0.034	0.011	4.521	1.434
0.45	1.378	0.034	0.017	2.474	1.208
1.08	1.472	0.032	0.017	2.187	1.177
1.45	1.000	0.000	0.000	0.000	0.000
1.95	1.481	0.034	0.016	2.264	1.048
2.42	2.085	0.166	0.025	7.940	1.214

Table A.1.1: Tables of statistical (stat) and systematic (sys) uncertainties on the scale factor (SF), in the centre of each bin of η. The systematic uncertainties are combined and averaged such that it is symmetrical around the point (sym), and uncertainties are also expressed as a percentage of the SF. The tables are given for each eVeto algorithm applied, for the eBDT @ 75%, 95% and 95% with eLLH (from top to bottom), with a medium tau ID applied.

Systematics Source: EL_EFF_Trigger_TOTAL_1NPCOR_PLUS_UNCOR

bin-center	SF	sys-up	sys-down	sys-up [%]	sys-down [%]
0.05	0.777	0.000	-0.000	0.001	-0.001
0.45	1.238	-0.000	0.000	-0.001	0.001
1.08	1.334	-0.000	0.000	-0.006	0.006
1.45	1.000	0.000	0.000	0.000	0.000
1.95	1.330	-0.000	0.000	-0.004	0.004
2.42	3.026	0.000	-0.000	0.008	-0.008

Systematics Source: EG_SCALE_ALLCORR

bin-center	SF	sys-up	sys-down	sys-up [%]	sys-down [%]
0.05	0.777	-0.000	-0.001	-0.025	-0.086
0.45	1.238	0.004	-0.003	0.293	-0.264
1.08	1.334	-0.001	-0.001	-0.042	-0.096
1.45	1.000	0.000	0.000	0.000	0.000
1.95	1.330	-0.001	0.000	-0.084	0.014
2.42	3.026	-0.025	0.012	-0.825	0.386

Systematics Source: EG_RESOLUTION_ALL

bin-center	SF	sys-up	sys-down	sys-up [%]	sys-down [%]
0.05	0.777	-0.001	0.000	-0.090	0.057
0.45	1.238	-0.002	-0.001	-0.152	-0.099
1.08	1.334	0.000	0.005	0.009	0.410
1.45	1.000	0.000	0.000	0.000	0.000
1.95	1.330	0.002	0.002	0.182	0.135
2.42	3.026	-0.010	-0.014	-0.339	-0.447

Systematics Source: Wjets_kf_OS

bin-center	SF	sys-up	sys-down	sys-up [%]	sys-down [%]
0.05	0.777	-0.000	0.000	-0.015	0.000
0.45	1.238	-0.001	0.000	-0.061	0.000
1.08	1.334	-0.001	0.000	-0.077	0.000
1.45	1.000	0.000	0.000	0.000	0.000
1.95	1.330	-0.003	0.000	-0.188	0.000
2.42	3.026	-0.011	0.000	-0.361	0.000

Systematics Source: RQCD

bin-center	SF	sys-up	sys-down	sys-up [%]	sys-down [%]
0.05	0.777	-0.002	0.002	-0.318	0.318
0.45	1.238	-0.007	0.007	-0.586	0.585
1.08	1.334	-0.004	0.004	-0.291	0.291
1.45	1.000	0.000	0.000	0.000	0.000
1.95	1.330	-0.003	0.003	-0.249	0.248
2.42	3.026	-0.012	0.012	-0.388	0.383

Systematics Source: EL_EFF_Iso_TOTAL_1NPCOR_PLUS_UNCOR

bin-center	SF	sys-up	sys-down	sys-up [%]	sys-down [%]
0.05	0.777	0.000	-0.000	0.004	-0.004
0.45	1.238	0.000	-0.000	0.001	-0.001
1.08	1.334	0.000	-0.000	0.001	-0.001
1.45	1.000	0.000	0.000	0.000	0.000
1.95	1.330	0.000	-0.000	0.001	-0.001
2.42	3.026	0.000	-0.000	0.008	-0.008

Systematics Source: PRW_DATASF

bin-center	SF	sys-up	sys-down	sys-up [%]	sys-down [%]
0.05	0.777	-0.003	-0.003	-0.395	-0.395
0.45	1.238	-0.007	-0.007	-0.540	-0.540
1.08	1.334	-0.011	-0.011	-0.846	-0.846
1.45	1.000	0.000	0.000	0.000	0.000
1.95	1.330	-0.008	-0.008	-0.582	-0.582
2.42	3.026	-0.019	-0.019	-0.642	-0.642

Systematics Source: FT_EFF_Eigen_Light_3

bin-center	SF	sys-up	sys-down	sys-up [%]	sys-down [%]
0.05	0.777	0.000	0.000	0.000	0.000
0.45	1.238	0.000	0.000	0.000	0.000
1.08	1.334	0.000	0.000	0.000	0.000
1.45	1.000	0.000	0.000	0.000	0.000
1.95	1.330	0.000	0.000	0.000	0.000
2.42	3.026	0.000	0.000	0.000	0.000

Systematics Source: FT_EFF_Eigen_Light_2

bin-center	SF	sys-up	sys-down	sys-up [%]	sys-down [%]
0.05	0.777	0.000	0.000	0.000	0.000
0.45	1.238	0.000	0.000	0.000	0.000
1.08	1.334	0.000	0.000	0.000	0.000
1.45	1.000	0.000	0.000	0.000	0.000
1.95	1.330	0.000	0.000	0.000	0.000
2.42	3.026	0.000	0.000	0.000	0.000

Systematics Source: FT_EFF_Eigen_Light_1

bin-center	SF	sys-up	sys-down	sys-up [%]	sys-down [%]
0.05	0.777	0.000	0.000	0.000	0.000
0.45	1.238	0.000	0.000	0.000	0.000
1.08	1.334	0.000	0.000	0.000	0.000
1.45	1.000	0.000	0.000	0.000	0.000
1.95	1.330	0.000	0.000	0.000	0.000
2.42	3.026	0.000	0.000	0.000	0.000

Systematics Source: FT_EFF_Eigen_Light_0

bin-center	SF	sys-up	sys-down	sys-up [%]	sys-down [%]
0.05	0.777	0.000	0.000	0.000	0.000
0.45	1.238	0.000	0.000	0.000	0.000
1.08	1.334	0.000	0.000	0.000	0.000
1.45	1.000	0.000	0.000	0.000	0.000
1.95	1.330	0.000	0.000	0.000	0.000
2.42	3.026	0.000	0.000	0.000	0.000

Systematics Source: JET_JvtEfficiency

bin-center	SF	sys-up	sys-down	sys-up [%]	sys-down [%]
0.05	0.777	0.000	-0.000	0.013	-0.013
0.45	1.238	0.000	-0.000	0.007	-0.007
1.08	1.334	0.000	-0.000	0.012	-0.012
1.45	1.000	0.000	0.000	0.000	0.000
1.95	1.330	0.000	-0.000	0.010	-0.010
2.42	3.026	0.000	-0.000	0.009	-0.009

Systematics Source: FT_EFF_Eigen_Light_4

bin-center	SF	sys-up	sys-down	sys-up [%]	sys-down [%]
0.05	0.777	0.000	0.000	0.000	0.000
0.45	1.238	0.000	0.000	0.000	0.000
1.08	1.334	0.000	0.000	0.000	0.000
1.45	1.000	0.000	0.000	0.000	0.000
1.95	1.330	0.000	0.000	0.000	0.000
2.42	3.026	0.000	0.000	0.000	0.000

Systematics Source: FT_EFF_Eigen_C_0

bin-center	SF	sys-up	sys-down	sys-up [%]	sys-down [%]
0.05	0.777	0.000	0.000	0.000	0.000
0.45	1.238	0.000	0.000	0.000	0.000
1.08	1.334	0.000	0.000	0.000	0.000
1.45	1.000	0.000	0.000	0.000	0.000
1.95	1.330	0.000	0.000	0.000	0.000
2.42	3.026	0.000	0.000	0.000	0.000

Systematics Source: FT_EFF_Eigen_C_1

bin-center	SF	sys-up	sys-down	sys-up [%]	sys-down [%]
0.05	0.777	0.000	0.000	0.000	0.000
0.45	1.238	0.000	0.000	0.000	0.000
1.08	1.334	0.000	0.000	0.000	0.000
1.45	1.000	0.000	0.000	0.000	0.000
1.95	1.330	0.000	0.000	0.000	0.000
2.42	3.026	0.000	0.000	0.000	0.000

Systematics Source: FT_EFF_Eigen_C_2

bin-center	SF	sys-up	sys-down	sys-up [%]	sys-down [%]
0.05	0.777	0.000	0.000	0.000	0.000
0.45	1.238	0.000	0.000	0.000	0.000
1.08	1.334	0.000	0.000	0.000	0.000
1.45	1.000	0.000	0.000	0.000	0.000
1.95	1.330	0.000	0.000	0.000	0.000
2.42	3.026	0.000	0.000	0.000	0.000

Systematics Source: JET_fJvtEfficiency

bin-center	SF	sys-up	sys-down	sys-up [%]	sys-down [%]
0.05	0.777	0.000	0.000	0.000	0.000
0.45	1.238	0.000	0.000	0.000	0.000
1.08	1.334	0.000	0.000	0.000	0.000
1.45	1.000	0.000	0.000	0.000	0.000
1.95	1.330	0.000	0.000	0.000	0.000
2.42	3.026	0.000	0.000	0.000	0.000

Systematics Source: FT_EFF_Eigen_B_1

bin-center	SF	sys-up	sys-down	sys-up [%]	sys-down [%]
0.05	0.777	0.000	0.000	0.000	0.000
0.45	1.238	0.000	0.000	0.000	0.000
1.08	1.334	0.000	0.000	0.000	0.000
1.45	1.000	0.000	0.000	0.000	0.000
1.95	1.330	0.000	0.000	0.000	0.000
2.42	3.026	0.000	0.000	0.000	0.000

Systematics Source: FT_EFF_Eigen_B_0

bin-center	SF	sys-up	sys-down	sys-up [%]	sys-down [%]
0.05	0.777	0.000	0.000	0.000	0.000
0.45	1.238	0.000	0.000	0.000	0.000
1.08	1.334	0.000	0.000	0.000	0.000
1.45	1.000	0.000	0.000	0.000	0.000
1.95	1.330	0.000	0.000	0.000	0.000
2.42	3.026	0.000	0.000	0.000	0.000

Systematics Source: FT_EFF_Eigen_B_2

bin-center	SF	sys-up	sys-down	sys-up [%]	sys-down [%]
0.05	0.777	0.000	0.000	0.000	0.000
0.45	1.238	0.000	0.000	0.000	0.000
1.08	1.334	0.000	0.000	0.000	0.000
1.45	1.000	0.000	0.000	0.000	0.000
1.95	1.330	0.000	0.000	0.000	0.000
2.42	3.026	0.000	0.000	0.000	0.000

Systematics Source: Wjets_kf_SS

bin-center	SF	sys-up	sys-down	sys-up [%]	sys-down [%]
0.05	0.777	0.000	0.000	0.000	0.000
0.45	1.238	0.000	0.000	0.000	0.000
1.08	1.334	0.000	0.000	0.000	0.000
1.45	1.000	0.000	0.000	0.000	0.000
1.95	1.330	0.000	0.000	0.000	0.000
2.42	3.026	0.000	0.000	0.000	0.000

Systematics Source: EL_EFF_Reco_TOTAL_1NPCOR_PLUS_UNCOR

bin-center	SF	sys-up	sys-down	sys-up [%]	sys-down [%]
0.05	0.777	0.000	-0.000	0.002	-0.002
0.45	1.238	-0.000	0.000	-0.000	0.000
1.08	1.334	-0.000	0.000	-0.001	0.001
1.45	1.000	0.000	0.000	0.000	0.000
1.95	1.330	0.000	-0.000	0.000	-0.001
2.42	3.026	0.000	-0.000	0.002	-0.002

Systematics Source: FT_EFF_extrapolation_from_charm

bin-center	SF	sys-up	sys-down	sys-up [%]	sys-down [%]
0.05	0.777	0.000	0.000	0.000	0.000
0.45	1.238	0.000	0.000	0.000	0.000
1.08	1.334	0.000	0.000	0.000	0.000
1.45	1.000	0.000	0.000	0.000	0.000
1.95	1.330	0.000	0.000	0.000	0.000
2.42	3.026	0.000	0.000	0.000	0.000

Systematics Source: EL_EFF_ID_TOTAL_1NPCOR_PLUS_UNCOR

bin-center	SF	sys-up	sys-down	sys-up [%]	sys-down [%]
0.05	0.777	-0.000	0.000	-0.036	0.036
0.45	1.238	-0.000	0.000	-0.019	0.019
1.08	1.334	-0.000	0.000	-0.020	0.020
1.45	1.000	0.000	0.000	0.000	0.000
1.95	1.330	-0.000	0.000	-0.001	0.001
2.42	3.026	0.000	-0.000	0.003	-0.003

Systematics Source: FT_EFF_extrapolation

bin-center	SF	sys-up	sys-down	sys-up [%]	sys-down [%]
0.05	0.777	0.000	0.000	0.000	0.000
0.45	1.238	0.000	0.000	0.000	0.000
1.08	1.334	0.000	0.000	0.000	0.000
1.45	1.000	0.000	0.000	0.000	0.000
1.95	1.330	0.000	0.000	0.000	0.000
2.42	3.026	0.000	0.000	0.000	0.000

Table A.1.2: Tables of systematic (sys) uncertainties on the scale factor (SF), in the centre of each bin of η. The systematic uncertainties are detailed individually for each variation, and uncertainties are also expressed as a percentage of the SF. The tables are given for the eLLH eVeto algorithm, with a medium tau ID applied.

Systematics Source: EL_EFF_Trigger_TOTAL_1NPCOR_PLUS_UNCOR

bin-center	SF	sys-up	sys-down	sys-up [%]	sys-down [%]
0.05	0.945	-0.000	0.000	-0.021	0.021
0.45	1.072	-0.000	0.000	-0.020	0.020
1.08	1.344	-0.000	0.000	-0.006	0.006
1.45	1.000	0.000	0.000	0.000	0.000
1.95	1.398	-0.000	0.000	-0.003	0.003
2.42	1.791	-0.000	0.000	-0.003	0.003

Systematics Source: EG_SCALE_ALLCORR

bin-center	SF	sys-up	sys-down	sys-up [%]	sys-down [%]
0.05	0.945	0.001	-0.004	0.144	-0.387
0.45	1.072	0.002	-0.003	0.169	-0.255
1.08	1.344	0.004	0.000	0.268	0.004
1.45	1.000	0.000	0.000	0.000	0.000
1.95	1.398	-0.003	0.003	-0.202	0.220
2.42	1.791	0.014	0.000	0.769	0.004

Systematics Source: EG_RESOLUTION_ALL

bin-center	SF	sys-up	sys-down	sys-up [%]	sys-down [%]
0.05	0.945	0.000	-0.011	0.019	-1.180
0.45	1.072	-0.001	-0.001	-0.122	-0.076
1.08	1.344	0.004	-0.000	0.271	-0.017
1.45	1.000	0.000	0.000	0.000	0.000
1.95	1.398	0.002	0.003	0.126	0.236
2.42	1.791	-0.019	0.023	-1.082	1.303

Systematics Source: Wjets_kf_OS

bin-center	SF	sys-up	sys-down	sys-up [%]	sys-down [%]
0.05	0.945	-0.001	0.000	-0.109	0.000
0.45	1.072	-0.001	0.000	-0.106	0.000
1.08	1.344	-0.002	0.000	-0.120	0.000
1.45	1.000	0.000	0.000	0.000	0.000
1.95	1.398	-0.005	0.000	-0.366	0.000
2.42	1.791	-0.006	0.000	-0.325	0.000

Systematics Source: RQCD

bin-center	SF	sys-up	sys-down	sys-up [%]	sys-down [%]
0.05	0.945	-0.006	0.006	-0.613	0.612
0.45	1.072	-0.006	0.006	-0.518	0.517
1.08	1.344	-0.002	0.002	-0.166	0.165
1.45	1.000	0.000	0.000	0.000	0.000
1.95	1.398	-0.004	0.004	-0.271	0.268
2.42	1.791	-0.012	0.012	-0.653	0.645

Systematics Source: EL_EFF_Iso_TOTAL_1NPCOR_PLUS_UNCOR

bin-center	SF	sys-up	sys-down	sys-up [%]	sys-down [%]
0.05	0.945	-0.000	0.000	-0.006	0.006
0.45	1.072	-0.000	0.000	-0.006	0.006
1.08	1.344	-0.000	0.000	-0.000	0.000
1.45	1.000	0.000	0.000	0.000	0.000
1.95	1.398	0.000	-0.000	0.000	-0.000
2.42	1.791	0.000	-0.000	0.003	-0.003

Systematics Source: PRW_DATASF

bin-center	SF	sys-up	sys-down	sys-up [%]	sys-down [%]
0.05	0.945	-0.010	-0.010	-1.063	-1.063
0.45	1.072	-0.004	-0.004	-0.403	-0.403
1.08	1.344	-0.013	-0.013	-1.003	-1.003
1.45	1.000	0.000	0.000	0.000	0.000
1.95	1.398	-0.011	-0.011	-0.816	-0.816
2.42	1.791	-0.014	-0.014	-0.759	-0.759

Systematics Source: FT_EFF_Eigen_Light_3

bin-center	SF	sys-up	sys-down	sys-up [%]	sys-down [%]
0.05	0.945	0.000	0.000	0.000	0.000
0.45	1.072	0.000	0.000	0.000	0.000
1.08	1.344	0.000	0.000	0.000	0.000
1.45	1.000	0.000	0.000	0.000	0.000
1.95	1.398	0.000	0.000	0.000	0.000
2.42	1.791	0.000	0.000	0.000	0.000

Systematics Source: FT_EFF_Eigen_Light_2

bin-center	SF	sys-up	sys-down	sys-up [%]	sys-down [%]
0.05	0.945	0.000	0.000	0.000	0.000
0.45	1.072	0.000	0.000	0.000	0.000
1.08	1.344	0.000	0.000	0.000	0.000
1.45	1.000	0.000	0.000	0.000	0.000
1.95	1.398	0.000	0.000	0.000	0.000
2.42	1.791	0.000	0.000	0.000	0.000

Systematics Source: FT_EFF_Eigen_Light_1

bin-center	SF	sys-up	sys-down	sys-up [%]	sys-down [%]
0.05	0.945	0.000	0.000	0.000	0.000
0.45	1.072	0.000	0.000	0.000	0.000
1.08	1.344	0.000	0.000	0.000	0.000
1.45	1.000	0.000	0.000	0.000	0.000
1.95	1.398	0.000	0.000	0.000	0.000
2.42	1.791	0.000	0.000	0.000	0.000

Systematics Source: FT_EFF_Eigen_Light_0

bin-center	SF	sys-up	sys-down	sys-up [%]	sys-down [%]
0.05	0.945	0.000	0.000	0.000	0.000
0.45	1.072	0.000	0.000	0.000	0.000
1.08	1.344	0.000	0.000	0.000	0.000
1.45	1.000	0.000	0.000	0.000	0.000
1.95	1.398	0.000	0.000	0.000	0.000
2.42	1.791	0.000	0.000	0.000	0.000

Systematics Source: JET_JvtEfficiency

bin-center	SF	sys-up	sys-down	sys-up [%]	sys-down [%]
0.05	0.945	-0.000	0.000	-0.008	0.008
0.45	1.072	-0.000	0.000	-0.009	0.009
1.08	1.344	-0.000	0.000	-0.007	0.007
1.45	1.000	0.000	0.000	0.000	0.000
1.95	1.398	-0.000	0.000	-0.010	0.010
2.42	1.791	-0.000	0.000	-0.007	0.007

Systematics Source: FT_EFF_Eigen_Light_4

bin-center	SF	sys-up	sys-down	sys-up [%]	sys-down [%]
0.05	0.945	0.000	0.000	0.000	0.000
0.45	1.072	0.000	0.000	0.000	0.000
1.08	1.344	0.000	0.000	0.000	0.000
1.45	1.000	0.000	0.000	0.000	0.000
1.95	1.398	0.000	0.000	0.000	0.000
2.42	1.791	0.000	0.000	0.000	0.000

Systematics Source: FT_EFF_Eigen_C_0

bin-center	SF	sys-up	sys-down	sys-up [%]	sys-down [%]
0.05	0.945	0.000	0.000	0.000	0.000
0.45	1.072	0.000	0.000	0.000	0.000
1.08	1.344	0.000	0.000	0.000	0.000
1.45	1.000	0.000	0.000	0.000	0.000
1.95	1.398	0.000	0.000	0.000	0.000
2.42	1.791	0.000	0.000	0.000	0.000

Systematics Source: FT_EFF_Eigen_C_1

bin-center	SF	sys-up	sys-down	sys-up [%]	sys-down [%]
0.05	0.945	0.000	0.000	0.000	0.000
0.45	1.072	0.000	0.000	0.000	0.000
1.08	1.344	0.000	0.000	0.000	0.000
1.45	1.000	0.000	0.000	0.000	0.000
1.95	1.398	0.000	0.000	0.000	0.000
2.42	1.791	0.000	0.000	0.000	0.000

Systematics Source: FT_EFF_Eigen_C_2

bin-center	SF	sys-up	sys-down	sys-up [%]	sys-down [%]
0.05	0.945	0.000	0.000	0.000	0.000
0.45	1.072	0.000	0.000	0.000	0.000
1.08	1.344	0.000	0.000	0.000	0.000
1.45	1.000	0.000	0.000	0.000	0.000
1.95	1.398	0.000	0.000	0.000	0.000
2.42	1.791	0.000	0.000	0.000	0.000

Systematics Source: JET_fJvtEfficiency

bin-center	SF	sys-up	sys-down	sys-up [%]	sys-down [%]
0.05	0.945	0.000	0.000	0.000	0.000
0.45	1.072	0.000	0.000	0.000	0.000
1.08	1.344	0.000	0.000	0.000	0.000
1.45	1.000	0.000	0.000	0.000	0.000
1.95	1.398	0.000	0.000	0.000	0.000
2.42	1.791	0.000	0.000	0.000	0.000

Systematics Source: FT_EFF_Eigen_B_1

bin-center	SF	sys-up	sys-down	sys-up [%]	sys-down [%]
0.05	0.945	0.000	0.000	0.000	0.000
0.45	1.072	0.000	0.000	0.000	0.000
1.08	1.344	0.000	0.000	0.000	0.000
1.45	1.000	0.000	0.000	0.000	0.000
1.95	1.398	0.000	0.000	0.000	0.000
2.42	1.791	0.000	0.000	0.000	0.000

Systematics Source: FT_EFF_Eigen_B_0

bin-center	SF	sys-up	sys-down	sys-up [%]	sys-down [%]
0.05	0.945	0.000	0.000	0.000	0.000
0.45	1.072	0.000	0.000	0.000	0.000
1.08	1.344	0.000	0.000	0.000	0.000
1.45	1.000	0.000	0.000	0.000	0.000
1.95	1.398	0.000	0.000	0.000	0.000
2.42	1.791	0.000	0.000	0.000	0.000

Systematics Source: FT_EFF_Eigen_B_2

bin-center	SF	sys-up	sys-down	sys-up [%]	sys-down [%]
0.05	0.945	0.000	0.000	0.000	0.000
0.45	1.072	0.000	0.000	0.000	0.000
1.08	1.344	0.000	0.000	0.000	0.000
1.45	1.000	0.000	0.000	0.000	0.000
1.95	1.398	0.000	0.000	0.000	0.000
2.42	1.791	0.000	0.000	0.000	0.000

Systematics Source: Wjets_kf_SS

bin-center	SF	sys-up	sys-down	sys-up [%]	sys-down [%]
0.05	0.945	0.000	0.000	0.000	0.000
0.45	1.072	0.000	0.000	0.000	0.000
1.08	1.344	0.000	0.000	0.000	0.000
1.45	1.000	0.000	0.000	0.000	0.000
1.95	1.398	0.000	0.000	0.000	0.000
2.42	1.791	0.000	0.000	0.000	0.000

Systematics Source: EL_EFF_Reco_TOTAL_1NPCOR_PLUS_UNCOR

bin-center	SF	sys-up	sys-down	sys-up [%]	sys-down [%]
0.05	0.945	-0.000	0.000	-0.005	0.005
0.45	1.072	-0.000	0.000	-0.007	0.007
1.08	1.344	-0.000	0.000	-0.003	0.003
1.45	1.000	0.000	0.000	0.000	0.000
1.95	1.398	-0.000	0.000	-0.005	0.005
2.42	1.791	-0.000	0.000	-0.007	0.007

Systematics Source: FT_EFF_extrapolation_from_charm

bin-center	SF	sys-up	sys-down	sys-up [%]	sys-down [%]
0.05	0.945	0.000	0.000	0.000	0.000
0.45	1.072	0.000	0.000	0.000	0.000
1.08	1.344	0.000	0.000	0.000	0.000
1.45	1.000	0.000	0.000	0.000	0.000
1.95	1.398	0.000	0.000	0.000	0.000
2.42	1.791	0.000	0.000	0.000	0.000

Systematics Source: EL_EFF_ID_TOTAL_1NPCOR_PLUS_UNCOR

bin-center	SF	sys-up	sys-down	sys-up [%]	sys-down [%]
0.05	0.945	-0.000	0.000	-0.037	0.038
0.45	1.072	-0.001	0.001	-0.064	0.065
1.08	1.344	-0.000	0.000	-0.034	0.034
1.45	1.000	0.000	0.000	0.000	0.000
1.95	1.398	-0.001	0.001	-0.045	0.046
2.42	1.791	-0.000	0.000	-0.017	0.018

Systematics Source: FT_EFF_extrapolation

bin-center	SF	sys-up	sys-down	sys-up [%]	sys-down [%]
0.05	0.945	0.000	0.000	0.000	0.000
0.45	1.072	0.000	0.000	0.000	0.000
1.08	1.344	0.000	0.000	0.000	0.000
1.45	1.000	0.000	0.000	0.000	0.000
1.95	1.398	0.000	0.000	0.000	0.000
2.42	1.791	0.000	0.000	0.000	0.000

Table A.1.3: Tables of systematic (sys) uncertainties on the scale factor (SF), in the centre of each bin of η. The systematic uncertainties are detailed individually for each variation, and uncertainties are also expressed as a percentage of the SF. The tables are given for the eBDT @ 75% eVeto algorithm, with a medium tau ID applied.

Systematics Source: EL_EFF_Trigger_TOTAL_1NPCOR_PLUS_UNCOR

bin-center	SF	sys-up	sys-down	sys-up [%]	sys-down [%]
0.05	0.898	-0.000	0.000	-0.017	0.017
0.45	1.045	-0.000	0.000	-0.016	0.016
1.08	1.360	-0.000	0.000	-0.006	0.006
1.45	1.000	0.000	0.000	0.000	0.000
1.95	1.359	-0.000	0.000	-0.003	0.003
2.42	1.876	-0.000	0.000	-0.002	0.002

Systematics Source: EG_SCALE_ALLCORR

bin-center	SF	sys-up	sys-down	sys-up [%]	sys-down [%]
0.05	0.898	0.002	-0.004	0.232	-0.410
0.45	1.045	0.002	-0.003	0.229	-0.281
1.08	1.360	0.004	-0.001	0.314	-0.090
1.45	1.000	0.000	0.000	0.000	0.000
1.95	1.359	-0.003	0.001	-0.199	0.086
2.42	1.876	-0.012	-0.004	-0.645	-0.198

Systematics Source: EG_RESOLUTION_ALL

bin-center	SF	sys-up	sys-down	sys-up [%]	sys-down [%]
0.05	0.898	0.003	-0.005	0.353	-0.603
0.45	1.045	-0.000	-0.002	-0.005	-0.177
1.08	1.360	0.002	0.001	0.160	0.059
1.45	1.000	0.000	0.000	0.000	0.000
1.95	1.359	-0.001	-0.001	-0.065	-0.081
2.42	1.876	0.005	0.001	0.291	0.048

Systematics Source: Wjets_kf_OS

bin-center	SF	sys-up	sys-down	sys-up [%]	sys-down [%]
0.05	0.898	-0.001	0.000	-0.074	0.000
0.45	1.045	-0.001	0.000	-0.081	0.000
1.08	1.360	-0.001	0.000	-0.090	0.000
1.45	1.000	0.000	0.000	0.000	0.000
1.95	1.359	-0.004	0.000	-0.283	0.000
2.42	1.876	-0.005	0.000	-0.248	0.000

Systematics Source: RQCD

bin-center	SF	sys-up	sys-down	sys-up [%]	sys-down [%]
0.05	0.898	-0.004	0.004	-0.432	0.431
0.45	1.045	-0.004	0.004	-0.365	0.364
1.08	1.360	-0.001	0.001	-0.100	0.100
1.45	1.000	0.000	0.000	0.000	0.000
1.95	1.359	-0.003	0.003	-0.201	0.199
2.42	1.876	-0.004	0.004	-0.233	0.231

Systematics Source: EL_EFF_Iso_TOTAL_1NPCOR_PLUS_UNCOR

bin-center	SF	sys-up	sys-down	sys-up [%]	sys-down [%]
0.05	0.898	-0.000	0.000	-0.004	0.004
0.45	1.045	-0.000	0.000	-0.004	0.004
1.08	1.360	0.000	-0.000	0.001	-0.001
1.45	1.000	0.000	0.000	0.000	0.000
1.95	1.359	0.000	-0.000	0.001	-0.001
2.42	1.876	0.000	-0.000	0.004	-0.004

Systematics Source: PRW_DATASF

bin-center	SF	sys-up	sys-down	sys-up [%]	sys-down [%]
0.05	0.898	-0.013	-0.013	-1.418	-1.418
0.45	1.045	-0.007	-0.007	-0.647	-0.647
1.08	1.360	-0.015	-0.015	-1.070	-1.070
1.45	1.000	0.000	0.000	0.000	0.000
1.95	1.359	-0.012	-0.012	-0.848	-0.848
2.42	1.876	-0.025	-0.025	-1.315	-1.315

Systematics Source: FT_EFF_Eigen_Light_3

bin-center	SF	sys-up	sys-down	sys-up [%]	sys-down [%]
0.05	0.898	0.000	0.000	0.000	0.000
0.45	1.045	0.000	0.000	0.000	0.000
1.08	1.360	0.000	0.000	0.000	0.000
1.45	1.000	0.000	0.000	0.000	0.000
1.95	1.359	0.000	0.000	0.000	0.000
2.42	1.876	0.000	0.000	0.000	0.000

Systematics Source: FT_EFF_Eigen_Light_2

bin-center	SF	sys-up	sys-down	sys-up [%]	sys-down [%]
0.05	0.898	0.000	0.000	0.000	0.000
0.45	1.045	0.000	0.000	0.000	0.000
1.08	1.360	0.000	0.000	0.000	0.000
1.45	1.000	0.000	0.000	0.000	0.000
1.95	1.359	0.000	0.000	0.000	0.000
2.42	1.876	0.000	0.000	0.000	0.000

Systematics Source: FT_EFF_Eigen_Light_1

bin-center	SF	sys-up	sys-down	sys-up [%]	sys-down [%]
0.05	0.898	0.000	0.000	0.000	0.000
0.45	1.045	0.000	0.000	0.000	0.000
1.08	1.360	0.000	0.000	0.000	0.000
1.45	1.000	0.000	0.000	0.000	0.000
1.95	1.359	0.000	0.000	0.000	0.000
2.42	1.876	0.000	0.000	0.000	0.000

Systematics Source: FT_EFF_Eigen_Light_0

bin-center	SF	sys-up	sys-down	sys-up [%]	sys-down [%]
0.05	0.898	0.000	0.000	0.000	0.000
0.45	1.045	0.000	0.000	0.000	0.000
1.08	1.360	0.000	0.000	0.000	0.000
1.45	1.000	0.000	0.000	0.000	0.000
1.95	1.359	0.000	0.000	0.000	0.000
2.42	1.876	0.000	0.000	0.000	0.000

Systematics Source: JET_JvtEfficiency

bin-center	SF	sys-up	sys-down	sys-up [%]	sys-down [%]
0.05	0.898	-0.000	0.000	-0.010	0.010
0.45	1.045	-0.000	0.000	-0.008	0.008
1.08	1.360	-0.000	0.000	-0.008	0.008
1.45	1.000	0.000	0.000	0.000	0.000
1.95	1.359	-0.000	0.000	-0.006	0.006
2.42	1.876	-0.000	0.000	-0.017	0.017

Systematics Source: FT_EFF_Eigen_Light_4

bin-center	SF	sys-up	sys-down	sys-up [%]	sys-down [%]
0.05	0.898	0.000	0.000	0.000	0.000
0.45	1.045	0.000	0.000	0.000	0.000
1.08	1.360	0.000	0.000	0.000	0.000
1.45	1.000	0.000	0.000	0.000	0.000
1.95	1.359	0.000	0.000	0.000	0.000
2.42	1.876	0.000	0.000	0.000	0.000

Systematics Source: FT_EFF_Eigen_C_0

bin-center	SF	sys-up	sys-down	sys-up [%]	sys-down [%]
0.05	0.898	0.000	0.000	0.000	0.000
0.45	1.045	0.000	0.000	0.000	0.000
1.08	1.360	0.000	0.000	0.000	0.000
1.45	1.000	0.000	0.000	0.000	0.000
1.95	1.359	0.000	0.000	0.000	0.000
2.42	1.876	0.000	0.000	0.000	0.000

Systematics Source: FT_EFF_Eigen_C_1

bin-center	SF	sys-up	sys-down	sys-up [%]	sys-down [%]
0.05	0.898	0.000	0.000	0.000	0.000
0.45	1.045	0.000	0.000	0.000	0.000
1.08	1.360	0.000	0.000	0.000	0.000
1.45	1.000	0.000	0.000	0.000	0.000
1.95	1.359	0.000	0.000	0.000	0.000
2.42	1.876	0.000	0.000	0.000	0.000

Systematics Source: FT_EFF_Eigen_C_2

bin-center	SF	sys-up	sys-down	sys-up [%]	sys-down [%]
0.05	0.898	0.000	0.000	0.000	0.000
0.45	1.045	0.000	0.000	0.000	0.000
1.08	1.360	0.000	0.000	0.000	0.000
1.45	1.000	0.000	0.000	0.000	0.000
1.95	1.359	0.000	0.000	0.000	0.000
2.42	1.876	0.000	0.000	0.000	0.000

Systematics Source: JET_fJvtEfficiency

bin-center	SF	sys-up	sys-down	sys-up [%]	sys-down [%]
0.05	0.898	0.000	0.000	0.000	0.000
0.45	1.045	0.000	0.000	0.000	0.000
1.08	1.360	0.000	0.000	0.000	0.000
1.45	1.000	0.000	0.000	0.000	0.000
1.95	1.359	0.000	0.000	0.000	0.000
2.42	1.876	0.000	0.000	0.000	0.000

Systematics Source: FT_EFF_Eigen_B_1

bin-center	SF	sys-up	sys-down	sys-up [%]	sys-down [%]
0.05	0.898	0.000	0.000	0.000	0.000
0.45	1.045	0.000	0.000	0.000	0.000
1.08	1.360	0.000	0.000	0.000	0.000
1.45	1.000	0.000	0.000	0.000	0.000
1.95	1.359	0.000	0.000	0.000	0.000
2.42	1.876	0.000	0.000	0.000	0.000

Systematics Source: FT_EFF_Eigen_B_0

bin-center	SF	sys-up	sys-down	sys-up [%]	sys-down [%]
0.05	0.898	0.000	0.000	0.000	0.000
0.45	1.045	0.000	0.000	0.000	0.000
1.08	1.360	0.000	0.000	0.000	0.000
1.45	1.000	0.000	0.000	0.000	0.000
1.95	1.359	0.000	0.000	0.000	0.000
2.42	1.876	0.000	0.000	0.000	0.000

Systematics Source: FT_EFF_Eigen_B_2

bin-center	SF	sys-up	sys-down	sys-up [%]	sys-down [%]
0.05	0.898	0.000	0.000	0.000	0.000
0.45	1.045	0.000	0.000	0.000	0.000
1.08	1.360	0.000	0.000	0.000	0.000
1.45	1.000	0.000	0.000	0.000	0.000
1.95	1.359	0.000	0.000	0.000	0.000
2.42	1.876	0.000	0.000	0.000	0.000

Systematics Source: Wjets_kf_SS

bin-center	SF	sys-up	sys-down	sys-up [%]	sys-down [%]
0.05	0.898	0.000	0.000	0.000	0.000
0.45	1.045	0.000	0.000	0.000	0.000
1.08	1.360	0.000	0.000	0.000	0.000
1.45	1.000	0.000	0.000	0.000	0.000
1.95	1.359	0.000	0.000	0.000	0.000
2.42	1.876	0.000	0.000	0.000	0.000

Systematics Source: EL_EFF_Reco_TOTAL_1NPCOR_PLUS_UNCOR

bin-center	SF	sys-up	sys-down	sys-up [%]	sys-down [%]
0.05	0.898	-0.000	0.000	-0.004	0.004
0.45	1.045	-0.000	0.000	-0.005	0.005
1.08	1.360	-0.000	0.000	-0.003	0.003
1.45	1.000	0.000	0.000	0.000	0.000
1.95	1.359	-0.000	0.000	-0.003	0.003
2.42	1.876	-0.000	0.000	-0.003	0.003

Systematics Source: FT_EFF_extrapolation_from_charm

bin-center	SF	sys-up	sys-down	sys-up [%]	sys-down [%]
0.05	0.898	0.000	0.000	0.000	0.000
0.45	1.045	0.000	0.000	0.000	0.000
1.08	1.360	0.000	0.000	0.000	0.000
1.45	1.000	0.000	0.000	0.000	0.000
1.95	1.359	0.000	0.000	0.000	0.000
2.42	1.876	0.000	0.000	0.000	0.000

Systematics Source: EL_EFF_ID_TOTAL_1NPCOR_PLUS_UNCOR

bin-center	SF	sys-up	sys-down	sys-up [%]	sys-down [%]
0.05	0.898	-0.000	0.000	-0.031	0.031
0.45	1.045	-0.001	0.001	-0.054	0.055
1.08	1.360	-0.000	0.000	-0.029	0.030
1.45	1.000	0.000	0.000	0.000	0.000
1.95	1.359	-0.001	0.001	-0.037	0.037
2.42	1.876	-0.000	0.000	-0.010	0.010

Systematics Source: FT_EFF_extrapolation

bin-center	SF	sys-up	sys-down	sys-up [%]	sys-down [%]
0.05	0.898	0.000	0.000	0.000	0.000
0.45	1.045	0.000	0.000	0.000	0.000
1.08	1.360	0.000	0.000	0.000	0.000
1.45	1.000	0.000	0.000	0.000	0.000
1.95	1.359	0.000	0.000	0.000	0.000
2.42	1.876	0.000	0.000	0.000	0.000

Table A.1.4: Tables of systematic (sys) uncertainties on the scale factor (SF), in the centre of each bin of η. The systematic uncertainties are detailed individually for each variation, and uncertainties are also expressed as a percentage of the SF. The tables are given for the eBDT @ 85% eVeto algorithm, with a medium tau ID applied.

Systematics Source: EL_EFF_Trigger_TOTAL_1NPCOR_PLUS_UNCOR

bin-center	SF	sys-up	sys-down	sys-up [%]	sys-down [%]
0.05	0.864	-0.000	0.000	-0.013	0.013
0.45	1.056	-0.000	0.000	-0.011	0.011
1.08	1.489	-0.000	0.000	-0.004	0.004
1.45	1.000	0.000	0.000	0.000	0.000
1.95	1.483	-0.000	0.000	-0.003	0.003
2.42	2.066	-0.000	0.000	-0.001	0.001

Systematics Source: EG_SCALE_ALLCORR

bin-center	SF	sys-up	sys-down	sys-up [%]	sys-down [%]
0.05	0.864	0.002	-0.002	0.215	-0.225
0.45	1.056	0.002	-0.003	0.224	-0.326
1.08	1.489	0.003	-0.001	0.234	-0.080
1.45	1.000	0.000	0.000	0.000	0.000
1.95	1.483	0.001	-0.001	0.071	-0.055
2.42	2.066	-0.000	-0.004	-0.022	-0.173

Systematics Source: EG_RESOLUTION_ALL

bin-center	SF	sys-up	sys-down	sys-up [%]	sys-down [%]
0.05	0.864	-0.000	-0.001	-0.032	-0.097
0.45	1.056	0.000	0.000	0.021	0.041
1.08	1.489	0.001	0.001	0.074	0.038
1.45	1.000	0.000	0.000	0.000	0.000
1.95	1.483	0.000	-0.002	0.014	-0.121
2.42	2.066	-0.007	0.013	-0.319	0.653

Systematics Source: Wjets_kf_OS

bin-center	SF	sys-up	sys-down	sys-up [%]	sys-down [%]
0.05	0.864	-0.000	0.000	-0.035	0.000
0.45	1.056	-0.001	0.000	-0.047	0.000
1.08	1.489	-0.001	0.000	-0.055	0.000
1.45	1.000	0.000	0.000	0.000	0.000
1.95	1.483	-0.002	0.000	-0.153	0.000
2.42	2.066	-0.002	0.000	-0.087	0.000

Systematics Source: RQCD

bin-center	SF	sys-up	sys-down	sys-up [%]	sys-down [%]
0.05	0.864	-0.002	0.002	-0.186	0.186
0.45	1.056	-0.002	0.002	-0.164	0.164
1.08	1.489	-0.000	0.000	-0.033	0.033
1.45	1.000	0.000	0.000	0.000	0.000
1.95	1.483	-0.001	0.001	-0.073	0.073
2.42	2.066	-0.000	0.000	-0.004	0.004

Systematics Source: EL_EFF_Iso_TOTAL_1NPCOR_PLUS_UNCOR

bin-center	SF	sys-up	sys-down	sys-up [%]	sys-down [%]
0.05	0.864	-0.000	0.000	-0.002	0.002
0.45	1.056	-0.000	0.000	-0.002	0.002
1.08	1.489	0.000	-0.000	0.001	-0.001
1.45	1.000	0.000	0.000	0.000	0.000
1.95	1.483	0.000	-0.000	0.001	-0.001
2.42	2.066	0.000	-0.000	0.003	-0.003

Systematics Source: PRW_DATASF

bin-center	SF	sys-up	sys-down	sys-up [%]	sys-down [%]
0.05	0.864	-0.011	-0.011	-1.301	-1.301
0.45	1.056	-0.011	-0.011	-1.074	-1.074
1.08	1.489	-0.021	-0.021	-1.395	-1.395
1.45	1.000	0.000	0.000	0.000	0.000
1.95	1.483	-0.019	-0.019	-1.312	-1.312
2.42	2.066	-0.035	-0.035	-1.682	-1.682

Systematics Source: FT_EFF_Eigen_Light_3

bin-center	SF	sys-up	sys-down	sys-up [%]	sys-down [%]
0.05	0.864	0.000	0.000	0.000	0.000
0.45	1.056	0.000	0.000	0.000	0.000
1.08	1.489	0.000	0.000	0.000	0.000
1.45	1.000	0.000	0.000	0.000	0.000
1.95	1.483	0.000	0.000	0.000	0.000
2.42	2.066	0.000	0.000	0.000	0.000

Systematics Source: FT_EFF_Eigen_Light_2

bin-center	SF	sys-up	sys-down	sys-up [%]	sys-down [%]
0.05	0.864	0.000	0.000	0.000	0.000
0.45	1.056	0.000	0.000	0.000	0.000
1.08	1.489	0.000	0.000	0.000	0.000
1.45	1.000	0.000	0.000	0.000	0.000
1.95	1.483	0.000	0.000	0.000	0.000
2.42	2.066	0.000	0.000	0.000	0.000

Systematics Source: FT_EFF_Eigen_Light_1

bin-center	SF	sys-up	sys-down	sys-up [%]	sys-down [%]
0.05	0.864	0.000	0.000	0.000	0.000
0.45	1.056	0.000	0.000	0.000	0.000
1.08	1.489	0.000	0.000	0.000	0.000
1.45	1.000	0.000	0.000	0.000	0.000
1.95	1.483	0.000	0.000	0.000	0.000
2.42	2.066	0.000	0.000	0.000	0.000

Systematics Source: FT_EFF_Eigen_Light_0

bin-center	SF	sys-up	sys-down	sys-up [%]	sys-down [%]
0.05	0.864	0.000	0.000	0.000	0.000
0.45	1.056	0.000	0.000	0.000	0.000
1.08	1.489	0.000	0.000	0.000	0.000
1.45	1.000	0.000	0.000	0.000	0.000
1.95	1.483	0.000	0.000	0.000	0.000
2.42	2.066	0.000	0.000	0.000	0.000

Systematics Source: JET_JvtEfficiency

bin-center	SF	sys-up	sys-down	sys-up [%]	sys-down [%]
0.05	0.864	-0.000	0.000	-0.005	0.005
0.45	1.056	-0.000	0.000	-0.007	0.007
1.08	1.489	-0.000	0.000	-0.007	0.007
1.45	1.000	0.000	0.000	0.000	0.000
1.95	1.483	-0.000	0.000	-0.006	0.006
2.42	2.066	-0.000	0.000	-0.013	0.013

Systematics Source: FT_EFF_Eigen_Light_4

bin-center	SF	sys-up	sys-down	sys-up [%]	sys-down [%]
0.05	0.864	0.000	0.000	0.000	0.000
0.45	1.056	0.000	0.000	0.000	0.000
1.08	1.489	0.000	0.000	0.000	0.000
1.45	1.000	0.000	0.000	0.000	0.000
1.95	1.483	0.000	0.000	0.000	0.000
2.42	2.066	0.000	0.000	0.000	0.000

Systematics Source: FT_EFF_Eigen_C_0

bin-center	SF	sys-up	sys-down	sys-up [%]	sys-down [%]
0.05	0.864	0.000	0.000	0.000	0.000
0.45	1.056	0.000	0.000	0.000	0.000
1.08	1.489	0.000	0.000	0.000	0.000
1.45	1.000	0.000	0.000	0.000	0.000
1.95	1.483	0.000	0.000	0.000	0.000
2.42	2.066	0.000	0.000	0.000	0.000

Systematics Source: FT_EFF_Eigen_C_1

bin-center	SF	sys-up	sys-down	sys-up [%]	sys-down [%]
0.05	0.864	0.000	0.000	0.000	0.000
0.45	1.056	0.000	0.000	0.000	0.000
1.08	1.489	0.000	0.000	0.000	0.000
1.45	1.000	0.000	0.000	0.000	0.000
1.95	1.483	0.000	0.000	0.000	0.000
2.42	2.066	0.000	0.000	0.000	0.000

Systematics Source: FT_EFF_Eigen_C_2

bin-center	SF	sys-up	sys-down	sys-up [%]	sys-down [%]
0.05	0.864	0.000	0.000	0.000	0.000
0.45	1.056	0.000	0.000	0.000	0.000
1.08	1.489	0.000	0.000	0.000	0.000
1.45	1.000	0.000	0.000	0.000	0.000
1.95	1.483	0.000	0.000	0.000	0.000
2.42	2.066	0.000	0.000	0.000	0.000

Systematics Source: JET_fJvtEfficiency

bin-center	SF	sys-up	sys-down	sys-up [%]	sys-down [%]
0.05	0.864	0.000	0.000	0.000	0.000
0.45	1.056	0.000	0.000	0.000	0.000
1.08	1.489	0.000	0.000	0.000	0.000
1.45	1.000	0.000	0.000	0.000	0.000
1.95	1.483	0.000	0.000	0.000	0.000
2.42	2.066	0.000	0.000	0.000	0.000

Systematics Source: FT_EFF_Eigen_B_1

bin-center	SF	sys-up	sys-down	sys-up [%]	sys-down [%]
0.05	0.864	0.000	0.000	0.000	0.000
0.45	1.056	0.000	0.000	0.000	0.000
1.08	1.489	0.000	0.000	0.000	0.000
1.45	1.000	0.000	0.000	0.000	0.000
1.95	1.483	0.000	0.000	0.000	0.000
2.42	2.066	0.000	0.000	0.000	0.000

Systematics Source: FT_EFF_Eigen_B_0

bin-center	SF	sys-up	sys-down	sys-up [%]	sys-down [%]
0.05	0.864	0.000	0.000	0.000	0.000
0.45	1.056	0.000	0.000	0.000	0.000
1.08	1.489	0.000	0.000	0.000	0.000
1.45	1.000	0.000	0.000	0.000	0.000
1.95	1.483	0.000	0.000	0.000	0.000
2.42	2.066	0.000	0.000	0.000	0.000

Systematics Source: FT_EFF_Eigen_B_2

bin-center	SF	sys-up	sys-down	sys-up [%]	sys-down [%]
0.05	0.864	0.000	0.000	0.000	0.000
0.45	1.056	0.000	0.000	0.000	0.000
1.08	1.489	0.000	0.000	0.000	0.000
1.45	1.000	0.000	0.000	0.000	0.000
1.95	1.483	0.000	0.000	0.000	0.000
2.42	2.066	0.000	0.000	0.000	0.000

Systematics Source: Wjets_kf_SS

bin-center	SF	sys-up	sys-down	sys-up [%]	sys-down [%]
0.05	0.864	0.000	0.000	0.000	0.000
0.45	1.056	0.000	0.000	0.000	0.000
1.08	1.489	0.000	0.000	0.000	0.000
1.45	1.000	0.000	0.000	0.000	0.000
1.95	1.483	0.000	0.000	0.000	0.000
2.42	2.066	0.000	0.000	0.000	0.000

Systematics Source: EL_EFF_Reco_TOTAL_1NPCOR_PLUS_UNCOR

bin-center	SF	sys-up	sys-down	sys-up [%]	sys-down [%]
0.05	0.864	-0.000	0.000	-0.003	0.003
0.45	1.056	-0.000	0.000	-0.004	0.004
1.08	1.489	-0.000	0.000	-0.003	0.003
1.45	1.000	0.000	0.000	0.000	0.000
1.95	1.483	-0.000	0.000	-0.003	0.003
2.42	2.066	-0.000	0.000	-0.001	0.001

Systematics Source: FT_EFF_extrapolation_from_charm

bin-center	SF	sys-up	sys-down	sys-up [%]	sys-down [%]
0.05	0.864	0.000	0.000	0.000	0.000
0.45	1.056	0.000	0.000	0.000	0.000
1.08	1.489	0.000	0.000	0.000	0.000
1.45	1.000	0.000	0.000	0.000	0.000
1.95	1.483	0.000	0.000	0.000	0.000
2.42	2.066	0.000	0.000	0.000	0.000

Systematics Source: EL_EFF_ID_TOTAL_1NPCOR_PLUS_UNCOR

bin-center	SF	sys-up	sys-down	sys-up [%]	sys-down [%]
0.05	0.864	-0.000	0.000	-0.028	0.028
0.45	1.056	-0.000	0.000	-0.029	0.030
1.08	1.489	-0.000	0.000	-0.016	0.017
1.45	1.000	0.000	0.000	0.000	0.000
1.95	1.483	-0.000	0.000	-0.024	0.025
2.42	2.066	0.000	-0.000	0.003	-0.003

Systematics Source: FT_EFF_extrapolation

bin-center	SF	sys-up	sys-down	sys-up [%]	sys-down [%]
0.05	0.864	0.000	0.000	0.000	0.000
0.45	1.056	0.000	0.000	0.000	0.000
1.08	1.489	0.000	0.000	0.000	0.000
1.45	1.000	0.000	0.000	0.000	0.000
1.95	1.483	0.000	0.000	0.000	0.000
2.42	2.066	0.000	0.000	0.000	0.000

Table A.1.5: Tables of systematic (sys) uncertainties on the scale factor (SF), in the centre of each bin of η. The systematic uncertainties are detailed individually for each variation, and uncertainties are also expressed as a percentage of the SF. The tables are given for the eBDT @ 95% eVeto algorithm, with a medium tau ID applied.

Systematics Source: EL_EFF_Trigger_TOTAL_1NPCOR_PLUS_UNCOR

bin-center	SF	sys-up	sys-down	sys-up [%]	sys-down [%]
0.05	1.041	-0.000	0.000	-0.012	0.012
0.45	1.608	-0.000	0.000	-0.011	0.011
1.08	1.538	-0.000	0.000	-0.011	0.011
1.45	1.000	0.000	0.000	0.000	0.000
1.95	1.550	-0.000	0.000	-0.008	0.008
2.42	1.966	-0.000	0.000	-0.003	0.003

Systematics Source: EG_SCALE_ALLCORR

bin-center	SF	sys-up	sys-down	sys-up [%]	sys-down [%]
0.05	1.041	0.003	-0.005	0.261	-0.462
0.45	1.608	0.006	-0.003	0.368	-0.167
1.08	1.538	-0.002	-0.002	-0.123	-0.135
1.45	1.000	0.000	0.000	0.000	0.000
1.95	1.550	-0.004	0.006	-0.251	0.367
2.42	1.966	-0.014	0.005	-0.724	0.237

Systematics Source: EG_RESOLUTION_ALL

bin-center	SF	sys-up	sys-down	sys-up [%]	sys-down [%]
0.05	1.041	-0.001	0.001	-0.086	0.117
0.45	1.608	-0.004	-0.003	-0.263	-0.200
1.08	1.538	-0.003	-0.002	-0.171	-0.099
1.45	1.000	0.000	0.000	0.000	0.000
1.95	1.550	0.003	-0.001	0.190	-0.072
2.42	1.966	0.007	-0.021	0.340	-1.088

Systematics Source: Wjets_kf_OS

bin-center	SF	sys-up	sys-down	sys-up [%]	sys-down [%]
0.05	1.041	-0.001	0.000	-0.096	0.000
0.45	1.608	-0.002	0.000	-0.123	0.000
1.08	1.538	-0.002	0.000	-0.124	0.000
1.45	1.000	0.000	0.000	0.000	0.000
1.95	1.550	-0.004	0.000	-0.248	0.000
2.42	1.966	-0.006	0.000	-0.298	0.000

Systematics Source: RQCD

bin-center	SF	sys-up	sys-down	sys-up [%]	sys-down [%]
0.05	1.041	-0.015	0.015	-1.401	1.398
0.45	1.608	-0.020	0.020	-1.233	1.229
1.08	1.538	-0.008	0.008	-0.503	0.502
1.45	1.000	0.000	0.000	0.000	0.000
1.95	1.550	-0.009	0.009	-0.569	0.565
2.42	1.966	-0.019	0.019	-0.978	0.968

Systematics Source: EL_EFF_Iso_TOTAL_1NPCOR_PLUS_UNCOR

bin-center	SF	sys-up	sys-down	sys-up [%]	sys-down [%]
0.05	1.041	0.000	-0.000	0.003	-0.003
0.45	1.608	-0.000	0.000	-0.002	0.002
1.08	1.538	0.000	-0.000	0.001	-0.001
1.45	1.000	0.000	0.000	0.000	0.000
1.95	1.550	0.000	-0.000	0.001	-0.001
2.42	1.966	0.000	-0.000	0.004	-0.004

Systematics Source: PRW_DATASF

bin-center	SF	sys-up	sys-down	sys-up [%]	sys-down [%]
0.05	1.041	-0.017	-0.017	-1.642	-1.642
0.45	1.608	-0.010	-0.010	-0.615	-0.615
1.08	1.538	-0.019	-0.019	-1.251	-1.251
1.45	1.000	0.000	0.000	0.000	0.000
1.95	1.550	-0.015	-0.015	-0.973	-0.973
2.42	1.966	-0.006	-0.006	-0.325	-0.325

Systematics Source: FT_EFF_Eigen_Light_3

bin-center	SF	sys-up	sys-down	sys-up [%]	sys-down [%]
0.05	1.041	0.000	0.000	0.000	0.000
0.45	1.608	0.000	0.000	0.000	0.000
1.08	1.538	0.000	0.000	0.000	0.000
1.45	1.000	0.000	0.000	0.000	0.000
1.95	1.550	0.000	0.000	0.000	0.000
2.42	1.966	0.000	0.000	0.000	0.000

Systematics Source: FT_EFF_Eigen_Light_2

bin-center	SF	sys-up	sys-down	sys-up [%]	sys-down [%]
0.05	1.041	0.000	0.000	0.000	0.000
0.45	1.608	0.000	0.000	0.000	0.000
1.08	1.538	0.000	0.000	0.000	0.000
1.45	1.000	0.000	0.000	0.000	0.000
1.95	1.550	0.000	0.000	0.000	0.000
2.42	1.966	0.000	0.000	0.000	0.000

Systematics Source: FT_EFF_Eigen_Light_1

bin-center	SF	sys-up	sys-down	sys-up [%]	sys-down [%]
0.05	1.041	0.000	0.000	0.000	0.000
0.45	1.608	0.000	0.000	0.000	0.000
1.08	1.538	0.000	0.000	0.000	0.000
1.45	1.000	0.000	0.000	0.000	0.000
1.95	1.550	0.000	0.000	0.000	0.000
2.42	1.966	0.000	0.000	0.000	0.000

Systematics Source: FT_EFF_Eigen_Light_0

bin-center	SF	sys-up	sys-down	sys-up [%]	sys-down [%]
0.05	1.041	0.000	0.000	0.000	0.000
0.45	1.608	0.000	0.000	0.000	0.000
1.08	1.538	0.000	0.000	0.000	0.000
1.45	1.000	0.000	0.000	0.000	0.000
1.95	1.550	0.000	0.000	0.000	0.000
2.42	1.966	0.000	0.000	0.000	0.000

Systematics Source: JET_JvtEfficiency

bin-center	SF	sys-up	sys-down	sys-up [%]	sys-down [%]
0.05	1.041	0.000	-0.000	0.015	-0.015
0.45	1.608	0.000	-0.000	0.000	-0.000
1.08	1.538	0.000	-0.000	0.010	-0.010
1.45	1.000	0.000	0.000	0.000	0.000
1.95	1.550	0.000	-0.000	0.007	-0.007
2.42	1.966	0.000	-0.000	0.003	-0.003

Systematics Source: FT_EFF_Eigen_Light_4

bin-center	SF	sys-up	sys-down	sys-up [%]	sys-down [%]
0.05	1.041	0.000	0.000	0.000	0.000
0.45	1.608	0.000	0.000	0.000	0.000
1.08	1.538	0.000	0.000	0.000	0.000
1.45	1.000	0.000	0.000	0.000	0.000
1.95	1.550	0.000	0.000	0.000	0.000
2.42	1.966	0.000	0.000	0.000	0.000

Systematics Source: FT_EFF_Eigen_C_0

bin-center	SF	sys-up	sys-down	sys-up [%]	sys-down [%]
0.05	1.041	0.000	0.000	0.000	0.000
0.45	1.608	0.000	0.000	0.000	0.000
1.08	1.538	0.000	0.000	0.000	0.000
1.45	1.000	0.000	0.000	0.000	0.000
1.95	1.550	0.000	0.000	0.000	0.000
2.42	1.966	0.000	0.000	0.000	0.000

Systematics Source: FT_EFF_Eigen_C_1

bin-center	SF	sys-up	sys-down	sys-up [%]	sys-down [%]
0.05	1.041	0.000	0.000	0.000	0.000
0.45	1.608	0.000	0.000	0.000	0.000
1.08	1.538	0.000	0.000	0.000	0.000
1.45	1.000	0.000	0.000	0.000	0.000
1.95	1.550	0.000	0.000	0.000	0.000
2.42	1.966	0.000	0.000	0.000	0.000

Systematics Source: FT_EFF_Eigen_C_2

bin-center	SF	sys-up	sys-down	sys-up [%]	sys-down [%]
0.05	1.041	0.000	0.000	0.000	0.000
0.45	1.608	0.000	0.000	0.000	0.000
1.08	1.538	0.000	0.000	0.000	0.000
1.45	1.000	0.000	0.000	0.000	0.000
1.95	1.550	0.000	0.000	0.000	0.000
2.42	1.966	0.000	0.000	0.000	0.000

Systematics Source: JET_fJvtEfficiency

bin-center	SF	sys-up	sys-down	sys-up [%]	sys-down [%]
0.05	1.041	0.000	0.000	0.000	0.000
0.45	1.608	0.000	0.000	0.000	0.000
1.08	1.538	0.000	0.000	0.000	0.000
1.45	1.000	0.000	0.000	0.000	0.000
1.95	1.550	0.000	0.000	0.000	0.000
2.42	1.966	0.000	0.000	0.000	0.000

Systematics Source: FT_EFF_Eigen_B_1

bin-center	SF	sys-up	sys-down	sys-up [%]	sys-down [%]
0.05	1.041	0.000	0.000	0.000	0.000
0.45	1.608	0.000	0.000	0.000	0.000
1.08	1.538	0.000	0.000	0.000	0.000
1.45	1.000	0.000	0.000	0.000	0.000
1.95	1.550	0.000	0.000	0.000	0.000
2.42	1.966	0.000	0.000	0.000	0.000

Systematics Source: FT_EFF_Eigen_B_0

bin-center	SF	sys-up	sys-down	sys-up [%]	sys-down [%]
0.05	1.041	0.000	0.000	0.000	0.000
0.45	1.608	0.000	0.000	0.000	0.000
1.08	1.538	0.000	0.000	0.000	0.000
1.45	1.000	0.000	0.000	0.000	0.000
1.95	1.550	0.000	0.000	0.000	0.000
2.42	1.966	0.000	0.000	0.000	0.000

Systematics Source: FT_EFF_Eigen_B_2

bin-center	SF	sys-up	sys-down	sys-up [%]	sys-down [%]
0.05	1.041	0.000	0.000	0.000	0.000
0.45	1.608	0.000	0.000	0.000	0.000
1.08	1.538	0.000	0.000	0.000	0.000
1.45	1.000	0.000	0.000	0.000	0.000
1.95	1.550	0.000	0.000	0.000	0.000
2.42	1.966	0.000	0.000	0.000	0.000

Systematics Source: Wjets_kf_SS

bin-center	SF	sys-up	sys-down	sys-up [%]	sys-down [%]
0.05	1.041	0.000	0.000	0.000	0.000
0.45	1.608	0.000	0.000	0.000	0.000
1.08	1.538	0.000	0.000	0.000	0.000
1.45	1.000	0.000	0.000	0.000	0.000
1.95	1.550	0.000	0.000	0.000	0.000
2.42	1.966	0.000	0.000	0.000	0.000

Systematics Source: EL_EFF_Reco_TOTAL_1NPCOR_PLUS_UNCOR

bin-center	SF	sys-up	sys-down	sys-up [%]	sys-down [%]
0.05	1.041	-0.000	0.000	-0.001	0.001
0.45	1.608	-0.000	0.000	-0.003	0.003
1.08	1.538	-0.000	0.000	-0.002	0.002
1.45	1.000	0.000	0.000	0.000	0.000
1.95	1.550	-0.000	0.000	-0.001	0.001
2.42	1.966	0.000	-0.000	0.004	-0.004

Systematics Source: FT_EFF_extrapolation_from_charm

bin-center	SF	sys-up	sys-down	sys-up [%]	sys-down [%]
0.05	1.041	0.000	0.000	0.000	0.000
0.45	1.608	0.000	0.000	0.000	0.000
1.08	1.538	0.000	0.000	0.000	0.000
1.45	1.000	0.000	0.000	0.000	0.000
1.95	1.550	0.000	0.000	0.000	0.000
2.42	1.966	0.000	0.000	0.000	0.000

Systematics Source: EL_EFF_ID_TOTAL_1NPCOR_PLUS_UNCOR

bin-center	SF	sys-up	sys-down	sys-up [%]	sys-down [%]
0.05	1.041	-0.000	0.000	-0.035	0.035
0.45	1.608	-0.001	0.001	-0.056	0.056
1.08	1.538	-0.001	0.001	-0.034	0.034
1.45	1.000	0.000	0.000	0.000	0.000
1.95	1.550	-0.000	0.000	-0.027	0.027
2.42	1.966	0.001	-0.001	0.038	-0.039

Systematics Source: FT_EFF_extrapolation

bin-center	SF	sys-up	sys-down	sys-up [%]	sys-down [%]
0.05	1.041	0.000	0.000	0.000	0.000
0.45	1.608	0.000	0.000	0.000	0.000
1.08	1.538	0.000	0.000	0.000	0.000
1.45	1.000	0.000	0.000	0.000	0.000
1.95	1.550	0.000	0.000	0.000	0.000
2.42	1.966	0.000	0.000	0.000	0.000

Table A.1.6: Tables of systematic (sys) uncertainties on the scale factor (SF), in the centre of each bin of η. The systematic uncertainties are detailed individually for each variation, and uncertainties are also expressed as a percentage of the SF. The tables are given for the eBDT @ 85% with eLLH eVeto algorithm, with a medium tau ID applied.

Systematics Source: EL_EFF_Trigger_TOTAL_1NPCOR_PLUS_UNCOR

bin-center	SF	sys-up	sys-down	sys-up [%]	sys-down [%]
0.05	0.761	-0.000	0.000	-0.008	0.008
0.45	1.378	-0.000	0.000	-0.008	0.008
1.08	1.472	-0.000	0.000	-0.009	0.009
1.45	1.000	0.000	0.000	0.000	0.000
1.95	1.481	-0.000	0.000	-0.006	0.006
2.42	2.085	-0.000	0.000	-0.007	0.007

Systematics Source: EG_SCALE_ALLCORR

bin-center	SF	sys-up	sys-down	sys-up [%]	sys-down [%]
0.05	0.761	0.000	-0.000	0.054	-0.045
0.45	1.378	0.005	-0.003	0.344	-0.216
1.08	1.472	-0.001	0.001	-0.039	0.034
1.45	1.000	0.000	0.000	0.000	0.000
1.95	1.481	-0.003	0.005	-0.173	0.317
2.42	2.085	-0.003	0.011	-0.146	0.534

Systematics Source: EG_RESOLUTION_ALL

bin-center	SF	sys-up	sys-down	sys-up [%]	sys-down [%]
0.05	0.761	-0.001	0.001	-0.133	0.167
0.45	1.378	-0.002	0.000	-0.116	0.018
1.08	1.472	-0.001	0.003	-0.085	0.173
1.45	1.000	0.000	0.000	0.000	0.000
1.95	1.481	0.003	-0.002	0.214	-0.165
2.42	2.085	-0.002	-0.014	-0.102	-0.654

Systematics Source: Wjets_kf_OS

bin-center	SF	sys-up	sys-down	sys-up [%]	sys-down [%]
0.05	0.761	-0.000	0.000	-0.032	0.000
0.45	1.378	-0.001	0.000	-0.087	0.000
1.08	1.472	-0.001	0.000	-0.101	0.000
1.45	1.000	0.000	0.000	0.000	0.000
1.95	1.481	-0.003	0.000	-0.196	0.000
2.42	2.085	-0.005	0.000	-0.239	0.000

Systematics Source: RQCD

bin-center	SF	sys-up	sys-down	sys-up [%]	sys-down [%]
0.05	0.761	-0.006	0.006	-0.751	0.751
0.45	1.378	-0.013	0.013	-0.947	0.945
1.08	1.472	-0.006	0.006	-0.399	0.398
1.45	1.000	0.000	0.000	0.000	0.000
1.95	1.481	-0.007	0.007	-0.451	0.448
2.42	2.085	-0.013	0.013	-0.613	0.608

Systematics Source: EL_EFF_Iso_TOTAL_1NPCOR_PLUS_UNCOR

bin-center	SF	sys-up	sys-down	sys-up [%]	sys-down [%]
0.05	0.761	0.000	-0.000	0.002	-0.002
0.45	1.378	-0.000	0.000	-0.001	0.001
1.08	1.472	0.000	-0.000	0.001	-0.001
1.45	1.000	0.000	0.000	0.000	0.000
1.95	1.481	0.000	-0.000	0.001	-0.001
2.42	2.085	0.000	-0.000	0.003	-0.003

Systematics Source: PRW_DATASF

bin-center	SF	sys-up	sys-down	sys-up [%]	sys-down [%]
0.05	0.761	-0.009	-0.009	-1.207	-1.207
0.45	1.378	-0.009	-0.009	-0.650	-0.650
1.08	1.472	-0.016	-0.016	-1.088	-1.088
1.45	1.000	0.000	0.000	0.000	0.000
1.95	1.481	-0.012	-0.012	-0.842	-0.842
2.42	2.085	-0.012	-0.012	-0.572	-0.572

Systematics Source: FT_EFF_Eigen_Light_3

bin-center	SF	sys-up	sys-down	sys-up [%]	sys-down [%]
0.05	0.761	0.000	0.000	0.000	0.000
0.45	1.378	0.000	0.000	0.000	0.000
1.08	1.472	0.000	0.000	0.000	0.000
1.45	1.000	0.000	0.000	0.000	0.000
1.95	1.481	0.000	0.000	0.000	0.000
2.42	2.085	0.000	0.000	0.000	0.000

Systematics Source: FT_EFF_Eigen_Light_2

bin-center	SF	sys-up	sys-down	sys-up [%]	sys-down [%]
0.05	0.761	0.000	0.000	0.000	0.000
0.45	1.378	0.000	0.000	0.000	0.000
1.08	1.472	0.000	0.000	0.000	0.000
1.45	1.000	0.000	0.000	0.000	0.000
1.95	1.481	0.000	0.000	0.000	0.000
2.42	2.085	0.000	0.000	0.000	0.000

Systematics Source: FT_EFF_Eigen_Light_1

bin-center	SF	sys-up	sys-down	sys-up [%]	sys-down [%]
0.05	0.761	0.000	0.000	0.000	0.000
0.45	1.378	0.000	0.000	0.000	0.000
1.08	1.472	0.000	0.000	0.000	0.000
1.45	1.000	0.000	0.000	0.000	0.000
1.95	1.481	0.000	0.000	0.000	0.000
2.42	2.085	0.000	0.000	0.000	0.000

Systematics Source: FT_EFF_Eigen_Light_0

bin-center	SF	sys-up	sys-down	sys-up [%]	sys-down [%]
0.05	0.761	0.000	0.000	0.000	0.000
0.45	1.378	0.000	0.000	0.000	0.000
1.08	1.472	0.000	0.000	0.000	0.000
1.45	1.000	0.000	0.000	0.000	0.000
1.95	1.481	0.000	0.000	0.000	0.000
2.42	2.085	0.000	0.000	0.000	0.000

Systematics Source: JET_JvtEfficiency

bin-center	SF	sys-up	sys-down	sys-up [%]	sys-down [%]
0.05	0.761	0.000	-0.000	0.013	-0.013
0.45	1.378	0.000	-0.000	0.004	-0.004
1.08	1.472	0.000	-0.000	0.010	-0.010
1.45	1.000	0.000	0.000	0.000	0.000
1.95	1.481	0.000	-0.000	0.005	-0.005
2.42	2.085	0.000	-0.000	0.002	-0.002

Systematics Source: FT_EFF_Eigen_Light_4

bin-center	SF	sys-up	sys-down	sys-up [%]	sys-down [%]
0.05	0.761	0.000	0.000	0.000	0.000
0.45	1.378	0.000	0.000	0.000	0.000
1.08	1.472	0.000	0.000	0.000	0.000
1.45	1.000	0.000	0.000	0.000	0.000
1.95	1.481	0.000	0.000	0.000	0.000
2.42	2.085	0.000	0.000	0.000	0.000

Systematics Source: FT_EFF_Eigen_C_0

bin-center	SF	sys-up	sys-down	sys-up [%]	sys-down [%]
0.05	0.761	0.000	0.000	0.000	0.000
0.45	1.378	0.000	0.000	0.000	0.000
1.08	1.472	0.000	0.000	0.000	0.000
1.45	1.000	0.000	0.000	0.000	0.000
1.95	1.481	0.000	0.000	0.000	0.000
2.42	2.085	0.000	0.000	0.000	0.000

Systematics Source: FT_EFF_Eigen_C_1

bin-center	SF	sys-up	sys-down	sys-up [%]	sys-down [%]
0.05	0.761	0.000	0.000	0.000	0.000
0.45	1.378	0.000	0.000	0.000	0.000
1.08	1.472	0.000	0.000	0.000	0.000
1.45	1.000	0.000	0.000	0.000	0.000
1.95	1.481	0.000	0.000	0.000	0.000
2.42	2.085	0.000	0.000	0.000	0.000

Systematics Source: FT_EFF_Eigen_C_2

bin-center	SF	sys-up	sys-down	sys-up [%]	sys-down [%]
0.05	0.761	0.000	0.000	0.000	0.000
0.45	1.378	0.000	0.000	0.000	0.000
1.08	1.472	0.000	0.000	0.000	0.000
1.45	1.000	0.000	0.000	0.000	0.000
1.95	1.481	0.000	0.000	0.000	0.000
2.42	2.085	0.000	0.000	0.000	0.000

Systematics Source: JET_fJvtEfficiency

bin-center	SF	sys-up	sys-down	sys-up [%]	sys-down [%]
0.05	0.761	0.000	0.000	0.000	0.000
0.45	1.378	0.000	0.000	0.000	0.000
1.08	1.472	0.000	0.000	0.000	0.000
1.45	1.000	0.000	0.000	0.000	0.000
1.95	1.481	0.000	0.000	0.000	0.000
2.42	2.085	0.000	0.000	0.000	0.000

Systematics Source: FT_EFF_Eigen_B_1

bin-center	SF	sys-up	sys-down	sys-up [%]	sys-down [%]
0.05	0.761	0.000	0.000	0.000	0.000
0.45	1.378	0.000	0.000	0.000	0.000
1.08	1.472	0.000	0.000	0.000	0.000
1.45	1.000	0.000	0.000	0.000	0.000
1.95	1.481	0.000	0.000	0.000	0.000
2.42	2.085	0.000	0.000	0.000	0.000

Systematics Source: FT_EFF_Eigen_B_0

bin-center	SF	sys-up	sys-down	sys-up [%]	sys-down [%]
0.05	0.761	0.000	0.000	0.000	0.000
0.45	1.378	0.000	0.000	0.000	0.000
1.08	1.472	0.000	0.000	0.000	0.000
1.45	1.000	0.000	0.000	0.000	0.000
1.95	1.481	0.000	0.000	0.000	0.000
2.42	2.085	0.000	0.000	0.000	0.000

Systematics Source: FT_EFF_Eigen_B_2

bin-center	SF	sys-up	sys-down	sys-up [%]	sys-down [%]
0.05	0.761	0.000	0.000	0.000	0.000
0.45	1.378	0.000	0.000	0.000	0.000
1.08	1.472	0.000	0.000	0.000	0.000
1.45	1.000	0.000	0.000	0.000	0.000
1.95	1.481	0.000	0.000	0.000	0.000
2.42	2.085	0.000	0.000	0.000	0.000

Systematics Source: Wjets_kf_SS

bin-center	SF	sys-up	sys-down	sys-up [%]	sys-down [%]
0.05	0.761	0.000	0.000	0.000	0.000
0.45	1.378	0.000	0.000	0.000	0.000
1.08	1.472	0.000	0.000	0.000	0.000
1.45	1.000	0.000	0.000	0.000	0.000
1.95	1.481	0.000	0.000	0.000	0.000
2.42	2.085	0.000	0.000	0.000	0.000

Systematics Source: EL_EFF_Reco_TOTAL_1NPCOR_PLUS_UNCOR

bin-center	SF	sys-up	sys-down	sys-up [%]	sys-down [%]
0.05	0.761	-0.000	0.000	-0.000	0.000
0.45	1.378	-0.000	0.000	-0.002	0.002
1.08	1.472	-0.000	0.000	-0.002	0.002
1.45	1.000	0.000	0.000	0.000	0.000
1.95	1.481	-0.000	0.000	-0.000	0.000
2.42	2.085	0.000	-0.000	0.002	-0.002

Systematics Source: FT_EFF_extrapolation_from_charm

bin-center	SF	sys-up	sys-down	sys-up [%]	sys-down [%]
0.05	0.761	0.000	0.000	0.000	0.000
0.45	1.378	0.000	0.000	0.000	0.000
1.08	1.472	0.000	0.000	0.000	0.000
1.45	1.000	0.000	0.000	0.000	0.000
1.95	1.481	0.000	0.000	0.000	0.000
2.42	2.085	0.000	0.000	0.000	0.000

Systematics Source: EL_EFF_ID_TOTAL_1NPCOR_PLUS_UNCOR

bin-center	SF	sys-up	sys-down	sys-up [%]	sys-down [%]
0.05	0.761	-0.000	0.000	-0.037	0.037
0.45	1.378	-0.001	0.001	-0.038	0.039
1.08	1.472	-0.000	0.000	-0.026	0.026
1.45	1.000	0.000	0.000	0.000	0.000
1.95	1.481	-0.000	0.000	-0.017	0.017
2.42	2.085	0.000	-0.000	0.017	-0.017

Systematics Source: FT_EFF_extrapolation

bin-center	SF	sys-up	sys-down	sys-up [%]	sys-down [%]
0.05	0.761	0.000	0.000	0.000	0.000
0.45	1.378	0.000	0.000	0.000	0.000
1.08	1.472	0.000	0.000	0.000	0.000
1.45	1.000	0.000	0.000	0.000	0.000
1.95	1.481	0.000	0.000	0.000	0.000
2.42	2.085	0.000	0.000	0.000	0.000

Table A.1.7: Tables of systematic (sys) uncertainties on the scale factor (SF), in the centre of each bin of η. The systematic uncertainties are detailed individually for each variation, and uncertainties are also expressed as a percentage of the SF. The tables are given for the eBDT @ 95% with eLLH eVeto algorithm, with a medium tau ID applied.

Appendix B: Search for new physics decaying into di-tau leptons

B.1 Event selection

Lepton	Trigger	Year
Electron	HLT_e24_lhmedium_L1EM20VH	2015
	HLT_e60_lhmedium	2015
	HLT_e120_lhloose	2015
	HLT_e26_lhtight_nod0_ivarloose	2016–2018
	HLT_e60_lhmedium_nod0	2016–2018
	HLT_e140_lhloose_nod0	2016–2018
Muon	HLT_mu20_iloose_L1MU15	2015
	HLT_mu26_ivarmedium	2016–2018
	HLT_mu50	2016–2018

Table B.1.1: List of CP-recommended single-lepton high-level triggers used in matching to each year of data-taking in the $\tau_{\text{lep}}\tau_{\text{had}}$ analysis. The p_{T} threshold for the triggers are the number given after the particle type (e or mu), often with additional quality and/or isolation requirements imposed.

```
### ttbar ###
mc16_13TeV.410470.PhPy8EG_A14_ttbar_hdamp258p75_nonallhad.deriv.DAOD_HIGG4D2.e6337_s3126_r10724_p3759
mc16_13TeV.410471.PhPy8EG_A14_ttbar_hdamp258p75_allhad.deriv.DAOD_HIGG4D2.e6337_s3126_r10724_p3759
mc16_13TeV.410472.PhPy8EG_A14_ttbar_hdamp258p75_dil.deriv.DAOD_HIGG4D2.e6348_s3126_r10724_p3759

### Zll ###
mc16_13TeV.361106.PowhegPythia8EvtGen_AZNLOCTEQ6L1_Zee.deriv.DAOD_HIGG4D2.e3601_s3126_r10724_p3759
mc16_13TeV.361107.PowhegPythia8EvtGen_AZNLOCTEQ6L1_Zmumu.deriv.DAOD_HIGG4D2.e3601_s3126_r10724_p3759
mc16_13TeV.361108.PowhegPythia8EvtGen_AZNLOCTEQ6L1_Ztautau.deriv.DAOD_HIGG4D2.e3601_s3126_r10724_p3759

### diboson ###
mc16_13TeV.363355.Sherpa_221_NNPDF30NNLO_ZqqZvv.deriv.DAOD_HIGG4D2.e5525_s3126_r10724_p3759
mc16_13TeV.363356.Sherpa_221_NNPDF30NNLO_ZqqZll.deriv.DAOD_HIGG4D2.e5525_s3126_r10724_p3759
mc16_13TeV.363357.Sherpa_221_NNPDF30NNLO_WqqZvv.deriv.DAOD_HIGG4D2.e5525_s3126_r10724_p3759
mc16_13TeV.363358.Sherpa_221_NNPDF30NNLO_WqqZll.deriv.DAOD_HIGG4D2.e5525_s3126_r10724_p3759
mc16_13TeV.363359.Sherpa_221_NNPDF30NNLO_WpqqWmlv.deriv.DAOD_HIGG4D2.e5583_s3126_r10724_p3759
mc16_13TeV.363360.Sherpa_221_NNPDF30NNLO_WplvWmqq.deriv.DAOD_HIGG4D2.e5983_s3126_r10724_p3759
mc16_13TeV.363489.Sherpa_221_NNPDF30NNLO_WlvZqq.deriv.DAOD_HIGG4D2.e5525_s3126_r10724_p3759
mc16_13TeV.364250.Sherpa_222_NNPDF30NNLO_llll.deriv.DAOD_HIGG4D2.e5894_s3126_r10724_p3759
mc16_13TeV.364253.Sherpa_222_NNPDF30NNLO_lllv.deriv.DAOD_HIGG4D2.e5916_s3126_r10724_p3759
mc16_13TeV.364254.Sherpa_222_NNPDF30NNLO_llvv.deriv.DAOD_HIGG4D2.e5916_s3126_r10724_p3759
mc16_13TeV.364255.Sherpa_222_NNPDF30NNLO_lvvv.deriv.DAOD_HIGG4D2.e5916_s3126_r10724_p3759

### single top ###
mc16_13TeV.410644.PowhegPythia8EvtGen_A14_singletop_schan_lept_top.deriv.DAOD_HIGG4D2.e6527_s3126_r10724_p3759
mc16_13TeV.410645.PowhegPythia8EvtGen_A14_singletop_schan_lept_antitop.deriv.DAOD_HIGG4D2.
    e6527_s3126_r10724_p3759
mc16_13TeV.410646.PowhegPythia8EvtGen_A14_Wt_DR_inclusive_top.deriv.DAOD_HIGG4D2.e6552_s3126_r10724_p3759
mc16_13TeV.410647.PowhegPythia8EvtGen_A14_Wt_DR_inclusive_antitop.deriv.DAOD_HIGG4D2.e6552_s3126_r10724_p3759
mc16_13TeV.410658.PhPy8EG_A14_tchan_BW50_lept_top.deriv.DAOD_HIGG4D2.e6671_s3126_r10724_p3759
mc16_13TeV.410659.PhPy8EG_A14_tchan_BW50_lept_antitop.deriv.DAOD_HIGG4D2.e6671_s3126_r10724_p3759

### ttbar (PMG systematics) ###
mc16_13TeV.410480.PhPy8EG_A14_ttbar_hdamp517p5_SingleLep.deriv.DAOD_HIGG4D2.e6454_a875_r10724_p3759
mc16_13TeV.410481.PhPy8EG_A14_ttbar_hdamp517p5_allhad.deriv.DAOD_HIGG4D2.e6520_a875_r10724_p3759
mc16_13TeV.410482.PhPy8EG_A14_ttbar_hdamp517p5_dil.deriv.DAOD_HIGG4D2.e6454_a875_r10724_p3759
```

```
mc16_13TeV.410464.aMcAtNloPy8EvtGen_MEN30NLO_A14N23LO_ttbar_noShWe_SingleLep.deriv.DAOD_HIGG4D2.
    e6762_a875_r10724_p3759
mc16_13TeV.410465.aMcAtNloPy8EvtGen_MEN30NLO_A14N23LO_ttbar_noShWe_dil.deriv.DAOD_HIGG4D2.e6762_a875_r10724_p3759
mc16_13TeV.410466.aMcAtNloPy8EvtGen_MEN30NLO_A14N23LO_ttbar_noShWe_AllHadronic.deriv.DAOD_HIGG4D2.
    e6762_a875_r10724_p3759
mc16_13TeV.410557.PowhegHerwig7EvtGen_H7UE_tt_hdamp258p75_704_SingleLep.deriv.DAOD_HIGG4D2.
    e6366_a875_r10724_p3759
mc16_13TeV.410558.PowhegHerwig7EvtGen_H7UE_tt_hdamp258p75_704_dil.deriv.DAOD_HIGG4D2.e6366_a875_r10724_p3759
mc16_13TeV.410559.PowhegHerwig7EvtGen_H7UE_tt_hdamp258p75_allhad.deriv.DAOD_HIGG4D2.e6567_a875_r10724_p3759

### bbH signals ###
mc16_13TeV.341856.aMcAtNloPythia8EvtGen_A14NNPDF23LO_bbH125_yb2_tautaulh.deriv.DAOD_HIGG4D2.
    e4482_a875_r10724_p3759
mc16_13TeV.341857.aMcAtNloPythia8EvtGen_A14NNPDF23LO_bbH150_yb2_tautaulh.deriv.DAOD_HIGG4D2.
    e5686_a875_r10724_p3759
mc16_13TeV.341858.aMcAtNloPythia8EvtGen_A14NNPDF23LO_bbH200_yb2_tautaulh.deriv.DAOD_HIGG4D2.
    e4482_a875_r10724_p3759
mc16_13TeV.341859.aMcAtNloPythia8EvtGen_A14NNPDF23LO_bbH250_yb2_tautaulh.deriv.DAOD_HIGG4D2.
    e5686_a875_r10724_p3759
mc16_13TeV.341860.aMcAtNloPythia8EvtGen_A14NNPDF23LO_bbH300_yb2_tautaulh.deriv.DAOD_HIGG4D2.
    e4482_a875_r10724_p3759
mc16_13TeV.341861.aMcAtNloPythia8EvtGen_A14NNPDF23LO_bbH350_yb2_tautaulh.deriv.DAOD_HIGG4D2.
    e4482_a875_r10724_p3759
mc16_13TeV.341862.aMcAtNloPythia8EvtGen_A14NNPDF23LO_bbH400_yb2_tautaulh.deriv.DAOD_HIGG4D2.
    e4298_a875_r10724_p3759
mc16_13TeV.341863.aMcAtNloPythia8EvtGen_A14NNPDF23LO_bbH500_yb2_tautaulh.deriv.DAOD_HIGG4D2.
    e4482_a875_r10724_p3759
mc16_13TeV.341864.aMcAtNloPythia8EvtGen_A14NNPDF23LO_bbH600_yb2_tautaulh.deriv.DAOD_HIGG4D2.
    e4482_a875_r10724_p3759
mc16_13TeV.341865.aMcAtNloPythia8EvtGen_A14NNPDF23LO_bbH700_yb2_tautaulh.deriv.DAOD_HIGG4D2.
    e4482_a875_r10724_p3759
mc16_13TeV.341866.aMcAtNloPythia8EvtGen_A14NNPDF23LO_bbH800_yb2_tautaulh.deriv.DAOD_HIGG4D2.
    e4482_a875_r10724_p3759
mc16_13TeV.341868.aMcAtNloPythia8EvtGen_A14NNPDF23LO_bbH1000_yb2_tautaulh.deriv.DAOD_HIGG4D2.
    e4298_a875_r10724_p3759
mc16_13TeV.341870.aMcAtNloPythia8EvtGen_A14NNPDF23LO_bbH1200_yb2_tautaulh.deriv.DAOD_HIGG4D2.
    e4482_a875_r10724_p3759
mc16_13TeV.341873.aMcAtNloPythia8EvtGen_A14NNPDF23LO_bbH1500_yb2_tautaulh.deriv.DAOD_HIGG4D2.
    e5314_a875_r10724_p3759
mc16_13TeV.345289.aMcAtNloPythia8EvtGen_A14NNPDF23LO_bbH2000_yb2_tautaulh.deriv.DAOD_HIGG4D2.
    e5686_a875_r10724_p3759
mc16_13TeV.345293.aMcAtNloPythia8EvtGen_A14NNPDF23LO_bbH2500_yb2_tautaulh.deriv.DAOD_HIGG4D2.
    e5686_a875_r10724_p3759

### ggH signals ###
mc16_13TeV.342305.PowhegPythia8EvtGen_CT10_AZNLOCTEQ6L1_ggH200W1_tautaulh.deriv.DAOD_HIGG4D2.
    e4284_s3126_r10724_p3759
mc16_13TeV.342308.PowhegPythia8EvtGen_CT10_AZNLOCTEQ6L1_ggH250W1_tautaulh.deriv.DAOD_HIGG4D2.
    e4284_s3126_r10724_p3759
mc16_13TeV.342310.PowhegPythia8EvtGen_CT10_AZNLOCTEQ6L1_ggH300W2_tautaulh.deriv.DAOD_HIGG4D2.
    e4284_s3126_r10724_p3759
mc16_13TeV.342312.PowhegPythia8EvtGen_CT10_AZNLOCTEQ6L1_ggH350W3_tautaulh.deriv.DAOD_HIGG4D2.
    e4284_s3126_r10724_p3759
mc16_13TeV.342314.PowhegPythia8EvtGen_CT10_AZNLOCTEQ6L1_ggH400W5_tautaulh.deriv.DAOD_HIGG4D2.
    e4284_s3126_r10724_p3759
mc16_13TeV.342316.PowhegPythia8EvtGen_CT10_AZNLOCTEQ6L1_ggH500W5_tautaulh.deriv.DAOD_HIGG4D2.
    e4284_s3126_r10724_p3759
mc16_13TeV.342318.PowhegPythia8EvtGen_CT10_AZNLOCTEQ6L1_ggH600W10_tautaulh.deriv.DAOD_HIGG4D2.
    e4284_s3126_r10724_p3759
mc16_13TeV.342320.PowhegPythia8EvtGen_CT10_AZNLOCTEQ6L1_ggH700W20_tautaulh.deriv.DAOD_HIGG4D2.
    e4284_s3126_r10724_p3759
mc16_13TeV.342322.PowhegPythia8EvtGen_CT10_AZNLOCTEQ6L1_ggH800W20_tautaulh.deriv.DAOD_HIGG4D2.
    e4284_s3126_r10724_p3759
mc16_13TeV.342326.PowhegPythia8EvtGen_CT10_AZNLOCTEQ6L1_ggH1000W30_tautaulh.deriv.DAOD_HIGG4D2.
    e4284_s3126_r10724_p3759
```

mc16_13TeV.342330.PowhegPythia8EvtGen_CT10_AZNLOCTEQ6L1_ggH1200W40_tautaulh.deriv.DAOD_HIGG4D2.
e4284_s3126_r10724_p3759
mc16_13TeV.342336.PowhegPythia8EvtGen_CT10_AZNLOCTEQ6L1_ggH1500W60_tautaulh.deriv.DAOD_HIGG4D2.
e4284_s3126_r10724_p3759
mc16_13TeV.345297.PowhegPythia8EvtGen_CT10_AZNLOCTEQ6L1_ggH2000W80_tautaulh.deriv.DAOD_HIGG4D2.
e5685_s3126_r10724_p3759
mc16_13TeV.345301.PowhegPythia8EvtGen_CT10_AZNLOCTEQ6L1_ggH2500W100_tautaulh.deriv.DAOD_HIGG4D2.
e5685_s3126_r10724_p3759

DYll (M slice)
mc16_13TeV.301000.PowhegPythia8EvtGen_AZNLOCTEQ6L1_DYee_120M180.deriv.DAOD_HIGG4D2.e3649_s3126_r10724_p3759
mc16_13TeV.301001.PowhegPythia8EvtGen_AZNLOCTEQ6L1_DYee_180M250.deriv.DAOD_HIGG4D2.e3649_s3126_r10724_p3759
mc16_13TeV.301002.PowhegPythia8EvtGen_AZNLOCTEQ6L1_DYee_250M400.deriv.DAOD_HIGG4D2.e3649_s3126_r10724_p3759
mc16_13TeV.301003.PowhegPythia8EvtGen_AZNLOCTEQ6L1_DYee_400M600.deriv.DAOD_HIGG4D2.e3649_s3126_r10724_p3759
mc16_13TeV.301004.PowhegPythia8EvtGen_AZNLOCTEQ6L1_DYee_600M800.deriv.DAOD_HIGG4D2.e3649_s3126_r10724_p3759
mc16_13TeV.301005.PowhegPythia8EvtGen_AZNLOCTEQ6L1_DYee_800M1000.deriv.DAOD_HIGG4D2.e3649_s3126_r10724_p3759
mc16_13TeV.301006.PowhegPythia8EvtGen_AZNLOCTEQ6L1_DYee_1000M1250.deriv.DAOD_HIGG4D2.e3649_s3126_r10724_p3759
mc16_13TeV.301007.PowhegPythia8EvtGen_AZNLOCTEQ6L1_DYee_1250M1500.deriv.DAOD_HIGG4D2.e3649_s3126_r10724_p3759
mc16_13TeV.301008.PowhegPythia8EvtGen_AZNLOCTEQ6L1_DYee_1500M1750.deriv.DAOD_HIGG4D2.e3649_s3126_r10724_p3759
mc16_13TeV.301009.PowhegPythia8EvtGen_AZNLOCTEQ6L1_DYee_1750M2000.deriv.DAOD_HIGG4D2.e3649_s3126_r10724_p3759
mc16_13TeV.301010.PowhegPythia8EvtGen_AZNLOCTEQ6L1_DYee_2000M2250.deriv.DAOD_HIGG4D2.e3649_s3126_r10724_p3759
mc16_13TeV.301011.PowhegPythia8EvtGen_AZNLOCTEQ6L1_DYee_2250M2500.deriv.DAOD_HIGG4D2.e3649_s3126_r10724_p3759
mc16_13TeV.301012.PowhegPythia8EvtGen_AZNLOCTEQ6L1_DYee_2500M2750.deriv.DAOD_HIGG4D2.e3649_s3126_r10724_p3759
mc16_13TeV.301013.PowhegPythia8EvtGen_AZNLOCTEQ6L1_DYee_2750M3000.deriv.DAOD_HIGG4D2.e3649_s3126_r10724_p3759
mc16_13TeV.301014.PowhegPythia8EvtGen_AZNLOCTEQ6L1_DYee_3000M3500.deriv.DAOD_HIGG4D2.e3649_s3126_r10724_p3759
mc16_13TeV.301015.PowhegPythia8EvtGen_AZNLOCTEQ6L1_DYee_3500M4000.deriv.DAOD_HIGG4D2.e3649_s3126_r10724_p3759
mc16_13TeV.301016.PowhegPythia8EvtGen_AZNLOCTEQ6L1_DYee_4000M4500.deriv.DAOD_HIGG4D2.e3649_s3126_r10724_p3759
mc16_13TeV.301017.PowhegPythia8EvtGen_AZNLOCTEQ6L1_DYee_4500M5000.deriv.DAOD_HIGG4D2.e3649_s3126_r10724_p3759
mc16_13TeV.301018.PowhegPythia8EvtGen_AZNLOCTEQ6L1_DYee_5000M.deriv.DAOD_HIGG4D2.e3649_s3126_r10724_p3759

mc16_13TeV.301020.PowhegPythia8EvtGen_AZNLOCTEQ6L1_DYmumu_120M180.deriv.DAOD_HIGG4D2.e3649_s3126_r10724_p3759
mc16_13TeV.301021.PowhegPythia8EvtGen_AZNLOCTEQ6L1_DYmumu_180M250.deriv.DAOD_HIGG4D2.e3649_s3126_r10724_p3759
mc16_13TeV.301022.PowhegPythia8EvtGen_AZNLOCTEQ6L1_DYmumu_250M400.deriv.DAOD_HIGG4D2.e3649_s3126_r10724_p3759
mc16_13TeV.301023.PowhegPythia8EvtGen_AZNLOCTEQ6L1_DYmumu_400M600.deriv.DAOD_HIGG4D2.e3649_s3126_r10724_p3759
mc16_13TeV.301024.PowhegPythia8EvtGen_AZNLOCTEQ6L1_DYmumu_600M800.deriv.DAOD_HIGG4D2.e3649_s3126_r10724_p3759
mc16_13TeV.301025.PowhegPythia8EvtGen_AZNLOCTEQ6L1_DYmumu_800M1000.deriv.DAOD_HIGG4D2.e3649_s3126_r10724_p3759
mc16_13TeV.301026.PowhegPythia8EvtGen_AZNLOCTEQ6L1_DYmumu_1000M1250.deriv.DAOD_HIGG4D2.e3649_s3126_r10724_p3759
mc16_13TeV.301027.PowhegPythia8EvtGen_AZNLOCTEQ6L1_DYmumu_1250M1500.deriv.DAOD_HIGG4D2.e3649_s3126_r10724_p3759
mc16_13TeV.301028.PowhegPythia8EvtGen_AZNLOCTEQ6L1_DYmumu_1500M1750.deriv.DAOD_HIGG4D2.e3649_s3126_r10724_p3759
mc16_13TeV.301029.PowhegPythia8EvtGen_AZNLOCTEQ6L1_DYmumu_1750M2000.deriv.DAOD_HIGG4D2.e3649_s3126_r10724_p3759
mc16_13TeV.301030.PowhegPythia8EvtGen_AZNLOCTEQ6L1_DYmumu_2000M2250.deriv.DAOD_HIGG4D2.e3649_s3126_r10724_p3759
mc16_13TeV.301031.PowhegPythia8EvtGen_AZNLOCTEQ6L1_DYmumu_2250M2500.deriv.DAOD_HIGG4D2.e3649_s3126_r10724_p3759
mc16_13TeV.301032.PowhegPythia8EvtGen_AZNLOCTEQ6L1_DYmumu_2500M2750.deriv.DAOD_HIGG4D2.e3649_s3126_r10724_p3759
mc16_13TeV.301033.PowhegPythia8EvtGen_AZNLOCTEQ6L1_DYmumu_2750M3000.deriv.DAOD_HIGG4D2.e3649_s3126_r10724_p3759
mc16_13TeV.301034.PowhegPythia8EvtGen_AZNLOCTEQ6L1_DYmumu_3000M3500.deriv.DAOD_HIGG4D2.e3649_s3126_r10724_p3759
mc16_13TeV.301035.PowhegPythia8EvtGen_AZNLOCTEQ6L1_DYmumu_3500M4000.deriv.DAOD_HIGG4D2.e3649_s3126_r10724_p3759
mc16_13TeV.301036.PowhegPythia8EvtGen_AZNLOCTEQ6L1_DYmumu_4000M4500.deriv.DAOD_HIGG4D2.e3649_s3126_r10724_p3759
mc16_13TeV.301037.PowhegPythia8EvtGen_AZNLOCTEQ6L1_DYmumu_4500M5000.deriv.DAOD_HIGG4D2.e3649_s3126_r10724_p3759
mc16_13TeV.301038.PowhegPythia8EvtGen_AZNLOCTEQ6L1_DYmumu_5000M.deriv.DAOD_HIGG4D2.e3649_s3126_r10724_p3759

mc16_13TeV.301040.PowhegPythia8EvtGen_AZNLOCTEQ6L1_DYtautau_120M180.deriv.DAOD_HIGG4D2.e3649_s3126_r10724_p3759
mc16_13TeV.301041.PowhegPythia8EvtGen_AZNLOCTEQ6L1_DYtautau_180M250.deriv.DAOD_HIGG4D2.e3649_s3126_r10724_p3759
mc16_13TeV.301042.PowhegPythia8EvtGen_AZNLOCTEQ6L1_DYtautau_250M400.deriv.DAOD_HIGG4D2.e3649_s3126_r10724_p3759
mc16_13TeV.301043.PowhegPythia8EvtGen_AZNLOCTEQ6L1_DYtautau_400M600.deriv.DAOD_HIGG4D2.e3649_s3126_r10724_p3759
mc16_13TeV.301044.PowhegPythia8EvtGen_AZNLOCTEQ6L1_DYtautau_600M800.deriv.DAOD_HIGG4D2.e3649_s3126_r10724_p3759
mc16_13TeV.301045.PowhegPythia8EvtGen_AZNLOCTEQ6L1_DYtautau_800M1000.deriv.DAOD_HIGG4D2.e3649_s3126_r10724_p3759
mc16_13TeV.301046.PowhegPythia8EvtGen_AZNLOCTEQ6L1_DYtautau_1000M1250.deriv.DAOD_HIGG4D2.e3649_s3126_r10724_p3759
mc16_13TeV.301047.PowhegPythia8EvtGen_AZNLOCTEQ6L1_DYtautau_1250M1500.deriv.DAOD_HIGG4D2.e3649_s3126_r10724_p3759
mc16_13TeV.301048.PowhegPythia8EvtGen_AZNLOCTEQ6L1_DYtautau_1500M1750.deriv.DAOD_HIGG4D2.e3649_s3126_r10724_p3759
mc16_13TeV.301049.PowhegPythia8EvtGen_AZNLOCTEQ6L1_DYtautau_1750M2000.deriv.DAOD_HIGG4D2.e3649_s3126_r10724_p3759
mc16_13TeV.301050.PowhegPythia8EvtGen_AZNLOCTEQ6L1_DYtautau_2000M2250.deriv.DAOD_HIGG4D2.e3649_s3126_r10724_p3759
mc16_13TeV.301051.PowhegPythia8EvtGen_AZNLOCTEQ6L1_DYtautau_2250M2500.deriv.DAOD_HIGG4D2.e3649_s3126_r10724_p3759
mc16_13TeV.301052.PowhegPythia8EvtGen_AZNLOCTEQ6L1_DYtautau_2500M2750.deriv.DAOD_HIGG4D2.e3649_s3126_r10724_p3759
mc16_13TeV.301053.PowhegPythia8EvtGen_AZNLOCTEQ6L1_DYtautau_2750M3000.deriv.DAOD_HIGG4D2.e3649_s3126_r10724_p3759
mc16_13TeV.301054.PowhegPythia8EvtGen_AZNLOCTEQ6L1_DYtautau_3000M3500.deriv.DAOD_HIGG4D2.e3649_s3126_r10724_p3759

```
mc16_13TeV.301055.PowhegPythia8EvtGen_AZNLOCTEQ6L1_DYtautau_3500M4000.deriv.DAOD_HIGG4D2.e3649_s3126_r10724_p3759
mc16_13TeV.301056.PowhegPythia8EvtGen_AZNLOCTEQ6L1_DYtautau_4000M4500.deriv.DAOD_HIGG4D2.e3649_s3126_r10724_p3759
mc16_13TeV.301057.PowhegPythia8EvtGen_AZNLOCTEQ6L1_DYtautau_4500M5000.deriv.DAOD_HIGG4D2.e3649_s3126_r10724_p3759
mc16_13TeV.301058.PowhegPythia8EvtGen_AZNLOCTEQ6L1_DYtautau_5000M.deriv.DAOD_HIGG4D2.e3649_s3126_r10724_p3759

### Zprime DYtautau LO signals ###
mc16_13TeV.305785.Pythia8EvtGen_A14NNPDF23LO_DYtautau_70M120.deriv.DAOD_HIGG4D2.e5200_s3126_r10724_p3759
mc16_13TeV.303437.Pythia8EvtGen_A14NNPDF23LO_DYtautau_120M180.deriv.DAOD_HIGG4D2.e4213_s3126_r10724_p3759
mc16_13TeV.303438.Pythia8EvtGen_A14NNPDF23LO_DYtautau_180M250.deriv.DAOD_HIGG4D2.e4213_s3126_r10724_p3759
mc16_13TeV.303439.Pythia8EvtGen_A14NNPDF23LO_DYtautau_250M400.deriv.DAOD_HIGG4D2.e4213_s3126_r10724_p3759
mc16_13TeV.303440.Pythia8EvtGen_A14NNPDF23LO_DYtautau_400M600.deriv.DAOD_HIGG4D2.e4213_s3126_r10724_p3759
mc16_13TeV.303441.Pythia8EvtGen_A14NNPDF23LO_DYtautau_600M800.deriv.DAOD_HIGG4D2.e4213_s3126_r10724_p3759
mc16_13TeV.303442.Pythia8EvtGen_A14NNPDF23LO_DYtautau_800M1000.deriv.DAOD_HIGG4D2.e4213_s3126_r10724_p3759
mc16_13TeV.303443.Pythia8EvtGen_A14NNPDF23LO_DYtautau_1000M1250.deriv.DAOD_HIGG4D2.e4213_s3126_r10724_p3759
mc16_13TeV.303444.Pythia8EvtGen_A14NNPDF23LO_DYtautau_1250M1500.deriv.DAOD_HIGG4D2.e4213_s3126_r10724_p3759
mc16_13TeV.303445.Pythia8EvtGen_A14NNPDF23LO_DYtautau_1500M1750.deriv.DAOD_HIGG4D2.e4213_s3126_r10724_p3759
mc16_13TeV.303446.Pythia8EvtGen_A14NNPDF23LO_DYtautau_1750M2000.deriv.DAOD_HIGG4D2.e4213_s3126_r10724_p3759
mc16_13TeV.303448.Pythia8EvtGen_A14NNPDF23LO_DYtautau_2250M2500.deriv.DAOD_HIGG4D2.e4213_s3126_r10724_p3759
mc16_13TeV.303449.Pythia8EvtGen_A14NNPDF23LO_DYtautau_2500M2750.deriv.DAOD_HIGG4D2.e4213_s3126_r10724_p3759
mc16_13TeV.303450.Pythia8EvtGen_A14NNPDF23LO_DYtautau_2750M3000.deriv.DAOD_HIGG4D2.e4213_s3126_r10724_p3759
mc16_13TeV.303451.Pythia8EvtGen_A14NNPDF23LO_DYtautau_3000M3500.deriv.DAOD_HIGG4D2.e4213_s3126_r10724_p3759
mc16_13TeV.303452.Pythia8EvtGen_A14NNPDF23LO_DYtautau_3500M4000.deriv.DAOD_HIGG4D2.e4213_s3126_r10724_p3759
mc16_13TeV.303453.Pythia8EvtGen_A14NNPDF23LO_DYtautau_4000M4500.deriv.DAOD_HIGG4D2.e4213_s3126_r10724_p3759
mc16_13TeV.303454.Pythia8EvtGen_A14NNPDF23LO_DYtautau_4500M5000.deriv.DAOD_HIGG4D2.e4213_s3126_r10724_p3759
mc16_13TeV.303455.Pythia8EvtGen_A14NNPDF23LO_DYtautau_5000M.deriv.DAOD_HIGG4D2.e4213_s3126_r10724_p3759

### Sherpa W+jets (pT slice) ###
mc16_13TeV.364170.Sherpa_221_NNPDF30NNLO_Wenu_MAXHTPTV0_70_CVetoBVeto.deriv.DAOD_HIGG4D2.e5340_s3126_r10724_p3759
mc16_13TeV.364171.Sherpa_221_NNPDF30NNLO_Wenu_MAXHTPTV0_70_CFilterBVeto.deriv.DAOD_HIGG4D2.
    e5340_s3126_r10724_p3759
mc16_13TeV.364172.Sherpa_221_NNPDF30NNLO_Wenu_MAXHTPTV0_70_BFilter.deriv.DAOD_HIGG4D2.e5340_s3126_r10724_p3759
mc16_13TeV.364173.Sherpa_221_NNPDF30NNLO_Wenu_MAXHTPTV70_140_CVetoBVeto.deriv.DAOD_HIGG4D2.
    e5340_s3126_r10724_p3759
mc16_13TeV.364174.Sherpa_221_NNPDF30NNLO_Wenu_MAXHTPTV70_140_CFilterBVeto.deriv.DAOD_HIGG4D2.
    e5340_s3126_r10724_p3759
mc16_13TeV.364175.Sherpa_221_NNPDF30NNLO_Wenu_MAXHTPTV70_140_BFilter.deriv.DAOD_HIGG4D2.e5340_s3126_r10724_p3759
mc16_13TeV.364176.Sherpa_221_NNPDF30NNLO_Wenu_MAXHTPTV140_280_CVetoBVeto.deriv.DAOD_HIGG4D2.
    e5340_s3126_r10724_p3759
mc16_13TeV.364177.Sherpa_221_NNPDF30NNLO_Wenu_MAXHTPTV140_280_CFilterBVeto.deriv.DAOD_HIGG4D2.
    e5340_s3126_r10724_p3759
mc16_13TeV.364178.Sherpa_221_NNPDF30NNLO_Wenu_MAXHTPTV140_280_BFilter.deriv.DAOD_HIGG4D2.e5340_s3126_r10724_p3759
mc16_13TeV.364179.Sherpa_221_NNPDF30NNLO_Wenu_MAXHTPTV280_500_CVetoBVeto.deriv.DAOD_HIGG4D2.
    e5340_s3126_r10724_p3759
mc16_13TeV.364180.Sherpa_221_NNPDF30NNLO_Wenu_MAXHTPTV280_500_CFilterBVeto.deriv.DAOD_HIGG4D2.
    e5340_s3126_r10724_p3759
mc16_13TeV.364181.Sherpa_221_NNPDF30NNLO_Wenu_MAXHTPTV280_500_BFilter.deriv.DAOD_HIGG4D2.e5340_s3126_r10724_p3759
mc16_13TeV.364182.Sherpa_221_NNPDF30NNLO_Wenu_MAXHTPTV500_1000.deriv.DAOD_HIGG4D2.e5340_s3126_r10724_p3759
mc16_13TeV.364183.Sherpa_221_NNPDF30NNLO_Wenu_MAXHTPTV1000_E_CMS.deriv.DAOD_HIGG4D2.e5340_s3126_r10724_p3759

mc16_13TeV.364156.Sherpa_221_NNPDF30NNLO_Wmunu_MAXHTPTV0_70_CVetoBVeto.deriv.DAOD_HIGG4D2.
    e5340_s3126_r10724_p3759
mc16_13TeV.364157.Sherpa_221_NNPDF30NNLO_Wmunu_MAXHTPTV0_70_CFilterBVeto.deriv.DAOD_HIGG4D2.
    e5340_s3126_r10724_p3759
mc16_13TeV.364158.Sherpa_221_NNPDF30NNLO_Wmunu_MAXHTPTV0_70_BFilter.deriv.DAOD_HIGG4D2.e5340_s3126_r10724_p3759
mc16_13TeV.364159.Sherpa_221_NNPDF30NNLO_Wmunu_MAXHTPTV70_140_CVetoBVeto.deriv.DAOD_HIGG4D2.
    e5340_s3126_r10724_p3759
mc16_13TeV.364160.Sherpa_221_NNPDF30NNLO_Wmunu_MAXHTPTV70_140_CFilterBVeto.deriv.DAOD_HIGG4D2.
    e5340_s3126_r10724_p3759
mc16_13TeV.364161.Sherpa_221_NNPDF30NNLO_Wmunu_MAXHTPTV70_140_BFilter.deriv.DAOD_HIGG4D2.e5340_s3126_r10724_p3759
mc16_13TeV.364162.Sherpa_221_NNPDF30NNLO_Wmunu_MAXHTPTV140_280_CVetoBVeto.deriv.DAOD_HIGG4D2.
    e5340_s3126_r10724_p3759
mc16_13TeV.364163.Sherpa_221_NNPDF30NNLO_Wmunu_MAXHTPTV140_280_CFilterBVeto.deriv.DAOD_HIGG4D2.
    e5340_s3126_r10724_p3759
mc16_13TeV.364164.Sherpa_221_NNPDF30NNLO_Wmunu_MAXHTPTV140_280_BFilter.deriv.DAOD_HIGG4D2.
    e5340_s3126_r10724_p3759
```

```
mc16_13TeV.364165.Sherpa_221_NNPDF30NNLO_Wmunu_MAXHTPTV280_500_CVetoBVeto.deriv.DAOD_HIGG4D2.
    e5340_s3126_r10724_p3759
mc16_13TeV.364166.Sherpa_221_NNPDF30NNLO_Wmunu_MAXHTPTV280_500_CFilterBVeto.deriv.DAOD_HIGG4D2.
    e5340_s3126_r10724_p3759
mc16_13TeV.364167.Sherpa_221_NNPDF30NNLO_Wmunu_MAXHTPTV280_500_BFilter.deriv.DAOD_HIGG4D2.
    e5340_s3126_r10724_p3759
mc16_13TeV.364168.Sherpa_221_NNPDF30NNLO_Wmunu_MAXHTPTV500_1000.deriv.DAOD_HIGG4D2.e5340_s3126_r10724_p3759
mc16_13TeV.364169.Sherpa_221_NNPDF30NNLO_Wmunu_MAXHTPTV1000_E_CMS.deriv.DAOD_HIGG4D2.e5340_s3126_r10724_p3759

mc16_13TeV.364184.Sherpa_221_NNPDF30NNLO_Wtaunu_MAXHTPTV0_70_CVetoBVeto.deriv.DAOD_HIGG4D2.
    e5340_s3126_r10724_p3759
mc16_13TeV.364185.Sherpa_221_NNPDF30NNLO_Wtaunu_MAXHTPTV0_70_CFilterBVeto.deriv.DAOD_HIGG4D2.
    e5340_s3126_r10724_p3759
mc16_13TeV.364186.Sherpa_221_NNPDF30NNLO_Wtaunu_MAXHTPTV0_70_BFilter.deriv.DAOD_HIGG4D2.e5340_s3126_r10724_p3759
mc16_13TeV.364187.Sherpa_221_NNPDF30NNLO_Wtaunu_MAXHTPTV70_140_CVetoBVeto.deriv.DAOD_HIGG4D2.
    e5340_s3126_r10724_p3759
mc16_13TeV.364188.Sherpa_221_NNPDF30NNLO_Wtaunu_MAXHTPTV70_140_CFilterBVeto.deriv.DAOD_HIGG4D2.
    e5340_s3126_r10724_p3759
mc16_13TeV.364189.Sherpa_221_NNPDF30NNLO_Wtaunu_MAXHTPTV70_140_BFilter.deriv.DAOD_HIGG4D2.
    e5340_s3126_r10724_p3759
mc16_13TeV.364190.Sherpa_221_NNPDF30NNLO_Wtaunu_MAXHTPTV140_280_CVetoBVeto.deriv.DAOD_HIGG4D2.
    e5340_s3126_r10724_p3759
mc16_13TeV.364191.Sherpa_221_NNPDF30NNLO_Wtaunu_MAXHTPTV140_280_CFilterBVeto.deriv.DAOD_HIGG4D2.
    e5340_s3126_r10724_p3759
mc16_13TeV.364192.Sherpa_221_NNPDF30NNLO_Wtaunu_MAXHTPTV140_280_BFilter.deriv.DAOD_HIGG4D2.
    e5340_s3126_r10724_p3759
mc16_13TeV.364193.Sherpa_221_NNPDF30NNLO_Wtaunu_MAXHTPTV280_500_CVetoBVeto.deriv.DAOD_HIGG4D2.
    e5340_s3126_r10724_p3759
mc16_13TeV.364194.Sherpa_221_NNPDF30NNLO_Wtaunu_MAXHTPTV280_500_CFilterBVeto.deriv.DAOD_HIGG4D2.
    e5340_s3126_r10724_p3759
mc16_13TeV.364195.Sherpa_221_NNPDF30NNLO_Wtaunu_MAXHTPTV280_500_BFilter.deriv.DAOD_HIGG4D2.
    e5340_s3126_r10724_p3759
mc16_13TeV.364196.Sherpa_221_NNPDF30NNLO_Wtaunu_MAXHTPTV500_1000.deriv.DAOD_HIGG4D2.e5340_s3126_r10724_p3759
mc16_13TeV.364197.Sherpa_221_NNPDF30NNLO_Wtaunu_MAXHTPTV1000_E_CMS.deriv.DAOD_HIGG4D2.e5340_s3126_r10724_p3759
```

Listing B.1.1: List of $\tau_{\text{lep}}\tau_{\text{had}}$ MC DAOD samples processed into Ntuples, for various background and signal processes. The naming scheme for each sample is broken down into several components, interspaced by a stop, in order: MC campaign and energy, unique dataset ID, summary generator and process name, file type, derivation cache, production tags. These production tags are further broken down to represent their version, in order: event generation, simulation, pileup reconstruction campaign, derivation production cache.

B.2 Background estimation

B.2.1 Multi-jet fake estimation

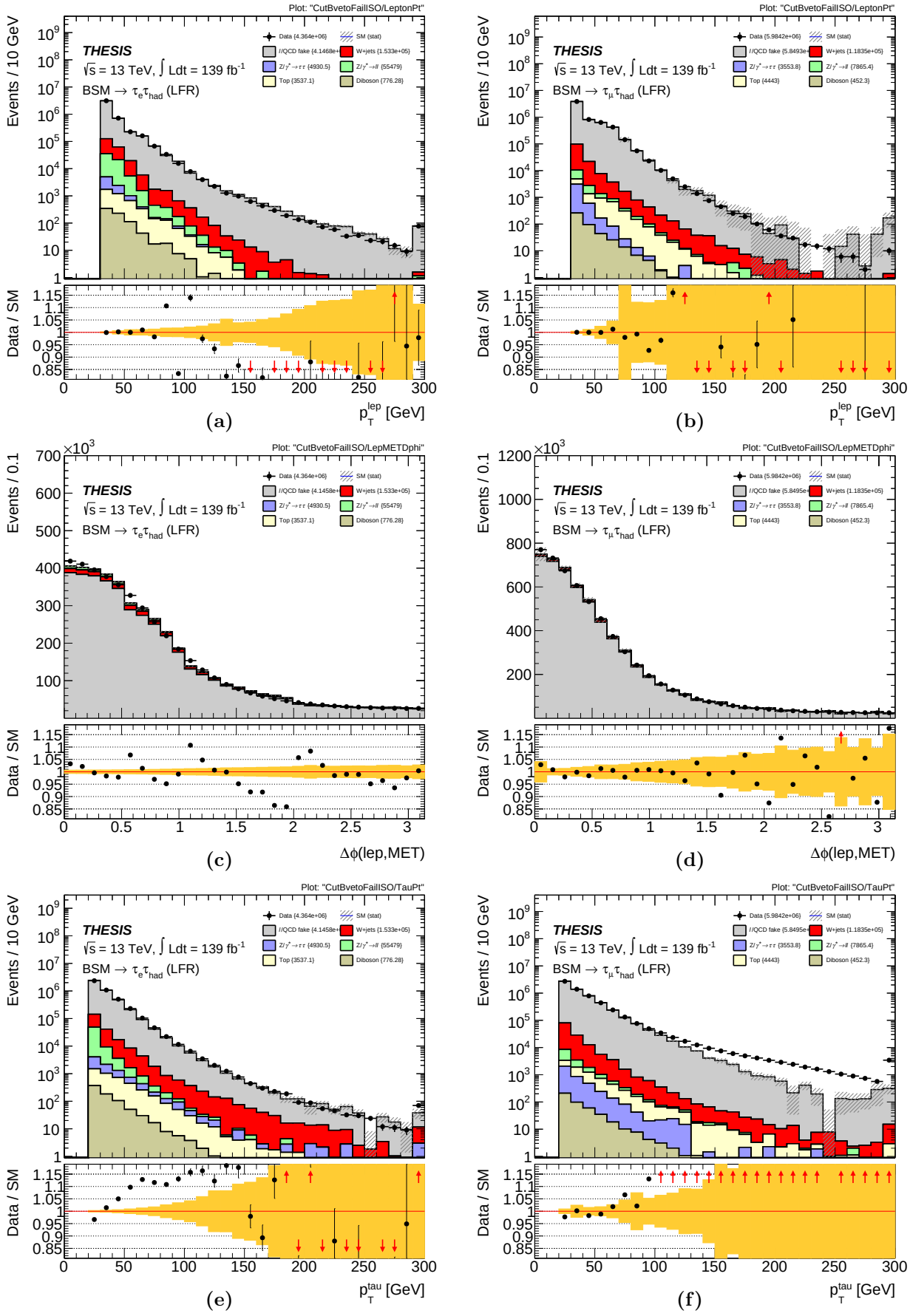

Figure B.2.1: Plots of the Lepton Fake Region which fail the lepton isolation requirement with the Lepton Fake Factor applied back, representing lepton p_{T}, $|\Delta\phi(\ell, E_{\mathrm{T}}^{\mathrm{miss}})|$ and tau p_{T} (from top to bottom). The region is divided into the $e\tau_{\mathrm{had}}$ (left) and $\mu\tau_{\mathrm{had}}$ (right) sub-channels, representing the b-veto category.

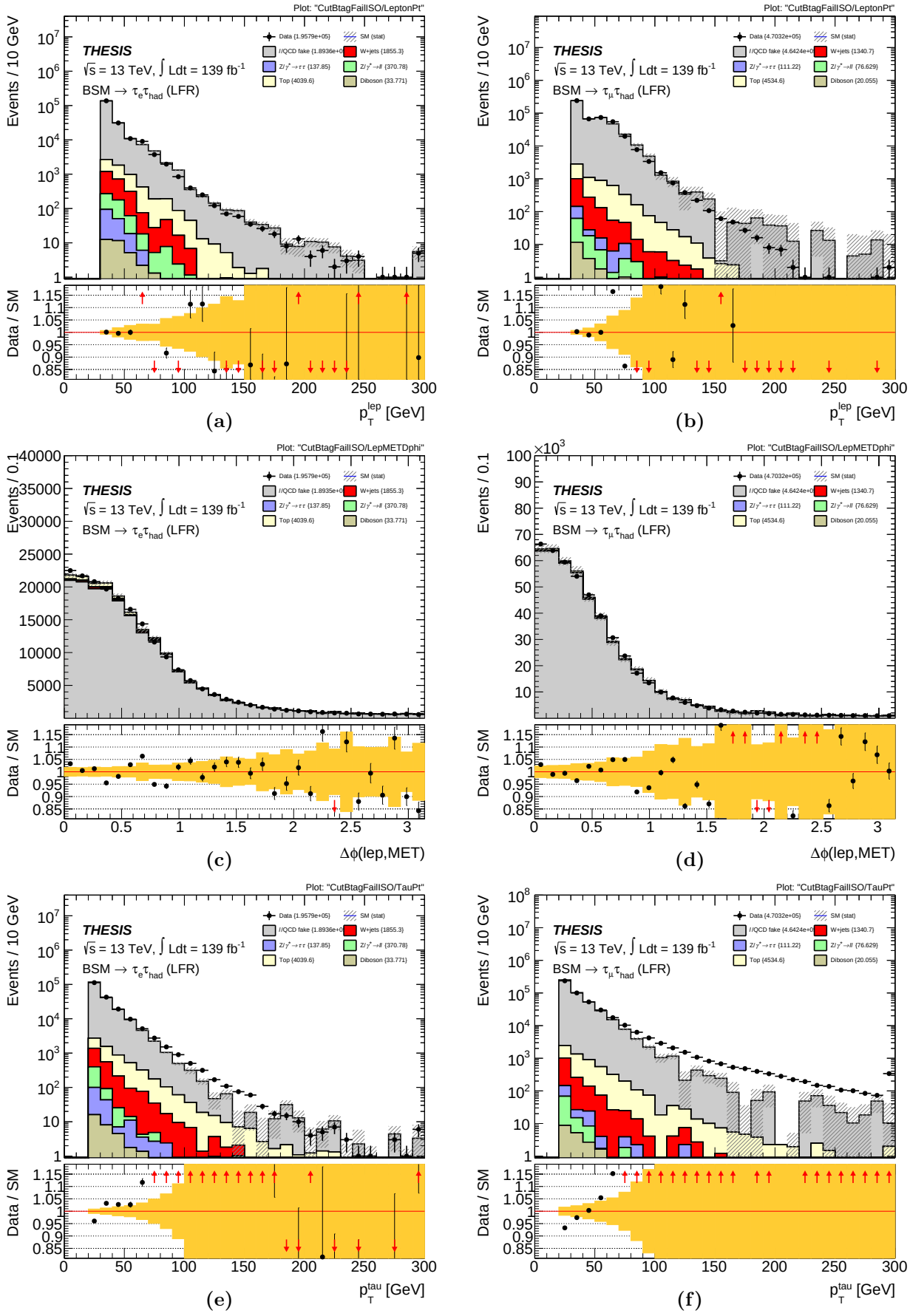

Figure B.2.2: Plots of the Lepton Fake Region which fail the lepton isolation requirement with the Lepton Fake Factor applied back, representing lepton p_{T}, $|\Delta\phi(\ell, E_{\mathrm{T}}^{\mathrm{miss}})|$ and tau p_{T} (from top to bottom). The region is divided into the $e\tau_{\mathrm{had}}$ (left) and $\mu\tau_{\mathrm{had}}$ (right) sub-channels, representing the b-tag category.

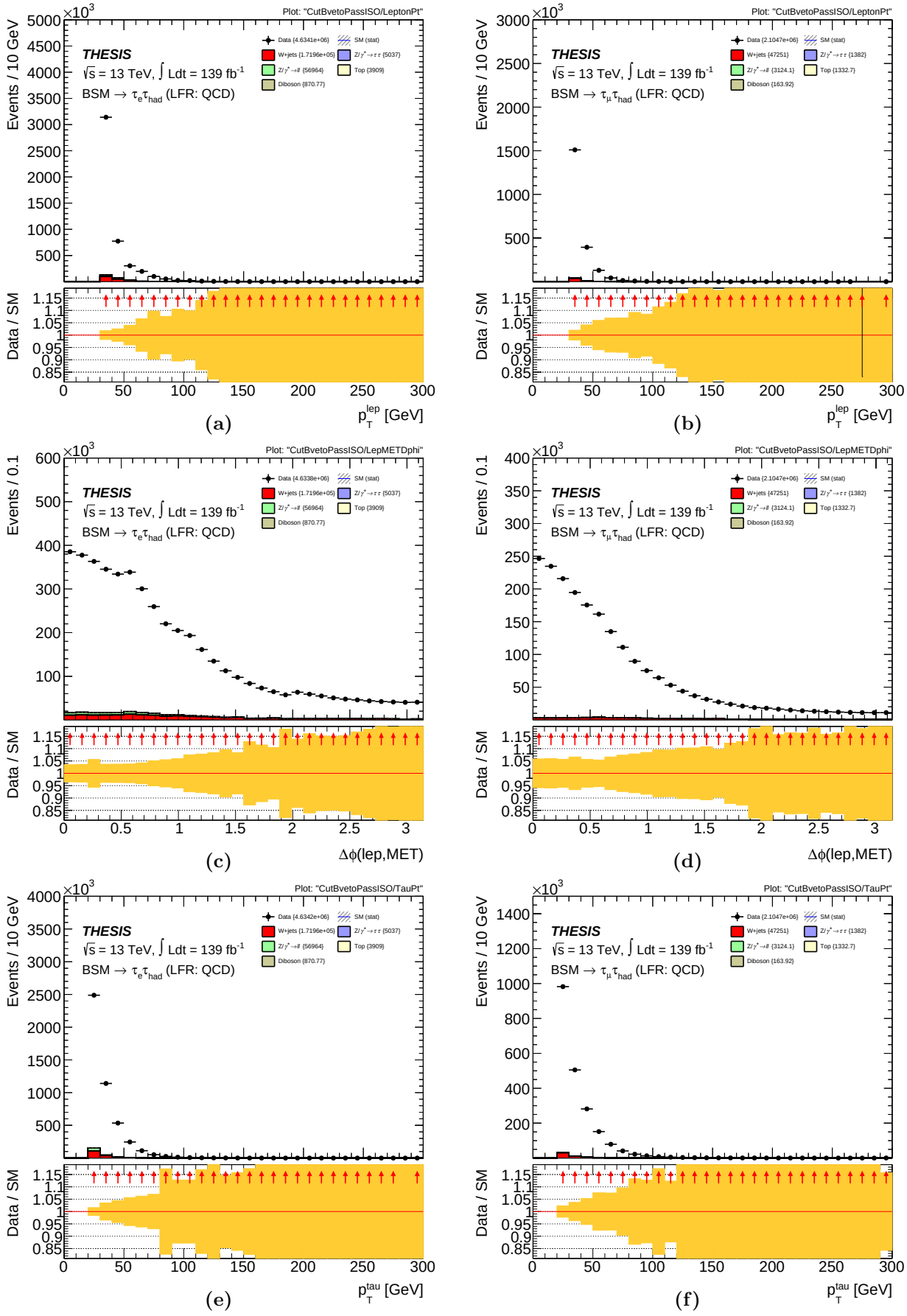

Figure B.2.3: Plots of the QCD fake component which pass the lepton isolation requirement within the Lepton Fake Region as used in the calculation of the Lepton Fake Factor, representing lepton p_{T}, $|\Delta\phi(\ell, E_{\mathrm{T}}^{\mathrm{miss}})|$ and tau p_{T} (from top to bottom). The region is divided into the $e\tau_{\mathrm{had}}$ (left) and $\mu\tau_{\mathrm{had}}$ (right) sub-channels, representing the b-veto category.

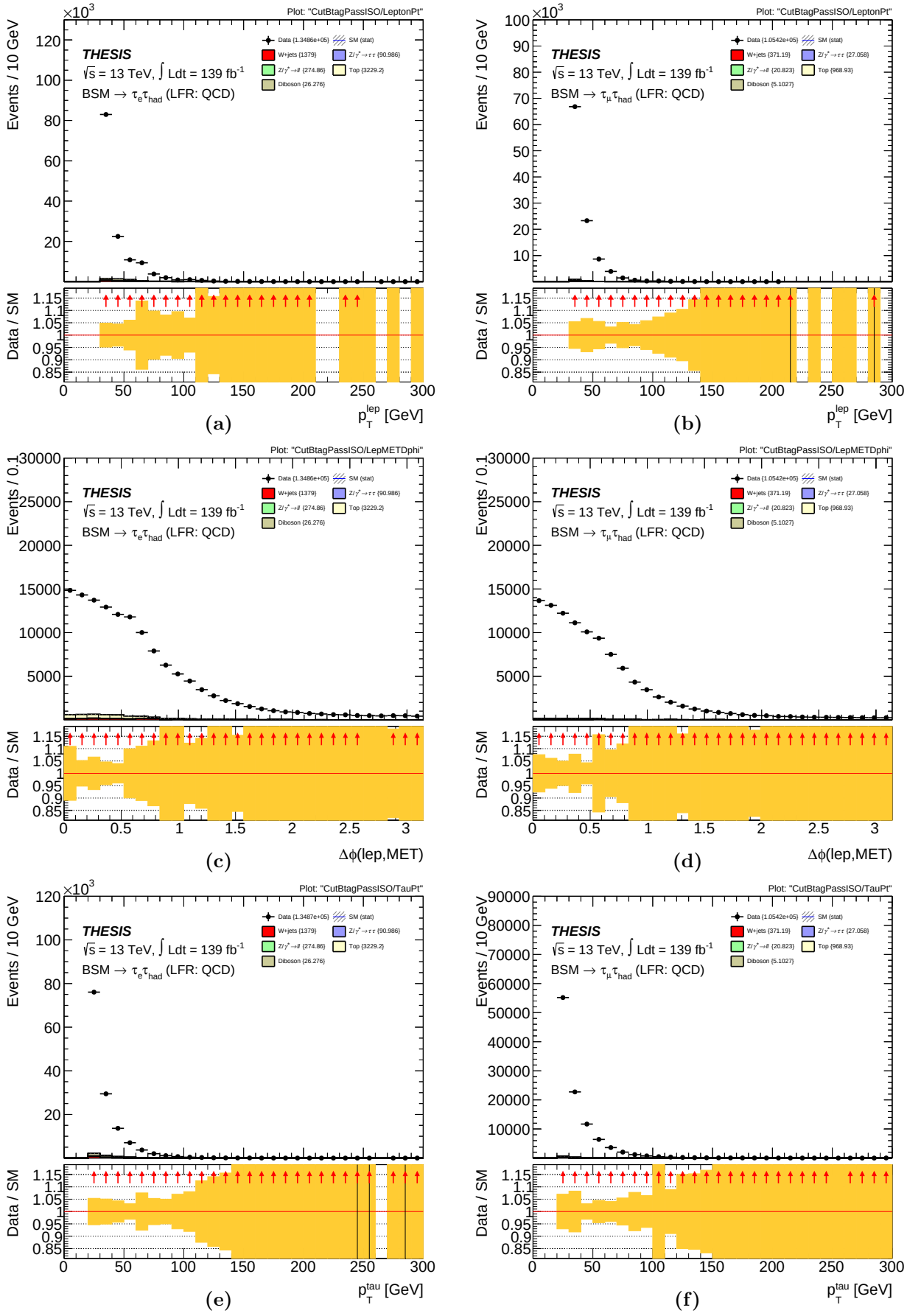

Figure B.2.4: Plots of the QCD fake component which pass the lepton isolation requirement within the Lepton Fake Region as used in the calculation of the Lepton Fake Factor, representing lepton p_{T}, $|\Delta\phi(\ell, E_{\mathrm{T}}^{\mathrm{miss}})|$ and tau p_{T} (from top to bottom). The region is divided into the $e\tau_{\mathrm{had}}$ (left) and $\mu\tau_{\mathrm{had}}$ (right) sub-channels, representing the b-tag category.

B.2.2 W boson and top quark fake estimation

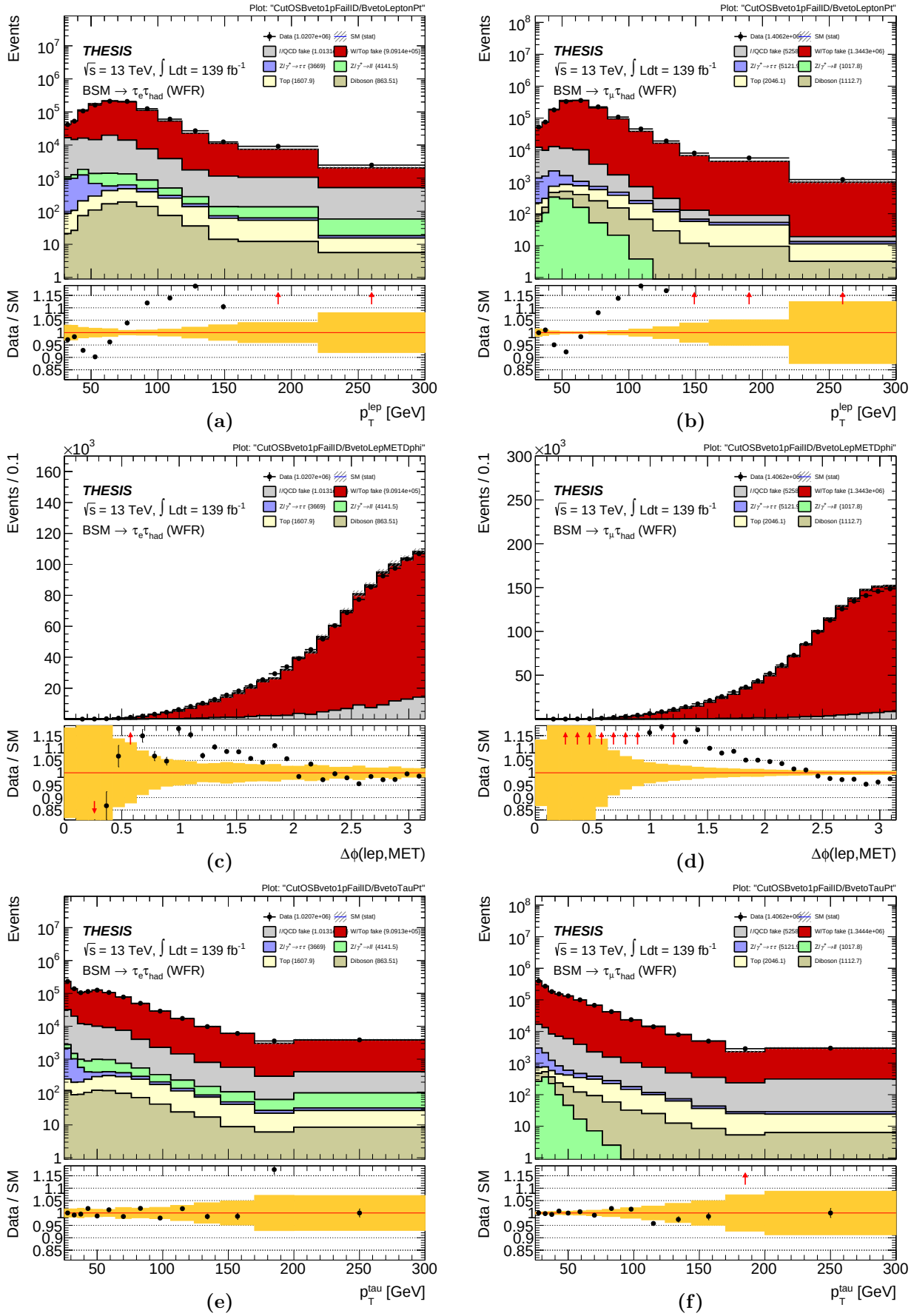

Figure B.2.5: Plots of the W+jets Fake Region which fail the tau identification requirement with the W+jets Fake Factor applied back, in the b-veto category, for the 1-prong tau decay mode, representing lepton p_{T}, $|\Delta\phi(\ell, E_{\mathrm{T}}^{\mathrm{miss}})|$ and tau p_{T} (from top to bottom). The region is divided into the $e\tau_{\mathrm{had}}$ (left) and $\mu\tau_{\mathrm{had}}$ (right) sub-channels.

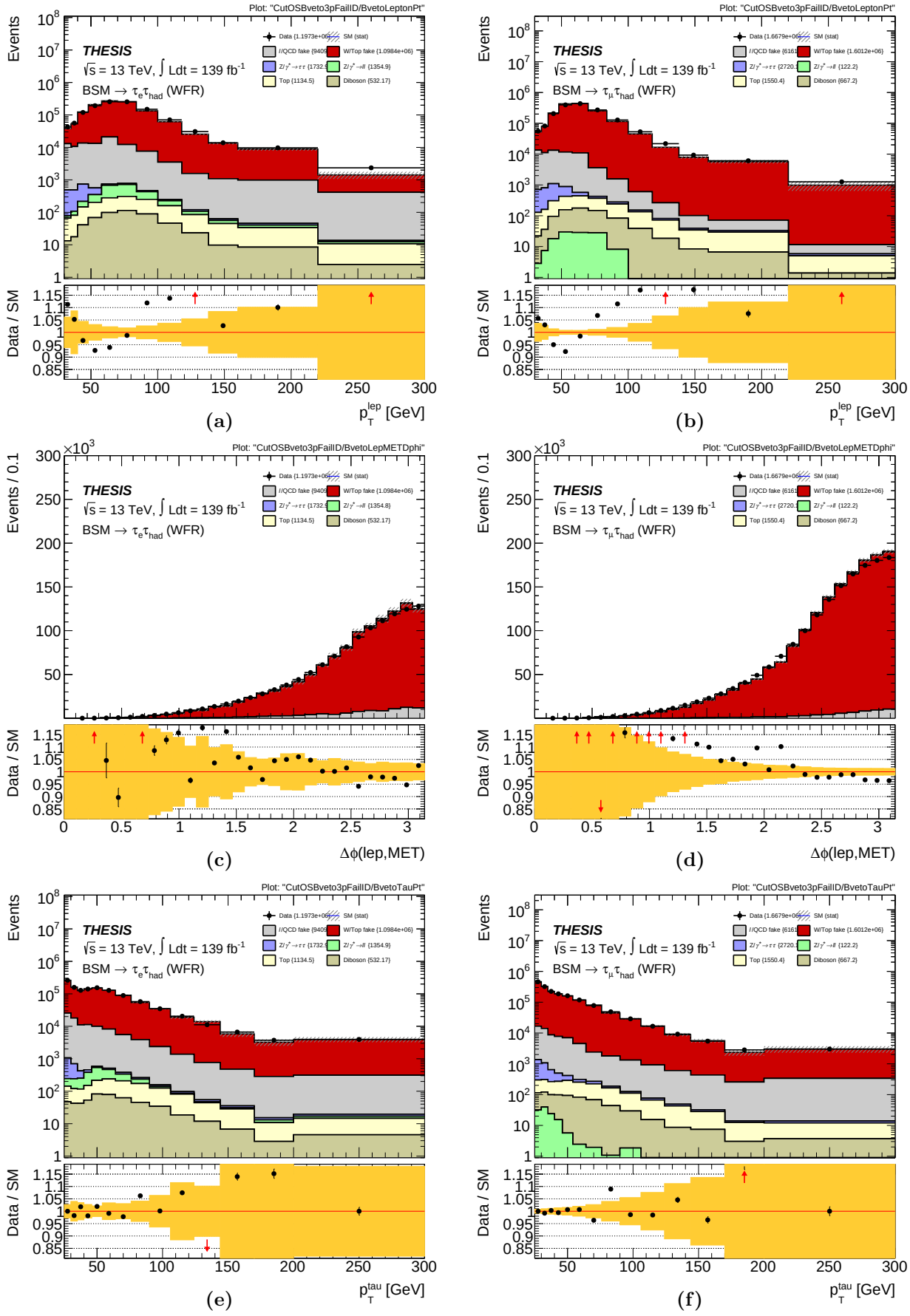

Figure B.2.6: Plots of the W+jets Fake Region which fail the tau identification requirement with the W+jets Fake Factor applied back, in the b-veto category, for the 3-prong tau decay mode, representing lepton p_{T}, $|\Delta\phi(\ell, E_{\mathrm{T}}^{\mathrm{miss}})|$ and tau p_{T} (from top to bottom). The region is divided into the $e\tau_{\mathrm{had}}$ (left) and $\mu\tau_{\mathrm{had}}$ (right) sub-channels.

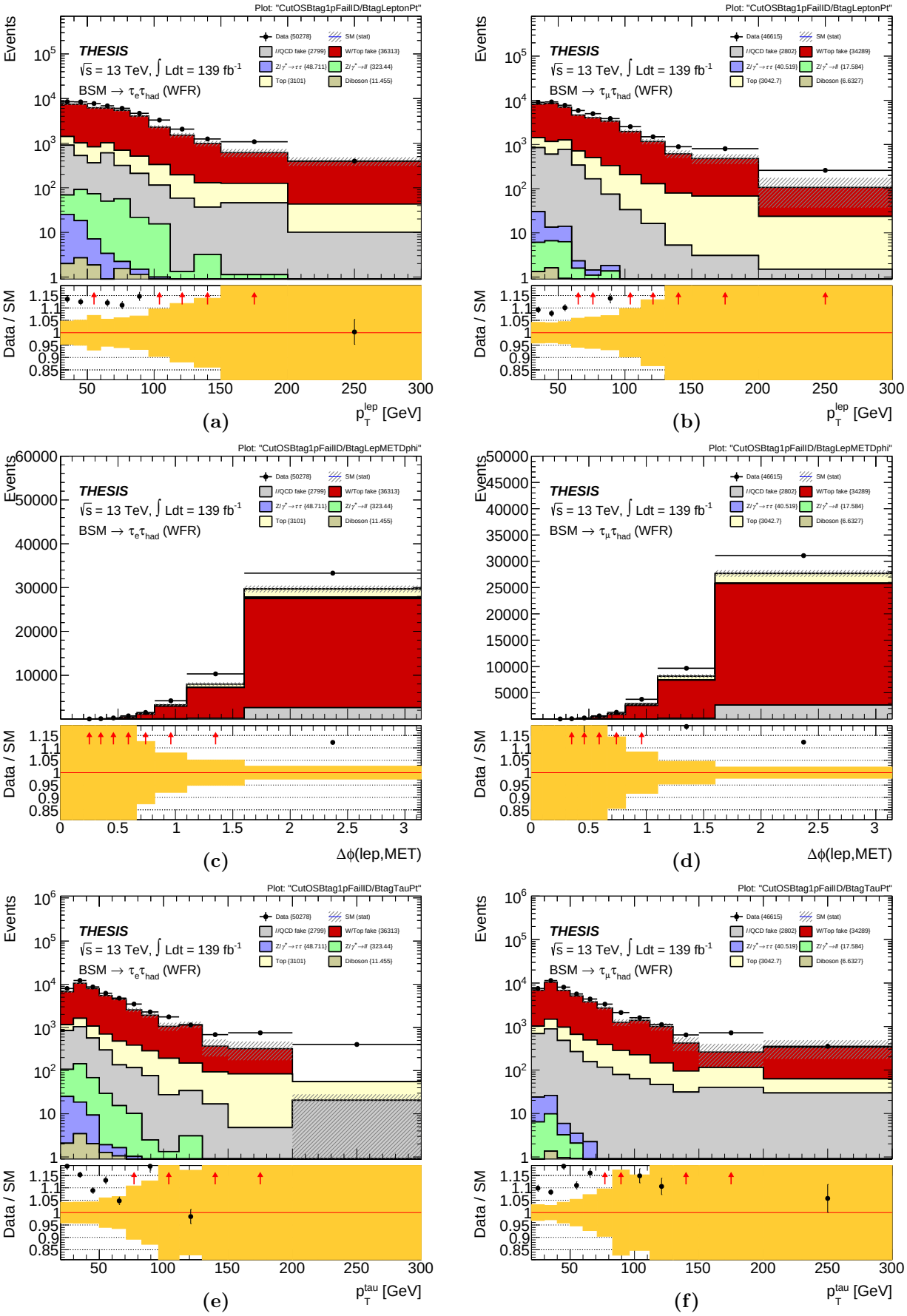

Figure B.2.7: Plots of the Top Fake Region which fail the tau identification requirement with the Top Fake Factor applied back, in the b-tag category, for the 1-prong tau decay mode, representing lepton p_{T}, $|\Delta\phi(\ell, E_{\mathrm{T}}^{\mathrm{miss}})|$ and tau p_{T} (from top to bottom). The region is divided into the $e\tau_{\mathrm{had}}$ (left) and $\mu\tau_{\mathrm{had}}$ (right) sub-channels.

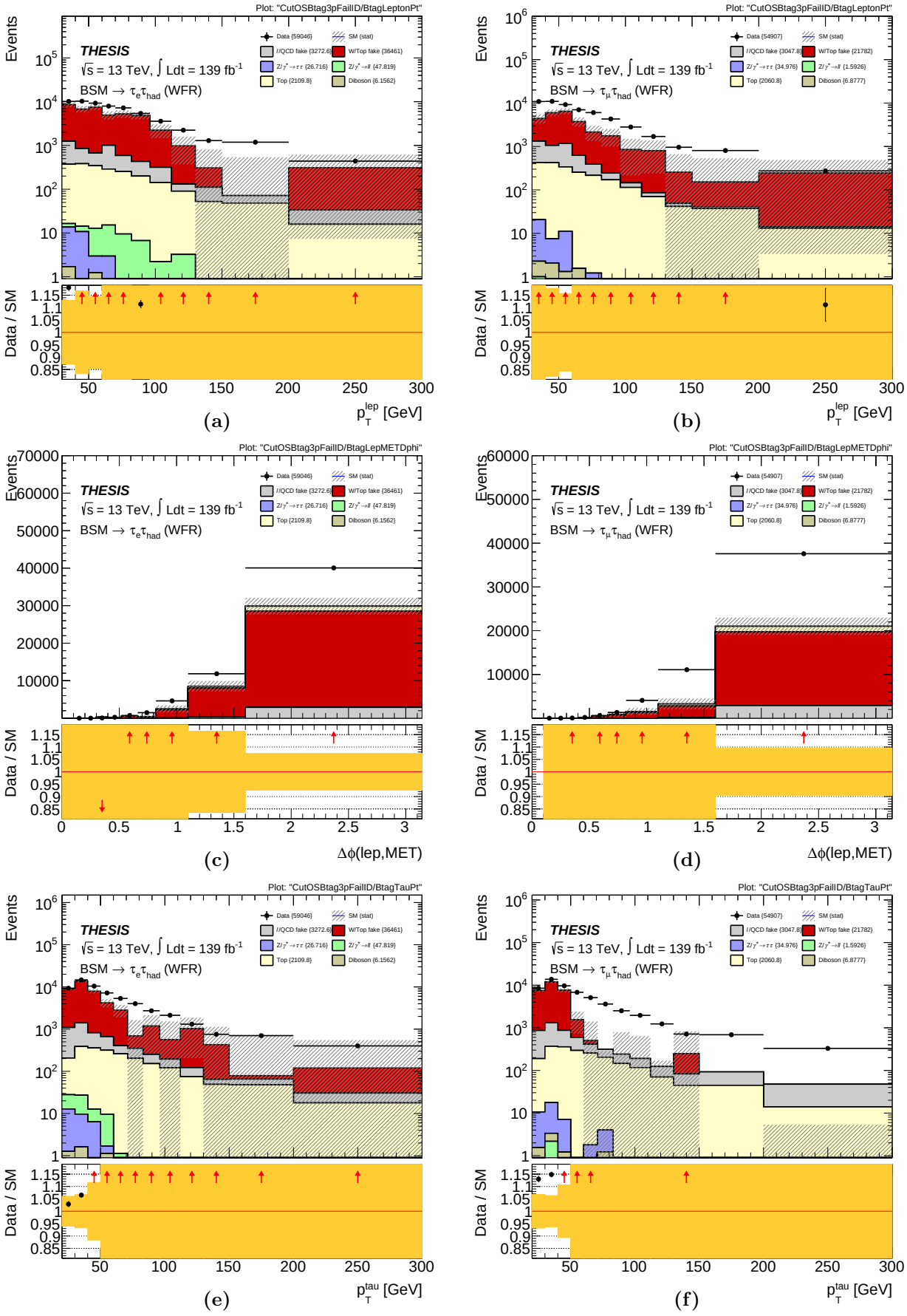

Figure B.2.8: Plots of the Top Fake Region which fail the tau identification requirement with the Top Fake Factor applied back, in the b-tag category, for the 3-prong tau decay mode, representing lepton p_{T}, $|\Delta\phi(\ell, E_{\mathrm{T}}^{\mathrm{miss}})|$ and tau p_{T} (from top to bottom). The region is divided into the $e\tau_{\mathrm{had}}$ (left) and $\mu\tau_{\mathrm{had}}$ (right) sub-channels.

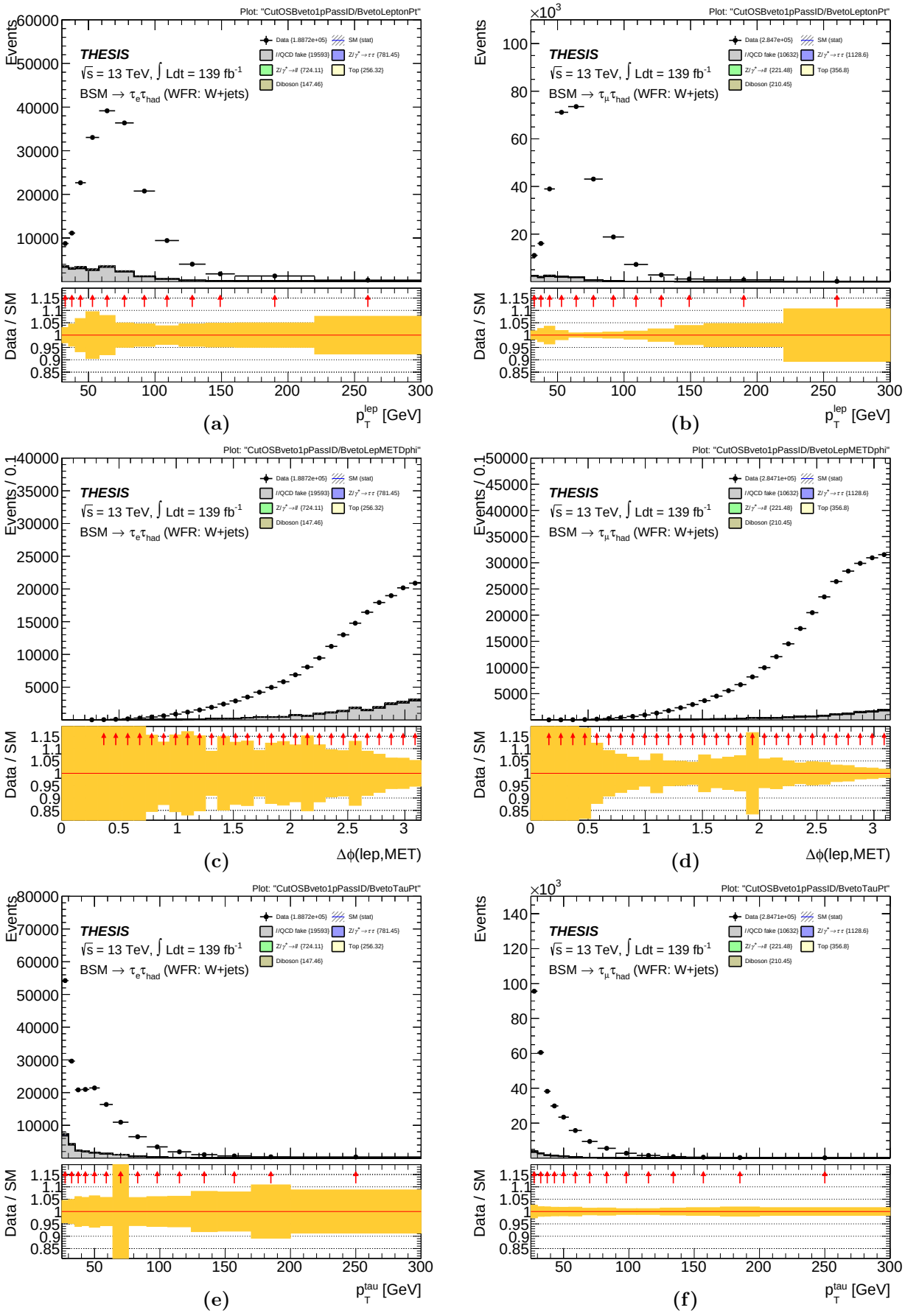

Figure B.2.9: Plots of the W+jets fake component which pass the tau identification requirement within the W+jets Fake Region as used in the calculation of the W+jets Fake Factor, in the b-veto category, for the 1-prong tau decay mode, representing lepton p_{T}, $|\Delta\phi(\ell, E_{\mathrm{T}}^{\mathrm{miss}})|$ and tau p_{T} (from top to bottom). The region is divided into the $e\tau_{\mathrm{had}}$ (left) and $\mu\tau_{\mathrm{had}}$ (right) sub-channels.

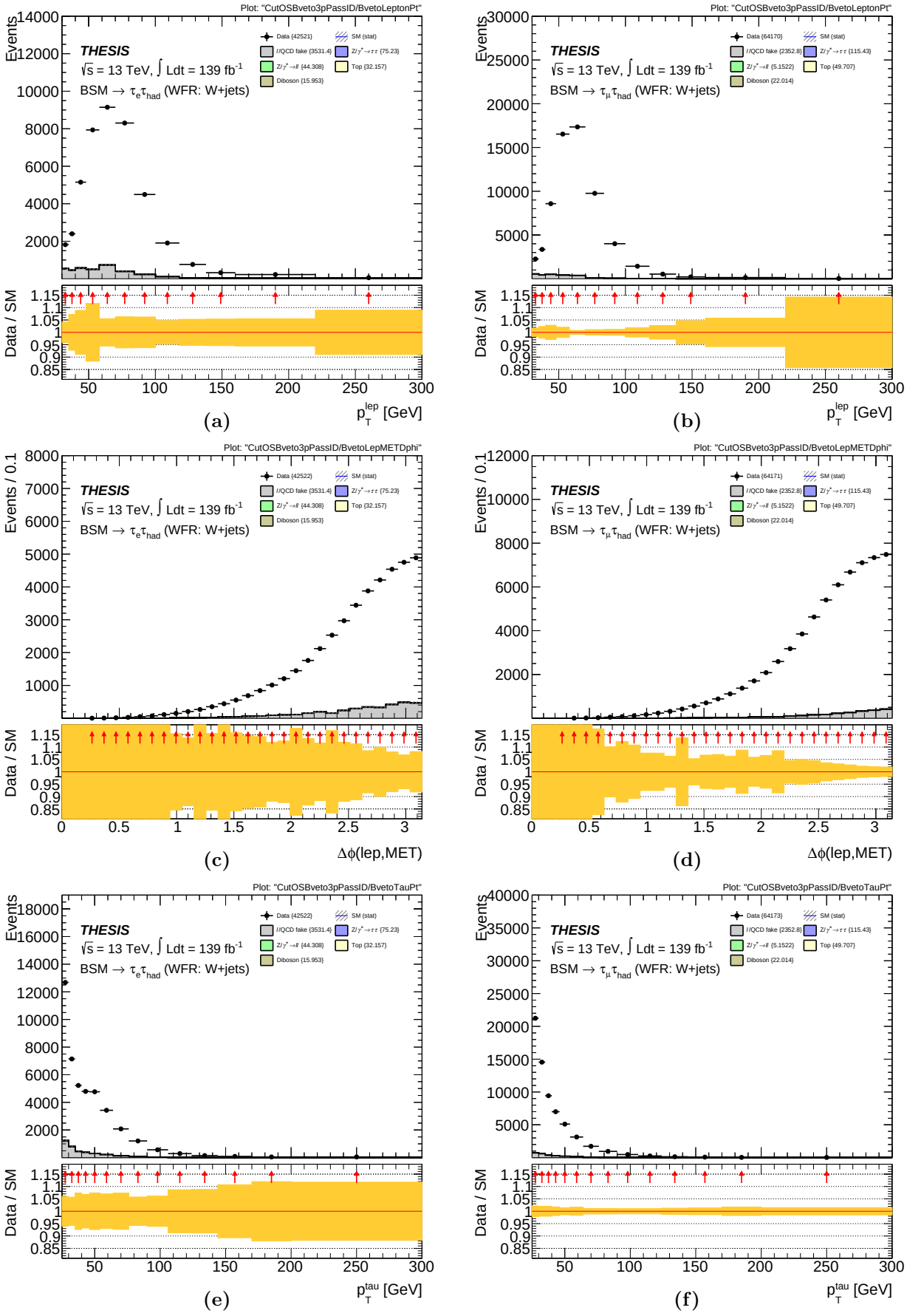

Figure B.2.10: Plots of the W+jets fake component which pass the tau identification requirement within the W+jets Fake Region as used in the calculation of the W+jets Fake Factor, in the b-veto category, for the 3-prong tau decay mode, representing lepton p_{T}, $|\Delta\phi(\ell, E_{\mathrm{T}}^{\mathrm{miss}})|$ and tau p_{T} (from top to bottom). The region is divided into the $e\tau_{\mathrm{had}}$ (left) and $\mu\tau_{\mathrm{had}}$ (right) sub-channels.

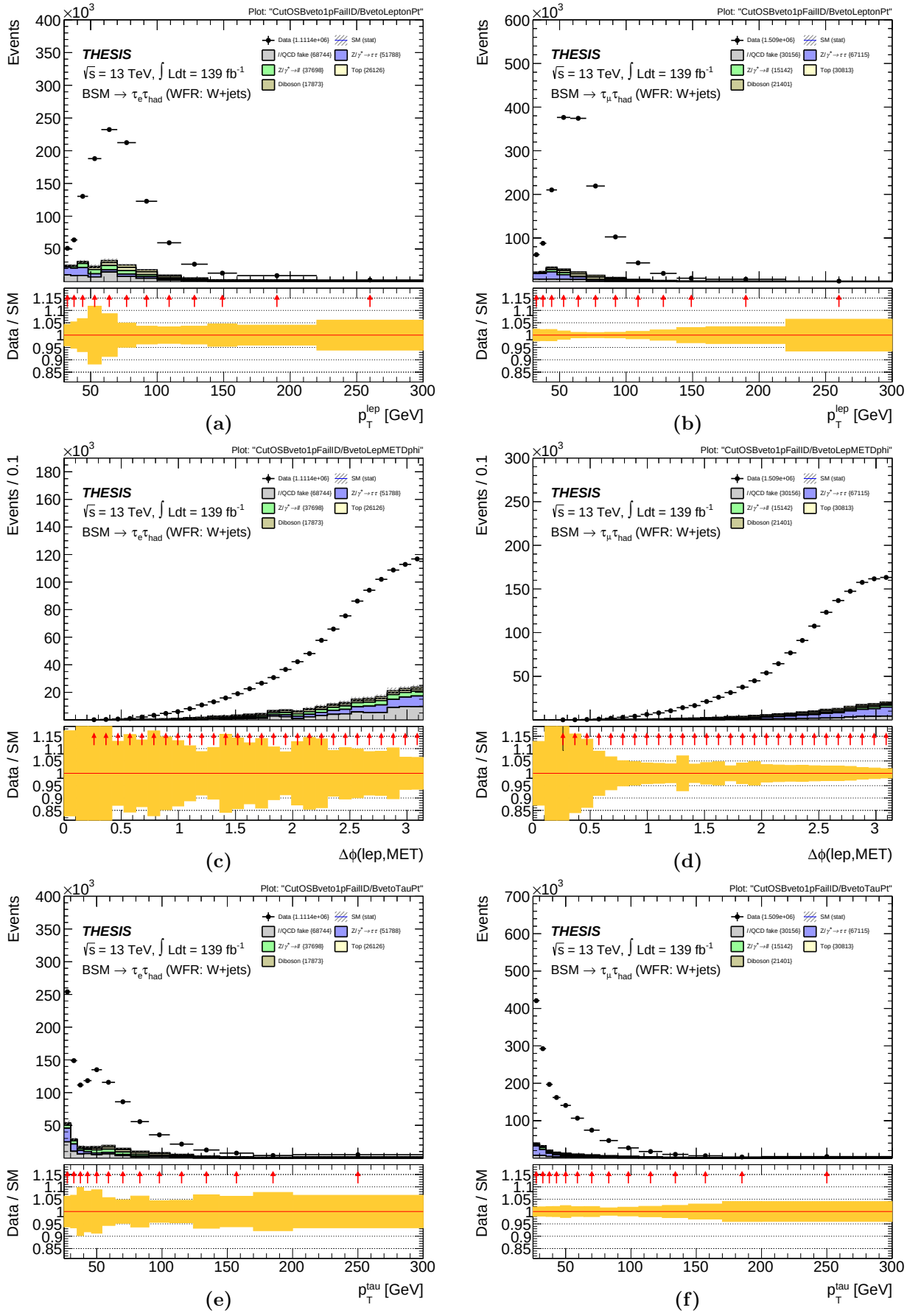

Figure B.2.11: Plots of the W+jets fake component which fail the tau identification requirement within the W+jets Fake Region as used in the calculation of the W+jets Fake Factor, in the b-veto category, for the 1-prong tau decay mode, representing lepton p_{T}, $|\Delta\phi(\ell, E_{\mathrm{T}}^{\mathrm{miss}})|$ and tau p_{T} (from top to bottom). The region is divided into the $e\tau_{\mathrm{had}}$ (left) and $\mu\tau_{\mathrm{had}}$ (right) sub-channels.

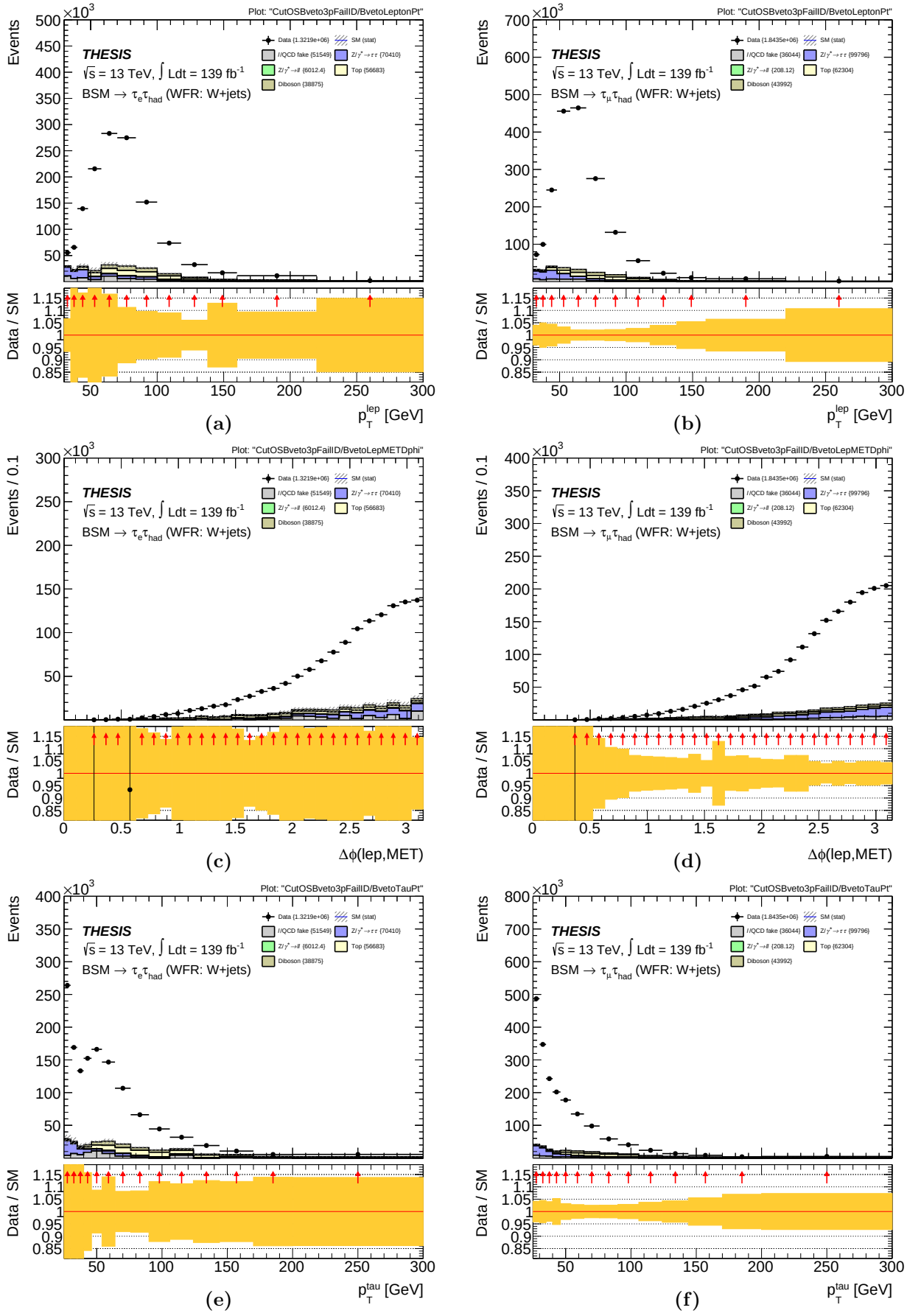

Figure B.2.12: Plots of the W+jets fake component which fail the tau identification requirement within the W+jets Fake Region as used in the calculation of the W+jets Fake Factor, in the b-veto category, for the 3-prong tau decay mode, representing lepton p_{T}, $|\Delta\phi(\ell, E_{\mathrm{T}}^{\mathrm{miss}})|$ and tau p_{T} (from top to bottom). The region is divided into the $e\tau_{\mathrm{had}}$ (left) and $\mu\tau_{\mathrm{had}}$ (right) sub-channels.

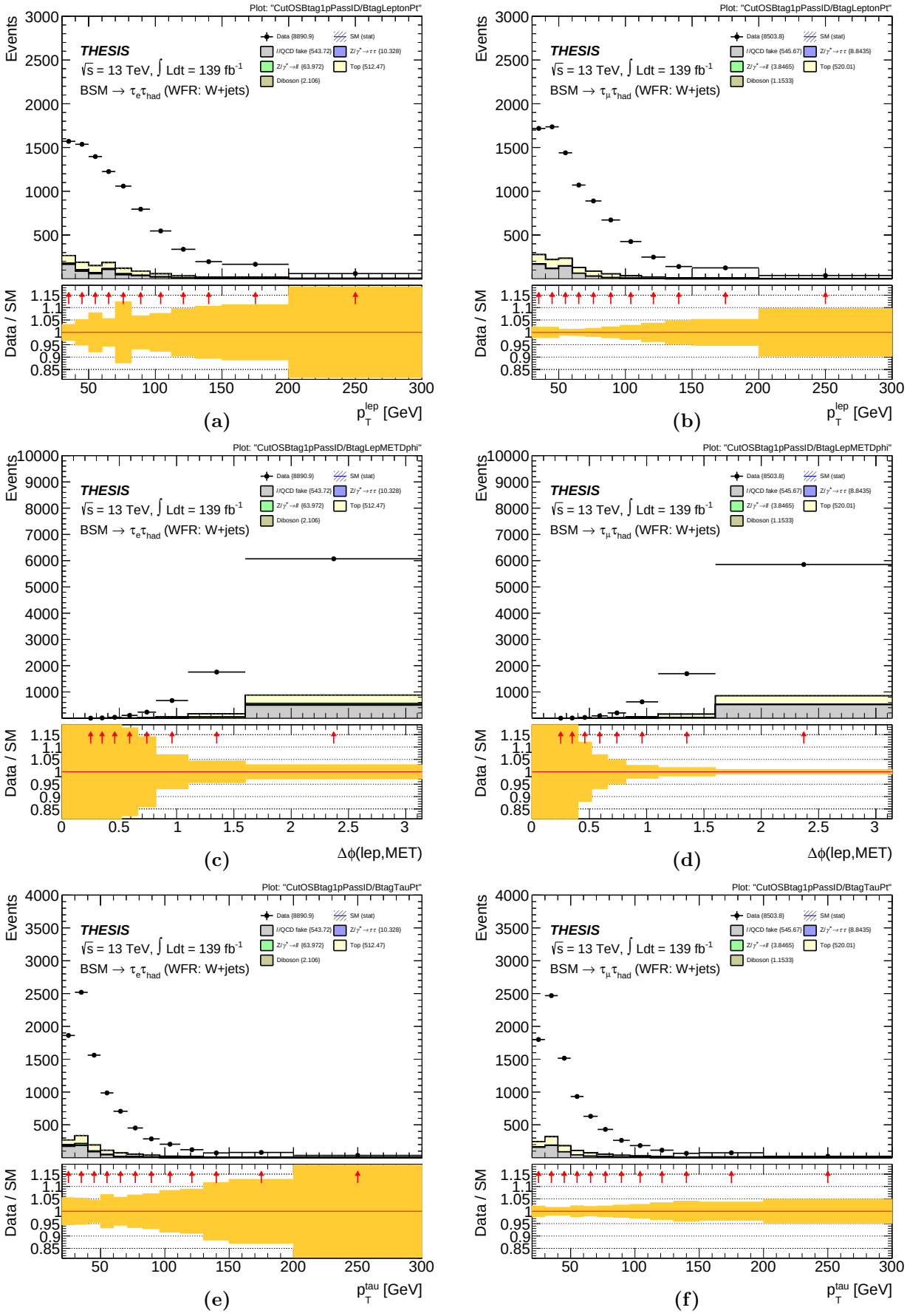

Figure B.2.13: Plots of the top quark fake component which pass the tau identification requirement within the Top Fake Region as used in the calculation of the Top Fake Factor, in the b-tag category, for the 1-prong tau decay mode, representing lepton p_{T}, $|\Delta\phi(\ell, E_{\mathrm{T}}^{\mathrm{miss}})|$ and tau p_{T} (from top to bottom). The region is divided into the $e\tau_{\mathrm{had}}$ (left) and $\mu\tau_{\mathrm{had}}$ (right) sub-channels.

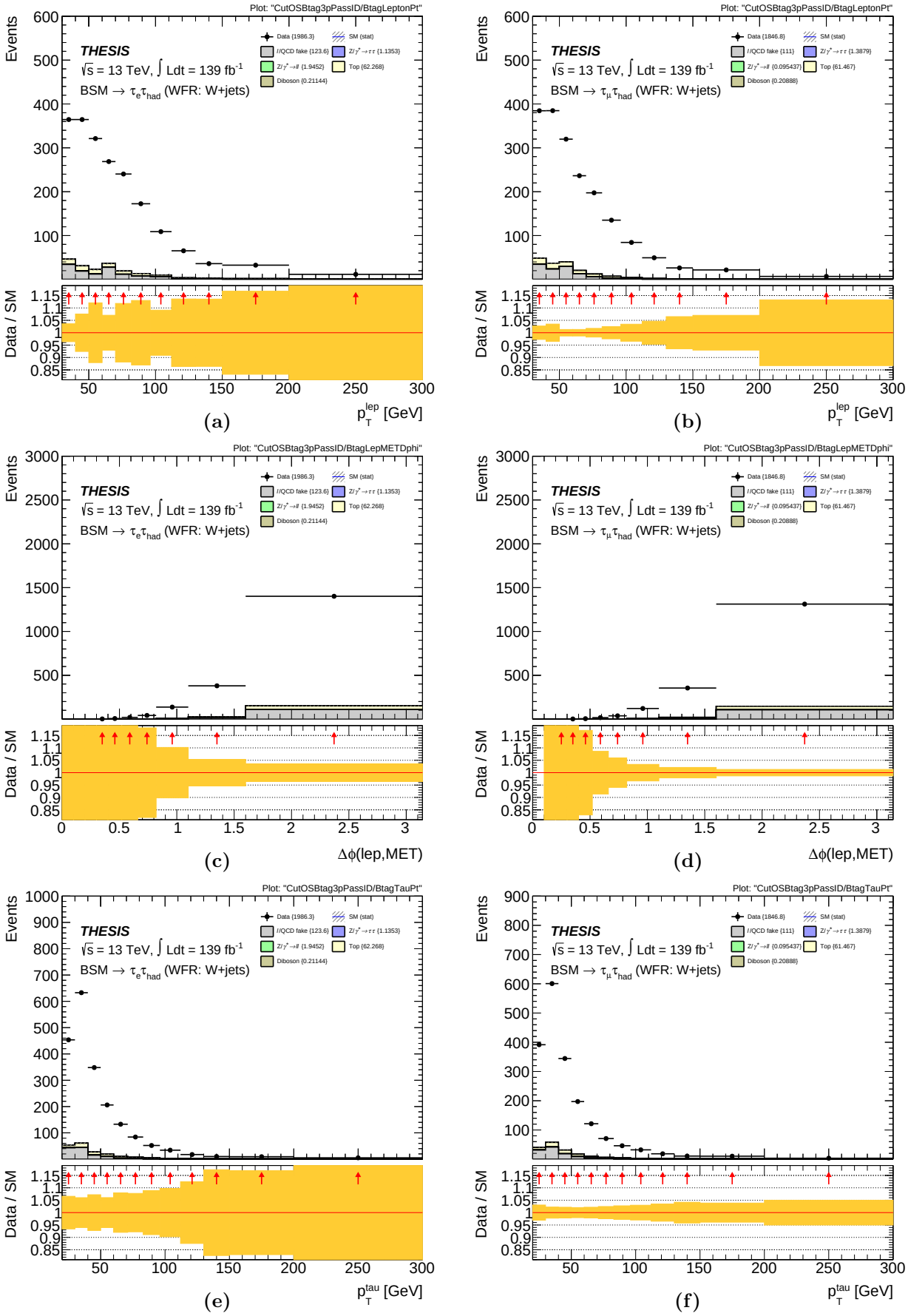

Figure B.2.14: Plots of the top quark fake component which pass the tau identification requirement within the Top Fake Region as used in the calculation of the Top Fake Factor, in the b-tag category, for the 3-prong tau decay mode, representing lepton p_{T}, $|\Delta\phi(\ell, E_{\mathrm{T}}^{\mathrm{miss}})|$ and tau p_{T} (from top to bottom). The region is divided into the $e\tau_{\mathrm{had}}$ (left) and $\mu\tau_{\mathrm{had}}$ (right) sub-channels.

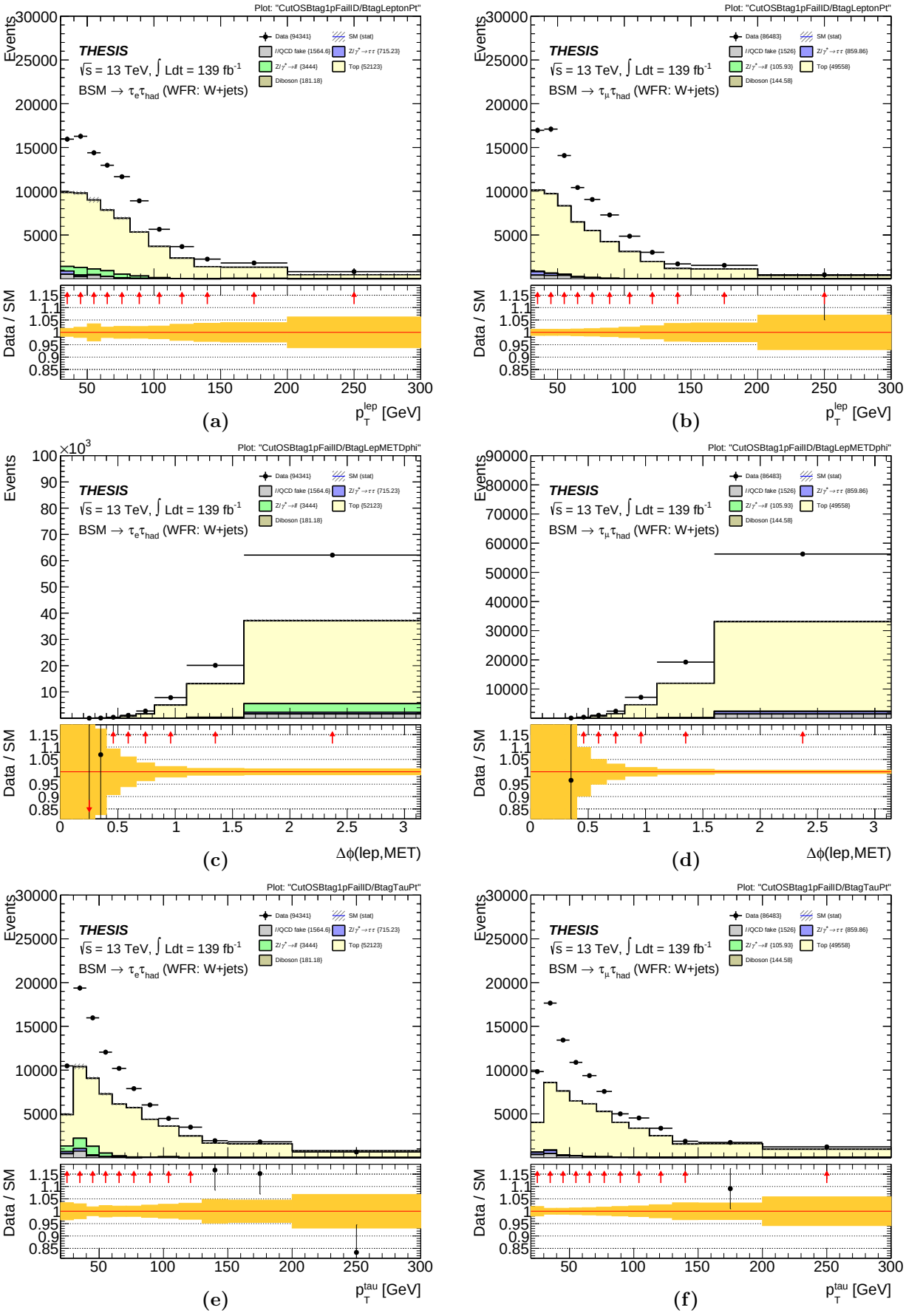

Figure B.2.15: Plots of the top quark fake component which fail the tau identification requirement within the Top Fake Region as used in the calculation of the Top Fake Factor, in the b-tag category, for the 1-prong tau decay mode, representing lepton p_{T}, $|\Delta\phi(\ell, E_{\mathrm{T}}^{\mathrm{miss}})|$ and tau p_{T} (from top to bottom). The region is divided into the $e\tau_{\mathrm{had}}$ (left) and $\mu\tau_{\mathrm{had}}$ (right) sub-channels.

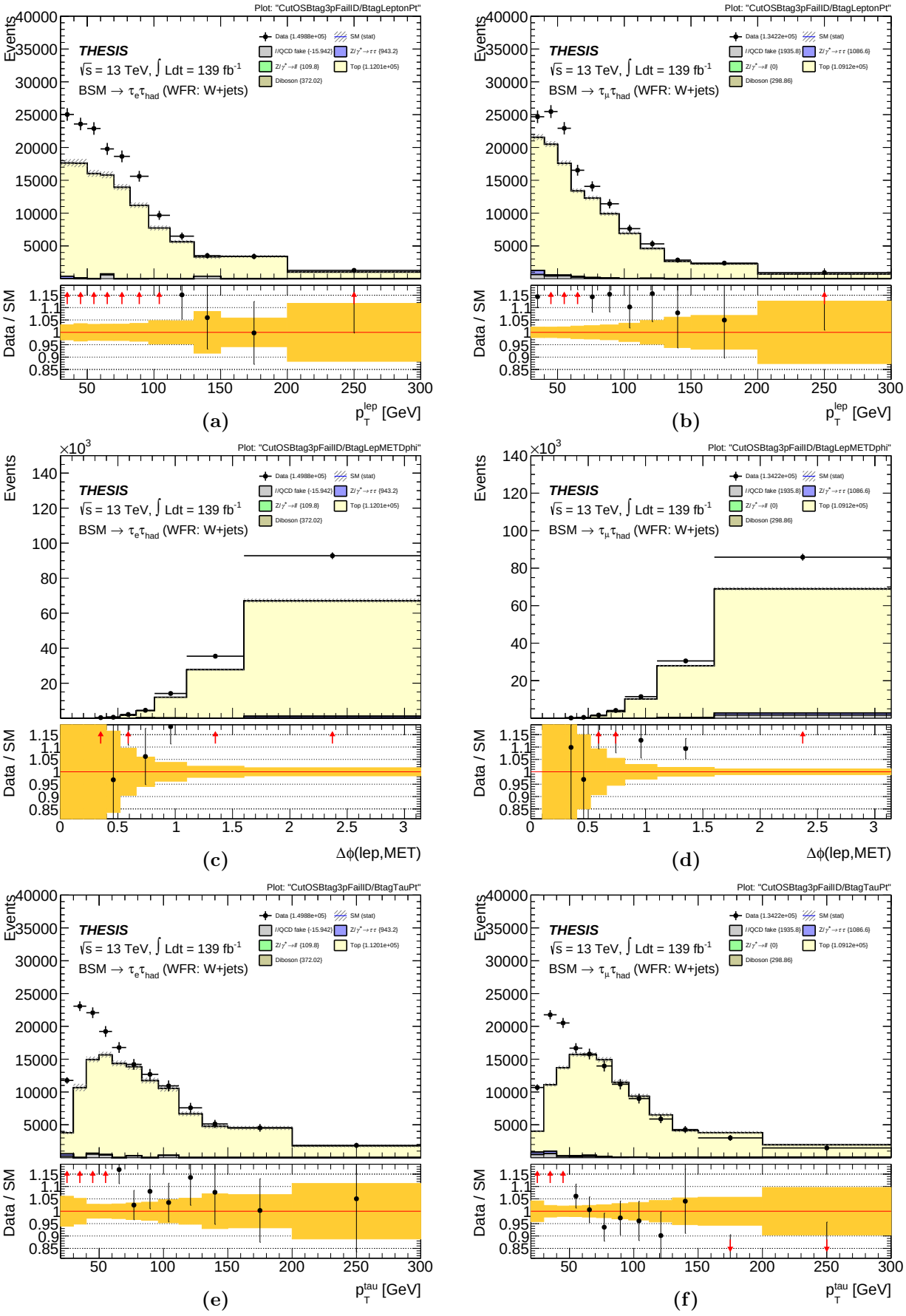

Figure B.2.16: Plots of the top quark fake component which fail the tau identification requirement within the Top Fake Region as used in the calculation of the Top Fake Factor, in the b-tag category, for the 3-prong tau decay mode, representing lepton p_{T}, $|\Delta\phi(\ell, E_{\mathrm{T}}^{\mathrm{miss}})|$ and tau p_{T} (from top to bottom). The region is divided into the $e\tau_{\mathrm{had}}$ (left) and $\mu\tau_{\mathrm{had}}$ (right) sub-channels.

B.3 Systematic uncertainties

Systematic	% yield
TTBar_PS	10.50
TTBar_ISR	8.50
TTBar_ME	5.55
FakeFactor_WjetsBtag1p	3.62
FakeFactor_WjetsReweight_ElHadBtag1p	1.46
TTBar_FSR	1.28
FakeFactor_ExtraSysBtag1p	1.21
JET_GroupedNP_2	0.93
JET_GroupedNP_1	0.86
TAUS_TRUEHADTAU_SME_TES_DETECTOR	0.81
TAUS_TRUEHADTAU_SME_TES_INSITU	0.59
JET_Flavor_Response	0.47
EG_SCALE_ALLCORR	0.41
TAUS_TRUEHADTAU_SME_TES_MODEL	0.35
MET_SoftTrk_ResoPara	0.16
MET_SoftTrk	0.11
JET_JER_EffectiveNP_7restTerm_1up	0.09
JET_JER_EffectiveNP_5_1up	0.09
JET_GroupedNP_3	0.08
MET_SoftTrk_ResoPerp	0.08
FakeFactor_LepElBtag	0.06
JET_JER_EffectiveNP_4_1up	0.05
JET_JER_DataVsMC_MC16_1up	0.04
JET_JER_EffectiveNP_1_1up	0.03
JET_JER_EffectiveNP_2_1up	0.03
JET_JER_EffectiveNP_3_1up	0.02
EG_RESOLUTION_ALL	0.02
MUON_SAGITTA_RHO	0.02
MUON_SAGITTA_RESBIAS	0.02
JET_JER_EffectiveNP_6_1up	0.02
MUON_SCALE	0.02
LPX_KFACTOR_CHOICE_HERAPDF20_Corr	0.02
LPX_KFACTOR_CHOICE_epWZ16_Corr	0.02
LPX_KFACTOR_PDF_Corr	0.01
EG_SCALE_E4SCINTILLATOR	0.01
LPX_KFACTOR_ALPHAS_Corr	0.01
LPX_KFACTOR_CHOICE_NNPDF30_Corr	0.00
LPX_KFACTOR_PDF_epWZ16_Corr	0.00
JET_EtaIntercalibration_NonClosure_posEta	0.00
LPX_KFACTOR_BEAM_ENERGY_Corr	0.00
MUON_ID	0.00
LPX_KFACTOR_SCALE_Z_Corr	0.00
LPX_KFACTOR_PI_Corr	0.00
JET_EtaIntercalibration_NonClosure_negEta	0.00
MUON_MS	0.00
LPX_KFACTOR_PDF_EW_Corr	0.00
LPX_KFACTOR_REDCHOICE_NNPDF30_Corr	0.00
JET_EtaIntercalibration_NonClosure_highE	0.00
EG_SCALE_AF2	0.00
EG_SCALE_ALL	0.00
EG_SCALE_LARCALIB_EXTRA2015PRE	0.00
EG_SCALE_LARTEMPERATURE_EXTRA2015PRE	0.00
EG_SCALE_LARTEMPERATURE_EXTRA2016PRE	0.00
JET_TILECORR_Uncertainty	0.00
LPX_KFACTOR_SCALE_W_Corr	0.00
btag_b_0	0.00
btag_b_1	0.00
btag_b_2	0.00
btag_c_0	0.00
btag_c_1	0.00

Systematic	% yield
TTBar_PS	10.94
TTBar_ISR	8.94
TTBar_ME	5.53
FakeFactor_WjetsBtag1p	3.53
FakeFactor_WjetsReweight_MuHadBtag1p	1.51
TTBar_FSR	1.28
JET_GroupedNP_2	1.05
FakeFactor_ExtraSysBtag1p	0.96
JET_GroupedNP_1	0.91
TAUS_TRUEHADTAU_SME_TES_DETECTOR	0.81
TAUS_TRUEHADTAU_SME_TES_INSITU	0.59
JET_Flavor_Response	0.55
TAUS_TRUEHADTAU_SME_TES_MODEL	0.31
FakeFactor_LepMuBtag	0.09
MUON_SCALE	0.08
JET_GroupedNP_3	0.08
MET_SoftTrk_ResoPerp	0.08
MET_SoftTrk_ResoPara	0.08
MET_SoftTrk	0.07
MUON_SAGITTA_RHO	0.06
JET_JER_EffectiveNP_4_1up	0.06
JET_JER_DataVsMC_MC16_1up	0.05
MUON_SAGITTA_RESBIAS	0.04
JET_JER_EffectiveNP_7restTerm_1up	0.03
JET_JER_EffectiveNP_6_1up	0.03
JET_JER_EffectiveNP_3_1up	0.03
FakeFactor_QCDReweight_MuHadBtag	0.03
MUON_ID	0.03
JET_JER_EffectiveNP_2_1up	0.03
EG_SCALE_ALLCORR	0.03
MUON_MS	0.02
EG_RESOLUTION_ALL	0.02
JET_JER_EffectiveNP_1_1up	0.02
LPX_KFACTOR_CHOICE_HERAPDF20_Corr	0.01
JET_EtaIntercalibration_NonClosure_negEta	0.01
LPX_KFACTOR_PDF_Corr	0.01
LPX_KFACTOR_CHOICE_epWZ16_Corr	0.01
LPX_KFACTOR_ALPHAS_Corr	0.01
LPX_KFACTOR_PI_Corr	0.01
LPX_KFACTOR_BEAM_ENERGY_Corr	0.01
LPX_KFACTOR_CHOICE_NNPDF30_Corr	0.01
LPX_KFACTOR_PDF_EW_Corr	0.01
LPX_KFACTOR_SCALE_Z_Corr	0.01
LPX_KFACTOR_REDCHOICE_NNPDF30_Corr	0.01
EG_SCALE_E4SCINTILLATOR	0.01
LPX_KFACTOR_SCALE_W_Corr	0.01
btag_b_0	0.01
btag_b_1	0.01
btag_b_2	0.01
btag_c_0	0.01
btag_c_1	0.01
btag_c_2	0.01
btag_c_3	0.01
btag_extrapolation	0.01
btag_extrapolation_from_charm	0.01
btag_light_0	0.01
btag_light_1	0.01
btag_light_2	0.01
btag_light_3	0.01
btag_light_4	0.01

Table B.3.1: Table of systematic uncertainties ranked in order as a percentage yield, in the $e\tau_{\text{had}}$ (left) and $\mu\tau_{\text{had}}$ (right) sub-channels, estimated in the Top Control Region, for the b-tag category and for 1-prong tau decays.

Systematic	% yield
TTBar_PS	11.04
TTBar_ISR	8.86
TTBar_ME	6.00
FakeFactor_ExtraSysBtag3p	3.24
FakeFactor_WjetsBtag3p	3.20
TAUS_TRUEHADTAU_SME_TES_DETECTOR	1.50
TTBar_FSR	1.36
FakeFactor_WjetsReweight_ElHadBtag3p	1.22
JET_GroupedNP_2	1.17
JET_GroupedNP_1	1.01
JET_Flavor_Response	0.65
EG_SCALE_ALLCORR	0.42
TAUS_TRUEHADTAU_SME_TES_INSITU	0.30
JET_JER_EffectiveNP_1_1up	0.23
JET_JER_EffectiveNP_7restTerm_1up	0.21
JET_JER_EffectiveNP_2_1up	0.16
MET_SoftTrk	0.10
JET_GroupedNP_3	0.09
TAUS_TRUEHADTAU_SME_TES_MODEL	0.06
JET_JER_EffectiveNP_3_1up	0.05
MET_SoftTrk_ResoPerp	0.05
JET_JER_EffectiveNP_5_1up	0.05
JET_JER_DataVsMC_MC16_1up	0.05
JET_JER_EffectiveNP_4_1up	0.05
MUON_SAGITTA_RESBIAS	0.03
MUON_SAGITTA_RHO	0.03
JET_JER_EffectiveNP_6_1up	0.02
FakeFactor_LepElBtag	0.02
MUON_SCALE	0.02
MUON_ID	0.01
MUON_MS	0.01
EG_SCALE_E4SCINTILLATOR	0.01
EG_RESOLUTION_ALL	0.01
JET_EtaIntercalibration_NonClosure_posEta	0.00
LPX_KFACTOR_CHOICE_HERAPDF20_Corr	0.00
JET_EtaIntercalibration_NonClosure_negEta	0.00
LPX_KFACTOR_PDF_Corr	0.00
LPX_KFACTOR_CHOICE_epWZ16_Corr	0.00
LPX_KFACTOR_ALPHAS_Corr	0.00
LPX_KFACTOR_PDF_epWZ16_Corr	0.00
LPX_KFACTOR_CHOICE_NNPDF30_Corr	0.00
LPX_KFACTOR_BEAM_ENERGY_Corr	0.00
LPX_KFACTOR_PI_Corr	0.00
LPX_KFACTOR_SCALE_Z_Corr	0.00
LPX_KFACTOR_PDF_EW_Corr	0.00
MET_SoftTrk_ResoPara	0.00
LPX_KFACTOR_REDCHOICE_NNPDF30_Corr	0.00
JET_EtaIntercalibration_NonClosure_highE	0.00
EG_SCALE_AF2	0.00
EG_SCALE_ALL	0.00
EG_SCALE_LARCALIB_EXTRA2015PRE	0.00
EG_SCALE_LARTEMPERATURE_EXTRA2015PRE	0.00
EG_SCALE_LARTEMPERATURE_EXTRA2016PRE	0.00
JET_TILECORR_Uncertainty	0.00
LPX_KFACTOR_SCALE_W_Corr	0.00
btag_b_0	0.00
btag_b_1	0.00
btag_b_2	0.00
btag_c_0	0.00
btag_c_1	0.00

Systematic	% yield
TTBar_PS	11.56
TTBar_ISR	9.39
TTBar_ME	5.96
FakeFactor_WjetsBtag3p	3.07
TAUS_TRUEHADTAU_SME_TES_DETECTOR	1.52
TTBar_FSR	1.37
JET_GroupedNP_2	1.34
FakeFactor_WjetsReweight_MuHadBtag3p	1.27
JET_GroupedNP_1	1.21
FakeFactor_ExtraSysBtag3p	0.99
JET_Flavor_Response	0.71
TAUS_TRUEHADTAU_SME_TES_INSITU	0.30
JET_JER_EffectiveNP_1_1up	0.16
JET_JER_EffectiveNP_2_1up	0.14
MET_SoftTrk	0.12
JET_JER_EffectiveNP_4_1up	0.11
FakeFactor_LepMuBtag	0.11
MUON_SAGITTA_RESBIAS	0.10
MUON_SAGITTA_RHO	0.10
JET_JER_DataVsMC_MC16_1up	0.09
MUON_SCALE	0.08
JET_JER_EffectiveNP_6_1up	0.07
MUON_MS	0.05
MET_SoftTrk_ResoPara	0.05
JET_JER_EffectiveNP_3_1up	0.05
JET_JER_EffectiveNP_5_1up	0.04
TAUS_TRUEHADTAU_SME_TES_MODEL	0.04
JET_JER_EffectiveNP_7restTerm_1up	0.04
JET_GroupedNP_3	0.03
EG_SCALE_ALLCORR	0.03
FakeFactor_QCDReweight_MuHadBtag	0.03
EG_RESOLUTION_ALL	0.02
JET_EtaIntercalibration_NonClosure_negEta	0.02
JET_EtaIntercalibration_NonClosure_posEta	0.01
LPX_KFACTOR_CHOICE_HERAPDF20_Corr	0.01
LPX_KFACTOR_PDF_Corr	0.01
MET_SoftTrk_ResoPerp	0.01
LPX_KFACTOR_CHOICE_epWZ16_Corr	0.01
LPX_KFACTOR_ALPHAS_Corr	0.01
LPX_KFACTOR_PI_Corr	0.01
LPX_KFACTOR_BEAM_ENERGY_Corr	0.01
LPX_KFACTOR_CHOICE_NNPDF30_Corr	0.01
LPX_KFACTOR_PDF_EW_Corr	0.01
LPX_KFACTOR_REDCHOICE_NNPDF30_Corr	0.01
JET_EtaIntercalibration_NonClosure_highE	0.01
EG_SCALE_AF2	0.01
EG_SCALE_ALL	0.01
EG_SCALE_E4SCINTILLATOR	0.01
EG_SCALE_LARCALIB_EXTRA2015PRE	0.01
EG_SCALE_LARTEMPERATURE_EXTRA2015PRE	0.01
EG_SCALE_LARTEMPERATURE_EXTRA2016PRE	0.01
JET_TILECORR_Uncertainty	0.01
LPX_KFACTOR_SCALE_W_Corr	0.01
btag_b_0	0.01
btag_b_1	0.01
btag_b_2	0.01
btag_c_0	0.01
btag_c_1	0.01
btag_c_2	0.01
btag_c_3	0.01

Table B.3.2: Table of systematic uncertainties ranked in order as a percentage yield, in the $e\tau_{\text{had}}$ (left) and $\mu\tau_{\text{had}}$ (right) sub-channels, estimated in the Top Control Region, for the b-tag category and for 3-prong tau decays.

Systematic	% yield
FakeFactor_WjetsReweight_ElHadBveto1p	3.81
FakeFactor_ExtraSysBveto1p	2.89
FakeFactor_WjetsBveto1p	2.24
LPX_KFACTOR_CHOICE_epWZ16_Corr	1.81
LPX_KFACTOR_CHOICE_HERAPDF20_Corr	1.56
LPX_KFACTOR_PDF_Corr	1.44
LPX_KFACTOR_ALPHAS_Corr	0.97
FakeFactor_LepElBveto	0.46
MET_SoftTrk	0.45
LPX_KFACTOR_CHOICE_NNPDF30_Corr	0.40
LPX_KFACTOR_PDF_epWZ16_Corr	0.36
LPX_KFACTOR_SCALE_Z_Corr	0.26
LPX_KFACTOR_BEAM_ENERGY_Corr	0.23
EG_SCALE_ALLCORR	0.21
TAUS_TRUEHADTAU_SME_TES_MODEL	0.18
MET_SoftTrk_ResoPerp	0.16
JET_GroupedNP_1	0.15
MET_SoftTrk_ResoPara	0.15
JET_GroupedNP_2	0.14
JET_JER_EffectiveNP_7restTerm_1up	0.10
JET_Flavor_Response	0.09
JET_JER_EffectiveNP_3_1up	0.08
JET_JER_EffectiveNP_6_1up	0.08
JET_JER_EffectiveNP_5_1up	0.07
JET_JER_EffectiveNP_4_1up	0.07
TTBar_PS	0.06
TTBar_ISR	0.06
TAUS_TRUEHADTAU_SME_TES_INSITU	0.05
JET_JER_EffectiveNP_2_1up	0.05
EG_RESOLUTION_ALL	0.04
LPX_KFACTOR_PI_Corr	0.02
LPX_KFACTOR_PDF_EW_Corr	0.02
TAUS_TRUEHADTAU_SME_TES_DETECTOR	0.01
TTBar_ME	0.01
JET_EtaIntercalibration_NonClosure_negEta	0.01
EG_SCALE_E4SCINTILLATOR	0.01
JET_JER_EffectiveNP_1_1up	0.01
JET_JER_DataVsMC_MC16_1up	0.01
JET_GroupedNP_3	0.00
JET_EtaIntercalibration_NonClosure_posEta	0.00
TTBar_FSR	0.00
MUON_MS	0.00
MUON_SAGITTA_RHO	0.00
MUON_ID	0.00
MUON_SAGITTA_RESBIAS	0.00
MUON_SCALE	0.00
JET_EtaIntercalibration_NonClosure_highE	0.00
LPX_KFACTOR_REDCHOICE_NNPDF30_Corr	0.00
EG_SCALE_AF2	0.00
EG_SCALE_ALL	0.00
EG_SCALE_LARCALIB_EXTRA2015PRE	0.00
EG_SCALE_LARTEMPERATURE_EXTRA2015PRE	0.00
EG_SCALE_LARTEMPERATURE_EXTRA2016PRE	0.00
JET_TILECORR_Uncertainty	0.00
LPX_KFACTOR_SCALE_W_Corr	0.00
btag_b_0	0.00
btag_b_1	0.00
btag_b_2	0.00
btag_c_0	0.00
btag_c_1	0.00

Systematic	% yield
FakeFactor_ExtraSysBveto1p	4.42
FakeFactor_WjetsReweight_MuHadBveto1p	3.30
LPX_KFACTOR_CHOICE_epWZ16_Corr	1.61
LPX_KFACTOR_CHOICE_HERAPDF20_Corr	1.37
LPX_KFACTOR_PDF_Corr	1.27
FakeFactor_WjetsBveto1p	1.16
LPX_KFACTOR_ALPHAS_Corr	0.86
FakeFactor_LepMuBveto	0.61
MET_SoftTrk	0.45
LPX_KFACTOR_CHOICE_NNPDF30_Corr	0.36
LPX_KFACTOR_PDF_epWZ16_Corr	0.32
FakeFactor_QCDReweight_MuHadBveto	0.29
MET_SoftTrk_ResoPara	0.24
LPX_KFACTOR_SCALE_Z_Corr	0.23
TAUS_TRUEHADTAU_SME_TES_MODEL	0.22
LPX_KFACTOR_BEAM_ENERGY_Corr	0.21
TAUS_TRUEHADTAU_SME_TES_INSITU	0.18
JET_JER_EffectiveNP_2_1up	0.17
JET_JER_EffectiveNP_3_1up	0.15
MET_SoftTrk_ResoPerp	0.15
MUON_SCALE	0.12
JET_JER_EffectiveNP_1_1up	0.11
MUON_MS	0.09
JET_GroupedNP_2	0.07
JET_GroupedNP_1	0.07
TTBar_PS	0.07
TTBar_ISR	0.06
JET_JER_EffectiveNP_7restTerm_1up	0.06
JET_JER_EffectiveNP_4_1up	0.06
JET_Flavor_Response	0.05
TAUS_TRUEHADTAU_SME_TES_DETECTOR	0.03
MUON_ID	0.02
JET_GroupedNP_3	0.02
MUON_SAGITTA_RESBIAS	0.02
JET_JER_DataVsMC_MC16_1up	0.02
LPX_KFACTOR_PI_Corr	0.02
MUON_SAGITTA_RHO	0.01
LPX_KFACTOR_PDF_EW_Corr	0.01
TTBar_ME	0.01
TTBar_FSR	0.00
JET_JER_EffectiveNP_6_1up	0.00
JET_EtaIntercalibration_NonClosure_posEta	0.00
JET_EtaIntercalibration_NonClosure_negEta	0.00
JET_JER_EffectiveNP_5_1up	0.00
EG_SCALE_ALLCORR	0.00
EG_RESOLUTION_ALL	0.00
LPX_KFACTOR_REDCHOICE_NNPDF30_Corr	0.00
JET_EtaIntercalibration_NonClosure_highE	0.00
EG_SCALE_AF2	0.00
EG_SCALE_ALL	0.00
EG_SCALE_E4SCINTILLATOR	0.00
EG_SCALE_LARCALIB_EXTRA2015PRE	0.00
EG_SCALE_LARTEMPERATURE_EXTRA2015PRE	0.00
EG_SCALE_LARTEMPERATURE_EXTRA2016PRE	0.00
JET_TILECORR_Uncertainty	0.00
LPX_KFACTOR_SCALE_W_Corr	0.00
btag_b_0	0.00
btag_b_1	0.00
btag_b_2	0.00
btag_c_0	0.00

Table B.3.3: Table of systematic uncertainties ranked in order as a percentage yield, in the $e\tau_{\text{had}}$ (left) and $\mu\tau_{\text{had}}$ (right) sub-channels, estimated in the Validation Region, for the b-veto category and for 1-prong tau decays.

Systematic	% yield
FakeFactor_ExtraSysBveto3p	4.87
FakeFactor_WjetsReweight_ElHadBveto3p	4.06
FakeFactor_WjetsBveto3p	2.41
LPX_KFACTOR_CHOICE_epWZ16_Corr	1.87
LPX_KFACTOR_CHOICE_HERAPDF20_Corr	1.59
LPX_KFACTOR_PDF_Corr	1.48
TAUS_TRUEHADTAU_SME_TES_INSITU	1.23
LPX_KFACTOR_ALPHAS_Corr	1.00
MET_SoftTrk_ResoPara	0.56
MET_SoftTrk	0.53
FakeFactor_LepElBveto	0.46
LPX_KFACTOR_CHOICE_NNPDF30_Corr	0.41
JET_JER_EffectiveNP_1_1up	0.40
LPX_KFACTOR_PDF_epWZ16_Corr	0.37
TAUS_TRUEHADTAU_SME_TES_MODEL	0.35
MET_SoftTrk_ResoPerp	0.30
JET_JER_EffectiveNP_3_1up	0.30
JET_JER_EffectiveNP_2_1up	0.29
LPX_KFACTOR_SCALE_Z_Corr	0.27
LPX_KFACTOR_BEAM_ENERGY_Corr	0.24
JET_GroupedNP_1	0.21
JET_GroupedNP_2	0.16
EG_SCALE_ALLCORR	0.14
JET_JER_EffectiveNP_4_1up	0.12
TTBar_PS	0.10
TTBar_ISR	0.10
JET_JER_EffectiveNP_5_1up	0.09
JET_JER_EffectiveNP_7restTerm_1up	0.09
JET_Flavor_Response	0.08
EG_RESOLUTION_ALL	0.05
JET_GroupedNP_3	0.03
TTBar_ME	0.02
JET_JER_DataVsMC_MC16_1up	0.02
LPX_KFACTOR_PI_Corr	0.02
LPX_KFACTOR_PDF_EW_Corr	0.02
JET_JER_EffectiveNP_6_1up	0.01
JET_EtaIntercalibration_NonClosure_negEta	0.01
TAUS_TRUEHADTAU_SME_TES_DETECTOR	0.01
MUON_ID	0.01
TTBar_FSR	0.00
EG_SCALE_E4SCINTILLATOR	0.00
JET_EtaIntercalibration_NonClosure_posEta	0.00
MUON_SAGITTA_RHO	0.00
MUON_MS	0.00
MUON_SAGITTA_RESBIAS	0.00
MUON_SCALE	0.00
LPX_KFACTOR_REDCHOICE_NNPDF30_Corr	0.00
EG_SCALE_AF2	0.00
EG_SCALE_ALL	0.00
EG_SCALE_LARCALIB_EXTRA2015PRE	0.00
EG_SCALE_LARTEMPERATURE_EXTRA2015PRE	0.00
EG_SCALE_LARTEMPERATURE_EXTRA2016PRE	0.00
JET_EtaIntercalibration_NonClosure_highE	0.00
JET_TILECORR_Uncertainty	0.00
LPX_KFACTOR_SCALE_W_Corr	0.00
btag_b_0	0.00
btag_b_1	0.00
btag_b_2	0.00
btag_c_0	0.00
btag_c_1	0.00

Systematic	% yield
FakeFactor_ExtraSysBveto3p	3.92
FakeFactor_WjetsReweight_MuHadBveto3p	3.54
LPX_KFACTOR_CHOICE_epWZ16_Corr	1.88
LPX_KFACTOR_CHOICE_HERAPDF20_Corr	1.60
LPX_KFACTOR_PDF_Corr	1.48
FakeFactor_WjetsBveto3p	1.31
LPX_KFACTOR_ALPHAS_Corr	1.00
TAUS_TRUEHADTAU_SME_TES_INSITU	0.73
MET_SoftTrk	0.67
JET_JER_EffectiveNP_1_1up	0.54
FakeFactor_LepMuBveto	0.51
JET_JER_EffectiveNP_2_1up	0.43
LPX_KFACTOR_CHOICE_NNPDF30_Corr	0.41
JET_GroupedNP_2	0.40
JET_GroupedNP_1	0.38
LPX_KFACTOR_PDF_epWZ16_Corr	0.37
TAUS_TRUEHADTAU_SME_TES_MODEL	0.30
JET_JER_EffectiveNP_3_1up	0.28
LPX_KFACTOR_SCALE_Z_Corr	0.27
LPX_KFACTOR_BEAM_ENERGY_Corr	0.24
FakeFactor_QCDReweight_MuHadBveto	0.22
JET_JER_EffectiveNP_4_1up	0.20
MET_SoftTrk_ResoPerp	0.17
JET_Flavor_Response	0.17
MUON_SCALE	0.15
JET_JER_EffectiveNP_5_1up	0.15
JET_JER_EffectiveNP_7restTerm_1up	0.14
MET_SoftTrk_ResoPara	0.13
JET_JER_EffectiveNP_6_1up	0.12
TTBar_PS	0.10
TTBar_ISR	0.10
MUON_MS	0.10
MUON_ID	0.05
JET_JER_DataVsMC_MC16_1up	0.04
MUON_SAGITTA_RHO	0.04
TAUS_TRUEHADTAU_SME_TES_DETECTOR	0.04
JET_GroupedNP_3	0.04
MUON_SAGITTA_RESBIAS	0.02
LPX_KFACTOR_PI_Corr	0.02
LPX_KFACTOR_PDF_EW_Corr	0.02
TTBar_ME	0.01
JET_EtaIntercalibration_NonClosure_posEta	0.01
TTBar_FSR	0.01
EG_SCALE_ALLCORR	0.01
EG_RESOLUTION_ALL	0.00
JET_EtaIntercalibration_NonClosure_negEta	0.00
LPX_KFACTOR_REDCHOICE_NNPDF30_Corr	0.00
EG_SCALE_AF2	0.00
EG_SCALE_ALL	0.00
EG_SCALE_E4SCINTILLATOR	0.00
EG_SCALE_LARCALIB_EXTRA2015PRE	0.00
EG_SCALE_LARTEMPERATURE_EXTRA2015PRE	0.00
EG_SCALE_LARTEMPERATURE_EXTRA2016PRE	0.00
JET_EtaIntercalibration_NonClosure_highE	0.00
JET_TILECORR_Uncertainty	0.00
LPX_KFACTOR_SCALE_W_Corr	0.00
btag_b_0	0.00
btag_b_1	0.00
btag_b_2	0.00
btag_c_0	0.00

Table B.3.4: Table of systematic uncertainties ranked in order as a percentage yield, in the $e\tau_{\text{had}}$ (left) and $\mu\tau_{\text{had}}$ (right) sub-channels, estimated in the Validation Region, for the b-veto category and for 3-prong tau decays.

Systematic	% yield
FakeFactor_WjetsBtag1p	12.55
TTBar_PS	4.62
FakeFactor_ExtraSysBtag1p	4.51
TTBar_ISR	4.37
FakeFactor_WjetsReweight_ElHadBtag1p	3.96
TAUS_TRUEHADTAU_SME_TES_DETECTOR	1.40
TTBar_ME	0.96
JET_GroupedNP_1	0.63
MET_SoftTrk_ResoPara	0.58
TAUS_TRUEHADTAU_SME_TES_INSITU	0.58
TAUS_TRUEHADTAU_SME_TES_MODEL	0.57
JET_GroupedNP_2	0.47
LPX_KFACTOR_CHOICE_epWZ16_Corr	0.43
JET_JER_EffectiveNP_4_1up	0.38
LPX_KFACTOR_CHOICE_HERAPDF20_Corr	0.38
MET_SoftTrk_ResoPerp	0.37
LPX_KFACTOR_PDF_Corr	0.34
EG_SCALE_ALLCORR	0.32
JET_JER_EffectiveNP_7restTerm_1up	0.29
FakeFactor_LepElBtag	0.25
JET_JER_DataVsMC_MC16_1up	0.24
LPX_KFACTOR_ALPHAS_Corr	0.23
JET_Flavor_Response	0.19
MET_SoftTrk	0.12
TTBar_FSR	0.12
JET_JER_EffectiveNP_6_1up	0.11
JET_JER_EffectiveNP_3_1up	0.11
JET_GroupedNP_3	0.10
LPX_KFACTOR_CHOICE_NNPDF30_Corr	0.10
LPX_KFACTOR_PDF_epWZ16_Corr	0.09
LPX_KFACTOR_SCALE_Z_Corr	0.07
LPX_KFACTOR_BEAM_ENERGY_Corr	0.06
JET_JER_EffectiveNP_2_1up	0.05
JET_JER_EffectiveNP_5_1up	0.05
JET_EtaIntercalibration_NonClosure_negEta	0.05
MUON_SAGITTA_RESBIAS	0.03
MUON_SAGITTA_RHO	0.03
JET_JER_EffectiveNP_1_1up	0.03
JET_EtaIntercalibration_NonClosure_posEta	0.03
EG_RESOLUTION_ALL	0.02
MUON_MS	0.02
MUON_SCALE	0.01
LPX_KFACTOR_PI_Corr	0.01
EG_SCALE_E4SCINTILLATOR	0.01
LPX_KFACTOR_PDF_EW_Corr	0.01
LPX_KFACTOR_REDCHOICE_NNPDF30_Corr	0.00
JET_EtaIntercalibration_NonClosure_highE	0.00
EG_SCALE_AF2	0.00
EG_SCALE_ALL	0.00
EG_SCALE_LARCALIB_EXTRA2015PRE	0.00
EG_SCALE_LARTEMPERATURE_EXTRA2015PRE	0.00
EG_SCALE_LARTEMPERATURE_EXTRA2016PRE	0.00
JET_TILECORR_Uncertainty	0.00
LPX_KFACTOR_SCALE_W_Corr	0.00
MUON_ID	0.00
btag_b_0	0.00
btag_b_1	0.00
btag_b_2	0.00
btag_c_0	0.00
btag_c_1	0.00

Systematic	% yield
FakeFactor_WjetsBtag1p	13.40
TTBar_PS	4.66
TTBar_ISR	4.59
FakeFactor_ExtraSysBtag1p	3.63
FakeFactor_WjetsReweight_MuHadBtag1p	3.26
TAUS_TRUEHADTAU_SME_TES_DETECTOR	1.04
TAUS_TRUEHADTAU_SME_TES_INSITU	0.78
TAUS_TRUEHADTAU_SME_TES_MODEL	0.74
TTBar_ME	0.58
FakeFactor_LepMuBtag	0.34
LPX_KFACTOR_CHOICE_epWZ16_Corr	0.32
JET_JER_EffectiveNP_3_1up	0.28
LPX_KFACTOR_CHOICE_HERAPDF20_Corr	0.28
TTBar_FSR	0.28
LPX_KFACTOR_PDF_Corr	0.24
JET_GroupedNP_2	0.19
LPX_KFACTOR_ALPHAS_Corr	0.16
FakeFactor_QCDReweight_MuHadBtag	0.16
JET_JER_EffectiveNP_4_1up	0.13
MET_SoftTrk_ResoPerp	0.13
MET_SoftTrk	0.13
JET_JER_EffectiveNP_2_1up	0.11
JET_Flavor_Response	0.10
MUON_MS	0.09
JET_JER_EffectiveNP_5_1up	0.08
LPX_KFACTOR_CHOICE_NNPDF30_Corr	0.08
MUON_ID	0.08
JET_JER_EffectiveNP_7restTerm_1up	0.07
LPX_KFACTOR_PDF_epWZ16_Corr	0.07
JET_JER_EffectiveNP_6_1up	0.06
MET_SoftTrk_ResoPara	0.06
LPX_KFACTOR_SCALE_Z_Corr	0.05
LPX_KFACTOR_BEAM_ENERGY_Corr	0.05
JET_GroupedNP_1	0.05
MUON_SAGITTA_RESBIAS	0.05
JET_GroupedNP_3	0.05
MUON_SCALE	0.03
JET_JER_EffectiveNP_1_1up	0.02
EG_SCALE_ALLCORR	0.02
MUON_SAGITTA_RHO	0.02
JET_JER_DataVsMC_MC16_1up	0.02
LPX_KFACTOR_PI_Corr	0.01
EG_RESOLUTION_ALL	0.01
LPX_KFACTOR_PDF_EW_Corr	0.01
JET_EtaIntercalibration_NonClosure_negEta	0.01
LPX_KFACTOR_REDCHOICE_NNPDF30_Corr	0.01
EG_SCALE_AF2	0.01
EG_SCALE_ALL	0.01
EG_SCALE_E4SCINTILLATOR	0.01
EG_SCALE_LARCALIB_EXTRA2015PRE	0.01
EG_SCALE_LARTEMPERATURE_EXTRA2015PRE	0.01
EG_SCALE_LARTEMPERATURE_EXTRA2016PRE	0.01
JET_EtaIntercalibration_NonClosure_highE	0.01
JET_TILECORR_Uncertainty	0.01
LPX_KFACTOR_SCALE_W_Corr	0.01
btag_b_0	0.01
btag_b_1	0.01
btag_b_2	0.01
btag_c_0	0.01
btag_c_1	0.01

Table B.3.5: Table of systematic uncertainties ranked in order as a percentage yield, in the $e\tau_{\text{had}}$ (left) and $\mu\tau_{\text{had}}$ (right) sub-channels, estimated in the Validation Region, for the b-tag category and for 1-prong tau decays.

Systematic	% yield
FakeFactor_WjetsBtag3p	10.16
FakeFactor_ExtraSysBtag3p	10.03
TTBar_PS	5.95
TTBar_ISR	5.60
FakeFactor_WjetsReweight_ElHadBtag3p	3.20
TAUS_TRUEHADTAU_SME_TES_DETECTOR	2.84
TAUS_TRUEHADTAU_SME_TES_INSITU	1.54
TTBar_ME	1.28
TAUS_TRUEHADTAU_SME_TES_MODEL	1.14
JET_GroupedNP_2	0.70
JET_JER_EffectiveNP_3_1up	0.65
JET_GroupedNP_1	0.64
EG_SCALE_ALLCORR	0.53
JET_Flavor_Response	0.41
JET_JER_EffectiveNP_1_1up	0.38
EG_RESOLUTION_ALL	0.37
MET_SoftTrk_ResoPara	0.36
JET_JER_EffectiveNP_2_1up	0.34
FakeFactor_LepElBtag	0.33
MET_SoftTrk	0.33
JET_GroupedNP_3	0.32
JET_JER_EffectiveNP_6_1up	0.28
JET_JER_EffectiveNP_5_1up	0.27
LPX_KFACTOR_CHOICE_epWZ16_Corr	0.26
LPX_KFACTOR_CHOICE_HERAPDF20_Corr	0.23
MET_SoftTrk_ResoPerp	0.22
JET_JER_EffectiveNP_4_1up	0.21
LPX_KFACTOR_PDF_Corr	0.21
TTBar_FSR	0.20
LPX_KFACTOR_ALPHAS_Corr	0.14
JET_JER_DataVsMC_MC16_1up	0.11
JET_EtaIntercalibration_NonClosure_posEta	0.08
JET_JER_EffectiveNP_7restTerm_1up	0.06
LPX_KFACTOR_CHOICE_NNPDF30_Corr	0.06
LPX_KFACTOR_PDF_epWZ16_Corr	0.05
LPX_KFACTOR_SCALE_Z_Corr	0.04
LPX_KFACTOR_BEAM_ENERGY_Corr	0.03
MUON_MS	0.02
JET_EtaIntercalibration_NonClosure_negEta	0.02
EG_SCALE_E4SCINTILLATOR	0.02
MUON_SAGITTA_RESBIAS	0.01
MUON_SAGITTA_RHO	0.01
LPX_KFACTOR_PI_Corr	0.01
LPX_KFACTOR_PDF_EW_Corr	0.00
LPX_KFACTOR_REDCHOICE_NNPDF30_Corr	0.00
EG_SCALE_AF2	0.00
EG_SCALE_ALL	0.00
EG_SCALE_LARCALIB_EXTRA2015PRE	0.00
EG_SCALE_LARTEMPERATURE_EXTRA2015PRE	0.00
EG_SCALE_LARTEMPERATURE_EXTRA2016PRE	0.00
FakeFactor_ExtraSysBtag1p	0.00
FakeFactor_ExtraSysBveto1p	0.00
FakeFactor_ExtraSysBveto3p	0.00
FakeFactor_LepElBveto	0.00
FakeFactor_LepMuBtag	0.00
FakeFactor_LepMuBveto	0.00
FakeFactor_QCDReweight_MuHadBtag	0.00
FakeFactor_QCDReweight_MuHadBveto	0.00
FakeFactor_WjetsBtag1p	0.00
FakeFactor_WjetsBveto1p	0.00

Systematic	% yield
FakeFactor_WjetsBtag3p	10.67
TTBar_PS	5.85
TTBar_ISR	5.75
FakeFactor_ExtraSysBtag3p	3.47
FakeFactor_WjetsReweight_MuHadBtag3p	2.78
TAUS_TRUEHADTAU_SME_TES_DETECTOR	1.38
TAUS_TRUEHADTAU_SME_TES_INSITU	0.99
JET_GroupedNP_2	0.86
TTBar_ME	0.80
JET_GroupedNP_1	0.60
JET_JER_EffectiveNP_3_1up	0.57
MET_SoftTrk_ResoPara	0.55
MET_SoftTrk_ResoPerp	0.54
JET_Flavor_Response	0.49
TAUS_TRUEHADTAU_SME_TES_MODEL	0.44
MUON_SAGITTA_RHO	0.41
MET_SoftTrk	0.38
MUON_SAGITTA_RESBIAS	0.37
LPX_KFACTOR_CHOICE_epWZ16_Corr	0.32
TTBar_FSR	0.31
FakeFactor_LepMuBtag	0.31
LPX_KFACTOR_CHOICE_HERAPDF20_Corr	0.28
LPX_KFACTOR_PDF_Corr	0.25
JET_GroupedNP_3	0.22
JET_JER_EffectiveNP_4_1up	0.21
JET_JER_EffectiveNP_1_1up	0.20
MUON_MS	0.19
JET_JER_EffectiveNP_6_1up	0.18
LPX_KFACTOR_ALPHAS_Corr	0.17
JET_JER_DataVsMC_MC16_1up	0.15
MUON_ID	0.15
FakeFactor_QCDReweight_MuHadBtag	0.13
JET_JER_EffectiveNP_5_1up	0.08
LPX_KFACTOR_CHOICE_NNPDF30_Corr	0.07
MUON_SCALE	0.07
LPX_KFACTOR_PDF_epWZ16_Corr	0.06
JET_EtaIntercalibration_NonClosure_negEta	0.05
LPX_KFACTOR_BEAM_ENERGY_Corr	0.04
LPX_KFACTOR_SCALE_Z_Corr	0.04
JET_EtaIntercalibration_NonClosure_posEta	0.03
JET_JER_EffectiveNP_7restTerm_1up	0.01
LPX_KFACTOR_PI_Corr	0.01
EG_RESOLUTION_ALL	0.01
EG_SCALE_ALLCORR	0.01
LPX_KFACTOR_PDF_EW_Corr	0.01
LPX_KFACTOR_REDCHOICE_NNPDF30_Corr	0.00
EG_SCALE_AF2	0.00
EG_SCALE_ALL	0.00
EG_SCALE_E4SCINTILLATOR	0.00
EG_SCALE_LARCALIB_EXTRA2015PRE	0.00
EG_SCALE_LARTEMPERATURE_EXTRA2015PRE	0.00
EG_SCALE_LARTEMPERATURE_EXTRA2016PRE	0.00
JET_EtaIntercalibration_NonClosure_highE	0.00
JET_TILECORR_Uncertainty	0.00
LPX_KFACTOR_SCALE_W_Corr	0.00
btag_b_0	0.00
btag_b_1	0.00
btag_b_2	0.00
btag_c_0	0.00
btag_c_1	0.00

Table B.3.6: Table of systematic uncertainties ranked in order as a percentage yield, in the $e\tau_{\text{had}}$ (left) and $\mu\tau_{\text{had}}$ (right) sub-channels, estimated in the Validation Region, for the b-tag category and for 3-prong tau decays.

Systematic	% yield
LPX_KFACTOR_CHOICE_epWZ16_Corr	3.12
LPX_KFACTOR_CHOICE_HERAPDF20_Corr	2.69
LPX_KFACTOR_PDF_Corr	2.48
FakeFactor_ExtraSysBveto1p	2.39
LPX_KFACTOR_ALPHAS_Corr	1.67
FakeFactor_WjetsReweight_ElHadBveto1p	1.67
FakeFactor_WjetsBveto1p	1.08
TAUS_TRUEHADTAU_SME_TES_INSITU	0.78
LPX_KFACTOR_CHOICE_NNPDF30_Corr	0.69
TAUS_TRUEHADTAU_SME_TES_MODEL	0.65
LPX_KFACTOR_PDF_epWZ16_Corr	0.62
JET_JER_EffectiveNP_1_1up	0.56
FakeFactor_LepElBveto	0.52
LPX_KFACTOR_SCALE_Z_Corr	0.45
JET_GroupedNP_1	0.44
MET_SoftTrk	0.43
LPX_KFACTOR_BEAM_ENERGY_Corr	0.41
JET_GroupedNP_2	0.39
JET_JER_EffectiveNP_2_1up	0.36
JET_JER_EffectiveNP_3_1up	0.31
MET_SoftTrk_ResoPara	0.25
EG_SCALE_ALLCORR	0.24
JET_JER_EffectiveNP_7restTerm_1up	0.20
JET_JER_EffectiveNP_4_1up	0.20
JET_JER_EffectiveNP_6_1up	0.16
JET_JER_EffectiveNP_5_1up	0.16
JET_Flavor_Response	0.13
TAUS_TRUEHADTAU_SME_TES_DETECTOR	0.11
MET_SoftTrk_ResoPerp	0.11
EG_RESOLUTION_ALL	0.09
LPX_KFACTOR_PI_Corr	0.05
TTBar_PS	0.04
TTBar_ISR	0.04
LPX_KFACTOR_PDF_EW_Corr	0.03
JET_JER_DataVsMC_MC16_1up	0.02
JET_GroupedNP_3	0.02
TTBar_ME	0.01
EG_SCALE_E4SCINTILLATOR	0.01
JET_EtaIntercalibration_NonClosure_negEta	0.00
TTBar_FSR	0.00
JET_EtaIntercalibration_NonClosure_posEta	0.00
MUON_SCALE	0.00
MUON_MS	0.00
MUON_SAGITTA_RHO	0.00
MUON_SAGITTA_RESBIAS	0.00
MUON_ID	0.00
JET_EtaIntercalibration_NonClosure_highE	0.00
LPX_KFACTOR_REDCHOICE_NNPDF30_Corr	0.00
EG_SCALE_AF2	0.00
EG_SCALE_ALL	0.00
EG_SCALE_LARCALIB_EXTRA2015PRE	0.00
EG_SCALE_LARTEMPERATURE_EXTRA2015PRE	0.00
EG_SCALE_LARTEMPERATURE_EXTRA2016PRE	0.00
JET_TILECORR_Uncertainty	0.00
LPX_KFACTOR_SCALE_W_Corr	0.00
btag_b_0	0.00
btag_b_1	0.00
btag_b_2	0.00
btag_c_0	0.00
btag_c_1	0.00

Systematic	% yield
FakeFactor_ExtraSysBveto1p	3.42
LPX_KFACTOR_CHOICE_epWZ16_Corr	3.10
LPX_KFACTOR_CHOICE_HERAPDF20_Corr	2.67
LPX_KFACTOR_PDF_Corr	2.46
LPX_KFACTOR_ALPHAS_Corr	1.66
TAUS_TRUEHADTAU_SME_TES_INSITU	1.50
FakeFactor_WjetsReweight_MuHadBveto1p	1.37
TAUS_TRUEHADTAU_SME_TES_MODEL	1.00
LPX_KFACTOR_CHOICE_NNPDF30_Corr	0.69
FakeFactor_WjetsBveto1p	0.61
LPX_KFACTOR_PDF_epWZ16_Corr	0.61
FakeFactor_LepMuBveto	0.59
JET_JER_EffectiveNP_1_1up	0.58
LPX_KFACTOR_SCALE_Z_Corr	0.45
MET_SoftTrk	0.41
LPX_KFACTOR_BEAM_ENERGY_Corr	0.40
JET_JER_EffectiveNP_2_1up	0.38
JET_GroupedNP_1	0.37
JET_GroupedNP_2	0.35
JET_JER_EffectiveNP_3_1up	0.30
MET_SoftTrk_ResoPara	0.26
FakeFactor_QCDReweight_MuHadBveto	0.22
MET_SoftTrk_ResoPerp	0.21
JET_JER_EffectiveNP_4_1up	0.19
JET_JER_EffectiveNP_7restTerm_1up	0.18
MUON_SCALE	0.13
JET_Flavor_Response	0.13
JET_JER_EffectiveNP_6_1up	0.12
JET_JER_EffectiveNP_5_1up	0.12
TAUS_TRUEHADTAU_SME_TES_DETECTOR	0.08
TTBar_PS	0.05
TTBar_ISR	0.05
LPX_KFACTOR_PI_Corr	0.04
LPX_KFACTOR_PDF_EW_Corr	0.03
JET_JER_DataVsMC_MC16_1up	0.03
MUON_SAGITTA_RHO	0.02
JET_GroupedNP_3	0.02
MUON_ID	0.02
MUON_MS	0.02
TTBar_ME	0.01
MUON_SAGITTA_RESBIAS	0.01
TTBar_FSR	0.00
JET_EtaIntercalibration_NonClosure_posEta	0.00
JET_EtaIntercalibration_NonClosure_negEta	0.00
EG_SCALE_ALLCORR	0.00
EG_RESOLUTION_ALL	0.00
LPX_KFACTOR_REDCHOICE_NNPDF30_Corr	0.00
EG_SCALE_E4SCINTILLATOR	0.00
LPX_KFACTOR_SCALE_W_Corr	0.00
btag_b_0	0.00
btag_b_1	0.00
btag_b_2	0.00
btag_c_0	0.00
btag_c_1	0.00
btag_c_2	0.00
btag_c_3	0.00
btag_extrapolation	0.00
btag_extrapolation_from_charm	0.00
btag_light_0	0.00
btag_light_1	0.00

Table B.3.7: Table of systematic uncertainties ranked in order as a percentage yield, in the $e\tau_{\text{had}}$ (left) and $\mu\tau_{\text{had}}$ (right) sub-channels, estimated in the Signal Region, for the b-veto category and for 1-prong tau decays.

Systematic	% yield
LPX_KFACTOR_CHOICE_epWZ16_Corr	3.56
LPX_KFACTOR_CHOICE_HERAPDF20_Corr	3.04
LPX_KFACTOR_PDF_Corr	2.82
LPX_KFACTOR_ALPHAS_Corr	1.90
FakeFactor_WjetsReweight_ElHadBveto3p	1.66
FakeFactor_ExtraSysBveto3p	1.46
FakeFactor_WjetsBveto3p	0.95
LPX_KFACTOR_CHOICE_NNPDF30_Corr	0.78
LPX_KFACTOR_PDF_epWZ16_Corr	0.70
JET_JER_EffectiveNP_1_1up	0.56
LPX_KFACTOR_SCALE_Z_Corr	0.51
LPX_KFACTOR_BEAM_ENERGY_Corr	0.46
TAUS_TRUEHADTAU_SME_TES_MODEL	0.41
FakeFactor_LepElBveto	0.40
MET_SoftTrk	0.38
JET_JER_EffectiveNP_2_1up	0.37
JET_GroupedNP_1	0.36
TAUS_TRUEHADTAU_SME_TES_INSITU	0.36
JET_GroupedNP_2	0.34
MET_SoftTrk_ResoPara	0.32
EG_SCALE_ALLCORR	0.32
JET_JER_EffectiveNP_3_1up	0.30
TAUS_TRUEHADTAU_SME_TES_DETECTOR	0.20
MET_SoftTrk_ResoPerp	0.20
JET_Flavor_Response	0.17
JET_JER_EffectiveNP_4_1up	0.15
JET_JER_EffectiveNP_7restTerm_1up	0.11
EG_RESOLUTION_ALL	0.07
TTBar_PS	0.07
TTBar_ISR	0.06
JET_JER_EffectiveNP_6_1up	0.06
LPX_KFACTOR_PI_Corr	0.04
JET_GroupedNP_3	0.04
LPX_KFACTOR_PDF_EW_Corr	0.03
JET_JER_EffectiveNP_5_1up	0.02
TTBar_ME	0.02
JET_JER_DataVsMC_MC16_1up	0.01
JET_EtaIntercalibration_NonClosure_negEta	0.01
EG_SCALE_E4SCINTILLATOR	0.01
MUON_SAGITTA_RESBIAS	0.01
MUON_SAGITTA_RHO	0.01
MUON_MS	0.01
JET_EtaIntercalibration_NonClosure_posEta	0.00
MUON_SCALE	0.00
MUON_ID	0.00
TTBar_FSR	0.00
LPX_KFACTOR_REDCHOICE_NNPDF30_Corr	0.00
JET_EtaIntercalibration_NonClosure_highE	0.00
EG_SCALE_AF2	0.00
EG_SCALE_ALL	0.00
EG_SCALE_LARCALIB_EXTRA2015PRE	0.00
EG_SCALE_LARTEMPERATURE_EXTRA2015PRE	0.00
EG_SCALE_LARTEMPERATURE_EXTRA2016PRE	0.00
JET_TILECORR_Uncertainty	0.00
LPX_KFACTOR_SCALE_W_Corr	0.00
btag_b_0	0.00
btag_b_1	0.00
btag_b_2	0.00
btag_c_0	0.00
btag_c_1	0.00

Systematic	% yield
LPX_KFACTOR_CHOICE_epWZ16_Corr	3.75
LPX_KFACTOR_CHOICE_HERAPDF20_Corr	3.22
LPX_KFACTOR_PDF_Corr	2.97
LPX_KFACTOR_ALPHAS_Corr	2.01
FakeFactor_ExtraSysBveto3p	1.95
TAUS_TRUEHADTAU_SME_TES_INSITU	1.94
FakeFactor_WjetsReweight_MuHadBveto3p	1.27
TAUS_TRUEHADTAU_SME_TES_MODEL	1.06
LPX_KFACTOR_CHOICE_NNPDF30_Corr	0.83
LPX_KFACTOR_PDF_epWZ16_Corr	0.74
JET_JER_EffectiveNP_1_1up	0.70
LPX_KFACTOR_SCALE_Z_Corr	0.54
FakeFactor_WjetsBveto3p	0.54
JET_GroupedNP_1	0.51
JET_GroupedNP_2	0.49
LPX_KFACTOR_BEAM_ENERGY_Corr	0.49
MET_SoftTrk	0.45
JET_JER_EffectiveNP_2_1up	0.41
JET_JER_EffectiveNP_3_1up	0.28
FakeFactor_LepMuBveto	0.26
JET_JER_EffectiveNP_4_1up	0.23
JET_Flavor_Response	0.22
MET_SoftTrk_ResoPara	0.19
MET_SoftTrk_ResoPerp	0.18
JET_JER_EffectiveNP_7restTerm_1up	0.18
JET_JER_EffectiveNP_6_1up	0.18
MUON_SCALE	0.18
JET_JER_EffectiveNP_5_1up	0.17
TAUS_TRUEHADTAU_SME_TES_DETECTOR	0.11
FakeFactor_QCDReweight_MuHadBveto	0.08
TTBar_PS	0.06
TTBar_ISR	0.06
LPX_KFACTOR_PI_Corr	0.05
MUON_SAGITTA_RESBIAS	0.04
LPX_KFACTOR_PDF_EW_Corr	0.03
JET_GroupedNP_3	0.02
MUON_MS	0.02
MUON_ID	0.02
MUON_SAGITTA_RHO	0.01
TTBar_ME	0.01
JET_JER_DataVsMC_MC16_1up	0.01
EG_SCALE_ALLCORR	0.01
TTBar_FSR	0.00
EG_RESOLUTION_ALL	0.00
JET_EtaIntercalibration_NonClosure_posEta	0.00
JET_EtaIntercalibration_NonClosure_negEta	0.00
LPX_KFACTOR_REDCHOICE_NNPDF30_Corr	0.00
JET_EtaIntercalibration_NonClosure_highE	0.00
EG_SCALE_AF2	0.00
EG_SCALE_ALL	0.00
EG_SCALE_E4SCINTILLATOR	0.00
EG_SCALE_LARCALIB_EXTRA2015PRE	0.00
EG_SCALE_LARTEMPERATURE_EXTRA2015PRE	0.00
EG_SCALE_LARTEMPERATURE_EXTRA2016PRE	0.00
JET_TILECORR_Uncertainty	0.00
LPX_KFACTOR_SCALE_W_Corr	0.00
btag_b_0	0.00
btag_b_1	0.00
btag_b_2	0.00
btag_c_0	0.00

Table B.3.8: Table of systematic uncertainties ranked in order as a percentage yield, in the $e\tau_{\text{had}}$ (left) and $\mu\tau_{\text{had}}$ (right) sub-channels, estimated in the Signal Region, for the b-veto category and for 3-prong tau decays.

Systematic	% yield
FakeFactor_WjetsBtag1p	9.42
TTBar_PS	4.74
TTBar_ISR	4.38
FakeFactor_ExtraSysBtag1p	3.48
FakeFactor_WjetsReweight_ElHadBtag1p	3.15
TAUS_TRUEHADTAU_SME_TES_DETECTOR	1.56
TTBar_ME	1.22
TAUS_TRUEHADTAU_SME_TES_INSITU	1.04
LPX_KFACTOR_CHOICE_epWZ16_Corr	0.76
JET_GroupedNP_1	0.74
TAUS_TRUEHADTAU_SME_TES_MODEL	0.72
JET_GroupedNP_2	0.70
LPX_KFACTOR_CHOICE_HERAPDF20_Corr	0.66
LPX_KFACTOR_PDF_Corr	0.61
FakeFactor_LepElBtag	0.44
LPX_KFACTOR_ALPHAS_Corr	0.41
JET_Flavor_Response	0.30
MET_SoftTrk	0.20
TTBar_FSR	0.19
EG_SCALE_ALLCORR	0.19
LPX_KFACTOR_CHOICE_NNPDF30_Corr	0.17
JET_JER_EffectiveNP_3_1up	0.16
LPX_KFACTOR_PDF_epWZ16_Corr	0.15
EG_RESOLUTION_ALL	0.14
JET_GroupedNP_3	0.12
JET_JER_EffectiveNP_5_1up	0.11
LPX_KFACTOR_SCALE_Z_Corr	0.11
JET_JER_EffectiveNP_2_1up	0.10
LPX_KFACTOR_BEAM_ENERGY_Corr	0.10
MET_SoftTrk_ResoPara	0.10
JET_JER_EffectiveNP_4_1up	0.06
JET_JER_DataVsMC_MC16_1up	0.05
MET_SoftTrk_ResoPerp	0.04
JET_JER_EffectiveNP_6_1up	0.03
JET_JER_EffectiveNP_1_1up	0.02
LPX_KFACTOR_PI_Corr	0.02
JET_EtaIntercalibration_NonClosure_negEta	0.02
MUON_ID	0.01
MUON_SCALE	0.01
LPX_KFACTOR_PDF_EW_Corr	0.01
JET_JER_EffectiveNP_7restTerm_1up	0.01
JET_EtaIntercalibration_NonClosure_posEta	0.01
EG_SCALE_E4SCINTILLATOR	0.00
MUON_SAGITTA_RESBIAS	0.00
LPX_KFACTOR_REDCHOICE_NNPDF30_Corr	0.00
EG_SCALE_AF2	0.00
EG_SCALE_ALL	0.00
EG_SCALE_LARCALIB_EXTRA2015PRE	0.00
EG_SCALE_LARTEMPERATURE_EXTRA2015PRE	0.00
EG_SCALE_LARTEMPERATURE_EXTRA2016PRE	0.00
JET_EtaIntercalibration_NonClosure_highE	0.00
JET_TILECORR_Uncertainty	0.00
LPX_KFACTOR_SCALE_W_Corr	0.00
btag_b_0	0.00
btag_b_1	0.00
btag_b_2	0.00
btag_c_0	0.00
btag_c_1	0.00
btag_c_2	0.00
btag_c_3	0.00

Systematic	% yield
FakeFactor_WjetsBtag1p	10.35
TTBar_PS	4.70
TTBar_ISR	4.51
FakeFactor_WjetsReweight_MuHadBtag1p	2.68
FakeFactor_ExtraSysBtag1p	2.66
TAUS_TRUEHADTAU_SME_TES_DETECTOR	1.16
TAUS_TRUEHADTAU_SME_TES_INSITU	1.05
TTBar_ME	0.84
TAUS_TRUEHADTAU_SME_TES_MODEL	0.71
JET_JER_EffectiveNP_1_1up	0.63
JET_JER_EffectiveNP_2_1up	0.60
LPX_KFACTOR_CHOICE_epWZ16_Corr	0.58
FakeFactor_LepMuBtag	0.52
LPX_KFACTOR_CHOICE_HERAPDF20_Corr	0.51
JET_JER_EffectiveNP_3_1up	0.46
LPX_KFACTOR_PDF_Corr	0.45
JET_JER_EffectiveNP_7restTerm_1up	0.40
JET_JER_EffectiveNP_5_1up	0.31
LPX_KFACTOR_ALPHAS_Corr	0.30
FakeFactor_QCDReweight_MuHadBtag	0.24
JET_JER_EffectiveNP_6_1up	0.24
TTBar_FSR	0.24
JET_GroupedNP_1	0.23
JET_JER_EffectiveNP_4_1up	0.23
MUON_SAGITTA_RHO	0.16
JET_Flavor_Response	0.14
LPX_KFACTOR_CHOICE_NNPDF30_Corr	0.13
JET_GroupedNP_2	0.12
LPX_KFACTOR_PDF_epWZ16_Corr	0.12
MUON_SAGITTA_RESBIAS	0.10
MUON_MS	0.09
MET_SoftTrk	0.09
LPX_KFACTOR_SCALE_Z_Corr	0.09
LPX_KFACTOR_BEAM_ENERGY_Corr	0.08
JET_JER_DataVsMC_MC16_1up	0.08
MET_SoftTrk_ResoPerp	0.05
JET_GroupedNP_3	0.05
MUON_ID	0.03
MET_SoftTrk_ResoPara	0.03
MUON_SCALE	0.02
LPX_KFACTOR_PI_Corr	0.02
JET_EtaIntercalibration_NonClosure_posEta	0.01
LPX_KFACTOR_PDF_EW_Corr	0.01
EG_SCALE_ALLCORR	0.01
EG_RESOLUTION_ALL	0.01
LPX_KFACTOR_REDCHOICE_NNPDF30_Corr	0.01
JET_EtaIntercalibration_NonClosure_highE	0.01
EG_SCALE_AF2	0.01
EG_SCALE_ALL	0.01
EG_SCALE_E4SCINTILLATOR	0.01
EG_SCALE_LARCALIB_EXTRA2015PRE	0.01
EG_SCALE_LARTEMPERATURE_EXTRA2015PRE	0.01
EG_SCALE_LARTEMPERATURE_EXTRA2016PRE	0.01
JET_TILECORR_Uncertainty	0.01
LPX_KFACTOR_SCALE_W_Corr	0.01
btag_b_0	0.01
btag_b_1	0.01
btag_b_2	0.01
btag_c_0	0.01
btag_c_1	0.01

Table B.3.9: Table of systematic uncertainties ranked in order as a percentage yield, in the $e\tau_{\text{had}}$ (left) and $\mu\tau_{\text{had}}$ (right) sub-channels, estimated in the Signal Region, for the b-tag category and for 1-prong tau decays.

Systematic	% yield
FakeFactor_WjetsBtag3p	6.79
FakeFactor_ExtraSysBtag3p	6.57
TTBar_PS	6.43
TTBar_ISR	5.95
TAUS_TRUEHADTAU_SME_TES_DETECTOR	2.67
FakeFactor_WjetsReweight_ElHadBtag3p	2.25
TTBar_ME	1.61
TAUS_TRUEHADTAU_SME_TES_MODEL	1.05
JET_JER_DataVsMC_MC16_1up	0.96
JET_JER_EffectiveNP_1_1up	0.93
JET_JER_EffectiveNP_4_1up	0.91
JET_JER_EffectiveNP_2_1up	0.81
LPX_KFACTOR_CHOICE_epWZ16_Corr	0.69
TAUS_TRUEHADTAU_SME_TES_INSITU	0.68
JET_JER_EffectiveNP_3_1up	0.67
JET_JER_EffectiveNP_7restTerm_1up	0.67
LPX_KFACTOR_CHOICE_HERAPDF20_Corr	0.60
LPX_KFACTOR_PDF_Corr	0.55
FakeFactor_LepElBtag	0.45
JET_GroupedNP_1	0.44
JET_JER_EffectiveNP_6_1up	0.41
LPX_KFACTOR_ALPHAS_Corr	0.37
EG_RESOLUTION_ALL	0.37
JET_GroupedNP_2	0.36
EG_SCALE_ALLCORR	0.31
JET_GroupedNP_3	0.27
TTBar_FSR	0.27
MET_SoftTrk_ResoPara	0.26
JET_JER_EffectiveNP_5_1up	0.22
JET_Flavor_Response	0.18
LPX_KFACTOR_CHOICE_NNPDF30_Corr	0.15
LPX_KFACTOR_PDF_epWZ16_Corr	0.14
MET_SoftTrk	0.12
LPX_KFACTOR_SCALE_Z_Corr	0.10
MET_SoftTrk_ResoPerp	0.10
LPX_KFACTOR_BEAM_ENERGY_Corr	0.09
MUON_ID	0.04
JET_EtaIntercalibration_NonClosure_posEta	0.02
MUON_SCALE	0.02
EG_SCALE_E4SCINTILLATOR	0.02
LPX_KFACTOR_PI_Corr	0.01
MUON_MS	0.01
MUON_SAGITTA_RHO	0.01
LPX_KFACTOR_PDF_EW_Corr	0.01
JET_EtaIntercalibration_NonClosure_negEta	0.01
MUON_SAGITTA_RESBIAS	0.00
LPX_KFACTOR_REDCHOICE_NNPDF30_Corr	0.00
EG_SCALE_AF2	0.00
EG_SCALE_ALL	0.00
EG_SCALE_LARCALIB_EXTRA2015PRE	0.00
EG_SCALE_LARTEMPERATURE_EXTRA2015PRE	0.00
EG_SCALE_LARTEMPERATURE_EXTRA2016PRE	0.00
JET_EtaIntercalibration_NonClosure_highE	0.00
JET_TILECORR_Uncertainty	0.00
LPX_KFACTOR_SCALE_W_Corr	0.00
btag_b_0	0.00
btag_b_1	0.00
btag_b_2	0.00
btag_c_0	0.00
btag_c_1	0.00

Systematic	% yield
FakeFactor_WjetsBtag3p	7.33
TTBar_PS	5.97
TTBar_ISR	5.73
FakeFactor_ExtraSysBtag3p	2.44
FakeFactor_WjetsReweight_MuHadBtag3p	2.00
TAUS_TRUEHADTAU_SME_TES_DETECTOR	1.82
TAUS_TRUEHADTAU_SME_TES_INSITU	1.32
TAUS_TRUEHADTAU_SME_TES_MODEL	1.27
TTBar_ME	1.07
LPX_KFACTOR_CHOICE_epWZ16_Corr	0.77
LPX_KFACTOR_CHOICE_HERAPDF20_Corr	0.67
LPX_KFACTOR_PDF_Corr	0.60
JET_JER_EffectiveNP_2_1up	0.50
JET_JER_EffectiveNP_3_1up	0.50
JET_GroupedNP_1	0.43
FakeFactor_LepMuBtag	0.41
LPX_KFACTOR_ALPHAS_Corr	0.40
MET_SoftTrk_ResoPara	0.37
JET_GroupedNP_2	0.36
MET_SoftTrk_ResoPerp	0.28
JET_Flavor_Response	0.24
TTBar_FSR	0.23
JET_JER_EffectiveNP_7restTerm_1up	0.22
MUON_MS	0.19
FakeFactor_QCDReweight_MuHadBtag	0.18
LPX_KFACTOR_CHOICE_NNPDF30_Corr	0.18
JET_JER_DataVsMC_MC16_1up	0.17
LPX_KFACTOR_PDF_epWZ16_Corr	0.16
MUON_SAGITTA_RHO	0.12
MUON_ID	0.12
LPX_KFACTOR_SCALE_Z_Corr	0.12
LPX_KFACTOR_BEAM_ENERGY_Corr	0.11
JET_JER_EffectiveNP_1_1up	0.10
JET_GroupedNP_3	0.10
MUON_SAGITTA_RESBIAS	0.09
MUON_SCALE	0.08
MET_SoftTrk	0.08
JET_JER_EffectiveNP_4_1up	0.08
JET_JER_EffectiveNP_5_1up	0.06
JET_JER_EffectiveNP_6_1up	0.05
LPX_KFACTOR_PI_Corr	0.02
LPX_KFACTOR_PDF_EW_Corr	0.01
EG_SCALE_ALLCORR	0.01
LPX_KFACTOR_REDCHOICE_NNPDF30_Corr	0.01
EG_RESOLUTION_ALL	0.01
EG_SCALE_AF2	0.01
EG_SCALE_ALL	0.01
EG_SCALE_E4SCINTILLATOR	0.01
EG_SCALE_LARCALIB_EXTRA2015PRE	0.01
EG_SCALE_LARTEMPERATURE_EXTRA2015PRE	0.01
EG_SCALE_LARTEMPERATURE_EXTRA2016PRE	0.01
JET_EtaIntercalibration_NonClosure_highE	0.01
JET_TILECORR_Uncertainty	0.01
LPX_KFACTOR_SCALE_W_Corr	0.01
btag_b_0	0.01
btag_b_1	0.01
btag_b_2	0.01
btag_c_0	0.01
btag_c_1	0.01
btag_c_2	0.01

Table B.3.10: Table of systematic uncertainties ranked in order as a percentage yield, in the $e\tau_{\text{had}}$ (left) and $\mu\tau_{\text{had}}$ (right) sub-channels, estimated in the Signal Region, for the b-tag category and for 3-prong tau decays.

Appendix C: ATLAS Phase-2 silicon Inner Tracker upgrade

C.1 Data acquisition testing

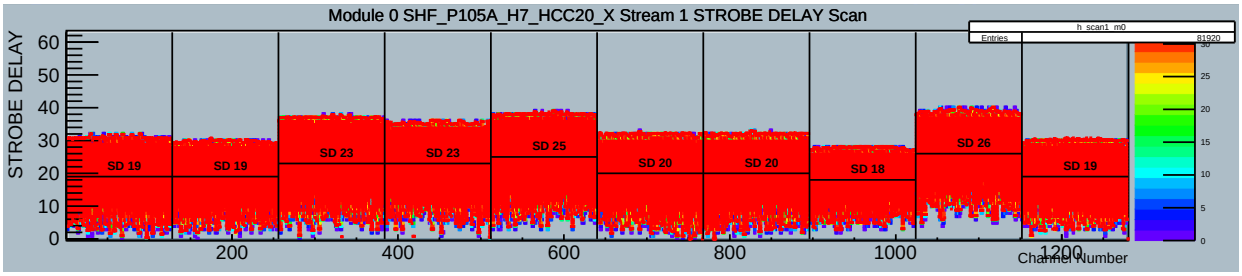

Figure C.1.1: ITSDAQ results representing the Strobe Delay test from the X-type hybrid on an MS SS module labelled *SHF_MS04*, for ABC Stream 1. The registered timing delays for each ABC all appear to be reasonably near the expected 20 µs.

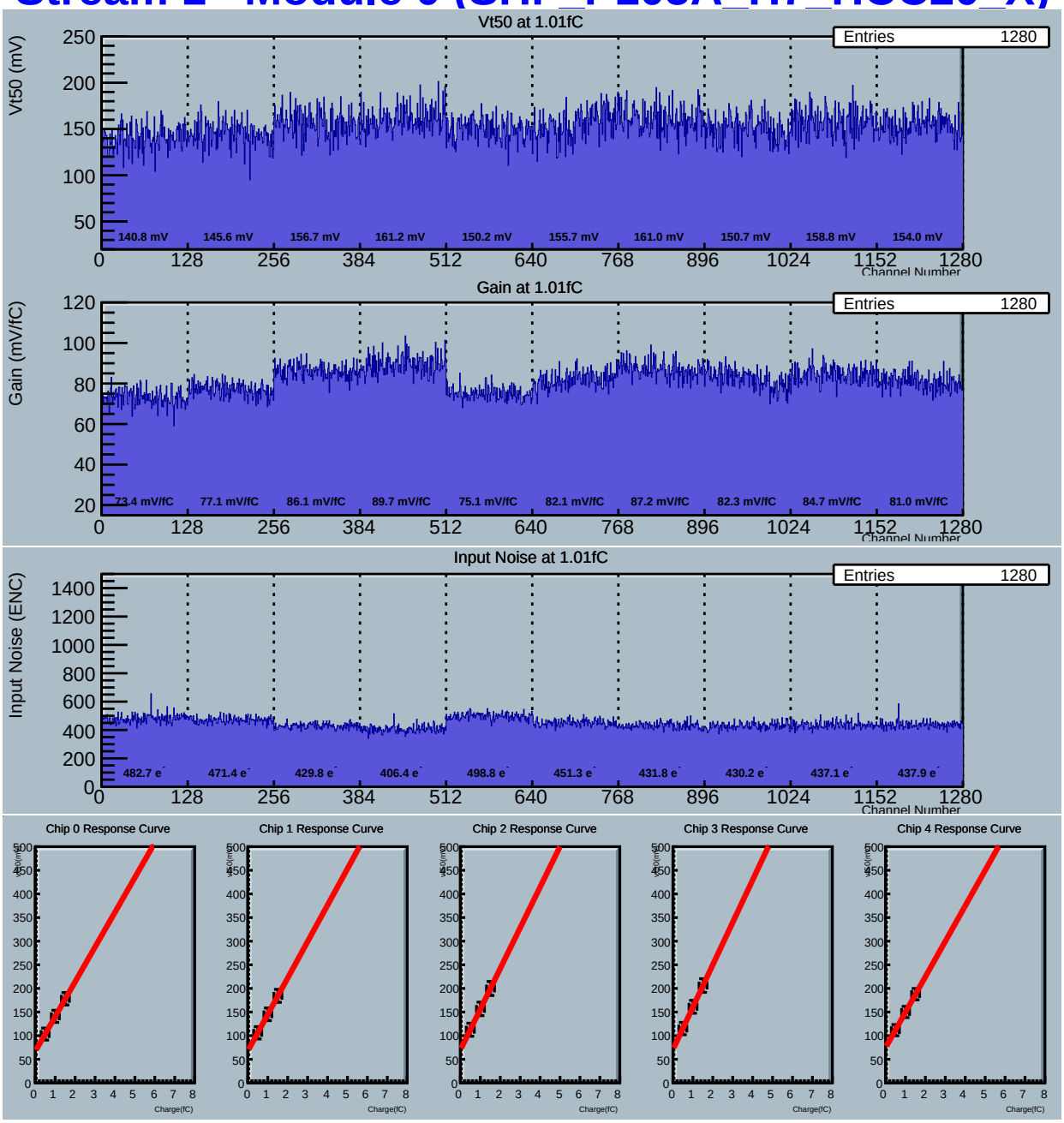

Figure C.1.2: ITSDAQ results representing the Three-Point Gain test from the X-type hybrid on an MS SS module labelled *SHF_MS04*, for ABC Stream 1. The plots show the threshold voltage, the gain, the input noise and the 3-point response curve as linear fit, for each ABC.

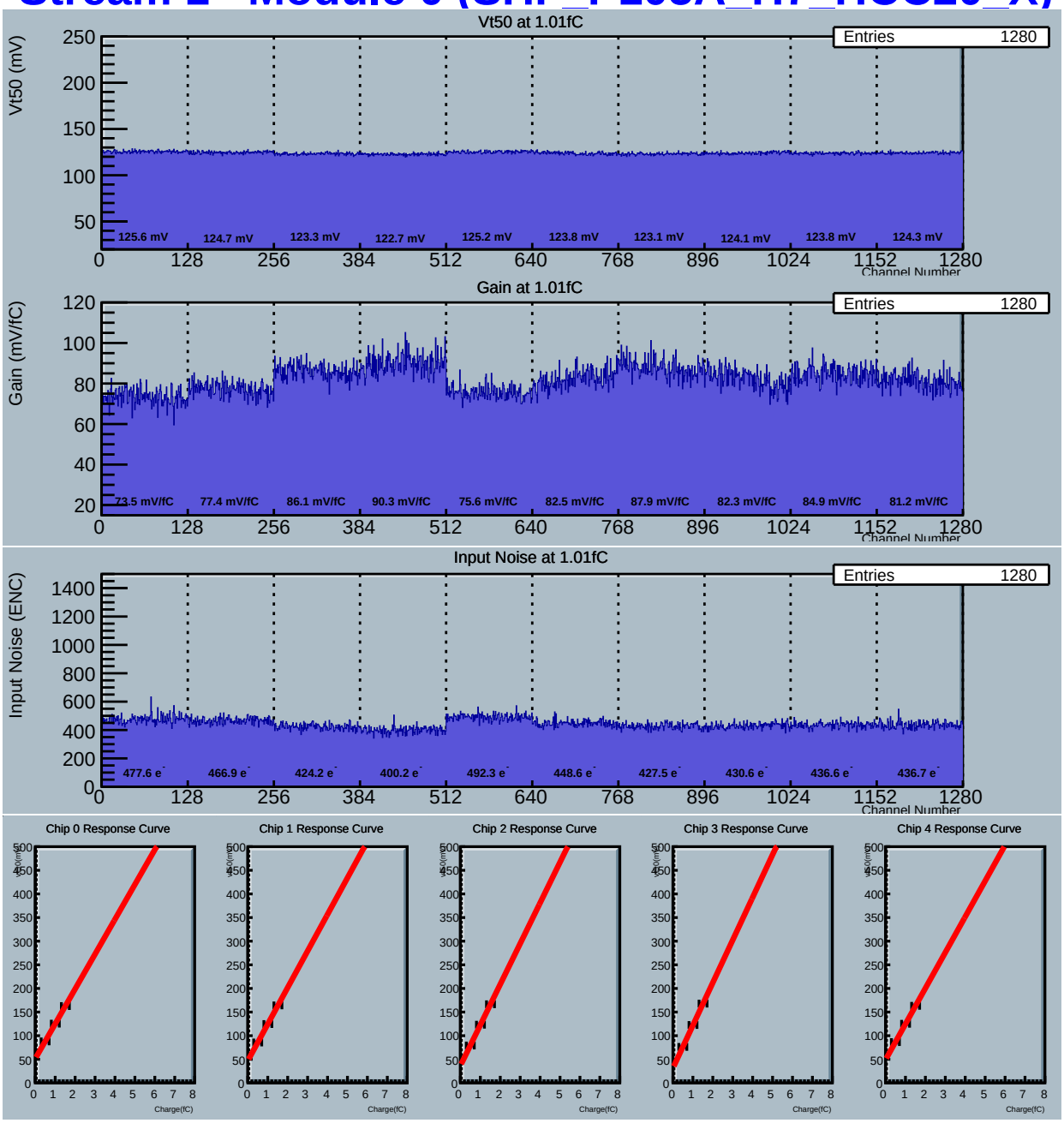

Figure C.1.3: ITSDAQ results representing the Three-Point Gain test, with trims and masks applied, from the X-type hybrid on an MS SS module labelled *SHF_MS04*, for ABC Stream 1. The plots show the threshold voltage, the gain, the input noise and the 3-point response curve as linear fit, for each ABC. The threshold voltage and their uncertainties in the response fit are constrained by the trim.

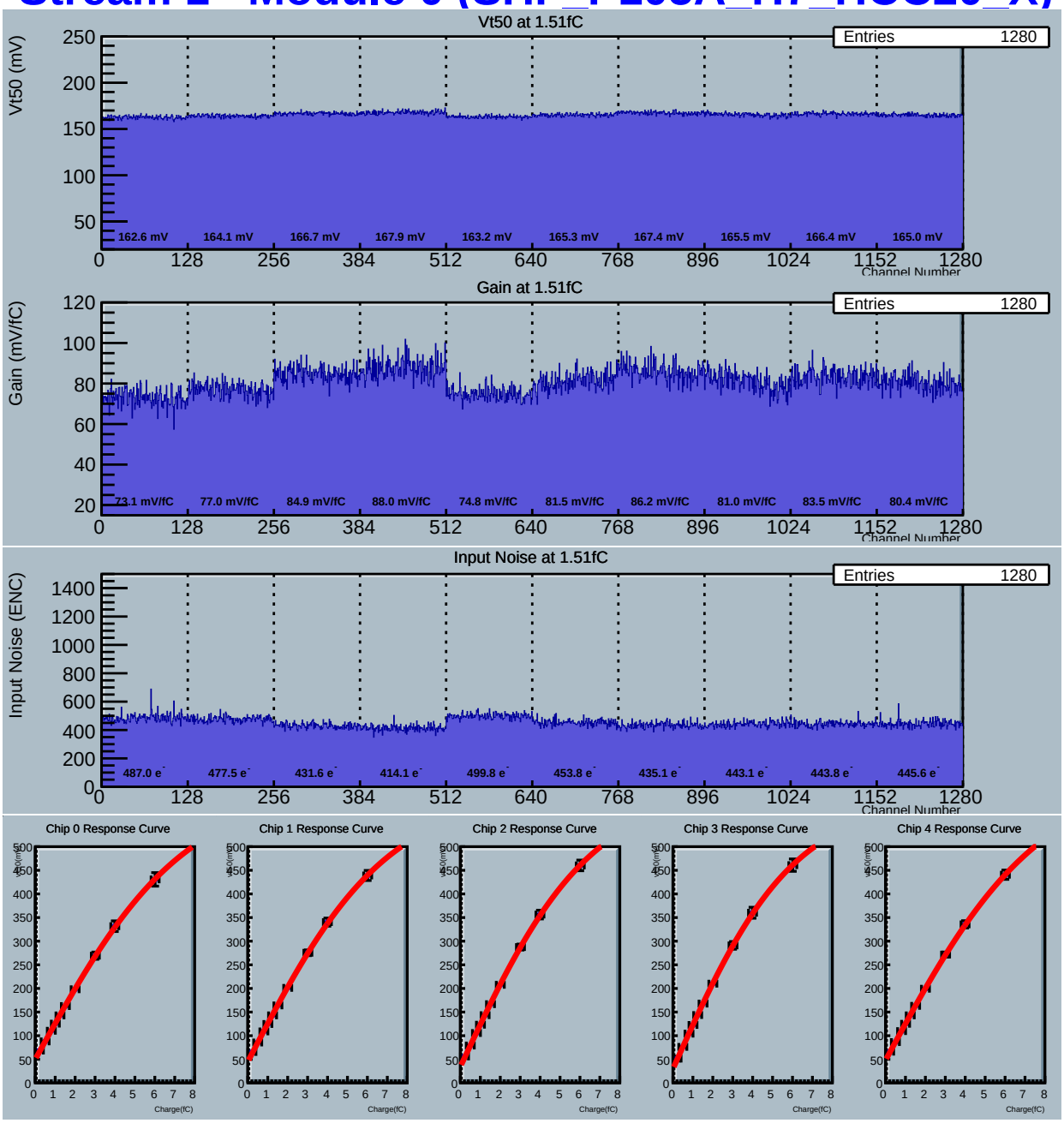

Figure C.1.4: ITSDAQ results representing the Response Curve test from the X-type hybrid on an MS SS module labelled *SHF_MS04*, for ABC Stream 1. The plots show the threshold voltage, the gain, the input noise and the 10-point response curve as exponential fit, for each ABC. As desired, the final input noise is reasonably minimal and the gain is maximal, while both are mostly consistent between ABCs.

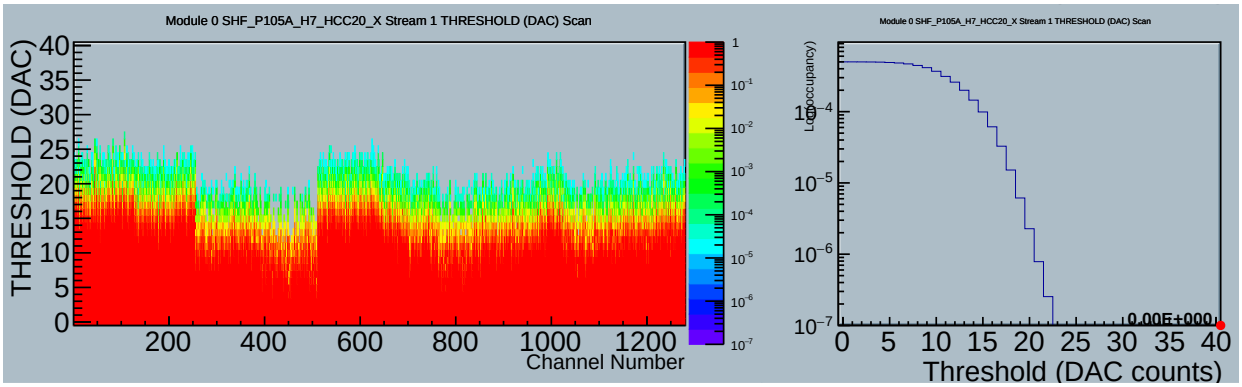

Figure C.1.5: ITSDAQ results representing the Noise Occupancy test from the X-type hybrid on an MS SS module labelled *SHF_MS04*, for ABC Stream 1. The plots show the threshold scan across each channel of the ABCs, and the resulting occupancy as a function of the threshold.

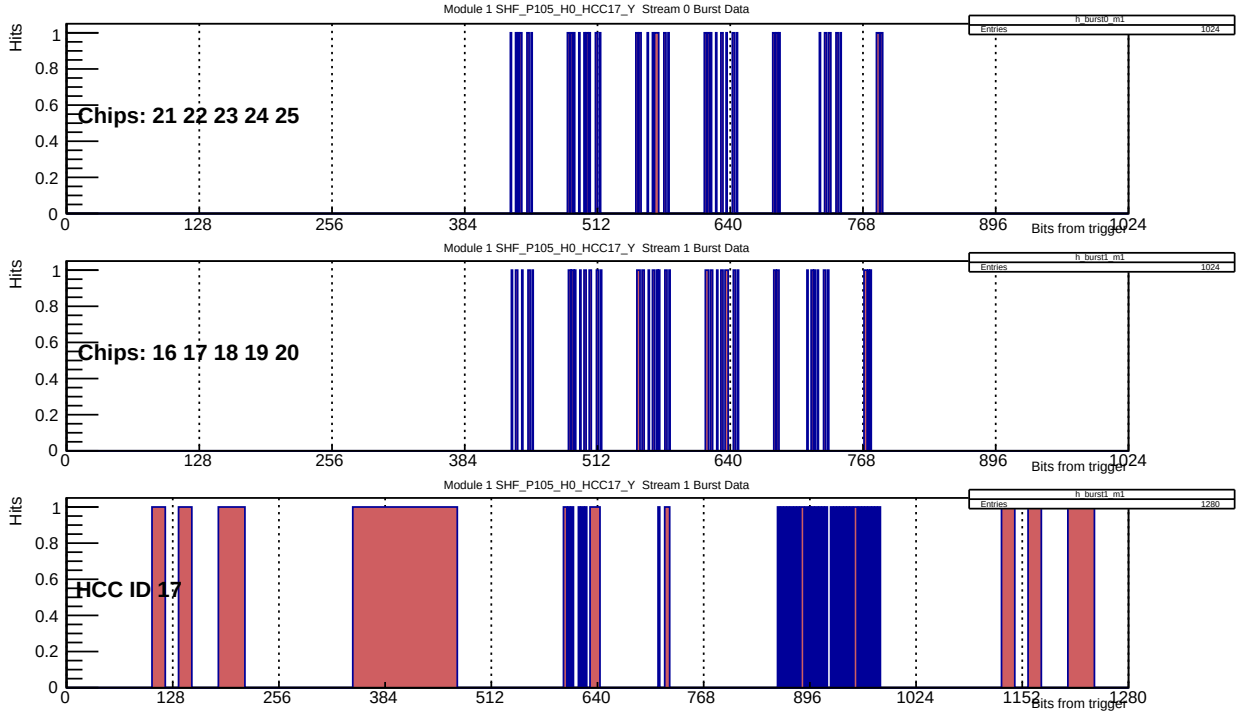

Figure C.1.6: ITSDAQ results representing the ABC and HCC IDs from the Y-type hybrid on an MS SS module labelled *SHF_MS04*, where the ABC IDs are shown for both streams. All expected addresses are correctly being received.

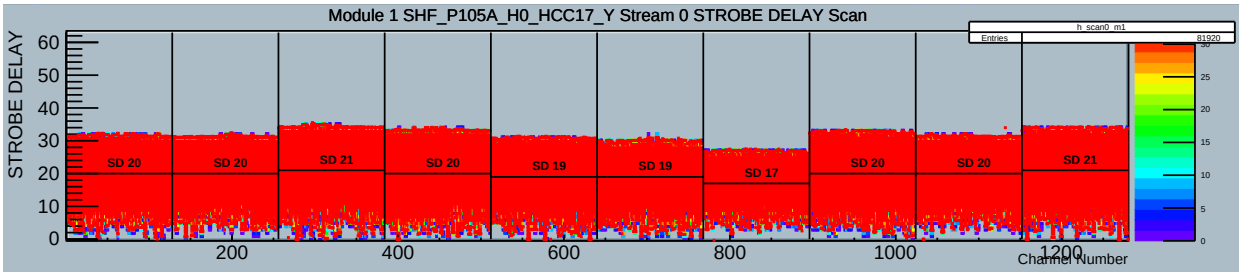

Figure C.1.7: ITSDAQ results representing the Strobe Delay test from the Y-type hybrid on an MS SS module labelled *SHF_MS04*, for ABC Stream 0. The registered timing delays for each ABC all appear to be reasonably near the expected 20 µs.

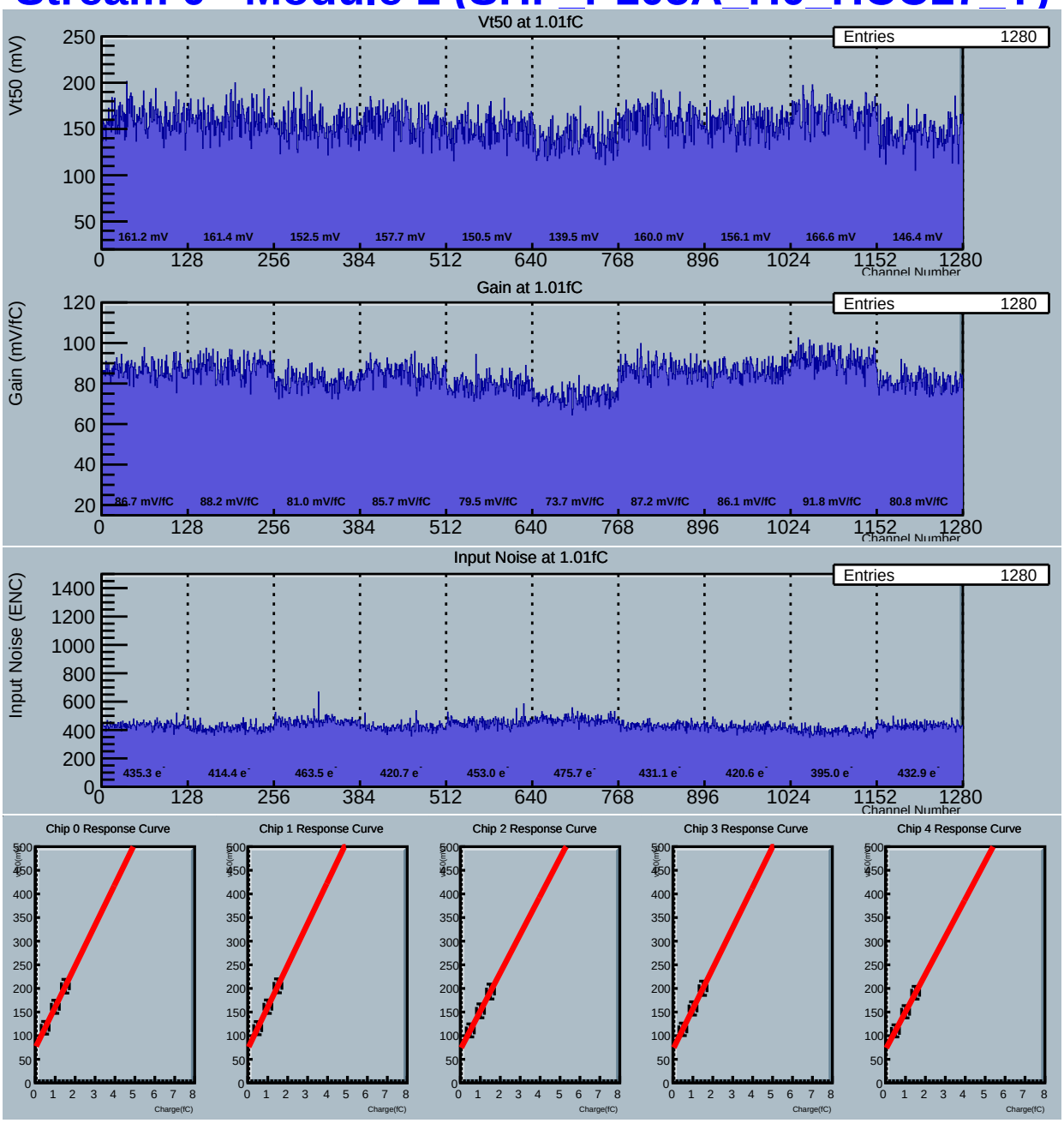

Figure C.1.8: ITSDAQ results representing the Three-Point Gain test from the Y-type hybrid on an MS SS module labelled *SHF_MS04*, for ABC Stream 0. The plots show the threshold voltage, the gain, the input noise and the 3-point response curve as linear fit, for each ABC.

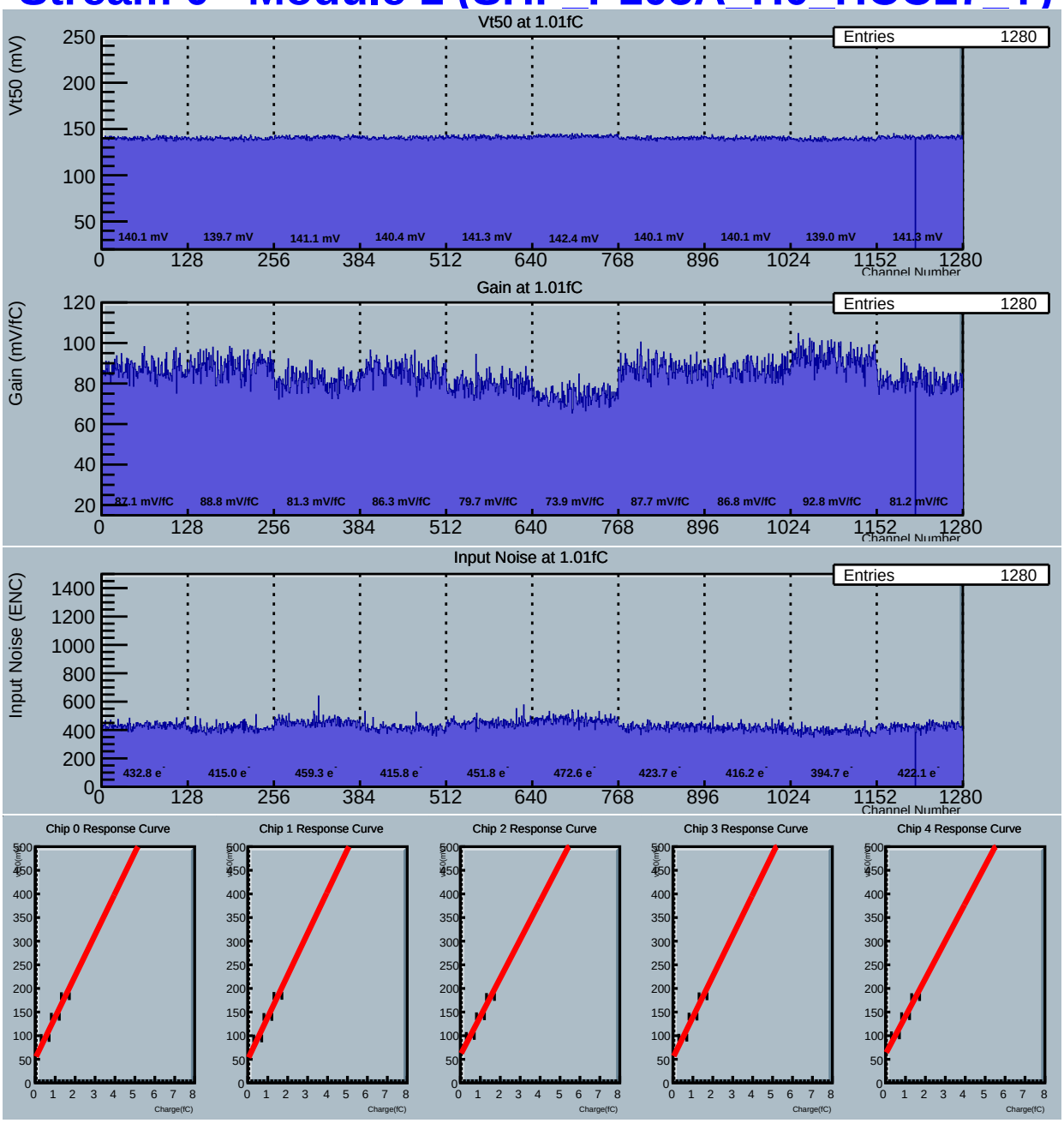

Figure C.1.9: ITSDAQ results representing the Three-Point Gain test, with trims and masks applied, from the Y-type hybrid on an MS SS module labelled *SHF_MS04*, for ABC Stream 0. The plots show the threshold voltage, the gain, the input noise and the 3-point response curve as linear fit, for each ABC. The threshold voltage and their uncertainties in the response fit are constrained by the trim, while 1 channel in the 10th ABC has been masked, which is reasonable.

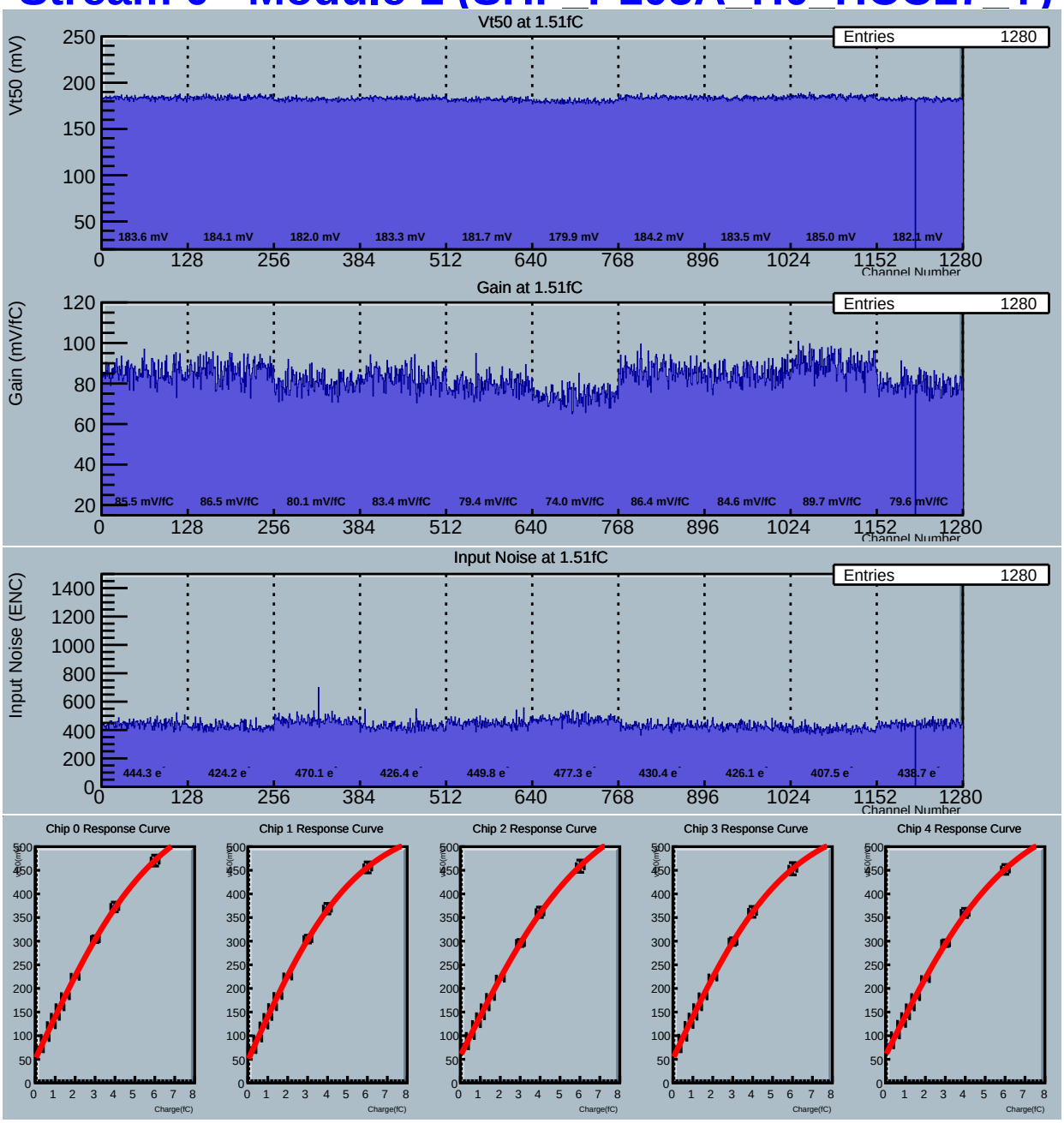

Figure C.1.10: ITSDAQ results representing the Response Curve test from the Y-type hybrid on an MS SS module labelled *SHF_MS04*, for ABC Stream 0. The plots show the threshold voltage, the gain, the input noise and the 10-point response curve as exponential fit, for each ABC. As desired, the final input noise is reasonably minimal and the gain is maximal, while both are mostly consistent between ABCs.

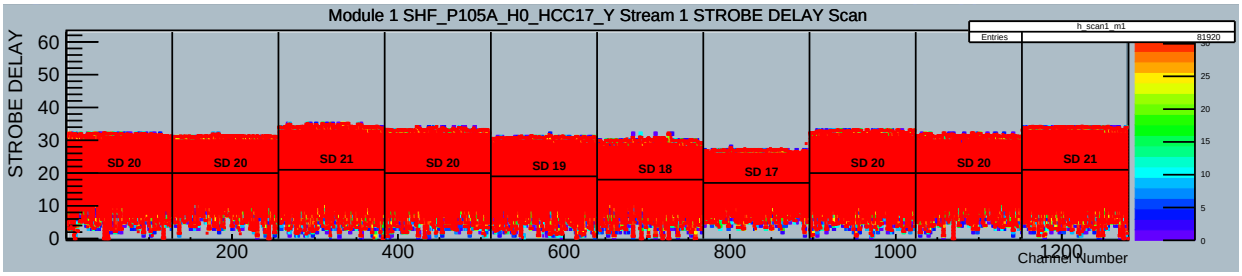

Figure C.1.11: ITSDAQ results representing the Strobe Delay test from the Y-type hybrid on an MS SS module labelled *SHF_MS04*, for ABC Stream 1. The registered timing delays for each ABC all appear to be reasonably near the expected 20 µs.

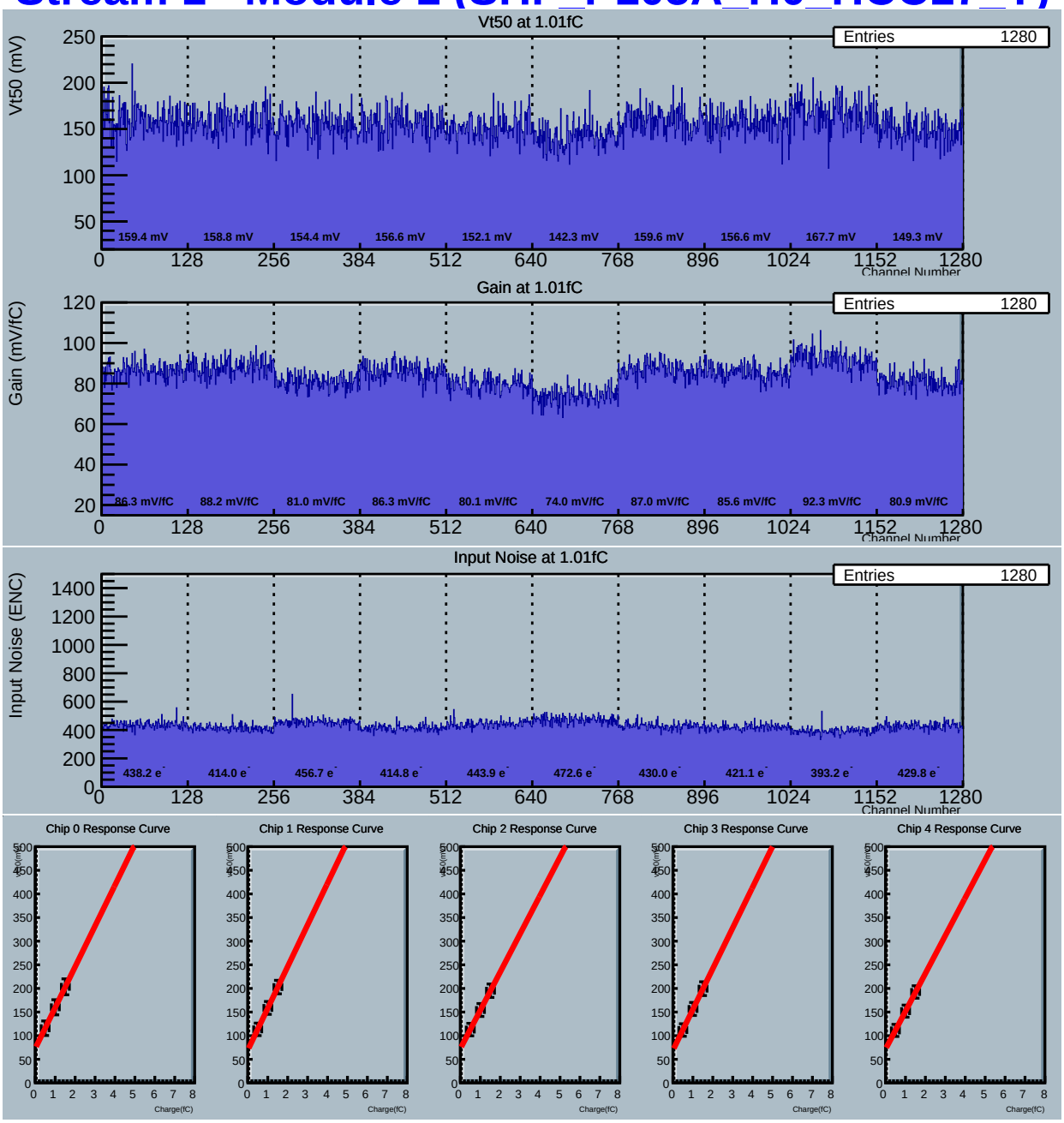

Figure C.1.12: ITSDAQ results representing the Three-Point Gain test from the Y-type hybrid on an MS SS module labelled *SHF_MS04*, for ABC Stream 1. The plots show the threshold voltage, the gain, the input noise and the 3-point response curve as linear fit, for each ABC.

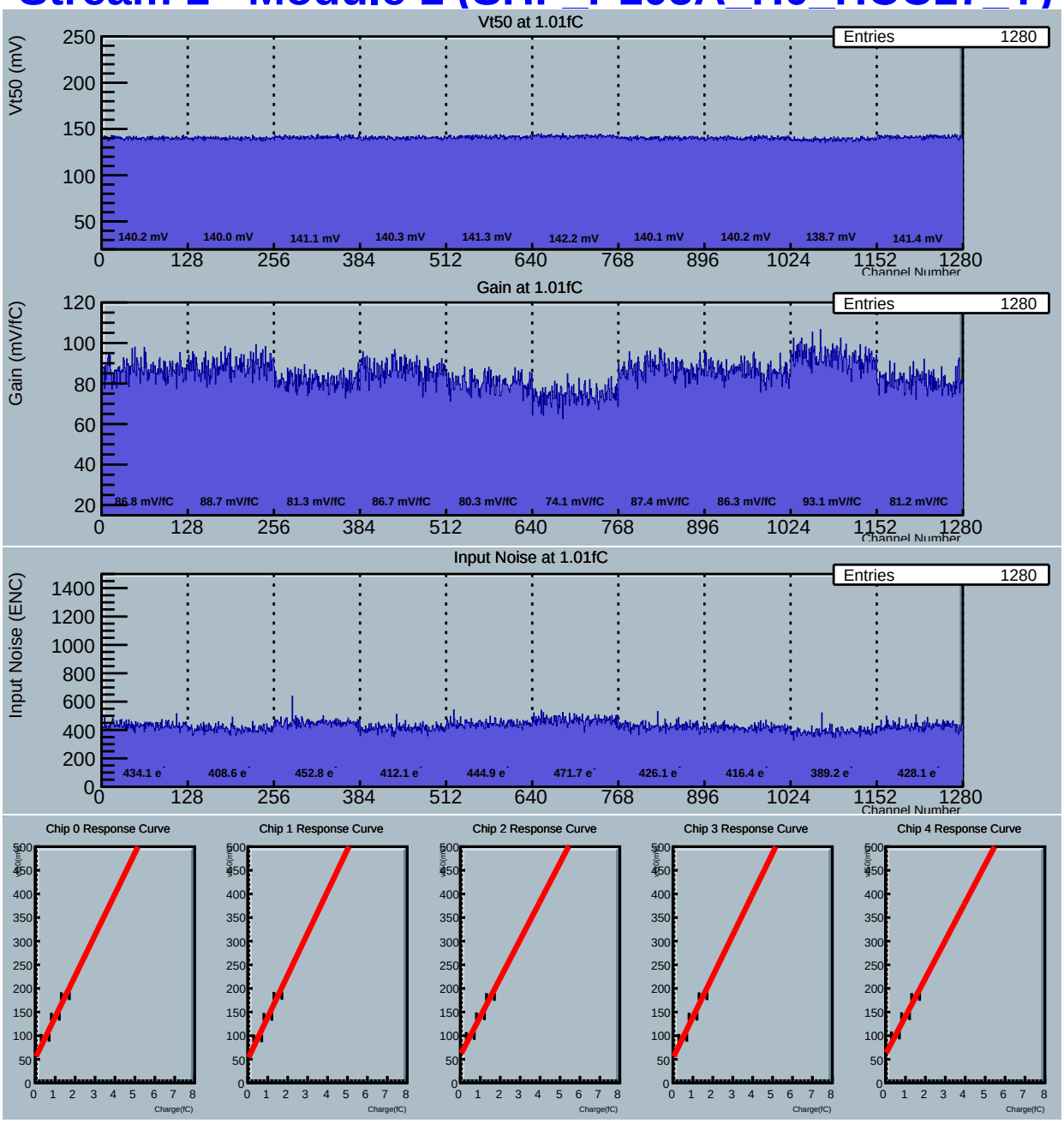

Figure C.1.13: ITSDAQ results representing the Three-Point Gain test, with trims and masks applied, from the Y-type hybrid on an MS SS module labelled *SHF_MS04*, for ABC Stream 1. The plots show the threshold voltage, the gain, the input noise and the 3-point response curve as linear fit, for each ABC. The threshold voltage and their uncertainties in the response fit are constrained by the trim.

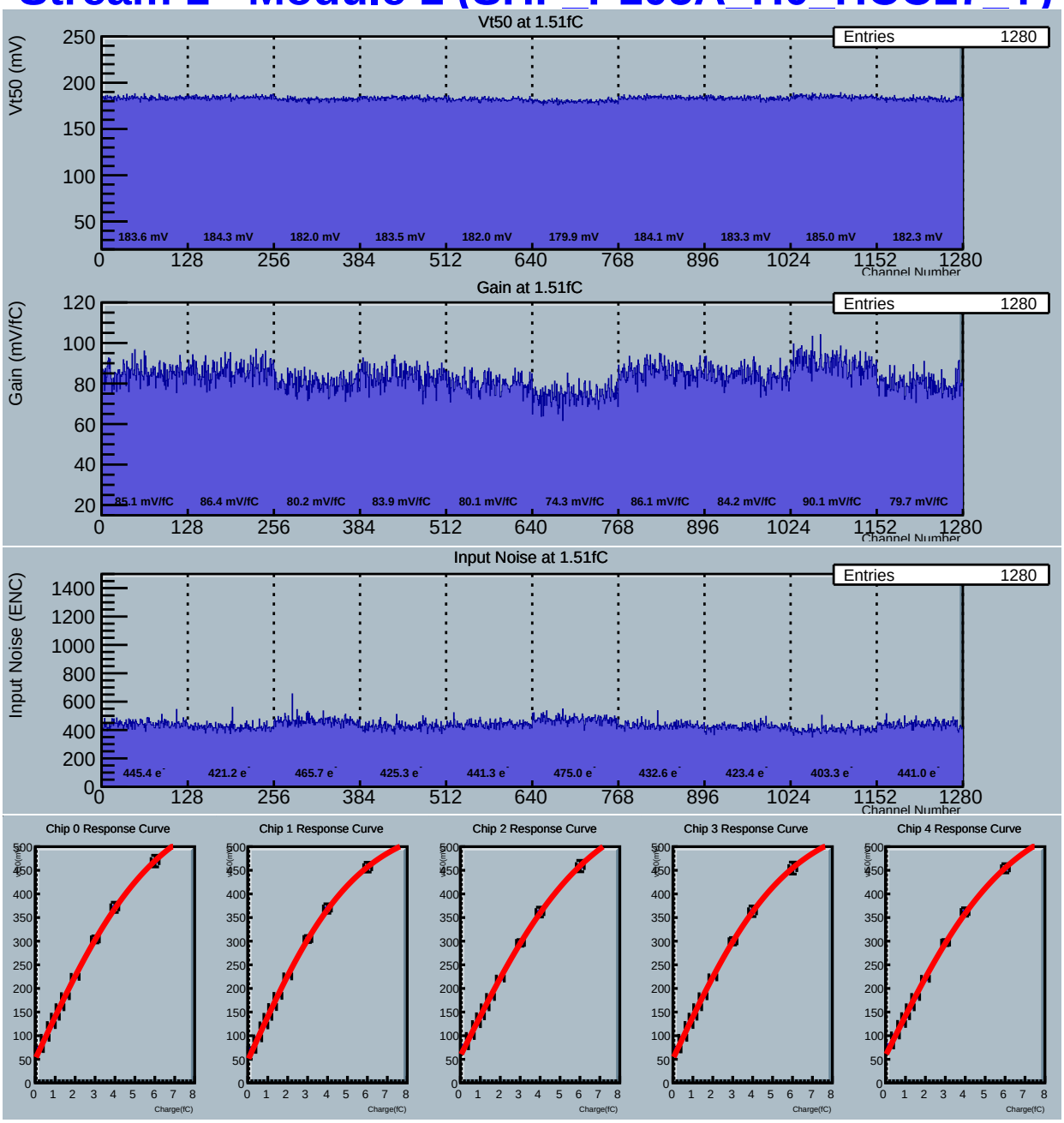

Figure C.1.14: ITSDAQ results representing the Response Curve test from the Y-type hybrid on an MS SS module labelled *SHF_MS04*, for ABC Stream 1. The plots show the threshold voltage, the gain, the input noise and the 10-point response curve as exponential fit, for each ABC. As desired, the final input noise is reasonably minimal and the gain is maximal, while both are mostly consistent between ABCs.